

ZAŠTITA MATERIJALA

Godina LXV

Beograd, 2024.

Broj 2

Editor in Chief

Prof. dr **Časlav Lačnjevac**, University of Belgrade, Faculty of Agriculture, Belgrade, Serbia

Co - editors

Dr **Nebojša Nikolić**, University of Belgrade, Serbia

Dr **Vladimir Panić**, University of Belgrade, Serbia

Prof.dr **Abd El-Aziz S. Fouda**, El-Mansoura University, Egypt

Prof.dr **Branimir Grgur**, University of Belgrade, Serbia

Prof.dr **Susai Rajendran**, Department of Chemistry, Thamarapady, India

Prof. dr **Iveta Vaskova**, Teknikal University of Kosice, Slovakia

Prof.dr.habil. **Marian Jaskula**, Jagiellonian University, Poland

Prof.dr **Leonid Dvorkin**, National University of Water and Environmental Engineering, Ukraine

Dr **Marija Ercegović**, Institute ITMNS, Serbia

Editorial Board

Prof.dr **Benedetto Bozzini**, Italy

Prof.dr **J. G. Gonzalez-Rodriguez**, México

Prof.dr **Heiner Jakob Gores**, Germany

Prof.dr **Tor Henning Hemmingsen**, Norway

Dr **Mirjana Stojanovic**, Serbia

Prof.dr **K. F. Khaled**, Egypt

Prof. dr **Miomir G. Pavlović**, Serbia

Prof. dr **Liudmila Tsygankova**, Russian Federation

Dr **Andrzej Kowal**, Poland

Prof.dr **Dragica Chamovska**, R.N.Macedonia

Prof. dr **Svetlana Kaluzhina**, Russian Federation

Prof.dr **Srdjan Roncevic**, Serbia

Prof.dr **Refik Zejnilović**, Montenegro

Dr **Ronald Latanision**, USA

Prof.dr **Miodrag Maksimović**, Serbia

Prof.dr **Vesna Mišković-Stanković**, Serbia

Dr **Dorothy Rajendran**, India

Prof.dr **Milan Jaić**, Serbia

Prof.dr **Kozeta Vaso**, Albania

Prof.dr **A. S. Sarac**, Turkey

Prof.dr **Vaso Manojlović**, Serbia

Prof.dr **Milorad Tomić**, BiH

Prof.dr **Jelena Bajat**, Serbia

Dr **Aleksandra Daković**, Serbia

Prof. dr **Ladislav Vrsalović**, Croacia

Prof.dr **Darko Vuksanović**, Montenegro

Prof.dr **Deana Wahyuningrum**, Indonesia

Dr **Nebojsa Marinkovic**, USA

Dr **Slavko Bernik**, Slovenia

Prof.dr **Milica Gvozdenovic**, Serbia

Dr **Tsvetina Dobrovoljska**, Bulgaria

Prof.dr **Oguike Raphael Shadai**, Nigeria

Dr **Miroslav Sokic**, Serbia

Prof.dr **Djendji Vaštag**, Serbia

Prof. dr **Maria Joany Rajendran**, India

Prof.dr **Regina Fuchs Godec**, Slovenia

Prof.dr **Aurel Nuro**, Albania

Dr **Muhammed Ernur Akiner**, Turkey

Dr **Branimir Jugovic**, Serbia

Dr **Petar Ljumovic**, Croacia

Prof.dr **Manjeet Singh Goyat**, India

Prof.dr **Aleksandar Kostic**, Serbia

Prof.dr **Borko Matijević**, Serbia

Dr **Miroslav Pavlovic**, Serbia

Prof.dr **Blažo Laličić**, Serbia

Izdavački savet – Publisher board

Dr **Sreco Pavlin**, predsednik, R. Slovenia

Mr **Ivan Burić**, Montenegro

Zoran Ivljanin, Serbia

Gordana Miljević, Serbia

Dr **Ilija Nasev**, R. S. Macedonia

Dr **Zoran Avramović**, Serbia

Momir Ilić, Serbia

Dosadašnji glavni i odgovorni urednici

Prof. dr **Sreten Mladenović** (1967–2001)

Prof.dr **Miodrag Maksimović** (2002 – 2005)

Prof.dr **Milan Antonijević** (2006-2012)

Technical editor: **Slavka Vukašinić**

Za izdavača – For publisher

Prof. dr **Časlav Lačnjevac**, predsednik

Izdavač- Publisher:

INŽENJERSKO DRUŠTVO ZA KOROZIJU, Beograd, Kneza Miloša 9/I,

Tel/fax (011) 3860 - 867 i (011) 3230–028,

E-mail: editor@idk.org.rs; idk@idk.org.rs, www.idk.org.rs, E-mail: caslav.lacnjevac@gmail.com

EVROPSKA FEDERACIJA ZA KOROZIJU (EFC) SMATRA OVAJ ČASOPIS ZVANIČNOM PUBLIKACIJOM ZA OBJAVLJIVANJE IZVEŠTAJA I INFORMACIJA

EUROPEAN FEDERATION OF CORROSION (EFC) CONSIDERES THIS JOURNAL TO BE THE OFFICIAL PUBLICATION FOR PUBLISHING THE REPORTS AND INFORMATION

SADRŽAJ – CONTENT

Alladi. Devi Sravanthi, Ponnuri. Bharath, Peddi. Kiranmayi, Dittakavi. Ramachandran	
Development and validation of RP-HPLC method for quantitative estimation of related substances in gatifloxacin drug substance.....	191
Agha Inya Ndukwe, Chukwuma Daniel Okolo, Benjamin Uchenna Nwadirichi	
Overview of corrosion behavior of ceramic materials in molten salt environments	202
Vijayalakshmi K. Arumugam, Judith Fennila, Thangavel K. Maheswari	
Blend of low cost electrode material for energy storage device under DC glow discharge plasma exposed ESAC.....	213
Naima Hadjadj, Bendaoud Mebarek, Yassine El Guerri, Mourad Keddou	
Dybkov model for the estimation of boron diffusion in the FeB/Fe₂B bilayer on AISI 316 steel.....	220
Aarudi Ranganth Shashikala, Kothakula Keerthi, Sridhar Bangarpet Shankar	
Electrochemical investigations of Ni-P/nano c-BN deposited on aluminum alloy	236
Narendhran Sadhasivam	
Synergistic effect of Fe and Co doped ZnO nanoparticles synthesized using <i>Alpinia galanga</i> against <i>Candida parasilopsis</i>.....	246
Emmanuel Rieborue Khama, Emmanuel Zeneboebi Loyibo, Wilfred Okologume, Stanley Too-chukwu Ekwueme, Chukwudi Victor Okafor, Nnaemeka Princewill Ohia	
Investigation of the performance of activated carbon derived from ripe plantain peels for CO₂ capture: Modelling and optimisation using response surface methodology	258
Svetlana Osadchuk, Lyudmila Nyrkova	
Investigation of properties of epoxy coating on X80 steel under cathodic polarization conditions	273
Natarajan Thiruvani, Ramu Mathammal, Dhanapal Prakash Babu, Sadasivam Ponkumar, Ramasamy Jayavell	
A novel Sr_{0.99}Zr(PO₄)₂:0.01Eu³⁺ ceramic glass viable for long term energy storage applications.....	279
Rajnish Grewal, Sunita Dahiya, Sunil Kumar, Naveen Kumar	
Structural, microstructural, magnetic and dielectric properties of Fe₂O₃ modified CuO composite	285
Ramaiah Prakash, Sundaresan Srividhya, Pitchaipillai Neelamegam, Karuppasamy Mukilan, Rajagopal Premkumar, Muthu Vinod Kumar	
Fresh and hardened characteristics of a novel alkali-activated geopolymer concrete with GGBFS.....	294
Abdel Hafiz A. Ali, Seddik S. Waheed, Salah M. Rabia, Nouby M. Ghazaly	
Assessment of the effect of mixing polystyrene (PS) with sawdust (SD) on copyrolysis products.....	307
Gayathri Thangavel, Kavitha Balakrishnan, Nirmala Murugesan	
NiO/MnO₂ nanocomposite in addition of layered Reduced Graphene Oxide (RGO) electrode for accountable supercapacitor application.....	315
Abd El-Aziz S. Fouda, Ibrahim S. El-Hallag, Ahmed A. El-Barbary, Fatma M. El Salamony	
Electrochemical and theoretical evaluations of 3-(4-chlorophenyl)-7-methyl-5H-[1, 2, 4] triazolo [3,4-b][1,3,4]thiadiazin-6(7H)-one as corrosion inhibitor for copper in nitric acid environment	331
Mukesh Kumar	
Studies of structural and optical properties of sputtered SiC thin films.....	343
Arunprasad Jaychandran, Murugan Ramaiyan, Christian Johnson Singaram, Anukarthika Balakrishnan	
Non-destructive evaluation of subsurface corrosion on hot steel angle sections embedded in concrete and its repair by cement slurry and nitro zinc coating.....	350
Rajasundaravadeivel Jeya Prakash, Balu Soundara, Singaram Christian Johnson	
Serviceability performance of fibre reinforced no fine concrete pavement.....	360
Recenzenti – Reviewers	371
Advertisements – Reklame	379

SUIZDAVAČI
INSTITUT ZA TEHNOLOGJU NUKLEARNIH I DRIGIH MINERALNIH SIROVINA, BEOGRAD
UDRUŽENJE INŽENJERA SRBIJE ZA KOROZIJU I ZAŠTITU MATERIJALA
CRNOGORSKO DRUŠTVO ZA ZAŠTITU MATERIJALA

DONATORI

JP ELEKTROMREŽA SRBIJE, BEOGRAD	TEHNOSAM, SUBOTICA
JKP DRUGI-OKTOBAR, VRŠAC	"PITURA", NOVI BEOGRAD
"NIS - FAM", KRUŠEVAC	UNIPROMET, ČAČAK
GALFOS, BEOGRAD	FAKULTET ZAŠTITE NA RADU, NIŠ
PD DRINSKO LIMSKE ELEKTRANE, BAJINA BAŠTA	INSTITUT ZA VODOPRIVREDU „JAROSLAV ČERNI“, BEOGRAD
INSTITUT ZA PREVENTIVU, NOVI SAD	„GALVA“, KRAGUJEVAC
MAŠINSKI FAKULTET, BEOGRAD	PERIĆ & PERIĆ, POŽAREVAC
TEHNOLOŠKO-METALURŠKI FAKULTET, BEOGRAD	HORIZONT PRES, BEOGRAD
TEHNIČKI FAKULTET, BOR	VISOKA TEHNOLOŠKA ŠKOLA STRUKOVNIH STUDIJA, NOVI BEOGRAD
TEHNOLOŠKI FAKULTET, LESKOVAC	VISOKA STRUKOVNA ŠKOLA, NIŠ
ALFA PLAM ad, VRANJE	VISOKA TEH. SKOLA STRUK. STUDIJA, NOVI SAD
„HELIOS“, DOMŽALE	INSTITUT ZA PUTEVE, BEOGRAD
ŠUMARSKI FAKULTET, BEOGRAD	IMPOL SEVAL, UŽICE
AGRONOMSKI FAKULTET, ČAČAK	ALFATERM, ČAČAK
GRAĐEVINSKO-ARHITEKTONSKI FAKULTET, NIŠ	METALAC A.D., GORNJI MILANOVAC
	SINVOZ DOO, ZRENJANIN

U finansiranju izdavanja časopisa "ZAŠTITA MATERIJALA" učestvuju:



MINISTARSTVO NAUKE, TEHNOLOŠKOG RAZVOJA I INOVACIJA REPUBLIKE SRBIJE



INŽENJERSKA KOMORA SRBIJE

CIP - Katalogizacija u publikaciji
Narodna biblioteka Srbije, Beograd

620.1

ZAŠTITA MATERIJALA = Materials Protection / Glavni urednik (Časlav Lačnjevac),
[Štampano izd.] - God. 1, br. 1 (1953)-god. 22, br. 3/4 (1974) ; god. 23, br. 1 (1982)-. - Beograd: Inženjersko
društvo za koroziju, 1953-1974; 1982- (Zemun : Akademska izdanja). - 29 cm

Dostupno i na: <https://www.zastita-materijala.org> - Tromesečno. - Drugo izdanje na drugom medijumu:
Zaštita materijala (Online) = ISSN 2466-2585
ISSN 0351-9465 = Zaštita materijala
COBISS.SR-ID 4506626

Redakcija: Beograd, Kneza Miloša 9/I, Tel/fax (011) 3860 - 867, i (011) 3230 - 028, E-mail: idx@idx.org.rs;
E-mail: editor@idx.org.rs, www.idx.org.rs; www.zastita-materijala.org/index.php/home/issue

Tekući račun: 205 - 24967 – 71, Komercijalna banka, Beograd; Časopis izlazi četiri puta godišnje
Rukopisi se ne vraćaju; Štampa: Akademska izdanja, Zemun

ISTORIJAT INŽENJERSKOG DRUŠTVA ZA KOROZIJU

Inženjersko društvo za koroziju, koji je pravni naslednik Saveza inženjera i tehničara za zaštitu materijala Srbije i Crne Gore, je društveno stručna organizacija koja je član Saveza inženjera i tehničara Srbije. Savez inženjera i tehničara za zaštitu materijala Jugoslavije, kako se prvobitno zvalo Inženjersko društvo za koroziju, početke svog delovanja je imao još 1952. godine preko Komisije za zaštitu od korozije. Ova komisija je postojala u okviru Društva hemičara i tehnologa DIT-a, mada se neki koreni iz zaštite od korozije pominju i pre drugog svetskog rata. Inicijatori za oformljenje ove Komisije bili su dr.inž Frano Podbrežnik, prof.dr Blažon, prof.dr Milan Pajević i Sveta Živanović. Komisija je imala 15 aktivnih članova i radila je u tri potkomisije.

Januara 1953. godine ova Komisija prerasta u Centar za zaštitu od korozije sa osnovnim zadatkom da radi na antikorozijskoj zaštiti svih materijala, uređaja, opreme i instalacija. Već u prvoj godini postojanja ovaj Centar je obrazovao svoju servisnu radionicu za fosfatiranje i pristupio izdavanju svojih stručnih publikacija.

Dalji rad Centra, do svog prerastanja u Društvo a kasnije u Savez, odvijao se u komisijama i servisnim radionicama preko kojih se intenzivno radilo na održavanju raznih kurseva i predavanja iz oblasti korozije materijala i zaštite od nje a, takođe, i na izradi projekata za korozionu zaštitu raznih objekata i opreme za mnoga preduzeća.

PREDSEDNIŠTVO IDK: Predsednik IDK prof.dr Časlav Lačnjevac Potpredsednik IDK Zoran Ivljanin, dipl.inž.tehn. Članovi Upravnog odbora – Srećko Stefanović, dipl.inž.tehn. – Dragan Petrović, dipl.elek.inž. – Momir Đurović, dipl.inž.tehn. Članovi Nadzornog odbora – Ljupče Milosavljević, dipl.inž.tehn. – Miodrag Jovanović, dipl.građ.inž. – Mirko Bačilović, dipl.ecc. Tehnički sekretar IDK – Srbislav Nešić, dipl.maš.inž.

Delatnost strukovnih udruženja (udruživanje u okviru profesije i tehničkih oblasti, uključujući i udruženja specijalista angažovanih u naučnoj delatnosti); – Obrazovanje odraslih (obrazovanje na seminarima, naučno-stručnim skupovima, specijalističkim kursovima i sl.); – Istraživanje procesa korozije i zaštite od korozije; – Izrada tehničke dokumentacije, ekspertiza i vršenje nadzora iz oblasti hidroizolacije, antikorozijske zaštite i protivpožarne zaštite.

Inženjersko društvo za koroziju Republike Srbije je izdavač časopisa Zaštita materijala, počlo je sa radom daleke 1953. godine, kao deo Centra za zaštitu od korozije u okviru Saveza inženjera i tehničara za zaštitu materijala Jugoslavije. Iste godine, Društvo je pokrenulo časopis Zaštita materijala, koji i danas aktivno izlazi. Pridružite se bezbrojnim čitaocima koji su imali koristi od njegovog zanimljivog naučnog sadržaja.



Otvaranje naučnog skupa

Zaštita materijala je recenzirani časopis koji sadrži radove o originalnom eksperimentalnom ili teorijskom istraživanju i značajno unapređuju razumevanje u oblastima korozije i zaštite materijala, zaštite životne sredine, ekološkog inženjerstva i tehnologija, inženjerstva materijala (keramika, polimeri, kompoziti; biomaterijali, materijali za skladištenje i konverziju energije, itd.); nanomaterijala i nanotehnologija; hemijskog i biohemijskog inženjerstva, primenjene hemije, upravljanja tehnologijom, i obrazovanja o održivom razvoju. Časopis prihvata radove koji prikazuju eksperimentalne i teorijske naučne i inženjerske rezultate na osnovu dostavljenih podataka.

Naučni radovi za ZM moraju biti dostavljeni na **engleskom jeziku** i treba da sadrže rezime na **engleskom i srpskom jeziku**. Za autore van srpskog govornog područja, izdavač će obezbediti rezimee i naslove tabela i slika na srpskom jeziku. Časopis izlazi 4 puta godišnje.

Časopis je indeksiran u Scopus, DOAJ, International Scientific Indexing (ISI), Journalspedia (JPSA), Sherpa Romeo itd.

Digitalne kopije časopisa su arhivirane u repozitorijumu.

Alladi. Devi Sravanthi¹, Ponnuri. Bharath², Peddi. Kiranmayi*¹, Dittakavi. Ramachandran²

¹Acharya Nagarjuna University, Department of Biochemistry, Nagarjuna Nagar, Guntur. Andhra Pradesh, India, ²Acharya Nagarjuna University, Department of Chemistry, Nagarjuna Nagar, Guntur. Andhra Pradesh, India.

Scientific paper

ISSN 0351-9465, E-ISSN 2466-2585

<https://doi.org/10.62638/ZasMat1148>



Zastita Materijala 65 (2)
191 - 201 (2024)

Development and validation of RP-HPLC method for quantitative estimation of related substances in gatifloxacin drug substance

ABSTRACT

The analysis of improved RP-HPLC method for the separation and quantification of Gatifloxacin and its impurities are described. Samples are analysed by means of reverse phase (RP-HPLC) using an Zorbax Eclipse C18, 50 x 4.6 mm 5 μ m and the mobile phase consists of two Channels A and B. Channel-A: 0.1% Trifluoroacetic acid buffer and Channel-B: Acetonitrile. The flow rate is 1.0 ml/min. The column temperature was maintained at 35°C and sample temperature was maintained at 25°C, injection volume 10 μ l and wavelength fixed at 220nm UV-detection. The developed LC method was validated with respect to specificity, precision, linearity, ruggedness and robustness. Validation study compared as per ICH guideline.

Keywords: Gatifloxacin, determination of related substances, liquid chromatography

1. INTRODUCTION

Gatifloxacin, 1-cyclopropyl-6-fluoro-8-methoxy-7-(3-methylpiperazin-1-yl)-4-oxoquinoline-3-carboxylic acid, is a fourth-generation antibiotic of the fluoroquinolone family which inhibits the bacterial enzymes DNA gyrase and topoisomerase IV [1]. The fluoroquinolones are quinolones with fluorine at position 6 of the naphthyridine ring [2]. Published structure–activity data show that the fluorine atom helps broadens their range of activity against both

Gram-negative and Gram-positive pathogens [3,4]. A simple reversed-phase high-performance liquid chromatographic (LC) method for assessment of the stability of Gatifloxacin in human plasma has been developed and validated [5]. A europium-sensitized fluorescence spectrophotometric method using an anionic surfactant, sodium dodecyl benzene sulphonate (SDBS), has also been developed for analysis of Gatifloxacin [6]. Papers have been published describing methods for analysis of Gatifloxacin in combination with ornidazole in tablet dosage forms [7].

Most of the methods reported involve troublesome mobile phases (buffers) and difficult detection methods (fluorescence). There are no published reports of methods for analysis of Gatifloxacin in bulk samples in the presence of degradation products and process-related impurities.

The objectives of the research work reported in this paper were to develop a suitable stability-indicating LC method for analysis of Gatifloxacin and to validate the method for specificity, LOD, LOQ, linearity, precision, accuracy, and robustness to show the stability-indicating power of the method and to ensure compliance with ICH Guidelines [8-12]. The molecule structure is shown in Figure: 1

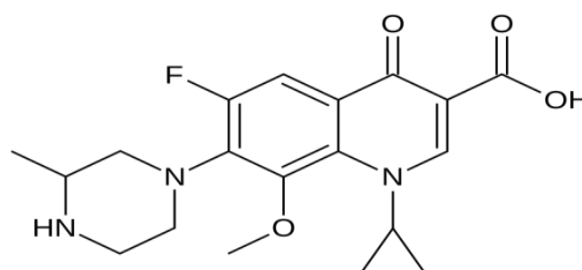


Figure: 1 Chemical structure of Gatifloxacin

Slika 1. Hemijska struktura Gatifloxacin-a

Impurity profiling of active pharmaceutical ingredients (API) in both bulk material and

*Corresponding author: Peddi Kiranmayi

E-mail: dittakavirc@gmail.com

Paper received: 08. 06. 2022.

Paper accepted: 16. 07. 2022.

Paper is available on the website: www.idk.org.rs/journal

formulations is one of the most challenging tasks. The presence of unwanted or in certain cases unknown chemicals, even in small amounts, may influence not only the therapeutic efficacy but also the safety of the pharmaceutical products. For these reasons, all major international pharmacopoeias have established maximum allowed limits for related compounds for both bulk and formulated APIs. As per the requirements of various regulatory authorities, the impurity profile study of drug substances and drug products has to be carried out using a suitable analytical method in the final product.

2. EXPERIMENTAL

2.1. Reagents and chemicals

Trifluoroacetic acid and Acetonitrile was procured from Merck. Water (Milli-Q). All chemicals were of an analytical grade and used as received.

Instrumentation

Chromatographic separation was achieved by using an Waters e2695, Empower³ software using, Zorbax Eclipse C18, 50 x 4.6 mm, 5 μ m and the mobile phase consists of two Channels A and B. Channel-A: 0.1% Trifluoroacetic acid buffer and Channel-B: Acetonitrile. The flow rate is 1.0 ml/min. The column temperature was maintained at 35°C and sample temperature was maintained at 25°C, injection volume 10 μ L and wavelength fixed at 220nm UV-detection. Retention times of impurities were 10.687 for impurity-A, 8.454 for Impurity-B, 13.018 for Impurity-C, 4.286 for impurity-D, 11.128 for impurity-E and 5.344 for Gatifloxacin.

Preparation of solutions:

Preparation of mobile phase-A:

Transferred 1.0 mL of Trifluoroacetic acid into 1000mL of milli-Q water and mixed well and sonicated to degas.

Preparation of mobile phase-B:

100% acetonitrile.

Preparation of diluent:

Prepared a mixture of 500mL of water and 500 mL of acetonitrile in the ratio of 50:50 (%v/v), filtered through 0.45 μ m membrane filter and sonicated to degas.

Preparation of standard solution:

Weigh accurately 35.00 mg of Gatifloxacin working standard in to a 100 mL volumetric flask, to it added 50 mL of diluent sonicate to dissolved and diluted to volume with diluent and mixed well. Further transferred 1.0mL of this solution into a 100

mL volumetric flask, diluted to volume with diluent and mixed well. Further transferred 1.0 mL of this solution into a 10mL volumetric flask, diluted to volume with diluent and mixed well.

Preparation of test solution:

Weighed accurately and transferred about 35 mg of test sample into a 100 mL volumetric flask, containing 50 mL of diluent sonicated it to dissolved and made up to the volume with diluent.

3. METHOD DEVELOPMENT

3.1. Method optimization parameters

An understanding of the nature of API (functionality, acidity, or basicity), the synthetic process, related impurities, the possible degradation pathways and their degradation products are needed for successful method development in reverse-phase HPLC. In addition, successful method development should result a robust, simple and time efficient method that is capable of being utilized in manufacturing setting.

3.2. Selection of wavelength

The sensitivity of the HPLC method depends upon the selection of detection wavelength. An ideal wavelength is one that gives good response for related substances and the drugs to be detected. The wavelength for measurement was selected as 220 nm from the absorption spectrum.

3.3. Selection of stationary phase

Proper selection of the stationary phase depends up on the nature of the sample and chemical profile. The drug selected for the present study was polar compound and could be separated either by normal phase chromatography or reverse phase chromatography. From literature survey, it was found that different C18 columns could be appropriately used for the separation of related substances for Gatifloxacin.

Poor peak shape and resolution was observed when Inertsil ODS-3V (50mm x 4.6mm, 5 μ) There was no proper resolution of impurities and analyte peak and efficiency of the peak is also not achieved and peak interferences are present. In second attempt made using Zorbax Eclipse C18, 50 x 4.6 mm, 5 μ m, and gradient mobile phase programmed of Mobile Phase. The resolution of both drug and impurities was achieved.

3.4. Selection of mobile phase

Different mobile phase and stationary phases were employed to develop a suitable LC method for the quantitative determination of impurities in

Gatifloxacin. A number of column chemistries supplied by different manufacturers and different mobile phase composition were tried to get good peak shapes and selectivity for the impurities present in Gatifloxacin.

Poor peak shape and resolution was observed mobile phase programmed of Mobile Phase: A phosphate buffer and Mobile Phase: B Acetonitrile. There was no proper resolution of impurities and analyte peak and efficiency of the peak is also not achieved and peak interferences are present. In second attempt made using mobile phase programmed of Mobile Phase: A 0.1% TFA buffer and Mobile Phase: B Acetonitrile. The resolution of both drug and impurities was achieved. These chromatographic conditions were selected for validation studies.

4. METHOD VALIDATION

4.1. Specificity

Blank interference

Specificity was demonstrated by injected blank solution, standard solution, sample solution, spiked sample and individual impurities and analyzed as per the test method.

Table 1 and Figures 2 to 4 illustrates that the specificity the chromatograms were recorded for blank, sample and spiked sample solutions of Gatifloxacin and its related substances. specificity studies reveal that the peaks are well separated from each other. Therefore the method is selective for the determination of related substances in Gatifloxacin. It was observed that known impurities are not co eluting with each other and main analyte peak. There is no interference of diluent at Gatifloxacin and impurities peaks.

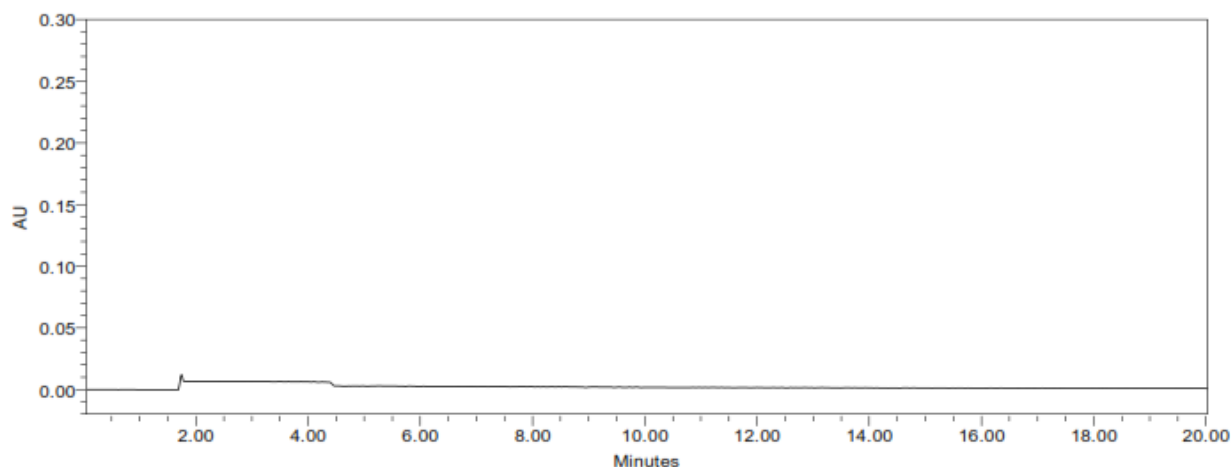


Figure 2. Typical chromatogram of Blank

Slika 2. Tipični hromatogram za prazno

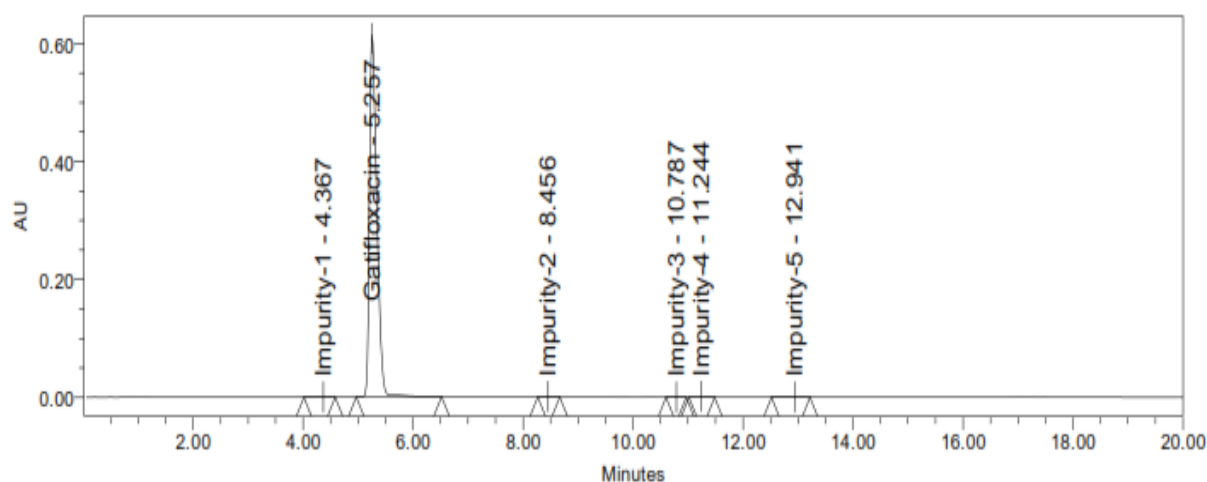


Figure 3. Typical chromatogram as such Sample

Slika 3. Tipičan hromatogram za uzorak

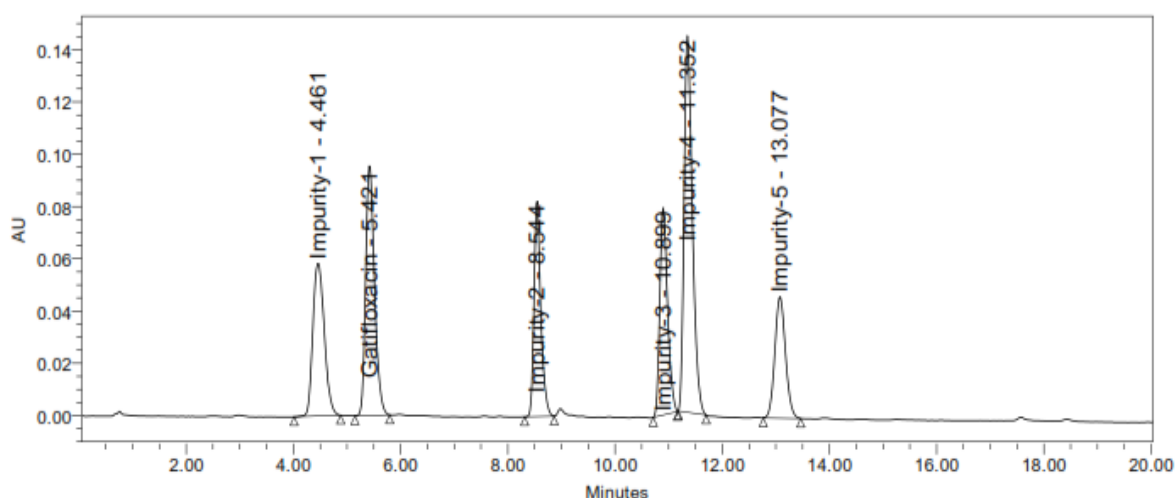


Figure 4. Typical chromatogram Spiked Sample

Slika 4. Tipični hromatogramski šiljasti dijagram za uzorak

Table 1. Impurity interference data (Specificity results)

Tabela 1. Podaci o interferenciji nečistoća (rezultati specifičnosti)

Peak Name	Retention Time	Blank	Placebo
Blank	ND	NA	NA
Impurity-1	4.461	No	No
Impurity-2	8.544	No	No
Impurity-3	10.899	No	No
Impurity-4	11.352	No	No
Impurity-5	13.077	No	No
Gatifloxacin	5.421	No	No

Force degradation

Forced degradation studies were performed to identify potential degradation products that might be formed in Gatifloxacin to elucidate the mechanisms of formation. From those studies it can be seen that there is a significant degradation in solution which exposed to acid, base and water, no significant change was observed. A mild degradation was observed under peroxide conditions. The observations are tabulated below Table 2.

Table 2. Force Degradation results of Gatifloxacin

Tabela 2. Rezultati razgradnje sile gatifloksacina

Name of the Sample	Stress condition	Results in %				
		Imp-01	Imp-02	Imp-03	Imp-04	Imp-05
Control sample	N/A	ND	ND	ND	0.08	0.18
Thermal sample	At 60°C for 2hrs	ND	ND	ND	0.06	0.14
UV exposure sample	2hrs	ND	ND	ND	0.06	0.16
Water hydrolysis sample	Heated at 60°C in H ₂ O for 2Hrs	ND	ND	ND	0.07	0.17
Acid hydrolysis sample	Heated at 60°C in 1.0NHCl for 2Hrs	ND	ND	ND	0.07	0.14
Base hydrolysis sample	Heated at 60°C in 1.0NNaOH for 2Hrs	ND	ND	ND	0.08	0.18
Oxidation sample	Heated at 60°C in 10% H ₂ O ₂ for 2Hrs	ND	ND	ND	0.38	1.56

The degradation studies indicate that the compound is stable upon exposed to thermal and UV exposed condition. It is concluded from the above observations; the present method is capable

to separate all the process and degradation impurities. Therefore the Related compounds by HPLC method is stability indicative.

4.2. Precision

4.2.1. System Precision

Prepared Gatifloxacin(0.1%) and its impurities standard solution (0.15%) and injected six replicates and calculated the %RSD for the peak areas of Gatifloxacin and its impurities. Table 3 and Figure 5 illustrates that the system precision of the method.

Table 3. System Precision data for Gatifloxacin

Tabela 3. Podaci o preciznosti sistema za gatifloksacin

Compound names	Average area	%RSD
Impurity-1	6397	1.4
Impurity-2	11307	0.8
Impurity-3	7332	0.8
Impurity-4	15539	0.4
Impurity-5	10052	0.3
Gatifloxacin	10597	1.3

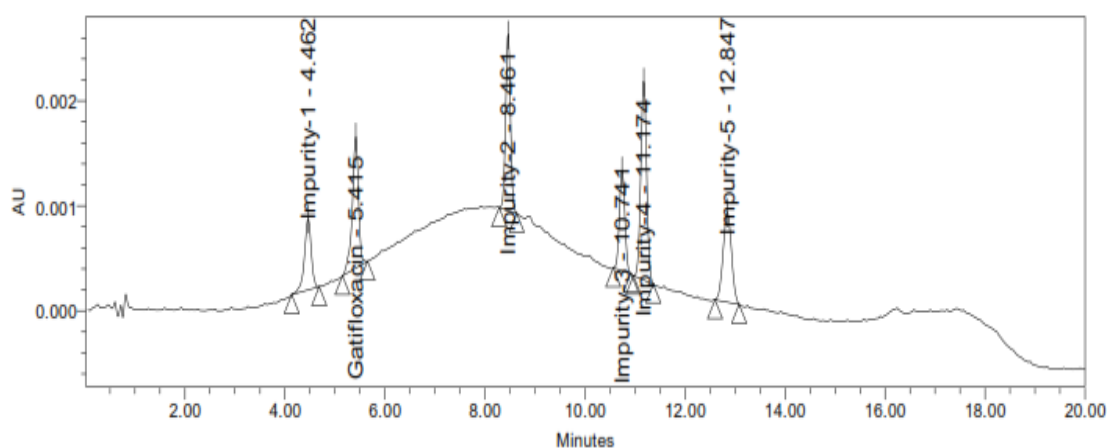


Figure 5. Typical chromatogram standard solution

Slika 5 Tipični hromatogram za standardni rastvor

The % RSD of peak area for Gatifloxacin and its impurities peak from the standard solution observed between 0.3%-1.4% which is below 5.0% indicates that the system gives precise result.

4.2.2. Method Precision

Method precision was demonstrated by prepared six samples by spiking of impurities at specification level and analyzed as per the method (Table 4).

Table 4. Results of method precision

Tabela 4. Rezultati preciznosti metode

S.No.	Sample Details	Impurity (%)				
		Imp-1	Imp-2	Imp-3	Imp-4	Imp-5
1	Prep-1	0.145	0.152	0.157	0.152	0.155
2	Prep-2	0.145	0.152	0.157	0.152	0.152
3	Prep-3	0.145	0.152	0.157	0.152	0.154
4	Prep-4	0.143	0.152	0.156	0.152	0.151
5	Prep-5	0.140	0.151	0.155	0.151	0.158
6	Prep-6	0.143	0.152	0.157	0.152	0.157
Avg.		0.144	0.152	0.157	0.152	0.155
Std. Dev.		0.002	0.000	0.001	0.000	0.003
%RSD		1.38	0.27	0.53	0.27	1.77

Table 4 illustrates that the method precision was demonstrated by prepared six samples by spiking of impurities at specification level and

analyzed as per the method. The results six samples were well within the limits. From the above results, it is concluded that method is precise.

4.3. Limit of detection (LOD) & Limit of Quantitation (LOQ)

Limit of detection: The worst found signal to noise ratio for each peak was greater than 3 in each injection. All the peaks were detected in all the three injections.

Limit of Quantitation: The worst found signal to noise ratio for each peak was greater than 10 in each injection. All the peaks were detected in all the six injections.

Table 5 and Figures 6 to 7 illustrates that the LOD and LOQ of the chromatograms were recorded. The limit of quantitation and limit of detection values obtained for each impurity and Gatifloxacin are within the acceptance criteria.

Table 5. LOD&LOQ concentrations and S/N values for Gatifloxacin and impurities

Tabela 5 LOD&LOQ koncentracije i S/N vrednosti za gatifloksacin i nečistoće

Name of the Impurity	Concentration in ppm		Signal to noise ratio value	
	LOD	LOQ	LOD	LOQ
Impurity-1	0.004	0.010	3.01	9.31
Impurity-2	0.004	0.011	4.87	9.26
Impurity-3	0.004	0.014	3.04	9.45
Impurity-4	0.004	0.012	4.87	9.81
Impurity-5	0.004	0.015	3.04	9.45
Gatifloxacin	0.004	0.014	3.02	9.75

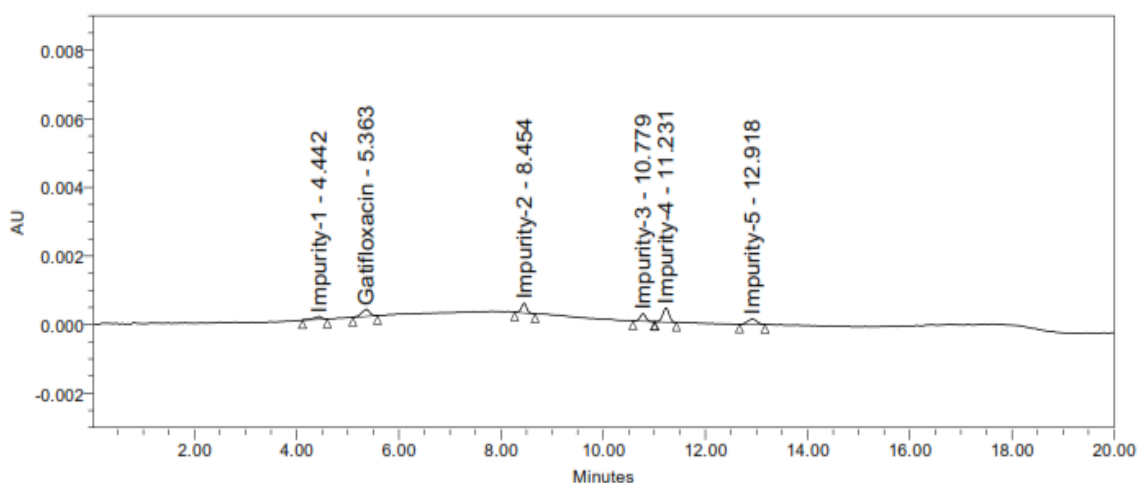


Figure 6. Typical chromatogram LOD solution

Slika 6. Tipični hromatogram za LOD rastvor

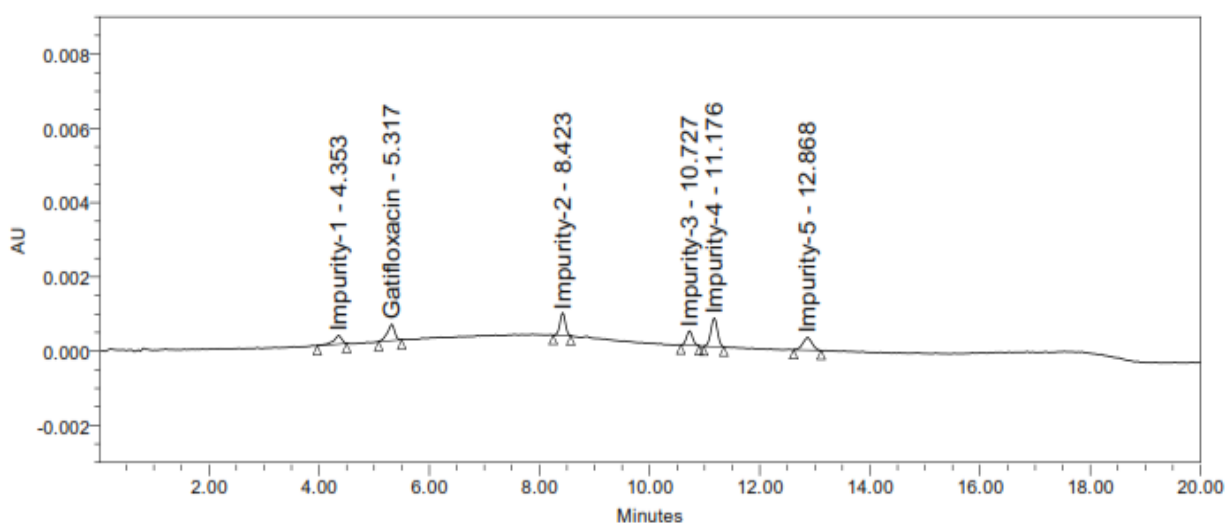


Figure 7. Typical chromatogram LOQ solution

Slika 7. Tipični hromatogram za LOQ rastvor

4.4. Linearity

The linearity of detector response for analytes was demonstrated by preparing solutions over the range of LOQ to 150% of specification limit with respect to sample concentration. These solutions were injected into the HPLC system and the responses of the same were recorded. A plot of concentration vs. peak area was done. The

Coefficient of determination between concentration and response was evaluated.

Table 6 to Table 10 and Figures 8 to 12 illustrates that the linearity results for Gatifloxacin and all the impurities in the specified concentration range are found satisfactory, with a correlation coefficient greater than 0.99 respectively.

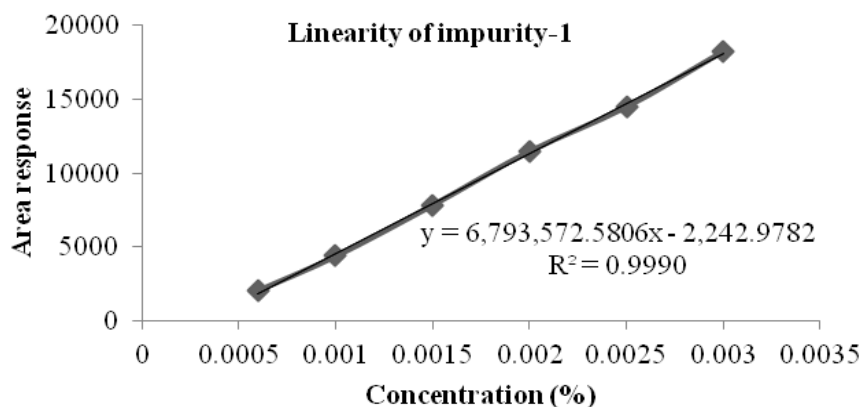


Figure 8. Linearity graph of Impurity-1

Slika 8. Grafik linearnosti nečistoće-1

Table 6. Linearity for Impurity-1

Tabela 6. Linearnost za nečistoću-1

S.No	Levels	Concentration in %	Area response
1	Linearity Level-1	0.0006	4069
2	Linearity Level-2	0.001	6538
3	Linearity Level-3	0.0015	11000
4	Linearity Level-4	0.002	14515
5	Linearity Level-5	0.0025	18297
6	Linearity Level-6	0.003	22655
Square root of Correlation coefficient (r^2)			0.9990
Slope			6793572.5806
Intercept			-2242.9782

Table 7. Linearity for Impurity-2

Tabela 7. Linearnost za nečistoću-2

S.No	Levels	Concentration in %	Area response
1	Linearity Level-1	0.0006	4216
2	Linearity Level-2	0.001	5995
3	Linearity Level-3	0.0015	8710
4	Linearity Level-4	0.002	11307
5	Linearity Level-5	0.0025	14144
6	Linearity Level-6	0.003	16774
Square root of Correlation coefficient (r^2)			0.9993
Slope			5288951.6129
Intercept			847.1855

Table 8. Linearity for Impurity-3

Tabela 8. Linearnost za nečistoću-3

S.No.	Levels	Concentration in %	Area response
1	Linearity Level-1	0.0006	3043
2	Linearity Level-2	0.001	4417
3	Linearity Level-3	0.0015	5697
4	Linearity Level-4	0.002	7332
5	Linearity Level-5	0.0025	8678
6	Linearity Level-6	0.003	10442
Square root of Correlation coefficient (r^2)			0.9984
Slope			3023564.5161
Intercept			1259.8694

Table 9. Linearity for Impurity-4

Tabela 9. Linearnost za nečistoću-4

S.No.	Levels	Concentration in %	Area response
1	Linearity Level-1	0.0006	6316
2	Linearity Level-2	0.001	8991
3	Linearity Level-3	0.0015	11993
4	Linearity Level-4	0.002	15539
5	Linearity Level-5	0.0025	18037
6	Linearity Level-6	0.003	21576
Square root of Correlation coefficient (r^2)			0.9986
Slope			6291145.1613
Intercept			2627.6435

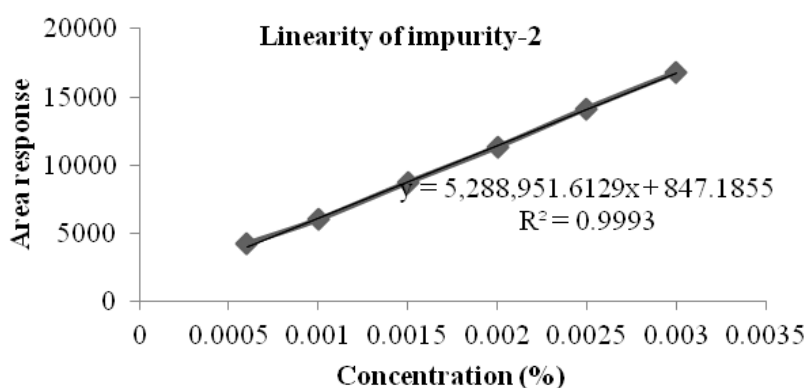


Figure 9. Linearity graph of Impurity-2

Slika 9. Grafik linearnosti nečistoće-2

Table 10. Linearity for Impurity-5

Tabela 10. Linearnost za nečistoću-5

S.No	Levels	Concentration in %	Area response
1	Linearity Level-1	0.0006	3868
2	Linearity Level-2	0.001	5688
3	Linearity Level-3	0.0015	7935
4	Linearity Level-4	0.002	10052
5	Linearity Level-5	0.0025	12790
6	Linearity Level-6	0.003	14768
Square root of Correlation coefficient (r^2)			0.9988
Slope			4584483.8710
Intercept			1084.2452

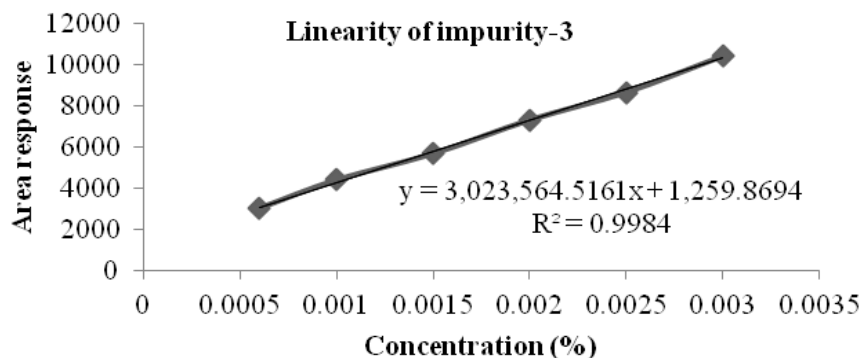


Figure 10. Linearity graph of Impurity-3

Slika 10. Grafik linearnosti nečistoće-3

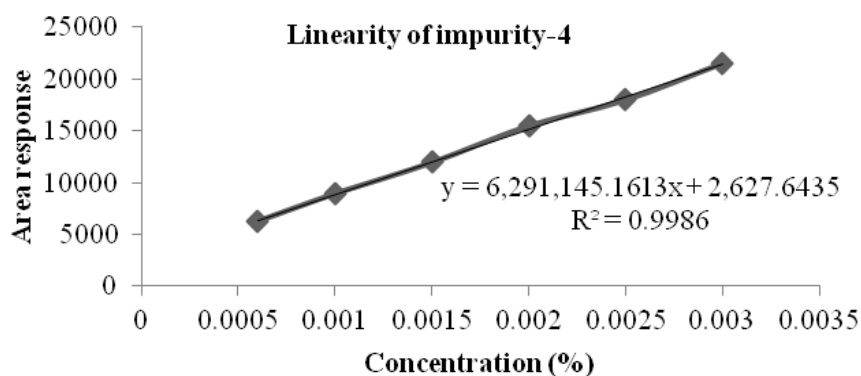


Figure 11. Linearity graph of Impurity-4

Slika 11. Grafik linearnosti nečistoće-4

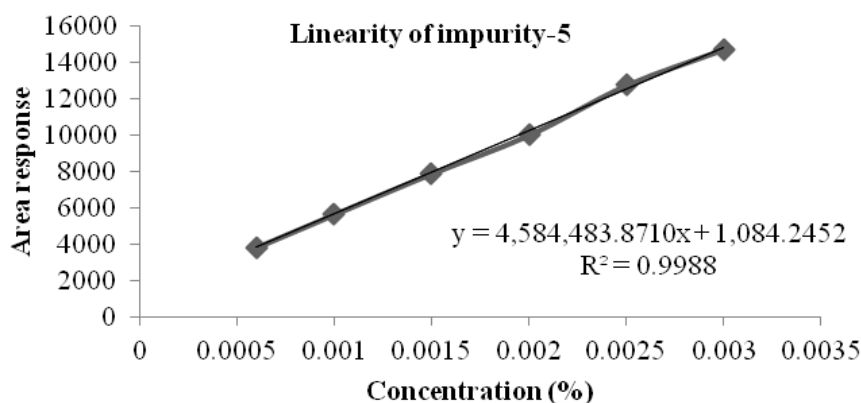


Figure 12. Linearity graph of Impurity-5

Slika 12. Grafik linearnosti nečistoće-5

4.5. Accuracy

Recovery of Gatifloxacin impurities in Gatifloxacin was performed. The sample was taken and varying amounts of Gatifloxacin impurities

representing LOQ to 150% of specification level were added to the flasks.

The spiked samples were prepared as per the method and the results are tabulated in Table 11.

Table 11. Accuracy study of Gatifloxacin

Tabela 11. Studija tačnosti gatifloksacina

S.No.	Theoretical (%)	% Mean Recovery				
		Imp-1	Imp-2	Imp-3	Imp-4	Imp-5
1	LOQ	110	93.9	92.9	93.9	92.9
2	50	97.4	97.3	96.4	97.3	96.4
3	100	98.5	99.1	98.2	99.1	98.2
4	150	99.0	100.0	100.6	100.0	100.6

4.6. Solution stability of analytical solutions

Reference solution and spiked test solution prepared, injected different time intervals and calculated the %RSD for the peak area of Gatifloxacin from reference solution, %RSD for the content of impurities from spiked test solution. The reference and test solution stable upto 48 hrs.

5. RESULTS AND DISCUSSION

A simple, economic, accurate and precise HPLC method was successfully developed. The method developed was statistically validated in terms of selectivity, accuracy, linearity, precision, and stability of solution.

For selectivity, the chromatograms were recorded for standard and sample solutions of Gatifloxacin and its related substances. Selectivity studies reveal that the peak is well separated from each other. Therefore the method is selective for the determination of related substances in Gatifloxacin. There is no interference of diluent at Gatifloxacin and impurities peaks. The elution order and the retention times of impurities and Gatifloxacin obtained from individual standard preparations and mixed standard preparations are comparable.

The limit of detection (LOD) and limit of quantitation (LOQ) for Gatifloxacin standard 0.014 and 0.004, impurity-1 0.010 and 0.004, impurity-2 0.011 and 0.004, impurity-3 0.014 and 0.004, impurity-4 0.0012 and 0.004 µg/mL and impurity-5 0.015 and 0.004 µg/mL respectively.

The linearity results for Gatifloxacin and all the impurities in the specified concentration range are found satisfactory, with a correlation coefficient greater than 0.99. Calibration curve was plotted and correlation co-efficient for Gatifloxacin and its impurities found to be 0.9990, 0.9993, 0.9984, 0.9986 and 0.9988 respectively.

The accuracy studies were shown as %recovery for Gatifloxacin and its impurities at

specification level. The limit of % recovered shown is in the range of 80 and 120% and the results obtained were found to be within the limits. Hence the method was found to be accurate.

For precision studies six replicate injections were performed. %RSD was determined from the peak areas of Gatifloxacin and its impurities. The acceptance limit should be not more than 10, and the results were found to be within the acceptance limits.

6. CONCLUSION

The new HPLC chromatographic method developed for Gatifloxacin and its related substances are rapid, simple, sensitive, precise, and accurate. Therefore, the proposed method can be successfully applied for the routine analysis of the active pharmaceutical ingredients for assurance of its quality during its formulation.

Acknowledgment

The authors are grateful to the Department of Biochemistry and Department of Chemistry, Acharya Nagarjuna University, Nagarjuna Nagar, Guntur, Andhra Pradesh, India, for providing the facilities to carry this research work.

Conflict of interests

The authors claim that there is no conflict of interest

Abbreviations

RP-HPLC: Reverse Phase High Performance Liquid Chromatography

LOD: Limit of Detection

LOQ: Limit of Quantification

7. REFERENCES

- [1] J.Gore, Z.Bryant, M.D.Stone, M.Nollmann, N.R.Cozzarelli (2006) Mechanochemical analysis of DNA gyrase using rotor bead tracking, *Bustamante C Nature*, 439, 100–104. doi: 10.1038/nature04319

- [2] A.H.Arteseros, J.Barbosa, O.R.Compan (2002) Nanotechnologies In Food And Agriculture, J. Chromatogr A, 945, 1–24. doi.org/10.1016/S0021-9673(01)01505-9
- [3] V.Lorian (ed) (1996) Antibiotics in laboratory medicine, 4th edn. Williams and Wilkins, Baltimore, p. 591–592. doi:10.1086/513670
- [4] V.F.Samanidou, C.E.Demetriou (2003) Papadoyannis IN Anal, Bioanal Chem, 375, 623–629. doi.org/10.1007/s00216-003-1749-9
- [5] S.Al-Dgither, S.N.Alvi, M.M.Hammami (2006), J.Pharm Biomed Anal, 41, 251–255.
- [6] L.Kothapalli, A.D.Deshpande (2007). 69(4), Indian J Pharm Sci, 69, 525–528.
- [7] W.Jiang, C.C.Guoa, P.Donga, Z.J.Chua, L.Wanga, W.Jiang (2008) A Validated, Specific Stability-Indicating RP-LC Method for Moxifloxacin and Its Related Substances, Luminescence, 23, 7–13. doi.org/10.1002/bio.1008
- [8] I.U.Khan, S.N.Razzaq, I.Mariam, M.Ashfaq, S.S.Razzaq (2014) Stability-indicating RP-HPLC method for simultaneous determination of Gatifloxacin and flurbiprofen in binary combination., Quím. Nova, 37, 349-354. doi.org/10.5935/0100-4042.20140058
- [9] M.I.Santoro, N.M.Kassab, A.K.Singh, E.R.Kedor-Hackmam (2006) Quantitative determination of Gatifloxacin, levofloxacin, lomefloxacin and pefloxacin fluoroquinolonic antibiotics in pharmaceutical preparations by high-performance liquid chromatography., J. Pharm.Biomed.Anal., 40(1), 179-184. doi.org/10.1016/j.jpba.2005.06.018
- [10] P.Sonali, K.Lata, T.Asha, A.Deshpande (2006) Simultaneous spectrophotometric estimation of Gatifloxacin and ornidazole in tablet dosage form., Ind. J. Pharm. Sci., 68, 819-821. doi.org/10.4103/0250-474X.31026
- [11] K.Venugopal, N.Ranendra (2005) New, simple and validated UV-spectrophotometric methods for the estimation of Gatifloxacin in bulk and formulations., Farmaco, 60, 906-912. doi.org/10.1016/j.farmac.2005.08.010
- [12] ICH (1994) Text on validation of analytical procedures, Q2A (R1). International Conference on Harmonization, IFPMA, Geneva

IZVOD

RAZVOJ I VALIDACIJA RP-HPLC METODE ZA KVANTITATIVNU PROCENU SRODNIH SUPSTANCI U SUPSTANCI LEKA GATIFLOKSACIN

Opisana je analiza poboljšane RP-HPLC metode za odvajanje i kvantifikaciju gatifloksacina i njegovih nečistoća. Uzorci se analiziraju pomoću reverzne faze (RP-HPLC) korišćenjem Zorbak Eclipse C18, 50 x 4,6 mm 5 µm, a mobilna faza se sastoji od dva kanala A i B. Kanal-A: 0,1% pufer trifluorosirćetne kiseline i kanal-B: acetonitril. Brzina protoka je 1,0 ml/min. Temperatura kolone je održavana na 35°C, a temperatura uzorka je održavana na 25°C, zapremina injekcije 10 µL and talasna dužina fiksirana na 220 nm UV-detekcija. Razvijena LC metoda je validirana s obzirom na specifičnost, preciznost, linearnost, robusnost i robusnost. Studija validacije upoređena prema ICH smernicama.

Ključne reči: Gatifloksacin, određivanje srodnih supstanci, tečna hromatografija

Naučni rad

Rad primljen: 08.06.2022.

Rad prihvaćen: 16.07.2022.

Rad je dostupan na sajtu: www.idk.org.rs/casopis

Agha Inya Ndukwe,^{1*} Chukwuma Daniel Okolo¹,
Benjamin Uchenna Nwadirichi¹

¹Department of Materials & Metallurgical Engineering, Federal
University of Technology, Owerri, Nigeria

Review paper

ISSN 0351-9465, E-ISSN 2466-2585

<https://doi.org/10.62638/ZasMat1128>



Zastita Materijala 65 (2)

202 - 212 (2024)

Overview of corrosion behaviour of ceramic materials in molten salt environments

ABSTRACT

This study reviewed previous studies between the years 2015 and 2021 on how ceramic materials degraded in the presence of molten salt environments. The processes of corrosion resistance of various ceramic compositions subjected to various molten salt compositions and temperatures were also scrutinized. The results offer important new insights into the variables affecting ceramics' corrosion behaviour and the production of corrosion products. The reported result reveals that the ceramic material with the composition $(Sm_{0.5}Sc_{0.5})_2Zr_2O_7$ performed better than that of $Sm_2Zr_2O_7$ in terms of hot corrosion resistance in molten salt ($V_2O_5 + Na_2SO_4$). It has also been reported that corrosion behaviour is influenced by particle size. Notably, zirconia (n-YSZ) with nanoscale grain sizes was more susceptible to hot corrosion, which was explained by increased specific surface areas. On the other hand, sintering and additives have been found to enhance corrosion resistance. The $Y-Y_2Si_2O_7$ ceramic's resistance to corrosion in ($V_2O_5 + Na_2SO_4$) molten salt was enhanced by the addition of alumina. The results of these investigations help us understand how corrosion works and what influences ceramic materials' susceptibility to deterioration in molten salt environment. This information can direct the development of more corrosive-resistant ceramic materials for use in high-temperature environments or molten salt-based energy systems, among other corrosive uses.

Keywords: hot corrosion, alumina, heat exchangers, nitrides, zirconia

1. INTRODUCTION

A process called "hot corrosion" occurs when molten salts attack a material's surface at the same time that they interact with the oxide layer that has formed there, often at a high temperature [1]. Hot corrosion is typically considered an accelerated deteriorating process that involves the deposition of corrosive species (like sulphates) from the environment (like combustion gas) to the surface of hot components, followed by the subsequent disintegration of the protective oxide scale [2]. Consequently, corrosive species are created that can enter the material and cause a variety of degradation processes, such as oxide spalling, grain boundary assault, and material embrittlement. Hot corrosion may dramatically lower a material's mechanical strength and lifespan, impairing the functionality and dependability of crucial parts [3].

In general, the menace of corrosion refers to the degradation of materials occasioned by electrochemical or chemical reactions. Unlike ceramics, metals tend to degrade in acidic environments and previous studies have shown that the corrosion of metals can be deterred in various acidic media using different plant extracts and pastes [4–13]. When exposed to acidic conditions, ceramics display improved corrosion resistance in comparison with metals [14]. In places where ceramics are used, such as heat engines and heat exchangers, molten salt deposits are significant corrodents and it has been reported that the Na_2SO_4 -induced corrosion can be quite serious [15].

Ceramics, including structural ceramics, are renowned for having extraordinary qualities including resistance to chemical reactivity, wear, and high temperature [16]. In the commercial world, these ceramics are utilized in a wide range of products, including gas turbine components, welding nozzles, heat exchangers, heat pipes, valves, cutting tools, turbochargers, crucibles, dental work, bone, and joint replacement

*Corresponding Author: Agha Inya Ndukwe

E-mail: agha.ndukwe@futo.edu.ng

Paper received: 08. 08. 2023.

Paper accepted: 22. 09. 2023.

Paper is available on the website: www.idk.org.rs/journal

prostheses [17]. In addition, these promising qualities make ceramics desirable for a wide range of applications, including heat barrier coatings, refractories, and catalytic supports [18]. However, the hot corrosive behaviour of ceramics in hostile conditions, such as molten salts, might restrict their performance and durability [19]. Designing and creating ceramic materials with better resistance to corrosive conditions, therefore, requires an understanding of the ability to characterize the hot corrosion behaviour of ceramics [20].

The extremely corrosive conditions of molten salts may seriously degrade materials [21]. They are made up of a combination of cations and anions, which can react with ceramic surfaces to cause corrosion [22]. Temperature, composition, and the presence of impurities are all factors that affect the corrosive attack in molten salts [23]. Various corrosive species, including chlorides, sulphates, and fluorides, can be introduced into the molten salt environment and speed up the deterioration of ceramics [24]. Further enhancing the corrosive assault may be the presence of impurities or strong gases.

Over a few decades, studies were done on hot corrosion of Na_2SO_4 -coated Ti_3AlC_2 in the air at 700–1000 °C [25]. No protective scales were reportedly seen, which led to significant hot corrosion of Ti_3AlC_2 by fused Na_2SO_4 at 900 and 1000 °C. The hot corrosion attack was minimal below the melting point of Na_2SO_4 , whereas Ti_3AlC_2 experienced a strong hot corrosion attack from fused sodium sulphate above the melting point of Na_2SO_4 . Another study examined the hot corrosion of Na_2SO_4 -coated and Ti_3SiC_2 -based ceramics at 900 and 1000 °C in air [26]. According to reports, the Ti_3SiC_2 ceramics covered with roughly 2 mg/cm² Na_2SO_4 experienced substantial damage.

Research has been conducted on the hot corrosion process of composite Alumina/Yttria-stabilized zirconia coating in molten sulphate-vanadate salt [27]. Results demonstrate that when the salt's V_2O_5 level was less than around 5 wt%, the Al_2O_3 overlay served as a barrier to prevent the molten salt from penetrating the YSZ coating. Due to this, ZrO_2 instability was greatly mitigated [27]. The hot corrosion behaviour of Ti_3SiC_2 in the combination of Na_2SO_4 - NaCl melts has been investigated [28]. When the concentration of Na_2SO_4 was more than 35 wt% at 850 °C, they reported that the Ti_3SiC_2 had a significant hot corrosion attack. There were some radial and transverse fissures in the outer and inner layers of the corrosion layer, which exhibited a duplex microstructure. Xie et al. [29] investigated the hot corrosion behaviour of double-ceramic-layer

$\text{LaTi}_2\text{Al}_9\text{O}_{19}$ and yttria-stabilized zirconia thermal barrier coatings. They reported that the bond coat in the $\text{LaTi}_2\text{Al}_9\text{O}_{19}$ /yttria-stabilized zirconia thermal barrier coatings significantly contributed to protecting the component against hot corrosion. In addition, the ceramic material, $\text{LaTi}_2\text{Al}_9\text{O}_{19}$ /yttria-stabilized zirconia was found to show good chemical stability in molten salts of Na_2SO_4 and NaCl . The disintegration of $\text{LaTi}_2\text{Al}_9\text{O}_{19}$ did not occur even after 1458 hot corrosion cycles at 1373 K, indicating high chemical stability in molten salt of Na_2SO_4 and NaCl , according to further observation [29]. The reason for this behaviour was attributed to the outstanding high-temperature performance and limited heat conductivity of the ceramic material ($\text{LaTi}_2\text{Al}_9\text{O}_{19}$).

The main objectives of this current study are to:

- 1. Review previous studies on the behaviour of ceramic materials in molten salt environments from 2015 to 2021, to better understand how they degrade and how well they can resist corrosion.
- 2. Identify and examine the variables, such as ceramic material composition, particle size, sintering methods, and salt composition, that affect the corrosion behaviour of ceramics in molten salt, and to
- 3. Identify knowledge gaps and potential directions for additional study in the hot corrosion behaviour of ceramics.

2. BEHAVIOUR OF CERAMICS IN MOLTEN SALTS

2.1. Ceramics attacked by molten salts – Nitrides and carbides

When different molten salts are present, the typically protective layer of SiO_2 that develops on SiC and Si_3N_4 can show accelerated corrosion. According to earlier research [30], an acid salt solution did not cause the protective layer to erode. Active corrosion was caused by the production of SiO gas at low oxygen pressures. It has been demonstrated that a key factor in the behaviour of molten sodium salts is the activity of Na_2O . The possible reactivity with silica increases as this activity rises [30]. Lin et al. [31] studied the 850–1000 °C hot corrosion behaviour of Na_2SO_4 -coated Ti_2AlC in air. Below the melting point of Na_2SO_4 , a protective Al_2O_3 scale was discovered to slow down further corrosion of the Ti_2AlC substrate. The hot corrosion kinetics were found to be parabolic. Because porous and non-protective scales failed to shield the Ti_2AlC substrate from hot corrosion assaults, severe hot corrosion attacks on Ti_2AlC were reported to occur at 900 and 1000 °C. Notably, it was observed that sulphur separated at

the scale/substrate interfaces and chemical interactions between Ti_2AlC and the Na_2SO_4 salt dominated the corrosion process. The hot corrosion resistance of Ti_2AlC can be improved by limiting the penetration of Na_2SO_4 to the Ti_2AlC substrate, and this was suggested as a practical and effective pre-oxidation treatment [31].

2.2. Ceramics' Hot Corrosion Mechanisms

Studies have shown that hot corrosion in ceramics involves several intricate processes that accelerate material deterioration, especially in the presence of sulphate-related salts [32]. On the other hand, yttria-stabilized zirconia's LZ_7C_3 coating was discovered to be flawless and degrading very little [33]. However, certain ceramics have been reported to exhibit relatively low corrosion when exposed to molten $NaCl-KCl-MgCl_2$ [34]. Designing solutions to reduce hot corrosion and increase the longevity of ceramic components in corrosive environments requires an understanding of the mechanisms behind the hot corrosion of ceramics.

2.2.1. Degradation owing to chemical processes

One of the main processes causing hot corrosion in ceramics is degradation owing to chemical processes. The ceramic surface may react with molten salts, producing soluble reaction products. The protective oxide layer on the ceramic surface may be removed by these reaction products, exposing the underlying material to more corrosion. The reactivity of the molten salt, the makeup of the ceramic material, and the system temperature all have an impact on the chemical assault process. A study to understand the hot corrosion deterrence of YSZ, $Gd_2Zr_2O_7$, and $Gd_2Zr_2O_7 + YSZ$ composite thermal barrier coatings in $Na_2SO_4 + V_2O_5$ at $1050\text{ }^\circ\text{C}$ has been conducted [35]. In heated corrosion testing, the authors observed that a series of linked chemical processes might be classified as the chemical degradation of common YSZ coatings. Additionally, it was discovered that $NaVO_3$ would occur when V_2O_5 and Na_2SO_4 salt combination were exposed to high heat ($1050\text{ }^\circ\text{C}$).

2.2.2. Degradation because of diffusion-controlled processes

Concentration gradients cause the transport of corrosive substances into the ceramic in the diffusion-controlled process of hot corrosion. Corrosive species infiltrate into the ceramic from the surrounding environment, and as they do so, their concentration rises. Temperature, concentration gradients, and material characteristics, such as diffusion coefficients, all affect the diffusion process. Costa-Oliveira and Baxter [36] investigated how salt corrosion affected a hot-pressed silicon nitride in combustion circumstances with

various sulphur concentrations. It was reported that depending on their concentration in the gas phase, pollutants including the salts, $NaCl$ and Na_2SO_4 frequently found in gas turbine atmospheres were expected to accelerate the corrosion of Si_3N_4 due to their absorption into the scale. This was clarified by assuming that corrosion in sodium-containing environments happened via an ionic diffusion process [36].

Corrosive species can react with the ceramic's components once they get within the material; for instance, if sulphur is present, it may interact with the metal ions in the ceramic lattice to generate sulphides. The creation of new phases like oxides, sulphides, or halides because of the interaction between corrosive species and ceramic elements might harm the material's characteristics. The porosity, grain boundaries, and flaws of the ceramic material can all have an impact on how easily corrosive species diffuse inside it. Corrosive species can enter through porous materials, which speeds up their transportation. They can operate as preferred diffusion channels for the ceramic material's grain boundaries, which are the interfaces between different ceramic grains. Cracks and gaps in materials can act as entrance routes for corrosive species, hastening the deterioration process. Electrochemical techniques have been used to assess the corrosion effect of zirconia addition at 1, 2, and 5 atomic percents (at.%) on the hot corrosion behaviour of Mo_3Si intermetallic alloy in 60 weight per cent $NaNO_3$ and 40 weight per cent KNO_3 at $600\text{ }^\circ\text{C}$ [37]. For the as-cast alloy or when 1 or 2 wt.% Zr was added, and the corrosion process was controlled by charge transfer, but when 5 wt.% Zr was added, and it was controlled by diffusion [37].

2.2.3. Degradation by electrochemistry

Electrochemical reactions may occur at the ceramic surface because of molten salts acting as electrolytes. As a result of these interactions, corrosive species are formed by the transfer of ions between the ceramic material and the corrosive environment. The presence of electrochemically active species in the molten salt, the electrical conductivity of the ceramic and the temperature all have an impact on the electrochemical attack process. Li et al. [38] used a molar ratio of 1:1 to study the hot corrosion behaviour of $Yb_2Zr_2O_7$ ceramic against V_2O_5 and $Na_2SO_4 + V_2O_5$ at temperatures of $900-1100\text{ }^\circ\text{C}$ for 2 hours in the air. They noticed that the $YbVO_4$, which resulted from the hot corrosion of $Yb_2Zr_2O_7$ coated in V_2O_5 , was particle-shaped as opposed to rod-like in the $Yb_2Zr_2O_7$ coated in $(Na_2SO_4 + V_2O_5)$. A dissolution-precipitation process-based model was put up to discover how hot corrosion products developed. The model could be used to explain the hot

corrosion mechanism. It showed that the larger driving force in the hot corrosion of V_2O_5 -coated $Yb_2Zr_2O_7$ contributed to the granular $YbVO_4$ whilst the relatively smaller driving force in the hot corrosion of $(Na_2SO_4 + V_2O_5)$ -coated $Yb_2Zr_2O_7$ resulted in the rod-like $YbVO_4$ [38].

3. OVERVIEW OF PREVIOUS STUDIES ON HOT CORROSION BEHAVIOUR OF CERAMICS IN MOLTEN SALT

The summary of the overview of earlier studies on the corrosion behaviour of ceramic materials in molten salts is presented in Table 1. Many scholars have worked on several aspects of the area to arrive at different conclusions. Guo et al. [39]

studied the degradation disposition of some ceramic materials $(Sm_{0.5}Sc_{0.5})_2Zr_2O_7$ and $Sm_2Zr_2O_7$ in the presence of molten salt ($V_2O_5 + Na_2SO_4$). They reported that the ceramic material with the composition $Sm_2Zr_2O_7$ was outperformed by the ceramic with the composition $(Sm_{0.5}Sc_{0.5})_2Zr_2O_7$ in terms of hot corrosion resistance to $(V_2O_5 + Na_2SO_4)$ 50 wt.% salt. In another study [40], the thermal barrier oxides with stabilized ZrO_2 doped with Gd_2O_3 and Yb_2O_3 were investigated to unravel their corrosion behaviour in $V_2O_5 + Na_2SO_4$ molten salt. It was observed that the YSZ ceramic material was more susceptible to corrosion in molten salt than GdYb-YSZ ceramic [40].

Table 1. An Overview of previous studies on hot corrosion behaviour of ceramics in molten salts

Tabela 1. Pregled prethodnih studija o ponašanju keramike u toploj koroziji u rastopljenim solima

Ceramic materials	Molten salt composition	Temperature range of study and maximum period of exposure	What to deduce from the study	Ref.
$(Sm_{0.5}Sc_{0.5})_2Zr_2O_7$ & $Sm_2Zr_2O_7$	50 wt.% V_2O_5 & 50 wt.% Na_2SO_4	700-900 °C/4 h	Compared to $Sm_2Zr_2O_7$, $(Sm_{0.5}Sc_{0.5})_2Zr_2O_7$ exhibited greater corrosion resistance to $Na_2SO_4+V_2O_5$ salt.	[39]
Thermal barrier oxides with stabilized ZrO_2 doped with Gd_2O_3 and Yb_2O_3	Gd_2O_3 (1 mol%) + Yb_2O_3 (1 mol%) doped with Y_2O_3 (3.5 mol%) stabilized ZrO_2 (GdYb-YSZ)	700-1000 °C / 4 h	Despite being vulnerable to molten salt attack, GdYb-YSZ demonstrated greater hot corrosion resistance than YSZ.	[40]
Zirconia with nanostructures	$NaVO_3$	700 °C/24–192 h	The YSZ-based thermal barrier coatings' hot corrosion deterioration was significantly accelerated by microcracks and open holes in the coatings.	[41]
Zirconia stabilized – yttria	$(Na_2SO_4 + V_2O_5)$ 50 wt.%	1000 °C / 4 h	The columnar holes that EB-PVD created contributed to the structure's degeneration brought on by the molten salts that seeped from the top layer, speeding up the rate of destruction.	[42]
Magnesia (Stabilized)	Lithium (Li_2O & $LiCl$)	300 – 650 °C/ 360 h	The introduction of lithium gave rise to the initiation of sudden cracks and pores.	[43]
$Y-Y_2Si_2O_7$	V_2O_5 & Na_2SO_4	20 h	The sample of the ceramic ($Y-Y_2Si_2O_7$) bearing alumina additive was reported to give outstanding resistance to corrosion in the presence of molten salt.	[44]
$(Gd_{0.9}Sc_{0.5})_2Zr_2O_7$	VO_5	700°C-1000°C/4h	At varying temperatures between 700-1000°C, the ceramic material $(Gd_{0.9}Sc_{0.5})_2Zr_2O_7$ displayed a potential corrosion resistance coating inhibitor.	[45]
$BaLa_2Ti_3O_{10}$	$V_2O_5, Na_2SO_4+V_2O_5$	900°C/4h	The ceramic material $(BaLa_2Ti_3O_{10})$ having reacted with V_2O_5 and $Na_2SO_4+V_2O_5$ appeared to have suitable corrosion resistance in V_2O_5	[46]

			compared to $\text{Na}_2\text{SO}_4+\text{V}_2\text{O}_5$.	
$\text{Yb}_2\text{O}_3\text{-Gd}_2\text{O}_3\text{-Y}_2\text{O}_3$	$\text{CaCl}_2\text{-CaF}_2\text{-CaO}$	1500°C-1600°C/11h	The ceramic material ($\text{Yb}_2\text{O}_3\text{-Gd}_2\text{O}_3\text{-Y}_2\text{O}_3$) sintered at 1500°C for 6h and experienced the highest degradation compared to 1600°C sintered ceramic material ($\text{Yb}_2\text{O}_3\text{-Gd}_2\text{O}_3\text{-Y}_2\text{O}_3$) for 11h	[47]
SrHfO_3	Na_2SO_4 & V_2O_5	1600°C/10h	A thinner corrosion layer at a higher temperature was observed due to the quick formation of corrosion products ($\text{Sr}_r\text{V}_2\text{O}_6\text{+m-H}_2\text{O}_{2(s)}\text{+Na}_2\text{O}$) which increases as temperature increases.	[48]
$\text{LaTi}_2\text{Al}_9\text{O}_{19}$	V_2O_5	700°C-950°C/10h	AlVO_4 production was the main reaction seen during a two-hour corrosion session at 700°C but was found to be unstable. It largely dissolved at 800 °C, forming Al_2O_3 . This shows the dynamic character of the corrosion reactions as well as the propensity of some phases to transform or alter under certain circumstances.	[49]
AlN	LiF-LiCl-LiBr-Li	500°C/300h	High levels of metallic Li (>0.1 weight per cent) were reported to hasten the corrosion of AlN .	[50]
$\text{Ba}_{1-x}\text{SxAx}$ (x=0,0.25,0.5,0.75,1)	Na_2SO_4	900°C-1100°C	At elevated temperatures, there was an enhancement in the diffusion of Na into $\text{Ba}_{1-x}\text{SxAx}$ which increased the rate of corrosion significantly.	[51]
$\text{La}_2\text{Hf}_2\text{O}_7$	$\text{Na}_2\text{SO}_4+\text{V}_2\text{O}_5$ & Na_2SO_4	900°C-1200°C/4h	The performance of $\text{La}_2\text{Hf}_2\text{O}_7$ in reaction with $\text{Na}_2\text{SO}_4+\text{V}_2\text{O}_5$ led to a decrease in the thickness of the corrosion product due to an increase in temperature as contact with V_2O_5 was made.	[52]
$\text{Cr}_2\text{AlC max}$ & CoNiCrAlY	$\text{Na}_2\text{SO}_4+\text{V}_2\text{O}_5$	950°C/30h	It was reported that $\text{Cr}_2\text{AlC Max}$ has a better hot corrosion resistance than the CoNiCrAlY sample.	[53]
$\text{YSZ, Gd}_2\text{Zr}_2\text{O}_7$ & $\text{YSZ/Gd}_2\text{Zr}_2\text{O}_7$	Na_2SO_4 and V_2O_5	1000°C/25h	Double coatings of $\text{YSZ/Gd}_2\text{Zr}_2\text{O}_7$ were found to resist hot corrosion than those of single coatings	[54]
Zirconia	NaVO_3 & Na_2SO_4	1100°C/ 6h-24h	The formation of a large polyhedron crystal of YVO_4 and m-ZrO_2 as corrosion products was obtained after 6h-24h. Also, the volume fraction of ZrO_2 in 8YSZ ceramics was found to increase after the corrosion test.	[55]
$\text{Ba}_2\text{REAlO}_5$	$\text{Na}_2\text{SO}_4+\text{V}_2\text{O}_5$	900°C-1000°C/4h	The Lewis acid-base rule, thermodynamics, and phase diagrams were used as the foundation for the postulated hot corrosion mechanisms.	[56]
$\text{Yb}_2\text{Si}_2\text{O}_7$	NaVO_3	1000°C-1500°C/2h	YbVO_4 was obtained on a bulk surface at 1000°C-1200°C owing to the acidity of the corrosion medium and a corrosion product ($\text{Yb}_2\text{Si}_2\text{O}_5$) was obtained.	[57]

Wang et al. [41] investigated how the particle size at the nanoscale can influence the corrosion of zirconia at 700°C in a NaVO_3 corrosive

environment. They reported that the samples (n-YSZ) powders having 30 nm grain sizes were vulnerable to hot corrosion. The reason was

attributed to specific surface areas that were larger when compared to those of other specimens. In another study, the hot corrosion of zirconia stabilized by yttria in ($\text{Na}_2\text{SO}_4 + \text{V}_2\text{O}_5$) 50 wt.% molten salt at 1000°C was undertaken [42]. To prevent edge effects, the corrosion salts were said to be applied to the specimen's surfaces at a concentration of 10 mg/cm^2 , about 1.5 mm away from the edge. It was reported that the interface between CoNiAlY bond (metallic) coating and YSZ ceramic coating existed thermally grown oxide layer including surface cracks.

Cho et al. [43] studied the corrosion of magnesia (stabilized) ceramic in molten salt. The molten salt is composed of lithium (Li_2O & LiCl). They reported that although the degradation of the magnesia ceramic occurred at both cyclic and isothermal conditions, the introduction of lithium increased the rate of corrosion to approximately 5 times compared to the initial degradation rate. On the other hand, the impact of sintering on the degradation of $\text{Y-Y}_2\text{Si}_2\text{O}_7$ ceramics in molten salt (V_2O_5 & Na_2SO_4) has been carried out [44]. The reaction of $\text{Y-Y}_2\text{Si}_2\text{O}_7$ ceramic with the following additives: Al, Li, and Mg resulted in 2 mol.% of Al_2O_3 , Li_2O , and MgO , producing three different samples. The ceramic ($\text{Y-Y}_2\text{Si}_2\text{O}_7$) sample with the alumina addition was said to have exceptional corrosion resistance in the presence of molten salt [44]. Zhang et al. [45] identified the effect of molten salt (V_2O_5) on ceramic material, bearing the composition, $\text{Gd}_{0.9}\text{Sc}_{0.5}\text{Zr}_2\text{O}_7$. They discovered that the corrosion product (Sc_2O_3), obtained following the interaction between the ceramic material ($\text{Gd}_{0.9}\text{Sc}_{0.5}\text{Zr}_2\text{O}_7$) and the molten salt (V_2O_5) possessed an outstanding resistance to corrosion due to the molten salt.

Liu et al. [46] discovered the influence of molten salts (Na_2SO_4 , and V_2O_5) on the ceramic material ($\text{BaLa}_2\text{Ti}_3\text{O}_{10}$). According to the results of this investigation, $\text{BaLa}_2\text{Ti}_3\text{O}_{10}$ ceramic, a potential candidate for Thermal Barrier Coating, exhibits greater resistance to V_2O_5 salt corrosion despite having strong resistance to both salts. On the other hand, the effect of molten salt ($\text{CaCl}_2\text{-CaF}_2\text{-CaO}$) on ceramic material ($\text{Yb}_2\text{O}_3\text{-Gd}_2\text{O}_3\text{-Y}_2\text{O}_3$) was carried out by Kim et al. [47]. They reported that the exposure time could act as a driving force for the penetration of the molten salt ($\text{CaCl}_2\text{-CaF}_2\text{-CaO}$) which further shows a higher degradation rate of the sample ($\text{Yb}_2\text{O}_3\text{-Gd}_2\text{O}_3\text{-Y}_2\text{O}_3$) sintered at 120h compared to the sample sintered at approximately 6h-11h.

Gu et al. [48] studied the influence of molten salts (Na_2SO_4 , V_2O_5 and the combination of $\text{Na}_2\text{SO}_4 + \text{V}_2\text{O}_5$ (in the molar proportion of 1:1) on the microstructure of the ceramic material (SrHfO_3).

A schematic illustration of what subsequently occurred and the nature of the corrosion product can be found in Fig. 1. The authors reported that while the thickness of the corrosion scale increased in mixed molten salt, the thickness of the corrosion layer reduced as the temperature increased in contact with V_2O_5 [48]. A thinner corrosion layer at a higher temperature was observed due to the quick formation of corrosion products ($\text{Sr}_r\text{V}_2\text{O}_6 + m\text{-HfO}_{2(s)} + \text{Na}_2\text{O}$) which increases as temperature increases.

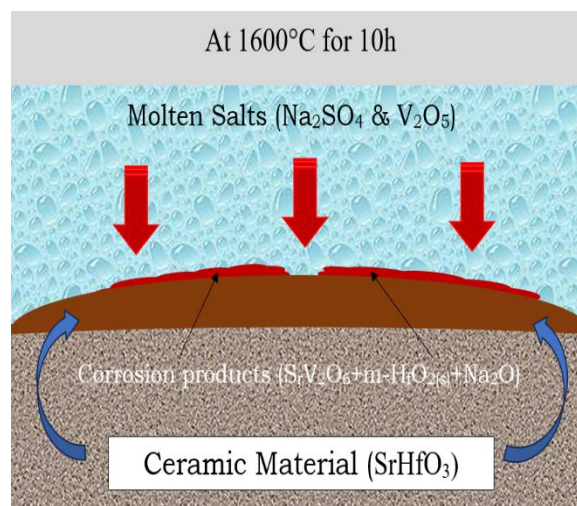


Figure 1. Formation of corrosion products ($\text{Sr}_r\text{V}_2\text{O}_6 + m\text{-HfO}_{2(s)} + \text{Na}_2\text{O}$) by the exposure of SrHfO_3 in Na_2SO_4 & V_2O_5

Slika 1. Formiranje produkata korozije ($\text{Sr}_r\text{V}_2\text{O}_6 + m\text{-HfO}_{2(s)} + \text{Na}_2\text{O}$) izlaganjem SrHfO_3 u Na_2SO_4 i V_2O_5

Evaluation of molten salt (V_2O_5) on ceramic material ($\text{LaTi}_2\text{Al}_9\text{O}_{19}$) has been carried out [49]. It was reported that the temperature and length of the corrosion process were found to dictate the nature of the corrosion products and microstructures of the $\text{LaTi}_2\text{Al}_9\text{O}_{19}$ ceramic. Variable reactions and phase formations were produced by altering temperatures and periods. In another interesting study, the AlN ceramics' corrosion behaviour in 500°C LiF-LiCl-LiBr-Li molten salt [50]. The researchers observed that high levels of metallic Li (>0.1 weight per cent) increased the corrosion of AlN. The interaction between Li and the YAG (yttrium aluminium garnet) found in AlN was reported to cause the observed accelerated corrosion. This implies that the existence of high Li concentrations encourages a corrosive environment, which damages AlN [50]. In a molten Na_2SO_4 environment, Jiang et al. [51] investigated the hot corrosion behaviour of barium-strontium aluminosilicates. They reported that the diffusion reaction of the Ba/Sr and Na cations had an impact on the hot corrosion behaviour of $\text{B}_{1-x}\text{S}_x\text{AS}$ compounds in a molten Na_2SO_4 environment. This

mechanism greatly aided the degradation process. Additionally, the order of cation migration during hot corrosion was impacted by the difference in atomic radius between strontium (Sr) and barium (Ba). It was discovered that strontium cations diffused out of the $B_{1-x}S_xAS$ structure before barium cations, suggesting that strontium should exit the structure first. A study to determine the performance of $La_2Hf_2O_7$ ceramic when exposed to the molten salt (sulphate-vanadate) at 900°C - 1200°C has been carried out [52]. They discovered nanoparticles (non-needle-like) were present and the corrosion rate was directly proportional to the increment in the temperature accompanied by $LaVO_4$ crystalline grain growing noticeably. Furthermore, the thickness of the corroded layer was reported to increase with an increase in corrosion temperature. A study on the behaviour of the Cr_2AlC max compound in the presence of V_2O_5 & Na_2SO_4 molten salts has been carried out [53]. The researchers discovered that under the test circumstances, the Cr_2AlC MAX-phase samples demonstrated greater hot corrosion resistance than the $CoNiCrAlY$ samples.

Ozgurluk et al. [54] experimented with the reaction of $YSZ/Gd_2Zr_2O_7$ when exposed to vanadate salt (V_2O_5) at 1000°C . They reported that after the conclusion of the experiment (25h) within 5h cycles at 1000°C , significant deterioration and spillage on the YSZ coatings was observed. On the other hand, a study on the effect of the presence of $NaVO_3+Na_2SO_4$ on Zirconia ceramics at 1100°C has been conducted [55].

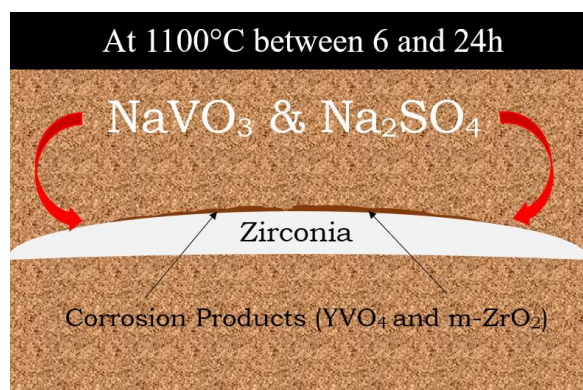


Figure 2. Effect of the presence of $NaVO_3+Na_2SO_4$ on Zirconia ceramics at 1100°C

Slika 2. Uticaj prisustva $NaVO_3+Na_2SO_4$ na cirkonijum keramiku na 1100°C

It was observed that Na_2SO_4 was a promoting factor of chemical reactions which increased the rate of corrosion. The process yielded Yttrium orthovanadate (YVO_4) and monoclinic zirconia dioxide ($m\text{-ZrO}_2$) as the corrosion products. Another study to evaluate the hot corrosion

mechanisms of Ba_2REAlO_5 when exposed to $Na_2SO_4+V_2O_5$ was successfully carried out [56]. According to the study, Ba_2REAlO_5 formed a reaction layer with a thickness of around $80\ \mu\text{m}$ after being exposed to a temperature of 1000°C for 4 hours. This implies that at this higher temperature, the material is more prone to corrosion. Finally, Zhang et al. [57] undertook a study to determine the behaviour of $Yb_2Si_2O_7$ ceramics when exposed to molten salt ($NaVO_3$) at 1000°C - 1500°C . They observed that the reaction between $Yb_2Si_2O_7$ and $NaVO_3$ produced rod-shaped $YbVO_4$ (ytterbium vanadate) grains at temperatures between 1000 and 1200°C . As the temperature increased, $YbVO_4$ concentration fell until it vanished at 1300°C . The hot corrosion product, Yb_2SiO_5 (ytterbium silicate), showed a polyhedral form at temperatures of 1300°C or higher. With an increase in temperature, the corrosion products contained more Yb_2SiO_5 .

4. CONCLUSION

From the present study on the overview of how ceramic materials behave when exposed to molten salt environments, the following conclusions may be drawn:

- The composition of ceramics has a big impact on corrosion resistance. In the presence of molten salt ($V_2O_5 + Na_2SO_4$), studies have shown that the ceramic material ($Sm_{0.5}Sc_{0.5}Zr_2O_7$) performed better than $Sm_2Zr_2O_7$ in terms of hot corrosion resistance. This emphasizes how crucial it is to choose ceramic compositions carefully to increase corrosion resistance in particular situations.
- The size of the particles affects corrosion behaviour. In a $NaVO_3$ corrosive environment, it was reported that zirconia ceramics with smaller particle sizes ($30\ \text{nm}$ grain sizes) were more susceptible to heat corrosion. This shows that certain surface areas, affected by particle size, contribute to the susceptibility of ceramic materials to corrosion.
- Additives can improve corrosion resistance. Studies have shown that using alumina (Al_2O_3) as an additive to $Y\text{-}Y_2Si_2O_7$ ceramics produced remarkable resistance to corrosion in molten salt (V_2O_5 & Na_2SO_4). This suggests that adding carefully chosen additives might enhance the corrosion resistance of ceramic materials.
- The alumina layer has been found to exhibit resistance to corrosion. The identification of an alumina layer (corrosion product) with exceptional corrosion resistance in a variety of molten salt conditions raises the possibility that this layer may play a significant role in

determining how quickly ceramic materials corrode. An alumina layer can serve as a barrier of defence against further deterioration.

These findings show the intricate interactions between the composition of ceramic materials, particle size, additives, molten salt composition, and the production of protective corrosion products that affect how they react to corrosion and how resistant they are to it. The development of corrosion-resistant ceramics for specific applications requires an understanding of these aspects.

5. KNOWLEDGE GAPS AND POTENTIAL RESEARCH AREAS

Following the overview of the behaviour of ceramics during hot corrosion in a variety of molten salts, the following areas have been identified as knowledge gaps. Additionally, some recommendations for possible future study areas have been made:

- Although the reviewed papers investigated the hot corrosion behaviour of several ceramics in molten salts, they did not go into detail about the precise corrosion mechanisms at play. It would be beneficial to comprehend the exact mechanisms by which corrosion occurs in various ceramic materials to help produce corrosion-resistant coatings or materials.
- The reviewed papers included the maximum exposure time for each investigation; however, they gave no details on how long the ceramic materials will last in hot corrosion environments. To determine if ceramics are suitable for use in practical applications, it would be crucial to look at the stability and degradation of ceramics, especially in the presence of sulphate-based molten salts over long periods.
- The reviewed studies discussed several ceramic compositions and how resistant they were to heat corrosion. The tuning of composition characteristics, such as dopants, additives, or material processing strategies to improve corrosion resistance, was not covered, nevertheless. Additional investigation is required to determine the composition's effect on hot corrosion behaviour and the best compositions for various applications.
- The major emphasis of many of the reviewed studies was on the temperature and the composition of molten salts as the main determinants of hot corrosion behaviour. The corrosion process, however, can also be impacted by other environmental variables such as gas atmospheres, contaminants, and thermal cycling. A deeper knowledge of the hot

corrosion behaviour of ceramics would result from examining the combined influence of these elements.

- The reviewed studies largely involved qualitative analyses of hot corrosion behaviour, concentrating on the relative resistance or susceptibility of various ceramics. To evaluate the performance of ceramics under hot corrosion circumstances, quantitative measurements of corrosion rates, mass loss, or other degradation characteristics would offer more accurate and comparable information.

It would be easier to create better corrosion-resistant materials if these information gaps were filled, which would lead to a better understanding of hot corrosion behaviour in ceramics.

6. REFERENCES

- [1] R. A. Rapp (2002) Hot corrosion of materials: A fluxing mechanism? *Corrosion Science*, 44(2), 209–221, [https://doi.org/10.1016/S0010-938X\(01\)00057-9](https://doi.org/10.1016/S0010-938X(01)00057-9)
- [2] D. A. Shifler (2018) Hot corrosion: A modification of reactants causing degradation. *Materials at High Temperatures*, 35(1–3), 225–235, <https://doi.org/10.1080/09603409.2017.1404692>
- [3] R. François, I. Khan, V. H. Dang (2013) Impact of corrosion on mechanical properties of steel embedded in 27-year-old corroded reinforced concrete beams. *Materials and Structures*, 46(6), 899–910, <https://doi.org/10.1617/s11527-012-9941-z>
- [4] A. I. Ndukwe (2022) Green inhibitors for corrosion of metals in acidic media: A review. *Academic journal of manufacturing engineering*, 20(2), 36–50, https://ajme.ro/PDF_AJME_2022_2/L5.pdf
- [5] A. I. Ndukwe, C. N. Anyakwo (2017) Modelling of corrosion inhibition of mild steel in hydrochloric acid by crushed leaves of *sida acuta* (malvaceae). *The International Journal of Engineering and Science*, 6(1), 22–33, <http://www.theijes.com/papers/vol6-issue1/Version-3/D0601032233.pdf>
- [6] A. I. Ndukwe, C. N. Anyakwo (2017) Predictive model for corrosion inhibition of mild steel in HCl by crushed leaves of *clerodendrum splendens*. *International Research Journal of Engineering and Technology*, 4(2), 679–688, <https://irjet.net/archives/V4/i2/IRJET-V4I2129.pdf>
- [7] A. I. Ndukwe, C. N. Anyakwo (2017) Modelling of corrosion inhibition of mild steel in sulphuric acid by thoroughly crushed leaves of *voacanga Africana* (apocynaceae). *American Journal of Engineering Research*, 6(1), 344–356, [http://www.ajer.org/papers/v6\(01\)/ZX060344356.pdf](http://www.ajer.org/papers/v6(01)/ZX060344356.pdf)
- [8] A. I. Ndukwe, C. N. Anyakwo (2017) Corrosion inhibition model for mild steel in sulphuric acid by crushed leaves of *clerodendrum splendens* (verbenaceae). *International Journal of Scientific Engineering and Applied Science*, 3(3), 39–49, <http://ijseas.com/volume3/v3i3/ijseas20170305.pdf>

- [9] A. I. Ndukwe, C. N. Anyakwo (2017) Predictive Corrosion-Inhibition Model for Mild Steel in Sulphuric Acid (H_2SO_4) by Leaf-Pastes of Sida Acuta Plant. *Journal of Civil, Construction and Environmental Engineering*, 2(5), 123–133, <https://doi.org/10.11648/j.jccee.20170205.11>
- [10] A. I. Ndukwe, N. E. Dan, J. U. Anaele, C. C. Ozoh, K. Okon, P. C. Agu (2023) The inhibition of mild steel corrosion by papaya and neem extracts. *Zastita Materijala*, 64(3), 274–282, <https://doi.org/10.5937/zasmat2303274N>
- [11] A.I. Ndukwe, Ihuoma, C. Akuwudike, D. O. Oluehi, F. A. Akaneme, E. U. Chibiko (2023) Predictive model for the corrosion inhibition of mild steel in 1.5 m HCl by the leaf-juice of Carica papaya, *Zastita Materijala*, 64(4), <https://doi.org/10.5937/zasmat2304413N>
- [12] C. N. Anyakwo, A. I. Ndukwe (2017) Mathematical model for corrosion inhibition of mild steel in hydrochloric acid by crushed leaves of tridaxpro-cumbens (asteraceae). *International journal of science and engineering investigations. International Journal of Science and Engineering Investigations*, 6(65), 81–89, <http://www.ijsei.com/papers/ijsei-66517-13.pdf>
- [13] C. N. Anyakwo, A. I. Ndukwe (2017) Prognostic model for corrosion-inhibition of mild steel in hydrochloric acid by crushed leaves of voacanga Africana. *International Journal of Computational and Theoretical Chemistry*, 5(3), 30-41. doi: 10.11648/j.ijctc.20170503.12
- [14] A. Valenzuela-Gutiérrez, J. López-Cuevas, A. González-Ángeles, N. Pilalua-Díaz (2019) Addition of ceramics materials to improve the corrosion resistance of alumina refractories. *SN Applied Sciences*, 1(7), 784-791, <https://doi.org/10.1007/s42452-019-0789-5>
- [15] N. S. Jacobson, J. L. Smialek, D. S. Fox (1994) Molten Salt Corrosion of Ceramics. In K. G. Nickel (Ed.), *Corrosion of Advanced Ceramics: Measurement and Modelling Proceedings of the NATO Advanced Research Workshop on Corrosion of Advanced Ceramics Tübingen, Germany August 30–September 3, 1993*, p. 205–222. Springer Netherlands, https://doi.org/10.1007/978-94-011-1182-9_16
- [16] J. M. Schoenung (2001) Structural Ceramics. In K. H. J. Buschow, R. W. Cahn, M. C. Flemings, B. Ilschner, E. J. Kramer, S. Mahajan, & P. Veyssiére (Eds.), *Encyclopedia of Materials: Science and Technology*, p.8921–8926. Elsevier, <https://doi.org/10.1016/B0-08-043152-6/01605-3>
- [17] D. P. Kaur, S. Raj, M. Bhandari (2022) Chapter 2—Recent advances in structural ceramics. In S. Singh, P. Kumar, & D. P. Mondal (Eds.), *Advanced Ceramics for Versatile Interdisciplinary Applications*, p.15–39. Elsevier, <https://doi.org/10.1016/B978-0-323-89952-9.00008-7>
- [18] X. Q. Cao, R. Vassen, D. Stoeber (2004) Ceramic materials for thermal barrier coatings. *Journal of the European Ceramic Society*, 24(1), 1–10. [https://doi.org/10.1016/S0955-2219\(03\)00129-8](https://doi.org/10.1016/S0955-2219(03)00129-8)
- [19] I. Gurrappa, A. Sambasiva Rao (2006) Thermal barrier coatings for enhanced efficiency of gas turbine engines. *Surface and Coatings Technology*, 201(6), 3016–3029, <https://doi.org/10.1016/j.surfcoat.2006.06.026>
- [20] M. Herrmann, H. Klemm (2014) 2.15—Corrosion of Ceramic Materials. In V. K. Sarin (Ed.), *Comprehensive Hard Materials*, p.413–446. Elsevier, <https://doi.org/10.1016/B978-0-08-096527-7.00034-9>
- [21] C. Falconer, M. Elbakhshwan (n.d.) Corrosion in Molten Salt Reactors – The UW-Madison Materials Degradation under Corrosion and Radiation (MADCOR) – UW–Madison. Retrieved July 12, 2023, from <https://madcor.labs.wisc.edu/previous-work/corrosion-in-molten-salt-reactors/>
- [22] Y. Iwadate (2014) Chapter 260—Structures and Properties of Rare-Earth Molten Salts. In J.-C. G. Bünzli & V. K. Pecharsky (Eds.), *Handbook on the Physics and Chemistry of Rare Earths*, 44, 87–168. Elsevier, <https://doi.org/10.1016/B978-0-444-62711-7.00260-7>
- [23] F. Ropital (2011) 15 - Environmental degradation in hydrocarbon fuel processing plant: Issues and mitigation. In M. R. Khan (Ed.), *Advances in Clean Hydrocarbon Fuel Processing* (pp. 437–462). Woodhead Publishing, <https://doi.org/10.1533/9780857093783.5.437>
- [24] A. Ibrahim, H. Peng, A. Riaz, M. Abdul Basit, U. Rashid, A. Basit (2021) Molten salts in the light of corrosion mitigation strategies and embedded with nanoparticles to enhance the thermophysical properties for CSP plants. *Solar Energy Materials and Solar Cells*, 219, 110768, <https://doi.org/10.1016/j.solmat.2020.110768>
- [25] X. H. Wang, Y. C. Zhou (2004) Hot Corrosion of Na₂SO₄-Coated Ti₃AlC₂ in Air at 700-1000°C. *Journal of The Electrochemical Society*, 151(9), B505. <https://doi.org/10.1149/1.1778171>
- [26] G. Liu, M. Y. Zhou (2003) Hot corrosion of Ti₃SiC₂-based ceramics coated with Na₂SO₄ at 900 and 1000 °C in air. *Corrosion Science*, 45(6), 1217–1226, [https://doi.org/10.1016/S0010-938X\(02\)00211-1](https://doi.org/10.1016/S0010-938X(02)00211-1)
- [27] N. Wu, Z. Chen, S. X. Mao (2005) Hot Corrosion Mechanism of Composite Alumina/Yttria-Stabilized Zirconia Coating in Molten Sulfate–Vanadate Salt. *Journal of the American Ceramic Society*, 88(3), 675–682, <https://doi.org/10.1111/j.1551-2916.2005.00120.x>
- [28] G. Liu, M. Li, Y. Zhou, Y. Zhang (2005) Hot corrosion behavior of Ti₃SiC₂ in the mixture of Na₂SO₄–NaCl melts. *Journal of the European Ceramic Society*, 25(7), 1033–1039, <https://doi.org/10.1016/j.jeurceramsoc.2004.04.013>
- [29] X. Xie, H. Guo, S. Gong, H. Xu (2012) Hot Corrosion Behavior of Double-ceramic-layer LaTi₂Al₉O₁₉/YSZ Thermal Barrier Coatings. *Chinese Journal of Aeronautics*, 25(1), 137–142, [https://doi.org/10.1016/S1000-9361\(11\)60372-5](https://doi.org/10.1016/S1000-9361(11)60372-5)
- [30] R. A. McCauley (2013) *Corrosion of Ceramic Materials*, Third Edition. CRC Press.

- [31] Z. Lin, Y. Zhou, M. Li, M. J. Wang. (2006) Hot corrosion and protection of Ti₂AlC against Na₂SO₄ salt in air. *Journal of the European Ceramic Society*, 26(16), 3871–3879, <https://doi.org/10.1016/j.jeurceramsoc.2005.12.004>
- [32] J. L. Trislancho-Reyes, J. G. Chacón-Nava, D. Y. Peña-Ballesteros, C. Gaona-Tiburcio, J. G. Gonzalez-Rodriguez, A. Martínez-Villafañe, F. Almeraya-Calderón (2011) Hot Corrosion Behaviour of NiCrFeNbMoTiAl Coating in Molten Salts at 700°C by Electrochemical Techniques. *International Journal of Electrochemical Science*, 6(2), 432–441, [https://doi.org/10.1016/S1452-3981\(23\)15006-1](https://doi.org/10.1016/S1452-3981(23)15006-1)
- [33] Z. Xu, L. He, R. Mu, S. He, G. Huang, X. Cao (2010) Hot corrosion behavior of rare earth zirconates and yttria partially stabilized zirconia thermal barrier coatings. *Surface and Coatings Technology*, 204(21), 3652–3661, <https://doi.org/10.1016/j.surfcoat.2010.04.044>
- [34] K. Sridharan, T. R. Allen (2013) Corrosion in Molten Salts. In F. Lantelme & H. Groult (Eds.), *Molten Salts Chemistry*, p. 241–267, Elsevier, <https://doi.org/10.1016/B978-0-12-398538-5.00012-3>
- [35] M. H. Habibi, L. Wang, S. M. Guo (2012) Evolution of hot corrosion resistance of YSZ, Gd₂Zr₂O₇, and Gd₂Zr₂O₇+YSZ composite thermal barrier coatings in Na₂SO₄+V₂O₅ at 1050°C. *Journal of the European Ceramic Society*, 32(8), 1635–1642, <https://doi.org/10.1016/j.jeurceramsoc.2012.01.006>
- [36] F. A. Costa Oliveira, D. J. Baxter (2001) Salt corrosion of a hot-pressed silicon nitride in combustion environments with different sulphur contents. *Materials at High Temperatures*, 18(1), 21–37, <https://doi.org/10.1179/mht.2001.003>
- [37] D. Brito-Hernández, I. Rosales-Cadena, J. G. González-Rodríguez, J. Uruchurtu-Chavarrín, R. Guardán-Tapia, J. G. Vera-Dimas, R. López-Sesenes (2023) Effect of zirconia in the corrosion behavior of intermetallic Mo₃Si alloy in molten salts mixture of NaNO₃ and KNO₃. *Materials and Corrosion*, 74(7), 1066–1075, <https://doi.org/10.1002/maco.202213223>
- [38] S. Li, Z. G. Liu, J. H. Ouyang. (2013) Growth of YbVO₄ crystals evolved from hot corrosion reactions of Yb₂Zr₂O₇ against V₂O₅ and Na₂SO₄+V₂O₅. *Applied Surface Science*, 276, 653–659, <https://doi.org/10.1016/j.apsusc.2013.03.149>
- [39] L. Guo, M. Li, F. Ye (2016) Comparison of hot corrosion resistance of Sm₂Zr₂O₇ and (Sm_{0.5}Sc_{0.5})₂Zr₂O₇ ceramics in Na₂SO₄+V₂O₅ molten salt. *Ceramics International*, 42(12), 13849–13854. <https://doi.org/10.1016/j.ceramint.2016.05.190>
- [40] L. Guo, C. Zhang, M. Li, W. Sun, Z. Zhang, F. Ye (2017) Hot corrosion evaluation of Gd₂O₃-Yb₂O₃ co-doped Y₂O₃ stabilized ZrO₂ thermal barrier oxides exposed to Na₂SO₄+V₂O₅ molten salt. *Ceramics International*, 43(2), 2780–2785, <https://doi.org/10.1016/j.ceramint.2016.11.109>
- [41] J. Wang, J. Sun, B. Zou, X. Zhou, S. Dong, L. Li, J. Jiang, L. Deng, X. Cao- (2017) Hot corrosion behaviour of nanostructured zirconia in molten NaVO₃ salt. *Ceramics International*, 43(13), 10415–10427, <https://doi.org/10.1016/j.ceramint.2017.05.077>
- [42] Y. Ozgurluk, K. Doleker, D. Ozkan, H. Ahlatci, A. Karaoglanli (2019) Cyclic Hot Corrosion Failure Behaviors of EB-PVD TBC Systems in the Presence of Sulfate and Vanadate Molten Salts. *Coatings*, 9(3), 166, <https://doi.org/10.3390/coatings9030166>
- [43] S. H. Cho, S. W. Kim, D. Y. Kim, J. H. Lee, J. M. Hur. (2017) Hot corrosion behavior of magnesia-stabilized ceramic material in a lithium molten salt. *Journal of Nuclear Materials*, 490, 85–93, <https://doi.org/10.1016/j.jnucmat.2017.04.012>
- [44] X. Fan, R. Sun, J. Dong, L. Wei, Q. Wang (2021) Effects of sintering additives on hot corrosion behavior of γ-Y₂Si₂O₇ ceramics in Na₂SO₄+V₂O₅ molten salt. *Journal of the European Ceramic Society*, 41(1), 517–525, <https://doi.org/10.1016/j.jeurceramsoc.2020.08.068>
- [45] C. Zhang, M. Li, Y. Zhang, L. Guo, J. Dong, F. Ye, L. Li, V. Ji (2017) Hot corrosion behavior of (Gd_{0.9}Sc_{0.1})₂Zr₂O₇ in V₂O₅ molten salt at 700–1000 °C. *Ceramics International*, 43(12), 9041–9046, <https://doi.org/10.1016/j.ceramint.2017.04.048>
- [46] H. Liu, J. Cai, J. Zhu (2019) Hot Corrosion Behavior of BaLa₂Ti₃O₁₀ Thermal Barrier Ceramics in V₂O₅ and Na₂SO₄ + V₂O₅ Molten Salts. *Coatings*, 9(6), 351, <https://doi.org/10.3390/coatings9060351>
- [47] W. B. Kim, S. C. Kwon, S. H. Cho, J. H. Lee (2020) Effect of the grain size of YSZ ceramic materials on corrosion resistance in a hot molten salt CaCl₂-CaF₂-CaO system. *Corrosion Science*, 170, 108664. <https://doi.org/10.1016/j.corsci.2020.108664>
- [48] S. Gu, S. Zhang, Y. Jia, W. Li, J. Yan (2017) Evaluation of hot corrosion behavior of SrHfO₃ ceramic in the presence of molten sulfate and vanadate salt. *Journal of Alloys and Compounds*, 728, 10–18, <https://doi.org/10.1016/j.jallcom.201708.279>
- [49] X. Zhou, Z. Xu, L. He, J. Xu, B. Zou, X. Cao (2016) Hot corrosion behavior of LaTi₂Al₉O₁₉ ceramic exposed to vanadium oxide at temperatures of 700–950 °C in air. *Corrosion Science*, 104, 310–318, <https://doi.org/10.1016/j.corsci.2015.12.024>
- [50] J. Zhang, J. Huang, R. Liu, G. Luo, Q. Shen (2021) Corrosion behaviour of AlN ceramics in LiF-LiCl-LiBr-Li molten salt at 500 °C. *Corrosion Science*, 190, 109672, <https://doi.org/10.1016/j.corsci.2021.109672>
- [51] F. Jiang, L. Cheng, Y. Wang, X. Huang (2017) Hot corrosion behaviour of barium-strontium aluminosilicates in a molten Na₂SO₄ environment. *Journal of the European Ceramic Society*, 37(2), 823–832, <https://doi.org/10.1016/j.jeurceramsoc.2016.09.007>
- [52] S. Gu, S. Zhang, Y. Jia, W. Li, J. Yan (2017) Evaluation of hot corrosion behavior of SrHfO₃ ceramic in the presence of molten sulfate and vanadate salt. *Journal of Alloys and Compounds*, 728, 10–18. <https://doi.org/10.1016/j.jallcom.2017.08.279>

- [53] A. Shamsipoor, M. Farvizi, M. Razavi, A. Keyvani, B. Mousavi, W. Pan (2021) Hot corrosion behavior of Cr₂AlC MAX phase and CoNiCrAlY compounds at 950 °C in presence of Na₂SO₄+V₂O₅ molten salts. *Ceramics International*, 47(2), 2347–2357, <https://doi.org/10.1016/j.ceramint.2020.09.077>
- [54] Y. Ozgurluk, K. M. Doleker, A. C. Karaoglanli (2018) Hot corrosion behavior of YSZ, Gd₂Zr₂O₇ and YSZ/Gd₂Zr₂O₇ thermal barrier coatings exposed to molten sulfate and vanadate salt. *Applied Surface Science*, 438, 96–113, <https://doi.org/10.1016/j.apsusc.2017.09.047>
- [55] Y. Hui, S. Zhao, J. Xu, B. Zou, Y. Wang, X. Cai, L. Zhu, X. Cao (2016) High-temperature corrosion behavior of zirconia ceramic in molten Na₂SO₄+NaVO₃ salt mixture. *Ceramics International*, 42(1), 341–350, <https://doi.org/10.1016/j.ceramint.2015.08.116>
- [56] L. Guo, C. Zhang, Q. He, J. Yu, Z. Yan, F. Ye, C. Dan, V. Ji (2018) Microstructure evolution and hot corrosion mechanisms of Ba₂REAlO₅ (RE = Yb, Er, Dy) exposed to V₂O₅ + Na₂SO₄ molten salt. *Journal of the European Ceramic Society*, 38(10), 3555–3563, <https://doi.org/10.1016/j.jeurceramsoc.2018.03.047>
- [57] Y. Zhang, B. Zou, X. Cai, Y. Wang, X. Cao (2020) Hot corrosion behavior of Yb₂Si₂O₇ ceramic under NaVO₃ salt attack. *Ceramics International*, 46(3), 2618–2623, <https://doi.org/10.1016/j.ceramint.2019.09.070>[58]

IZVOD

PREGLJED KOROZIONOG PONAŠANJA KERAMIČKIH MATERIJALA U OKRUŽENJIMA RASTOPLJENE SOLI

Ova studija je pregledala prethodne studije između 2015. i 2021. o tome kako su keramički materijali degradirali u prisustvu rastopljene soli. Takođe, ispitani su procesi otpornosti na koroziju različitih keramičkih kompozicija izloženih različitim sastavima rastopljene soli i temperaturama. Rezultati nude važne nove uvide u varijable koje utiču na koroziono ponašanje keramike i proizvodnju proizvoda korozije. Prijavljeni rezultat otkriva da je keramički materijal sastava (Sm_{0.5}Sc_{0.5})₂Zr₂O₇ imao bolji učinak od Sm₂Zr₂O₇ u pogledu otpornosti na toplu koroziju u rastopljenoj soli (V₂O₅ + Na₂SO₄). Takođe, prijavljeno je da na ponašanje korozije utiče veličina čestica. Značajno je da je cirkonijum (n-ISZ) sa veličinom zrna na nanoskali bio podložniji vrućoj koroziji, što se objašnjava povećanim specifičnim površinama. S druge strane, utvrđeno je da sinterovanje i aditivi povećavaju otpornost na koroziju. Otpornost I-I₂Si₂O₇ keramike na koroziju u (V₂O₅ + Na₂SO₄) rastopljenoj soli je poboljšana dodatkom glinice. Rezultati ovih istraživanja pomažu nam da razumemo kako korozija funkcioniše i šta utiče na podložnost keramičkih materijala propadanju u rastopljenim slanim medijima. Ove informacije mogu da usmere stvaranje keramičkih materijala otpornijih na koroziju za upotrebu u okruženjima sa visokim temperaturama ili energetskim sistemima na bazi rastopljene soli, između ostalih korozivnih upotreba.

Ključne reči: vruća korozija, glinica, izmenjivači toplote, nitridi, cirkonijum

Pregledni rad

Rad primljen: 08.08.2023.

Rad prihvaćen: 22.09.2023.

Rad je dostupan na sajtu: www.idk.org.rs/casopis

Vijayalakshmi K. Arumugam^{1*}, Judith Fennila¹,
Thangavel K. Maheswar²

¹Department of Physics, Sri Vasavi College, Erode -638316, India

²Department of Electrical and Electronics Engineering, Bannari Amman
Institute of Technology, Sathyamangalam, Erode-638402, India

Scientific paper

ISSN 0351-9465, E-ISSN 2466-2585

<https://doi.org/10.62638/ZasMat1123>



Zastita Materijala 65 (2)

213 - 219 (2024)

Blend of low cost electrode material for energy storage device under DC glow discharge plasma exposed ESAC

ABSTRACT

The waste biomass in the form of eucalyptus globulus seeds activated carbon, which is employed as the electrode material and is environmentally acceptable, provides the good specific capacitance in the current work which is used for the energy storage application. A sample carbonization and physical activation procedure was used to create the activated carbon from the eucalyptus seeds. As prepared activated carbon was exposed to a DC glow discharge plasma, which modifies the surface of the material without altering its core characteristics. The investigation of the activated carbon was done utilizing structural, morphological, and electrochemical techniques of both pure and plasma treated. The increasing intensity of the X-ray diffraction indicates the carbon's amorphous and disorderly character. More oxygen-containing functional groups are present, according to an FTIR analysis. The FESEM/EDAX investigation has demonstrated the less appearance and more graphitic porosity with random orientation. Moreover, the electrochemical investigations were examined for utilization of the material of Electrochemical Impedance Spectroscopy (EIS) and Galvanostatic charge-discharge (GCD) which has a specific capacitance of 150F/g for a 1.5mA/g current density. The results revealed that the activated carbon made from Eucalyptus seeds after plasma treatment has good surface characteristics, improved specific capacitance, and is a low-cost electrode material for fabrication of energy storage device.

Keywords: Eucalyptus seeds, Activated carbon, Plasma treatment, Surface modification, Specific capacitance

1. INTRODUCTION

Now a day's energy storage device has been recent trends in the modern world where the world is depending on the energy sources. The focus of energy research has turned to advancing the development of sustainable and renewable energy sources due to the ever-increasing global energy demand, the decreasing availability of fossil fuels, and increasing environmental issues[1]. To full fill the next generation requirements its need, a major improvement in the energy density and cyclic life of present energy storage device. Batteries have exploring innovative energy material and associated high energy density storage for longer time period in order towards archiving its goal in the

energy storage system[2]. Recently, bio-mass, which is primarily agricultural waste, has become a different source of porous carbon and has been used in energy storage technologies. Here activated carbon derived from the Eucalyptus seeds serves as the good carbon material for the energy storage application. This Eucalyptus seeds activated carbon (ESAC) was undergoes the pyrolysis carbonization with the physical activation[3]. The ESAC was investigated using the structural and morphological characteristics, which observes that the carbon has the more porous morphology, whereas the electrochemical investigation shows the energy density of the material. The as prepared electrode of ESAC undergoes the electrochemical studies such as EIS and GCD to check the electrical conductivity of the material and the specific capacitance and cyclic stability and power density of the ESAC electrode material. On this results, we make an effort to present a summary of the most recent developments in the use of carbons obtained from

*Corresponding author: K A Vijayalakshmi

E-mail: kavijayalakshmi@yahoo.com

Paper received: 28. 09. 2023.

Paper accepted: 07. 11. 2023.

Paper is available on the website: www.idk.org.rs/journal

the ESAC biomass as electrodes for new rechargeable batteries[4].

1.1. Plasma Introduction

The fourth state of matter is called a plasma, which is made up of extremely excited atoms, molecules, ions, and free radical species. Recently, plasma processing has taken over as the main source for altering a material's surface without affecting its fundamental qualities or bulk characteristics[5]. Plasma modification is used to create certain functional groups that can interact with other groups, change the surface's free energy, increase its ability to resist corrosion, alter its porous morphology, remove contaminants, or create cross-linking. The plasma surface modification could lead to the development of interaction of the carbon material with the increase and formation of new covalent bonds in the functional groups[6]. Along with this the adhesion strength, wettability and biocompatibility are also enhanced. When carbon materials are subjected to plasma treatment, the most significant features that can alter are an increase in surface area compared to untreated carbon materials. Normally, carbon is hydrophobic however, after plasma treatment, ESAC's wettability transforms to hydrophilic[7]. The as prepared carbon electrode material has the increased wettability of hydrophilic nature which have the redox behavior and the transfer of electrons. Thus the specific capacitance of carbon material can be improved by adding some more oxygen containing molecules in to the carbon

framework. It has been shown that after air plasma treatment addition of oxygen containing groups to carbon based material can increase the capacitance, improve surface wettability and to some extent boost electrical conductivity[8].

2. MATERIALS AND METHODS

2.1. Materials

The eucalyptus seed was viewed as the activated carbon's primary raw source. This raw materials were gathered in the Niligris area which serves as the basic resource. Before beginning the carbonization process, the raw material was cleaned several times with distilled water, dried in the sun, and then roughly crushed with a mortar and pestle to break up the globulus (spherical) shape for an easier carbonization process.

2.2. Carbonization

The pyrolysis method was used to carbonize the dried eucalyptus seed for an hour in a muffle furnace at a temperature of about 400°C at the heating temperature of 5°C/min. The hard carbonized particles were crushed into nanoparticle size using a mortar and pestle.

2.3. Activation

Followed by the carbonization process the nanoparticles sized carbon material undergoes the physical activation process in the same muffle furnace for about 600°C for an hour at the heating temperature of about 5°C/minute [9] shown in fig.1

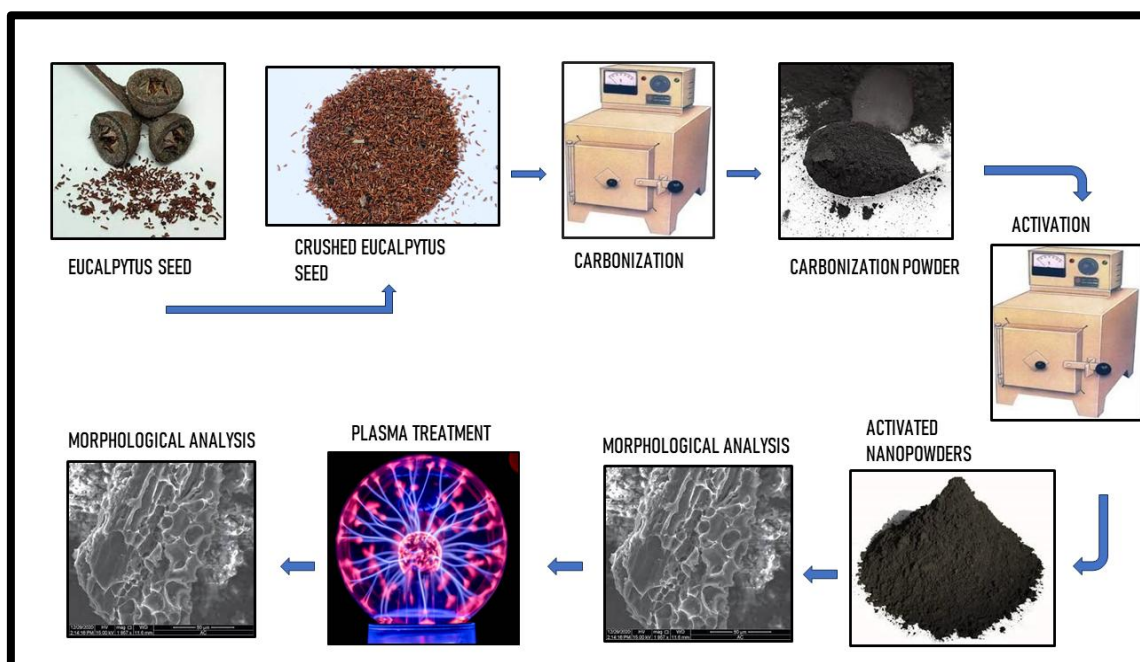


Figure 1. Schematic diagram of synthesized ES nanoparticles

Slika 1. Sematski dijagram sintetizovanih ES nanočestica

2.4. Plasma processing

The plasma chamber consist of two aluminum electrodes, a Pirani gauge power source, and stainless steel chamber 50*30-diameter gas valve which are all included. Using acetone and distilled water, the entire chamber was cleaned. The activated ES was collected in a sample holder that was sandwiched between two electrodes that were spaced 6 cm apart. The operatory parameters of DC glow discharge plasma is of about 450 V and 0.03 mbar pressure were used to create the atmospheric air plasma.

2.5. Electrode preparation

In order to get the active electrode material of ESAC, air plasma treated ESAC were developed by mixing as-prepared nanoparticles carbon black, and poly vinylidene difluoride (PVDF) were mixed in a mass ratio of 80:10:10 with 0.3 mL of N-methyl 2-pyrrolidone (NMP) to obtain the homogeneous slurry mixture. In a hot air oven, the active electrode was dried for three hours at 60 °C. Ag/AgCl and platinum act as the reference electrode and counter electrode. In a three-electrode configuration. The untreated ESAC and the plasma treated ESAC was used as the working electrode.

2.6. Characterization

The formation of the crystalline structure was investigated using XRD (XPERT-PRO with CuK

radiation).By using the Shimadzu 8400S FT-IR Spectroscopy instruments functional groups was analyzed. The crystal surface morphology was examined using a JEOL version JSM 6390LV, and the components and component ratios were verified using a JEOL version JED-2300 for EDAX technique. Three electrode systems were utilized to test the electrochemical properties with the PG LITE 1.0 electrochemical apparatus.

3. RESULT AND DISCUSSION

3.1. XRD (X- ray diffraction)

Fig. 2(A) displays the XRD patterns of the ESAC, These broad peaks for the activated carbon are located at around 23°, which corroborate the amorphous properties and disordered nature of the carbon due to (002) with the plane that indicates the graphitic nature[10]. Following the plasma treatment, the ESAC's intensity was proceed to increase without changing its basic properties[11]. By applying the Debye-Scherrer (Eq. 1), which determine the crystalline size between 30 to 40nm.

$$D = K\lambda/\beta \cos \theta \quad (1)$$

Along with this, the ESAC material's micro strain lies between 0.0081 to 0.01 and dislocation density ranges from 0.000170 to 0.020 was observed.

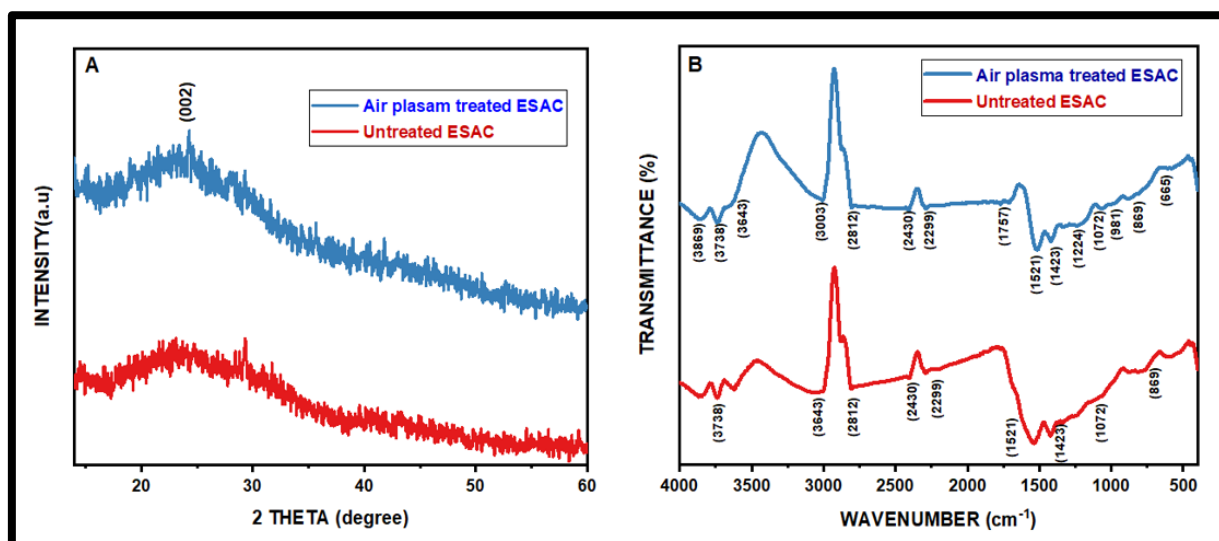


Figure 2. (a) The XRD diffraction peaks and (b) The FTIR spectra of untreated and plasma treated ESAC

Slika 2. (a) XRD difrakcioni pikovi i (b) FTIR spektri netretiranog i ESAC tretiranog plazmom

3.2. FTIR (Fourier Transform infrared spectroscopy)

The FTIR spectra of untreated ESAC was investigated which is ranging from 4000cm⁻¹to

400cm⁻¹ shown in fig 2(B). The peak at 3738 cm⁻¹-3643cm⁻¹ in the spectra is due to the stretching vibrations of the carboxylic group's O-H bond. The vibration band at 2812cm⁻¹ corresponds to the

methyl and methylene groups. The vibration peaks corresponds from 2430cm^{-1} to 2299cm^{-1} are assigned to the stretching of C-H mode[12]. The peaks ranging from 1521cm^{-1} to 1072cm^{-1} observed as stretching vibration of C=O as the carboxyl and carbonyl groups along with the aromatic ring, at 869cm^{-1} as C-H stretching. But after the air plasma treatment the increase in wettability has more polar region with covalent bonds. Thus shows the 3869cm^{-1} of O-H stretching of bonds and 3003cm^{-1} to 2812cm^{-1} has the carboxylic acid, phenols and alcohol groups. The peak at 1757cm^{-1} has the C=C aromatic ring. The vibration peaks ranging from 981cm^{-1} to 665cm^{-1} has the weak band of aromatic rings of C-H groups [13]. The material's surface area helps by supplying more active sites for adsorption peaks in the ESAC material.

3.3. FESEM (Field Emission Scanning Electron Microscope)

As shown in (Fig. 3).with the FESEM image of pure ESAC and the plasma treated, the ESAC is

created as a byproduct of the conversion of cellulose, hemicellulose, and lignin by the process of structural disordering of the remaining carbon. (Fig 3a) shows the no pores for the untreated ESAC whereas for the Air plasma treated ESAC the (Fig. 3b, 3c) shows the more porous and open porous as a result of the interaction of the free radicals with the ESAC, which has good morphology. The porous construction may offer a large number of pores, which would help to improve electrolyte ion transfer and thus increase the surface area. The quantity and type of oxygen-containing surface groups which remains almost constant throughout the activation process, but after the plasma treatment, the number of oxygen-containing groups increases. Additionally, the EDAX investigations reveals that elemental makeup of untreated and air plasma treated ESAC, which adds to the carbon and oxygen content of different levels and peaks. In this results, there is 82% of carbon and 18% of oxygen present in the air plasma treated sample (Fig. 3d, 3e).

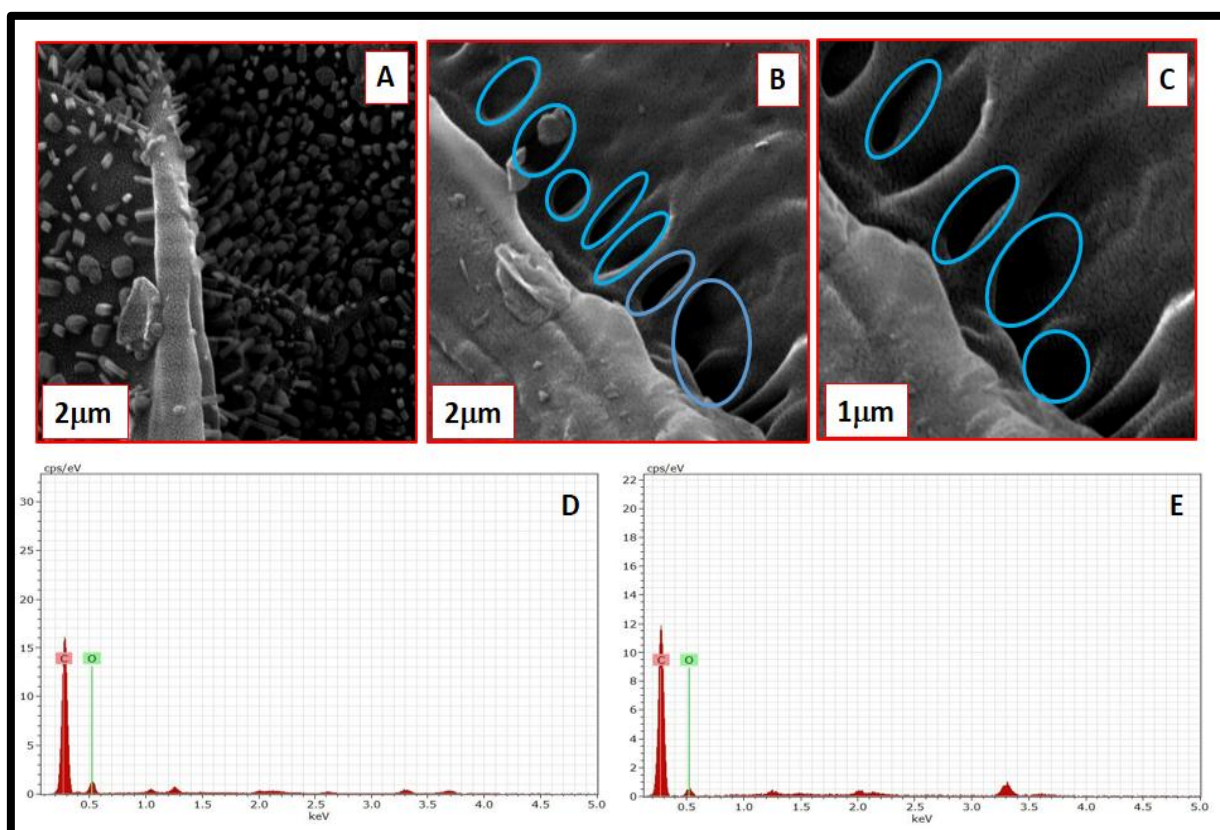


Figure 3. The FESEM /EDAX images (a) The untreated ESAC, (b) The air plasma treated ESAC, (c) The EDAX for untreated and (d) the air plasma treated ESAC

Slika 3. FESEM/EDAX slike (a) Netretirani ESAC, (b) ESAC tretiran vazdušnom plazmom, (c) EDAX za neobrađeni i (d) ESAC tretiran vazdušnom plazmom

ELECTROCHEMICAL INVESTIGATION

3.4. EIS (Electrostatic Impedance Spectroscopy)

In general, real- Z' and imaginary- Z'' value were carried out by electrochemical impedance analysis (EIS) for the Nyquist plot. The electrodes of both untreated and plasma-treated ESAC were examined using a 0.1MHz to 100 KHz frequency window, illustrated in (Fig.4). To describe Polarization Resistance (R_s) and Charge Transfer

Resistance (R_{ct}), the Nyquist plot indicates that the untreated ESAC in the frequency range is not a well-defined semicircle. However, after plasma treatment, the appropriate semicircle is a result of the charge transfer resistance, which suggests good charge conductivity. The equivalent polarisation resistance and the charge transfer resistance are calculated from the graph as for R_s 269 Ω and 1041 Ω for untreated ESAC and R_{ct} 103 Ω and 227 Ω for air plasma treated ESAC [14]-[15].

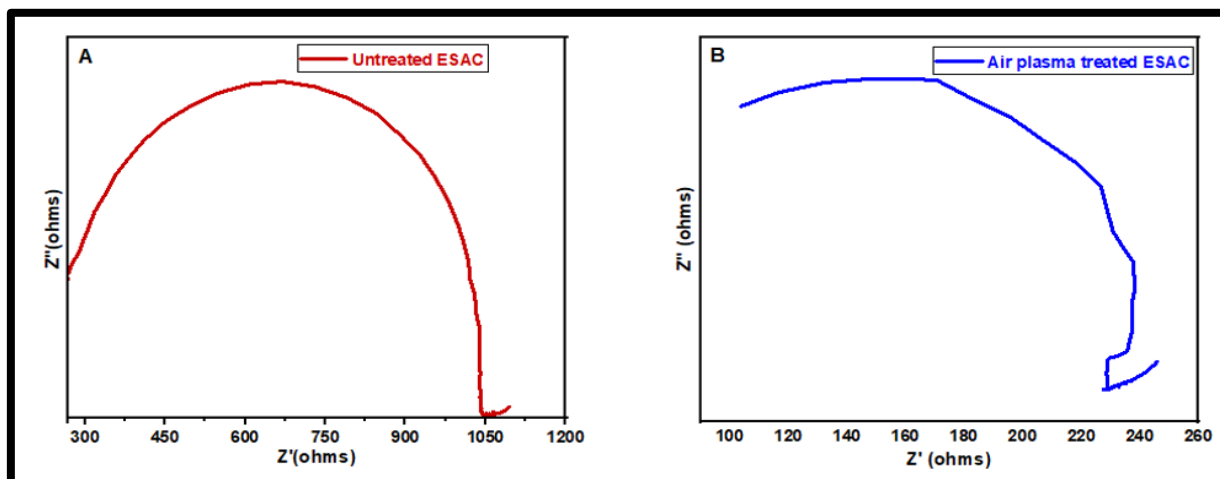


Figure 4. The EIS result (a) untreated electrode material ESAC and (b) The Air plasma treated ESAC electrode material

Slika 4. Rezultat EIS (a) neobrađen elektrođni materijal ESAC i (b) ESAC elektrođni materijal tretiran vazdušnom plazmom

3.5. GCD (Galvanostatic charge-discharge)

To further understand the electrochemical behavior the galvanostatic charge and discharge has been investigated using a three electrode system in 2M of KOH with potentials ranging from 0

to 0.5V and different current densities. The specific capacitance was investigated using the formula

$$C = \frac{I \cdot \Delta t}{M \cdot \Delta V} \quad (2)$$

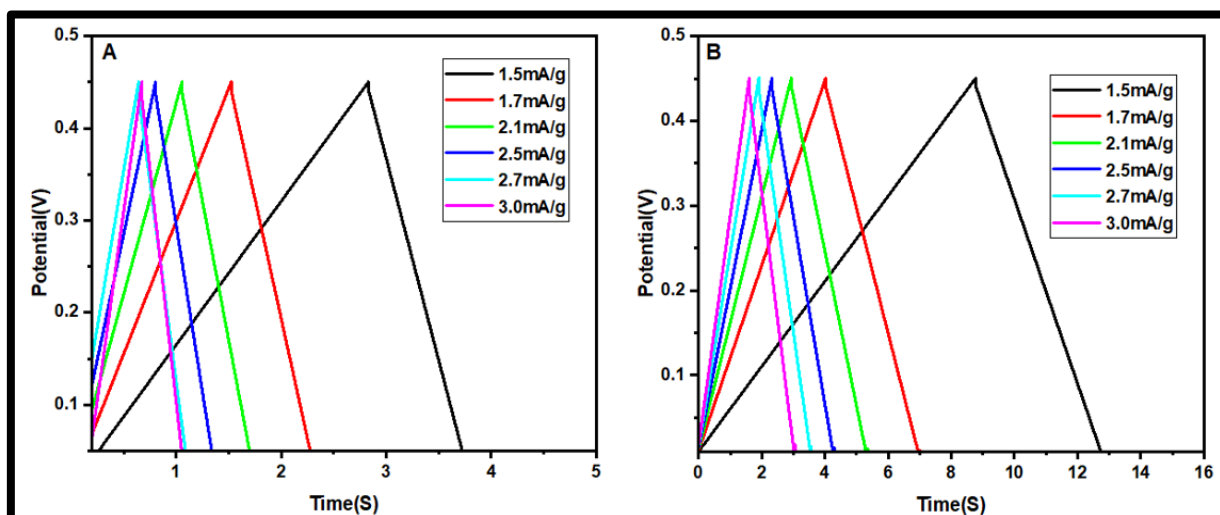


Figure 5. The GCD profile. (a) The untreated of ESAC and (b) The Air plasma treated ESAC electrode
Slika 5. Profil GCD. (a) Netretirana ESAC elektroda i (b) ESAC elektroda tretirana vazdušnom plazmom

The GCD profile in the figure 5 shows the current densities ranging from 1.5mA/g, 1.7mA/g, 2.1mA/g, 2.5mA/g, 2.7mA/g, 3.0mA/g. The specific capacitance has been calculated for both the electrodes of untreated and plasma treated ESAC, the untreated electrode shows the specific capacitance value of about 208F/g, 140F/g, 97F/g, 80F/g, 71F/g, 64F/g and [16], the plasma treated electrode shows the specific capacitance of about 613F/g, 444F/g, 375F/g, 350F/g, 323F/g thus the plasma treated ESAC electrode material due to its enhanced functional groups and the greater porous in the surface which render the material to hydrophilic nature and the plasma treatment thus increases the specific capacitance.

4. CONCLUSION

It was possible to create an activated carbon using the method of carbonizing and activating ESAC. The structural and morphological characteristics were investigated for both untreated and air plasma treated ESAC. The plasma treatment results in the formation of new functional groups that enhance the wettability, adhesion, and biocompatibility. The electrochemical results in the specific capacitance of 613F/g with the current density of 1.5 mA/g for KOH electrolyte. Thus it clearly shows how the plasma-treated carbon material improves in all of the aforementioned investigations and exhibits good electrochemical performance as well as environmental friendliness and economic viability.

5. REFERENCE

- [1] R.Thangavel, A.G.Kannan, R.Ponraj, V.Thangavel, D. W. Kim, Y. S. Lee (2018) High-energy green supercapacitor driven by ionic liquid electrolytes as an ultra-high stable next-generation energy storage device, *J. Power Sources*, 383, 102–109. doi 10.1016/j.jpowsour.2018.02.037.
- [2] G.S.Dos Reis, S.H.Larsson, H.P. de Oliveira, M. Thyrel, E. C. Lima.(2020) Sustainable biomass activated carbons as electrodes for battery and supercapacitors—a mini-review, *Nanomaterials*, 10(7), 1–22. doi 10.3390/nano10071398
- [3] S.P.Chand, A.Joshi (2021) Biomass derived carbon for supercapacitor applications: Review. *J. Energy Storage*, 39, 102646. doi 10.1016/j.est.2021.102646
- [4] A.Pistone, C.Espro (2020) Current trends on turning biomass wastes into carbon materials for electrochemical sensing and rechargeable battery applications *Curr. Opin. Green Sustain. Chem.*, 26, 100374. doi 10.1016/j.cogsc.2020.100374.
- [5] R.K.Gupta, M.Dubey, P.Kharel, Z.Gu, Q.H.Fan (2015) Biochar activated by oxygen plasma for supercapacitors, *J. Power Sources*, 274, 1300–1305. doi:10.1016/j.jpowsour.2014.10.169
- [6] C.Saka (2018) Overview on the Surface Functionalization Mechanism and Determination of Surface Functional Groups of Plasma Treated Carbon Nanotubes, *Crit. Rev. Anal. Chem.*, 48(1), 1–14. doi:10.1080/10408347.2017.1356699.
- [7] R.Wolf, A.C.Sparavigna (2010) Role of Plasma Surface Treatments on Wetting and Adhesion, *Engineering*, 02(06), 397–402. doi: 10.4236/eng.2010.26052.
- [8] W.M.Chang, C.C.Wang, C.Y.Chen (2015) Plasma Treatment of Carbon Nanotubes Applied to Improve the High Performance of Carbon Nanofiber Supercapacitors, *Electrochim. Acta*, 186, 530–541. doi: 10.1016/j.electacta.2015.11.038
- [9] C.Grima-Olmedo, R.Gómez, D.Gómez-Limón, C. Clemente-Jul (2016) Activated carbon from flash pyrolysis of eucalyptus residue, *Heliyon*, 2(9), 1-18. doi: 10.1016/j.heliyon.2016.e00155.
- [10] S.J.Rajasekaran, V.Raghavan (2020) Facile synthesis of activated carbon derived from Eucalyptus globulus seed as efficient electrode material for supercapacitors, *Diam. Relat. Mater.*, 109, 108038. doi 10.1016/j.diamond.2020.108038.
- [11] K.A.Vijayalakshmi, K.Vignesh, N.Karthikeyan. (2015) Synthesis and surface characterization of bamboo charcoal carbon using low temperature plasma treatment, *Mater. Technol.*, 30(A2), A99–A103. doi 10.1179/17535557A15Y.000000005.
- [12] S.Mopoung, N.Dejang (2021) Activated carbon preparation from eucalyptus wood chips using continuous carbonization–steam activation process in a batch intermittent rotary kiln, *Sci. Rep.*, 11(1),1–9. doi 10.1038/s41598-021-93249-x.
- [13] S.Saveetha, K.A.Vijayalakshmi (2021) Influence of Low temperature Plasma on activated bamboo charcoal employed in energy storage system, 16(1001), 12–22. <https://doi.org/10.37896/jxu16.6/002>.
- [14] D. Jain, J. Kanungo, S. K. Tripathi (2020) Enhancement in performance of supercapacitor using eucalyptus leaves derived activated carbon electrode with CH₃COONa and HQ electrolytes: A step towards environment benign supercapacitor, *J. Alloys Compd.*, 832, 154956. doi 10.1016/j.jallcom.2020.154956
- [15] E.Adhamash et al. (2020) High-energy plasma activation of renewable carbon for enhanced capacitive performance of supercapacitor electrode, *Electrochim. Acta*, 362, 1-9, doi: 10.1016/j.electacta.2020.137148
- [16] Y.Wen, L.Chi, K.Wenelska, X.Wen, X.Chen, E. Mijowska (2020) Eucalyptus derived heteroatom-doped hierarchical porous carbons as electrode materials in supercapacitors, *Sci. Rep.*, 10(1),1–12 doi:10.1038/s41598-020-71649-9

IZVOD

MEŠAVINA JEFTINOG ELEKTRODNOG MATERIJALA ZA UREĐAJ ZA SKLADIŠTENJE ENERGIJE ISPOD ESAC-A IZLOŽENOG DC SJAJNOM PRAŽNENJU PLAZMI

Otpadna biomasa u vidu aktivnog uglja semena eukaliptusa globulosa, koji se koristi kao materijal elektrode i ekološki prihvatljiv, obezbeđuje dobar specifični kapacitet u trenutnom radu koji se koristi za primenu za skladištenje energije. Korištena je procedura karbonizacije uzorka i fizičke aktivacije za stvaranje aktivnog uglja iz semena eukaliptusa. Kao pripremljen, aktivni ugalj je bio izložen DC usijanoj plazmi, koja modifikuje površinu materijala bez promene njegovih osnovnih karakteristika. Ispitivanje aktivnog uglja je obavljeno korišćenjem strukturnih, morfoloških i elektrohemijskih tehnika, kako čistih tako i tretiranih plazmom. Povećani intenzitet difrakcije rendgenskih zraka ukazuje na amorfnu i neuređeni karakter ugljenika. Prisutno je više funkcionalnih grupa koje sadrže kiseonik, prema FTIR analizi. FESEM/EDAKS istraživanje je pokazalo manji izgled i veću grafitnu poroznost sa nasumičnom orijentacijom. Štaviše, elektrohemijska ispitivanja su ispitana za korišćenje materijala elektrohemijske impedansne spektroskopije (EIS) i galvanostatskog pražnjenja-pražnjenja (GCD) koji ima specifičnu kapacitivnost od 150F/g za gustinu struje od 1,5mA/g. Rezultati su otkrili da aktivni ugalj napravljen od semena eukaliptusa nakon tretmana plazmom ima dobre površinske karakteristike, poboljšanu specifičnu kapacitivnost i da je jeftin elektrodni materijal za izradu uređaja za skladištenje energije.

Ključne reči: seme eukaliptusa, aktivni ugalj, tretman plazmom, modifikacija površine, specifična kapacitivnost.

Naučni rad

Rad primljen: 28.09.2023.

Rad prihvaćen: 07.11.2023.

Rad je dostupan na sajtu: www.idk.org.rs/casopis

Naima Hadjadj^{1,2}, Bendaoud Mebarek³,
Yassine El Guerri⁴, Mourad Keddam⁵

¹Département Sciences de la Matière, Faculté des Sciences et Technologie, Université de Tissemsilt, BP 182, 38000 Tissemsilt, Algérie, ²Laboratoire d'Etudes Physique des Matériaux, Université des Sciences et de Technologies USTO-MB, BP 1505 El M'Naouar, Oran, Algérie, ³Laboratoire de Recherche en Intelligence Artificielle et Systèmes (LRIAS), University of Tiaret, Algeria, ⁴Research laboratory of industrial technologies, University of Tiaret, Algeria, ⁵Laboratoire de Technologie des Matériaux, Faculté de Génie Mécanique et Génie des Procédés, USTHB, B.P No. 32, 16111, El-Alia, Bab-Ezzouar, Alger, Algérie

Scientific paper

ISSN 0351-9465, E-ISSN 2466-2585

<https://doi.org/10.62638/ZasMat1125>



Zastita Materijala 65 (2)
220 - 235 (2024)

Dybkov model for the estimation of boron diffusion in the FeB/Fe₂B bilayer on AISI 316 steel

ABSTRACT

The aim of this work is to apply three models to simulate the boron diffusion in AISI 316 steel, with an approach based on classical mass balance equations, the Dybkov model and the integral method. From the numerical solutions of both models, the predicted values of layers' thicknesses have been compared to the experimental results. In addition, in order to improve the predictability of the two models, it is necessary to find precise measurements on the diffusion of boron in each phase. The comparison of experimental and theoretical results allows us to confirm the validity of both models. After validation, the root mean square error and the diffusion coefficient were calculated to achieve good performance and better accuracy. The comparison of the results from the two simulation models with confronted with the experimental data to verify the validity of this theoretical study. Finally, the comparison of the derived results gave the values of the root mean square error equal to 1.6 μm for Fe₂B and 0.75 μm for FeB.

Keywords: Boriding, diffusion, Iron borides, Dybkov model, Integral method

1. INTRODUCTION

The purpose of treating materials is to improve or modify the mechanical and physical properties of a part [1-2], electrical conductivity, resistance to wear or friction, etc., to control its performance, resistance to corrosion, solidity, and to improve its external appearance [3]. The treatment of a material increases the life of a product [2].

For this reason, several processes have been developed to give the active surfaces of mechanical parts optimal properties in relation to the conditions of their use in service [1-4]. Among these surface treatments, emphasis may be put into the thermochemical treatments which include (nitriding, carburizing and boriding) [2].

The boriding treatment used to achieve hard layers that withstand wear and corrosion [2]. It can be carried out either in solid, liquid or gaseous phase [4].

The borides that are produced have interesting physico-chemical and mechanical properties for different industrial applications [1,5]. Single-phase or two-phase boride layers can be produced with this technique [6]. The thermochemical method of boriding hardening can be applied to many ferrous, non-ferrous and cermet materials [1,2]. The process involves the diffusion of boron atoms into the base metal lattice by forming a hard interstitial boron compound on the surface [7].

The boriding process is based on a two-step reaction; the first step occurs between the boron source and the treated material [2,3]. Depending on time and temperature, the second step generates a boride layer at the substrate surface [8] by thermal diffusion.

The boride layer can be either mono-phased or bi-phased [9]. The morphology of the layers can be tooth shaped or planar depending on the alloying elements present in the steel [1,10]. For carbon steel, the diffusion of boron atoms into the substrate gives rise to the formation of a (boride layers/substrate) interface with saw-tooth morphology [2]. For the high alloy steels, the generated (boride layer/substrate) interface tend to flatten [1-3].

Corresponding author: Naima Hadjadj

E-mail: naima.hadjadj@univ-tissemsilt.dz

Paper received: 27. 09. 2023.

Paper accepted: 15. 11. 2023.

Paper is available on the website: www.idk.org.rs/journal

Like all thermochemical surface treatments, boriding can be carried out by various processes and techniques in a solid medium in powders or with pastesor in a gaseous medium [11].

Powder boriding is realized in a temperature range between 1100-1300 K and a boriding time ranging from 2 to 24 hours [12]. In powder boriding, parts are placed in cases filled with powder and inserted into muffle furnaces. The advantages of such a process are, is the ability of changing the composition of the mixture powder [1,13].

Boriding provides a hardness gradient decreasing from the surface to the material core [14]. The hardness is much higher than that achieved through any other surface hardening process[15]. The combination of high hardness and low coefficient of friction improves the properties of resistance to fatigue, abrasion and wear [1,15]. Other benefits associated with boriding are retainingof hardness at elevated temperature, corrosion resistance in an acidic environment, and reduction in the use of lubricants [2,16].

The thickness of the resulting layer varies from 50 to 350 μm . This treatment makes it possible to obtain a very high surface hardness: from 1800 to 2000 HV for non-alloy steels, and up to 4000 HV for certain titanium alloys [1,2,17].

The thickness and proportion of each of the two borides depend on the chemical composition of the boriding medium, the temperature and the holding time[13,18].

Boron coatings are often developed on steels or iron to give them better resistance to corrosion and erosion[1,19]. Very hard layers of iron borides (FeB, Fe₂B) are formed on the surface of these materials [1,2]. FeB is harder than Fe₂B, but it is more brittle and more easily fractured during impact[1,2,20]. The structures of FeB and Fe₂B were known to be interstitial, FeB is orthorhombic and Fe₂B phase crystallizes in a body-centered tetragonal structure[21].

Several researchers have carried out the modeling of boriding kinetics among them, Keddami et al [22, 23] who presented a simple model and the integral method to simulate the boriding kinetics in powders. With the integral diffusion model, one can determine the diffusion coefficients of boron in the FeB and Fe₂B layers and predict their thicknesses. Two different models have been proposed by Campos et al [24], their first model was based on artificial intelligence with the use of an artificial neural network and the second one used the least square approach. The alternative method called pulsed direct current powder boriding (PDCPB) process was also presented in [25]. To study the boriding kinetics, Mebarek et al. [26] used fuzzy

logic (FL) approach to model the diffusion of boron in steel, which is mainly based on a number of assumptions to estimate the kinetics of boride layer. To determine the effect of different parameters (temperature, boriding time, boron concentration) on this process, an LS-SVM method was employed[27], in another study, Dybkov et al.[28] have proposed and developed a kinetic approach. Their mathematical model consisting in studying the growth of the bilayer (FeB/Fe₂B) on binary alloys. Through this approach, the parabolic growth law for boride layers was assumed and the kinetics can alternatively be described by a system of two nonlinear differential equations. For the calculation of the diffusion coefficient, many models exist and being used to estimate the value of this parameter [29,30]. In another work, ElGuerrri et al [31] studied the impact of the diffusion coefficient calculation on predicting the boride layer thickness.

In this work, we were interested in studying the growth kinetics of FeB and Fe₂B layers using the three diffusion models based on Fick's second law. Subsequent calculations performed using these models aim to predict the boride layer thickness and boron concentration profiles in each phase, Generally the boron coefficient diffusion is calculated by an expression based on the experimental data. In this work we used three different models to calculate the boron diffusion coefficients in the boride layers produced on an AISI 316 steel by the powder technique and we have studied the impact of the boron diffusivity on the kinetic simulation. In addition, the mass gains relative to the formation of FeB and Fe₂B layers were also evaluated. Finally, the three models were experimentally validated in the considered temperature range.

2. MATHEMATICAL MODEL OF DIFFUSION

The formation of iron borides layers is a phenomenon which is controlled by the diffusion process of boron atoms into the steel surface. The boron concentration profile is described by the solution of second Fick's diffusion equation for a semi-infinite medium given by Equation (1):

$$\frac{\partial C_i}{\partial t} = D_i \frac{\partial^2 C_i(x,t)}{\partial x^2} \quad (1)$$

The partial differential Equation (1) is of a parabolic type. It has analytical solution for the specific initial conditions detailed below. Where $C_i(x, t)$ is the concentration of boron at depth x after diffusion time (t) , and D_i is the diffusion coefficient.

The growth process of FeB and Fe₂B layers will continue at the considered interface under the

two partial chemical reactions at the further stage, over prolonged time duration:

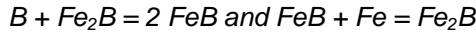


Figure 1 illustrates the boron concentration distribution along the depth of surface-hardened layer for a given temperature and under a boron potential that allows the formation of a two-phase layer (FeB/Fe₂B) on the substrate:

$C_{up}^{Fe_2B}$ and $C_{low}^{Fe_2B}$ represent the values of the upper and lower boron levels in the Fe₂B layer,

C_{ads} is given as the amount of boron adsorbed on the surface of the material.

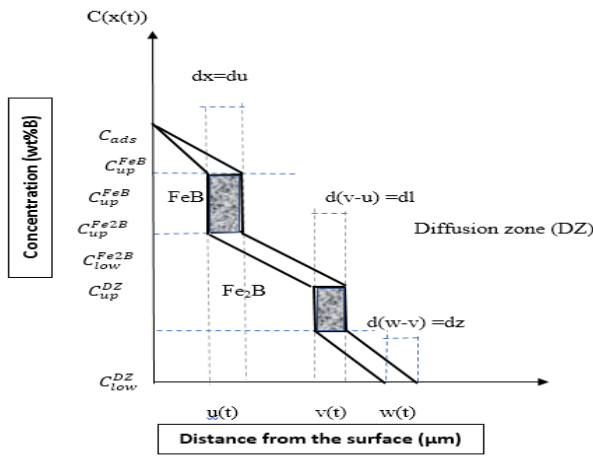


Figure 1. Schematic profile of boron concentration along the FeB and Fe₂B layers

Slika 1. Šematski profil koncentracije bora duž slojeva FeB i Fe₂B

C_0 is the limit of boron solubility in the substrate for which we subscribe a value of 35×10^{-4} % in weight of Boron, u and v are respectively the thicknesses of the FeB and (FeB+ Fe₂B) layers, which vary with the processing time according to the following equations:

$$u = k_1 t^{1/2} \tag{2}$$

$$v = k_2 t^{1/2} \tag{3}$$

where k_1 and k_2 the parabolic growth rate constants at the first and second interfaces.

The development of the models which we aim at proposing will be based on a set of conditions that will facilitate the calculations and render simpler mathematical formulae without prejudicing the integrity of the models when compared to experimental results. Thus, we firstly we consider only a flux of boron atoms perpendicular to the material surface, the temperature of the sample is set to be constant during the process, we also

assume that the concentration of boron on the surface does not change with time and temperature. Iron boride is considered to grow parabolically over time, the boride layer is assumed to be sufficiently thin relative to the thickness of the sample, and finally the diffusion of Fe may be disregarded. Furthermore, the solution of the equation (1) can be obtained using the following boundary conditions set as follows:

$$C_i \{x(t > 0)\} = 0,$$

$$C_{FeB} \{x(t = 0)\} = C_{up}^{FeB} = C_B^{S/FeB}$$

if $C_{ads} > 16.23\%$ in boron weight (wt.% B),

$$C_{FeB} \{x(t = 0)\} = C_{low}^{FeB} \text{ if } C_{ads} < 16.23\%$$

in wt.% B and with the FeB phase,

$$C_{Fe_2B} \{x(t = 0)\} = C_{up}^{Fe_2B} \text{ if } 8.83 \text{ in mass}$$

$B < C_{ads} < 16.23\%$ B weight and without the FeB phase,

$C_{Fe_2B} \{x(t = 0)\} = C_{low}^{Fe_2B}$ if $C_{ads} < 8.83\%$ B weight and without the FeB phase,

$$C_{FeB} \{x(t = t) = u\} = C_{low}^{FeB},$$

$$C_{Fe_2B} \{x(t = t) = u\} = C_{up}^{Fe_2B},$$

$$C_{Fe_2B} \{x(t = t) = v\} = C_{low}^{Fe_2B},$$

$$C_{Fe} \{x(t = t) = v\} = C_0.$$

The models which we aim at developing are designed to predict the thickness of bilayer based on the following parameters: (boron surface concentration, time and temperature). This model is used to predict the thickness of the boride layers based on the following parameters: (boron surface concentration, time and temperature).

A simple model of the boride layer growth (FeB/Fe₂B)

For the phase (Fe₂B or FeB), as proposed by Kirkaldy [32], the general solution of the equation (01) is given by the following equation:

$$C_i(x, t) = A_i + B_i \operatorname{erf} \left(\frac{x}{2\sqrt{D_i t}} \right) \tag{4}$$

Where *erf* the Gauss errorfunction; A_i and B_i are constants to be determined according to the boundary conditions. The interfaces (FeB/Fe₂B) and (Fe₂B/Fe), shift by an infinitely small distance dx , which results from the flows in and out of the surface concerned, and is expressed by the following formulae:

$$W_{FeB} \frac{du}{dt} = (J_{FeB} - J_{Fe_2B})_{x=u} \tag{5}$$

$$W_{Fe_2B} \frac{dv}{dt} + \sigma \frac{du}{dt} = (J_{Fe_2B} - J_{Fe})_{x=v} \tag{6}$$

The models which we aim at developing are designed to predict the thickness of bilayer based on the following parameters: (boron surface concentration, time and temperature). This model is used to predict the thickness of the boride layers based on the following parameters: (boron surface concentration, time and temperature).

A simple model of the boride layer growth (FeB/Fe₂B)

For the phase (Fe₂B or FeB), as proposed by Kirkcaldy [32], the general solution of the equation (01) is given by the following equation:

$$C_i(x, t) = A_i + B_i \operatorname{erf}\left(\frac{x}{2\sqrt{D_i t}}\right) \quad (4)$$

where *erf* the Gauss errorfunction; A_i and B_i are constants to be determined according to the boundary conditions. The interfaces(FeB/Fe₂B) and (Fe₂B/Fe), shift by an infinitely small distance *dx*, which results from the flows in and out of the surface concerned, and is expressed by the following formulae:

$$W_{FeB} \frac{du}{dt} = (J_{FeB} - J_{Fe_2B})_{x=u} \quad (5)$$

$$W_{Fe_2B} \frac{dv}{dt} + \sigma \frac{du}{dt} = (J_{Fe_2B} - J_{Fe})_{x=v} \quad (6)$$

with

$$W_1 \frac{k_1}{2} = (-B_1 D_1 \frac{2}{\sqrt{\pi}} \frac{1}{2\sqrt{D_1 t}} e^{-\frac{x^2}{4D_1 t}} - A_2 D_2 \frac{2}{\sqrt{\pi}} \frac{1}{2\sqrt{D_2 t}} e^{-\frac{x^2}{4D_2 t}}) \quad (11)$$

$$W_1 \frac{k_1}{2} = (-B_1 D_1 \frac{2}{\sqrt{\pi}} \frac{1}{2\sqrt{D_1 t}} e^{-\frac{x^2}{4D_1 t}} - A_2 D_2 \frac{2}{\sqrt{\pi}} \frac{1}{2\sqrt{D_2 t}} e^{-\frac{x^2}{4D_2 t}}) \quad (12)$$

where

$$A_1 = C_{FeB}^{up}, B_1 = \frac{C_{FeB}^{low} - C_{FeB}^{up}}{\operatorname{erf}\left(\frac{u}{2\sqrt{D_1 t}}\right)}, A_2 = \frac{C_{Fe_2B}^{up}}{\operatorname{erfc}\left(\frac{v}{2\sqrt{D_2 t}}\right)}, B_2 = -A_2, A_3 = \frac{C_{Fe_2B}^{low}}{\operatorname{erfc}\left(\frac{v}{2\sqrt{D_3 t}}\right)}, B_3 = -A_2$$

After solving these two equations, the solution (k₁ and k₂) is used to calculate the thickness of the boride layers(u and v), and also to determine the boron concentration with respect to the depth.

A diffusion model based on the integral method

This model considers [23] the growth of the Fe₂B and FeB layers in steel, the distribution of boron concentration along the two layers is described by a parabolic relationship.

In the integral method, the variation of boron concentration with respect to time and the depth

$$C_{FeB}(x, t) = C_{low}^{FeB} + a_1(t)(u(t) - x) + b_1(t)(u(t) - x)^2 \quad (13)$$

$$C_{Fe_2B}(x, t) = C_{low}^{Fe_2B} + a_2(t)(v(t) - x) + b_2(t)(v(t) - x)^2 \quad (14)$$

$$W_{FeB} = \frac{1}{2} \left(C_B^{s/FeB} - C_B^{FeB} \right) + (C_B^{Fe_2B/FeB} - C_B^{FeB/Fe_2B}) \quad (7)$$

$$W_{Fe_2B} = \frac{1}{2} \left(C_B^{FeB} - C_B^{Fe} \right) + (C_B^{Fe/Fe_2B} - C_B^{Fe_2B/Fe}) \quad (8)$$

$$\sigma = \frac{1}{2} (C_B^{FeB/Fe_2B} - C_B^{Fe/Fe_2B}) \quad (9)$$

$$J_i = -D_i \frac{\partial C_i(x, t)}{\partial x} \quad (10)$$

with

$$i = (FeB, Fe_2B, Fe).$$

The kinetics of the evolution of the thickness of the Fe₂B layer is a process limited by the diffusion of boron atoms in the Fe₂B layer. The evolution of this layer follows a parabolic law as a function of time. Where; j_i is the flows of boron atoms in phase i at depth x, and it is related to the gradient of the concentration. k₁ and k₂ can be obtained by solving the non-linear equations (04) and (05). And by simplifying equations (4) and (5) we get:

(distance) of diffusion in each boride layer is not linear and satisfies the second Fick law given by Equation (1).

The mathematical expressions of boron concentrations in each phase are essential to apply this approach, where they are considered to have a parabolic form as suggested by the Goodman method[33]. Therefore, boron concentrations along the FeB(0 ≤ x ≤ u) and Fe₂B(u ≤ x ≤ v) layers are given respectively by the equations (14) and (15) as follows:

The parameters $a_1(t), b_1(t), a_2(t), b_2(t), u(t), v(t)$ must meet boundary conditions. Thus, when applying these conditions at the surface and at the (FeB/ Fe₂B) we get respectively, equation (16 and 17):

$$a_1(t)u(t) + b_1(t)u^2(t) = (C_{up}^{FeB} - C_{low}^{FeB}) \tag{15}$$

$$a_2(t)[v(t) - u(t)] + b_1(t)[v(t) - u(t)]^2 = (C_{up}^{Fe_2B} - C_{low}^{Fe_2B}) \tag{16}$$

By integrating Fick second law between 0 and $u(t)$ for the FeB phase, and between $u(t)$ and $v(t)$ for the Fe₂B phase, and then by applying the Leibniz rule, we arrive at the following ordinary differential equations:

$$\frac{d}{dt} \left[\frac{u^2(t)}{2} a_1(t) + \frac{u^3(t)}{3} b_1(t) \right] = 2D_1 b_1(t)u(t) \tag{17}$$

$$2 w_{12} \frac{dv(t)}{dt} + \frac{[v(t)-u(t)]^2}{2} \frac{da_2(t)}{dt} + \frac{[v(t)-u(t)]^3}{3} \frac{db_2(t)}{dt} = 2D_2 b_2(t)[v(t) - u(t)] \tag{18}$$

The two algebraic constraints applied on this diffusion problem can be derived Equations (17 and 18) from the continuity equation at the (Fe₂B/Substrate) interface as follows:

$$2 w_1 b_1(t)D_1 = D_1 a_1^2(t) - D_2 a_1(t)(a_2(t) + 2b_2(t)[v(t) - u(t)]) \tag{19}$$

with $w_1 = \left[\frac{(C_{up}^{FeB} + C_{low}^{FeB})}{2} - C_{up}^{Fe_2B} \right]$.

$$2 w_{12} b_1(t)D_1 a_2(t) + 2 w_2 b_2(t)D_2 a_1(t) = D_2 a_2^2(t)a_1(t) \tag{20}$$

with $w_2 = \left[\frac{(C_{up}^{Fe_2B} + C_{low}^{Fe_2B})}{2} - C_0 \right]$ and $w_{12} = \frac{(C_{up}^{Fe_2B} - C_{low}^{Fe_2B})}{2}$.

Equations 16 and 21 form a Differential-algebraic system of equations (DAE) whose unknowns are $a_1(t), b_1(t), a_2(t), b_2(t), u(t), v(t)$, which satisfy the given algebraic constraints. This system (DAE) can therefore be solved analytically using the equation for the variation in the boride layer thickness in each phase.

To determine the coefficients of boron diffusion in each phase (FeB and Fe₂B), the following variable changes are made:

$$a_l(t) = \frac{\alpha_l}{u(t)}, b_l(t) = \frac{\beta_l}{u(t)^2}, a_2(t) = \frac{\alpha_2}{[v(t)-u(t)]}, b_2(t) = \frac{\beta_2}{[v(t)-u(t)]^2} \tag{21}$$

In which, the constants $\alpha_1, \beta_1, \alpha_2$ and β_2 should satisfy the boundary conditions. Thus, the expression of boron diffusion coefficients in the FeB and Fe₂B phases are calculated as follows:

$$D_1 = k_1^2 \left[\frac{(C_{up}^{FeB} - C_{low}^{FeB})}{8\beta_1} - \frac{1}{24} \right], \text{ for } \beta_1 < 3 (C_{up}^{FeB} - C_{low}^{FeB}) \tag{22}$$

$$D_2 = \frac{k_2(k_2 - k_1)(C_{up}^{Fe_2B} - C_{low}^{Fe_2B})}{4\beta_2} - (k_2 - k_1)^2 \left[\frac{(C_{up}^{Fe_2B} - C_{low}^{Fe_2B})}{8\beta_1} - \frac{1}{24} \right] \tag{23}$$

The relationships between constants α_1 and β_1 , and between α_2 and β_2 are given respectively by:

$$\alpha_1 + \beta_1 = (C_{up}^{Fe_2B} - C_{low}^{Fe_2B}) \tag{24}$$

$$\alpha_2 + \beta_2 = (C_{up}^{FeB} - C_{low}^{FeB}) \tag{25}$$

To determine the value of boron diffusion in each phase, it is important to calculate the value of β_2 from the β_1 using the following equation:

$$(\alpha_1^2 - 2 W_1 \beta_1)(\alpha_2^2 - 2 W_2 \beta_2) = 2 W_{12} \beta_1 \alpha_2 (2 W_{12} + \beta_2) \tag{26}$$

Dybkov Model

The further growth of boride layers is controlled by the diffusion step at the expense of boron element [34,35]. The growth kinetics of boride

layers at the diffusion stage of their formation is described by a system of two differential equations in dependence of treatment time at a given boriding temperature:

$$\frac{du(t)}{dt} = \frac{D_1}{u(t)} - \frac{rg}{p} \frac{D_2}{l(t)} \quad (27)$$

$$u^2 = D_1 t = D_0^1 t \cdot \exp\left(-\frac{Q_1}{RT}\right) \quad (29)$$

$$\frac{dv(t)}{dt} = \left(1 - \frac{q}{sg}\right) \frac{D_1}{u(t)} + \left(1 - \frac{rg}{p}\right) \frac{D_2}{(v(t)-u(t))} \quad (28)$$

$$v^2 = D_2 t = D_0^2 t \cdot \exp\left(-\frac{Q_2}{RT}\right) \quad (30)$$

With $u(t)$ and $l(t)$ the thicknesses of FeB and Fe₂B layers. The constant g depends on the molar volume of FeB and Fe₂B phases with $g=0.60$. As obtained from the stoichiometric coefficients for phases FeB and Fe₂B the constants were the following: $p = 1$, $q = 1$, $r = 1$ and $s = 2$.

3. CALCULATION OF THE BORON COEFFICIENT DIFFUSION

By the Dybkov Model (DM)

Based on this approach, [34,35] we can calculate the values of boron diffusion coefficients in FeB and Fe₂B by the two following equations:

$$D_1 = \frac{0.5 k_1}{\left(p - \frac{rg}{s}\right)} \left[(p - rg)k_1 + rgk_2 \right]$$

$$D_2 = \frac{0.5 (k_2 - k_1)}{\left(1 - \frac{rg}{sp}\right)} \left[k_2 + \left(\frac{q}{sg} - 1\right) k_1 \right]$$

Therefore, the determination of these two parameters D_1 and D_2 , requires the fitting of experimental results with Equations (2) and (3) to obtain the k_1 and k_2 values.

By Arrhenius expression (AE)

The diffusion coefficient can be related to the processing time and thickness of the boride layer by Arrhenius expression. To estimate the boron activation energy, we must have a minimum of three processing temperatures with three durations for each temperature to obtain the corresponding layers' thicknesses. Based on the experimental data, we can estimate the activation energy of boron diffusion in the treated steel using the following Equation (30):

The variable u represents the thickness of FeB layer and v that of (FeB + Fe₂B) layer given in (μm), D_0^i is the boron diffusion coefficient ($\mu\text{m}^2/\text{s}$), t is the boriding time, Q_i is the value of the activation energy measured in Joule/mol, R is the gas constant and T is the temperature in Kelvin. It is easy to estimate the value of the activation energy Q_i using Arrhenius's Law in a linear form given by equation (29), where Q_i can be easily deduced from the slope of the straight line expressed in (kJ/mol).

$$\ln(D_i) = \ln(D_0^i) - \frac{Q_i}{RT} \quad i=1,2 \quad (31)$$

By the Integral method (IM)

Using the following equations provided for the Integral method, [23] we can calculate the boron coefficient diffusion in each phase using Equation (32 and 32):

$$D_1 = k_1^2 \left[\frac{(C_{up}^{FeB} - C_{low}^{FeB})}{8\beta_1} - \frac{1}{24} \right] \quad (32)$$

$$D_2 = \frac{k_2(k_2 - k_1)(C_{up}^{Fe_2B} - C_{low}^{Fe_2B})}{4\beta_2} - (k_2 - k_1)^2 \left[\frac{(C_{up}^{Fe_2B} - C_{low}^{Fe_2B})}{8\beta_1} - \frac{1}{24} \right] \quad (33)$$

4. EXPERIMENTAL PROCEDURE

We use the experimental of reference work [36], the process of boriding of AISI 316 steel was carried out with the powder technique using B₄C Durborid. This treatment was done at different temperatures 1123, 1173, 1223 and 1273 K with processing duration between 2 and 10h. The chemical composition of the AISI 316 steel is given in Table 1.

Table 1. The chemical composition of AISI 316 steel (in % mass) [36]

Tabela 1. Hemijski sastav čelika AISI 316 (u % mase) [36]

Elements	C	Mn	Si	Ni	Mo	Cr	P	S
(wt %)	0.07	1.99	1.0	12.5	2.2	17.3	0.04	0.02

According to reference [36] and just before processing, all samples underwent a surface pre-treatment (preparation) with abrasive elements to eliminate any contamination that may interfere with boron diffusion. The thickness of the resulting boride layer (FeB and Fe₂B) was measured by optical microscopy. To ensure the accuracy of the layer thickness measurements, an average of ten

measurements were taken on different locations of the cross-sections of the borided samples.

The measurement of the thickness of the boride layer adopts the following method, that consists in measuring with an optical microscope the lengths of the two deepest needles and those of the two shallowest needles and taking the average length of these four needles as the value

of the thickness of the boride layer at the selected location.

Table 2. Experimental data of k_1 and k_2 [36]

Tabela 2. Eksperimentalni podaci za k_1 i k_2 [36]

Temperature	Growth rate constant ($\mu\text{m/s}^{0.5}$)	
	k_1	k_2
1123	0.068	0.145
1173	0.118	0.254
1223	0.157	0.337
1273	0.241	0.542

Table 3. Data used in the simulation

Tabela 3. Podaci korišćeni u simulaciji

$C_{up}^{FeB} = 16.40 \text{ wt. \%}$ and $C_{low}^{FeB} = 16.23\%$	The maximum and minimum boron contents in FeB
$C_{up}^{Fe2B} = 9\%$ and $C_{low}^{Fe2B} = 8.83\%$	Stand for the maximum and minimum boron contents in Fe ₂ B
C_{ads}	The adsorbed concentration of boron
$C_0 = 35 \times 10^{-4}\%$	Stands for the solubility limit of boron within the matrix

Calculation of diffusion coefficients in FeB and Fe₂B

Figure 2 represents the calculated diffusion coefficients of boron in the FeB layer which varies exponentially as a function of temperature based on the three approaches (the integral model, Dybkov model and the Arrhenius expression). It is observed that the coefficient of the Arrhenius

The experimental data facilitates the computation of growth rate constants; Table 2 illustrates the experimental growth rate constants for the two phases, where k_1 and k_2 represent the growth rate constants in the FeB and Fe₂B phases, respectively.

5. SIMULATION RESULT AND DISCUSSION

The data concerning the boron diffusivity and the different concentrations are collected in Tab.3, these data were used in our simulation code.

expression increases faster compared to the coefficients of other models which increase slowly with the temperature rise, for the calculation of the boron diffusion coefficient a good agreement between the three models at the temperature 1123 K and a good agreement between the integral model and the Dybkov model at the temperature 1273 K.

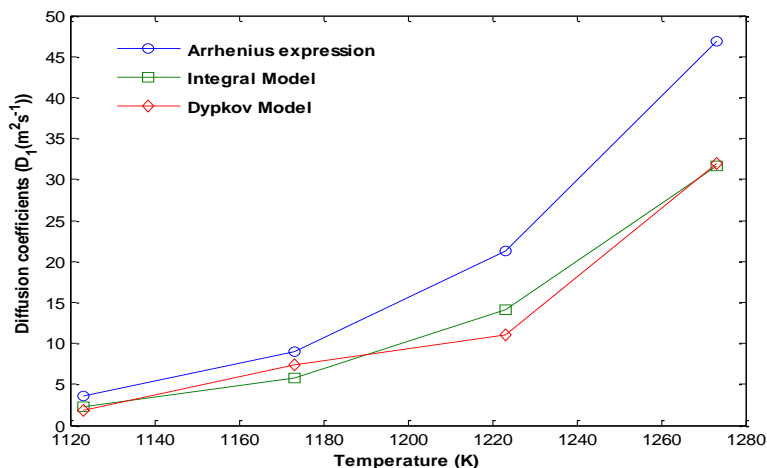


Figure 2. Calculation of boron diffusion coefficients in the FeB layers using the three models

Slika 2. Proračun koeficijenta difuzije bora u slojevima FeB koristeći tri modela

Figure 3 shows the calculated diffusion coefficients of boron in Fe₂B which vary exponentially versus the processing temperature with the integral model, Dybkov model and the Arrhenius relationship. It is noticed that the coefficient estimated from the Arrhenius relationship increases speedily compared to the values determined from the integral method and Dybkov model.

Table 4 represents the estimated values of boron diffusion coefficients in Fe₂B and FeB at temperatures between 1173 K and 1273 K for Arrhenius expression, integral model and Dybkov model. From the results of Table 4, we determined the corresponding values of D₀ and Q in FeB and Fe₂B layers with different models (see Table 5).

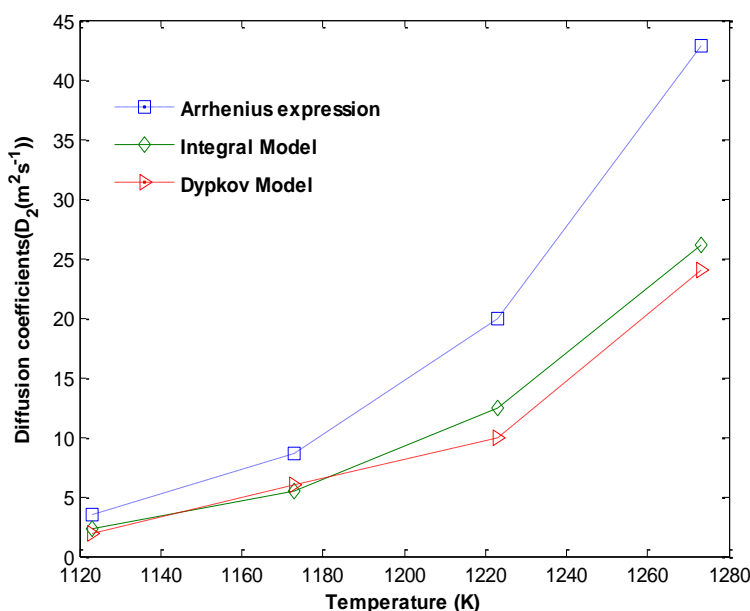


Figure 3. Calculation of boron diffusion coefficients in the Fe₂B layers using the three models

Slika 3. Proračun koeficijena difuzije bora u slojevima Fe₂B korišćenjem tri modela

Table 4 represents the estimated values of boron diffusion coefficients in Fe₂B and FeB at temperatures between 1173 K and 1273 K for Arrhenius expression, integral model and Dybkov model. From the results of Table 4, we determined the corresponding values of D₀ and Q in FeB and Fe₂B layers with different models (see Table 5).

Table 4. Calculated values of boron diffusion coefficients in the Fe₂B layers using different models

Tabela 4. Izračunate vrednosti koeficijena difuzije bora u slojevima Fe₂B korišćenjem različitih modela

Temperature (K)	Calculated boron diffusion coefficient (m ² /s)					
	D ₁			D ₂		
	Arrhenius expression	Integral Model	Dybkov Model	Arrhenius expression	Integral Model	Dybkov Model
1123	3.56 × 10 ⁻¹³	2.23 × 10 ⁻¹³	1.80 × 10 ⁻¹³	3.51 × 10 ⁻¹³	2.28 × 10 ⁻¹³	1.90 × 10 ⁻¹³
1173	9.05 × 10 ⁻¹³	5.83 × 10 ⁻¹³	7.38 × 10 ⁻¹³	8.67 × 10 ⁻¹³	5.52 × 10 ⁻¹³	5.95 × 10 ⁻¹³
1223	2.13 × 10 ⁻¹²	1.41 × 10 ⁻¹²	1.11 × 10 ⁻¹²	1.99 × 10 ⁻¹²	1.24 × 10 ⁻¹²	10 ⁻¹²
1273	4.68 × 10 ⁻¹²	3.16 × 10 ⁻¹²	3.20 × 10 ⁻¹²	4.28 × 10 ⁻¹²	2.61 × 10 ⁻¹²	2.40 × 10 ⁻¹²

Table 5. Calculated values of D₀ and Q in FeB and Fe₂B employing different models

Tabela 5. Izračunate vrednosti D₀ i Q u FeB i Fe₂B primenom različitih modela

Temperature (K)	Boron diffusion coefficients (m ² /s)					
	D ₁			D ₂		
	Arrhenius Expression + (AE)	Integral Model + (AE)	Dybkov Model + (AE)	Arrhenius expression + (AE)	Integral Model + (AE)	Dybkov Model + (AE)
D ₀ (× 10 ⁻⁴)	11	14	22	5.5308	2.2487	2.0347
Q (kJ/mol)	207.85	207.85	216.164	199.536	191.222	191.222

Table 6 provides a comparison between the activation energies of boron in various steels, as reported in previous research [37-42], and the values obtained in our study. An initial evaluation indicates variations in the activation energies.

These variations can be related to a multitude of influential factors: the selection of the boronizing method, the temperature range applied, the methodology employed for the determination of boron activation energies, and the chemical composition of the substrate.

Table 6. Values of boron activation energies obtained in the case of borided steels using different methods

Tabela 6. Vrednosti bora na energijama aktivacije dobijene u slučaju boriranih čelika različitim metodama

Material	Boriding Method	Q (kJ.mol ⁻¹)		Ref
		FeB	Fe ₂ B	
AISI 316	Powder technique	204	198	Campos et al [37]
AISIM2	Powder	220.2	213	NaitAbdellah et al.[38]
AISID2	Powder	a/ 207.84	197.04	Keddam et al [39] a:Dybkov model b:Integral model
		b/208.04	197.46	
AISI316	Plasma paste	118.12 (FeB+Fe ₂ B)		Keddam et al [40]
Royalloy steel	Powder	242.79	223	Orihel et al [41]
AISIM2	Paste	283	239.4	Campos et al [42]
AISI 316	Powder technique	a/207.85	199.536	This work a: Arrhenius expression b: Integral model c: Dybkov model
		b/207.85	191.222	
		c/216.164	191.222	

Layers' thicknesses of FeB and Fe₂B by the proposed models

In order to run numerical simulations of the phenomena using the proposed model, the parameters needed are the temperature, boriding time and diffusivity of boron in each phase, as well as the concentration of boron. Whereas the kinetic data and boron activation energies for iron boriding were taken from the reference [6].

For the first model, the values of boron diffusion coefficients in the α-Fe and γ-Fe phases were found in references [6]. The boron diffusion coefficients in iron borides (m²/s) are given in the previous section. For the simple model, we used the values of k₁ and k₂ to calculate the thickness of the boride layer (u and v).

For the diffusion integral method, to solve the system of algebraic-differential equations [23] a numerical method is employed, moreover, the thickness of the borided layer (Fe₂B) can be calculated using the following equation:

$$k_1 = \frac{D_1}{\sqrt{\frac{C_{up}^{FeB} - C_{low}^{FeB}}{8\beta_1} - \frac{1}{24}}} \tag{34}$$

$$D_2 = \frac{k_2(k_2 - k_{*1})(C_{up}^{Fe_2B} - C_{low}^{Fe_2B})}{4\beta_2} - (k_2 - k_1)^2 \left[\frac{(C_{up}^{Fe_2B} - C_{low}^{Fe_2B})}{8\beta_1} - \frac{1}{24} \right] \tag{35}$$

From the values of α₁/β₁/α₂/β₂ we! Calculate the parameter a₁, a₂, b₁, b₂, the estimation of this value allow to simulate the layer thickness FeB and Fe₂B.

The calculation of these thicknesses was done with Equations (36) and (37):

$$u(t) = \frac{\alpha_1}{a_1(t)} \tag{36}$$

$$v(t) = \frac{\alpha_2}{a_2(t)} + u(t) \tag{37}$$

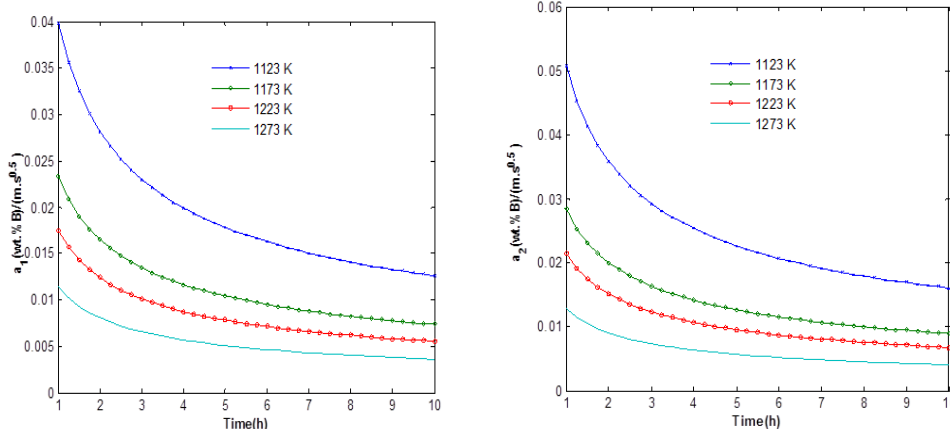


Figure 4. Values of a₁, a₂ parameters as function of time

Slika 4. Vrednosti parametara a₁, a₂ u funkciji vremena

Table 5 shows increase in the temperature-related growth rate constants for the two phases FeB and Fe₂B, there is a good agreement between the simulation results and experimental data.

The growth rate constants are noticed to change exponentially, and we obtained a good

match between the simulation results and the experimental data. A comparison was made between the calculated values of growth rate constants and those determined empirically [36] and the results are displayed in Table 7.

Table 7. Comparing the calculated growth rate constants with the experimental ones

Tabela 7. Poređenje izračunatih konstanti brzine rasta sa eksperimentalnim

Temperature (K)	Growth rate Constants (μm/s ^{0.5})							
	FeB				Fe ₂ B			
	Exp [36]	Simulation			Exp [36]	Simulation		
Simple Model		Integral Model	Dybkov Model	Simple Model		Integral Model	Dybkov Model	
1123	0.069	0.07156	0.05712	0.0581	0.145	0.1522	0.1527	0.1561
1173	0.118	0.10970	0.09099	0.1110	0.254	0.2326	0.2399	0.2520
1223	0.157	0.16560	0.13950	0.1421	0.337	0.3592	0.3633	0.3600
1273	0.241	0.23830	0.20690	0.2201	0.542	0.5332	0.5325	0.5542

After determining the diffusivity of boron in each phase, the layers' thickness $u(t)$ and $v(t)$ can be estimated for a given time and temperature.

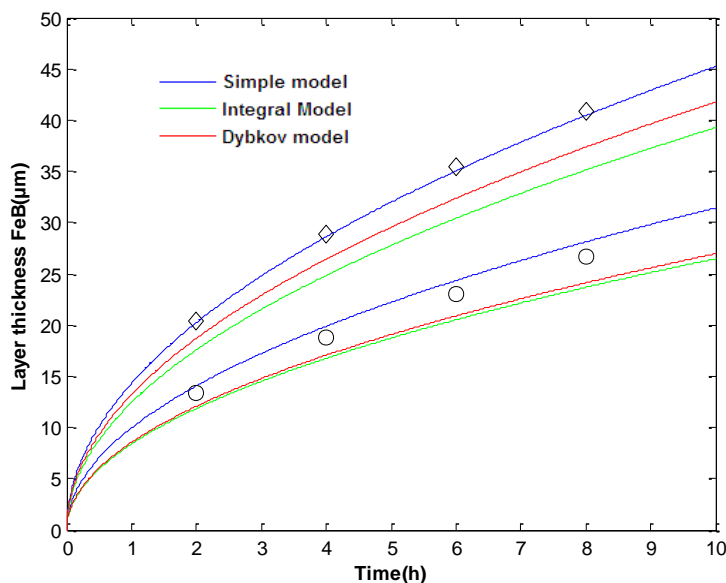


Figure 5. Comparison of calculated layers' thicknesses of FeB with the experimental data [36], using three models at 1223K and 1273K

Slika 5. Poređenje izračunatih debljina slojeva FeB sa eksperimentalnim podacima [36], korišćenjem tri modela na 1223K i 1273K

Figure 5 and 6 give the time evolution of estimated thicknesses of FeB and Fe₂B layers at the two temperatures 1223K and 1273K, using three models. We note that when the temperature increases, the diffusion process becomes very fast.

Table 7 shows that the three models have consistent results with the experimental data, which

confirms their validity. With the proposed models we can calculate the thickness of each boride layer.

We can calculate the instantaneous velocities of the (FeB/Fe₂B) and (Fe₂B/diffusion zone) interfaces as follows:

$$v_{FeB} = \frac{du}{dt} = \frac{k_1}{2\sqrt{t}} \quad v_{Fe_2B} = \frac{dv}{dt} = \frac{k_2}{2\sqrt{t}} \quad (38)$$

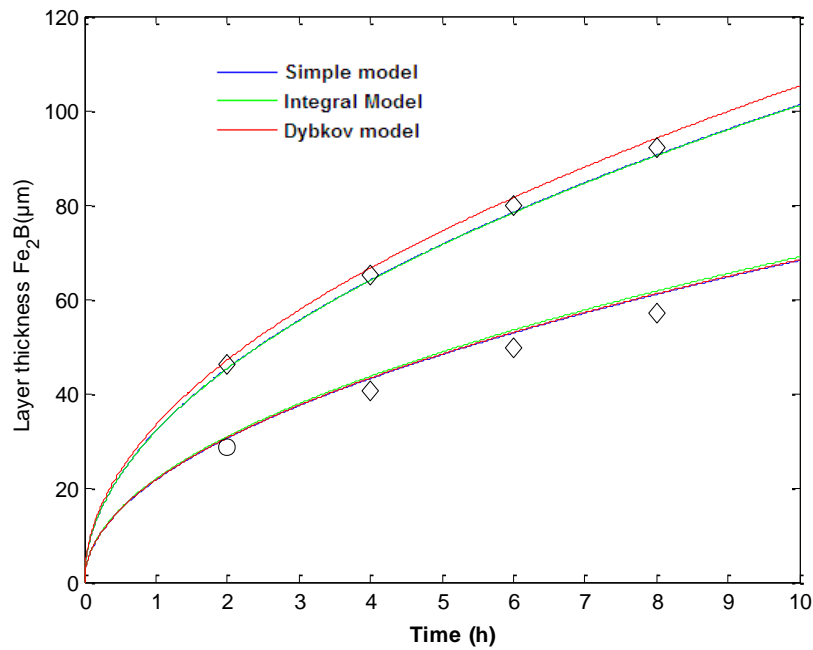


Figure 6. Comparison of calculated layers' thicknesses of FeB with the experimental data [36], using three models at 1223K and 1273K

Slika 6. Poređenje izračunatih debljina slojeva FeB sa eksperimentalnim podacima [36], korišćenjem tri modela na 1223K i 1273K

Figure 7 and 8 describe the time dependencies of the instantaneous velocities at the two growing interfaces using the three approaches: the simple model, the integral method and Dybkov model.

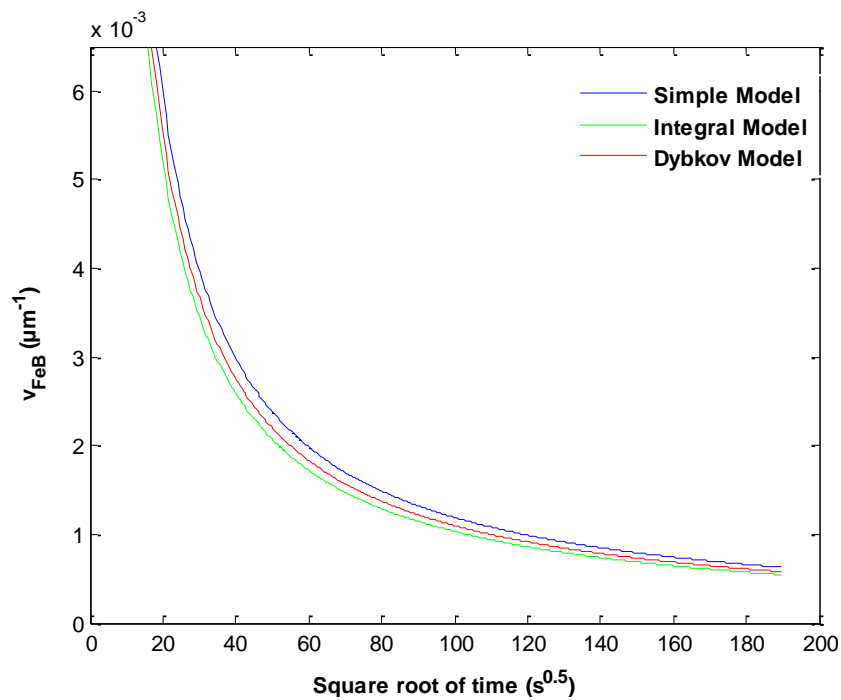


Figure 7. Calculated velocity at the first interface as a function of square root of time at 1273K

Slika 7. Izračunata brzina na prvom interfejsu kao funkcija kvadratnog korena vremena na 1273K

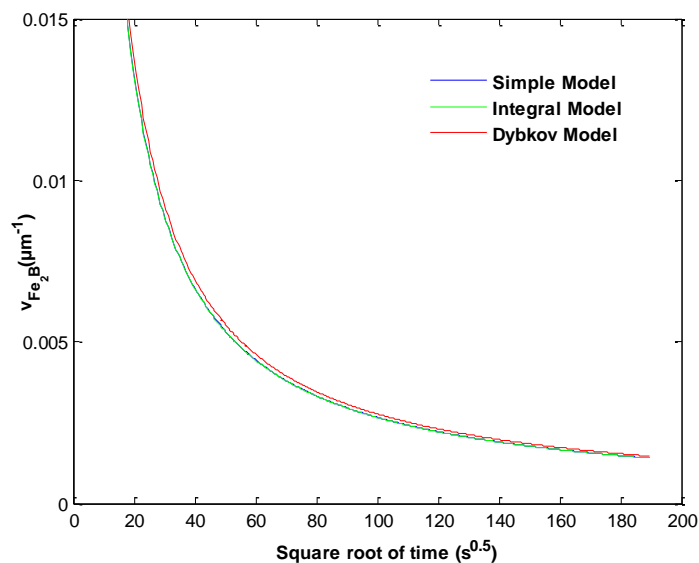


Figure 8. Calculated velocity at the second interface as a function of square root of time at 1273K
 Slika 8. Izračunata brzina na drugom interfejsu kao funkcija kvadratnog korena vremena na 1273K

6. MASS GAIN DETERMINATION

The mass gain for FeB and Fe₂B phases per unit surface [44] can be calculated using the following equations given by Equations (39) and (40):

$$G_{FeB} = \rho_{Fe_2B} w_2 t \frac{du}{dt} \tag{39}$$

$$G_{Fe_2B} = \rho_{Fe} t \left((w_2 + w') \frac{du}{dt} + w_2 \frac{dl}{dt} \right) \tag{40}$$

With $\rho_{Fe_2B} = 7.336 \text{ g/cm}^3$ and $\rho_{Fe} = 7.86 \text{ g/cm}^3$ is the density of Fe₂B layer and the density of iron.

$$\omega_1 = \frac{(C_{up}^{FeB} + C_{low}^{FeB})}{2} - C_{up}^{Fe_2B}$$

$$\omega_2 = \frac{(C_{up}^{Fe_2B} + C_{low}^{Fe_2B})}{2} - C_0$$

$$\omega_{12} = \frac{(C_{up}^{Fe_2B} + C_{low}^{Fe_2B})}{2}$$

With the assumption that the Fe₂B and FeB layers form instantly. $G_{FeB}(t)$ and $G_{Fe_2B}(t)$ are the values of mass gain per unit surface (g/cm^2).

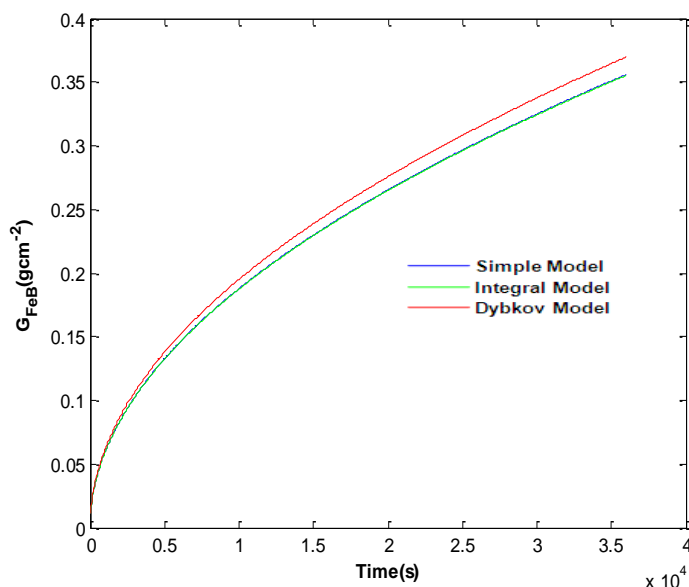


Figure 9. Calculated mass gain of the FeB layer versus the time duration at 1273 K
 Slika 9. Izračunato povećanje mase sloja FeB u odnosu na vremensko trajanje na 1273 K

Figure 9 and 10 give the time dependences of calculated mass gain at a temperature of 1273 K using the three models. It is seen that that the values of mass gain determined for both phases

increase with the treatment time. It is also worth noting that the mass gain relative to the FeB phase is greater than that of the Fe₂B phase.

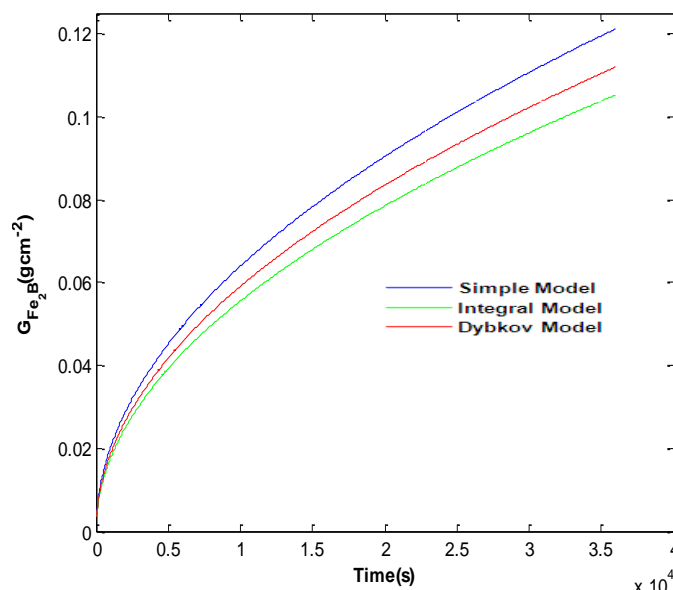


Figure 10. Calculated mass gain of the Fe₂B layer versus the time duration at 1273 K

Slika 10. Izračunato povećanje mase sloja Fe₂B u odnosu na vremensko trajanje na 1273 K

Figure 11 illustrates the calculated ratio (FeB to Fe₂B) in terms of thickness for different temperatures. It is noticed that the results from the integral and Dybkov models are very comparable except for 1173K. However the calculation results given by the simple model are higher than the values provided by Dybkov model and integral method.

We can notice that the simple method yield results close to the experimental values compared to the integral method and Dybkov model.

Figure 12 displays the comparative ratios in terms of thickness for different processing temperatures by considering FeB and Fe₂B layers.

Figure 13 gives the estimated values of absolute error in terms of layers' thicknesses when comparing the three approaches. It is observed that the simple model yields minimum value of absolute error in comparison to the two other models. However, for the Fe₂B layer, the value of error absolute is minimum when applying the Dybkov model.

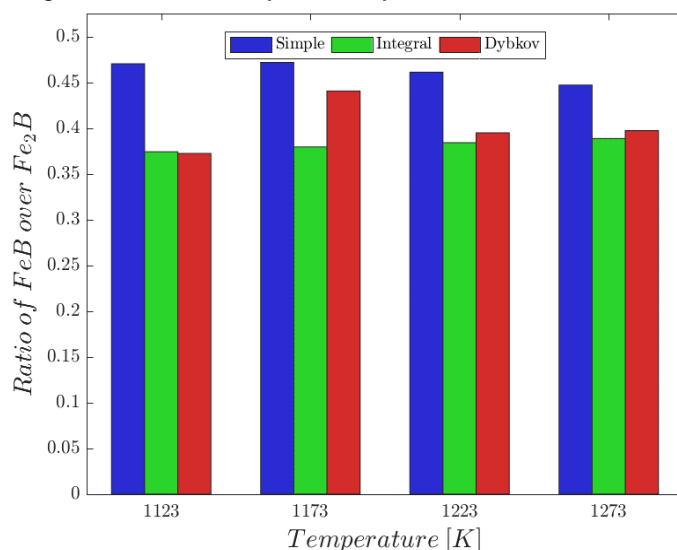


Figure 11. Calculated thickness ratio (FeB to Fe₂B) at increasing temperatures using three models

Slika 11. Izračunati odnos debljine (FeB prema Fe₂B) pri rastućim temperaturama korišćenjem tri modela

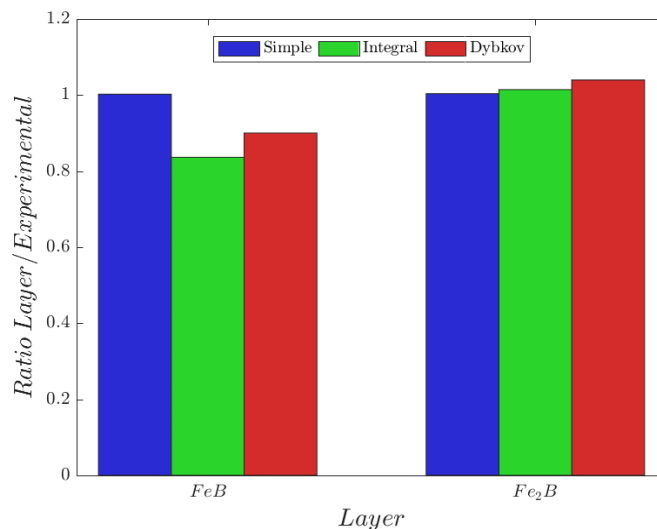


Figure 12. Ratio Simulation/Experimental vs layer

Slika 12. Odnos simulacije/eksperimentalnog prema sloju

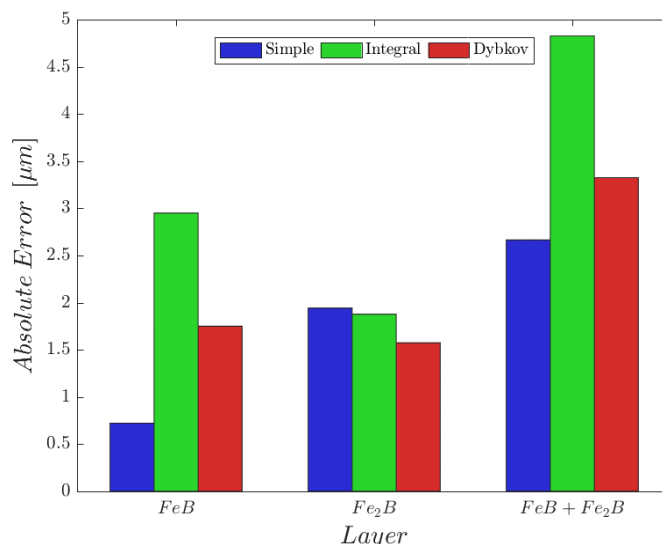


Figure 13. Estimation of absolute errors in terms of layers' thicknesses

Slika 13. Procena apsolutnih grešaka u smislu debljina slojeva

7. CONCLUSION

In the present work, three different approaches were applied to estimate the boron diffusion coefficients in the FeB and Fe₂B layers formed on AISI 316 steel. The first kinetic approach used a simple model based on the Fick's laws while the second model employed the integral model. The third approach called the Dybkov model was also adopted by considering the experimental fitting parameters as the values of boron diffusion coefficients in FeB and Fe₂B.

These three models have been validated empirically by contrasting the simulated results with the experimental data found in the literature. A comparative study between the three models was

achieved by calculating the absolute errors. In addition, the mass gain resulting from the formation of FeB and Fe₂B layers was estimated versus the time duration at 1273 K. The instantaneous velocities for the two growing interfaces were also evaluated. It is concluded that the estimated mass gain within the FeB layer was significant in comparison with that of Fe₂B layer.

8. REFERENCES

- [1] M.Kulka (2019) Current Trends in Boriding. Techniques, Engineering Materials book series, Springer International Publishing. <https://doi.org/10.1007/978-3-030-06782-3>
- [2] A.G.Matuschka (1980) Boronizing, Hayden and Son Inc, Philadelphia.

- [3] A.K.Sinha, N.Boronizing (1991) ASM Int. handbook, The Materials International Society, *Materials Park*, OH, USA, 4, 437-447.
- [4] O.Allaoui, N.Bouaouadja, G.Sainderman (2006) Characterization of boronized layers on a XC38 steel, *Surf. Coat. Tech.* 201, 3475-3483. <https://doi.org/10.1016/j.surfcoat.2006.07.238>
- [5] S.A.Bouaziz, N.Boudaoud, A.Zanoun (2009) Boruration thermochimique d'un acier C38 dans un bain de sels borax-SiC, *Matériaux et Techniques*, 97, 253-261. <https://doi.org/10.1051/mattech/2009036>
- [6] M Keddama, SM Chentouf (2005) A diffusion model for describing the bilayer growth (FeB/Fe₂B) during the ironpowder-packboriding ; *Applied Surface Science*, 252(2),393-399. <https://doi.org/10.1016/j.apsusc.2005.01.016>
- [7] B.Mebarek, D.Madouri, A.Zanoun, A.Belaidi (2015) Simulation model of monolayer growth kinetics of Fe₂B phase, *Matériaux et Techniques*, 103, 703 . <https://doi.org/10.1051/mattech/2015058>
- [8] B.Mebarek, A.Benguelloula, A.Zanoun (2018) Effect of Boride Incubation Time During the Formation of Fe₂B Phase, *Materials Research*, 21(1), 23-32. <http://dx.doi.org/10.1590/1980-5373-MR-2017-0647>.
- [9] L.G.Yu, X.J.Chen, K.A.Khor, G.Sundararajan (2005) FeB/Fe₂B phase transformation during SPSPack-boronizing: Boride layer growth kinetics, *Acta Materialia* 53, 2361-2368. <https://doi.org/10.1016/j.actamat.2005.01.043>
- [10] B.Mebarek, M.Keddama, M.Kulka (2021) Simulation of the incubation time for the formation of (FeB/Fe₂B) bilayer on pure iron , *KOM – Corrosion and Material Protection Journal*, 65(2)49-56. <https://doi.org/10.2478/kom-2021-0006>
- [11] B.Mebarek, S.A.Bouaziz, A.Zanoun (2012) Modèle de simulation pour l'étude de la boruration thermochimique de l'acier inoxydable «AISI 316» (X5CrNiMo17-12-2), *Matériaux & Techniques*, 100, 167-175, <https://doi.org/10.1051/mattech/2012009>
- [12] S.Şahin (2009) Effects of boronizing process on the surface roughness and dimensions of AISI 1020, AISI 1040 and AISI 2714, *Journal of Materials Processing Technology*, 209(4),1736-1741, <https://doi.org/10.1016/j.jmatprotec.2008.04.040>
- [13] B.Mebarek (2012) thèse de doctorat, Ecole Nationale Polytechnique d'Oran Maurice Audin.
- [14] O.Delai, C.Xia, L.Shiqiang (2021) Growth kinetics of the FeB/Fe₂B boride layer on the surface of 4Cr5MoSiV1 steel: experiments and modelling, *Journal of Materials Research and Technology*, 11, 1272-1280, <https://doi.org/10.1016/j.jmrt.2021.01.109>
- [15] M.X.Wei, S.Q.Wang, L.Wang, X.H.Cui, K.M.Chen (2011) Effect of tempering conditions on wear resistance in various wear mechanisms of H13 steel, *Tribol Int*, 44(7), 898-905, <https://doi.org/10.1016/j.triboint.2011.03.005>
- [16] A.Günen et al (2019) Properties and Corrosion Resistance of AISI H13 Hot-Work Tool Steel with Borided B₄C Powders. *Metals and Materials International*. 26(9), 329-1340. doi.org/10.1007/s12540-019-00421-0
- [17] I.E.Campos-Silva, G.A.Rodriguez-Castro (2015) Boriding to improve the mechanical properties and corrosion resistance of steels, in *Thermochemical surface engineering of steels Elsevier*. 651-702. <https://doi.org/10.1533/9780857096524.5.651>
- [18] B.Mebarek, M.Keddama (2019) Prediction model for studying the growth kinetics of Fe₂B boride layers during boronizing. *Ingénierie des Systèmes d'Information*, 24(2), 201-205. <https://doi.org/10.18280/isi.240212>
- [19] S.Sahin, C.Meric (2002) Investigation of the effect of boronizing on cast irons, *Materials Research Bulletin*, 37(5), 971-979, [https://doi.org/10.1016/S0025-5408\(02\)00697-9](https://doi.org/10.1016/S0025-5408(02)00697-9).
- [20] B.Mebarek, M.Keddama, H.Boussebha (2020) Simulation model of the Growth Kinetics of Fe₂B Layers with Consideration of the Boride Incubation Time Effect, *Surface Review and Letters*, 27(04), 1950127 <https://doi.org/10.1142/S0218625X19501270>
- [21] Ch.Kapfenberger, A.Barbara, P.Rainer, H.Hubert (2006) Structure refinements of iron borides Fe₂B and FeB; *Zeitschrift für Kristallographie - Crystalline Materials*, 221(5-7), 477-481. <https://doi.org/10.1524/zkri.2006.221.5-7.477>
- [22] M.Keddama (2004) A kinetic model for the borided layers by the paste-boronizing process, *Applied Surface Science*, 236, 451-455. <https://doi.org/10.1016/j.apsusc.2004.05.141>
- [23] M.Keddama, M.Kulka (2018) Simulation of the growth kinetics of FeB and Fe₂B layers on AISI D2 steel by the integral method. *Physics of Metals and Metallography*, 119(9), 842-851. doi.org/10.1134/S0031918X18090065
- [24] I.Campos, M.Islas, G.Ramírez, C. Villa Velázquez, C.Mota (2007) Growth kinetics of borided layers: Artificial neural network and least square approaches, *Applied Surface Science*, 253(14), 6226-6231, <https://doi.org/10.1016/j.apsusc.2007.01.070>
- [25] I.Campos-Silva, E.J.Hernández-Ramirez, A. Contreras-Hernández, J.L.Rosales-Lopez, E. Valdez-Zayas, I.Mejía-Caballero, J.Martínez-Trinidad (2021) Pulsed-DC powder-pack boriding: Growth kinetics of boride layers on an AISI 316 L stainless steel and Inconel 718 superalloy, *Surface and Coatings Technology*, 421, 127-404, <https://doi.org/10.1016/j.surfcoat.2021.127404>
- [26] B.Mebarek, M.Keddama (2018) A fuzzy neural network approach for modeling the growth kinetics of FeB and Fe₂B layers during the boronizing process, *Matériaux et Techniques*, 06, 603-609. <https://doi.org/10.1051/mattech/2019002>
- [27] B.Mebarek, M.Keddama, H.Aboshighiba (2018) LS-SVM approach for modeling the growth kinetics of FeB and Fe₂B layers formed on Armco iron, *Revue des Sciences et Technologie de l'information*, 23 (5), 29-41. <https://doi.org/10.3166/ISI.23.5.29-41>
- [28] V.I.Dybkov, L.V.Goncharuk, V.G.Khoruzha, K.A. Meleshevich, A.V.Samelyuk, V.R.Sidorko (2008) Diffusional growth kinetics of boride layers on iron-chromium alloys. *Solid State Phenomena*. 138, 181-188. <https://doi.org/10.4028/www.scientific.net/SSP.138.181>

- [29] M. Keddad, B. Bouarour, Z.Nait Abdellah, R. Chegroune (2013) The effective diffusion coefficient of boron in the Fe_2B layers formed on the iron substrate, *MATEC Web of Conferences* 3, 01012, doi.org/ 10.1051/mateconf/20130301012
- [30] S.Taktak (2006) A study on the diffusion kinetics of borides on boronized Cr-based steels, *J. Mater. Sci.*, 41, 7590–7596. https://doi.org/10.1007/s10853-006-0847-4
- [31] Y.ElGuerrri, B.Mebarek, M.Keddad (2022) Impact of the diffusion coefficient calculation on predicting Fe_2B boride layer thickness, *KOM – Corrosion and Material Protection Journal*, 66(1), 25-35. https://doi.org/10.2478/kom-2022-0005
- [32] J.S.Kirkaldy (1958) diffusion in multicomponent metallic systems: iii. The motion of planar phase interfaces, *Can. J. Phys.* 36, 917-926.
- [33] T.R.Goodman (1964) Application of integral methods to transient nonlinear heat transfer. *Adv. Heat Transfer*, 1,51-122. https://doi.org/10.1016/S0065-2717(08)70097-2
- [34] V.I.Dybkov (2010) Reaction Diffusion and Solid-State Chemical Kinetics, 2nd ed., Trans Tech Publications, Zuerich. ISBN, 3038134457
- [35] V.I.Dybkov (2013) Chemical Kinetics, IPMS Publications, Kyiv, Free online version http://www.dybkov.kiev.ua
- [36] I.Campos-Silva, M.Ortiz-Domínguez, O.Bravo Bárcenas, M.A.Doñu-Ruiz, D.Bravo-Bárcenas, C. Tapia-Quintero, M.Y. Jiménez-Reyes (2010) Formation and kinetics of FeB/Fe_2B layers and diffusion zone at the surface of AISI 316 borided steels, *Surf. Coat. Technol.* 205, 403-214. https://doi.org/10.1016/j.surfcoat.2010.06.068
- [37] I.Campos-Silva, M.Ortiz-Domínguez, C.Tapia-Quintero et al (2012) Kinetics and Boron Diffusion in the FeB/Fe_2B Layers Formed at the Surface of Borided High-Alloy Steel. *J. of Mater Eng and Perform*, 21, 1714–1723. https://doi.org/10.1007/s11665-011-0088-9
- [38] Z.NaitAbellah, M.Keddad (2014) Estimation of the boron diffusion coefficients in the FeB and Fe_2B layers during the pack-boriding of a high-alloy steel. *Mater. Tehnol.*, 48, 237–242. http://mit.imt.si/Revija/izvodi/mit142/abdellah.pdf
- [39] M.Keddad, M.Kulka (2020) Simulation of Boriding kinetics of AISI D2 steel by using two different approaches, *Met, Sci, Heat Treat*, 61,756–763. https://doi.org/10.1007/s11041-020-00496-2
- [40] M.Keddad, R.Chegroune, M.Kulka, N.Makuch, D.Panfil, P.Siwak, S.Taktak (2018) Characterization tribological and mechanical properties of plasma paste borided AISI 316 steel. *Trans. Indian Inst. Met.* 71, 79–90. doi:10.1007/s12666-017-1142-6
- [41] P.Orihel, M.Drienovský, Z.Gabalcová, P.Jurčí, M.Keddad (2023) Characterization and Boron Diffusion Kinetics on the Surface-Hardened Layers of Royalloy Steel, *Coatings*, 13,113-122. https://doi.org/10.3390/coatings13010113
- [42] I.Campos, R.Torres, O.Bautista, G.Ramírez, L. Zúñiga (2006) Effect of boron paste thickness on the growth kinetics of polyphase boride coatings during the boriding process. *Appl. Surf. Sci.* 252, 2396–2403. http://dx.doi.org/10.1016/j.apsusc.2005.04.022
- [43] T.B.Massalski, H.Okamoto, P.R.Subramanian, L. Kacprzak (1990) Binary Alloy Phase Diagrams, Eds. ASM,480. ISBN: 978-0-87170-403-0
- [44] M.Keddad (2011) Simulation of the growth kinetics of the (FeB/Fe_2B) bilayer obtained on a borided stainless steel, *Applied Surface Science*, 257(6), 2004–2010, https://doi.org/10.1016/j.apsusc. 2010.09.043

IZVOD

DIBKOV MODEL ZA PROCENU DIFUZIJE BORA U DVOSLOJU FeB/Fe_2B NA ČELIKU AISI 316

Cilj ovog rada je primena tri modela za simulaciju difuzije bora u čeliku AISI 316, sa pristupom zasnovanim na klasičnim jednačinama bilansa mase, Dibkovljevom modelu i integralnoj metodi. Iz numeričkih rešenja oba modela, upoređene su predviđene vrednosti debljine slojeva sa eksperimentalnim rezultatima. Pored toga, da bi se poboljšala predvidljivost ova dva modela, neophodno je pronaći precizna merenja difuzije bora u svakoj fazi. Poređenje eksperimentalnih i teorijskih rezultata nam omogućava da potvrdimo validnost oba modela. Nakon validacije, izračunati su srednja kvadratna greška i koeficijent difuzije da bi se postigle dobre performanse i bolja tačnost. Poređenjem rezultata iz dva simulaciona modela suočena su sa eksperimentalnim podacima da bi se potvrdila validnost ove teorijske studije. Konačno, poređenje izvedenih rezultata dalo je vrednosti srednje kvadratne greške jednake 1,6 mm za Fe_2B i 0,75 mm za FeB .

Ključne reči: Boriranje, difuzija, boridi gvožđa, Dibkov model, Integralna metoda

Naučni rad

Rad primljen: 27.09.2023.

Rad prihvaćen: 15.11.2023.

Rad je dostupan na sajtu: www.idk.org.rs/casopis

Aarudi Ranganth Shashikala^{1*}, Kothakula Keerthi¹,
Sridhar Bangarpet Shankar²

^{1,2}Department of Chemistry, Presidency University, Itgalpura,
Bengaluru-64, India, ²Department of Industrial Engineering and
Management, MSRIT, Bengaluru-54, India.

Scientific paper

ISSN 0351-9465, E-ISSN 2466-2585

<https://doi.org/10.62638/ZasMat1135>



Zastita Materijala 65 (2)
236 - 245 (2024)

Electrochemical investigations of Ni-P/nano c-BN deposited on aluminum alloy

ABSTRACT

Electrochemical investigations were carried out on the Ni-P/nano cubic-Boron Nitride (c-BN) coatings obtained by using sodium hypophosphite reduced electrolyte bath solution with complexing agents. The screening of complexing agents was carried out by UV-Visible spectrophotometric studies. The deposits obtained using optimized bath composition was tested by EDAX, SEM and XRD in order to understand the structural morphology of the coatings. Electrochemical studies conducted by Potentiodynamic polarization and Electrochemical Impedance Spectroscopy (EIS) revealed the greater stability of coatings in acidic and alkaline environment. To evaluate the behavior of the coatings in marine environment, Salt spray test was conducted using sodium chloride solution. Results indicate the improved resistance to corrosion with the incorporation of nano c-BN in the coatings.

Keywords: cubic-Boron Nitride, Corrosion resistance, Polarization, EIS, Salt spray

1. INTRODUCTION

Over the years, electroless nickel phosphorous (Ni-P) coatings is used extensively for industrial applications as it provides protection against corrosion, has enhanced mechanical properties and the coatings have superior uniformity with improved life span to the work pieces [1-4]. Electroless nickel deposits can be obtained uniformly on complex shaped objects. The mechanical and chemical properties of Ni-P plating depends on phosphorus content, degree of crystallinity, crystal size and plating bath conditions [5-7]. After annealing, hardness of the binary Ni-P coatings decreased due to increase in crystal structure [8]. Ternary Ni-P-Cu, Ni-Zn-P, Ni-W-P, Ni-Cr-P and Ni-Mo-P have been studied by many authors [9-16]. These ternary coatings enhance the durability of alloy coatings at elevated temperatures. Incorporation of multiple metals in the coatings found to improve the thermal and mechanical properties at higher temperature. However, controlling the phosphorous content and composition of third element in coating will be a challenge [17].

It is difficult to reduce few metals while obtaining ternary electro less deposits. When a metal is difficult to get reduced, its share in the composite cannot reach appreciable values [18]. Ni-Cr-P coatings containing 4% chromium has been studied by Tadashi [19]. Ni-Cr-P deposition by ion exchange method was carried out by researchers [20]. A review related to the deposition of ternary alloys was published [21]. Among the ternary alloys developed only Ni-P coatings with Fe, Co and Cu found to have more practical applications, as they provide uniform thickness deposits on complex, irregular objects with critical dimensions. They also provide coatings with higher hardness, wear resistance and corrosion resistance.

It is reported in literature that addition of nano particles in the binary plating bath enhances the mechanical properties of the composite coating [22-28]. Over the years, Ni-P composite coatings with nano ZnO, TiO₂, Ti, WC, h-BN, SiO₂, SiC and Al₂O₃ have been studied by several researchers [29-32]. Dense, uniform, crack free coatings with higher protection against corrosion were obtained by the incorporation of nano particles. Hexagonal BN (h-BN) offers high corrosion resistance, thermal stability and can function as excellent lubricant [33]. However, h-BN has poor wettability and friction control properties below 400°C [34-35]. Nano c-BN, being extremely hard, improves the micro hardness of the composite coating and corrosion resistance. Dispersion and dissolution of these nano powders

*Corresponding author: A. R. Shashikala¹

Email: aarudirs@gmail.com

Paper received: 25. 09. 2023.

Paper corrected: 29.11.2023.

Paper accepted: 07. 12. 2023.

Paper is available on the website: www.idk.org.rs/journal

in the electrolyte bath solution is a challenge. Continuous agitation through ultra-sonication is required to disperse the same in the bath solution effectively [36].

Acidic hypophosphite plating baths have a number of advantages over the alkaline ammonical baths due to its higher plating rates, good stability and produce deposits with improved properties. Many formulations for acidic hypophosphite based electroless nickel baths have been reported in literature [37-41].

Owing to excellent properties of nano c-BN, in the present study nano c-BN reinforced electroless Ni-P composite coatings (Ni-P/nano c-BN) were produced in a hypophosphite reduced bath solution on 6061- Al substrate in acidic medium. The influence of nano c-BN on the tribological and anticorrosion behaviour of the coatings were studied.

2. EXPERIMENTAL PROCEDURE

2.1. Electroless Ni-P/nano c-BN coatings

Analytical grade reagents were used for the development of Ni-P/nano c-BN on aluminum alloy substrates. The deposition was carried out as per the below mentioned steps [42]. Ball milled nano c-BN with particle size 63-70nm was used for the development of composite coating.

1. Solvent degreasing: Substrate surface was degreased using an organic solvent by ultra-sonication at 25°C.
2. Alkaline cleaning: Alkali cleaning was carried out by dipping the specimens in an alkaline solution at 55 to 60°C for five minutes.
3. De-smutting: Acid scales and other impurities were removed by dipping the substrate in a solution containing mixture of acids for 50 seconds at 25°C.
4. Alloy zincating was carried out at 25°C, followed by electroless plating [43].
5. Electroless Ni-P/nano c-BN plating was obtained on pre-cleaned 6061 –Al substrates in an electrolytic bath solution containing NiSO₄·7H₂O, NaH₂PO₂, Na₃C₄H₆O₄·6H₂O, NH₂-CH₂-COOH, NH₄SO₄, PbNO₃, CHNaSO and nano c-BN, at pH 4.5 and temperature 90±2 °C as indicated in Table 1.

NiSO₄·7H₂O and nano c-BN was used as source of nickle and nano particle respectively, NaH₂PO₂ acts as reducing agent, Na₃C₄H₆O₄·6H₂O and NH₂-CH₂-COOH are the complexing agents, NH₄SO₄ is used as conducting salt, PbNO₃ provides lead ions in the solution facilitating bright coating, sodium lauryl sulphate acts as wetting agent.

2.2. Measurement techniques

2.2.1. Characterization techniques

Double beam UV-Visible spectrophotometer 2202, Sytronics, was used for screening the complexing agents. To examine the morphology and composition of the coatings Scanning electron microscope (Noran scientific analyzer, USA) was used. X-ray diffraction patterns of the coatings were obtained by X-ray diffractometer with CuK α radiation.

2.2.2. Corrosion studies

Protection efficiency of the coatings in acidic and alkaline medium was evaluated by the following techniques:

- a. Polarization studies: Potentiodynamic polarisation studies were conducted in 0.5 N NaOH and 0.5 N HCl solutions by using electrochemical work station. Electroless Ni-P and Ni-P/nano c-BN coated specimens were used as working electrodes. The specimens were immersed in the aqueous media for 45 minutes of equilibrate time before recording the data. All the experiments were conducted at room temperature. Repeated experiments were carried out to get accurate results.
- b. Electrochemical impedance studies: Impedance measurements were conducted by AC signal with amplitude of 0.01 V at open-circuit potential in the frequency range from 10⁻⁵ to 1 Hz. Before performing experiments, a stabilization time of 45 minutes was provided to achieve a stable open-circuit potential. The cell impedance was measured at the frequency from 1 Hz to 10⁵ Hz.
- c. Salt spray test: The stability of the coatings in acidified Sodium chloride solution was evaluated by neutral salt spray test according to ASTM-B117 standard. Every two hours of salt spray, the samples were removed and observed for any degradation.

All the experiments were carried out on multiple samples prepared under optimum conditions and the results obtained is provided in the experimental section.

3. RESULTS AND DISCUSSION

3.1. Optimization of the plating bath

Complexing agents play very important role in producing good quality deposit [15]. Different complexing agents were screened for Ni²⁺ ions in an electrolytic acidic solution at pH 3.0. Tri sodium citrate and glycine were found to form weak complexes with Ni²⁺ ions in presence of nano c-BN which is one of the main requirements to get even

and non-porous deposit. Figure 1, provides the UV-visible absorption spectrum of complexing agents. The absorption spectrum of the Ni^{2+} ions with glycine and c-BN gives two bands characteristic of metal-ligand complexes of octahedral geometry. The absorption spectrum of Ni^{2+} ions with tri sodium citrate and c-BN also gives two bands characteristic of metal-ligand complexes of octahedral geometry. Whereas the absorption spectrum obtained with both the complexing agents and nano c-BN, has three bands characteristic of metal-ligand complexes of octahedral geometry. As glycine and tri sodium citrate complexing agents form weak bonds with the metal ions, both were used as complexing agents in the plating bath solution.

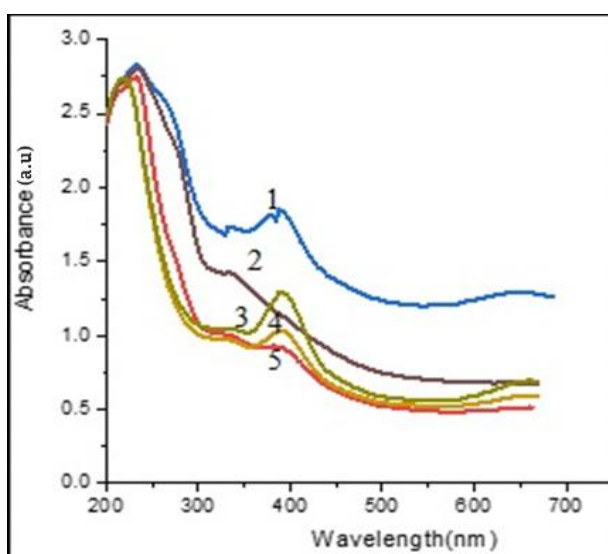


Figure 1. UV absorption spectra 1: Ni^{2+} +TSC+Gly+ c-BN, 2) Nano c-BN, 3) Ni^{2+} +c-BN, 4) Ni^{2+} +Gly+ c-BN, 5) Ni^{2+} +TSC+ c-BN

Slika 1. UV spektri apsorpcije 1: Ni^{2+} +TSC+Gly+ c-BN, 2) Nano c-BN, 3) Ni^{2+} +c-BN, 4) Ni^{2+} +Gly+ c-BN, 5) Ni^{2+} +TSC+ c-BN

Composition of different constituents in the plating bath was varied to optimize the bath composition along with pH and temperature. Concentration of one of the constituent was varied at a time keeping the other constituent's concentration constant. Nickel sulphate concentration was varied from 10 g/L to 40 g/L, sodium hypophosphite and tri sodium citrate concentration was varied from 5 g/L to 35 g/L individually, sodium sulphate concentration was varied from 5 g/L to 20 g/L and nano c-BN concentration was varied from 0.5 g/L to 3 g/L. Nano c-BN with particle size ~66 nm was dispersed in the plating bath solution and subjected to 6 hours of ultra-sonication as solubility of nano particles is low in aqueous solutions. After 6 hours, the solution was filtered and the filtrate was used

for electroless plating on 6061-Al substrates. The concentration of the lead nitrate and sodium lauryl sulphate was kept constant.

The pH of the bath solution was varied from 3.5 to 7.0. Temperature of the plating bath was varied from 70 to 95 °C. At lower pH values the coating obtained was rough and consisted of surface roughness and irregularities. When the pH was increased above 5.5, precipitation of metal oxides and hydroxides was observed. Similarly, the coatings obtained at lower temperatures <90° C was uneven when observed under 4X magnification lens. At higher temperatures, decomposition of bath constituents was observed.

Based on the repeated trials and visual observation of the coatings under 4X magnification lens, the plating bath composition was optimised and the same is tabulated in Table 1. The coatings obtained under optimised conditions were used for the characterization and corrosion studies.

Table 1. Optimised plating bath

Tabela 1. Optimizovana kupka za oplatu

Composition of the plating bath (g/L)	Optimum conditions
NiSO ₄ . 6H ₂ O: 30 NaH ₂ PO ₂ : 20-25 Nano c-BN: 2 Na ₃ C ₆ H ₅ O ₇ : 25 Glycine: 5 NH ₄ SO ₄ : 10-15 Lead Nitrate: 0.001 Sodium Lauryl Sulphate: 0.01	Temp: 90 °C pH: 5 Plating duration: 60 minutes

3.2. Surface morphology and microstructure

The percentage weight composition of the elements in the coatings is provided in Table 2 which indicates the presence of boron and nitrogen along with nickel and phosphorous.

Table 2. Elemental composition of the coating

Tabela 2. Elementarni sastav prevlake

Element	Atomic weight(%)
Boron	20.90
Nitrogen	12.17
Oxygen	18.69
Phosphorous	8.27
Nickel	39.97

Surface morphology of the coatings with and without c-BN at different plating time intervals is shown in Figure 2. Ni-P plating without c-BN was found to have spherical structure. With the incorporation of nano c-BN the coating was found to have uniform distribution with needle like structure. Few nodular lumps were seen at higher plating time.

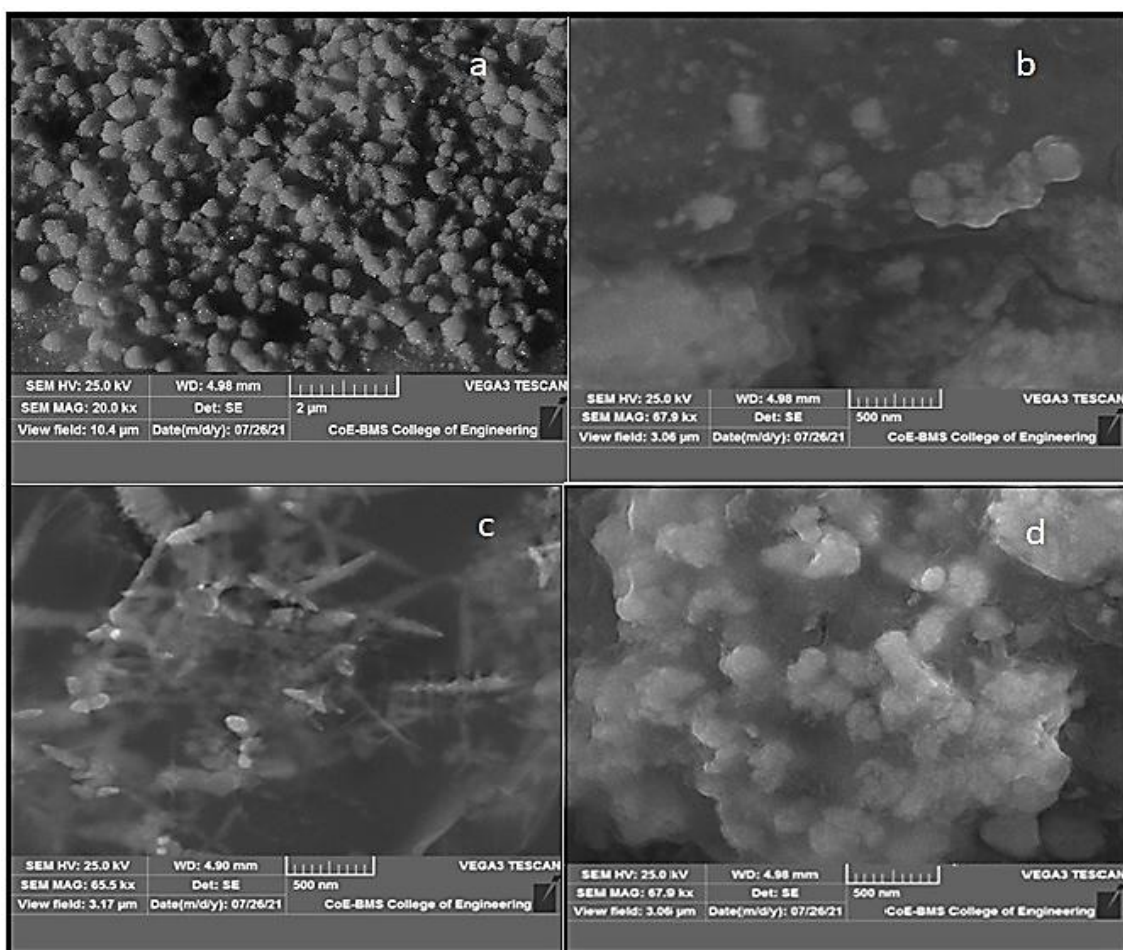


Figure 2. Microstructure of the deposits: a) Ni-P b) Ni-P/nano c-BN at 30 minutes of plating time c) Ni-P/nano c-BN at 1 hour of plating time d) Ni-P/nano c-BN at 2 hours of plating time

Slika 2. Mikrostruktura naslaga: a) Ni-P b) Ni-P/nano c-BN na 30 minuta nanošenja c) Ni-P/nano c-BN na 1 sat vremena nanošenja d) Ni-P/ nano c-BN na 2 sata nanošenja

The XRD pattern of the nano c-BN reinforced electroless coating is presented in Figure 3 and it exhibit five distinct peaks. The diffraction pattern indicates the crystalline nature of the coatings. The maximum peak (111) corresponds to FCC structured crystalline nickel. In addition to nickel (111) peak, well defined peaks of Ni_3P (110) and BN (220) was observed. Other small peaks (311) and (211) corresponds to nickel and phosphorous. The studies also indicate that the nano c-BN is embedded well into the matrix of Ni-P. The average crystallite size of the ball milled nano c-BN was also calculated from the Debye-Scherrer formula [24] with the help of FWHM values of the peaks in the XRD pattern as epr our earlier publication [44]. The average crystallite size observed was 76nm.

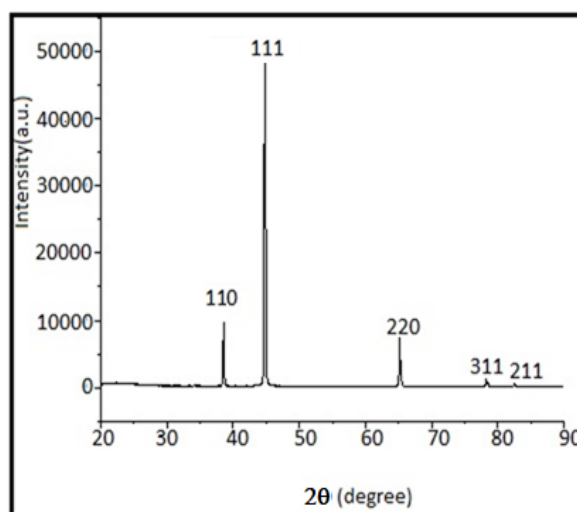


Figure 3. XRD pattern for Ni-P/nano c-BN plating
Slika 3. XRD uzorak za Ni-P/nano c-BN prevlaku

3.3. Electrochemical investigations

Electroless Ni-P/ nano c-BN composite coatings obtained from optimised plating bath (Table 1) were subjected to electrochemical corrosion measurements. The measurements were carried out for multiple samples and the concordant results obtained is reported.

3.3.1. Potentiodynamic polarization studies

Potentiodynamic polarisation experiments were carried out for electroless Ni-P/ nano c-BN composite coatings to investigate the corrosion behaviour of the coatings in both alkaline and acidic environments. The results were compared with bare aluminium and electroless Ni-P coatings. Figure 4a and 4b depicts the tafel plots of the samples measured in sodium hydroxide and hydrochloric acid medium respectively. It is evident that the composite coatings exhibit better protection irrespective of the type of medium compared to binary coatings. The corrosion current (I_{corr}) was calculated by using the equation given below. Polarization resistance was obtained from the Tafel slopes. The corrosion data is tabulated in Table 3.

$$b = \frac{\beta_a \beta_c}{(\beta_a + \beta_c) 2.303} \quad (1)$$

$$I_{corr} = b/R_p \quad (2)$$

where

b is Stern-Geary coefficient and R_p is polarization resistance

The nano c-BN reinforced coatings possess lower corrosion current values and offer high efficiency compared to bare Al 6061 and electroless Ni-P coatings. Higher electrochemical resistance of c-BN nano particles might be the reason for improved protection ability of the coatings [45]. Incorporation of nano c-BN has significant impact on the corrosion resistance of the composite coatings compared to that reported for other composite coatings with zirconium boron nitride, SiC and h-BN [46-49].

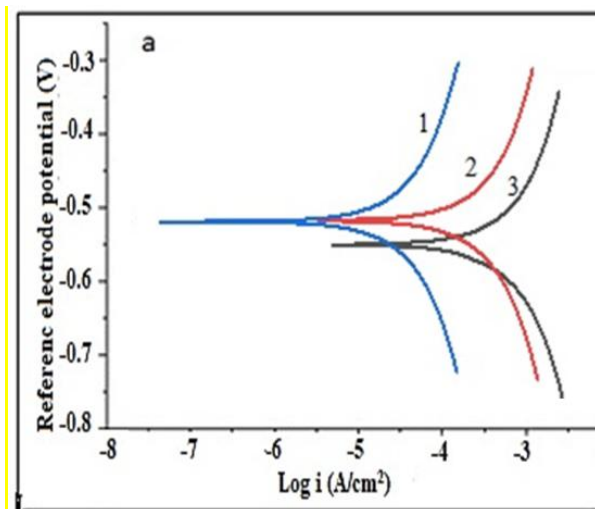


Figure 4 a. Current-Potential diagrams in 0.5N NaOH (1. Ni-P/nano c-BN 2. Electroless Ni-P 3. Al alloy)

Slika 4 a. Dijagrami strujnog potencijala u 0,5N NaOH (1. Ni-P/nano c-BN 2. Bezelektrični Ni-P 3. Al legura)

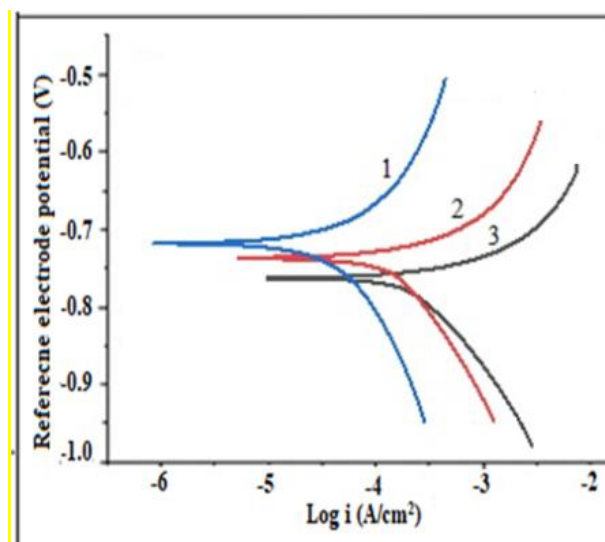


Figure 4 b. Current-Potential diagrams in 0.5N HCl (1. Ni-P/nano c-BN 2. Electroless Ni-P 3. Al alloy)

Slika 4 b. Dijagrami struja-potencijal u 0,5N HCl (1. Ni-P/nano c-BN 2. Bezelektrični Ni-P 3. Al legura)

Table 3. Polarization data of the samples in 0.5N NaOH and 0.5N HCl solution

Tabela 3. Podaci o polarizaciji uzoraka u 0.5N rastvoru NaOH i 0.5N HCl

Type of coating	Aluminium alloy		Ni/P		Ni-P/nano c-BN	
	NaOH	HCl	NaOH	HCl	NaOH	HCl
E_{corr} (V vs SCE)	-0.57	-0.79	-0.53	-0.75	-0.51	-0.71
β_a (V/dec)	0.068	0.075	0.292	0.395	0.316	0.422
β_c (V/dec)	-0.42	-0.69	-0.36	-0.61	-0.32	-0.52
I_{corr} ($\mu\text{A}/\text{cm}^2$)	18.2	22.6	9.8	14.3	4.3	6.8
PE (%)	-	-	79.8	71.8	94.8	86.2

3.3.2. Impedance studies

Nyquist plots obtained in corrosive media is presented in Figure 5a and 5b respectively for alkaline and acidic medium. Increase in the semicircle diameter of the specimen indicates higher impedance values as observed in case of composite coating [50].

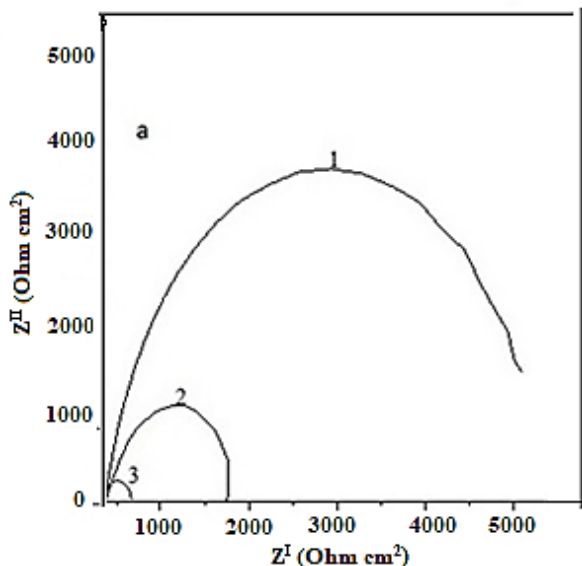


Figure 5a. Nyquist diagrams in 0.5N NaOH (1. Ni-P/nano c-BN, 2. Ni/P, 3. Aluminium alloy)

Slika 5a. Nyquist-ovi dijagrami u 0.5N NaOH (1. Ni-P/nano c-BN, 2. Ni/P, 3. legura aluminijuma)

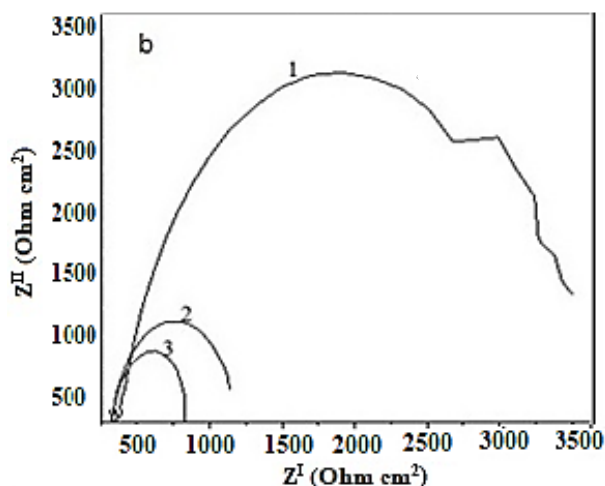


Figure 5b. Nyquist diagrams in 0.5N HCl (1. Ni-P/nano c-BN, 2. Ni/P, 3. Aluminium alloy)

Slika 5b. Nyquist-ovi dijagrami u 0.5N HCl (1. Ni-P/nano c-BN, 2. Ni/P, 3. legura aluminijuma)

The Bode plots of bare aluminium alloy, binary Ni-P as well as Ni-P/nano c-BN in acidic and alkaline media is provided in Figure 6 and 7. The higher impedance values were observed in case of composite coatings which confirms the higher corrosion resistance of the coatings. The minute voids in the Ni-P coatings is occupied by the nano c-BN particles leading to the improved resistance of the composite coatings [51]. The protection efficiency of nano composite coatings is less in acidic medium compared to that in alkaline medium. The Randel equivalent circuit for the above system is presented in Figure 8.

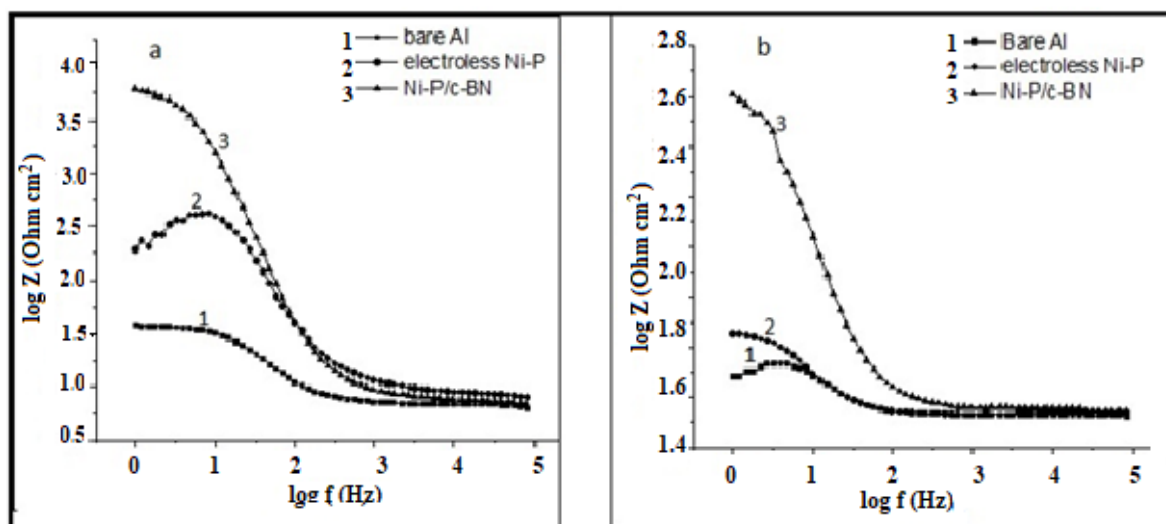


Figure 6. Bode amplitude plots of 1. Aluminium alloy 2. Ni/P 3. Ni-P/nano c-BN (a. 0.5N NaOH and b. 0.5N HCl)

Slika 6. Bode-ovi grafikoni amplitude 1. Legura aluminijuma 2. Ni/P 3. Ni-P/nano c-BN (a. 0.5N NaOH i b. 0.5N HCl)

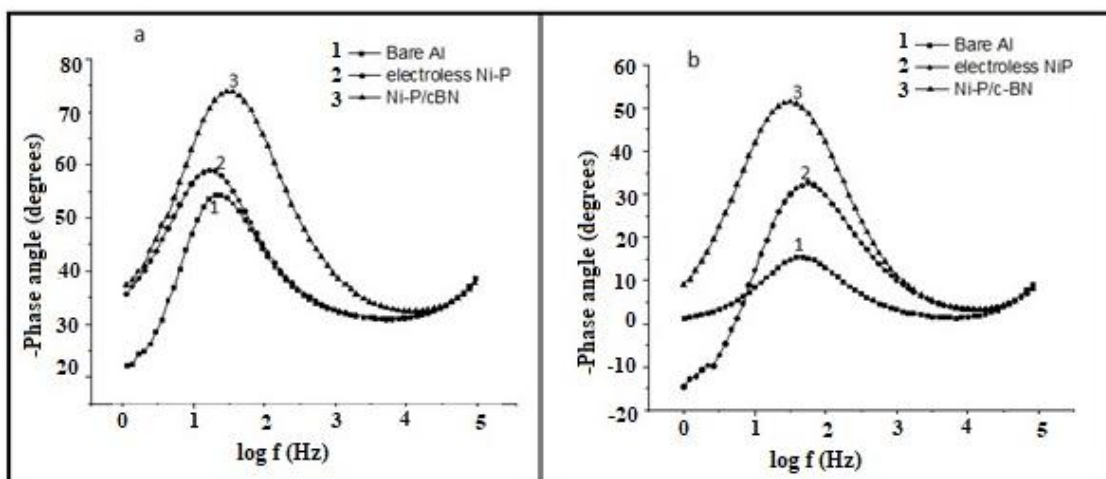


Figure 7. Bode Phase angle diagrams of 1. Aluminium alloy 2. Ni/P 3. Ni-P/nano c-BN (a. 0.5N NaOH and b. 0.5N HCl)

Slika 7. Bode-ovi dijagrami faznog ugla 1. Legura aluminijuma 2. Ni/P 3. Ni-P/nano c-BN (a. 0.5N NaOH i b. 0.5N HCl)

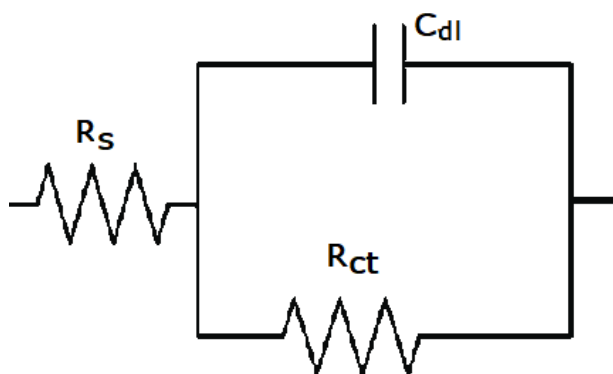


Figure 8. Randel circuit for the system

Slika 8. Rendel-ovo kolo za sistem

3.3.3. Neutral salt spray test

Salt spray tests were conducted by spraying 5% sodium chloride solution on the substrates for four days continuously. The specimens were observed for degradation under 4X magnification lens after every 2 hours by taking the specimens out of the fog chamber. After four days, the samples were removed, washed and dried in air [25]. The composite coating was stable up to 92 hours while the binary Ni-P coating started to degrade after 3days. The observation is in agreement with the electrochemical studies. Pin holes and grey spots were observed in both the samples after 4 days of exposure to fog.

3.4. Microhardness

Micro hardness of the electroless Ni-P plated specimens with and without nano c-BN, before and after heat treatment at 250°C for 2 hours was

determined by Vickers hardness method with 50 g load. The test was repeated for multiple samples and average microhardness recorded is tabulated in Table 4. Higher microhardness of composite coating may be attributed to the presence of hard nano c-BN in the coating. A remarkable increase in microhardness was observed after heat treatment owing to precipitation of the intermetallic Ni₃P in the coatings at high temperatures [51-52].

Table 4. Microhardness of the samples before and after heat treatment

Tabela 4. Mikrotvrdoća uzoraka pre i posle termičke obrade

Microhardness (VHN)→ ↓Type of coating	Before heat treatment	After heat treatment
Electroless Ni-P	96	101
Electroless Ni-P/nano c-BN	185	202

3.5. Testing evaluation

All the samples were inspected visually for defects under 4X magnification lens. Deposits were found to be uniform and even over the entire surface of the substrate.

3.5.1. Adhesion test

The adherence strength of the composite coating to the substrate was investigated by scotch tape peel off method. In this test 100 squares of 4 mm² were scribed through the coatings. A pressure sensitive tape of one- inch was then applied tightly

over the coating by rolling a roller covered with rubber over the tape twice. The pressure sensitive tape was taken off at right angle to the coating. The samples were later inspected visually for any detachment in the coating. The coating was found to adhere to the surface firmly.

3.5.2. Heat treatment

The binary Ni-P and nano c-BN reinforced composite coatings were heat treated in a hot air oven at 250°C for 6 hours to study the effect of high temperature on the physical nature of the coating and hardness. After 6 hours the test samples were taken out of the oven and inspected for any physical changes. No degradation like discolouration, blisters or pits were observed.

3.5.3. Humidity test

Humidity test is conducted to study the effect of relative humidity and high temperature on the samples, which in turns related to corrosion protection efficiency [53]. This test is conducted by placing the samples in a thermostatically controlled humidity chamber for two days under $95 \pm 5\%$ relative humidity at 50°C. After 48 hours, the specimens were removed from the chamber and observed for any defects or degradation under 4X lens. Blisters and discoloration was observed on electroless Ni-P coatings and no degradation was observed in case of Ni-P/nano c-BN coatings indicating higher stability under humid conditions.

4 CONCLUSIONS

The Ni-P/nano c-BN composite coatings were obtained by eco-friendly electroless method. EDX and XRD studies confirms the presence of nickel, phosphorous, boron and nitrogen in the composite coatings. Needle like structure with few agglomerates were observed in scanning electron micrographs. Electroless Ni-P/nano c-BN coatings exhibited better protection against corrosion in both acidic and alkaline media as indicated by polarization, impedance and salt spray studies. Incorporation of nano c-BN enhanced the barrier properties of the coatings providing higher protection indicating these coatings can be used for corrosion protection applications both in acidic and alkaline environments. Nano c-BN reinforced coatings exhibited improved hardness compared to electroless Ni-P coatings. The improved hardness is attributed to the incorporation of hard nano c-BN in the coatings. The micro hardness of the composite coatings increased after heat treatment due to precipitation of Ni_3P . The composite coatings exhibited excellent stability to higher temperatures and humid environment.

5. REFERENCES

- [1] L.Ramesh et al. (1999) Electrolytic preparation and characterization of Ni-Fe-Mo alloys: Cathode materials for alkaline water electrolysis, *Int. J. Energy Res.*, 23(10), 919-924, [https://doi.org/10.1002/\(SICI\)1099-114X\(199908\)23:10%3C919::AID-ER524%3E3.0.CO;2-D](https://doi.org/10.1002/(SICI)1099-114X(199908)23:10%3C919::AID-ER524%3E3.0.CO;2-D)
- [2] G.O.Mallory et al. (1990) *Electroless plating: Fundamentals and Applications*, AESF, Orlando, FL., 207(a), 189 (b).
- [3] Chintada et al. (2021) State of Art Review on Nickel-Based Electroless Coatings and Materials, *J. Bio. Tribo.*, 7, 134, 3-14, <https://doi.org/10.1007/s40735-021-00568-7>.
- [4] M.Yan et al. (2008) Improved microhardness and wear resistance of the as-deposited electroless Ni-P coating, *Surf. Coat. Technol.*, 20(24), 5909-5913, <https://doi.org/10.1016/j.surfcoat.2008.06.180>.
- [5] T. Mimani et al. (1996) The effect of microstructure on the corrosion behaviour of electroless Ni-P alloys in acidic media, *Surf. Coat. Technol.*, 79 (1), 246-251, [https://doi.org/10.1016/0257-8972\(95\)02446-8](https://doi.org/10.1016/0257-8972(95)02446-8)
- [6] J. Flis et al. (1985) Effect of phosphorous on Anodic Dissolution and passivation on Nickel in near-neutral solution, *Corrosion*, 41, 700-706, <https://doi.org/10.5006/1.3583006>.
- [7] K.Sugita et al. (1984) Composition and Crystallinity of Electroless Nickel, *J. Electrochem. Soc.*, 131(1), 111-114, <https://doi.org/10.1149/1.2115488>.
- [8] P. Murukesan et al. (2007) Hardness and structural correlation for electroless Ni alloy deposits, *J. Mater. Sci.*, 42, 6600-6607, <https://doi.org/10.1007/s10853-007-1501-5>.
- [9] M. Meng et al. (2019) Mechanical properties and tribological behaviour of electroless Ni-P-Cu coatings on corrosion-resistant alloys under ultrahigh contact stress with sprayed nanoparticles, *Tribology International*, 139, 59-66, <https://doi.org/10.1016/j.triboint.2019.06.031>.
- [10] C.J. Chen et al. (1999) A Mathematical Model of an Electrochemical Capacitor with Double-Layer and Faradaic Processes, *J. Electrochem Soc.*, 146(9), 3168-3175, <https://doi.org/10.1149/1.1392450>.
- [11] Fan-Bean Wu et al. (2007) Fabrication and characterization of the Ni-P-Al-W multicomponent coatings, *Surf. Coat. Technol.*, 202, 762-767, <https://doi.org/10.1016/j.surfcoat.2007.06.070>.
- [12] Shu et al. (2015) Parameter optimization for Electroless Ni-P-W coatings, *Surf. Coat. Technol.*, 276, 195-201, <https://doi.org/10.1016/j.surfcoat.2015.06.068>.
- [13] M.S.Ali Eltoun (2016) Electroless and corrosion of Nickel-Phosphorus-Tungsten Alloy, *The J of Middle East and North Africa Sciences*, 2(2), 16-24, <https://doi.org/10.12816/0032658>.
- [14] C.F.Conde et al. (1989) Non-isothermal crystallization and isothermal transformation kinetics of the Ni-Cr-P metallic glass, *J. Mater. Sci.*, 24, 139-142, <https://doi.org/10.1007/BF00660945>.

- [15] A.R.Shashikala et al. (2007) Studies and characterisation of electroless Ni–Cr–P alloy coatings, *Trans. IM.*, 85(6), 320-325, <https://doi.org/10.1179/174591907X246483>.
- [16] K Parker (1996) The Effect of Nickel Salts on Electroless Nickel Plating, *Plat. Surf. Finish.*, 83(1), 70-71, 70, 71 (nmfrc.org).
- [17] Wei-Yu Chen et al. (2004) Thermal stability of sputtered Ni–P and Ni–P–Cr coatings during cycling test and annealing treatment, *Surf. Coat. Technol.*, 177–178 (6), 222-226, <https://doi.org/10.1016/j.surfcoat.2003.09.036>.
- [18] G.G. Gawrilov (1979) Chemical electroless nickel plating, Portullis press, Redhill, p.168.
- [19] S.Singh Siwal et al. (2023) A review on electrochemical techniques for metal recovery from waste resources, *Current Opinion in Green and Sustainable Chemistry*, 39, 100722, <https://doi.org/10.1016/j.cogsc.2022.100722>.
- [20] Sh. Liu et al. (2021) Mechanistic study of Ni–Cr–P alloy electrodeposition and characterization of deposits, *Journal of Electroanalytical Chemistry*, 897, 115582, <https://doi.org/10.1016/j.jelechem.2021.115582>.
- [21] C.R.Shipley (1984) Historical highlights of electroless plating, *Plating and Surface Finishing*, 71(6), 24-27.
- [22] S.Karthikeyan et al. (2014) Effect of reducing agent and nano Al₂O₃ particles on the properties of electroless Ni-P coating, *Appl Surf Sci.*, 307, 654-660, <https://doi.org/10.1016/j.apsusc.2014.04.092>.
- [23] S. Sadreddini et al. (2014) Corrosion resistance enhancement of Ni-P-nano SiO₂ Composite coatings on Aluminium, *Appl Surf sci.*, 303, 125-130. <https://doi.org/10.1016/j.apsusc.2014.02.109>.
- [24] Y.Y.Liu et al. (2007) Synthesis and tribological behavior of electroless Ni-P-WC nano composite coatings, *Surf Coat Tech.*, 201(16-17), 7246-7251, <https://doi.org/10.1016/j.surfcoat.2007.01.035>.
- [25] A.R.Shashikala et al. (2021) Co-deposition of electroless Ni-P-ZnO composites and evaluation of corrosion resistance of the coatings, *Mater. Today proceed.*, 45, 3837-3840, <http://doi.org/10.1016/j.matpr.2020.05.447>.
- [26] Kh.Shahzad et al. (2020) Corrosion &Heat treatment study of electroless Ni-P-Ti nanocomposite coatings deposited on HSLA steel, *Nanomaterials.*, 10, 1-19, <https://doi.org/10.3390/nano10101932>.
- [27] A.V.Sreenu (2018) Aluminium-Boron Nitride nano composite coating by friction surfacing on low carbon steel substrate-a feasibility study, *Mater. today proceed.*, 5, 26829-26835, <https://doi.org/10.1016/j.matpr.2018.08.164>.
- [28] Ch. Zhao et al. (2014) Preparation and mechanical properties of electroless Ni–P–WC nano composite coatings, *JMEP*, 23, 193-197, <http://doi.org/10.1007/s11665-013-0753-2>.
- [29] He.-Zhi Zhou et al. (2016) Preparation research of Nano-SiC/Ni-P composite coating under a compound field, *IOP Conf. Series: Materials Science and Engineering* 137, 012066, <http://doi.org/10.1088/1757-899X/137/1/012066>.
- [30] S.R.All. Karam et al. (2012) An Investigation on Effects of TiO₂ Nano-Particles Incorporated in Electroless NiP Coatings Properties, *International J. Modern physics conference series.*, 05, 833-840, <https://doi.org/10.1142/S2010194512002814>.
- [31] S.Sharma et al. (2016) Co-deposition of Synthesized ZnO Nanoparticles into Ni-P Matrix Using Electroless Technique and Their Corrosion Study, *JMEP.*, 25, 4383-4393, <http://doi.org/10.1007/s11665-016-2292-0>.
- [32] H. Luo et al. (2015) Development of electroless Ni-P/nano WC composite coatings and investigation on its properties, *Surf Coat Tech*, 277, 99-106, <https://doi.org/10.1016/j.surfcoat.2015.07.011>.
- [33] K.A.Bello et al. (2015) Synthesis and characterization of Ni-P coated Hexagonal Boron Nitride by electroless Nickel Deposition, *Surf Engg & appl Electrochem.*, 51 (6), 523-529, <https://doi.org/10.3103/S1068375515060058>.
- [34] Zh. Shitang et al. (2008) Friction and Wear Behavior of Laser Cladding NiAl/hBN Self-Lubricating Composite Coating, *Mater. Sci Eng., A* 491 (1), 47-54, <http://doi.org/10.1016/j.msea.2007.12.015>.
- [35] Bi.-Cuong et al. (2019) Operational and environmental conditions regulate the frictional behavior of two-dimensional materials, *Appl Surf Sci.*, 483, 34-44, <https://doi.org/10.1016/j.apsusc.2019.03.249>.
- [36] S Kumari et al. (2019) Electrochemical behavior of nanostructured graphene nickel phosphorus composite coating on copper, *J Appl Electrochem.*, 49, 1157-1166, <https://doi.org/10.1007/s10800-019-01333-y>.
- [37] P.P.Krishnamoorthy et al. (1992) Properties of electroless nickel-phosphorus deposits after crystallization, *Metal Finishing.*, 90, 13-17.
- [38] A.Talat El-Mallah et al. (1993) Autocatalytic (Electroless) deposition of nickel-phosphorus-boron alloys - Part III, *Metal Finishing.*, 91, 19-21.
- [39] D.Baudrand (1996) Nickel sulfamate plating, its mystique and practicality, *Metal Finishing.*, 94 (7), 15-18, [https://doi.org/10.1016/0026-0576\(96\)81353-5](https://doi.org/10.1016/0026-0576(96)81353-5)
- [40] W.Sha et al. (2011) Crystallisation of nickel–phosphorus (Ni–P) deposits with medium and low phosphorus content”, Editor(s): W. Sha, X. Wu, K.G. Keong, In *Woodhead Publishing Series in Metals and Surface Engineering, Electroless Copper and Nickel–Phosphorus Plating*”, Woodhead Publishing, 163, <http://doi.org/10.1533/9780857090966.2.163>.
- [41] K.Parker (1987) The Formulation of Electroless Nickel-Phosphorus Plating Bath, *Plating and Surface Finishing*”, 74(2), 60-65, <https://api.semanticscholar.org/CorpusID:102381908>
- [42] A.R.Shashikala et al. (2006) Studies on solar selective black chrome plating on Al alloys, *Galvanotechnik.*, 10, 1-14.
- [43] C.R.Raghavendra (2016) Electrodeposition of Ni-Al₂O₃ nano composite coating and evaluation of wear characteristics, *IOP Conf. Ser.: Mater. Sci.*

- Eng, 149, 012110, <http://doi.org/10.1088/1757-899X/149/1/012110>.
- [44] A.R.Shashikala et al. (2023) The effect of ball milling on the morphology of cubic boron nitride, Malaysian Journal of Science, 42 (3), 19-25, <https://doi.org/10.22452/mjs.vol42no3.4>.
- [45] M.Alishahi et al. (2012) The effect of carbon nanotubes on the corrosion and tribological behavior of electroless Ni-P-CNT composite coating, Appl Surf Sci., 258, 2439-2446, <https://doi.org/10.1016/j.apsusc.2011.10.067>.
- [46] M.Urgen et al. (1995) Corrosion of zirconium boride and zirconium boron nitride coated steels, Surf. Coat. Tech., 71(1), 60-66, [https://doi.org/10.1016/0257-8972\(94\)02316-1](https://doi.org/10.1016/0257-8972(94)02316-1).
- [47] A.Kumar et al. (2022) Sputter-grown hierarchical nitride (TiN & h-BN) coatings on BN nanoplates reinforced Al7079 alloy with improved corrosion resistance, Surf. Coat. Tech., 432, 128-161, <https://doi.org/10.1016/j.surfcoat.2021.128061>.
- [48] Y.Fan et al. (2020) Corrosion Resistance of Modified Hexagonal Boron Nitride (h-BN) Nanosheets Doped Acrylic Acid Coating on Hot-Dip Galvanized Steel, Materials, 13 (10), 2340-2350, <https://doi.org/10.3390/ma13102340>.
- [49] X.Fu et al. (2020) Corrosion resistance of Ni-P/SiC and Ni-P composite coatings prepared by magnetic field-enhanced jet electrodeposition, RSC Adv., 10(56), 34167-34176, <https://doi.org/10.1039/D0RA06735K>.
- [50] A.R.Shashikala et al. (2008) Chemical conversion coatings on Magnesium Alloys-A comparative study, Int. J. Electrochem. Sci., 3(9), 993-1004, [https://doi.org/10.1016/S1452-3981\(23\)15498-8](https://doi.org/10.1016/S1452-3981(23)15498-8).
- [51] B.Radwan, K.Ali et al. (2018) Properties enhancement of Ni-P electrodeposited coatings by the incorporation of nanoscale Y2O3 particles, Appl. Surf. Sci., 457, 956-967, <https://doi.org/10.1016/j.apsusc.2018.06.241>.
- [52] I.Apachitei et al. (1998) Electroless Ni-P Composite Coatings: The Effect of Heat Treatment on the Microhardness of Substrate and Coating, Scripta Materialia, 38(9), 1347-1353, [https://doi.org/10.1016/S1359-6462\(98\)00054-2](https://doi.org/10.1016/S1359-6462(98)00054-2).
- [53] W.Ya Li et al. (2011) Effect of vacuum heat treatment on microstructure and microhardness of cold-sprayed TiN particle-reinforced Al alloy-based composites, Mater & Design., 32(1), 388-394, <https://doi.org/10.1016/j.matdes.2010.06.002>.

IZVOD

ELEKTROHEMIJSKA ISPITIVANJA Ni-P/NANO c-BN NANESENIH NA LEGURU ALUMINIJUMA

Elektrohemijska ispitivanja su obavljena na prevlakama Ni-P/nano kubni bor nitridom (c-BN) dobijenim korišćenjem rastvora u kupatilu elektrolita redukovanog natrijum hipofosfitom sa agensima za stvaranje kompleksa. Skrining agenasa za stvaranje kompleksa je sproveden UV-Visible spektrofotometrijskim studijama. Naslage dobijene korišćenjem optimizovanog sastava kupatila su testirane pomoću EDAX, SEM i XRD da bi se razumela strukturna morfologija premaza. Elektrohemijske studije sprovedene pomoću potenciodinamičke polarizacije i elektrohemijske impedansne spektroskopije (EIS) otkrile su veću stabilnost premaza u kiseloj i alkalnoj sredini. Da bi se procenilo ponašanje premaza u morskom okruženju, sprovedeno je ispitivanje slanim sprejom korišćenjem rastvora natrijum hlorida. Rezultati ukazuju na poboljšanu otpornost na koroziju ugradnjom nano c-BN u prevlake.

Ključne reči: kubni-bor nitrid, otpornost na koroziju, polarizacija, EIS, slani sprej

Naučni rad

Rad primljen: 25.09.2023.

Rad korigovan: 29.11.2023.

Rad prihvaćen: 07.12.2023.

Rad je dostupan na sajtu: www.idk.org.rs/casopis

Narendhran Sadhasivam*

Department of Biotechnology, Sri Krishna Arts and Science College,
Kuniamuthur, Coimbatore, India

Scientific paper

ISSN 0351-9465, E-ISSN 2466-2585

<https://doi.org/10.62638/ZasMat1131>



Zastita Materijala 65 (2)

246 - 257 (2024)

Synergistic effect of Fe and Co doped ZnO nanoparticles synthesized using *Alpinia galanga* against *Candida parasilopsis*

ABSTRACT

In this investigation, nanoparticles such as ZnO, Fe doped ZnO and Co doped ZnO NPs prepared by the co-precipitation method were tested against the pathogenic yeast. The spectroscopic analyses were carried out to identify the morphological and chemical composition of the synthesized nanoparticles. The results of XRD analysis revealed that the synthesized nanoparticles were crystalline in nature with average size ranges between 32 – 34 nm approximately. EDX and SEM analysis were carried out to identify the element composition (Co, Fe and Zn) and spherical shape of nanoparticles. The functional group that is responsible for the capping and stability of nanoparticles was confirmed by FTIR analysis, to compare the antifungal efficiency of ZnO, Fe doped ZnO and Co doped ZnO from the resultant zone of inhibition.

Keywords: Antifungal activity, *Candida parasilopsis*, Copper, Iron, Zinc

1. INTRODUCTION

Fungal infections are concerned to be a serious case of health conditions. The severity of the infections seems to be higher in the case of immune compromised people as they are more susceptible which in turn impairs their disease conditions. The administration of drugs resulting from modern medical inventions potentially have immune suppressive actions which is also considered to be one of the causes of high incidence of fungal infections. It is high time for the world to get cautious about fungal infections [1]. *Candida* species are opportunistic fungal pathogens in which both *Candida albicans* and non *albicans candida* species (eg, *Candida parasilopsis*) have caused increased incidence of diseases recently. The severity of the infections is complex due to its associated virulence factors and the emergence of drug resistant strains. In such cases, a direct administration of such antifungal agents has many limitations such as toxicities, drug resistance etc [2]. The unavailability of many antifungal drugs as well as cost expenses limits its usage in many of the developing countries. Hence science and technology for developing a novel medication that will be affordable as well as effective in invading fungal diseases [3].

Over the last two decades, nanotechnology has been in high demand which changed the conventional drug administration processes. It is possible to have a targeted drug delivery as it emphasizes on submicron size particles in which mono or poly therapeutic compounds may either dispersed, adsorbed, covalently bonded, or encapsulated in vesicles, capsules, or polymeric matrix. Furthermore, the nanodrug delivery system enhances the bioavailability and decreases the possible side effects of the drug. Considering the wider perspective of nanotechnology in medicine, several researchers are making an exceptional effort to raise the standards of nano drugs by putting forward various methodologies to fabricate novel nano drug formulations [4]. Now-a days, metallic nanoparticles have gained immense attention as antimicrobial agents due to their high surface area to volume ratio, availability and ease of synthesis. Interestingly, green synthesis of nanoparticles from plant extracts is a striking area of research in nanotechnology. It is economically feasible and eco-friendly compared to physical and chemical routes [5].

Alpinia galanga is a plant belonging to zingiberacea family and is widely distributed in South East Asia. It has a role as a traditional medicine to cure inflammation, HIV, diabetes and ulcers. The *Alpinia galanga* leaf extracts contain pharmacologically significant metabolites such as galanolactones, quercetin, galangin, kaempferol, and labdane [6]. Consequently, due to their diverse pharmacological activities, these extracts could be extensively utilized in the synthesis of ZnO

*Corresponding author: Sadhasivam Narendhran

Email: narendhrans@skasc.ac.in

Paper received: 27. 09. 2023.

Paper accepted: 09. 12. 2023.

Paper is available on the website: www.idk.org.rs/journal

nanoparticles. Generally, metal and metal oxide nanoparticles have more application due to their stability when compared to other organic materials. ZnO have a very attractive attributes such as selective toxicity targeting prokaryotic cells, anticancer activities etc. They trigger mechanisms like apoptosis, necrosis, and the generation of reactive oxygen species (ROS) in their effects. Studies indicate that ZnO has proven to be a potent antibacterial agent, capable of selectively damaging membrane structures and compromising their integrity. Additionally, these nanoparticles can efficiently penetrate intracellular of bacteria, leading to damage to both DNA and proteins [5]. Usually ZnO is a chemically stable and biocompatible material with optical, electronic and magnetic properties.

Formulation of doped nanoparticles is another advancement made in the field of nanotechnology. As far as doping is concerned, transition metals like Fe and Co can be largely utilized and it enhances the physico-chemical properties of the nanoparticles [8]. Moreover, doping of ZnO nanoparticle with transition metals in which the metal site functions as trapping sites by acting as electron acceptors from ZnO there by detaining electron hole recombination and its subsequent reduction in band gap energy. Doping process could be made possible with various methods where sol-gel technique, solid state reaction, co precipitation and pulsed laser decomposition are some of them. Accordingly, doping of transition metals like Fe and Co can complement the antimicrobial properties of ZnO. Certain studies propose that introducing dopants such as Fe and Co into ZnO creates defects in the crystalline lattice. This, in turn, leads to the generation of a higher amount of Reactive Oxygen Species, consequently enhancing antimicrobial activity [9]. Literally cobalt and zinc have similar atomic radii of 0.58 Å and 0.6 Å, respectively. In general doping generally enhances the efficiencies of ZnO in terms of increasing the optical absorption which ultimately reduces the band gap and increases the antimicrobial activity [8].

The present study is focused on exploiting *Alpinia galanga* as a raw material for the green synthesis of ZnO nanoparticles. The aim is to enhance the functionality of the nanoparticles by doping them with Fe and Co to form Fe/ZnO NP and Co/ZnO NP using a co-precipitation method. Furthermore, the pure ZnO and transition metal doped (Fe and Co) ZnO nanoparticles were characterized using FT-IR, EDAX, DLS, UV-Visible spectroscopy, SEM and XRD analysis. Additionally, an antifungal susceptibility test is done by carrying out a well diffusion method against *Candida parapsilopsis*.

2. MATERIALS AND METHODS

Healthy leaves of *Alpinia galanga* were collected from kanthalloor region (10.2135°N, 77.1972°E), Idukki District, Kerala, India. *Candida parapsilopsis* culture was obtained from Institute of Microbial Technology Chandigarh, India. Precursors such as Zinc Chloride ($ZnCl_2$), Ferrous Sulphate ($FeSO_4$) and Cobalt Nitrate ($Co(NO_3)_2$) were purchased from Sigma Aldrich.

2.1 Methodology

2.1.1. Preparation of plant extract

Alpinia galanga leaves were rinsed with purified Milli Q water to remove impurities, dried under shade for 8-10 days, and blend to a fine powder. About 20g of powdered leaf sample were dissolved in 100 ml of Milli Q water and followed by a water bath at 65°C for 25 minutes. Upon cooling the extract was filtered using Whatmann No1 filter paper. The filtrate was used further for the synthesis of ZnO nanoparticles.

2.1.2. Synthesis of ZnO nanoparticles

ZnO nanoparticles were synthesized by gently adding 0.1M zinc chloride solution ($ZnCl_2$) to 25ml of leaf extract in a magnetic stirrer at 60°C for 2 hours [10]. Subsequently, 20ml of 1% NaOH solution was added to the mixture of zinc chloride and leaf extract. When a light yellow coloured precipitate was formed it was allowed to settle for 10 hrs. The particles were separated by centrifugation at 6000 rpm for 20 minutes and were then rinsed three times with distilled water and 70% ethanol to eliminate any traces of impurities. The purified yellow color precipitant was dried overnight at 80°C in hot air oven and powdered to obtain ZnO nanoparticles.

2.1.3. Synthesis of Co doped ZnO and Fe doped ZnO nanoparticles

To synthesize Co-doped ZnO nanoparticles, 1 gram of ZnO nanoparticles was mixed in a conical flask containing 50ml of deionized water (solution A) and stirred continuously for 30 minutes [11,12]. An estimated aliquot of (0.1M) cobalt nitrate solution (solution B) was then added to solution A and stirred further. To this homogeneous mixture, 1g of NaOH and 1% Polyvinylpyrrolidone (PVP) were added. The reaction was proceeded for 2hrs at 5°C to form precipitate of Co doped ZnO nanoparticles. The precipitate was left undisturbed for few hours followed by rinsing with distilled water and 70% ethanol remove any traces of impurities. The purified precipitant was dried overnight in hot air oven at 80°C for 2 days and then powdered.

To synthesize Fe-doped ZnO nanoparticles, 1 gram of ZnO nanoparticles was mixed in a conical

flask containing 50ml of deionized water (solution A) and stirred continuously for 30 minutes [13,14]. An estimated aliquot of (0.1M) ferrous sulfate solution (solution B) was then added to solution A and stirred further. To this homogeneous mixture, 1g of NaOH and 1% PVP were added. The reaction was proceeded for 2hrs at 5°C to form precipitate of Co doped ZnO nanoparticles. The precipitate was left undisturbed for few hours followed by rinsing with distilled water and 70% ethanol remove any traces of impurities. The purified precipitant was dried overnight in hot air oven at 80°C for 2 days and then powdered.

2.2. Characterization of ZnO/Fe doped ZnO/ Co doped ZnO nanoparticles

The crystalline structure and quality of ZnO, Fe doped ZnO and Co doped ZnO NPs were examined using XRD by step scan technique with Cu-K α radiation (1500A°, 40KV, 30 mA) to determine the crystal density [15]. Optical properties of nanoparticles were characterized on the basis of UV-Visible absorption spectra within the wavelength range of 300-700nm [16]. Elemental composition and surface morphology were analyzed using EDAX (Energy Dispersive analysis of X-Ray) and SEM (Scanning electron microscopy model, Hi tech model-s-3400n) [17]. A Perker Elmer 1725X Fourier transform infrared spectrophotometer was used to obtain information about the bond formation in the fabricated nanoparticles. Simultaneously the average size and distribution of nanoparticles were determined by Dynamic Light Scattering analysis [18]

2.3. Antifungal activity of ZnO NPs, Fe doped ZnO NPs and Co doped ZnO NPs

Antifungal activities of ZnO, Fe doped ZnO and Co doped ZnO nanoparticles were performed by agar well diffusion method against *Candida parapsilopsis* [18]. Pure culture of *Candida parapsilopsis* was sub cultured in potato dextrose broth at room temperature in an orbital shaking incubator (Remi, India) at 200rpm. A 100 μ l of subculture was swabbed on potato dextrose agar plates. Following culture absorption after 10 minutes, wells of 6mm size were punched with the help of a sterile gel puncher. Samples of ZnO, Fe doped ZnO and Co doped ZnO nanoparticles with varying concentrations of 50mg/ml and 100mg/ml were loaded to individually labelled plates. A 10mg/ml concentration of positive control (Amphotericin B) was added to every single well in the plates and a negative control of distilled water was also loaded appropriately using micropipettes. The plates were incubated at room temperature for 48hrs. After 48hrs of incubation, the zone of

inhibition was measured in diameter and the mean values are recorded.

2.4. Determination of Minimum Bactericidal Concentration (MBC), and Minimum Fungicidal Concentration (MFC)

Following a broth dilution method [19] the solutions of nanoparticles (ZnO, Fe doped ZnO and Co doped ZnO) were serially diluted in two folds. A 100 μ g/ml of sterile PDA broth was added to each well of a 96 well microtitre plates. To the first well, a 100 μ g/ml concentration of respective nanoparticles was added and mixed uniformly. The suspensions were further transferred and the process continued to obtain a series of dilutions with concentrations of 100, 50, 25, 12.5, and 3.125 μ g/ml respectively. The wells were further inoculated with 2 μ l of inoculum and were incubated at room temperature. Further the plates were monitored for turbidity which indicates the presence of growth and non-turbidity indicating the absence of growth. Thus from the experiment the MIC values were investigated. MIC refers to the lowest concentration of nanoparticles which will inhibit the visible growth appearance of microbes after incubating for a required period of time [19,20]. The minimum fungal concentration (MFC) was considered to be the lowest concentration of ZnO, Fe doped ZnO and Co doped ZnO nanoparticles that prevent the development of any single colony of *Candida parapsilopsis* on PDA agar plates following incubation at room temperature.

2.5. Statistical analysis

Every result was shown as mean \pm standard deviation. Applying SPSS statistical tool, growth attributes were examined at the significant level of ≤ 0.005 using T-test to compare the differences between ZnO, Fe doped ZnO, Co doped ZnO, and control, respectively. The possible effects of ZnO, Fe doped ZnO, and Co doped ZnO nanoparticles were evaluated by performing one-way analysis of variance (ANOVA) if P values of ≤ 0.005 were proved to be statistically significant.

3. RESULTS AND DISCUSSION

3.1. Structural analysis

The structural information of *Alpinia galanga* synthesized ZnO and transition metal doped ZnO (Fe and Co) NPs were analyzed from X-ray diffraction pattern (Fig 1). Figure 1 which shows the XRD spectrum of ZnO, Fe doped ZnO, and Co doped ZnO NPs revealed strong diffraction peaks at 2 θ value matching to the crystal plane of (100), (002), (101), (102), (110), (103), (112) of respective NPs. In fact, the intense peaks at (100), (101) reveal a crystalline hexagonal wurtzite structure [21].

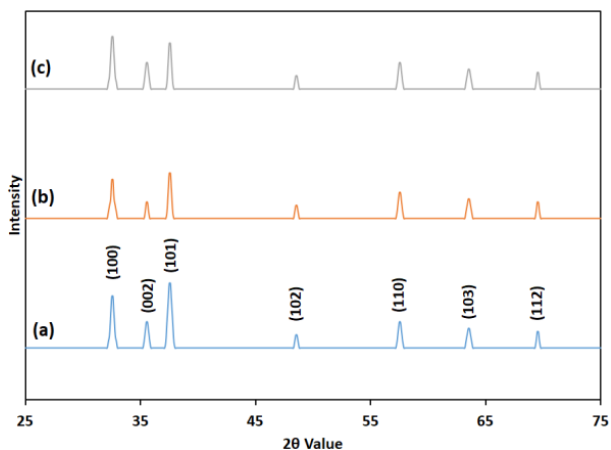


Figure 1. XRD analysis of synthesized nanoparticles (a) ZnO, (b) Co-ZnO and (c) Fe-ZnO
 Slika 1. XRD analiza sintetizovanih nanočestica (a) ZnO, (b) Co-ZnO i (c) Fe-ZnO

A single phase with no additional peaks (secondary phases) was observed in the Fe, Co, and Fe/Co doped clusters when indexing the peaks with the assistance of the JCPDS-file 36-1451. A similar case was reported by Mohamed et al. [22] in which the fabricated Co/ZnO NPs matched with a standard XRD pattern of ZnO. Hence, XRD pattern add more evidence to the current analysis as it proves the lack of extra peaks in doped ZnO NPs as well as an unaltered hexagonal wurtzite structure in doped ZnO NPs. Therefore all the three NPs have a same XRD spectrum. Elumalai et al. [23] recorded the mean crystalline size (D) of powdered ZnO to be 18nm using Scherrer equation $D=0.89\lambda/(\beta\cos\theta)$. Ta et al. [24] reports that there is no significant change in the lattice structure and quality of ZnO crystal upon doping. Hence, the current study reports estimated particle size of 34.64nm, 32nm and 32.19nm for ZnO, Co-ZnO and Fe-ZnO, respectively.

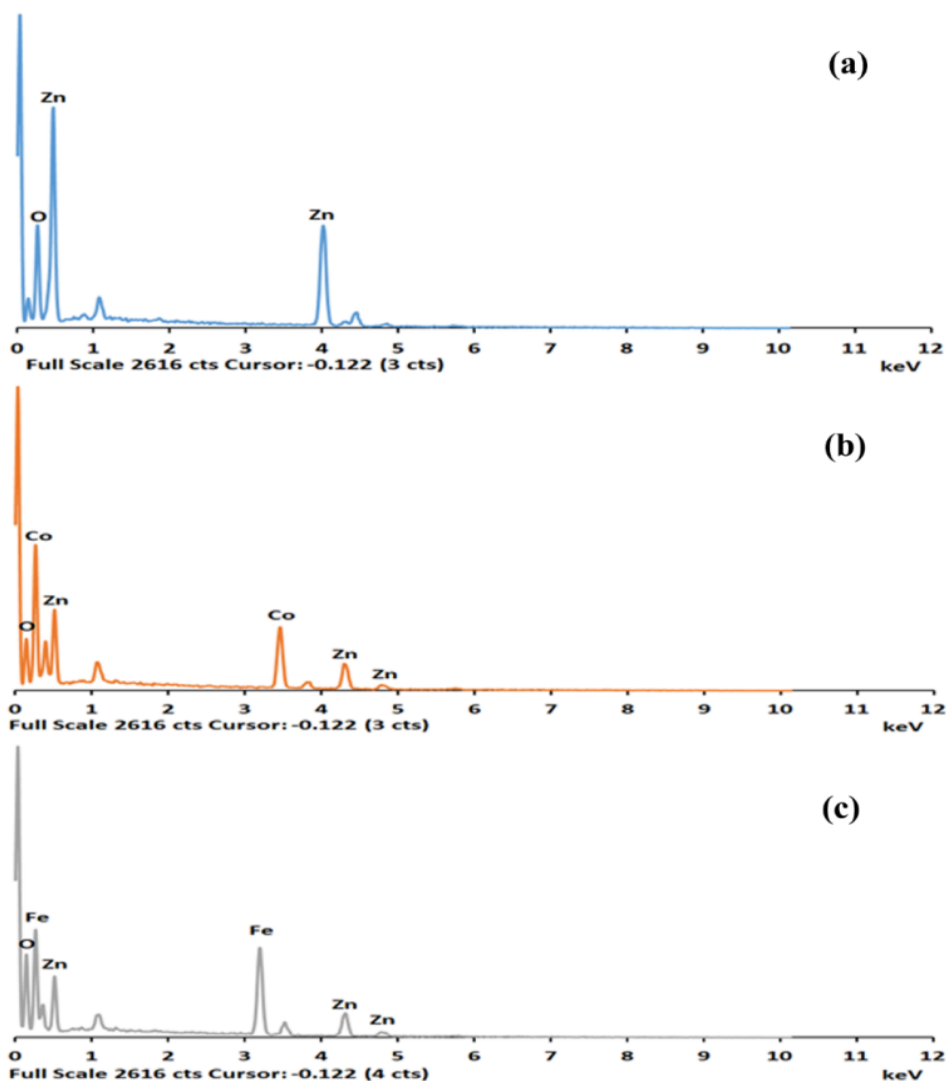


Figure 2. EDX analysis of synthesized nanoparticles (a) ZnO, (b) Co-ZnO and (c) Fe-ZnO
 Slika 2. EDX analiza sintetizovanih nanočestica (a) ZnO, (b) Co-ZnO i (c) Fe-ZnO

Surface morphology of the ZnO NPs and doped ZnO NPs were investigated using Scanning Electron Microscopy (Fig 2, Fig 3 and Fig 4). Figure recorded under different magnifications reveals that particles are agglomerated with spherical-like and hexagonal-like appearance with a relatively uniform size distribution. Furthermore, the elemental analysis of the synthesized ZnO and doped ZnO NPs was obtained from the corresponding Energy

dispersive X-ray spectrum shown in Fig 5. The accurate elemental composition of NPs in atomic% and weight% recorded are shown in Table 1. A qualitative analysis performed by Sharma et al. [21] confirms the purity of the NPs with the absence of any other foreign materials within the individual spectrum of nanoparticles. This supports the validity of the current study.

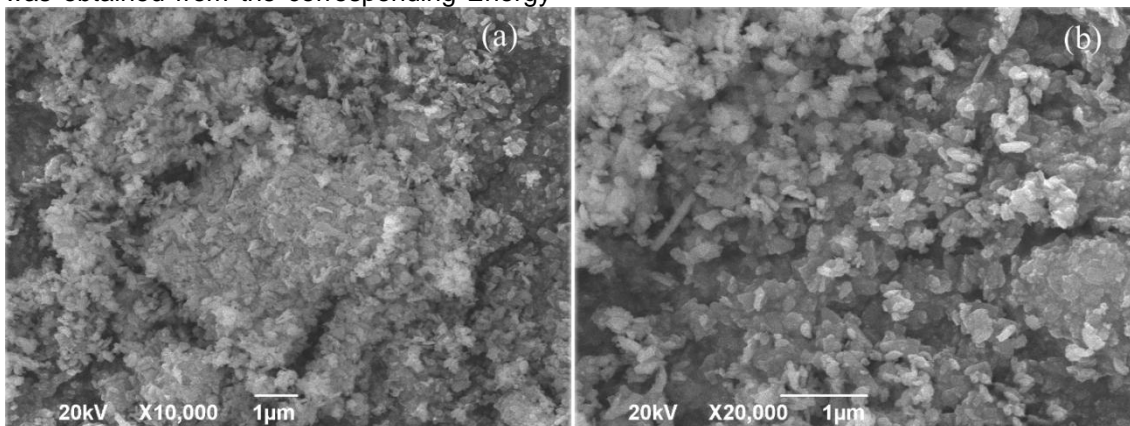


Figure 3. SEM image of *Alpinia galanga* mediated ZnO NPs

Slika 3. SEM slika ZnO NP posredovanih *Alpinia galanga*

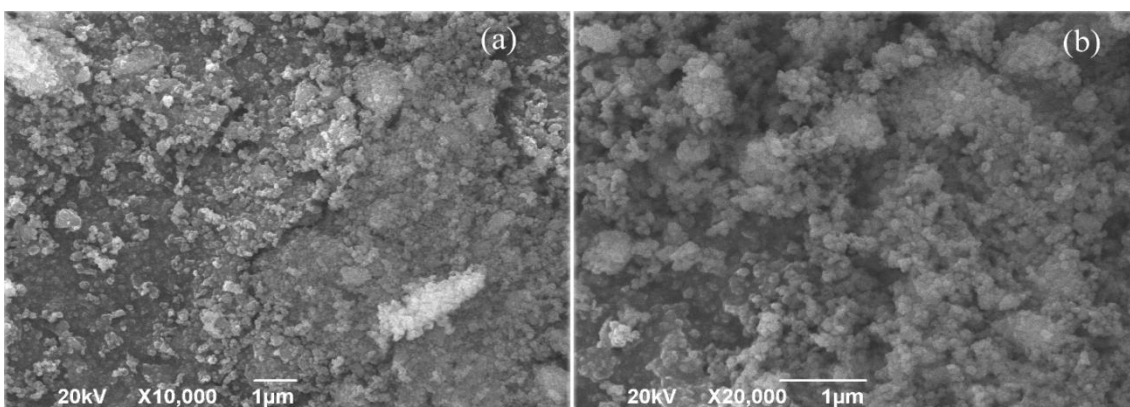


Figure 4. SEM image of Co-ZnO NPs

Slika 4. SEM slika Co-ZnO NP

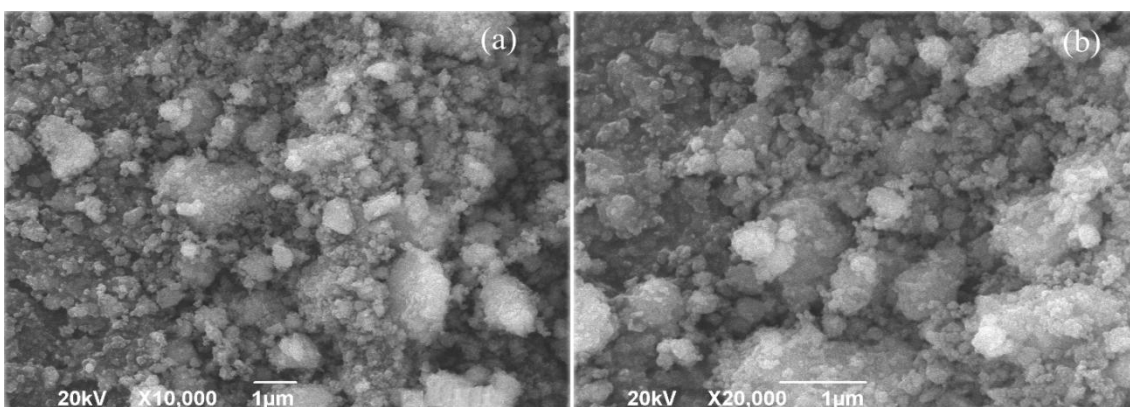


Figure 5. SEM image of Fe-ZnO NPs

Slika 5. SEM slika Fe-ZnO NP

Table 1. EDX analysis of ZnO, Co-ZnO and Fe-ZnO NPs

Tabela 1. EDX analiza ZnO, Co-ZnO i Fe-ZnO NP

Elements	Atomic percentage (%)				Weight percentage (%)			
	Zn	Co	Fe	O	Zn	Co	Fe	O
ZnO	36.71	-	-	63.29	69.73	-	-	30.27
Co-ZnO	11.28	13.91	-	74.81	26.78	29.76	-	43.46
Fe-ZnO	11.49	-	20.37	68.15	25.21	-	38.19	36.61

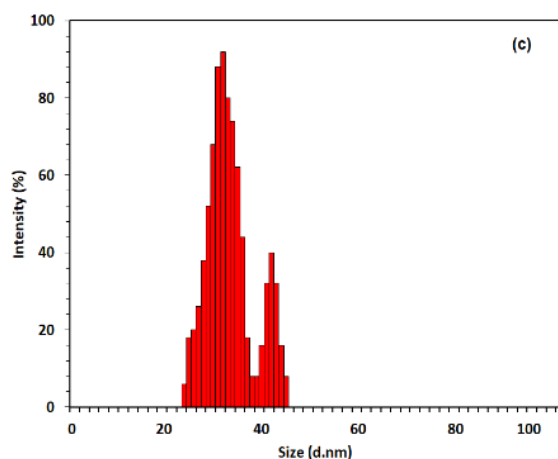
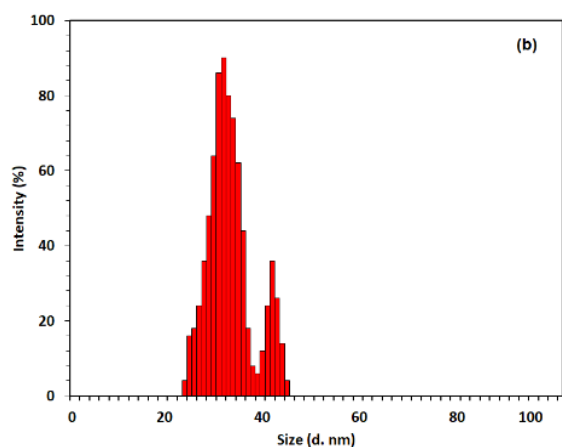
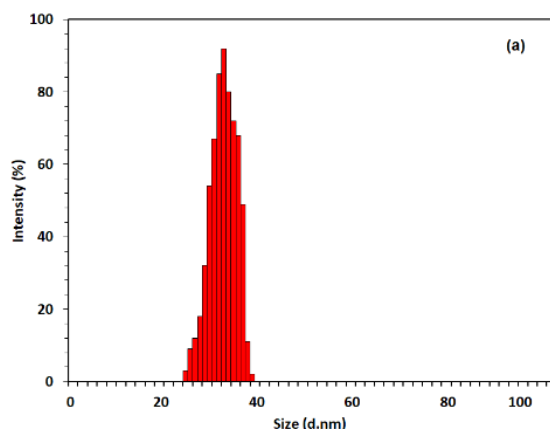


Figure 6. Particle size analysis of (a) ZnO, (b) Co-ZnO and (c) Fe-ZnO NPs

Slika 6. Analiza veličine čestica (a) ZnO, (b) Co-ZnO i (c) Fe-ZnO NP

3.3. Particle size analysis

Dynamic Light Scattering studies is used to determine the average size distribution profile of the ZnO, Fe doped ZnO and Co doped ZnO nanoparticles (Fig 6).

Table 2 shows the average size distribution of the NPs and which confirm the results obtained by XRD and SEM. The average size (Z) of ZnO, Co-ZnO and Fe-ZnO was found to be 36, 32 and 32 nm, respectively.

Table 2. The average size distribution of ZnO, Co-ZnO and Fe-ZnO NPs estimated by using Particle size analysis

Tabela 2. Prosečna distribucija veličine ZnO, Co-ZnO i Fe-ZnO NP procenjena korišćenjem analize veličine čestica

Nanoparticles	Size distribution (d.nm)	Z- Average size (d.nm)
ZnO	24-38	36
Co-ZnO	22-44	32
Fe-ZnO	22-44	32

3.4. Fourier Transform Infrared spectroscopy (FTIR)

The characteristic major peaks in the FTIR spectrum of *A. galanga* leaf extract show a broad band at 3143 cm^{-1} and 3444 cm^{-1} due to O-H stretching and bending vibrations of polyphenols (Fig 7 and Table 3). A slender band at 1768 cm^{-1} reveals the C=O stretch corresponding to carboxylic acid. Similarly, the peak at 1056 cm^{-1} is attributed to an O-H bend. Intense sharp bands at 1400 cm^{-1} and 1637 cm^{-1} correspond to aromatic (C=C stretch) functional groups [17]. The band at 1637 cm^{-1} represents the N-H bending vibrations of primary amines. Moreover, the bands at 619 cm^{-1} correspond to bending vibrations of alkynes (=C-H) and stretching vibrations of alkyl halides respectively.

FTIR spectrum revealed the function of phytochemicals as a capping agent during the synthesis of ZnO NPs. When the bioactive compound is bound to the surface of ZnO NPs it subsequently results in the reduction and stabilization of NPs (phenolic compounds, amines, ether, carboxylic acids, and hydroxyl groups) [18].

For the reduction of Zn^{2+} to Zn^0 O-H, C-N and N-H groups are involved [17]. Furthermore, ZnO/Co-ZnO/Fe-ZnO NPs spectrum exhibit a similar broad absorption band at 3142 cm^{-1} , 3379 cm^{-1} , 3140 cm^{-1} [18] corresponding to stretching vibration H bending vibrations in alcohol (Fig 8 and Table 4). The band at 3140 cm^{-1} in Co doped ZnO NP corresponds to H bending vibrations. Similarly, an intense band at 1402 cm^{-1} and 1400 cm^{-1} corresponds to C=C stretch in aromatic ring. There is an absence of C=O stretching vibrations in

synthesized ZnO, Co-ZnO, Fe-ZnO spectrums. Vijayakumar et al. [18] reported that the peaks from $700\text{--}900\text{ cm}^{-1}$ in FTIR spectra of ZnO particles are attributed to the bond formation between Fe and O, confirming the synthesis of Fe-doped ZnO nanoparticles. Similarly Sharma et al. [21] also confirmed the presence of a band at 875 cm^{-1} which was referred as the frequency of metal oxide vibrations due to the changes in the features of metal resulting from doping of cobalt metal oxide precursor.

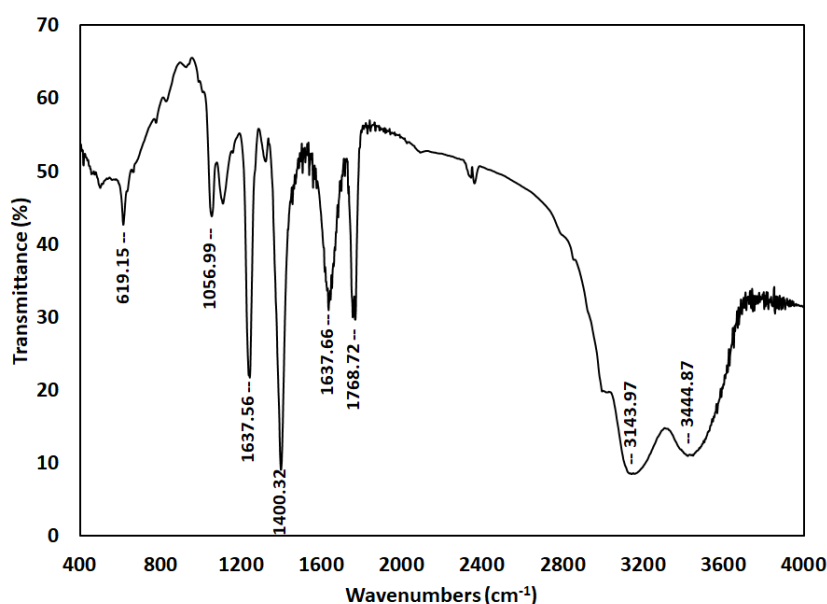


Figure 7. FTIR analysis of *Alpinia galangal* aqueous extract

Slika 7. FTIR analiza vodenog ekstrakta *Alpinia galangal*

Table 3. FTIR analysis of ZnO, Co-ZnO and Fe-ZnO NPs

Tabela 3. FTIR analiza ZnO, Co-ZnO i Fe-ZnO NP

Functional group and bond		<i>A. galanga</i>	ZnO	Co:ZnO	Fe:ZnO
Alkynes	=C-H (Bending)	619.15	617.22	688.59	617.22
Alkyl halides	C-Cl stretch		-	-	831.32
carboxylic acids	O-H bend	1056.99	-	941.26	-
Primary amines	N-H bend	1637.56	1639.49	1624.06	1639.49
Amine	C-N (Stretch)		1128.36	1128.36	1130.29
Aromatic	C=C (Stretch)	1400.32, 1637.66	1402.25	1402.25	1400.32
Carboxylic acid	C=O stretch	1768.72	-	-	-
Alcohol	O-H (Stretch, H-bending)	3143.97, 3444.87	3142.04	3379.29, 3140.11	3140.11

3.5. Antifungal Assay

Antifungal assay of ZnO, Co doped ZnO and Fe doped ZnO NPs against *Candida parapsilopsis* was determined by the well diffusion method. Table 4 shows the details of resulting zone of inhibition

against standard Amphotericin B (AmB). A concentration dependent antifungal activity is observed from these results. An ANOVA test clarifies that the results obtained were statistically significant.

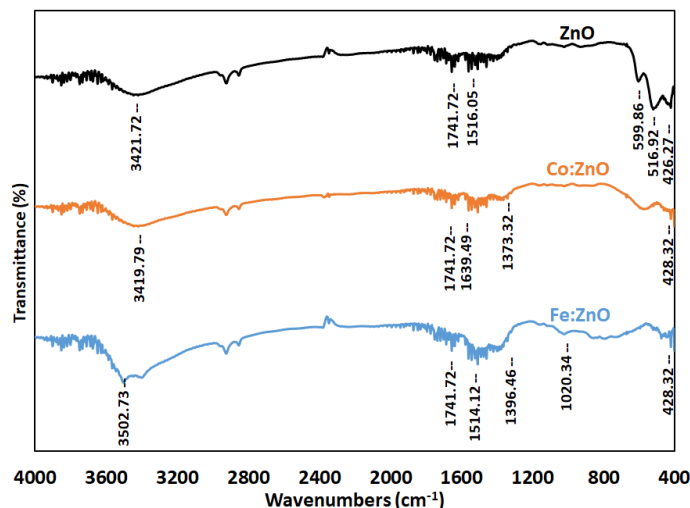


Figure 8. FTIR analysis of ZnO, Co-ZnO and Fe-ZnO NPs

Slika 8. FTIR analiza ZnO, Co-ZnO i Fe-ZnO NPs

Table 4. Antifungal activity of ZnO, Co-ZnO and Fe-ZnO NPs against candida parasilopsis. The resulted zone of inhibition (mm) are expressed in Mean ± SD

Tabela 4. Antifungalna aktivnost ZnO, Co-ZnO i Fe-ZnO NP protiv candida parasilopsis. Dobijena zona inhibicije (mm) je izražena kao srednja vrednost ± SD

Nanoparticles	Different concentration of Nanoparticles		Control (Amphotericin B 10 mg/ml)	Mean ± SD	t test	F	Sig.
	50 mg/L	100 mg/L					
ZnO	8.66 ± 0.57	9.50 ± 0.50		8.27 ± 1.34	11.738	20.818	0.002*
Co-ZnO	8.33 ± 0.57	9.00 ± 1.00	5.77 ± 0.57	7.77 ± 1.56	9.168	17.357	0.006*
Fe-ZnO	8.66 ± 0.57	12.00 ± 1.00		8.88 ± 1.71	6.512	34.857	0.000*

Figure 9 shows the zone of inhibition of ZnO/Co-ZnO/Fe-ZnO at 50 and 100mg/L. The highest zone of inhibition against *Candida parasilopsis* observed had with a diameter of 9.50±0.50 at a concentration of 100mg/L (Fig 9). Likewise zone of inhibition is 9.00±1.00 and 12.00±1.00 for Co-ZnO and Fe-ZnO NPs, respectively. The observed zone of inhibition against *Candida parasilopsis* is specified for ZnO/Co-ZnO/Fe-ZnO at concentrations of 50 and 100mg/L. The data shows the highest zone of inhibition (with a diameter of 9.50±0.50) at a concentration of 100mg/L. Additionally, specific values for the zone of inhibition are provided for

Co-ZnO and Fe-ZnO NPs. The concluding statement ties these results together by attributing the increased antifungal activity to the synergistic effect of doping in the nanoparticles. The supporting evidence comes from the observed zone of inhibition values for different nanoparticle formulations at varying concentrations. Additionally, the present analysis supports the fact that particles in nano dimensions have effective properties compared to their macro dimensions. Upon comparing the zones of clearance observed around both the standard and samples, it was found that all three types of nanoparticles were effective in inhibiting growth [23].

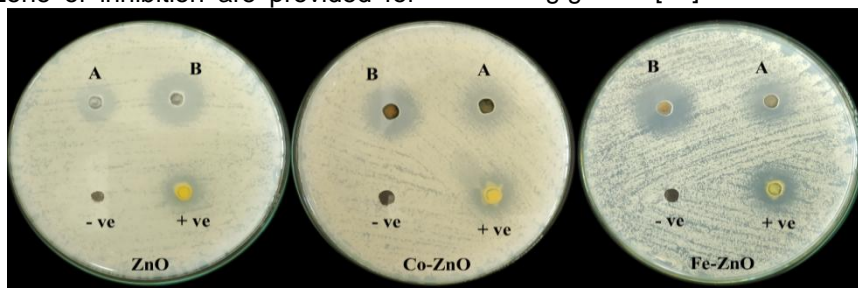


Figure 9. Antifungal activity of ZnO, Co-ZnO and Fe-ZnO NPs on candida parasilopsis

Slika 9. Antifungalna aktivnost ZnO, Co-ZnO i Fe-ZnO NP na candida parasilopsis

The MIC and MFC values of synthesized ZnO, Fe doped ZnO and Co doped ZnO NPs are shown (Table 5). From these values, The MIC for ZnO NPs is observed at a concentration of 12.5 $\mu\text{g/ml}$, while both Co-ZnO and Fe-ZnO NPs share identical MIC values at a concentration of 3.125 $\mu\text{g/ml}$. The MFC values show significant value of 25 $\mu\text{g/ml}$ for ZnO NPs, 3.125 $\mu\text{g/ml}$ for Fe-ZnO and Co-ZnO NPs. Thus evaluating MIC and MFC, a potential MIC/MFC ratio was calculated to be 2;1;1 for ZnO; Fe-ZnO; Co-ZnO NPs.

Table 5. MIC ($\mu\text{g/ml}$) and MBC ($\mu\text{g/ml}$) values of ZnO, Co-ZnO and Fe-ZnO NPs against *Candida parasilopsis*

Tabela 5. MIC ($\mu\text{g/ml}$) i MBC ($\mu\text{g/ml}$) vrednosti ZnO, Co-ZnO i Fe-ZnO NP protiv *parasilopsis kandide*

Nanoparticles	MIC ($\mu\text{g/ml}$)	MBC ($\mu\text{g/ml}$)	MBC/MIC ratio
ZnO	12.5	25	2
Co-ZnO	3.125	3.125	1
Fe-ZnO	3.125	3.125	1

The biofilm inhibitory activity of synthesized nanoparticles was determined by a standard crystal violet method performed on micro titration plates. Figures 10 reveal the light microscopic observation of the biofilm and the image recorded using an inverted microscope under 40X magnification (Fig 11). Figure 10 shows the effective inhibition of fungal hyphae according to standard 10mg AmB and 100mg, 50mg, and 25mg of Fe-ZnO. The figure 10 shows a synergistic effect in the biofilm inhibitory activity by Fe-ZnO compared to that Co-ZnO in the same concentration range. Nevertheless, the rest of the concentrations also exhibit an appreciating inhibitory activity against a pathogenic *Candida parapsilopsis* biofilm. Eventually, there is a decreased aggregation of planktonic cells in the biofilm compared to control (absence of nanomaterial). In the case of both light and inverted microscopic observations both the nanoparticles appeared to have a concentration dependent anti biofilm activity against the *Candida parapsilopsis* strain.

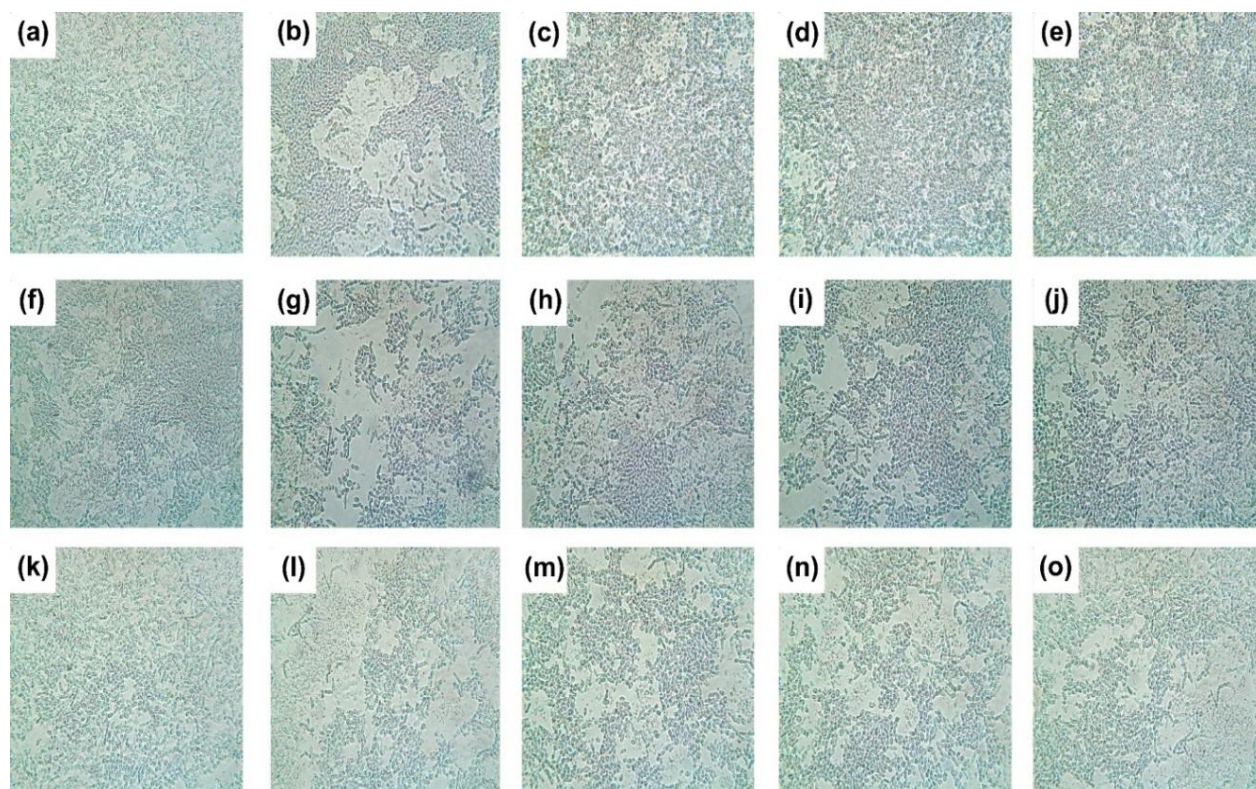


Figure 10. CV stained light microscopic observation of the biofilm inhibitory assay of ZnO (a-e), Co-ZnO (f-j) and Fe-ZnO (k-o) NPs on *C.parasilopsis*

Slika 10. CV obojeno svetlosnim mikroskopskim posmatranjem testa inhibitora biofilma ZnO (a-e), Co-ZnO (f-j) i Fe-ZnO (k-o) NP na *C.parasilopsis*

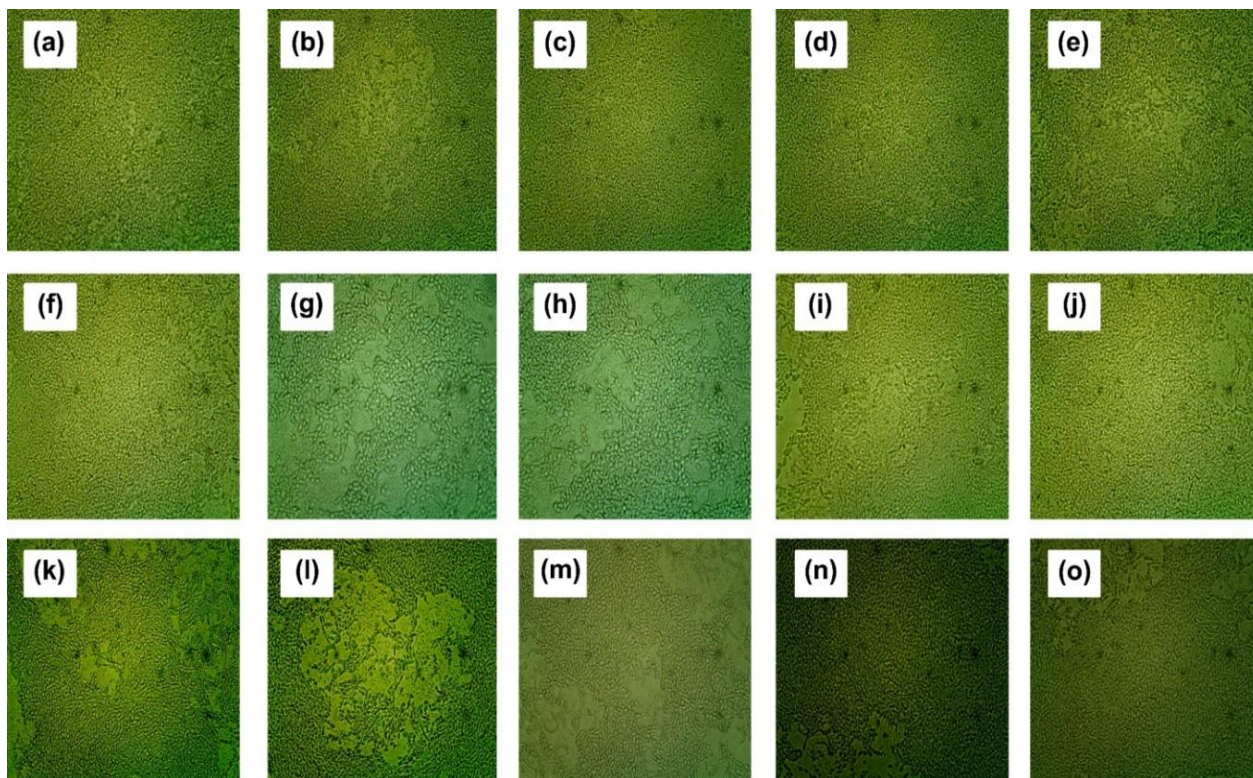


Figure 11. The image obtained from inverted microscope under 40X magnification for of ZnO (a-e), Co-ZnO (f-j) and Fe-ZnO (k-o) NPs

Slika 11. Slika dobijena invertovanim mikroskopom pod uvećanjem od 40Ks za ZnO (a-e), Co-ZnO (f-j) i Fe-ZnO (k-o) NPs

4. CONCLUSION

The present study was carried out on the synergistic effect of Fe and Co doped ZnO nanoparticles synthesized using *Alpinia galanga* leaf extract and their in vitro antifungal activity. ZnO NPs were successfully synthesized and doped with transition metal precursors to generate Fe doped ZnO and Co doped ZnO NPs by co precipitation method. The nanoparticles fabricated under optimized process conditions were characterized using FTIR, XRD, SEM, DLS, EDAX and the results were evaluated. In vitro antifungal susceptibility tests revealed the fascinating antifungal efficiencies of three NPs against *Candida parapsilopsis* when compared to a standard Amphotericin B. Hence, these nanoparticles could be largely exploited for biomedical applications. Moreover, it strongly emphasizes the need to execute a green synthesis approach for synthesizing metallic/metal oxide nanoparticles rather than a chemical approach. This particular work is regarded as an environmentally safe, inexpensive method and the process could be effectively practiced on large scales. The nanoparticles can be explored as a novel nano therapeutic medicine in future.

Acknowledgment

We thank to the Management of Sri Krishna Arts and Science College, Coimbatore, Tamil Nadu, India for the Seed money grant and providing necessary facilities to carry out this work.

5. REFERENCES

- [1] E.J. Baron, J.M. Miller (2008) Bacterial and fungal infections among diagnostic laboratory workers: evaluating the risks. *Diagn. Micr. Infec. Dis.*, 60(3), 241–246, <https://doi.org/10.1016/j.diagmicrobio.2007.09.016>
- [2] J. Kaur, C.J. Nobile (2023) Antifungal drug-resistance mechanisms in *Candida* biofilms. *Curr. Opin. Microbiol.*, 71, 102237, <https://doi.org/10.1016/j.mib.2022.102237>
- [3] A. Espinel-Ingroff (2009) Novel antifungal agents, targets or therapeutic strategies for the treatment of invasive fungal diseases: a review of the literature (2005-2009). *Rev. Iberoam. Micol.*, 26(1), 15–22, [https://doi.org/10.1016/s1130-1406\(09\)70004-x](https://doi.org/10.1016/s1130-1406(09)70004-x)
- [4] A. Chaturvedi, S. Shambhakar (2024) Nanotechnology in Drug Delivery: Overcoming Poor Solubility Challenges through Nanoformulations. *Nanomed. J.*, 14, In Press, <https://doi.org/10.2174/0124681873276732231207051324>

- [5] T.A.Wani, G.Suresh (2022) Plant-Mediated Green Synthesis of Magnetic Spinel Ferrite Nanoparticles: A Sustainable Trend in Nanotechnology. *Adv. Sustain. Syst.*, 6(6), <https://doi.org/10.1002/adsu.202200035>
- [6] A.Burhan, D.Ratnadewi, A.Setiyono, R.Astuti, A. Umar (2024) Phytochemical Profiling of Hippobroma longiflora Leaf Extract Using LC-MS/MS Analysis and Pharmacological Potential. *Egypt. J. Chem.*, 23, <https://doi.org/10.21608/ejchem.2024.242541.8740>
- [7] S.Chandrasekaran, V.Anbazhagan (2023) Green Synthesis of ZnO and V-Doped ZnO Nanoparticles Using Vinca rosea Plant Leaf for Biomedical Applications. *Appl. Biochem. Biotechnol.*, 196(1), 50–67. <https://doi.org/10.1007/s12010-023-04546-2>
- [8] M.Duan, J.G.Shapter, W.Qi, S.Yang, G.Gao (2018) Recent progress in magnetic nanoparticles: synthesis, properties, and applications. *Nanotechnol.*, 29(45), 452001, <https://doi.org/10.1088/1361-6528/aadcec>
- [9] M.S.Nadeem, T.Munawar, F.Mukhtar, M.Naveed, U. Rahman, M.Riaz, F.Iqbal (2021) Enhancement in the photocatalytic and antimicrobial properties of ZnO nanoparticles by structural variations and energy bandgap tuning through Fe and Co co-doping. *Ceram. Int.*, 47(8), 11109–11121, <https://doi.org/10.1016/j.ceramint.2020.12.234>
- [10] R.R.Muthu Chudarkodi, A.Rajalaxshmi (2016) Synthesis, Electrochemical Characterization and Photocatalytic Application of Ceion Doped ZnO nanoparticles using Leaf Extract of SesbaniaGrandiflora by Green Method. *Int. J. Sci. Res.*, 5(3), 1073–1080. <https://doi.org/10.21275/v5i3.15031601>
- [11] S.Chandrasekaran, V.Anbazhagan (2023) Green Synthesis of ZnO and V-Doped ZnO Nanoparticles Using Vinca rosea Plant Leaf for Biomedical Applications. *Appl. Biochem. Biotechnol.*, 196(1), 50–67. <https://doi.org/10.1007/s12010-023-04546-2>
- [12] D.Giram, A.Das (2024) Synthesis and characterization of Fe doped ZnO nanoparticles for the photocatalytic degradation of Eriochrome Black-T dye. *Indian J. Chem. Techn.*, In press, <https://doi.org/10.56042/ijct.v31i1.4985>
- [13] D.Gupta, R.K.Ghanshyam Kotnala, N.S.Negi (2013) Synthesis and characterization of Cu, Fe co-doped ZnO nano-particles synthesized by solution combustion method. *AIP Conference Proceedings*. <https://doi.org/10.1063/1.4810156>
- [14] P.Dhiman, R.Rani, M.Singh (2012) Structural and electrical properties of Fe doped ZnO nanoparticles synthesized by solution combustion method. *AIP Conference Proceedings*. <https://doi.org/10.1063/1.4710002>
- [15] P.Dhiman, J.Chand, S.Verma Sarveena, M.Singh (2014) Ni, Fe Co-doped ZnO nanoparticles synthesized by solution combustion method. *AIP Conference Proceedings*. <https://doi.org/10.1063/1.4872990>
- [16] N.Madkhali (2022) Analysis of Structural, Optical, and Magnetic Properties of (Fe,Co) Co-Doped ZnO Nanoparticles Synthesized under UV Light. *Condens. Matter.*, 7(4), 63-71, <https://doi.org/10.3390/condmat7040063>
- [17] P.Malathy, S.Selvarajan (2018) Visible Light Assisted Photocatalytic Activity of Co-doped ZnO, In-Doped ZnO and (Co, In) co-doped ZnO Nanoparticles. *Int. J. Nanotechnol. App.*, 8(1), 1–14, <https://doi.org/10.24247/ijnajun20181>
- [18] T.S.Boopathi, S.Suksom, J.Suriyaprakash, A.H. Hirad, A.A.Alarfaj, I.Thangavelu (2024) Psidium guajava-mediated green synthesis of Fe-doped ZnO and Co-doped ZnO nanoparticles: a comprehensive study on characterization and biological applications. *Biopro. Biosyst. Eng.*, in press, <https://doi.org/10.1007/s00449-024-03002-7>
- [19] W.Kejela Tolossa, P.Taddesse Shibeshi (2022) Structural, optical and enhanced antibacterial activities of ZnO and (Co, Fe) co-doped ZnO nanoparticles by sol-gel combustion method. *Chem. Phys. Lett.*, 795, 139519, <https://doi.org/10.1016/j.cplett.2022.139519>
- [20] I.O.Chikezie (2017) Determination of minimum inhibitory concentration (MIC) and minimum bactericidal concentration (MBC) using a novel dilution tube method. *Afr. J. Microbiol. Res.*, 11(23), 977–980, <https://doi.org/10.5897/ajmr2017.8545>
- [21] D.Sharma, R.Jha (2017) Transition metal (Co, Mn) co-doped ZnO nanoparticles: Effect on structural and optical properties. *J. Alloys Compd.*, 698, 532–538, <https://doi.org/10.1016/j.jallcom.2016.12.227>
- [22] M.Ram, K.Bala, H.Sharma, A.Kumar, N.S.Negi (2016) Investigation on structural and electrical properties of Fe doped ZnO nanoparticles synthesized by solution combustion method. *AIP Conference Proceedings*. <https://doi.org/10.1063/1.4946078>
- [23] M.D.Sahadat Hossain, S.Ahmed (2023) Easy and green synthesis of TiO₂ (Anatase and Rutile): Estimation of crystallite size using Scherrer equation, Williamson-Hall plot, Monshi-Scherrer Model, size-strain plot, Halder- Wagner Model. *Results Mater.*, 20, 100492, <https://doi.org/10.1016/j.rinma.2023.100492>
- [24] X.Han, S.Wahl, P.Russo, N.Pinna (2018) Cobalt-Assisted Morphology and Assembly Control of Co-Doped ZnO Nanoparticles. *Nanomater.*, 8(4), 249, <https://doi.org/10.3390/nano8040249>
- [25] M.Mittal, M.Sharma, O.P.Pandey (2014) UV-Visible light induced photocatalytic studies of Cu doped ZnO nanoparticles prepared by co-precipitation method. *J. Sol. Energy.*, 110, 386–397, <https://doi.org/10.1016/j.solener.2014.09.026>
- [26] D.Sharma, R.Jha (2017) Analysis of structural, optical and magnetic properties of Fe/Co co-doped ZnO nanocrystals. *Ceram. Int.*, 43(11), 8488–8496, <https://doi.org/10.1016/j.ceramint.2017.03.201>
- [27] Y.Köseoğlu (2015) Rapid synthesis of room temperature ferromagnetic Fe and Co co-doped ZnO DMS nanoparticles. *Ceram. Int.*, 41(9), 11655–11661, <https://doi.org/10.1016/j.ceramint.2015.05.127>

IZVOD

SINERGISTIČKI EFEKAT NANOČESTICA ZnO DOPIRANIH Fe I Co SINTETIZOVANIH KORIŠĆENJEM *ALPINIA GALANGA* PROTIV *CANDIDA* *PARASILOPSIS*

U ovom istraživanju, nanočestice kao što su ZnO, ZnO dopiran Fe i ZnO NP dopiran Co pripremljene metodom koprecipitacije su testirane protiv patogenog kvasca. Spektroskopske analize su sprovedene radi identifikacije morfološkog i hemijskog sastava sintetizovanih nanočestica. Rezultati XRD analize su otkrili da su sintetizovane nanočestice kristalne prirode sa prosečnim rasponom veličine između 32 – 34 nm približno. EDKS i SEM analize su sprovedene da bi se identifikovao sastav elemenata (Co, Fe i Zn) i sferni oblik nanočestica. Funkcionalna grupa koja je odgovorna za zatvaranje i stabilnost nanočestica je potvrđena FTIR analizom, da bi se uporedila antifungalna efikasnost ZnO, ZnO dopiranog Fe i ZnO dopiranog Co iz rezultujuće zone inhibicije.

Ključne reči: *Antifungalna aktivnost, Candida parapsilosis, bakar, gvožđe, cink*

Naučni rad

Rad primljen: 27. 09. 2023.

Rad prihvaćen: 09. 12. 2023.

Rad je dostupan na sajtu: www.idk.org.rs/casopis

Emmanuel Rieborue Khama¹, Emmanuel Zeneboebi Loyibo²,
Wilfred Okologume², Stanley Too-chukwu Ekwueme^{3*},
Chukwudi Victor Okafor², Nnaemeka Princewill Ohia³

¹Nigeria Maritime University, Okerenkoko, Delta State, Nigeria,

²Department of Petroleum Engineering, Federal University of
Petroleum Resources, Effurun, Nigeria, ³Department of Petroleum
Engineering, Federal university of Technology, Owerri, Nigeria

Scientific paper

ISSN 0351-9465, E-ISSN 2466-2585

<https://doi.org/10.62638/ZasMat1149>



Zastita Materijala 65 (2)
258 - 272 (2024)

Investigation of the performance of activated carbon derived from ripe plantain peels for CO₂ capture: Modelling and optimisation using response surface methodology

ABSTRACT

This study investigates the potential of activated carbon derived from ripe plantain peels (PPAC) for carbon dioxide (CO₂) capture. PPAC was prepared through carbonization and activation using H₃PO₄, and its unique properties were extensively characterized which revealed irregular sponge-like protrusions and well-defined pores under Scanning Electron Microscopy (SEM). Elemental analysis identified carbon, silicon, and oxygen as major components, corroborated by X-ray Diffraction (XRD) analysis indicating the presence of silicon oxide (SiO₂), potassium oxide (K₂O), and calcium oxide (CaO). Fourier Transform Infrared (FTIR) spectroscopy highlighted diverse functional groups on PPAC's surface. CO₂ adsorption tests were conducted at 27°C and 40°C with varying pressures on PPAC particles of 150µm and 845µm sizes. Results revealed that CO₂ adsorption capacity increased with escalating pressures. Remarkably, at 27°C, PPAC exhibited superior performance than at 40°C, attributed to a higher-pressure drop enhancing the driving force for CO₂ adsorption. Larger particles (845µm) demonstrated higher adsorption capacity due to increased surface area, enhanced pore accessibility, and faster mass transfer. The Response Surface Methodology (RSM) conducted gave 2FI model as the most representative of the design data and showed high accuracy (R²=0.9973) and low error metrics (MSE=0.01697, RMSE=0.130269, MAE=0.109, MAPE=2.7244). The Adeq Precision value of 76.26 validated the model's reliability. Optimization using RSM yielded optimal CO₂ adsorption values (9.69 mmol/g) at 27°C and 100 bars. PPAC emerges as a promising solution for CO₂ capture, offering valuable prospects in mitigating emissions and addressing climate change challenges.

Keywords: Ripe Plantain peel activated carbon, Response surface methodology, Characterization, optimisation, CO₂ adsorption

1. INTRODUCTION

The utilization of fossil fuels has resulted in substantial CO₂ emissions, a major contributor to global warming and climate change [1,2]. CO₂ emissions constitute a significant portion of global greenhouse gas emissions, posing challenges such as climate change and ocean acidification [3, 4]. Currently, atmospheric CO₂ levels have exceeded 415 ppm, surpassing the Earth's capacity. Rising global temperatures, particularly beyond 2°C, could lead to severe environmental consequences [5,6].

Efforts to mitigate global warming include the exploration of Carbon Capture and Storage (CCS) technologies. Among these, post-combustion CO₂ capture techniques, have gained prominence due to their low technological risk and retrofittable nature [7,8]. Various methods, such as adsorption, membrane processes, cryogenic distillation, and absorption, have been suggested for CO₂ separation [6, 9]. Among these options, cryogenic distillation is the most established, but its extensive use is hindered by significant energy consumption and high costs [10,11].

Absorption methods, especially those utilizing amine-based solvents, offer high CO₂ absorption rates but are hindered by high costs, energy consumption, corrosion issues, and environmental concerns [11,12]. Additionally, liquid sorbents like polyamines and organic-inorganic hybrids necessitate thermal energy for desorption [13,14].

*Corresponding author: Stanley Too-chukwu Ekwueme

E-mail: stanleyekwueme@yahoo.com

Paper received: 17. 11. 2023.

Paper accepted: 10. 12. 2023.

Paper is available on the website: www.idk.org.rs/journal

Membrane separation, on the other hand, has emerged as a promising technology for CO₂ capture. Both polymeric and inorganic membranes have been extensively studied [15,16]. Inorganic membranes have demonstrated high permeability and selectivity but face challenges related to fabrication costs and scalability [17,18]. Polymeric membranes, following the solution-diffusion mechanism, encounter limitations due to the trade-off between selectivity and permeability, hindering their industrial applicability [19,20].

Adsorption-based CO₂ capture, employing materials like activated carbon (AC), metal-organic frameworks (MOFs), zeolite molecular sieves, and porous organic polymers (POPs), has gained attention, especially for smaller-scale applications [17, 20]. Among these, AC stands out due to its low regeneration energy, thermal stability, large porosity, and cost-effectiveness. While commercially-produced AC exhibits good performance, its production process is prohibitively expensive in developing nations, leading to increased operational costs [21,22].

To address these challenges, there is a growing interest in affordable methods of producing activated carbon. Utilizing biomass from agricultural waste materials such as rice husk, coconut husk, plantain peels, sawdust, bagasse, and other agricultural residues presents an economical and environmentally sustainable alternative [23,24]. These biomass-derived sources significantly reduce production costs compared to commercial counterparts and hold great potential for future commercialization [25-27].

Researchers have extensively explored the utilization of biomass and waste materials for the preparation of activated carbon with promising applications in CO₂ adsorption [28,29]. For instance, Sabri et al. [30] investigated the use of palm kernel shell for activated carbon synthesis, which was further modified with imidazoles. This modified activated carbon demonstrated outstanding performance in CO₂ capture during pressure swing adsorption processes [31,32].

Serafin et al. [20] explored the use of Amazonian andiroba shell for producing porous activated carbon as a CO₂ adsorbent. They employed physical activation techniques and studied the effect of activation times on the material's characteristics. The resulting activated carbon exhibited high surface area, microporosity, and excellent CO₂ adsorption capacity. Additionally, their research highlighted the material's superior cyclic stability and charge transfer processes, indicating its potential for practical applications.

Patel et al. [19] investigated activated porous carbon derived from pine sawdust using a hybrid synthesis protocol. This research compared the effectiveness of activated carbon derived via physicochemical, chemical, and physical activation methods. The optimized material exhibited a high BET surface area and remarkable CO₂ adsorption capacity. It displayed strong physisorption behaviour for CO₂, making it suitable for repeated adsorption-desorption cycles.

Yanti et al. [21] explored the synthesis of activated carbon from banana peel, which was further modified with magnetite for enhanced iron metal ion recovery. The activated carbon exhibited improved thermal stability after alkali activation. Their study showcased the material's potential in CO₂ adsorption and highlighted its thermal stability after modification.

In recent years, Response Surface Methodology (RSM) has gained widespread popularity for exploring the intricate relationships between responses and independent variables in various chemical processes. RSM has been recognised for its ability to comprehensively consider interactions among variables, both in combination and independently [6]. Unlike the conventional method of altering one variable at a time (OVAT), which is time-consuming, costly, and fails to capture interactions between input variables, RSM modelling and optimization provide a more efficient approach. To facilitate RSM studies, several design techniques are available, such as Box-Behnken Design (BBD), central composite design, and optimal design methods. Among these, the Box-Behnken Design (BBD) has emerged as the most extensively explored method for RSM modelling and optimization. BBD not only reduces the number of experiments required but also offers valuable insights into how processes are influenced by the interactions between various parameters [33].

Many scholars have investigated the use of RSM for modelling and optimisation of activated carbons prepared using biomass precursors. Greco et al. [6] investigated activated carbon prepared from wheat straw using a one-step synthesis approach, comparing it with conventional two-step production methods. Their research demonstrated that the one-step activated carbon exhibited comparable textural properties, CO₂ uptake, and selectivity to the two-step counterparts. Breakthrough curve simulations also emphasized its effectiveness in CH₄/CO₂ separation under dynamic conditions, making the one-step process an economically attractive route for large-scale production systems.

Khoshraftar and Ghaemi [10] investigated the use of pistachio shells for creating microporous activated carbon with high CO₂ adsorption capacity. They employed various analytical techniques such as X-ray diffraction, Fourier transform infrared spectrometry, and scanning electron microscopy to characterize the material. The activated carbon derived from pistachio shells exhibited specific surface area and excellent CO₂ sorption properties. Their study also utilized response surface methodology and artificial neural network models to optimize CO₂ adsorption conditions, achieving highly accurate predictions.

Li et al. [24] explored the synthesis of low-cost activated carbons using apple tree pruning waste and waste polyethylene terephthalate (PET) plastic bottles. Their research focused on understanding the synergistic mechanism between these precursors during carbonization. Through response surface methodology, they analysed the impact of PET ratio and carbonization conditions on pore structure and CO₂ adsorption performance. The optimized conditions led to a significant CO₂ uptake, demonstrating the potential of this activated carbon for CO₂ adsorption.

Mukherjee et al. [30] utilized spent coffee grounds as a feedstock for activated carbon synthesis via physical activation. They optimized the activation parameters using the Box-Behnken design method, achieving high specific surface area. Additionally, they employed a natural deep eutectic solvent to modify the activated carbon's surface functionalities. The resulting material displayed excellent CO₂ capture performance, selectivity, and cyclic stability, making it a promising solution for CO₂ emission mitigation.

2. MATERIALS AND METHODS

2.1. Materials and Apparatus

The study used ripe plantain peel as the precursor material which was obtained from Effurun market in Delta State, Nigeria. H₃PO₄, pure CO₂ gas and distilled water were obtained from the lab. The Apparatus used include SEM device, FTIR device, XRD device, EDX device, grinding machine, stirrer, pH meter, cylindrical glass beaker, oven, furnace, CO₂ adsorption setup.

2.2. Methods

The methods comprise the preparation of plantain peel activated carbon (PPAC), the characterization of the PPAC, the CO₂ adsorption test and the RSM modelling.

2.2.1. Preparation of Activated Carbon

The ripe plantain-peels were thoroughly washed with tap followed by distilled water and sun

dried for three weeks. The sun-dried sample was then taken to the lab for extra effective drying using oven at 100°C. The resulting oven-dried sample was taken to the furnace for carbonization. Carbonisation of the oven-dried sample was done at 500°C in the furnace after which the resulting sample was grinded to obtain a smooth powdered sample. The resulting powdered sample was then sieved to several sizes including 150 microns and 840 microns respectively.



Figure 1. PPAC preparation process

Slika 1. Proces pripreme PPAC-a

The resulting sieved carbonized sample was then taken for activation. Phosphoric acid (H₃PO₄) was used as the activator. First, a cylindrical glass beaker was filled with phosphoric acid and then the sieved carbonized sample was added to it. The resulting mixture was vigorously stirred using electric stirrer for 24 hours to achieve a strong cohesion between the activator (H₃PO₄) and the carbonized plantain peel sample. Furthermore, the stirring enabled the H₃PO₄ to achieve strong internal contact with the carbonized material.

The stirring was immediately proceeded with the filtration of the H₃PO₄ acid from the activated sample. Then warm water was added and stirred again to remove residual acid. The pH of the activated carbon was then checked and recorded. The pH was recorded to be 7.60. then the activated carbon was then dried in the oven at 100°C.

2.2.2. Characterisation of the Plantain Peel Activated Carbon

Various characterization techniques were employed to analyze the structural and morphological properties of the plantain peel activated carbon (PPAC). Fourier-Transform Infrared (FTIR) Spectroscopy was used to examine the functional groups in PPAC by analyzing infrared spectra at different wavelengths. A PerkinElmer FTIR spectrometer identified functional groups on PPAC surfaces after mixing PPAC and potassium bromide (KBr) at a weight ratio of 1:200 (g adsorbent/g KBr) and compacting the powder with a hydraulic press to form pellets.



Figure 2. The Activated carbon preparation process (a) ripe plantain peel, (b) carbonized plantain peel, (c) activation of carbonised plantain peel carbon (d) activated plantain peel carbon.

Slika 2. Proces pripreme aktivnog uglja (a) zrela kora banane, (b) karbonizovana kora banane, (c) aktivacija karbonizovanog ugljenika od kore banane (d) aktivni ugljen od kore banana

Scanning Electron Microscopy (SEM) was utilized to observe the morphology of PPAC using a TESCAN Vega 3 model operating at 25 kV. The Micromeritics ASAP 2020 porosimeter measured nitrogen adsorption/desorption isotherms at 77 K to determine the structural parameters of activated carbon. Energy Dispersive X-ray (EDX) analysis was conducted to analyze the chemical composition of the PPAC sample.

The crystalline structure of the sample was determined using X-ray diffraction analysis performed with a D8 Advance X-ray diffractometer (model: D8 Advance, BRUKER, Germany) coupled with a P2 Phaser Bruker and an XFlash silicon drift detector. During the analysis, the sample was ground into a fine powder and placed inside the device. The X-ray motion moved in a circular path from 5 to 90 degrees relative to the horizon line, directing the beam onto the sample from different angles. Diffraction measurements were taken at every 0.015 θ , generating a diffraction pattern.

2.2.3. CO₂ Adsorption Experiment

An experimental setup illustrated in Figure 3a was setup to determine the CO₂ adsorption

capacity of PPAC under post-combustion conditions, adhering to Sieverts law [34]. Initially, a 59.06-inch flowline with a diameter of 1/4 inches was established to facilitate the passage of CO₂ gas from the storage cylinder to the Staging Manifold (SM) depicted in Figure 3b, measuring 8 inches in length and 2.16 inches in diameter. Within the SM, the pressure of CO₂ was gradually allowed to increase, reaching post-combustion conditions ranging from 0.15 to 1 bar.

Subsequently, a Reactor (R) housed in a water bath, as shown in Figure 4, was connected to V1 through a 13-inch flow line with a diameter of 1/4 inches. Finally, a vacuum pump with a capacity of 1 horsepower was linked to a 47-inch flow line with a diameter of 1/4 inches, positioned between the CO₂ storage cylinder and V1. This setup was instrumental in evacuating CO₂ from the flow loop at the conclusion of each sorption cycle conducted at specific pressure and temperature conditions.

During the CO₂ adsorption test: first, the vacuum pump (VP) was used to eliminate air molecules from the airtight apparatus, ensuring the absence of other gases in the system before the

adsorption process. Subsequently, the Dosing Valve (DV) and Bleeding Valve (BV) were closed, while the Inlet Valve (IV) was opened to allow the passage of CO₂ gas. A specific mass of adsorbent

(CS – 1.08g, AC – 1.08g) was precisely measured using a weighing balance and placed inside Reactor (V2) to occupy its volume.



Figure 3. CO₂ adsorption equipment (a) Experimental setup for evaluation of CO₂ adsorption capacity (b) Reactors for storing adsorbents

Slika 3. Oprema za adsorpciju CO₂ (a) Eksperimentalna postavka za procenu kapaciteta adsorpcije CO₂ (b) Reaktori za skladištenje adsorbenata

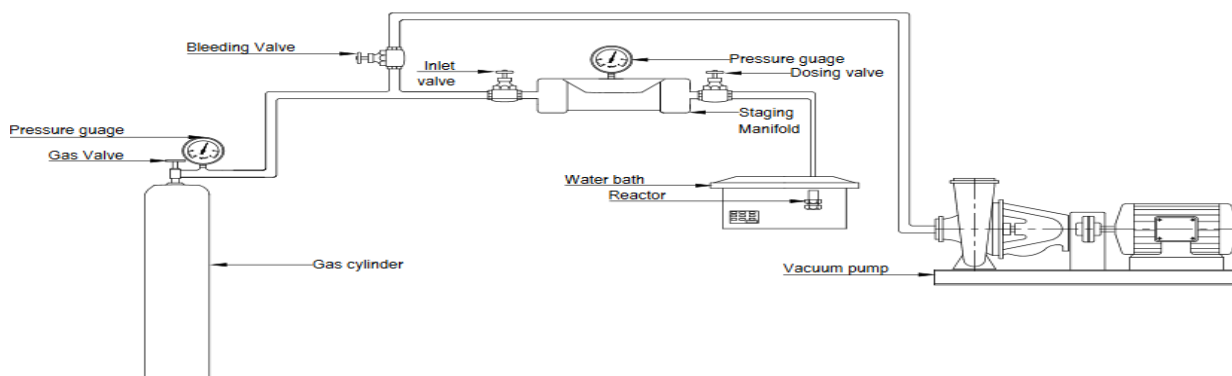


Figure 4. Schematic of CO₂ adsorption experimental setup

Slika 4. Šema eksperimentalne postavke za adsorpciju CO₂

Next, CO₂ gas was gently introduced into the Staging Manifold (V1) from the CO₂ gas cylinder (CGC) while DV and BV were closed, allowing the pressure to build up in V1 to a specific pressure of interest (P1 – 2.0, 3.0, 4.0, 5.0, 6.0, 8.0, 10.0, and 15.0 psi). Once the desired pressure was reached, IV was promptly closed to maintain a constant pressure in V1. The Staging Manifold was sealed for 15 minutes to check for any leakages, which were monitored through any noticeable pressure drop indicated by the Pressure Gauge (PG).

Following this, an equilibration temperature was maintained for 30 minutes. DV was then cautiously opened, allowing CO₂ gas to flow into V2 submerged in a water bath (WB) kept at a specific temperature. This initiated contact with the

adsorbents, allowing the adsorption process to occur over a period of 60 minutes. The final pressure, denoted as P2, was recorded by the PG. DV was closed, and BV was opened to enable CO₂ entry from CGC into V1 until the pressure of interest was achieved. This experiment was repeated for each sorption cycle under incremental pressure and constant temperature conditions.

At the end of each sorption cycle, with pressure increment and constant temperature, DV was closed, and V1 was detached from the apparatus. The apparatus was sealed, and residual gas molecules were removed using VP. A specific mass of adsorbent was re-measured and placed in V1, occupying its volume, and the experiment was repeated as described above. The temperatures

utilized in this experiment were 26°C, 40°C, and 70°C, while the pressures of interest were 5 psi, 10 psi, and 15 psi.

2.2.4. RSM Modelling

The RSM modelling involved the examination of two variables from the CO₂ adsorption test: temperature (ranging from 27°C to 40°C) and pressure (ranging from 20 psi to 100 psi) to understand their impact on CO₂ adsorption (measured in mmol/g). These variables were used as input data for the BBD-RSM modelling. The BBD generated 10 experimental runs, which were utilized in the modelling process. Various regression analysis models were assessed to identify the most accurate one that could approximate the experimental data precisely. The outcomes were analysed using 3D response plots and an analysis of variance (ANOVA). The suitability of the model was evaluated through ANOVA, coefficient of determination (R²), F-value, P-value, and residual analysis. The 2FI model exhibited superior performance and was chosen based on statistical parameters such as R², adjusted R², predicted R², standard deviation, and coefficient of variance (COV). Through multiple regression analyses, these models were fitted to the experimental data, enabling the estimation of responses from independent variables using the provided general equations below. The general form of the 2FI regression model is given as

$$y = a_0 + \sum_{i=1}^k a_i x_i + \sum_{i=1}^k \sum_{j=i+1}^k a_{ij(i<j)} x_i x_j + e \quad (1)$$

where x_i , x_j , x_l , are the input variables and a_i , a_{ij} , a_{ii} , and a_{ijl} are the coefficient of each of the terms, a_0 is the offset and e is the residual or error term.

The statistical metrics which are used to assess the performance of the RSM comprise the coefficient of determination (R²), the mean-square error (MSE), the root-mean-square error (RMSE), the mean absolute error (MAE), the mean absolute percentage error (MAPE) and the standard deviation as given below

$$R^2 = \frac{\sum_{i=1}^n (x_{a,i} - x_{p,i})^2}{\sum_{i=1}^n (x_{p,i} - x_{a,ave})^2} \quad (2)$$

$$MSE = \frac{1}{n} \sum_{i=1}^n (x_{p,i} - x_{a,i})^2 \quad (3)$$

$$RMSE = \sqrt{\frac{1}{n} \sum_{i=1}^n (x_{p,i} - x_{a,i})^2} \quad (4)$$

$$MAE = \frac{1}{n} \sum_{i=1}^n |(x_{a,i} - x_{p,i})| \quad (5)$$

$$MAPE = \frac{\frac{1}{n} \sum_{i=1}^n |(x_{a,i} - x_{p,i})|}{\frac{1}{n} \sum_{i=1}^n x_{a,i}} \quad (6)$$

$$std\ dev = \sum_{i=1}^n \frac{(x_{di} - m)^2}{n-1} \quad (7)$$

where n is the number of experimental runs, $x_{p,i}$ is the estimated values, $x_{a,i}$ is the experimental values, $x_{a,ave}$ is the average experimental values, x_{di} is the difference between the actual and estimated value, m is the mean value of x_d dataset, k is the number of input variables.

3. RESULTS AND DISCUSSION

3.1. PPAC Characterization Result

The SEM image depicted in figure 5 shows the morphology of the PPAC at 500µm.

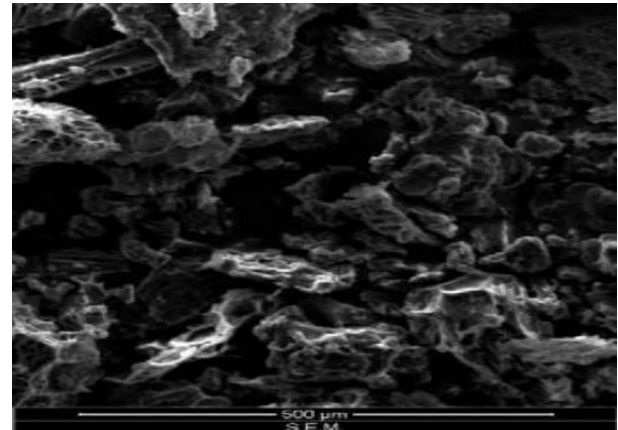


Figure 5. SEM images of PPAC

Slika 5. SEM slika PPAC-a

The morphology of PPAC from in 5 shows irregular sponge-like protrusions distributed unevenly, with well-defined pores. These protrusions are indicative of the organic content present in plantain peels, while the clearly visible pores are the outcome of thermal and chemical treatments, involving processes like carbonization and activation. These treatments removed volatile components from the sample, resulting in the distinctive microstructure observed in PPAC. This microstructure signifies an enhanced surface area, essential for effective adsorption of gaseous substances.

The EDX analysis depicted in Figure 6 reveals the elemental composition of PPAC, indicating the presence of oxygen (20.23 wt%), carbon (33.4 wt%), potassium (5.32 wt%), magnesium (1.35 wt%), calcium (4.50 wt%), silicon (30.0 wt%), and iron (5.20 wt%). The predominant components in PPAC are carbon, silicon, and oxygen, with lower proportions of potassium, iron, calcium, and magnesium, each decreasing in percentage weight. The oxygen content in PPAC holds critical significance, as oxygen functional groups play a pivotal role in determining the surface properties of carbons, influencing their suitability as ion exchangers, adsorbents, etc.

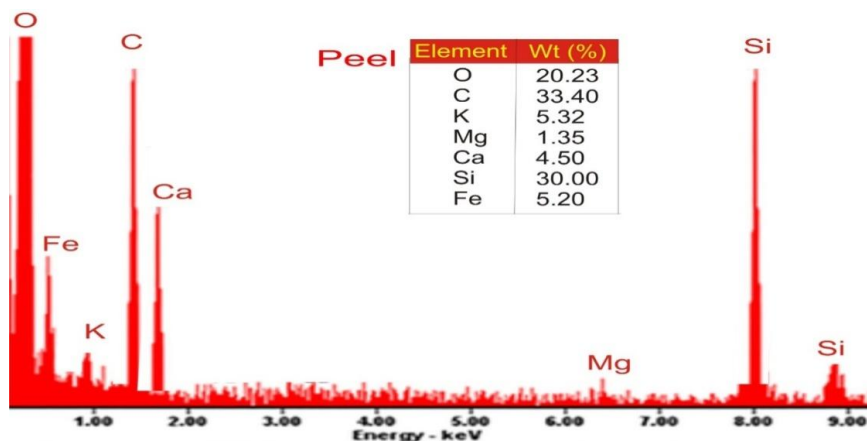


Figure 6. EDX analyses showing the chemical composition of PPAC

Slika 6. EDX analize koje pokazuju hemijski sastav PPAC-a

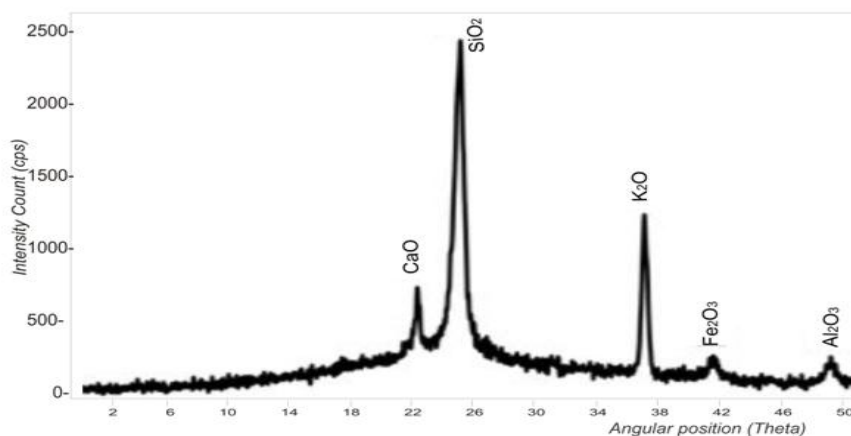


Figure 7. XRD analyses results of PPAC

Slika 7. Rezultati XRD analize za PPAC

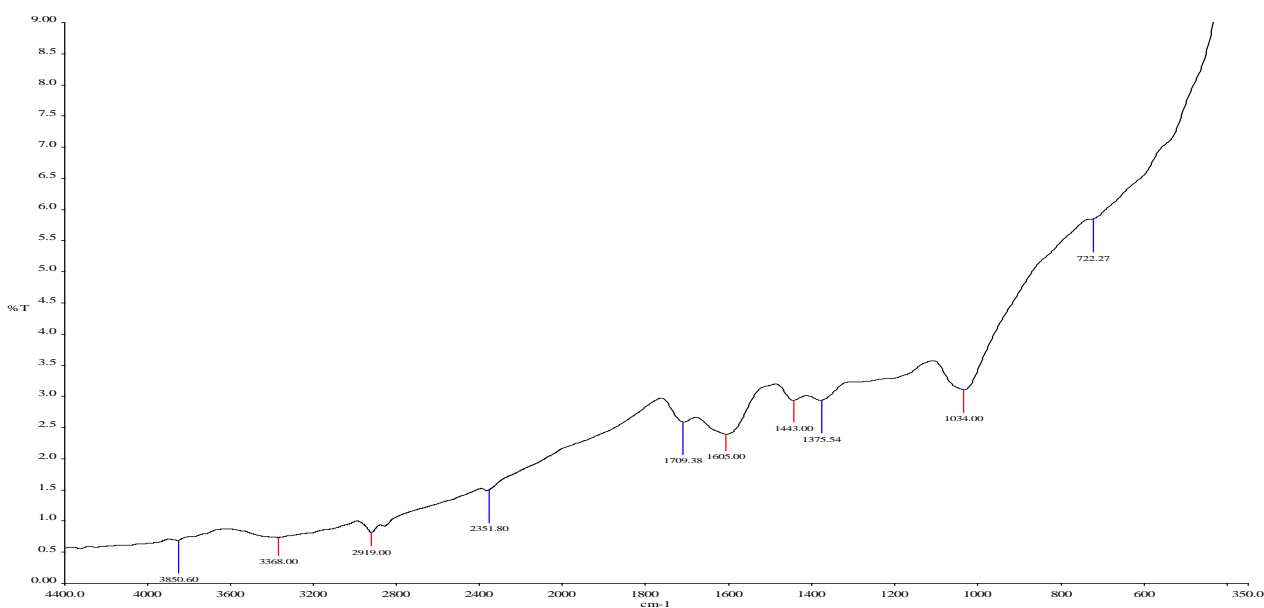


Figure 8. FTIR analyses of PPAC

Slika 8. FTIR analize PPAC

The XRD results of the PPAC shown in Figure 7 reveal the crystallinity of the and hence indicate the oxide composition of the PPAC. Diffraction angles were observed within the range of 0 to 51.6°. Prominent peaks were identified at 22°, 25°, and 36.5°, while minor peaks were noted at 42° and 49°. The major peaks indicate the presence of silicon oxide (SiO₂) as the predominant component in PPAC, followed by potassium oxide (K₂O) and calcium oxide (CaO). Additionally, the minor peaks suggest the existence of iron (III) oxide (Fe₂O₃) and aluminium oxide (Al₂O₃). The prevalence of these oxides, particularly SiO₂, K₂O, and CaO in PPAC, signifies the transformation of activated carbon from its precursors due to the thermal and chemical treatments applied during its preparation

The FTIR analysis of PPAC, as depicted in figure 8, displayed peaks at specific wavenumbers: 3850.60 cm⁻¹, 3368 cm⁻¹, 2919 cm⁻¹, 2315.8 cm⁻¹, 1709.38 cm⁻¹, 1605 cm⁻¹, 1443 cm⁻¹, 1375.54 cm⁻¹, 1034 cm⁻¹, and 722.27 cm⁻¹. Bands within and above 3850 cm⁻¹ signified OH stretching vibrations, while those within the range of 3500-3860 cm⁻¹ indicates OH stretching of proteins or polyphenols. Bands between 3300-3500 cm⁻¹ represented bonded N-H/C-H/O-H stretches typical of amines

and amides. Aliphatic stretches involving C-H and C-H₂ bonds were denoted by bands in the 2850-2950 cm⁻¹ range. The presence of C-N bonds was indicated by bands around 2100-2350 cm⁻¹. Double bonds of C=O, characteristic of ketones, were noted within the 1700-1750 cm⁻¹ range. Inorganic carbonate groups (-C=O groups) were identified in the 1400-1470 cm⁻¹ range, while CH and CH₂ aliphatic bending groups were present in the 1350-1440 cm⁻¹ range. Silica was evidenced by the bands at 1054 cm⁻¹, and out-of-plane CH bending was observed in the 700-800 cm⁻¹ range.

The specific surface area and pore size distribution of PPAC were determined through BET and BJH analyses. The BET analyses revealed a surface area of 1062.350 m²/g. Additionally, the adsorption and desorption average pore widths were found to be 28.25Å and 28.22Å, respectively, as per the BET analyses. On the other hand, the BJH analyses indicated average pore widths of 28.55Å (adsorption) and 30.55Å (desorption). The single-point adsorption total pore volume of pores measured 0.554500 cm³/g, whereas the desorption cumulative volume of pores was 0.452220 cm³/g. The isotherm linear plot for the BET/BJH analyses is presented in figure 9.

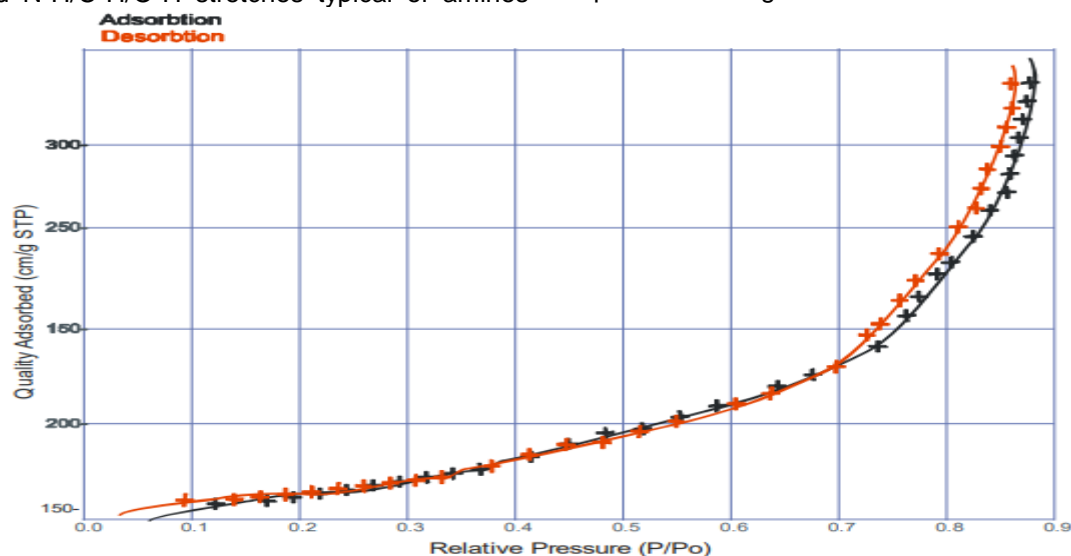


Figure 9. Isotherm linear plot of the PPAC subjected to BET/BJH analyses

Slika 9. Izotermni linearni dijagram za PPAC podvrgnut BET/BJH analizama

From figure 9 shows that the quality of absorbed species from the PPAC would increase exponentially with increase in the relative pressure (P/Po)

3.2. Results for CO₂ Adsorption

CO₂ adsorption results are given for PPAC samples of 150µm and 845µm. For the 150µm PPAC sample, the CO₂ adsorption capacities were

found to be 2.1558 mmol/g and 9.6126 mmol/g at pressures of 20 psi and 100 psi, respectively, and at an adsorption temperature of 27°C. However, at 40°C, the CO₂ adsorption capacities at 20 psi and 100 psi were recorded as 1.4438 mmol/g and 7.7154 mmol/g, respectively. Figure 10 illustrates the differences in both the final adsorption pressure and CO₂ adsorption capacity for different temperatures under the same applied initial

pressures. The CO₂ adsorption capacity as a function of initial and final pressures is depicted in

figures 10a and 10b for 27°C and 40°C, respectively.

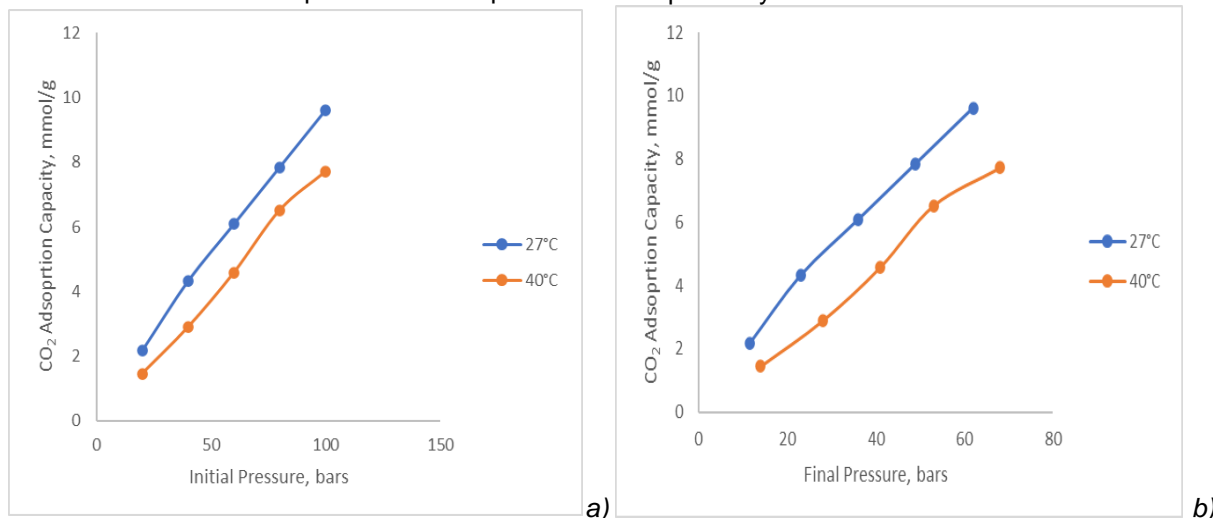


Figure 10. CO₂ adsorption capacities for 150µm (a) as a function of Initial pressure (b) As a function of final pressure

Slika 10. Kapaciteti adsorpcije CO₂ za 150µm (a) u funkciji početnog pritiska (b) u funkciji konačnog pritiska

As shown in Figure 10, it is evident that the CO₂ adsorption capacity rises with increasing pressures, both initial and final. However, at 27°C, the PPAC exhibited a higher CO₂ adsorption capacity compared to that at 40°C, as pressures were varied. This indicates that for the 150µm activated carbon, CO₂ adsorption decreased with

an increase in adsorption temperature. The increased CO₂ adsorption observed at the higher temperature of 150µm PPAC is attributed to the greater pressure drop across the membrane material at lower temperatures. This condition created a stronger driving force, leading to higher CO₂ adsorption, as illustrated in Figure 11.

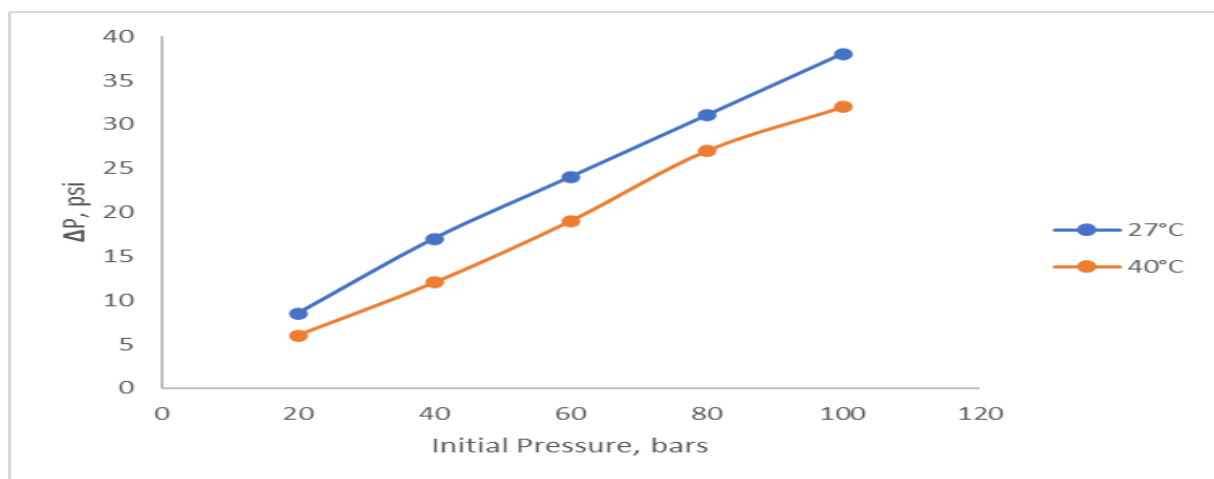


Figure 11. Pressure drop across PPAC for various adsorption temperatures

Slika 11. Pad pritiska na PPAC za različite temperature adsorpcije

Figure 11 reveals that with an increase in temperature, the pressure drop across the PPAC material diminishes, leading to a lower CO₂ adsorption capacity. The pressure drop refers to the disparity between the final resultant pressure

and the initial pressure applied across the activated carbon material. The driving force for gas adsorption is intricately linked to the difference in partial pressure of the gas across the adsorbent material. A higher-pressure drop indicates a more

substantial difference in CO₂ partial pressure, thereby facilitating more significant adsorption.

For the 845µm PPAC sample, the CO₂ adsorption capacities were 2.542 mmol/g and 12.7103 mmol/g at 20 psi and 100 psi pressures, respectively, at 27°C temperature. At 40°C

temperature, the CO₂ adsorption capacities were 3.6775 mmol/g and 8.451 mmol/g at 20 psi and 100 psi pressures, respectively. Figure 12 shows the CO₂ adsorption capacities as a function of the initial and final pressures for the 845µm PPAC.

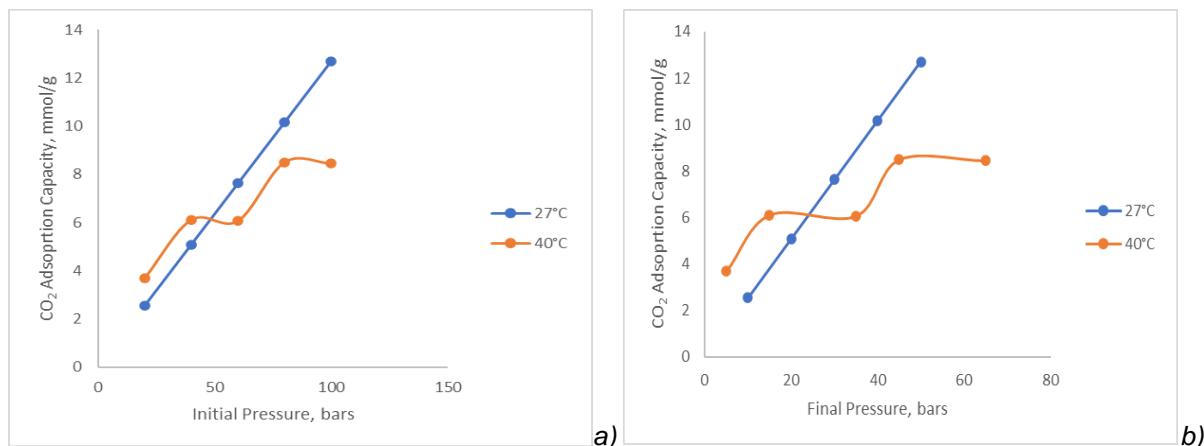


Figure 12. CO₂ adsorption capacities for 845µm (a) as a function of Initial pressure (b) As a function of final pressure

Slika 12. Kapacitet adsorpcije CO₂ za 845µm (a) kao funkcija početnog pritiska (b) Kao funkcija konačnog pritiska

The CO₂ adsorption capacities of 845µm size PPAC exhibit variations with temperature and pressure. At 27°C, the CO₂ adsorption capacity of 845µm PPAC demonstrated a linear increase with both initial and final pressures. The initial pressure corresponds to the applied inlet pressure of the feed CO₂, while the final pressure corresponds to the recorded pressure of the adsorbed CO₂ species. Conversely, at 40°C adsorption temperature, the CO₂ adsorption displayed an erratic trend. The adsorption showed both

increasing and decreasing patterns with both applied and final pressures. CO₂ adsorption increased between inlet pressures of 20 psi to 40 psi and then decreased between 40 psi and 60 psi pressures. It then increased again from 60 psi to 80 psi pressures and subsequently decreased between 80 psi and 100 psi pressures.

Figure 13 shows the comparison of the CO₂ adsorption capacities of the PPAC for the 150µm and 845µm at several pressures and temperatures.

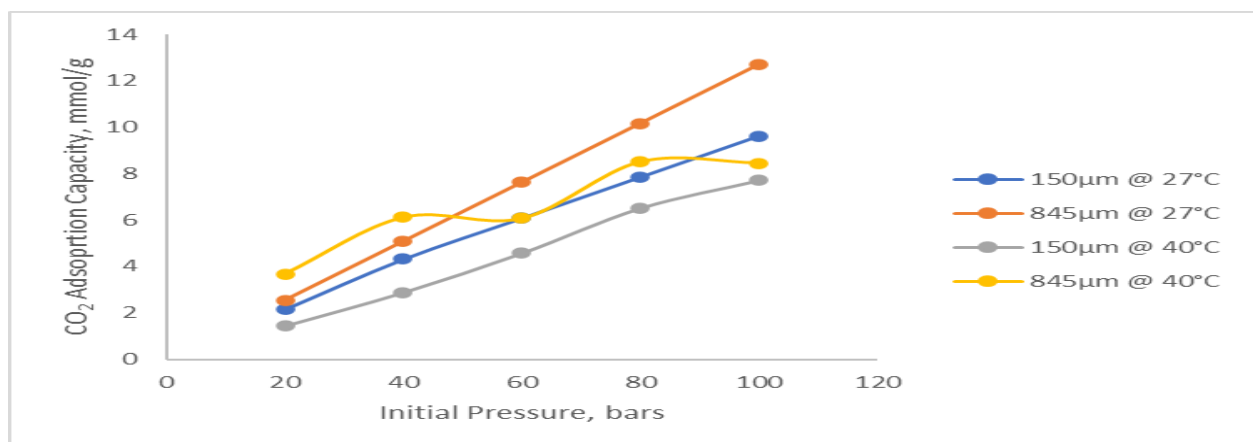


Figure 13. CO₂ adsorption capacities at several particle sizes of PPAC

Slika 13. Kapacitet adsorpcije CO₂ pri nekoliko veličina čestica PPAC-a

From figure 13, it is observed that CO₂ adsorption exhibited higher values for 845µm particles compared to 150µm particles. This finding indicates that CO₂ adsorption increases with larger particle size of activated carbon, a trend consistent across both 27°C and 40°C adsorption temperatures. Several factors contribute to this phenomenon:

Activated carbon materials possess a porous structure, characterized by a network of tiny pores and a high surface area. Larger particle sizes provide more space for these pores, creating a greater surface area available for adsorption. Consequently, larger particles offer ample room for CO₂ molecules to be adsorbed onto the surface of the activated carbon. In contrast, smaller particles result in crowded pores, limiting the accessibility of CO₂ molecules to the interior of the pores.

Furthermore, smaller particles tend to impede the diffusion of CO₂ molecules into the internal pores due to increased resistance. Larger particles, on the other hand, offer open pathways for CO₂ molecules to enter the porous structure, enhancing adsorption capacity. Additionally, larger particles provide a greater number of active adsorption sites due to their larger surface area. This abundance of adsorption sites allows for more interactions between CO₂ molecules and the adsorption sites, resulting in a higher adsorption capacity.

In contrast, smaller particles tend to agglomerate, reducing the overall surface area available for adsorption. Larger particles, being less prone to agglomeration, maintain a larger accessible surface area for CO₂ adsorption, facilitating faster and more efficient adsorption and mass transfer of CO₂ molecules. These characteristics collectively contribute to the observed increase in CO₂ adsorption capacity with larger particle size of activated carbon.

4.2. RSM Modelling Results

The RSM model was developed by fitting the experimental data to the RSM model. The 2FI model gave the highest fit to the actual data and was selected. The equation for the 2FI model generated by RSM is given as

$$Y = +5.32 - 0.6858X_1 + 3.46X_2 - 0.22721X_1X_2 \quad (8)$$

Equation 8 generated by RSM shows CO₂ adsorption represented as Y while temperature and pressure are represented by X₁ and X₂ respectively. The equation 7 shows that CO₂ adsorption is affected by temperature and pressure of the CO₂ gas. Equation 8, expressed in terms of the actual factors, provides a tool for predicting the response for specific levels of each factor. To use this equation effectively, the levels must be specified in the original units of each factor for both input parameters and the response variable.

The RSM model demonstrated strong predictive capability, proven by high coefficients of determination ($R^2=0.9973$, Adjusted $R^2=0.9959$, and predicted $R^2=0.9909$). R^2 values exceeding 0.8 typically indicate a significant fit between experimental and model-predicted results. The low coefficient of variance (CV) at 3.24% highlights the reliability of the experiment. The results from the analysis of variance (ANOVA), summarized in Table 1, confirmed the significance of the input parameters and the 2FI model. In the 2FI model, each term was assessed for significance using p-values at a confidence level of 95%. Terms with p-values less than or equal to 0.05 were considered significant, indicating their impact on the response. Additionally, higher F-values for model terms highlighted their substantial influence on the response variable. Notably, the p-value less than 0.0001 and the f-value of 731.21 further validate the acceptability of the 2FI model.

Table 1. Model coefficient based on ANOVA

Tabela 1. Koeficijent modela na osnovu ANOVA

Source	Sum of Squares	df	Mean Square	f-value	p-value	
Model	64.9	3	2.63	731.21	<0.0001	Significant
A-Temperature	4.7	1	4.7	158.97	<0.0001	
B-Pressure	59.94	1	59.94	2025.92	<0.0001	
AB	0.2581	1	0.2581	8.73	0.0255	
Residual	0.1775	6	0.0296			
Cor Total	65.08	9				

Figure 14 shows the actual vs. predicted response for the reduced cubic regression model.

In Figure 14a, the actual and predicted values are closely aligned and exhibit good agreement, as

indicated by their proximity to the 45° line. Figure 14b illustrates the graphical analysis of the model through a normal plot of residuals. The majority of data points fall within the range of 1.0 and -1.0

when represented as residuals. This alignment along a straight line suggests a normal distribution of residuals as the focus progresses. Equation (8) has proven to be the most suitable model for

interpreting historical data related to CO₂ adsorption responses. The model highlights that all independent parameters significantly influence the response parameter.

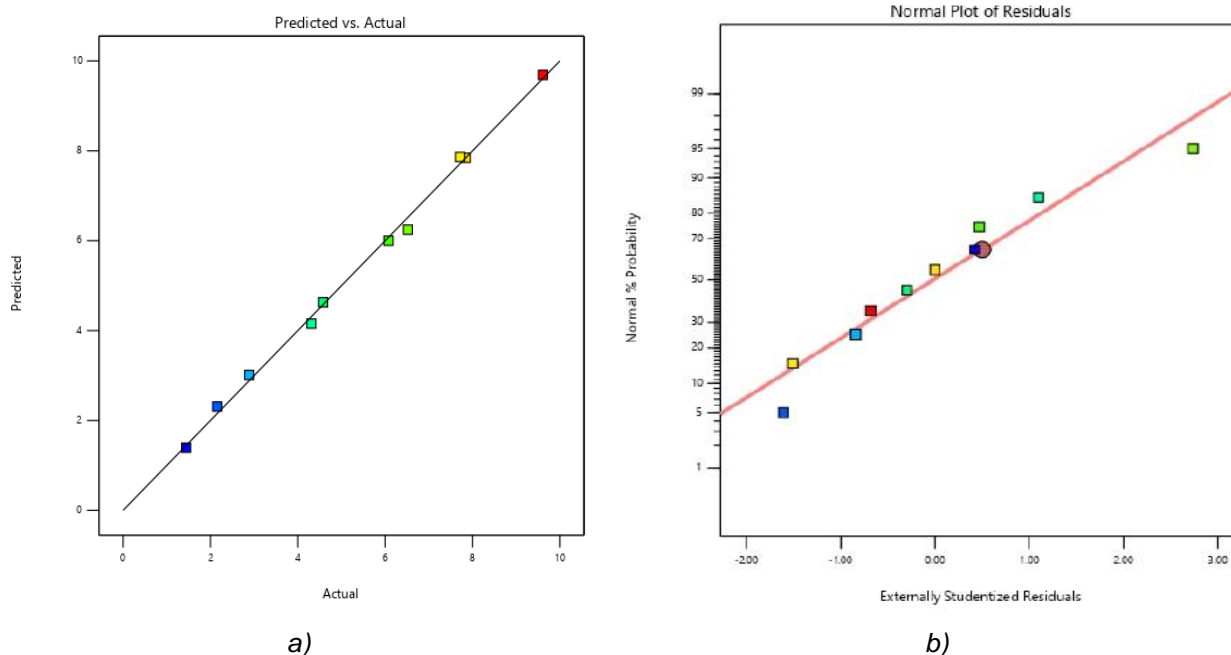


Figure 14. RSM diagnostic plots: a) Predicted vs actualm b) Normal plot of residuals

Slika 14. RSM dijagnostički grafici: a) Predviđeni naspram stvarnih (b) Normalni grafikon reziduala

Table 2. Actual and predicted results for CO₂ adsorption

Tabela 2. Stvarni i predviđeni rezultati za adsorpciju CO₂

Run	Temperature °C	Pressure psi	CO ₂ Adsorption, mmol/g	
			Actual	Predicted
1	27	20	2.16	2.31
2	27	40	4.31	4.16
3	27	60	6.08	6
4	27	80	7.85	7.85
5	27	100	9.61	9.69
6	40	20	1.44	1.39
7	40	40	2.89	3.01
8	40	60	4.58	4.63
9	40	80	6.52	6.25
10	40	100	7.72	7.86

Table 3 shows the performance metrics for the RSM model.

Table 3 shows that the RSM model provided accurate predictions of the experimental data based on the considered error metrics. The R² values exceeding 0.9 indicate highly accurate predictions of the test data. The low MSE (0.017)

and RMSE (0.13) values signify minimal errors between the actual data and the predicted response. Additionally, the MAE (0.109) and MAPE (2.72) values emphasize the high accuracy of the predictions.

Table 3. Performance metrics for RSM indicating model validation

Tabela 3. Metrika performansi za RSM koja ukazuje na validaciju modela

Parameter	Result
MSE	0.01697
RMSE	0.130269
MAE	0.109
MAPE	2.7244
R ²	0.9973
Adjusted R ²	0.9959
Predicted R ²	0.9909
CV	3.24
Adeq Precision	76.26
Std Dev.	0.172

The reliability of the model and fit are further supported by its low C.V. % value (3.34%), indicating a strong correlation between the actual

and expected values. Adeq Precision, which measures the signal-to-noise ratio, is desirable when greater than 4. The Adeq Precision value of 76.262 signifies a robust signal. This model is well-suited for navigating the design space. The optimization conducted using RSM resulted in optimized values for temperature, pressure, and CO₂ adsorption at 27°C, 100 bars, and 9.69 mmol/g, respectively.

4. CONCLUSION

Comprehensive investigation of activated carbon derived from ripe plantain peels has been achieved. Through carbonization and activation with H₃PO₄, plantain-peel activated carbon (PPAC) was created and extensively analysed. Characterisation tests, CO₂ adsorption test and RSM modelling were performed. The characterisation reveals that PPAC was effective for CO₂ adsorption as evidenced by the SEM analyses, XRD analyses, FTIR analyses, BET and BJH analyses etc. CO₂ adsorption (mmol/g) increased with increasing pressures (both initial and final). However, at 27°C, PPAC exhibited higher CO₂ adsorption capacity than at 40°C for the same pressure range. This suggests that CO₂ adsorption decreased with increasing adsorption temperature. The higher CO₂ adsorption at lower temperatures (27°C) was attributed to a higher pressure drop across the PPAC material. The pressure drop difference served as a driving force for enhanced CO₂ adsorption. Comparing two particle sizes (150µm and 845µm) of PPAC, CO₂ adsorption capacity was higher for larger particle size (845µm). Larger particles offered more surface area, better pore accessibility, and facilitated faster mass transfer, resulting in increased adsorption capacity.

From the Response Surface Methodology (RSM) model, the developed 2FI model demonstrated exceptional accuracy, as observed by high coefficients of determination ($R^2=0.9973$) and low error metrics (MSE=0.01697, RMSE=0.130269, MAE=0.109, MAPE=2.7244). The reliability of the model was confirmed by the Adeq Precision value of 76.26. Utilizing the optimized model. The optimisation conducted using RSM determined the optimal values for CO₂ adsorption as 9.69 mmol/g at temperature and pressure values of 27°C, 100 bars respectively. Generally, PPAC demonstrated favourable characteristics for CO₂ adsorption, making it a promising solution for mitigating CO₂ emissions and addressing climate change challenges.

Acknowledgement

Special recognition goes to TETFUND for the funding that enabled this was to be accomplished.

5. REFERENCES

- [1] A.H.Jagaba, I.M.Lawal, A.A.Ghfar, A.K.Usman, N.S. Yaro, Noor, A.HBirniwa (2023) Biochar-based geopolymer nanocomposite for COD and phenol removal from agro-industrial biorefinery wastewater: Kinetic modelling, microbial community, and optimization by response surface methodology. *Chemosphere*, 339, 139620. doi: 10.1016/j.chemosphere.2023.139620
- [2] C.U.Uzoho, I.F.Okorafor, D.O.Olomu, N.E.Achilike, O.D.Adesina, M.O.Onyekonwu (2023) Determination of Minimum Miscibility Pressure Between Heavy Oil–Supercritical Carbon Dioxide System Using the Slim Tube Method. In *SPE Nigeria Annual International Conference and Exhibition* (p. D021S002R001). SPE.
- [3] A.H.Jawad, A.S.Abdulhameed, T.A.Khadiran, Z.A. Othman, L.D.Wilson, S.Algburi (2023) Response surface methodology for optimizing methylene blue dye removal by mesoporous activated carbon derived from renewable woody Bambusoideae waste. *Int. J. of Phytoremediation*, 26(5), 727-739, doi: 10.1080/15226514.2023.2262040.
- [4] C.Owusu, E.A.Mends, G.Acquah (2022) Enhancing the physical qualities of activated carbon produced from palm kernel shell via response surface methodology—process variable optimization. *Biomass Conversion and Biorefinery*, ID 254561779, doi:10.1007/s13399-022-03595-7
- [5] Z.Khosrafi, H.Masoumi, A.Ghaemi (2023) Characterization and evaluation of low-cost biomass-based-AC for CO₂ capture: A review. *Case Studies in Chemical and Environmental Engineering*, 100373. <http://dx.doi.org/10.1016/j.cscee.2023.100373>
- [6] G. Greco, R.L.Canevesi, C.Di Stasi, A.Celzard, V. Fierro, J.J. Manya (2022) Biomass-derived carbons physically activated in one or two steps for CH₄/CO₂ separation. *Renewable Energy*, 191, 122-133, doi: 10.1016/j.renene.2022.04.035
- [7] M.M.Bade, A.A.Dubale, D.F.Bebizuh, M. Atlabachew (2022) Highly efficient multisubstrate agricultural waste-derived activated carbon for enhanced CO₂ Capture. *ACS omega*, 7(22), 18770-18779, <https://doi.org/10.1021/acsomega.2c01528>
- [8] J.A.Sosa, J.R.Laines, D.S.García, R.Hernández, M. Zappi, A.E. de los Monteros (2023) Activated Carbon: A Review of Residual Precursors, Synthesis Processes, Characterization Techniques, and Applications in the Improvement of Biogas. *Environmental Engineering Research*, 28(3), 220100, <https://doi.org/10.4491/eer.2022.100>
- [9] A.Inam, S.S.Oncel (2021) Photobioreactors as potential tools for environmentally friendly and sustainable buildings. *International Journal of Environmental Science and Technology*, 19(4), 1-12, <http://dx.doi.org/10.1007/s13762-021-03281-7>

- [10] Z.Khosraftar, A.Ghaemi (2022) Evaluation of pistachio shells as solid wastes to produce activated carbon for CO₂ capture: isotherm, response surface methodology (RSM) and artificial neural network (ANN) modeling. *Current Research in Green and Sustainable Chemistry*, 5, 100342, <https://doi.org/10.1016/j.crgsc.2022.100342>.
- [11] M.Gorbounov, B.Petrovic, S.Ozmen, P.Clough, S.M.Soltani (2023) Activated carbon derived from Biomass combustion bottom ash as solid sorbent for CO₂ adsorption. *Chemical Engineering Research and Design*, 194, 325-343, <https://doi.org/10.1016/j.cherd.2023.04.057>
- [12] A.Dey, B.Saini, S.C.Balchandani, S.K.Dash (2022) Investigation of equilibrium CO₂ solubility in 35 wt% aqueous 1-(2-aminoethyl) piperazine (AEP) and performance study over monoethanolamine for CO₂ absorption. *Materials Today: Proceedings*, 61(2), 498-503, <http://dx.doi.org/10.1016/j.matpr.2021.12.357>
- [13] Y.Yang, C.Zhu, Q.Huang (2021) Progress on preparation and adsorption application of solid waste derived hierarchical porous carbon. *Chemical Industry and Engineering Progress*, 40(1), 427-439, doi, 10.16085/j.issn.1000-6613.2020-0439.
- [14] H.Yang, C.He, L.Fu, J.Huo, C.Zhao, X.Li, Y.Song (2021) Capture and separation of CO₂ on BC3nanosheets: A DFT study. *Chinese Chemical Letters*, 32(10), 3202-3206, <http://dx.doi.org/10.1016/j.cclet.2021.03.038>
- [15] S.Janakiram, J.L.M.Espejo, K.K.Høisæter, A.Lindbråthen, L.Ansaloni, L.Deng (2020) Three-phase hybrid facilitated transport hollow fiber membranes for enhanced CO₂ separation. *Applied Materials Today*, 21, 100801, <https://doi.org/10.1016/j.apmt.2020.100801>
- [16] Y.Bao, J.Li, Q.Guo, B.Jiang, C.Su (2022) Review on technologies of geological resources exploitation by using carbon dioxide and its synchronous storage. *Coal Science and Technology*, 50(6), 84-95. doi : 10.13199/j.cnki.cst.2021-0552.
- [17] Y.Devarajan, N.Lakshmaiya (2022) Effective utilization of waste banana peel extracts for generating activated carbon-based adsorbent for emission reduction. *Biomass Conversion and Biorefinery*, 1-7, <http://dx.doi.org/10.1007/s13399-022-03470-5>
- [18] J.Maharjan, V.K.Jha (2022) Activated carbon obtained from banana peels for the removal of As (III) from water. *Scientific World*, 15(15), 145-157, <https://doi.org/10.3126/sw.v15i15.45665>
- [19] H.Patel, H.Weldekidan, A.Mohanty, M.Misra (2023) Effect of physicochemical activation on CO₂ adsorption of activated porous carbon derived from pine sawdust. *Carbon Capture Science Technology*, 8, 100128, <https://doi.org/10.1016/j.ccst.2023.100128>
- [20] J.Serafin, M.Ouzzine, C.Xing, H.El Ouahabi, A.Kamińska, J.Sreńscek-Nazzal (2022) Activated carbons from the Amazonian biomass andiroba shells applied as a CO₂ adsorbent and a cheap semiconductor material. *Journal of CO₂ Utilization*, 62, 102071, <https://doi.org/10.1016/j.jcou.2022.102071>
- [21] I.Yanti, P.P.Sationo, W.F.Winata, M.Anugrahwati, A.K.Anas, Y.A.Swasono (2023) Effectiveness of activated carbon magnetic composite from banana peel (*Musa acuminata*) for recovering iron metal ions. *Case Studies in Chemical and Environmental Engineering*, 8(4), 100378, <http://dx.doi.org/10.1016/j.cscee.2023.100378>
- [22] K.Jasri, A.S.Abdulhameed, A.H.Jawad, Z.A.ALothman, T.A.Yousef, O.K.Al Duaij. (2023) Mesoporous activated carbon produced from mixed wastes of oil palm frond and palm kernel shell using microwave radiation-assisted K₂CO₃ activation for methylene blue dye removal: Optimization by response surface methodology. *Diamond and Related Materials*, 131, 109581, <https://doi.org/10.1016/j.diamond.2022.109581>
- [23] Y.Vasilev, P.Vasileva, A.Tsvetkova (2020) The Study of Spreading Information on Carbon Capture, Utilization and Storage Technologies in the Social Media. 20th International Multidisciplinary Scientific GeoConference Proceedings SGEM, 20(5), 833-839, <http://dx.doi.org/10.5593/sgem2020/5.1/s20.105>
- [24] Y.Li, G.Zhang, J.Liu, G.Li, Y.Wang (2023) Optimized preparation of multi-matrix activated carbon for CO₂ capture by response surface methodology: The advantages of co-pyrolysis of biomass and plastics. *J. of the Energy Institute*, 101415, doi:10.1016/j.joei.2023.101415
- [25] M.Ounis, E.Sanz-Santos, F.Fakhfakh, M.K. Younes, B.Hadrich, S.Álvarez-Torrellas, J.García (2023) Optimisation of Adsorption Removal of Bisphenol A Using Sludge-Based Activated Carbons: Application of Response Surface Methodology with a Box–Behnken Design. *Arabian Journal for Science and Engineering*, 49(3), 1-18, doi:10.1007/s13369-023-08203-y
- [26] J.Fito, S.Tibebu, T.T.Nkambule (2023) Optimization of Cr (VI) removal from aqueous solution with activated carbon derived from *Eichhorniacrassipes* under response surface methodology. *BMC chemistry*, 17(1), 4, <https://doi.org/10.1186/s13065-023-00913-6>
- [27] Z.Tariq, Z.Xu, M.Gudala, B.Yan, S.Sun (2023 January). Deep-Learning-Based Surrogate Model to Predict CO₂ Saturation Front in Highly Heterogeneous Naturally Fractured Reservoirs: A Discrete Fracture Network Approach. In SPE Reservoir Characterisation and Simulation Conference and Exhibition? (p. D021S007R006). SPE. <https://doi.org/10.2118/212658-ms>
- [28] S.Kumar, K.Prasad, J.M.Gil, A.J.Sobral, J.Koh (2018) Mesoporous zeolite-chitosan composite for enhanced capture and catalytic activity in chemical fixation of CO₂. *Carbohydrate Polymers*, 198, 401-406, <https://doi.org/10.1016/j.carbpol.2018.06.100>
- [29] D.Chaturvedi, O.P.Misra (2019) Modeling impact of varying pH due to carbondioxide on the dynamics of prey–predator species system. *Nonlinear Analysis: Real World Applications*, 46, 374-402, <https://doi.org/10.1016/j.nonrwa.2018.09.024>
- [30] A.Mukherjee, B.Saha, C.Niu, A.K.Dalai (2022) Preparation of activated carbon from spent coffee

- grounds and functionalization by deep eutectic solvent: Effect of textural properties and surface chemistry on CO₂ capture performance. *Journal of Environmental Chemical Engineering*, 10(6), 108815, <http://dx.doi.org/10.1016/j.jece.2022.108815>
- [31] N.H.Sabri, N.H.A.Rani, N.F.Mohamad, N.M. Muhsen, M.M.Zaini (2023) Simulation of CO₂ capture for amine impregnated activated carbon-palm kernel shell (AC-PKS) adsorbent in pressure swing adsorption (PSA) using Aspen Adsorption. *Materials Today: Proceedings*, <https://doi.org/10.1016/j.matpr.2022.12.206>
- [32] H.Vogtenhuber, R.Hofmann, F.Helminger, G. Schöny (2018) Process simulation of an efficient temperature swing adsorption concept for biogas upgrading. *Energy*, 162, 200-209, doi: 10.1016/j.energy.2018.07.193
- [33] R.Maniarasu, S.K.Rathore, S.Murugan (2023) Biomass-based activated carbon for CO₂ adsorption—A review. *Energy & Environment*, 34(5), 1674-1721, doi: 10.1177/0958305X221093465
- [34] A.Helmi, F.Gallucci, M. van Sint Annaland. (2014) Resource scarcity in palladium membrane applications for carbon capture in integrated gasification combined cycle units. *International journal of hydrogen energy*, 39(20), 10498-10506, <https://doi.org/10.1016/j.ijhydene.2014.05.009>

IZVOD

ISTRAŽIVANJE UČINKA AKTIVNOG UGLJA DOBIJENOG IZ KORE ZRELE BANANE ZA HVATANJE CO₂: MODELIRANJE I OPTIMIZACIJA KORIŠĆENJEM METODOLOGIJE POVRŠINE ODGOVORA

Ova studija istražuje potencijal aktivnog uglja dobijenog iz kore zrele banane (PPAC) za hvatanje ugljen-dioksida (CO₂). PPAC je pripremljen karbonizacijom i aktivacijom pomoću H₃PO₄, a njegova jedinstvena svojstva su opsežno okarakterisana što je otkrilo nepravilne izbočine nalik sunderu i dobro definisane pore pod skenirajućom elektronskom mikroskopijom (SEM). Elementarna analiza identifikovala je ugljenik, silicijum i kiseonik kao glavne komponente, što je potvrđeno analizom rendgenske difrakcije (XRD) koja ukazuje na prisustvo silicijum oksida (SiO₂), kalijum oksida (K₂O) i kalcijum oksida (CaO). Fourier Transform Infrared (FTIR) spektroskopija je istakla različite funkcionalne grupe na površini PPAC-a. Testovi adsorpcije CO₂ su sprovedeni na 27°C i 40°C sa različitim pritiscima na PPAC čestice veličine 150µm i 845µm. Rezultati su otkrili da se kapacitet adsorpcije CO₂ povećava sa eskalirajućim pritiscima. Izvanredno, na 27°C, PPAC je pokazao superiorne performanse nego na 40°C, što se pripisuje većem padu pritiska koji povećava pokretačku snagu za adsorpciju CO₂. Veće čestice (845 µm) su pokazale veći kapacitet adsorpcije zbog povećane površine, poboljšane dostupnosti pora i bržeg prenosa mase. Sprovedena metodologija površine odgovora (RSM) dala je 2FI model kao najreprezentativniji od projektnih podataka i pokazala je visoku tačnost (R²=0,9973) i nisku metriku greške (MSE=0,01697, RMSE=0,130269, MAE=0,109, MAPE=2,7244). Vrednost Adek Precision od 76,26 potvrdila je pouzdanost modela. Optimizacija korišćenjem RSM-a je dala optimalne vrednosti adsorpcije CO₂ (9,69 mmol/g) na 27°C i 100 bara. PPAC se pojavljuje kao obećavajuće rešenje za hvatanje CO₂, nudeći vredne izgleda za smanjenje emisija i rešavanje izazova klimatskih promena.

Ključne reči: aktivni ugalj od kore zrele banane, metodologija površine odgovora, karakterizacija, optimizacija, adsorpcija CO₂

Naučni rad

Rad primljen: 17.11.2023.

Rad prihvaćen: 10.12.2023.

Rad je dostupan na sajtu: www.idk.org.rs/casopis

Svetlana Osadchuk, Lyudmila Nyrkova*

E.O. Paton Electric Welding Institute of the National Academy of Sciences of Ukraine, Kyiv, Ukraine

Scientific paper

ISSN 0351-9465, E-ISSN 2466-2585

<https://doi.org/10.62638/ZasMat1130>



Zastita Materijala 65 (2)
273 - 278 (2024)

Investigation of properties of epoxy coating on X80 steel under cathodic polarization conditions

ABSTRACT

The effect of cathodic polarization on the properties of the protective epoxy coating on X80 steel samples under cyclic changes in temperature from 20 to 75 °C over a period ~3.5 months was investigated. It is shown that in a 3% NaCl solution, with decreasing polarization potential from -1.05 to -0.85 V, the disbondment radius of the epoxy coating decreased by ~3.48 times (from 10.8 to 3.1 mm). At -0.75 V and in the absence of polarization, disbondment of the coating from the steel don't observed. By potential -0.75 V coating retains its protective properties according to the transient specific electrical resistance indicator, and its aging is slowed down.

Keywords: epoxy coating, X80 steel, cathodic polarization, protective potential, cathodic disbondment, transient specific electrical resistance, coating degradation

1. INTRODUCTION

Polyurethane and epoxy coatings, which are used in oil and gas pipelines, have high resistance to cathodic disbondment, and according to DSTU 4219 with amendment No. 1 [1], they are classified as class B (very reinforced) and are recommended for use in areas with a potentially high probability of corrosion cracking. Under such conditions, using polarizing potentials more negative than -850 mV is not recommended to minimize coating disbondment [2]. In addition, important characteristics of coatings are their resistance to the development of defects over time and their preservation of transient electrical resistance values [3].

Cathodic polarization affects the properties of the environment around the pipe under the disbonded coating, which contributes to the degradation of the coating matrix and its disbondment. It is believed that the causes of disbondment are the dissolution of iron oxides at the metal/coating interface [4, 5], the formation and accumulation of hydroxide ions, which increases the pH of the medium to 14, crevice corrosion due to the cathodic reduction of hydrogen [6], the state

of the surface [7], the presence of soluble salts on the surface [8], the level of the cathodic polarization potential, and the size of the gap between the exfoliated coating and the steel [9], which affects the change in corrosion and electrochemical conditions on the surface of the pipe near the area of disbondment.

To increase the resistance of coatings against cathodic disbondment, the use of inhibitors in the environment (for example, thiourea) [10], nanostructured films [11, 12], the addition of zinc filler in epoxy compositions [13], lowering the level of cathodic polarization, etc., is proposed.

This investigation aimed to determine the influence of the cathodic polarization level on the protective properties of modern epoxy coatings applied to the surface of X80 steel, as well as the changes in the solution's properties under the influence of polarization and its effect on steel.

2. MATERIALS AND METHODS

A two-component epoxy coating, amine-approved (further - the coating), which does not contain solvents, with a dry residue of (98±2) %, intended for application to the outer surface of pipelines, was used in this work. The coating was applied in one layer on X80 pipe steel specimens with dimensions of 100 mm × 100 mm × 20 mm after sandblasting. The chemical composition of the X80 steel is listed in Table 1.

*Corresponding author: Lyudmila Nyrkova

E-mail: lnyrkova@gmail.com

Paper received: 12. 12. 2023.

Paper accepted: 21. 12. 2023.

Paper is available on the website: www.idk.org.rs/journal

Table 1. Chemical composition of X80 steel

Tabela 1. Hemijski sastav čelika X80

Element	C	Mn	V	Nb	Ti	Cu	Mo	Cr
Wt. %	0.06	1.635	0.036	0.040	0.015	0.07	0.012	0.03

All defined indicators of physical, mechanical and protective properties of the coating corresponds to the requirements of DSTU 4219 [1]. Particularly, the thickness of the coating in the initial state was 2 mm, the dielectric continuity – $17.5 \cdot 10^3$ V (according to DSTU 4219 the dielectric constant must be equal not less than $5 \cdot 10^3$ V/(mm of the thickness of the coating)), the transient specific electrical resistance from $1.2 \cdot 10^{10}$ to $1.5 \cdot 10^{10}$ Ohm·m². Cathodic disbondment of the coating was studied in 3% NaCl according to [1] in the range of protective polarization potentials from -0.75 to -1.05 V relative to the silver chloride reference electrode (which is corresponds to the range from -0.85 to -1.15 V relative to the copper sulfate reference electrode). A polarization potential of -1.05 V was maintained using a magnesium anode, and other potentials (-0.75 and -0.85 V) were set using a multi-channel potentiostatic device using a laboratory stand with a clamping electrochemical cell. A defect with a diameter of 6 mm was artificially created in the epoxy coating. Polarization potentials were adjusted using the device. Potentials were measured by a voltmeter with an accuracy of 0.08%, and polarization currents using an ammeter.

The research was carried out under cyclic temperature changes from 20 to 75 °C, close to the maximum operating temperature of the coating. One cycle continued for 24 h (1 day): at a temperature of 75 °C – 12 h; at a temperature of 20 °C – 12 h. On weekends, the specimens were kept at a temperature of 20 °C. The total duration of the cover study was 3.5 months, of which 29 days were spent at elevated temperatures. According to the results of previous studies, at a temperature of 20 °C, disbondment of the coating was not observed, therefore, the duration of exposure at this temperature was not taken into account.

After the research, the disbondment radius was determined according to [1], the dielectric continuity was determined using a spark gap detector DKI-1, and the transient resistivity of the coating was determined using a teraohmmeter E6-13.

In the solutions before and after the coating study, electrical conductivity and pH were measured by standard methods, redox potential by potentiometry using platinum and silver chloride electrodes.

The density of the limiting diffusion current j_{O_2} was determined from the cathodic polarization curves, which were recorded on a PI-50.1.1 potentiostat with a sweep speed of $1 \cdot 10^{-3}$ V/sec in 3% NaCl after tests of the coating in that solutions without polarization and under polarization.

The residual corrosion rate i_{res} in mm/year in the coating defect was counted according to the method [1] by the formula:

$$i_{res} = i_{cor} \cdot 10^{\frac{E_{pol} - E_{cor}}{b_a}} \quad (1)$$

Where i_{cor} is corrosion rate of metal in the studied environment, determined by the polarization resistance method in a 3% NaCl solution, equal to 0.101 mm/year [14];

E_{pol} – polarization potential, V;

E_{cor} – corrosion potential, V;

b_a – Tafel slope of the anodic polarization curve, equal to 0.06 V [15].

3. RESULTS AND DISCUSSION

When the potential decreases from -1.05 to -0.75 V, the polarization current naturally decreases by almost 3 orders of magnitude (Fig. 1).

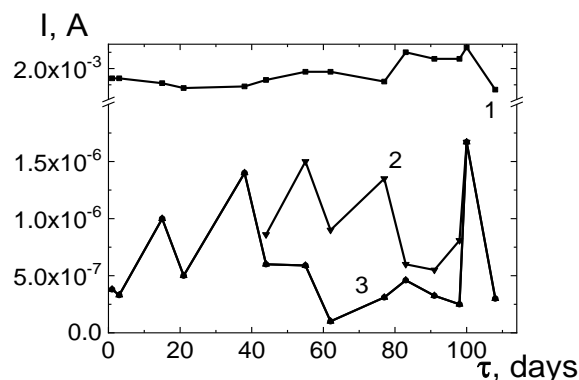


Figure 1. Change of polarization currents in time at the potential -1.05 V (1), -0.85 V (2), and -0.75 V (3)

Slika 1. Promena polarizacionih struja u vremenu na potencijalu -1.05 V (1), -0.85 V (2) i -0.75 V (3).

This type of current change corresponds to a decrease in the disbondment radius (Fig. 2). At a

potential of -1.05 V, the disbondment radius was 10.8 mm (Fig. 2, b). The disbondment nature of the coating was adhesive, so coating disbonding was not detected. When the potential decreases from -1.05 to -0.85 V, the disbondment radius of the coating decreased by nearly 3.48 times (from 10.8 to 3.1 mm). When the potential was further reduced to -0.75 V and when polarization was not applied, coating disbondment from the steel was not observed (Fig. 2, c-e).

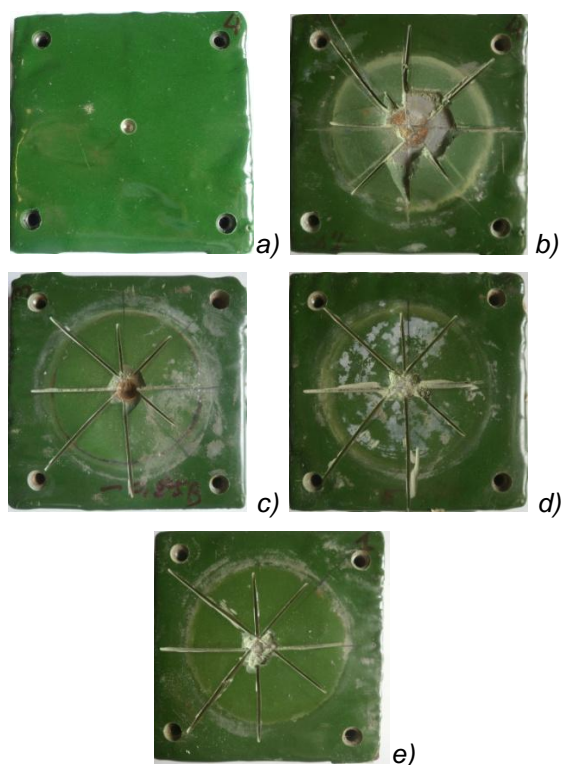


Figure 2. The appearance of the epoxy coating in the area of the artificial defect in the initial state (a) and after tests for cathodic disbondment in a solution of 3% NaCl with cyclic temperature changes for 3,5 months and determination of the disbondment radius: b – for polarization -1.05 V; c – with a polarization of -0.85 V; d – at polarization -0.75 V; e – without polarization

Slika 2. Izgled epoksidnog premaza u predelu veštačkog defekta u početnom stanju (a) i nakon ispitivanja katodnog odvajanja u rastvoru 3% NaCl uz ciklične promene temperature tokom 3,5 meseca i određivanje odvajanja. poluprečnik: b – za polarizaciju $-1,05$ V; c – sa polarizacijom od $-0,85$ V; d – pri polarizaciji $-0,75$ V; e – bez polarizacije.

Change of the cover properties depending on polarization potential, namely disbondment radius, and transient electrical resistivity are shown in Fig. 3, changes in the properties of a 3% NaCl solution after testing the cathodic disbondment

coating at different potential are presented in Fig. 4. Coating aging was evaluated by the change in transient electrical resistance. It was established that the transient electrical resistance increased from $2.06 \cdot 10^6$ Ohm \cdot m 2 after coating testing at a potential of -1.05 V to $8.42 \cdot 10^6$ Ohm \cdot m 2 after coating disbondment investigation at a potential of -0.75 V and up to $1.45 \cdot 10^7$ Ohm \cdot m 2 when coating disbondment was tested without polarization (Fig. 3). Such values of transient electrical resistance correspond to normalized indicator for a new coating of a highly reinforced type according to [1] ($1 \cdot 10^7$ Ohm \cdot m 2 after exposure to a 3% NaCl solution for 100 days at a temperature of 20 °C). The dielectric integrity of the coating was changed only in cells in which the coating was tested at polarization -1.05 V, and its value was $12.5 \cdot 10^3$ V, while in the initial state, it was $17.5 \cdot 10^3$ V. A change in the color of the solution was also noted, which is obviously associated with coating degradation.

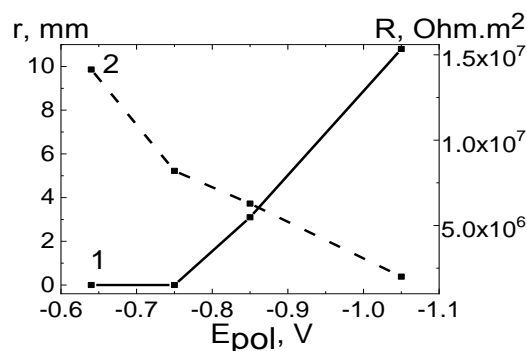


Figure 3. Change of the cover properties depending on polarization potential: 1 – disbondment radius; 2 – transient electrical resistivity

Slika 3. Promena svojstava poklopca u zavisnosti od polarizacionog potencijala: 1 – radijus odvajanja; 2 – prolazna električna otpornost

An increase in the pH of the solutions in which the coating disbondment was studied under potentials -0.75 , -0.85 , and -1.05 V, respectively, from 7.0 (in the initial state) to 12.2 was established. A decrease in the redox potential from 0.518 V (in the initial state) to 0.313 V was noted (Fig. 4).

Therefore, the properties of the solution changed from moderately oxidizing (from 0.5 to 0.6 V) to weakly reducing (from 0.3 to 0.4 V). In addition, the electrical conductivity of the solution (in Sm/cm) varies non-monotonically in the rows $1.1 \cdot 10^{-2}$ (before the tests) $\rightarrow 1.23 \cdot 10^{-2}$ (after coating disbondment tests at E_{cor}) $\rightarrow 4.30 \cdot 10^{-2}$ (after coating disbondment tests at -0.75 V) $\rightarrow 4.14 \cdot 10^{-2}$ (after coating disbondment tests at -0.85 V) $\rightarrow 7.82 \cdot 10^{-2}$ (after coating disbondment tests at -1.05 V). It is obvious that such changes in the solution due to cathodic polarization can lead to a change in the corrosion rate of steel.

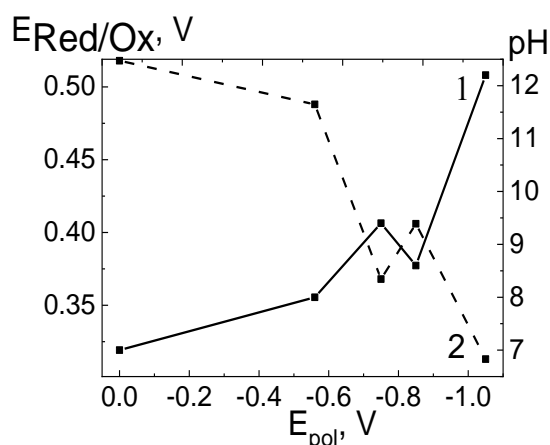


Figure 4. Changes in the properties of a 3% NaCl solution after testing the coating by the cathodic disbondment method at different potentials: 1 – pH; 2 – Red Ox potential

Slika 4. Promene svojstava 3% rastvora NaCl nakon ispitivanja prevlake metodom katodnog odvajanja pri različitim potencijalima: 1 – pH; 2 – Red Ox Potencijal

The corrosion resistance of X80 pipe steel in solutions (with different pH) after coating tests were evaluated by the limiting diffusion current, as well as other related characteristics such as the ratio of the cathodic protection current to the limiting diffusion current j_{cp}/j_o and the residual corrosion rate. In Fig. 5 the cathodic polarization curves of this steel in solutions with different pH after coating degradation tests are shown, from which the limiting diffusion current was determined. Electrochemical corrosion of steel in 3% NaCl solution occurs with diffusion control (curves 1-4) and mixed control (curve 5). From the analysis of the nature of the curves, it was established that in the original solution, the limiting diffusion current on the steel was equal to 0.47 A/m^2 . In the solutions after coating disbondment testing at potentials of -0.75 and -0.85 V, the limiting diffusion current density of oxygen was, respectively, 0.28 and 0.26 A/m^2 . In the solution, in which coating disbondment tests were carried out at potential of -1.05 V, the absence of the limiting diffusion current was explained by a change in the properties of the solution under the action of cathodic polarization of the steel (Fig. 4), presumably due to the reduction of compounds with the participation of iron ions (oxides, hydroxides, and hydroxyl chlorides) and degradation of the coating. From the analysis of the obtained results, it follows that the susceptibility of steel to uniform corrosion in the corresponding solution after disbondment of the coating is lower the higher the level of polarization.

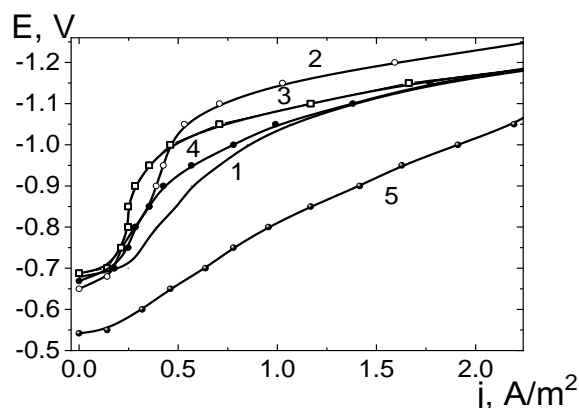


Figure 5. Cathodic polarization curves of X80 steel in a solution of 3% NaCl after testing the coating by the cathodic disbondment method at different potentials: 1 – initial state; 2 – E_{cor} ; 3 – -0.75 V; 4 – -0.85 V; 5 – -1.05 V

Slika 5. Krive katodne polarizacije čelika Ks80 u rastvoru 3% NaCl nakon ispitivanja prevlake metodom katodnog odvajanja pri različitim potencijalima: 1 – početno stanje; 2 – E_{cor} ; 3 – -0.75 V; 4 – -0.85 V; 5 – -1.05 V.

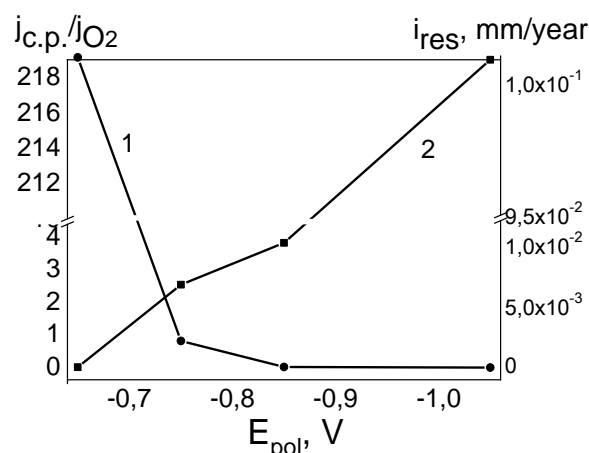


Figure 6. Change in the ratio j_{cp}/j_o at potential -1.05 V (1) after testing coating on cathodic disbondment in cells and residual corrosion rate of X80 steel (2) in 3% NaCl solution at different polarization potentials

Slika 6. Promena odnosa j_{cp}/j_o od potencijala -1.05 V (1) nakon ispitivanja prevlake na katodno odvajanje u ćelijama i zaostale brzine korozije čelika X80 (2) u 3% rastvoru NaCl pri različitim potencijalima polarizacije

It was previously established [14] that the analysis of the relationship between cathodic protection current, limiting diffusion current $j_{c.p.}/j_o$, and the residual corrosion rate makes it possible to assess the protection state of the

coating defect and the corrosion resistance of the steel. Calculating these ratios $j_{c,p}/j_{O_2}$ at a potential of -1.05 V from the polarization curves (Fig. 5) for X80 steel in the corresponding solutions, it was found that the ratio in the solution after polarization of the steel at a potential of -1.05 V is higher than 4, which indicates the possibility of steel hydrogenating. Residual corrosion rate values calculated according to [1], Fig. 6, (curve 2), showed that in all tested solutions, a technically sufficient protective effect, for which the residual corrosion rate is less than 0.01 mm/year, is achieved at a potential of -0.75 V. That is, if the values of the protective potentials are exceeded by the absolute value of -0.75 V, it is possible to accelerate the degradation of the epoxy coating in the defect area, and the probability of hydrogenation of X80 steel will increase with time, which can create favorable conditions for the development of stress-corrosion cracking.

4. CONCLUSIONS

It was established that the protective properties of the epoxy coating applied to X80 steel in a solution of 3% NaCl for 3.5 months with a cyclic temperature change from 20 to 75 °C, which simulates a temperature close to the maximum operating temperature, with a decrease in the absolute value of the polarization potential from -1.05 to -0.75 V relative to the silver chloride reference electrode, are preserved: the disbondment radius decreases from 10.8 to 0 mm, and the transient resistivity of the coating is from $2.03 \cdot 10^6$ to $8.42 \cdot 10^6$ Ohm·m². Polarization potentials that are less negative than -0.85 V help minimize cathodic exfoliation.

Acknowledgment

The work was carried out with the support of the National Academy of Sciences of Ukraine (state registration number 0118U100537)

5. REFERENCES

- [1] DSTU 4219-2003 Main steel pipelines. General requirements for protection against corrosion. Kyiv. State Consumer Standard of Ukraine. 86 p. Change No. 1. 2018.
- [2] RP, N.S. (1969) Control of External Corrosion on Underground or Submerged Metallic Piping Systems. Mater. Prot., 8(9), 1.
- [3] J.A.Beavers, N.G.Thompson (2006) External corrosion of oil and natural gas pipelines. ASM handbook, 13 (05145), <https://doi.org/10.31399/asm.hb.v13c.a0004213>
- [4] D.Hill et al. (2009) Performance of composite materials in corrosive conditions: cathodic disbondment of composite materials and modeling of a composite repair patch for pipelines. In NACE CORROSION (pp. NACE-09329). NACE. <https://onepetro.org/NACECORR/proceedings-abstract/CORR09/All-CORR09/128711>
- [5] Q.Ding et al. (2021) Influence of AC Stray Current on Cathodic Disbondment of Epoxy Coatings. International journal of electrochemical science, 16(1), 1-16, <https://doi.org/10.20964/2021.01.30>
- [6] Jr.Leidheiser (1982) Corrosion of painted metals – a review. Corrosion, 38(7), 374-383, <https://doi.org/10.5006/1.3581899>
- [7] N.Wint et al. (2020) Combinatorial Studies into the Effect of Thermally Inter-Diffused Magnesium on the Kinetics of Organic Coating Cathodic Delamination from Zinc Galvanized Steel. Journal of The Electrochemical Society, 167(2), 021502. <https://doi.org/10.1149/1945-7111/ab6289>
- [8] M.Zamanzadeh (2016) March. Fusion Bonded Epoxy Coatings (FBE) and Disbondmen. In NACE CORROSION (pp. NACE-2016). NACE, <https://onepetro.org/NACECORR/proceedings-abstract/CORR16/All-CORR16/123533>
- [9] R.Ashari et al. (2020) Corrosion and electrochemical conditions of pipeline steel under tape coating disbondments: effect of disbondment gap size and morphology. Journal of pipeline systems engineering and practice, 11(1), 04019051, [https://doi.org/10.1061/\(ASCE\)PS.1949-1204.0000413](https://doi.org/10.1061/(ASCE)PS.1949-1204.0000413)
- [10] C.Gu et al. (2020) The coating delamination mitigation of epoxy coatings by inhibiting the hydrogen evolution reaction. Progress in Organic Coatings, 147, 105774, <https://doi.org/10.1016/j.porgcoat.2020.105774>
- [11] A.H.Mofidabadi. et al. (2020) Explorations of the adhesion and anti-corrosion properties of the epoxy coating on the carbon steel surface modified by Eu2O3 nanostructured film. Journal of Molecular Liquids, 314, 113658, <https://doi.org/10.1016/j.molliq.2020.113658>
- [12] S.Akbarzadeh et al. (2020) Inspection the corrosion prevention performance and dry/wet interfacial adhesion qualities of the melamine-cured polyester coating applied on the treated mild steel surface with a nanostructured composite cerium-neodymium film. Colloids and Surfaces A: Physicochemical and Engineering Aspects, 590, 124472, <https://doi.org/10.1016/j.colsurfa.2020.124472>
- [13] L.Zhang et al. (2014) The influence of cathodic polarization on performance of two epoxy coatings on steel. International Journal of Electrochemical Science, 9(11), pp.6266-6280, [https://doi.org/10.1016/S1452-3981\(23\)10887-X](https://doi.org/10.1016/S1452-3981(23)10887-X).
- [14] L.I.Nyrkova et all. (2020) Influence of the corrosiveness of a medium on the ratio of the cathodic protection current to the ultimate diffusion current for KH70 pipe steel. Materials Science, 56, 417-424, <https://doi.org/10.1007/s11003-020-00445-7>.
- [15] M.G.Fontana, R.W.Staehle, (1970) Advances in corrosion science and technology. Plenum Press.

IZVOD

ISTRAŽIVANJE SVOJSTVA EPOKSI PREMAZA NA ČELIKU X80 U USLOVIMA KATODNE POLARIZACIJE

Ispitivan je uticaj katodne polarizacije na svojstva zaštitnog epoksidnog premaza na uzorcima čelika X80 pri cikličnim promenama temperature od 20 do 75°C u periodu ~3,5 meseca. Pokazano je da se u 3% rastvoru NaCl, sa smanjenjem potencijala polarizacije sa -1,05 na -0,85 V, radijus odvajanja epoksidnog premaza smanjio za ~3,48 puta (sa 10,8 na 3,1 mm). Na -0,75 V i u odsustvu polarizacije, odvajanje prevlake od čelika nije primećeno. Potencijal -0,75 V premaz zadržava zaštitna svojstva prema prolaznom specifičnom indikatoru električnog otpora, a njegovo starenje se usporava.

Ključne reči: epoksidni premaz, X80 čelik, katodna polarizacija, zaštitni potencijal, katodno odvajanje, prolazni specifični električni otpor, degradacija premaza

Naučni rad

Rad primljen: 12.12.2023.

Rad prihvaćen: 21.12.2023.

Rad je dostupan na sajtu: www.idk.org.rs/casopis

Natarajan Thiruvani^{1,2}, Ramu Mathamma², Dhanapal Prakash Babu³, Sadasivam Ponkumar⁴, Ramasamy Jayavel⁵

¹Department of Physics, Government Arts College for Women, Salem, India, ²Department of Physics, Sri Sarada college for women (Autonomous), Salem, India, ³School of Applied Sciences, Department of Physics, REVA University, Bangalore, India, ⁴Department of Physics, Thiruvalluvar Government Arts College, Namakkal, India, ⁵Crystal Growth Centre, Anna University, Chennai -600 025

Scientific paper

ISSN 0351-9465, E-ISSN 2466-2585

<https://doi.org/10.62638/ZasMa1133>



Zastita Materijala 65 (2)
279 - 284 (2024)

A novel $\text{Sr}_{0.99}\text{Zr}(\text{PO}_4)_2:0.01\text{Eu}^{3+}$ ceramic glass viable for long term energy storage applications

ABSTRACT

This paper reports the first-time synthesis of $\text{Sr}_{0.99}\text{Zr}(\text{PO}_4)_2:0.01\text{Eu}^{3+}$ ceramic glass were synthesized via solution combustion using glycine as fuel (1:1 fuel-to-oxidizer ratio). X-ray diffraction confirmed the desired crystalline phase, while Scherrer analysis indicated an average particle size of approximately 60 nm. This was further supported by scanning electron microscopy, which revealed a particle size around 75 nm. Notably, the material exhibited a characteristic mesoporous structure, a signature feature of the solution combustion technique. Dielectric studies revealed a double exponential decay profile, signifying the presence of voids within the material. Importantly, the significantly smaller time constant (t_2) compared to t_1 highlights the material's suitability for long-term energy storage applications.

Keywords: SZO nanoceramics, solution combustion synthesis, energy storage, dielectric properties

1. INTRODUCTION

For decades, phosphates have captivated researchers due to their diverse applications, encompassing everything from phosphors and nuclear waste forms to thermal barrier coatings, catalysts, and solid electrolytes [1]. These materials boast remarkable characteristics, including exceptional chemical stability, low thermal conductivity, high melting points, a high thermal expansion coefficient, and the ability to readily accommodate defects [2]. Recently, zirconia-based materials have attracted significant attention for their potential as energy storage materials. This surge in interest on Eu^{3+} doped materials has spurred extensive research into their preparation and functional properties, leading to the development of diverse synthesis methods like solid-state reaction, sol-gel, combustion, stearic acid, solution combustion, and hydrothermal techniques [3].

While solid-state synthesis remains popular due to its simplicity, its limitations, such as high temperatures (often exceeding 1200°C) and lengthy reaction times (lasting several days), can lead to large agglomerates [4].

Building upon our previous success in overcoming limitations like high temperatures and long reaction times through solution combustion [5], this work delves deeper into the preparation and characterization of $\text{Sr}_{0.99}\text{Zr}(\text{PO}_4)_2:0.01\text{Eu}^{3+}$ nanopowders. This efficient route yielded materials with a desirable mesoporous structure and enhanced chemical homogeneity, paving the way for simpler and more cost-effective synthesis compared to traditional methods. Here, we focus on comprehensively understanding these promising materials, paving the way for their potential applications in energy storage of $\text{Sr}_{0.99}\text{Zr}(\text{PO}_4)_2:0.01\text{Eu}^{3+}$.

Driven by the pressing need for efficient, durable, sustainable, and affordable energy storage solutions [7], researchers are exploring novel materials with exceptional properties. Supercapacitors, bridging the gap between capacitors and batteries, offer promising possibilities for applications requiring rapid energy cycling due to their fast charging/discharging capabilities [8]. This has sparked significant interest

*Corresponding author: Natarajan Thiruvani

E-mail: thiruvaninatarajan23@gmail.com

Paper received: 15. 12. 2023.

Paper accepted: 26.12.2023.

Paper is available on the website: www.idk.org.rs/journal

in materials with supercapacitive potential. Preliminary studies suggest that $\text{SrZr}(\text{PO}_4)_2$ exhibits promising supercapacitive properties and corrosion protection coatings [9], making it a prime candidate for further exploration and optimization.

Its unique combination of desirable properties, including high stability, low thermal expansion, and superionic conductivity [10, 11], makes it an attractive candidate for various technological advancements. Continued research and development are crucial to unlock the full potential of $\text{SrZr}(\text{PO}_4)_2$ and contribute to the advancement of diverse industries [12].

Orthophosphates have emerged as prominent host materials for dielectric applications due to their exceptional properties, including a large band gap, moderate phonon energy and high chemical stability [13]. $\text{Sr}_{0.99}\text{Zr}(\text{PO}_4)_2:0.01\text{Eu}^{3+}$ ceramic material was specifically chosen for this study due to its advantageous characteristics:

- Ionic conductivity: Facilitates efficient charge transport.
- Anisotropy: Enables tailoring material properties for specific applications.
- Lower thermal expansion: Enhances material stability [13].
- Larger ionic radii: Allows effective incorporation of rare-earth ions without altering the crystal structure [14].
- Presence of zirconium and phosphate: Provides a well-defined crystal field for structural applications.

Despite the promising potential of $\text{SrZr}(\text{PO}_4)_2$, limited research has been conducted on its dielectric properties, particularly regarding Eu^{3+} doping. This work aims to address this gap by exploring dielectric properties of this material. To

the best of our knowledge, no reports are available on these specific aspects of $\text{Sr}_{0.99}\text{Zr}(\text{PO}_4)_2:0.01\text{Eu}^{3+}$.

Significance of the Study: This study ventures into the uncharted territory of $\text{Sr}_{0.99}\text{Zr}(\text{PO}_4)_2:0.01\text{Eu}^{3+}$'s dielectric properties, shedding light on its potential for innovative technological advancements. Unveiling its dielectric behavior offers valuable insights into the material's suitability for specific applications.

2. PREPARATION:

$\text{Sr}_{0.99}\text{Zr}(\text{PO}_4)_2:0.01\text{Eu}^{3+}$ was prepared by solution combustion method with F/O ratio maintained at unity. Stoichiometric amounts of $\text{ZrO}(\text{NO}_3)_2$, $\text{NH}_6(\text{PO}_4)_2$, $\text{Eu}(\text{NO}_3)_3$, $\text{Sr}(\text{NO}_3)_2$, and Glycine were dissolved in 50 ml of double distilled water to obtain a homogenous solution. The precursor solution was then transferred to a crystalline dish and placed in a preheated muffle furnace at 500°C . Upon completion of the reaction, the sample was removed from the furnace and allowed to cool to room temperature. Finally, the powder was calcined at 800°C for 6 hours.

3. RESULT AND DISCUSSION

3.1. XRD analysis

To ascertain the crystallinity, phase purity, and structural information of $\text{Sr}_{0.99}\text{Zr}(\text{PO}_4)_2:0.01\text{Eu}^{3+}$, powder X-ray diffraction (XRD) measurements were conducted, Fig. 1. The observed diffraction patterns aligned well with ICSD file number 150336 [14]. The crystalline sizes of the prepared samples were calculated using the Scherrer method and were about 60nm.

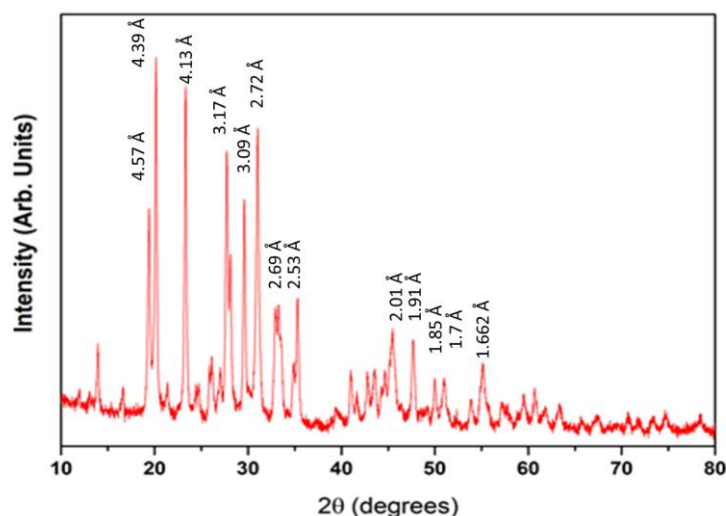


Figure 1. PXR spectrum of $\text{Sr}_{0.99}\text{Zr}(\text{PO}_4)_2:0.01\text{Eu}$

Slika 1. PXR spektar $\text{Sr}_{0.99}\text{Zr}(\text{PO}_4)_2:0.01\text{Eu}$

The Scherer equation is given by:

$$D = k\lambda/\beta\cos\theta \quad (1)$$

where λ is the wavelength of X-rays (1.5406 Å), β is the full width half maxima of diffraction peaks, k is the Scherer's constant (0.9), and θ is the Bragg's angle.

3.3. SEM

Figure 2 presents SEM images of the sample, highlighting microstructure of the sample. This

reveal mesoporous nature of the sample with particle distribution in nano meter range. These observations can be attributed to the evolution of a substantial amount of gases during the combustion process, leading to the formation of voids and pores. The measured particle size in the SEM micrographs, around 75 nm, coincides with the results obtained from PXRD studies, suggesting consistency between the two characterization techniques.

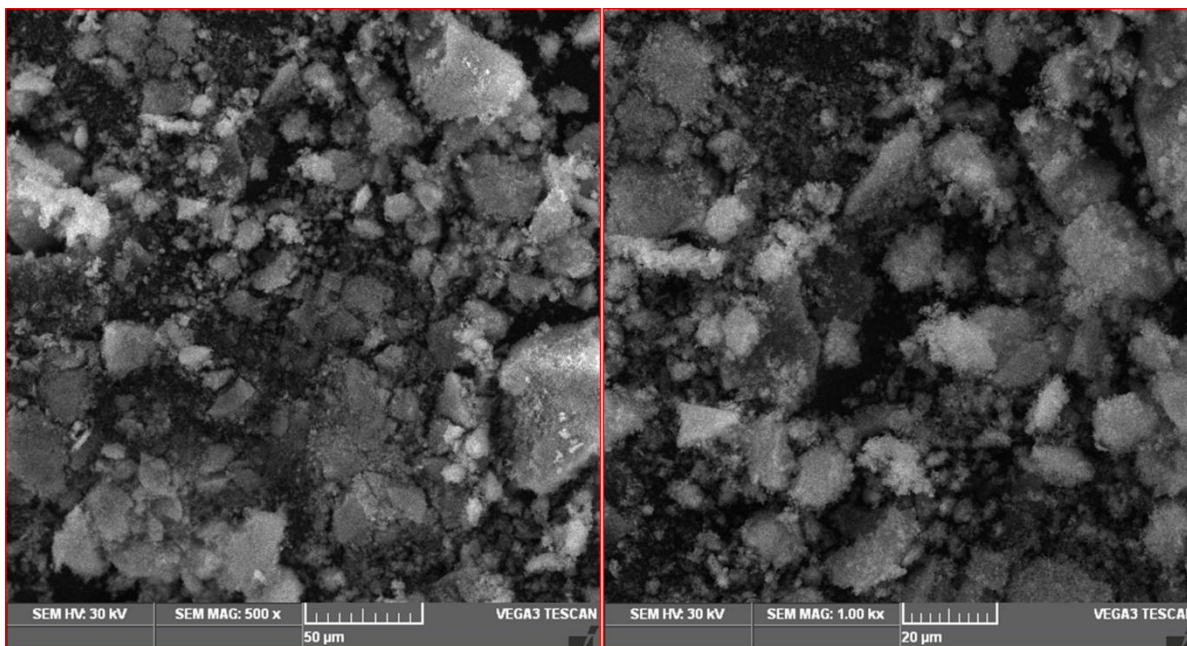


Figure 2. SEM micrograph of $\text{Sr}_{0.99}\text{Zr}(\text{PO}_4)_2:0.01\text{Eu}$ at 50 and 20 μm magnification

Slika 2. SEM mikrofografija $\text{Sr}_{0.99}\text{Zr}(\text{PO}_4)_2:0.01\text{Eu}$ pri uvećanju od 50 i 20 μm

3.4. Dielectric studies

Understanding the interplay between electric fields and materials forms the cornerstone of designing and developing materials for various applications. This interaction, governed by several key parameters, manifests in the form of dielectric properties [15].

Two crucial concepts in dielectric studies are relaxation time and correlation function. Relaxation time dictates how quickly a material responds to an applied electric field, representing the average time it takes for its internal dipoles to align with the field. A single relaxation time translates to an exponential decay of the material's polarization, while a distribution of relaxation times results in a more complex decay profile [16]. Analyzing the relaxation time sheds light on the dynamics of the dipoles and their response to external stimuli.

The correlation function, denoted by $C(\tau)$, mathematically quantifies the relationship between

a material's dielectric response at different times. Essentially, it measures how well the polarization at a specific moment relates to the polarization at a later one [17]. This function is calculated using dielectric relaxation data, typically involving measurements of the material's dielectric constant at various frequencies. By analyzing the frequency dependence of this constant, researchers can extract the relaxation time and subsequently calculate the correlation function, as per the provided formula [18].

$$C(\tau) = \lim_{T \rightarrow \infty} \frac{1}{T} \int_0^T \varepsilon(t) \varepsilon(t + \tau) dt \quad (6)$$

where: $\varepsilon(t)$ is the dielectric constant of the material at time t , τ is the time lag between the two measurements of $\varepsilon(t)$, T is the total time of the measurement

The relaxation time (τ) characterizes the time taken for the dielectric permittivity to decay to half its initial value following an electric field

perturbation [19]. Its relationship to the correlation function, C(τ), is described by:

$$C(\tau) = \frac{1}{2} \exp\left(-\frac{\tau}{\tau_R}\right) \tag{7}$$

The decay curves were fit using the double exponential equation:

$$y = A_1 \exp\left(\frac{-x}{t_1}\right) + A_2 \exp\left(\frac{-x}{t_2}\right) + y_0 \tag{8}$$

Table 1 showcases our calculated data, while Figure 3 visually dissects the dielectric decay behavior of Sr_{0.99}Zr(PO₄)₂:0.01Eu³⁺. Here, the blue squares (■) represent the experimental data, the

red line depicts the fitted curve, and the individual decay components are shown for analysis. In this figure, "y₀" signifies the initial offset level, A₁ and A₂ represent the initial amplitudes of the two exponential decay components, τ₁ and τ₂ are the time constants reflecting the decay time for each component, and k₁ and k₂ are the respective rate constants.

τ₁ and τ₂ are the time constants or decay time represented as follows:

$$\tau_1 = \frac{1}{k_1} \text{ And } \tau_2 = \frac{1}{k_2} \tag{9}$$

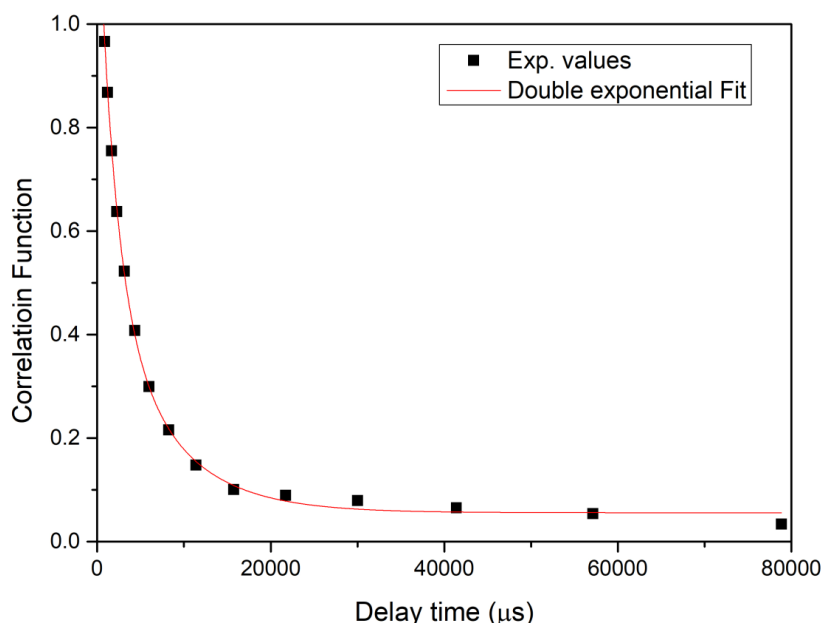


Figure 3. Di-electric decay curves of Sr_{0.99}Zr(PO₄)₂:0.01Eu

Slika 3. Krive dielektričnog raspada Sr_{0.99}Zr(PO₄)₂:0,01Eu

Table 1. Calculated decay parameters for Sr_{0.99}Eu_{0.01}Zr(PO₄)₂ by double exponential fit

Tabela 1. Izračunati parametri raspada za Sr_{0.99}Eu_{0.01}Zr(PO₄)₂ dvostrukim eksponencijalnim uklapanjem

Parameter	Value
y ₀	0.06
A ₁	0.48
τ ₁ (μs)	7078
A ₂	0.751
τ ₂ (μs)	1953
k ₁	1.41E-04
k ₂	5.12E-04
τ ₁	4906
τ ₂	1354

The speed of the two exponential decay components depends on their respective time

constants. Simply put, the larger the time constant, the slower the decay. Each component's decay time is the time it takes for its signal to drop to a tiny fraction (about 0.693) of its initial strength [20].

This double-decay behavior, a hallmark of bi-exponential decay, indicates the material stores energy at two different rates. This can be attributed to the presence of two distinct mechanisms for storing charge within the material [21].

- Fast decay (t₂): This rapid decline reflects the release of energy stored in the material's pores, as seen in the SEM images.
- Slow decay (t₁): This slower decline corresponds to the release of energy stored deeper within the material, in its bulk.

Importantly, the much smaller value of t₂ compared to t₁ in our studies suggests this material is promising for long-term energy storage applications [22].

4. CONCLUSION

For the first time, we report the synthesis of $\text{Sr}_{0.99}\text{Zr}(\text{PO}_4)_2:0.01\text{Eu}^{3+}$ using a simple solution combustion method. XRD analysis confirms the triclinic phase of the synthesized materials, with particle sizes about 60 nm. SEM micrographs show mesoporous particle formation with lot of voids and agglomeration. Di-electric studies reveal double exponential nature of decay, confirming the presence of voids in the system. In the present studies t_2 is much smaller than t_1 , implying suitability of the material for long-term energy storage applications.

Author Contribution

All authors contributed to the study conception and design. Material preparation, data collection and analysis were performed by N. Thiruvani, R. Mathammal, S. Ponkumar, D. Prakash Babu. R. Jayavel

Declaration of competing interest

The authors declare that they have no known competing financial interest of personal relationships that could have appeared to influence the work reported in this paper.

Data Availability statement

The data that support the findings of this study are available from the corresponding author, upon reasonable request.

Declaration of generative AI and AI-assisted technologies in the writing process

During the preparation of this work the author(s) used Bard.ai in order to remove typo errors. After using this tool/service, the author(s) reviewed and edited the content as needed and take(s) full responsibility for the content of the publication.

5. REFERENCE

- [1] K. Munirathnam, G. R. Dillip, B. D. P. Raju, S. W. Joo, S. J. Dhoble, B. M. Nagabhushana, R. Hari Krishna, K. P. Ramesh, S. Varadharaj Perumal, D. Prakashbabu (2015) Synthesis, photoluminescence and Judd–Ofelt parameters of $\text{LiNa}_3\text{P}_2\text{O}_7: \text{Eu}^{3+}$ orthorhombic microstructures. *Applied Physics A*, 120, 1615–1623. <https://doi.org/10.1007/s00339-015-9371-1>
- [2] J. Fojt, L. Joska, L. Cvrček, V. Březina (2013) ZrO coatings for bioapplication. *KOM–Corrosion and Material Protection Journal*, 57(4), 93–98. <https://doi.org/10.2478/kom-2013-001>
- [3] B. Glorieux, V. Jubera, A. I. Orlova, A. E. Kanunov, A. Garcia, C. Pallier, T. A. Oleneva (2013) Phosphors based on $\text{NaZr}_2(\text{PO}_4)_3$ -type calcium and strontium phosphates activated with Eu^{2+} and Sm^{3+} . *Inorganic Materials*, 49, 82–88. <https://doi.org/10.1134/S0020168513010032>
- [4] M. Muralimanokar, V. R. Vaira, R. Padmanaban, P. G. Suganya (2020) Characterization of AZ31-NbC surface composite fabricated by friction stir processing. *KOM–Corrosion and Material Protection Journal*, 64(1), 29–37. <https://doi.org/10.2478/kom-2020-0005>
- [5] Y. H. Mohan Prakash, D. Prakash Babu, M. Madesh Kumar, S. Ponkumar, K. M. Rahulan (2021) Orange photoluminescence emission of samarium ion doped in calcium zirconium orthophosphate. *Spectroscopy Letters*, 54(4), 292–298. <https://doi.org/10.1080/00387010.2021.1930923>
- [6] D. Prakashbabu, R. H. Krishna, B. M. Nagabhushana, H. Nagabhushana, C. Shivakumara, R. P. S. Chakradar, H. B. Ramalingam, S. C. Sharma, R. Chandramohan (2014) Low temperature synthesis of pure cubic ZrO₂ nanopowder: Structural and luminescence studies. *Spectrochimica Acta Part A: Molecular and Biomolecular Spectroscopy*, 122, 216–222. <https://doi.org/10.1016/j.saa.2013.11.043>
- [7] F. Tudorache, K. Popa, L. Mitoseriu, N. Lupu, D. Bregiroux, G. Wallez (2011) Dielectric investigation of $\text{MIIMIV}(\text{PO}_4)_2$ double orthophosphates (MI= Ca, Sr, Ba, Pb; MIV= Ti, Zr, Hf, Ge, Sn). *Journal of Alloys and Compounds*, 509(37), 9127–9132. <https://doi.org/10.1016/j.jallcom.2011.06.072>
- [8] D. Prakash Babu, S. Ponkumar (2023) Uv Irradiation Induced Capacitance Enhancement in $\text{Pani}/\text{SrZr}(\text{Po}_4)_2$ Composite. Available at SSRN: <https://ssrn.com/abstract=4575454> or <http://dx.doi.org/10.2139/ssrn.4575454>
- [9] K. Fukuda, T. Iwata, A. Moriyama, S. Hashimoto (2006) Crystal structures and phase transitions of $\text{SrZr}(\text{PO}_4)_2\text{–BaZr}(\text{PO}_4)_2$ solid solutions. *Journal of Solid State Chemistry*, 179(12), 3870–3876. <https://doi.org/10.1016/j.jssc.2006.08.024>
- [10] Y. H. Mohan Prakash, D. Prakash Babu, M. Madesh Kumar, S. Ponkumar, K. M. Rahulan (2021) Orange photoluminescence emission of samarium ion doped in calcium zirconium orthophosphate. *Spectroscopy Letters*, 54(4), 292–298. <https://doi.org/10.1080/00387010.2021.1930923>
- [11] V. D. Sharma, P. Khajuria, S. Kumar, R. Prakash, R. J. Choudhary (2023) A novel yellow whitish Dy^{3+} activated $\text{NaZr}_2(\text{PO}_4)_3$ phosphor: Structural, spectral and optical investigations. *Optik*, 291, 171354. <https://doi.org/10.1016/j.ijleo.2023.171354>
- [12] Y. Liu, M. S. Molokeev, Q. Liu, Z. Xia (2018) Crystal structures, phase transitions and thermal expansion properties of $\text{NaZr}_2(\text{PO}_4)_3\text{–SrZr}_4(\text{PO}_4)_6$ solid solutions. *Inorganic Chemistry Frontiers*, 5(3), 619–625. <https://doi.org/10.1039/C7QI00782E>
- [13] D. Kajánek, B. Hadzima, F. Pastorek, M. N. Jacková (2018) Evolution of the dicalcium phosphate-dihydrate (DCPD) coating created by large amplitude sinusoidal voltammetry (LASV) on corrosion resistance of the ZW3 magnesium alloy in chloride containing environment. *KOM–Corrosion and Material Protection Journal*, 62(1), 14–18. <https://doi.org/10.2478/kom-2018-0003>
- [14] K. Fukuda, A. Moriyama, S. Hashimoto (2004) Crystal structure and phase transitions of strontium zirconium diorthophosphate, $\text{SrZr}(\text{PO}_4)_2$. *Journal of Solid State Chemistry*, 177(10), 3514–3521. <https://doi.org/10.1016/j.jssc.2004.06.002>

- [15] J.M.Arroyo, M.G.S. Rao, M.S. de U.Ventura, M.-L.T.B.Daunis, O.Rodríguez, J.W.P.Hsu, R.R.Bon (2023) All solution-processed hafnium rich hybrid dielectrics for hysteresis free metal-oxide thin-film transistors. *Journal of Materials Chemistry C*, 11(5), 1824–1841. <https://doi.org/10.1039/D2TC03761K>
- [16] W. Zhou, G. Cao, M. Yuan, S. Zhong, Y. Wang, X. Liu, D. Cao et al. (2023) Core–shell engineering of conductive fillers toward enhanced dielectric properties: a universal polarization mechanism in polymer conductor composites. *Advanced Materials*, 35(2), 2207829. <https://doi.org/10.1002/adma.202207829>
- [17] S. Sahoo, M. Bhuyan, D. Sahoo (2023) Tuning of dielectric and magnetic performance of graphene oxide via defect regulation by metal oxide nanoparticle for high temperature device. *Journal of Alloys and Compounds*, 935, 168097. <https://doi.org/10.1016/j.jallcom.2022.168097>
- [18] L.M.Al-Harbi, Q.A.Alsulami, M.O.Farea, A.Rajeh (2023) Tuning optical, dielectric, and electrical properties of Polyethylene oxide/Carboxymethyl cellulose doped with mixed metal oxide nanoparticles for flexible electronic devices. *Journal of Molecular Structure*, 1272, 134244. <https://doi.org/10.1016/j.molstruc.2022.134244>
- [19] S.J.Rzoska, A.Drozd-Rzoska, W.Bulejak, J.Los, S.Starzonek, M.Szafran, F.Gao (2023) A Critical Insight into Pretransitional Behavior and Dielectric Tunability of Relaxor Ceramics. *arXiv preprint arXiv:2310.13326*. <https://doi.org/10.3390/ma16247634>
- [20] O.I.Sallam, M.M.Atta, E.O.Taha, A.M. Elbasiony, A.M.A.Henaish, R.M.Ahmed (2023) Synthesis and modification of photoluminescence and dielectric properties of novel fluorophosphate glass by incorporating different transition metal oxides for optoelectronic applications. *Optical Materials*, 136, 113413. <https://doi.org/10.1016/j.optmat.2022.113413>
- [21] K.G.Mondal, B.S.Kar, S.Rakshit, S. Saha, P.C.Jana, M.N.Goswami (2023) Optical, structural and dielectric properties of solvothermally grown molybdenum sulfide nanosheets. *Journal of Alloys and Compounds*, 969, 172356. <https://doi.org/10.1016/j.jallcom.2023.172356>
- [22] W. Xu, Y. Li, Q. Cui, H. Zhang, C. Xia, H. Guo, G. Zhou (2023) All-optical generation, detection, and manipulation of picosecond acoustic pulses in 2D semiconductor/dielectric heterostructures. *Photonics Research*, 11(12), 2000–2010. <https://doi.org/10.1364/PRJ.491805>

IZVOD

NOVO $\text{Sr}_{0.99}\text{Zr}(\text{PO}_4)_2:0.01\text{Eu}^{3+}$ KERAMIČKO STAKLO ODRŽIVO ZA DUGOROČNE APLIKACIJE ZA SKLADIŠTENJE ENERGIJE

U ovom radu je prikazana prva sinteza $\text{Sr}_{0.99}\text{Zr}(\text{PO}_4)_2:0.01\text{Eu}^{3+}$ keramičkog stakla sintetizovana sagorevanjem rastvora korišćenjem glicina kao goriva (odnos goriva i oksidatora 1:1). Difrakcija rendgenskih zraka je potvrdila željenu kristalnu fazu, dok je Šererova analiza pokazala prosečnu veličinu čestica od približno 60 nm. Ovo je dodatno podržano skenirajućim elektronskim mikroskopom, koji je otkrio veličinu čestica oko 75 nm. Primetno je da je materijal pokazao karakterističnu mezoporoznu strukturu, prepoznatljivu karakteristiku tehnike sagorevanja rastvora. Dielektrične studije su otkrile dvostruki eksponencijalni profil raspadanja, što označava prisustvo praznina unutar materijala. Važno je da značajno manja vremenska konstanta (t_2) u poređenju sa t_1 naglašava pogodnost materijala za dugoročne aplikacije za skladištenje energije.

Ključne reči: SZO nanokeramika, sinteza sagorevanja rastvora, skladište energije, dielektrična svojstva.

Naučni rad

Rad primljen: 15.12.2023.

Rad prihvaćen: 26.12.2023.

Rad je dostupan na sajtu: www.idk.org.rs/casopis

Rajnish Grewal¹, Sunita Dahiya², Sunil Kumar^{3*},
Naveen Kumar⁴

^{1,2}Department of Physics, Baba Mastnath University Rohtak, Haryana, India, ³Department of Physics, RR BAWA DAV College, Batala (143505), Punjab, India, ⁴Department of Physics, Panjab University Chandigarh, Chandigarh, India

Scientific paper

ISSN 0351-9465, E-ISSN 2466-2585

<https://doi.org/10.62638/ZasMat1136>



Zastita Materijala 65 (2)
285 - 293 (2024)

Structural, microstructural, magnetic and dielectric properties of Fe₂O₃ modified CuO composite

ABSTRACT

1-xCuO-xFe₂O₃ composites where x = 0.05, 0.10, 0.15 and 0.20 have been synthesized using ball milling mixing method. The structural, microstructural, elemental analysis, magnetic and dielectric properties of prepared ceramic composites have been investigated using the advanced characterization techniques. The influence of sintering temperature on structural, dielectric and magnetic properties have been investigated. The structural phase analysis has been carried out using X-ray diffraction and effect of sintering temperature clearly depicted in graphs. As increase in sintering temperature from 700 °C to 900 °C, diffraction peaks shift towards higher angles, indicating changes in crystal lattice parameters and potential crystal structure distortions. However, after careful consideration of the XRD results and a comprehensive analysis, we concluded that a synthesis temperature of 700 °C is preferable. The SEM micrographs shows an increase in grain size of ceramic composites as concentration of Fe₂O₃ increases. The Energy Dispersive X-Ray spectroscopy affirms presence of elements according to stoichiometric proportion whereas S-shaped M vs. H. loop confirms presence of magnetic ordering. Variation of Real (ε') and Imaginary (ε'') parts of dielectric permittivity with frequency shows general dielectric behavior.

Keywords: Composites, Ball milling mixing method, Dielectric properties, Magnetic properties

1. INTRODUCTION

Semiconducting nano crystalline materials draw attention for their vast usage in micro-electronics industry due to their small band gap. Transition metal oxide (CuO) based semiconductor having small band gap (1.2-1.5 eV) become important candidates for their usage in digital as well as in electronic industry. CuO is unique and important for wide range applications such as including photochemical cells, gas sensors, biosensors, solar cells, and photocatalytic properties. Current research on pure and modified CuO provides significant potential in realm of microelectronics because of its extraordinarily high dielectric constant. It has been reported in literature that synthesis methods impact on particle size as well as on dielectric behavior of CuO.

These are so many synthesis methods to synthesize CuO reported in literature such as sol-gel and sono-chemical method, thermal decomposition method and precipitation method [1-8].

According to Zhu et. al.'s investigation into structural characterization of CuO nano-particles created by microwave irradiating copper (II) acetate and sodium hydroxide as starting material. The particles have a regular shape and limited size distribution as well as high degree of purity. Kim et al. investigated structural, optical, and electrical characteristics of CuO nano-particles with a monoclinic structure phase [9]. From x-ray photoelectron spectroscopy profile, O 1s and Cu 2p peaks corresponding to the CuO nano-particle were seen. The band gap of CuO nano-particle at room temperature was discovered to be 3.63 eV [9].

In this paper, we report structural, elemental, magnetic as well as dielectric properties of Fe₂O₃ modified CuO composites (1-xCuO-xFe₂O₃ where x=0.05, 0.10, 0.15 & 0.20) synthesized using Ball mixing method. The major aspect of choosing Fe₂O₃ is modification in magnetic and dielectric properties of CuO ceramics.

*Corresponding author: Sunil Kumar

E-mail: sunil_nano@yahoo.com

Paper received: 28. 09. 2023.

Paper accepted: 30. 12. 2023.

Paper is available on the website: www.idk.org.rs/journal

2. EXPERIMENTAL

1-xCuO-xFe₂O₃ composites where $x = 0.05, 0.10, 0.15$ & 0.20 have been successfully synthesized using ball mixing method. For synthesis of composites, CuO & Fe₂O₃ mixed in required stoichiometric proportion. The CuO and Fe₂O₃ purchased from Sigma Aldrich. The weighed powders of oxides (CuO & Fe₂O₃) transferred in a plastic bottle contains zirconia ball and ball milled in high-energy ball milling machine for 12 hours. After 12 hours, mixture of powder and acetone has been taken out from bottle and heated at 100 °C for ~ 1 hour so that acetone get evaporated and powder dried. Dried powder mixed with polyvinyl alcohol (2%wt) as binder and pressed into circular disc (Diameter ~ 12 mm, Thickness ~ 1 mm and Pressure ~ 1.5 ton).

The pallets have been sintered at 700° & 900°C for 2 hours for optimization of sintering temperature at which sample exhibits enhanced magnetic and dielectric properties. The presence of both phases (Structural Phase of CuO & Fe₂O₃) confirmed from X-Ray diffractograms whereas morphological analysis (Grain Growth as well as Grain Size) studied from SEM micrographs. The

presence of elements as per stoichiometric proportion mentioned above confirmed using Energy Dispersive X-ray Dispersive spectroscopy whereas elemental mapping shows uniform distribution of different-different metal ions. The density of sintered pellet was measured using lab made set up based on Archimedes principle. The magnetic ordering has been confirmed using Vibrating Sample Magnetometer. The ϵ' , ϵ'' & σ_{ac} vs. Frequency measurements were carried out using impedance analyser.

3. RESULTS AND DISCUSSION

Room temperature structural phase formation has been studied using x-ray diffractograms of CuO, Fe₂O₃ & 1-xCuO-xFe₂O₃ composites where $x = 0.05, 0.10, 0.15$ & 0.20 sintered at 700°C and 900°C shown in figure 1. Sharp high intensity diffraction peaks reveal crystalline nature of prepared ceramic composites whereas noise in background data of Fe₂O₃ results due to fluorescence effect. The diffraction data (diffraction peaks) have been matched with reported JCPDS cards which gives crystallographic information of structural phase of CuO and Fe₂O₃.

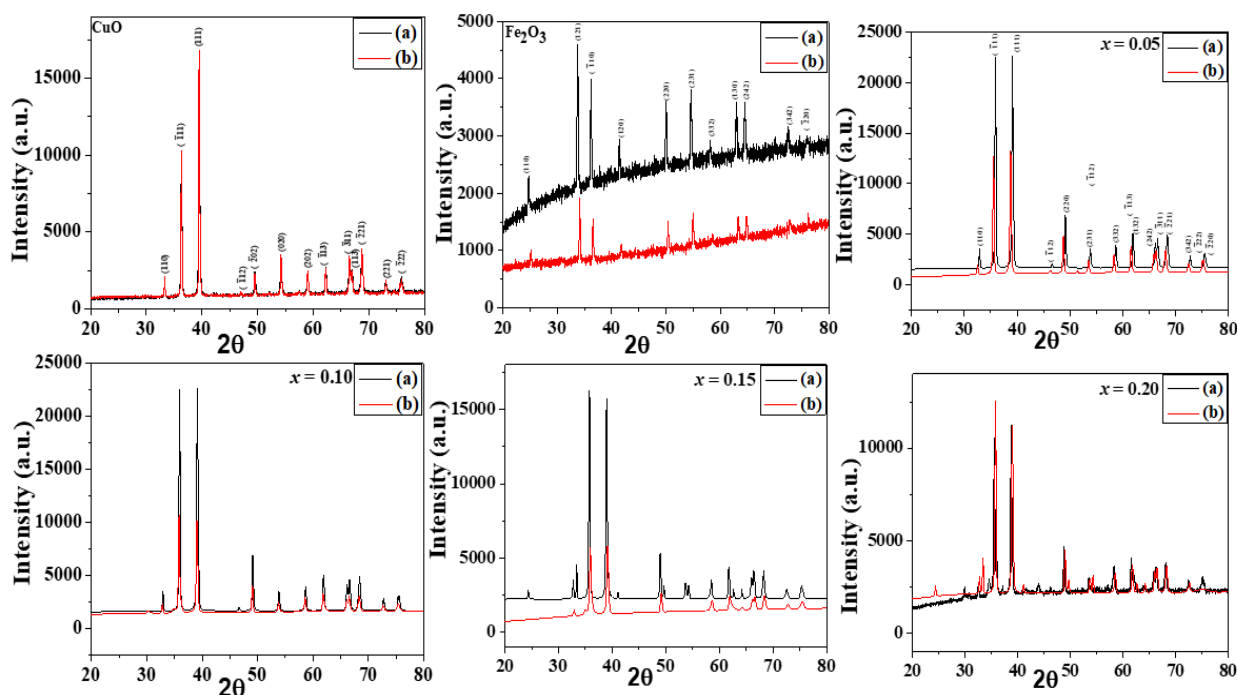


Figure 1. X-Ray Diffraction data of 1-xCuO-xFe₂O₃ where (a) = Sintered at 700°C & (b) 900°C for CuO, Fe₂O₃ and $x = x = 0.05, 0.10, 0.15$ & 0.20 ceramic composites

Slika 1. Podaci difrakcije rendgenskih zraka 1-xCuO-xFe₂O₃ gde je (a) = sinterovano na 700°C & (b) 900°C za CuO, Fe₂O₃ i $x = x = 0,05, 0,10, 0,15$ i $0,20$ keramičkih kompozita

The experimental data has been indexed according to JCPDS card no 80-1917 (ICDS # 069750) represent for Monoclinic phase space group Cc No. 9 for pure CuO and no. 73-2234 (ICDS # 024791) reports Hexagonal phase space group $R\bar{3}c$ for Fe_2O_3 . No diffraction peak left unassigned shows that CuO and Fe_2O_3 exhibits its own phase reported in literature. In graphs, for $x = 0.05$ & 0.10 , diffraction peaks quiet well overlapped at both temperatures shows that sample exhibits similar phases but as 'x' increases up to $x = 0.15$ to 0.20 , diffraction peaks shift towards higher 2θ shows change in structural phase with sintering temperature and maximum in $x = 0.20$. This change in structural phase may result due to strain produced with increasing sintering temperature or increasing concentration of Fe_2O_3 in ceramic composites. Therefore it has been concluded that

sample sintered at $700^\circ C$ demonstrtaed structural phase of CuO (Monoclinic Phase).

The microstructural analysis of CuO, Fe_2O_3 & $1-xCuO-xFe_2O_3$ composites where $x = 0.05, 0.10, 0.15$ & 0.20 sintered at $700^\circ C$ has been studied from FESEM micrographs and shown in figure 2. Micrographs clearly expresses presence grains with irregular in shape, size and randomly orientated with proper grain growth. All the micrographs were recorded using in-lens detector at 20k magnification & 10 kV accelerating voltage. The increase in grain size with increasing 'x' shows increase in grain growth with least porosity. The grain size has been calculated using Smart SEM software equipped with FESEM. The grain size increases from $\sim 1.46 \mu m$ to $\sim 2.26 \mu m$ as 'x' increases from 0.05 to 0.20. The density has also been increased from from 6.98 to $7.38 g/cm^3$, respectively as 'x' increases.

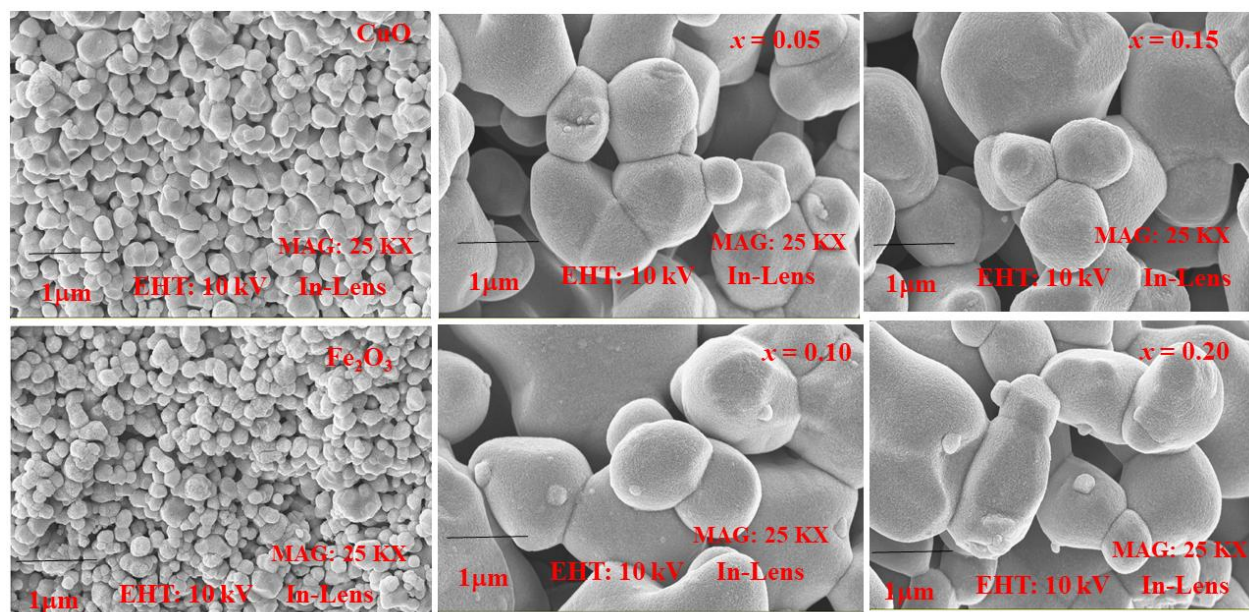


Figure 2. FESEM Micrographs of CuO, Fe_2O_3 and $1-xCuO-xFe_2O_3$ where $x = x = 0.05, 0.10, 0.15$ & 0.20 ceramic composites

Slika 2. FESEM Mikrogrami CuO, Fe_2O_3 i $1-xCuO-xFe_2O_3$ gde je $x = x = 0.05, 0.10, 0.15$ i 0.20 keramičkih kompozita

The presence of elements as per stoichiometric formula have been confirmed from Energy Dispersive X-ray spectroscopy (EDS) analysis. The EDS spectra of pure CuO, Fe_2O_3 and $0.8CuO-0.2Fe_2O_3$ ceramic composite sintered at $700^\circ C$ have been shown in Figure 3. The Binding Energy

vs. Intensity electro micrographs shows that peak corresponding to 8.04 eV, 0.542 & 6.39 eV of K α evident for presence Cu & O in CuO and Fe and O in Fe_2O_3 . The presence of Cu, O & Fe in wt% as well as in mol% has been shown in Table shown in figure 4.

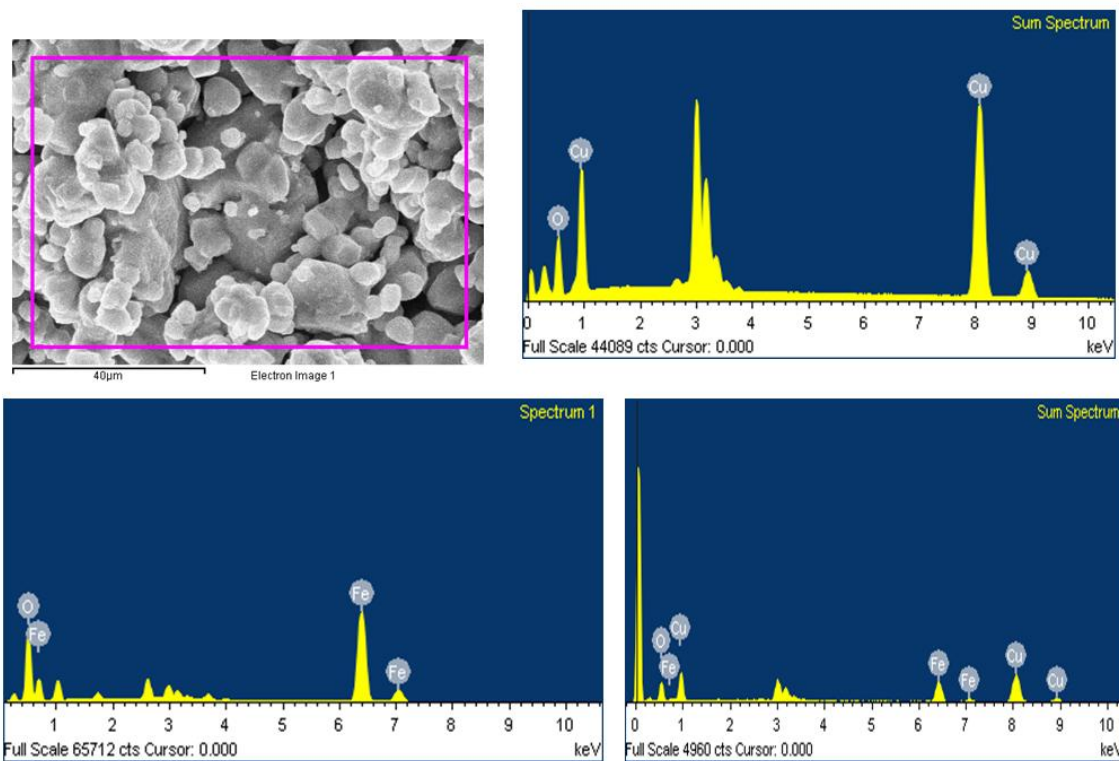


Figure 3. Energy Dispersive Spectral Micro Graphs of CuO, Fe₂O₃ and 0.8CuO-0.2Fe₂O₃ ceramic composites sintered at 700°C

Slika 3. Energetski disperzivni spektralni mikrografovi CuO, Fe₂O₃ i 0.8CuO-0.2Fe₂O₃ keramičkih kompozita sinterovanih na 700°C

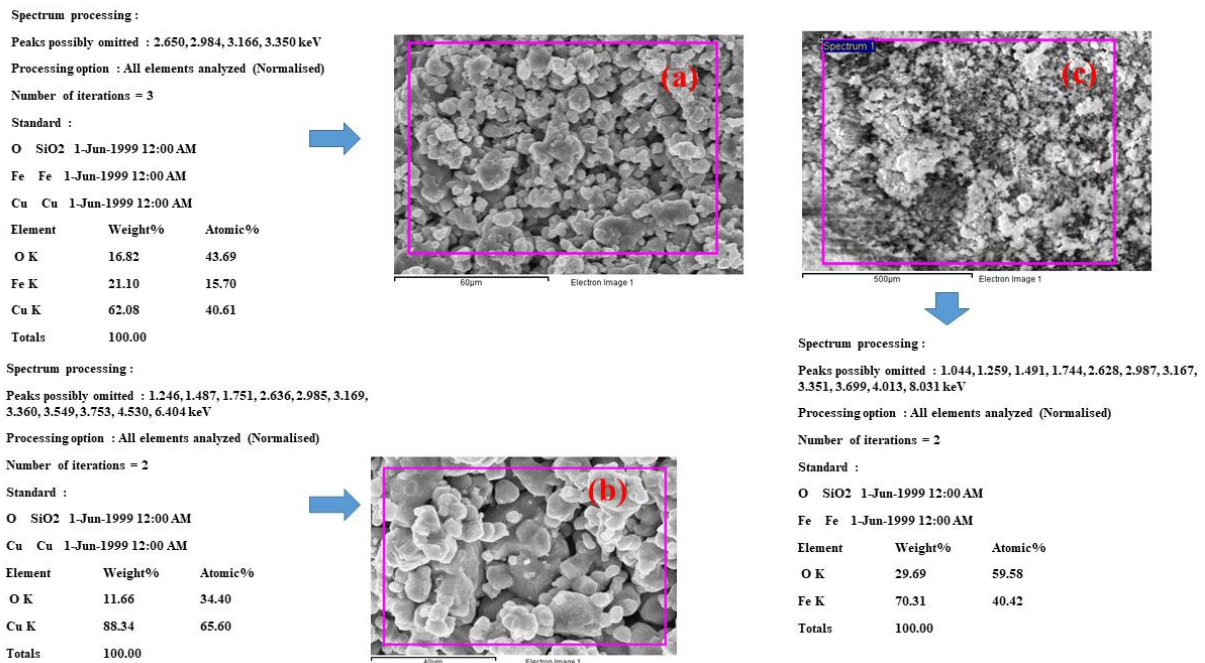


Figure 4. Weight (%) and Mol (%) of CuO, Fe₂O₃ and 0.8CuO-0.2Fe₂O₃ ceramic composites sintered at 700°C

Slika 4. Težina (%) i mol (%) CuO, Fe₂O₃ i 0.8CuO-0.2Fe₂O₃ keramičkih kompozita sinterovanih na 700°C

The distribution of different metal ions as per stoichiometric formula, Elemental mapping in selected area has been carried out. The elemental mapped electron micrographs of CuO , Fe_2O_3 & $0.8\text{CuO}-0.2\text{Fe}_2\text{O}_3$ ceramic composites sintered at 700°C shown in figure 5. The different colours have been assigned to different metal ions. The

micro-graphs with all coloured dot show that all metal ions distributed uniformly. The red colour assigned to Cooper (Cu) whereas Oxygen (O) and Iron (Fe) green and yellow colour. The micrograph in which all colour represents uniformly presence of all metal ions in selected area.

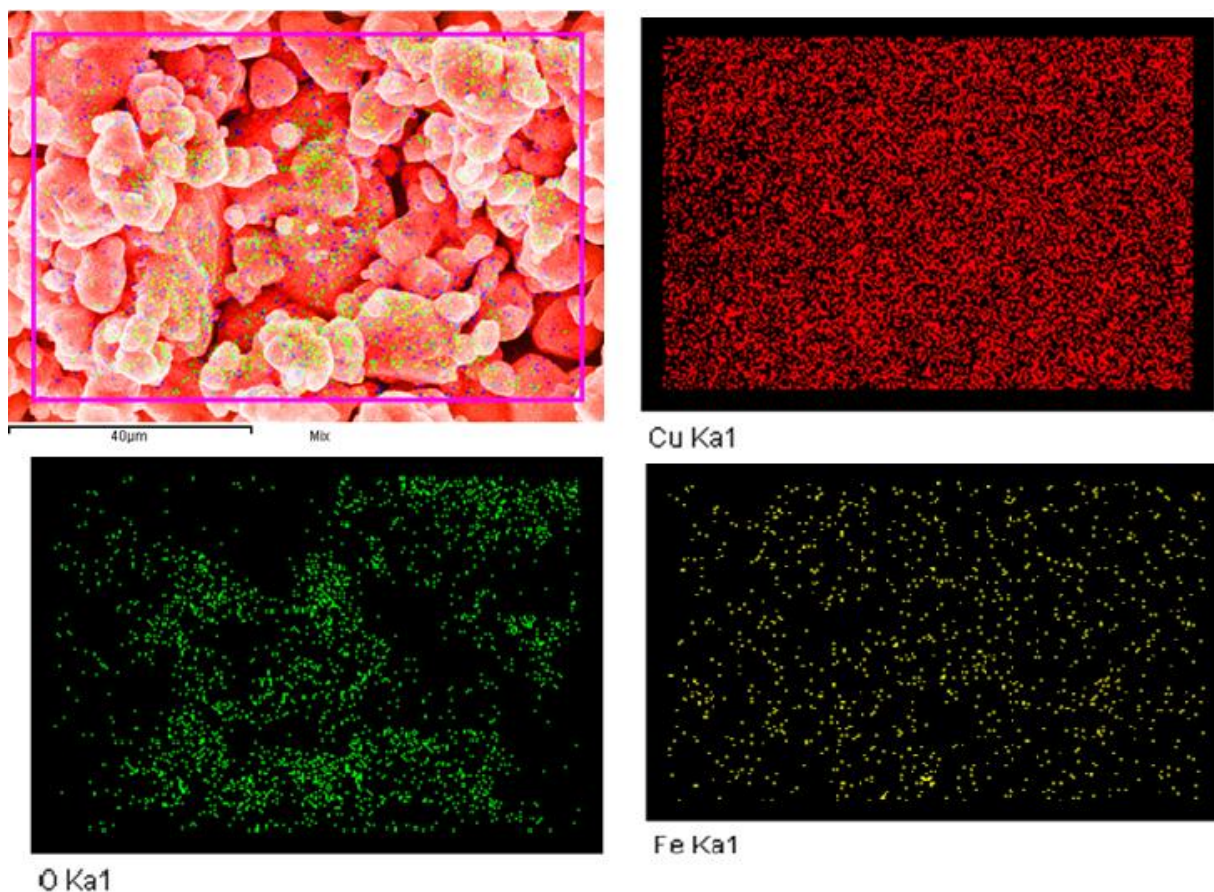


Figure 5. Elemental Mapping along with mixed micrograph of $0.8\text{CuO}-0.2\text{Fe}_2\text{O}_3$ ceramic composites sintered at 700°C

Slika 5. Elementarno mapiranje zajedno sa mešovitim mikrografijom $0.8\text{CuO}-0.2\text{Fe}_2\text{O}_3$ keramičkih kompozita sinterovanih na 700°C

Magnetization vs. Magnetic Field measurements of CuO , Fe_2O_3 & $1-x\text{CuO}-x\text{Fe}_2\text{O}_3$ composites where $x = 0.05, 0.10, 0.15$ & 0.20 , sintered at 700°C have been shown in figure 6. The magnetic data clearly reveal that (a) Small remnant magnetization value and narrow coercivity of CuO results for superparamagnetic or week magnetic ordering as already reported (b) magnetic hysteresis of Fe_2O_3 sintered at 700°C magnetically ordered behavior. The hysteresis in $1-x\text{CuO}-x\text{Fe}_2\text{O}_3$ samples sintered at 700°C reveals dominance of ferromagnetic ordering over antiferromagnetic (Presence of Both Ferromagnetic as well as antiferromagnetic confirmed from unsaturated hysteresis curve). Such kind of

behavior (Presence of both Ferromagnetic and Antiferromagnetic ordering) may be due to oxygen vacancies created which results in pinched hysteresis loop. The remnant magnetization (M_r) of prepared ceramic composites increases from 0.068 emu/g for $x = 0.05$ to 0.118 emu/g for $x = 0.15$ and then decreases to 0.099 emu/g for $x = 0.20$ whereas coercivity also varies from 393.8 Oe for $x = 0.05$ to 438.6 Oe for $x = 0.15$ and then decreases to 296.2 Oe for $x = 0.20$. Since CuO exhibits weakly magnetic or superparamagnetic behavior. This increase in remnant magnetization may result due to increase in creation of oxygen, which create multi valance state of Fe (Fe^{2+} & Fe^{3+}) during sintering in oxygen deficient environment. These

oxygen vacancies responsible for strong negative super exchange interaction between Fe^{3+} and Fe^{3+} through oxygen (O^{2-}) anion responsible for antiferromagnetic ordering whereas direct exchange interaction between $\text{Fe}^{3+}/\text{Fe}^{3+}$ and $\text{Fe}^{3+}/\text{Fe}^{2+}$ through vacancies (V_o) results in ferromagnetic ordering. The increase in value of M_r may be due to increased effect of $\text{Fe}^{3+}/\text{Fe}^{3+}$ and $\text{Fe}^{3+}/\text{Fe}^{2+}$ through vacancies (V_o) which results in ferromagnetic ordering [10]. The value of remnant

magnetization (emu/g) and coercivity (Oe) tabulated in Table 1. It is clear that direct exchange interaction between $\text{Fe}^{3+}/\text{Fe}^{3+}$ and $\text{Fe}^{3+}/\text{Fe}^{2+}$ through vacancies (V_o) dominates over strong negative super exchange interaction between Fe^{3+} and Fe^{3+} through oxygen (O^{2-}) anion up to $x = 0.15$ and then reverses responsible for increase in remnant magnetization up to $x = 0.15$ and then decreases.

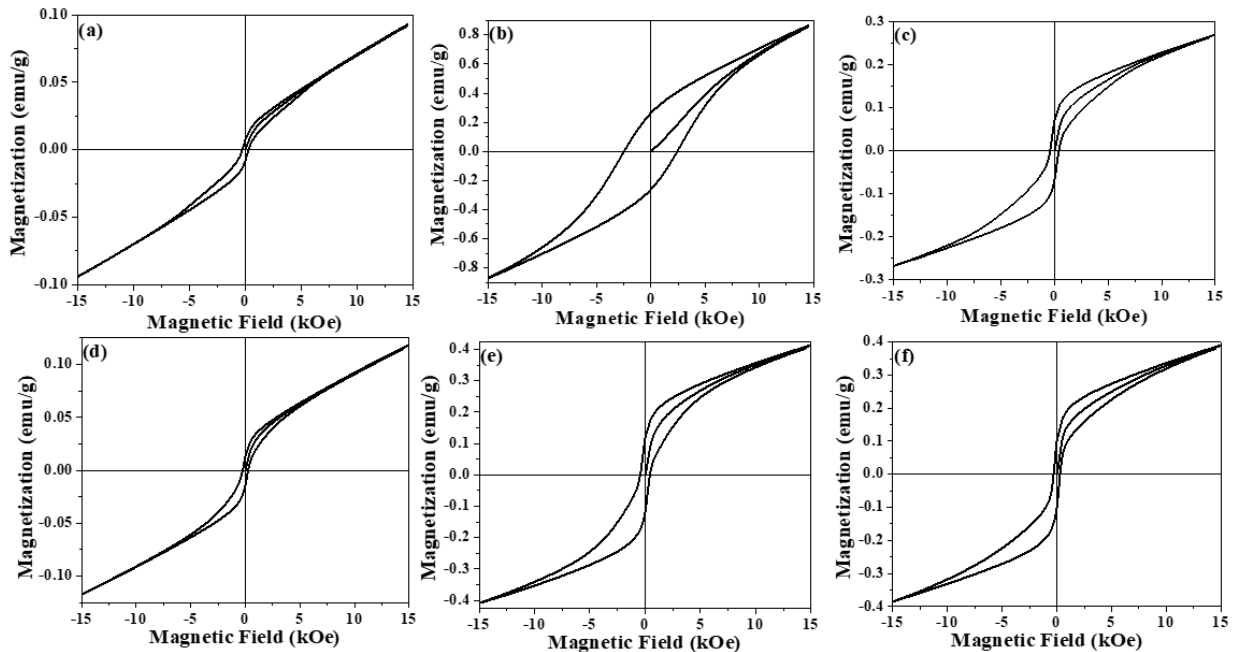


Figure 6. Magnetization vs. Applied Magnetic Field of CuO , Fe_2O_3 & $1-x\text{CuO}-x\text{Fe}_2\text{O}_3$ where (a) = CuO , (b) = Fe_2O_3 (c) = 0.05, (d) = 0.10, (e) = 0.15 & (f) = 0.20 ceramic composites sintered at 700°C

Slika 6. Magnetizacija u odnosu na primenjeno magnetno polje CuO , Fe_2O_3 i $1-\text{CuP}-\text{Fe}_2\text{O}_3$ gde je (a) = CuP , (b) = Fe_2O_3 (c) = 0.05, (d) = 0.10, (e) = 0.15 & (f) = 0.20 keramičkih kompozita sinterovanih na 700°C

Table 1. The Value of Remnant Magnetization & Coercive Field of CuO , Fe_2O_3 & $1-x\text{CuO}-x\text{Fe}_2\text{O}_3$ where (a) = CuO , (b) = Fe_2O_3 (c) = 0.05, (d) = 0.10, (e) = 0.15 & (f) = 0.20 ceramic composites sintered at 700°C

Tabela 1. Vrednost preostale magnetizacije i koercitivnog polja CuO , Fe_2O_3 i $1-\text{CuO}-\text{Fe}_2\text{O}_3$ gde je (a) = CuO , (b) = Fe_2O_3 (c) = 0.05, (d) = 0.10, (e) = 0.15 & (f) = 0.20 keramičkih kompozita sinterovanih na 700°C

Sample	M_r (emu/g)	H_c (Oe)
(a)	0.007	276.6
(b)	0.262	2461
(c)	0.068	393.8
(d)	0.013	254.9
(e)	0.118	438.6
(f)	0.099	296.2

Room temperature variation of Real & Imaginary part of dielectric permittivity (ϵ') & (ϵ'') of CuO & $1-x\text{CuO}-x\text{Fe}_2\text{O}_3$ composites where $x = 0.05, 0.10, 0.15$ & 0.20 in frequency range varies from $100\text{Hz} - 1\text{MHz}$ have been shown in figure 7 & 8. It has been clearly revealed from graphs that value of both Real (ϵ') and Imaginary (ϵ'') part of dielectric permittivity decreases as frequency increases up to a certain value and afterward varies linear. In lower frequency range, both Real & Imaginary part of dielectric permittivity (ϵ') & (ϵ'') exhibits maximum value and decreases continuously with increasing frequency and become almost linear after certain value of frequency. Such types of behavior of represent general dielectric behavior of any dielectric, which follow either Debye, or Non-Debye behavior. In lower frequency range, maximum of all polarizations (Dipolar, Ionic, Electronic &

Interfacial) effectively contributes to dielectric permittivity results in maximum value of both Real (ϵ') and Imaginary (ϵ'') part of dielectric permittivity [11,12].

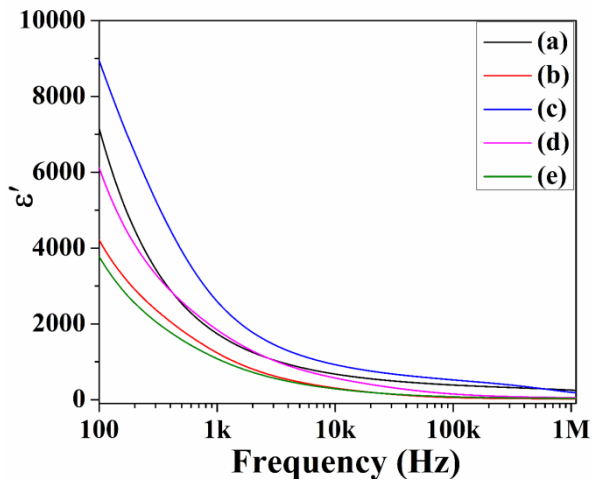


Figure 7. ϵ' vs. Frequency of CuO , Fe_2O_3 & $1-x\text{CuO}-x\text{Fe}_2\text{O}_3$ where (a) = CuO , (b) = Fe_2O_3 (c) = 0.05, (d) = 0.10, (e) = 0.15 & (f) = 0.20 ceramic composites sintered at 700°C

Slika 7. ϵ' u odnosu na učestalost CuO , Fe_2O_3 i $1-x\text{CuO}-x\text{Fe}_2\text{O}_3$ gde je (a) = CuO , (b) = Fe_2O_3 (c) = 0.05, (d) = 0.10, (e) = 0.15 & (f) = 0.20 keramički kompoziti sinterovani na 700°C

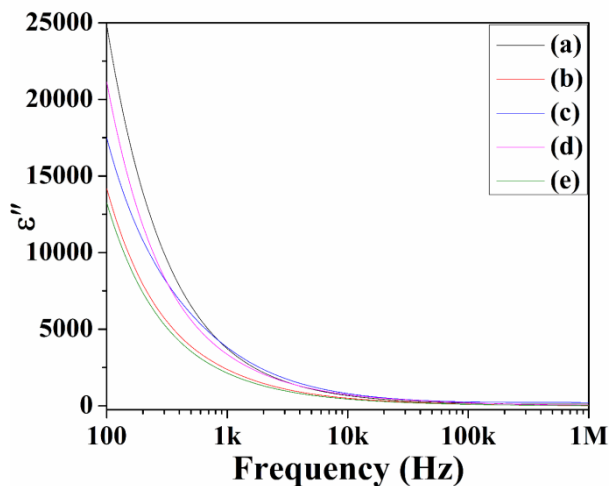


Figure 8. ϵ'' vs. Frequency of CuO , Fe_2O_3 & $1-x\text{CuO}-x\text{Fe}_2\text{O}_3$ where (a) = CuO , (b) = Fe_2O_3 (c) = 0.05, (d) = 0.10, (e) = 0.15 & (f) = 0.20 ceramic composites sintered at 700°C

Slika 8. ϵ'' naspram učestalosti CuO , Fe_2O_3 i $1-x\text{CuO}-x\text{Fe}_2\text{O}_3$ gde je (a) = CuO , (b) = Fe_2O_3 (c) = 0.05, (d) = 0.10, (e) = 0.15 & (f) = 0.20 keramički kompoziti sinterovani na 700°C

As frequency increases towards higher regime, value of both Real (ϵ') and Imaginary (ϵ'') part of dielectric permittivity starts decreases and after

certain value of frequency, value of both Real (ϵ') and Imaginary (ϵ'') part of dielectric permittivity become almost constant. This may be due to elimination of contribution of polarization in dielectric permittivity. It has been clearly seen from graph that value dielectric permittivity first decreases and then increases up to maximum value as 'x' increases and again decreases with further increase of 'x' may be due to interfacial polarization.

The Cole-Cole relaxation model (modified form of Debye relaxation model) has been used to explain the relaxation phenomenon [12]. According to this model, the ϵ' and ϵ'' vary with frequency as:

$$\epsilon'(\omega) = \epsilon_\infty + (\epsilon_s - \epsilon_\infty) \frac{1 + (\omega\tau_0)^{1-\alpha} \sin \frac{1}{2}\alpha\pi}{1 + 2(\omega\tau_0)^{1-\alpha} \sin \frac{1}{2}\alpha\pi + (\omega\tau_0)^{2(1-\alpha)}}$$

$$\epsilon''(\omega) = (\epsilon_s - \epsilon_\infty) \frac{(\omega\tau_0)^{1-\alpha} \cos \frac{1}{2}\alpha\pi}{1 + 2(\omega\tau_0)^{1-\alpha} \sin \frac{1}{2}\alpha\pi + (\omega\tau_0)^{2(1-\alpha)}}$$

Where ϵ_∞ = dielectric constant measured at high frequency, ϵ_s = dielectric constant measured at low frequency, $\omega = 2\pi f$ the angular frequency of applied field and τ = characteristics relaxation time of the medium. The exponent parameter α usually varies between 0 and 1, and it describes shape of spectral curves. It may be noted that for $\alpha = 0$, Cole-Cole model reduces to Debye model.

Room temperature σ_{ac} vs. Frequency at room temperature CuO , Fe_2O_3 & $1-x\text{CuO}-x\text{Fe}_2\text{O}_3$ composites where $x = 0.05, 0.10, 0.15$ & 0.20 , sintered at 700°C have been shown in figure 8. The ac conductivity calculated from recorded dielectric parameters using following formula

$$\sigma_{ac} = 2\pi f \epsilon_0 \epsilon' \tan \delta$$

Where the parameters have their usual meaning. Ac conductivity profile with frequency has been divided into two regions. First linearly varied region with frequency known as dc conductivity whereas dispersion region which corresponds to ac conductivity. Frequency varied ac conductivity in ceramics is generally analyzed by Jonscher's power law;

$$\sigma_{ac} = \sigma_{dc} + A \omega^n,$$

Where "A" is dispersion parameter representing the strength of polarizability and "n" dimensionless frequency exponent representing interaction between mobile ions with lattice around them.

According to Jonscher, origin of frequency dependence of conductivity may be due to relaxation phenomenon arising due to hopping of mobile charge carriers [13-16]. The conductivity also follows similar behavior like dielectric behavior. This may also due to variation in concentration of oxygen vacancies created which also effect magnetic properties means remnant magnetization first decreases and then increases may result due to processing of Fe_2O_3 with CuO in CuO- Fe_2O_3 composites as shown in figure 9.

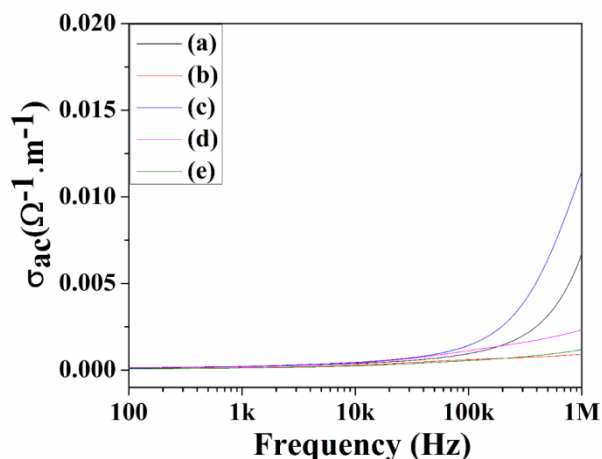


Figure 9. σ_{ac} vs. Frequency variation of CuO, Fe_2O_3 & $1-x\text{CuO}-x\text{Fe}_2\text{O}_3$ where (a) = CuO, (b) = Fe_2O_3 , (c) = 0.05, (d) = 0.10, (e) = 0.15 & (f) = 0.20 ceramic composites sintered at 700°C

Slika 9. σ_{ac} naspram varijacije frekvencije CuO, Fe_2O_3 i $1-x\text{CuO}-x\text{Fe}_2\text{O}_3$ gde je (a) = CuO, (b) = Fe_2O_3 (c) = 0.05, (d) = 0.10, (e) = 0.15 i (f) = 0.20 keramički kompoziti sinterovani na 700°C

4. CONCLUSION

CuO, Fe_2O_3 and $1-x\text{CuO}-x\text{Fe}_2\text{O}_3$ where $x = 0.05, 0.10, 0.15$ & 0.20 ceramic composites sintered at 700°C & 900°C where $x = 0.05, 0.10, 0.15$ & 0.20 have been successfully prepared using ball milling mixing method. X-ray diffraction pattern confirms that optimized sintering temperature for ceramic composites is 700°C at which composites exhibits crystalline phase of both CuO and Fe_2O_3 as reported in JCPDS cards. Microstructural analysis gives densification as well as grain growth whereas energy dispersive x-ray spectroscopy and elemental mapping reveals presence of elements according to mentioned stoichiometric proportion and uniform distribution of metal ions.

Magnetic hysteresis data confirms that variation in magnetization directly follows competition of AFM and FM interaction whereas dielectric data follow similar behavior to magnetic ordering which results from creation of oxygen

vacancies. The oxygen vacancies also play an important role in conduction behavior of dielectrics whereas interfacial polarization also plays effective role in dielectric properties of composites.

5. REFERENCES

- [1] M.Fterich, F.B.Nasr, R.Lefi, M.Toumi, S.Guermazi (2016) Effect of concentration of hexamethylenetetramine in structure, microstructure and optical properties of CuO nanoparticles synthesized by hydrothermal route. *Materials Science in Semiconductor Processing*, 43, 114-122. <https://doi.org/10.1016/j.mssp.2015.11.023>
- [2] S.Heikal, H.M.Mokhtar, W.A.E.Ghany (2023) Effect of CuO addition on the structural, electrical and dielectric properties of the sodium borate glasses. *Physica B: Condensed Matter*, 667, 415142. <https://doi.org/10.1016/j.physb.2023.415142>
- [3] C.Oruç, A.Altındal (2017) Structural and dielectric properties of CuO nanoparticles. *Ceramics international*, 43(14), 10708-10714. <https://doi.org/10.1016/j.ceramint.2017.05.006>
- [4] M.E.Grigore, E.R.Biscu, A.M.Holban, M.C.Gestal, A.M.Grumezescu (2016) Methods of synthesis, properties and biomedical applications of CuO nanoparticles. *Pharmaceuticals*, 9(4), 75-83. <https://doi.org/10.3390/ph9040075>
- [5] K.S.Siddiqi, A.Husen (2020) Current status of plant metabolite-based fabrication of copper/copper oxide nanoparticles and their applications: a review. *Biomaterials Research*, 24(1), 1-15. <https://doi.org/10.1186/s40824-020-00188-1>
- [6] W.Hao, P.Xu, L.Sun, E.Cao (2023) Influence of CuO addition on the sintering temperature and giant dielectric properties of $(\text{In}_{0.5}\text{Nb}_{0.5})_{0.05}\text{Ti}_{0.95}\text{O}_2$ ceramics. *Ceramics International*, 49(24), 40650-40658. <http://dx.doi.org/10.1016/j.ceramint.2023.10.046>
- [7] E.Arulkumar, S.S.Shree, S.Thanikaikarasan (2023) Structure, morphology, composition, optical properties of CuO/NiO nanocomposite for electrochemical energy storage devices. *Results in Chemistry*, 6, 101087. <http://dx.doi.org/10.1016/j.rechem.2023.101087>
- [8] O.I.Sallam, M.M. Atta, E.O.Taha, A.M.Elbasiony, A. M.A.Henaish, R.M.Ahmed (2023) Synthesis and modification of photoluminescence and dielectric properties of novel fluorophosphate glass by incorporating different transition metal oxides for optoelectronic application. *Optical Materials*, 136, 113413. https://ui.adsabs.harvard.edu/link_gateway/2023OptMa.13613413S/doi:10.1016/j.optmat.2022.113413
- [9] M.E.Grigore, E.R.Biscu, A.M.Holban, M.C.Gestal, A. M. Grumezescu (2016) Methods of synthesis, properties and biomedical applications of CuO nanoparticles. *Pharmaceuticals*, 9(4), 75-84. <https://doi.org/10.3390/ph9040075>
- [10] K.S.Siddiqi, A.Husen (2020) Current status of plant metabolite-based fabrication of copper/copper oxide

- nanoparticles and their applications: a review. *Biomaterials Research*, 24(1),1-15.
<https://doi.org/10.1186/s40824-020-00188-1>
- [11] S.Kumar, J.Pal, S.Kaur, R.Kaur, M.Singh, A.Singh (2018) The Effect of Aliovalent Pb^{2+} Dopant on the Magnetic and Magnetodielectric Properties of $LaFeO_3$ Solid Solutions. *Journal of Magnetism and Magnetic Materials*, 467, 89-95.
<https://doi.org/10.1016/j.jmmm.2018.07.037>
- [12] M.Kumar, K.L.Yadav (2007) Study of dielectric, magnetic, ferroelectric and magnetoelectric properties in the $PbMn_xTi_{1-x}O_3$ system at room temperature. *Journal of Physics: Condensed Matter*, 19, 242202.
<https://doi.org/10.1088/0953-8984/19/24/242202>
- [13] K.S.Cole, H.Robert (1941) Dispersion and Absorption in Dielectrics:-Alternating Current Characteristics. *Journal of Chemical Physics*, 9, 341–351. <http://dx.doi.org/10.1063/1.1750906>
- [14] S.Havriliak, S.Negami (1967) A complex plane representation of dielectric and mechanical relaxation processes in some polymers. *Polymer*, 3861(67), 90021-3.
[https://doi.org/10.1016/0032-3861\(67\)90021-3](https://doi.org/10.1016/0032-3861(67)90021-3)
- [15] V.Prakasha, S.N.Choudharya, T.P.Sinhab (2008) Dielectric relaxation in complex perovskite oxide $BaCo_{1/2}W_{1/2}O_3$. *Physica B*, 403, 103-108.
<http://dx.doi.org/10.1016/j.physb.2007.08.015>
- [16] A.K.Jonscher (1977) The Universal Dielectric Response. *Nature*, 267, 673-679.
https://ui.adsabs.harvard.edu/link_gateway/1977Natur.267..673J/doi:10.1038/267673a0

IZVOD

STRUKTURNA, MIKROSTRUKTURNA, MAGNETNA I DIELEKTRIČNA SVOJSTVA CuO KOMPOZITA MODIFIKOVANOG Fe_2O_3

1-xCuO-xFe2O3 kompoziti, gde je x = 0,05, 0,10, 0,15 i 0,20, su sintetizovani metodom mešanja sa kugličnim mlevenjem. Pripremljena keramika je okarakterisana po različitim osobinama kao što su strukturna i mikrostrukturalna, elementarni sastav prema navedenoj stehiometrijskoj proporciji i magnetna svojstva. Takođe, istraživana su dielektrična svojstva pripremljenih keramičkih kompozita, sinterovanih na različitim temperaturama, na sobnoj temperaturi. Kako povećavamo temperaturu sinteze sa 700 °C na 900 °C, vrhovi difrakcije se pomeraju ka većim uglovima, što ukazuje na promene u parametrima kristalne rešetke i potencijalne izobličenja kristalne strukture. Ova primećena promena ukazuje na povećanu toplotnu energiju koja utiče na raspored atoma u materijalu. Međutim, nakon pažljivog razmatranja XRD rezultata i sveobuhvatne analize, zaključili smo da je temperatura sinteze od 700°C poželjnija. Na ovoj nižoj temperaturi održava se željena kristalna struktura, minimizirajući rizik od strukturnih promena ili faznih transformacija koje bi mogle uticati na svojstva i performanse materijala. Pored toga, izbor od 700°C obezbeđuje ravnotežu između postizanja željenih karakteristika materijala i izbegavanja potencijalnih nedostataka povezanih sa višim temperaturama sinteze. SEM mikrografije pokazuju povećanje veličine zrna keramičkih kompozita. Energetska disperzivna rendgenska spektroskopija potvrđuje prisustvo elemenata u skladu sa stehiometrijskom proporcijom, dok S-oblika M protiv H. petlje potvrđuje prisustvo magnetnog uređenja. Realni (ϵ') i imaginarni (ϵ'') delovi dielektrične permitivnosti u odnosu na frekvenciju pokazuju dielektrično ponašanje.

Ključne reči: Kompoziti, metoda mešanja sa kugličnim mlevenjem, dielektrična svojstva, magnetna svojstva

Naučni rad

Rad primljen: 28.09.2023.

Rad prihvacen: 30.12.2023.

Rad je dostupan na sajtu: www.idk.org.rs/casopis

Ramaiah Prakash^{1*}, Sundaresan Srividhya²,
Pitchaipillai Neelamegam³, Karuppasamy Mukilan⁴,
Rajagopal Premkumar⁴, Muthu Vinod Kumar⁵

¹Department of Civil Engineering, Government College of Engineering, Tirunelveli, India, ²Department of Civil Engineering, Builders Engineering College, Kangeyam, Tirupur, India, ³Department of Civil Engineering, SRM Valliammai Engineering College, Kattankulathur, India, ⁴Department of Civil Engineering, Kalasalingam Academy of Research and Education, Krishnankoil, India, ⁵Department of Civil Engineering, Vel Tech Rangarajan Dr.Sagunthala R&D Institute of Science, Chennai, India

Scientific paper

ISSN 0351-9465, E-ISSN 2466-2585

<https://doi.org/10.62638/ZasMat1121>



Zastita Materijala 65 (2)

294 - 306 (2024)

Fresh and hardened characteristics of a novel alkali-activated geopolymer concrete with GGBFS

ABSTRACT

The development of a country's infrastructure relies heavily on the use of cement concrete as the major building material. The cement industry significantly contributes to global warming due to its substantial carbon dioxide (CO₂) emissions. Reducing the consumption of cement in concrete while maintaining its essential features can lead to a more cost-effective and environmentally friendly advancement of the construction sector.

By looking at a new concrete mix that includes fly ash (FA) and Ground Granulated Blast Furnace Slag (GGBFS), this study aims to develop cement less concrete. An Alkali-Activated Solution (AAS) was used as the liquid binder along with a dry mix of FA and GGBFS. This study examines the utilization and impact of liquid and solid binders in the production of alkali-activated GGBFS-based Geopolymer Concrete (GPC), as well as the optimal quantities required for their incorporation. Various ratios of AAS to GSB were experimented with to determine the optimum mixture. To find optimum mixture of GGBFS for the GPC, different amounts of GGBFS were utilised as a Partial substitution for fly ash. At 28 days, test specimens, such as cubes, cylinders, and beams, were cast and put to the test. The GPC has also decided to use heat curing to get good results. It is found that the ratio 0.5 between AAS and GSB and a makeup of 75% GGBFS made the strongest material. The results of the study show that using AAS and GGBFS in geopolymer concrete makes a better product, which could be used in places where there is not enough water.

Keywords: Geopolymer; Geopolymer Solid Binder; Alkali-Activated Solution; Fly Ash; GGBFS

1. INTRODUCTION

Portland cement has been the most often utilized substance to bind the components of traditional concrete. The strength and durability characteristics of Portland cement concrete have improved significantly as well. On the one hand, cement manufacture uses the natural resources and huge energy, and also, it releases solid waste and carbon dioxide (CO₂) gas that pollutes the environment. The cement sector is responsible for approximately 5-7 percent of global CO₂ emissions. [1, 2]. Fly ash and slag from the first stages of the

iron industry have accumulated in enormous amount. Industrial waste disposal is a difficult task. Although it may not be feasible to dispose of industrial and construction trash, the necessity of using these by-product wastes has grown due to rising raw material prices and demand, as well as irreparable environmental harm [3]. However, with the help of contemporary green engineering techniques, more energy-efficient and environmentally friendly binding materials are now feasible. Anthracite or bituminous coal is used to create "Class F" fly ash which is a natural pozzolonic materials and have low calcium content [4]. Class F fly ash undergoes a chemical reaction with a solution called alkali-activated solution (AAS), which consists of a combination of sodium hydroxide and sodium silicate solution, at elevated temperatures. An inorganic alumino-silicate

*Corresponding author: Ramaiah Prakash

E-mail: rprakash024@gmail.com

Paper received: 19. 12. 2023.

Paper accepted: 08. 01. 2024.

Paper is available on the website: www.idk.org.rs/journal

polymer known as geopolymer is the reaction's end product [5,6]. The GGBFS-alkali activated geopolymer concrete utilizes fly ash and slag as the geopolymer solid binder (GSB), while AAS functions as the geopolymer liquid binder (GLB). Comparing Class F fly ash to other classes, greater alumina and silica compounds are present [7]. Calcium oxide, silica, and alumina are found in slag. The poor reaction between the solid binder and the liquid binder results in a delay in the geopolymerisation process when conducted under ambient conditions. [8]. The reaction between the solid binder and the liquid binder happens more quickly as the curing temperature rises.

During the heat curing process, the solid binders react with an alkali-activated solution, leading to the creation of sodium aluminosilicate and calcium aluminosilicate gels. The sodium aluminosilicate gel changes into calcium aluminosilicate gel at greater GGBFS/slag concentration levels. Due to its greater density, the matrix of the changed product benefits from increased strength and durability [9,10]. In order to improve the geopolymer's acid and temperature resistance as well as early strength, fly ash may be employed [7,11]. The strength qualities of geopolymer concrete are collectively influenced by various factors, including the concentration of the sodium hydroxide solution, the ratio of silicate to sodium hydroxide solution, the ratio of AAS to GSB, the quantity of fly ash, and the curing procedure. The mechanical properties of the geopolymer concrete is improved by the sodium hydroxide concentration. Numerous researchers [10,12–16] have discovered the ideal sodium silicate to hydroxide ratio to be between 1.5 and 2.5 while maintaining a higher sodium hydroxide molarity (10–16 M) to achieve higher strength. Geopolymer concrete composed of fly ash exhibits a gradual increase in strength when exposed to normal room temperatures. However, using oven curing at temperatures between 40 and 90 °C has resulted in a respectable increase in strength [17]. The fly ash-based geopolymer concrete strengthened the most when it was dried for 24 hours at a temperature between 60 and 75 °C [18,19]. Additionally, the strength and durability qualities of geopolymer concrete have been enhanced by the addition of GGBS and slag [1,7-10,20]. Furthermore, it has been documented that the production of geopolymer concrete utilizing a composition of 75% fly ash, 25% slag, and a NaOH concentration of 14 M yielded a compressive strength measurement of 35 MPa, which remained consistent even after a 28-day period of ambient curing [7]. With an increase in slag content and NaOH solution concentration, geopolymer concrete's compressive strength improved [10,20].

Bellum (2019) conducted a study that found geopolymer concrete, consisting of 30% fly ash and 70% ground granulated blast furnace slag (GGBS), displayed a compressive strength of 34.15 MPa. The concrete specimens underwent a curing process that consisted of 24 hours of oven curing at a temperature of 70°C, followed by an additional 28 days of ambient curing. The ratio of alkali-activated slag (AAS) to GGBS in the mixture was 0.35 [21]. Ma et al. (2019) found that including 30% slag in geopolymer concrete led to the maximum level of compressive strength. Nevertheless, it is important to acknowledge that the concentration of NaOH had a minimal effect on the strength after a 28-day duration [22]. Studies indicate that the utilization of fly ash and alkali-activated solution (AAS) in geopolymer concrete yields the most significant compressive strength. This outcome is achieved by maintaining a sodium hydroxide (NaOH) concentration within the range of 15.5 to 16M, and a silicate to sodium hydroxide solution ratio ranging from 1.5 to 2.5. Only a limited amount of study has examined the mechanical properties of geopolymer concrete (GPC) made with fly ash and ground granulated blast furnace slag (GGBFS), as well as the ratio of alkali-activated slag (AAS) to GGBFS.

The objective of this study is to create a concrete material by combining fly ash, blast furnace slag, and coarse and fine aggregates. This will serve the purpose of mitigating environmental pollution caused by the utilization of fly ash and blast furnace slag, while also eliminating the need for energy-intensive binding materials like cement. To create a better concrete material, different binding agents AAS have been tested. As a solid binder, fly ash and GGBFS have also been combined in a dry condition, in addition to the liquid binder. This research paper focuses on calculating the ideal proportion of GGBFS to fly ash to provide the highest fresh, hardened and durability characteristics.

Investigation has been done to find out how alkali activated GPC's mechanical properties are affected by the ratio of AAS to GSB. Heat curing at 60°C for 24 hours was used to test for any beneficial effects. The mechanical properties of GPC were examined by conducting experiments on compressive strength, flexural strength, modulus of rigidity, and split tensile strength. The objective was to improve these qualities by replacing a portion of fly ash with varied fractions of GGBFS.

2. EXPERIMENTAL PART

2.1. Materials

The geopolymer binding material is created via the process of geopolymerization, wherein a solid

binder composed of "Class F" fly ash and GGBFS reacts with a liquid binder called "AAS". Tables 1 and 2 display the physical properties and compositions of Class F fly ash and GGBFS. The liquid binder mostly comprises sodium hydroxide

and sodium silicate solutions. The procurement of fine and well-graded coarse aggregates from a local source was done for the purpose of using them in geopolymer concrete.

Table 1. Physical properties: GGBFS and Fly ash

Tabela 1. Fizička svojstva: GGBFS i leteći pepeo

Properties	Specific gravity	Specific surface area (Blaine), (m ² /kg)	Autoclave expansion, (%)	Residue on 45 µm (%)	Moisture content, (%)
GGBS	2.79	380	0.40	2.25	0.12
Fly ash	2.25	389	0.05	1.25	0.10

Table 2. Fly ash and GGBF: Chemical composition

Tabela 2. Leteći pepeo i GGBF: Hemijski sastav

	CaO	Al ₂ O ₃	SiO ₂	Fe ₂ O ₃	MgO	K ₂ O	SO ₃	Na ₂ O	LOI
GGBS	40.5	13.9	32.0	1.8	6.0	0.40	1.70	0.6	3.9
Fly ash	2.9	26.0	59.9	3.9	0.9	1.9	0.70	0.78	1.95

2.2. Preparation of the Binder

The Solution Sodium hydroxide was made the day before the GPC was cast. Pellets of sodium hydroxide were stored in a plastic container with tap water that was 97% pure and had a pH between 7.12 and 7.20. They were thoroughly stirred with a magnetic stirrer until they dissolved. As a substantial amount of heat was produced by exothermic chemical reactions, safety precautions were taken. After that, the alkaline solution was covered and let to cool. Based on the findings of earlier research, the ideal sodium hydroxide to sodium silicate ratio of 1.8 and 16 M, respectively, were maintained. In a 16M NaOH solution, the specific gravity and pH value were 1.44 and 12.4, respectively. The silicon dioxide (SiO₂) content of the sodium silicate solution was 30.4%, disodium oxide (Na₂O) was 11.6%, water was 56.9%, and the other components were filler materials. Sodium silicate has a specific gravity of 1.38. The sodium hydroxide solution and the sodium silicate gel were combined. This mixture underwent rigorous stirring for 5 minutes, which caused an exothermic reaction to produce an alkaline-activator solution (liquid binder) [23]. This solution was stored in a container with a tight lid.

2.3. Mix Proportion, Mixing, and Preparation of Sample

Geopolymer concrete can be prepared using either a dry blending technique or a wet blending technique. The experiment employed a dry mix approach. The composition of "Class F" Fly ash, GGBFS, alkaline-activator solution (AAS), fine aggregate, coarse aggregate, and water were established. The impact of the AAS to GSB ratio on

the strength parameters of fly ash-based GPC was examined using various ratios (0.30, 0.40, 0.50, and 0.60). In addition, varying quantities of GGBFS were employed to substitute the fly ash in the mixture to assess the effectiveness of GGBFS in geopolymer concrete.

In amounts of 25, 50, 75 and 100% by the weight of fly ash in the mixture, GGBFS partially replaced the fly ash. Due to the lack of a precise design approach, the concrete constituents were proportioned using the trial-and-error method [15]. The specific gravity of the ingredients serves as the basis for the mix design criterion in this investigation. Table 3 lists the weights and ratios of each element in the GPC mix. The solid binder's weight, which was 460 kg/m³, remained consistent throughout. The quantity of aggregates has been determined by the utilization of absolute volume, aggregate grading curve, and material specific gravity.

A mixer machine was utilized for a duration of 120 seconds to blend surface-dried coarse and fine aggregates, fly ash, and GGBFS. The AAS and water (pH=7.12–7.20) were gradually mixed together for 60 seconds to form a uniform concrete mixture. Then, the mixture of coarse and fine aggregates, fly ash, and GGBFS was continuously mixed for an additional 180 seconds. In 150 mm cube, 150x300 mm cylinder, and 100x100x500 mm beam moulds, this freshly mixed geopolymer concrete was cast. On a vibration table, concrete moulds were compacted. To prevent free water from the green concrete from evaporating, a plastic wrapping sheet was placed around the concrete-filled moulds.

Table 3. Mix proportion of fly ash and slag based geopolymer concrete

Tabela 3. Udeo mešavine geopolimer betona na bazi letećeg pepela i šljake

Mix No.	AAS/GSB	W/GSB	Molarity of SH	SS/SH	% of GGBFS by weight of GSB	FA by weight of GSB	CA by weight of GSB
M0.20	0.30	0.25	16	1.8	0	1.07	2.47
M0.30	0.40	0.25	16	1.8	0	1.06	2.44
M0.40	0.50	0.25	16	1.8	0	1.05	2.41
M0.50	0.50	0.25	16	1.8	0	1.04	2.35
M25.50	0.50	0.25	16	1.8	25	1.07	2.46
M50.50	0.50	0.25	16	1.8	50	1.09	2.51
M75.50	0.50	0.25	16	1.8	75	1.11	2.55
M100.50	0.50	0.25	16	1.8	100	1.13	2.60

2.4. Slump Test

The workability of freshly mixed geopolymer concrete was assessed using a Slump cone. The gadget consists mostly of a steel mould shaped like a frustum of a cone and a steel rod used for tampering. The frustum has an inner diameter of 200 mm at its top and 100 mm at its bottom. The height of the frustum measures 300 mm. Workability was evaluated in accordance with the Indian Standard (IS: 7320)

2.5. Curing of Samples

The plastic-wrapped moulds, filled with concrete, were left at room temperature for a duration of 60 minutes. The moulds [24,25] underwent heat curing in an oven at a precisely controlled temperature of 60°C for a duration of 24 hours, after 60 minutes of ambient curing. Prior to testing, the oven-cured specimen moulds shown in Figure 1 were kept at a consistent temperature ranging from 24 to 26 degrees Celsius and a relative humidity ranging from 60 to 5%



Figure 1. GPC Specimens

Slika 1. GPC uzorci

2.6. Compressive Strength Test

The compressive strengths of GPC cubes were evaluated using a hydraulic digital compression

testing machine with a capacity of 2000 kN and a least count of 0.1 kN as shown in Figure 2.a, following the guidelines of the Indian Standard IS: 516 [26]. The assessments were conducted after 3, 7, and 28 days. The test was conducted with a displacement rate ranging from 1.4 to 1.6 kilograms per minute. The compressive strength of each mix was evaluated by conducting tests on three cubes, and the mean value was determined.

2.7. Flexure Test

The flexural strength test was conducted using a digital flexure testing system that had a capacity of 100 kN and a minimum resolution of 0.1 kN as shown in Figure 2.b. A 100x100x500 mm beam was loaded at its centre point following the guidelines of ASTM Standard ASTM C-293-02, 2002, to determine its flexural strength [27]. Following the testing of three beams for each mixture, an average value for flexural strength was established.

2.8. Modulus of Elasticity

An extensometer equipped with a dial gauge was affixed to the centre of the cylindrical sample to quantify its deformation for testing modulus of elasticity as shown in Figure 2.c [28,29]. Experiments were performed on cylindrical samples utilizing a single-direction compression force at a displacement rate of 1.4 to 1.6 kg per minute.

2.9. Split Tensile Test

The split tensile test was conducted using the identical compressive testing instrument, as specified by the Indian standard IS:5816 [30]. The split strength of 150x300 mm cylinders, which were subjected to compression force perpendicular to the cylinder's longitudinal axis, as shown in Figure 2.d. The displacement rate was maintained at a consistent level of 1.4–1.6 kg/min. The average findings were calculated by conducting tests on three cylinders of each mixture after a period of 28 days.



Figure 2. (a) Compressive strength test (b) Flexural strength test (c) Modulus of elasticity test (d) Split tensile strength test

Slika 2. (a) Ispitivanje čvrstoće na pritisak (b) Ispitivanje čvrstoće na savijanje (c) Ispitivanje modula elastičnosti (d) Ispitivanje zatezne čvrstoće rascepa

3. RESULTS AND DISCUSSION

3.1. Slump

The geopolymer concrete mixes were formulated using solid binders such as GGBFS and fly ash, a liquid binder known as alkaline activated solution, aggregates, and water. The water quantity acquired has been standardized for all design mixtures in the current investigation. The acquired water was divided into two equal parts. One component is allocated for the preparation of the AAS solution, while the other half is designated for the production of slump. Increasing the AAS to GSB ratios necessitated a greater amount of water for AAS preparation, with the excess water being utilized for slump. Due to the reduced water content in the preparation of AAS and increased water content in the creation of a more manageable GPC, the concrete mixture exhibited cohesiveness and excellent plasticity, even though it had a smaller proportion of AAS to GSB content. Figure 3 depicts the slump values corresponding to

different ratios of AAS to GSB. The data demonstrated a decline in slump values as the ratio of AAS to GSB increased. Figure 4 illustrates the slump value of concrete mixes with GGBS replacement. The rigidity of the geopolymer concrete mixture escalates proportionally with the concentration of GGBFS in the mixture. Furthermore, there is a distinction in the rheological properties between Portland cement concrete and geopolymer concrete. The slump and hydration of Portland cement concrete were influenced by reactive and excess water, while in the case of GPC, water is exclusively utilized to prepare AAS and enhance workability. Previous studies have shown that the inclusion of slag in the GPC mix resulted in a decrease in workability [24,31]. To enhance the workability of the geopolymer mix at higher concentrations of GGBFS, the use of a superplasticizer is recommended. The workability of concrete can affect the mechanical and physical properties of the hardened material.

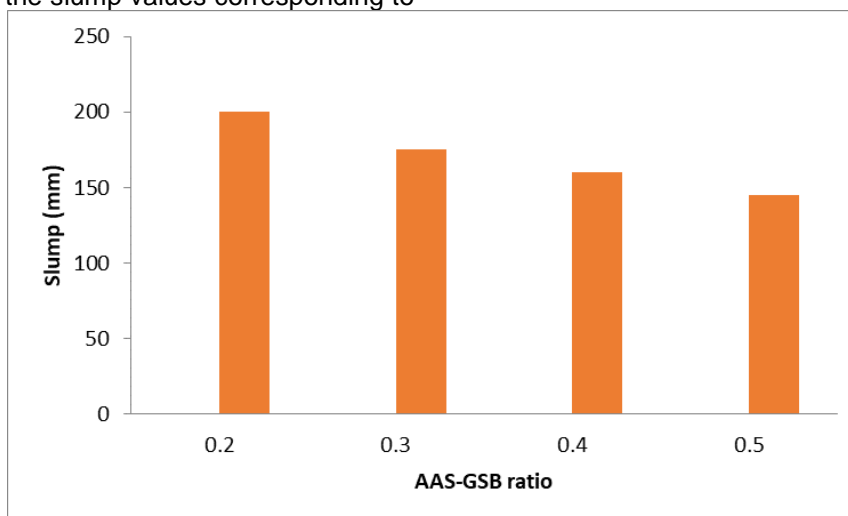


Figure 3. Slump of GPC concrete for various AAS-GSB ratios

Slika 3. Sleganje GPC betona za različite AAS-GSB odnose

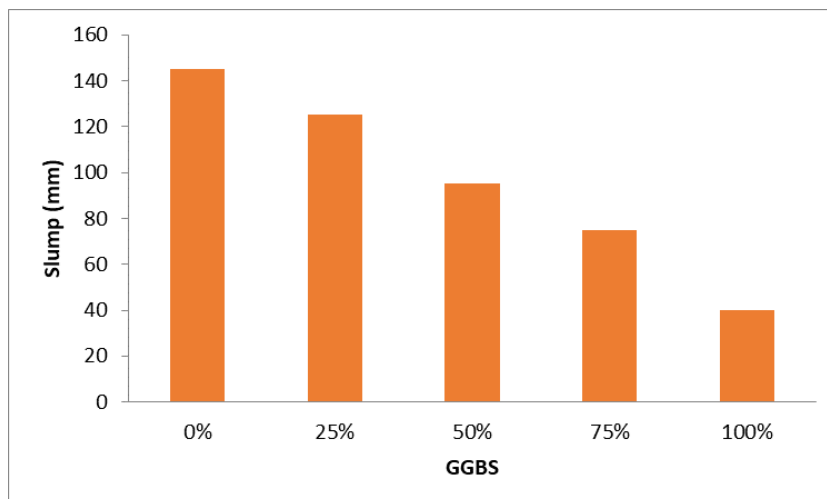


Figure 4. Slump of GPC concrete for various GGBS substitute

Slika 4. Sleganje GPC betona za različite GGBS zamene

3.2. Compressive Strength

Two significant GPC adjustments were taken into consideration in this analysis. Four different ratios of geopolymer solid binder (GSB) to alkali activated solutions (AAS) were used in the first experiment. These proportions were 0.2, 0.3, 0.4

and 0.5. Five different GGBFS substitutes for fly ash were used in the second. By weight of the entire fly ash, these replacements represented 25%, 50%, 75% and 100%. These modified GPC samples underwent testing. In Figures 5 and 6, the outcomes of compressive strengths are displayed.

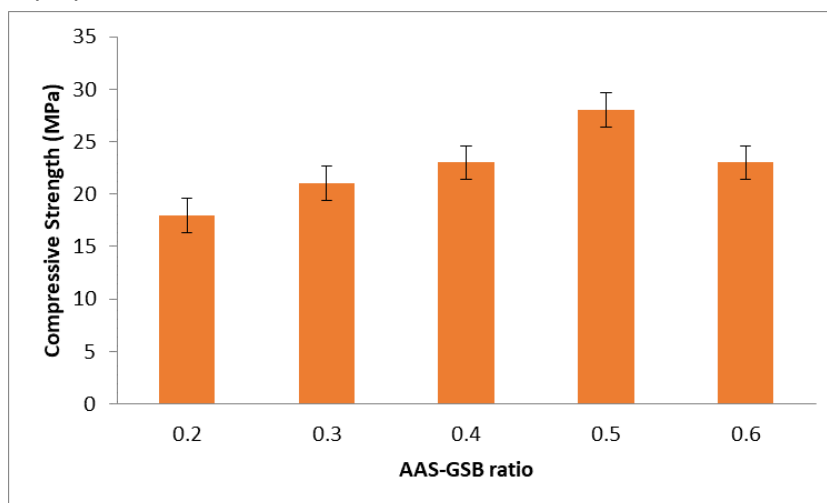


Figure 5. Compressive Strength of GPC for various AAS-GSB ratios

Slika 5. Čvrstoća na pritisak GPC za različite AAS-GSB odnose

Figure 5 displays a graph of the compressive strengths of GPC at 28 days for various AAS-to-GSB ratios. Figure 6 displays a graph of the compressive strengths of GPC at 28 days for various GGBS content. It can be seen that an AAS to GSB ratio of 0.5 results in the greatest gain in compressive strength value. AAS to GSB ratio was set at 0.50 while various GGBFS proportions were used to evaluate the impact of GGBFS content in the GPC. The effect of different GGBFS on

compressive strengths at 28 days after curing is depicted in Figure 5. When 25%, 50%, 75 % and 100% of the fly ash was substituted by GGBFS, the compressive strength values at 28 days were found to rise by 7.1%, 13.3%, 25% and 10.7%, respectively, above the conventional (fly ash based) geopolymer concrete. It can be noticed that 75% fly ash substitution by GGBFS, a substantial increase in strength has been noted. A slight increase in strength is shown when GPC contains 100%

GGBFS. At 75% GGBFS concentration, the GPC had the best compressive strength.

No surface cracks were observed after the curing process in a 60°C oven. Nevertheless, certain researchers have observed the presence of surface fissures caused by the contraction of the alkali-activated slag concrete [10]. Several studies have reported that the addition of slag to geopolymer concrete (GPC) during ambient curing results in a moderate increase in compressive

strength [21, 25, 32–34]. At a temperature of 60 °C, fly ash, GGBFS, and AAS demonstrate the most rapid rates of polymerization [25,35]. The greater enhancement in compressive strength is ascribed to the elevated calcium content of GGBFS [35]. The GGBFS primarily facilitates the interaction between calcium silicate, calcium aluminosilicate, and sodium aluminosilicate gel hydrates, which is responsible for the increase in compressive strength.

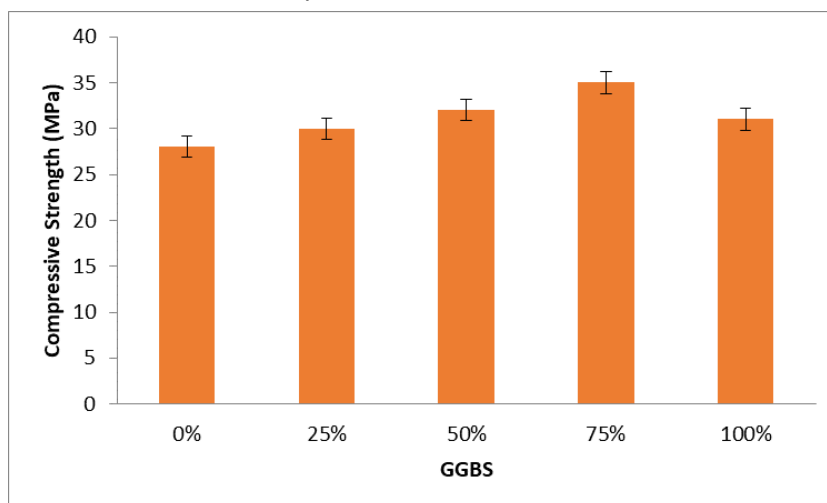


Figure 6. Compressive Strength of GPC for various GGBS substitute

Slika 6. Čvrstoća na pritisak GPC za različite GGBS zamene

3.3. Flexural strength

Flexural strength is the ability of a beam to withstand failure under bending forces. The discovery was made that the ratio of AAS (alkali-activated slag) to GSB (ground granulated blast furnace slag) in GPC (geopolymer concrete) had an influence on the flexural strength. The flexural strength of geopolymer concrete reached its peak

when the AAS-to-GBS ratio was 0.5, without the presence of GGBFS. Figure 7 depicts the flexural strength of different ratios of AAS-GBS. At a GGBFS level of 75%, the flexural strength reaches its peak. Figure 8 displays the flexural strength of GPC concrete at different levels of GGBS substitution.

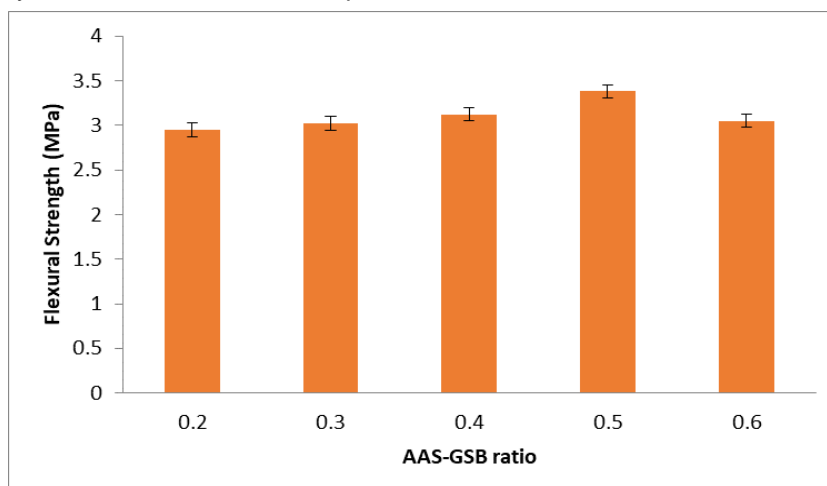


Figure 7. Split tensile Strength of GPC for various AAS-GBS ratios

Slika 7. Zatezna čvrstoća rascepa GPC za različite AAS-GBS odnose

Figure 8 displays the flexural strength of GPC concrete at different levels of GGBS substitution. Figure 8 demonstrates a notable link between the compressive and flexural strengths. The ACI 318 Building Code [36] can be used to determine the anticipated flexural strength of Portland cement concrete, and an expression for it can be expressed as f_c as per Equation 1.

$$f_r = 0.62 \sqrt{f_c} \tag{1}$$

Most of the specimens' flexural strengths were discovered to be between 20 and 30 percent greater than those predicted by Equation 2 (Figure 9). The authors arrived a formula for calculating the flexural strength of alkali-activated GGBFS-based geopolymer concrete as follows.

$$f_r = 0.682 \sqrt{f_c} \tag{2}$$

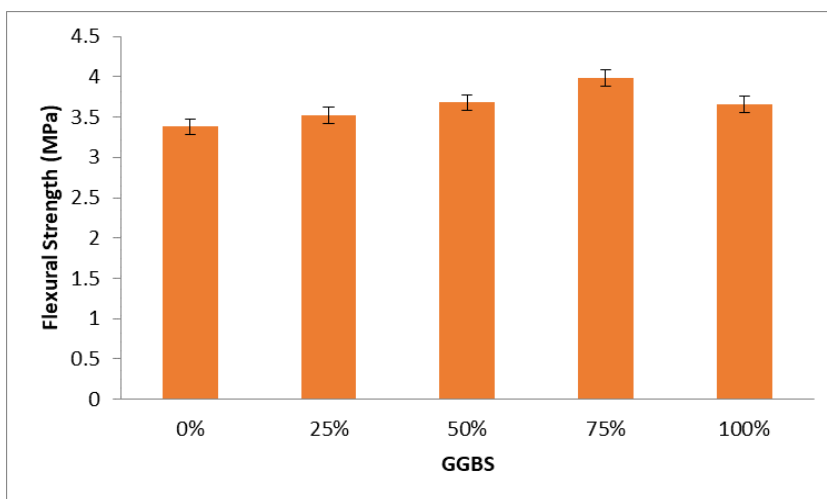


Figure 8. Split tensile Strength of GPC for GGBS substitute

Slika 8. Zatezna čvrstoća rascepa GPC za GGBS zamenu

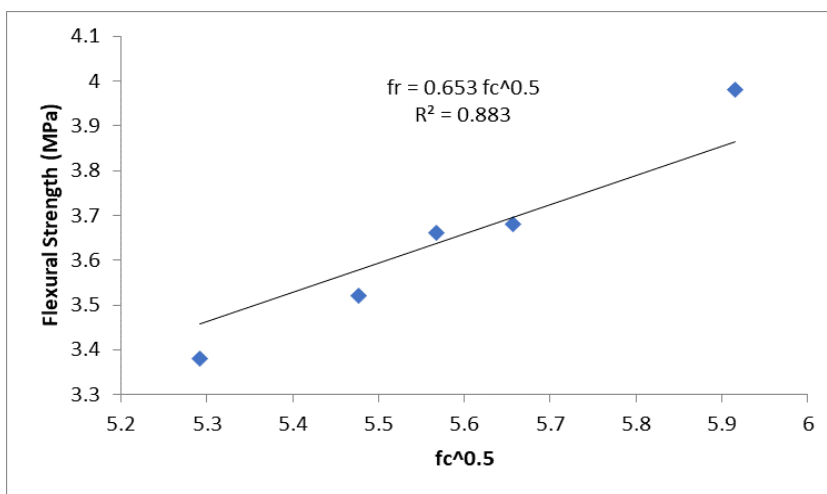


Figure 9. Correlation between flexural strength versus compressive strength

Slika 9. Korelacija između čvrstoće na savijanje i čvrstoće na pritisak

3.4. Modulus of Elasticity

Figure 10 depicts the modulus of elasticity of GPC wfor various AAS-GSB ratios. Figure 11 compares the elastic modulus of "class F" fly ash with geopolymer-based GGBFS concrete for various GGBS replacements. When the AAS-to-GSB ratio was raised to 0.50, the elastic modulus values began to rise. ACI Building Code [36] and

"IS code" [26] compare the elastic modulus values to those expected for Portland cement concrete. Equation 3 & 4 represents to ACI code, and IS code for the elastic modulus of Portland cement concrete respectively.

$$E_c = 4700 \sqrt{f_c} \text{ MPa.} \tag{3}$$

$$E_c = 5000 \sqrt{f_c} \text{ MPa.} \tag{4}$$

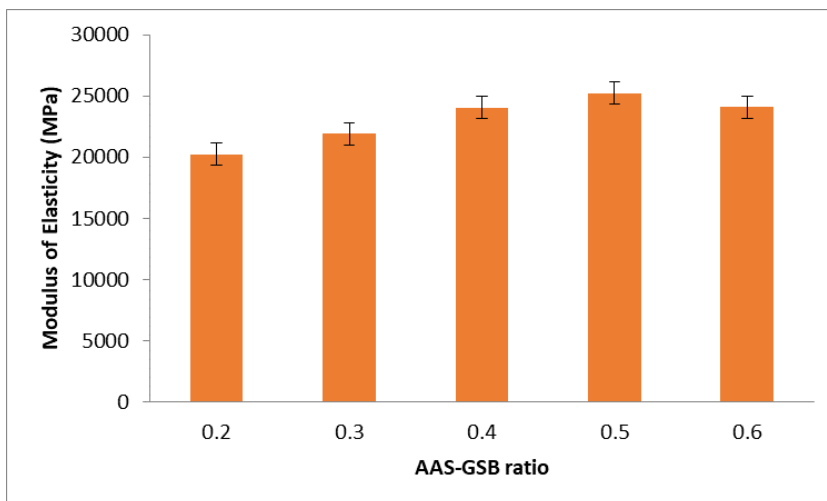


Figure 10. Modulus of elasticity of GPC for various AAS-GSB ratios

Slika 10. Modul elastičnosti GPC za različite AAS-GSB odnose

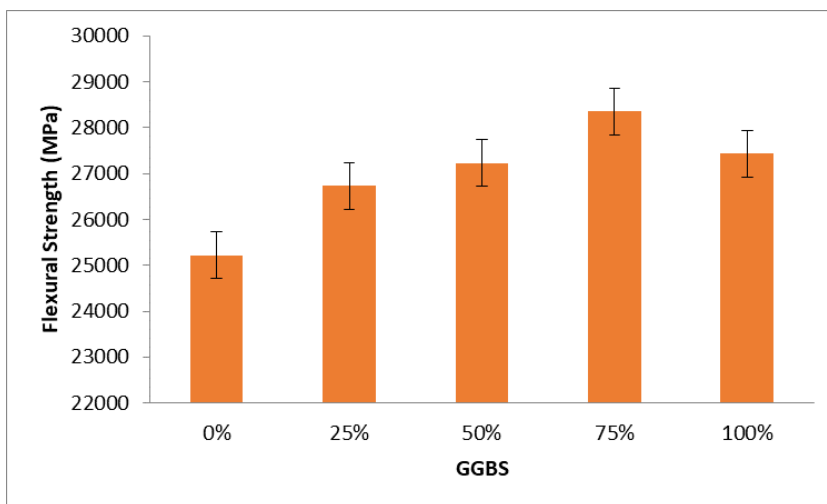


Figure 11. Modulus of elasticity of GPC for various GGBS substitute

Slika 11. Modul elastičnosti GPC za različite zamene GGBS

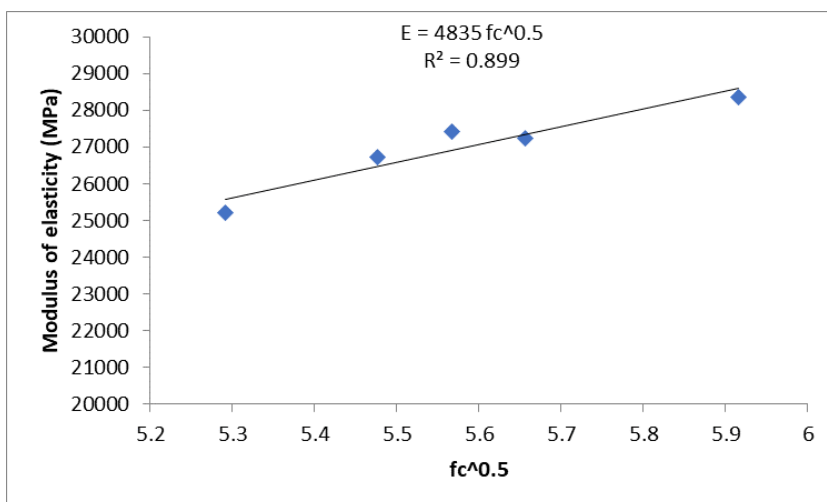


Figure 12. Correlation between Modulus of elasticity versus compressive strength

Slika 12. Korelacija između modula elastičnosti i čvrstoće na pritisak

Figure 12 illustrates the relationship between the modulus of elasticity and compressive strength. Equation 5 presents the authors' anticipated formula for determining the flexural strength of alkali-activated GGBFS-based geopolymer concrete.

$$E_c = 4950 \sqrt{f_c} \text{ MPa.} \quad (5)$$

3.5. Split tensile strength

The split tensile test is an indirect way of evaluating the tensile test of concrete [37]. Figure 13 illustrates the split tensile strength of GPC (Glass Powder Concrete) for different ratios of AAS (Alkali Activated Slag) to GSB (Ground Granulated Blast Furnace Slag). Figure 14 presents a comparison of the split tensile strength between "class F" fly ash and geopolymer-based GGBFS concrete at different levels of GGBS replacements. The split tensile strength of GPC is known to be associated with different aspects of crack initiation and

propagation in the concrete structure [38]. An increase in the quantity of GGBFS in alkali-activated, GGBFS-based geopolymer concrete, while keeping the AAS/GSB ratio constant at 0.50, resulted in an improvement in the split tensile strength. The splitting tensile strength (f_t) for Portland cement concrete can be determined using the CEB-FIP Model Code 95 [39] (Equation 6) and the ACI 318 Building Code [36] (Equation 7).

$$f_t = 0.62 \sqrt{f_c} \quad (6)$$

$$f_t = 0.50 \sqrt{f_c} \quad (7)$$

Figure 15 illustrates the relationship between the modulus of elasticity and compressive strength. The authors proposed a mathematical formula, denoted as Equation (8), to estimate the flexural strength of alkali-activated GGBFS-based geopolymer concrete.

$$f_t = 0.53 \sqrt{f_c} \quad (8)$$

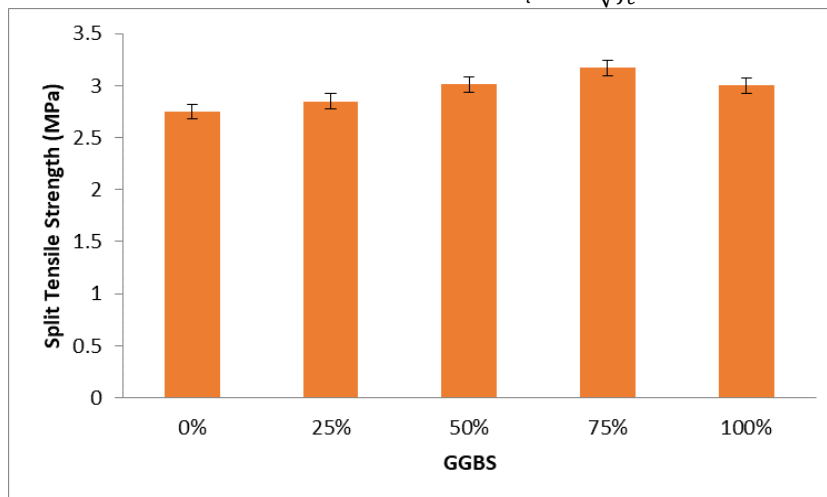


Figure 13. Split tensile strength of GPC for various AAS-GSB ratios

Slika 13. Zatezna čvrstoća rascepa GPC za različite AAS-GSB odnose

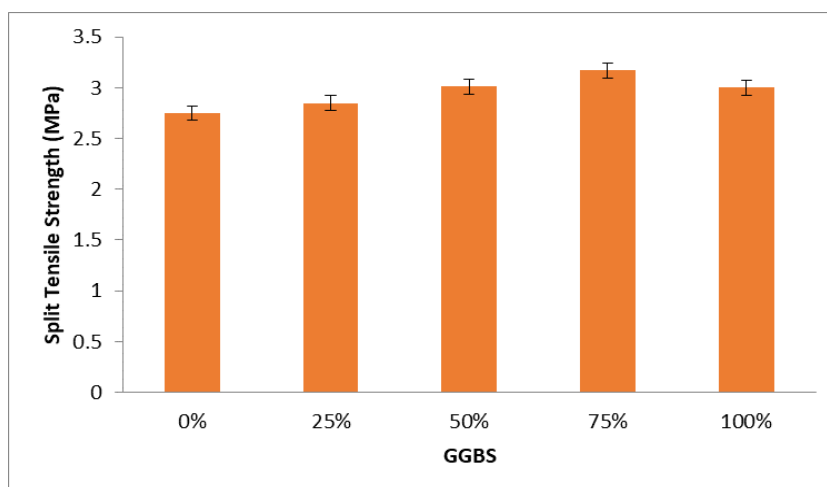


Figure 14. Split tensile strength of GPC for various GGBS substitute

Slika 14. Zatezna čvrstoća GPC-a za različite GGBS zamene

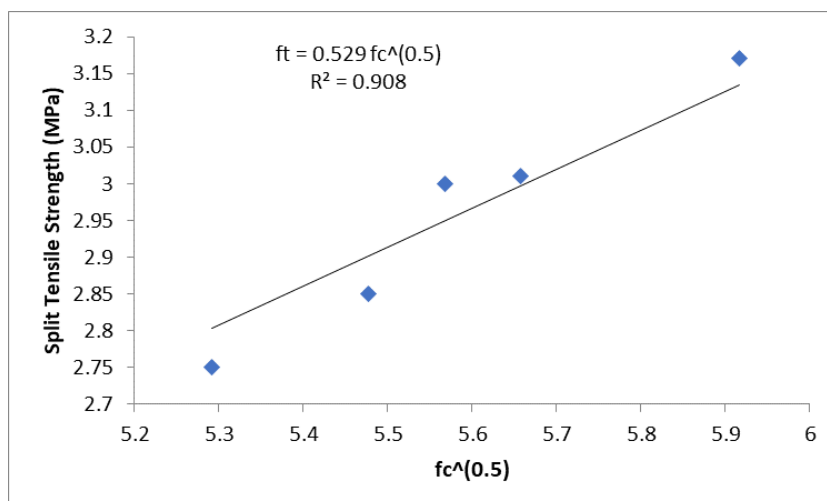


Figure 15. Correlation between Split tensile strength versus compressive strength

Slika 15. Korelacija između zatezne čvrstoće rascepa i čvrstoće na pritisak

4. CONCLUSION

The objective of this study is to develop a geopolymer concrete that exhibits a superior level of strength by utilizing an alkali-activated ground granulated blast furnace slag (GGBFS) as its primary component. The strength of this is attributed to the alkali-activated solution (AAS), which consists of sodium hydroxide and silicate solutions, as well as GGBFS. The subsequent information was revealed during an examination of strength and workability.

- The geopolymer concrete's workability rises when the AAS-to-GSB ratio rises but falls when the GGBFS content rises.
- The higher AAS-to-GSB ratio in fly ash-based GPC accounts for the increased strength. A ratio rise above 0.5, however, has no appreciable impact on the strength. An AAS-to-GSB ratio of 0.50 results in the fly ash-based GPC's highest compressive strength value.
- With the addition of more GGBFS, the mechanical properties of GPC are significantly improved. It can be shown that 80% GGBFS in GPC has generated the strongest results. When GPC contains more than 80% GGBFS, the increase in strength is minimal.
- GPC can reach high early strengths of up to 77-86% of the 28-day compressive strength when it is cured at 60° C for 24 hours.
- Empirical equations have been formulated to determine the flexural strength, elastic modulus, and split tensile strength of GPC that has undergone a curing process at 60°C for 24 hours, based on its compressive strength. These equations are expected to be advantageous for professionals in the field of concrete technology.

The objective of the present investigation was to develop a novel concrete material that has notable mechanical properties by utilizing industrial waste materials. It was based on GGBFS and an AAS. It is anticipated that this concrete would find extensive use as structural concrete. In places without access to mixing water, it would be considerably more useful.

Acknowledgement

The authors express their sincere gratitude for the support provided by the Department of Civil Engineering at Alagappa Chettiar Government College of Engineering and Technology in Karaikudi, Tamilnadu, India.

5. REFERENCES

- [1] P.Zhang, Z.Gao, J.Wang, J.Guo, S.Hu, Y.Ling (2020) Properties of fresh and hardened fly ash/slag based Geopolymer Concrete: A Review; *Journal of Cleaner Production*, 270, 122389. <https://doi.org/10.1016/j.jclepro.2020.122389>.
- [2] E.Benhelal, G.Zahedi, E.Shamsaei, A.Bahadori (2013) Global strategies and potentials to curb CO₂ emissions in Cement Industry; *Journal of Cleaner Production*, 51, 142–161. <https://doi.org/10.1016/j.jclepro.2012.10.049>.
- [3] A.Sabbagh Moghadam, N.Hadiani (2018) Stabilizing the excavation materials to be used in fill layers; *Civil Engineering Journal*, 4(5), 1165-1172. doi:10.28991/cej-0309165
- [4] D.Joseph (1994) Geopolymers: man-made rock geosynthesis and the resulting development of very early high strength cement; *Journal of Materials education*, 16, 91-91
- [5] F.Pacheco-Torgal, J.Castro-Gomes, S.Jalali (2008) Alkali-activated binders: A Review; *Construction and Building Materials*, 22(7), 1305–1314. <https://doi.org/10.1016/j.conbuildmat.2007.10.015>

- [6] C.K.Ma, A.Z.Awang, W.Omar (2018) Structural and material performance of Geopolymer Concrete: A Review; *Construction and Building Materials*, 186, 90–102. <https://doi.org/10.1016/j.conbuildmat.2018.07.111>
- [7] B.Singh, M.R.Rahman, R.Paswan, S.K. Bhattacharyya (2016) Effect of activator concentration on the strength, Itz and drying shrinkage of fly ash/slag geopolymer concrete; *Construction and Building Materials*, 118, 171–179. <https://doi.org/10.1016/j.conbuildmat.2016.05.008>
- [8] S.A.Bernal, J.L.Provis, B.Walkley, R.San Nicolas, J.D.Gehman, D.G.Brice, J.S.J.Van Deventer (2013) Gel nanostructure in alkali-activated binders based on slag and fly ash, and effects of accelerated carbonation; *Cement and Concrete Research*, 53, 127–144. <https://doi.org/10.1016/j.cemconres.2013.06.007>
- [9] M.Mastali, P.Kinnunen, A.Dalvand, R.Mohammadi Firouz, M.Illikainen (2018) Drying shrinkage in alkali-activated binders – A critical review; *Construction and Building Materials*, 190, 533–550. <https://doi.org/10.1016/j.conbuildmat.2018.09.125>
- [10] N.K.Lee, H.K.Lee (2013) Setting and mechanical properties of alkali-activated fly ash/slag concrete manufactured at room temperature; *Construction and Building Materials*, 47, 1201–1209. <https://doi.org/10.1016/j.conbuildmat.2013.05.107>
- [11] J.J.Ekaputri, M.B.Ulum, R.Triwulan Bayuaji, T.E.Susanto, M.M.Al Bakri Abdullah (2015) A comprehensive characterization and determination of Fly Ashes in Indonesia using different methods; *Applied Mechanics and Materials*, 754–755, 320–325. doi:10.4028/www.scientific.net/amm.754-755.320
- [12] G.S.Ryu, Y.B.Lee, K.T.Koh, Y.S.Chung (2013) The mechanical properties of fly ash-based geopolymer concrete with alkaline activators; *Construction and Building Materials*, 47, 409–418. <https://doi.org/10.1016/j.conbuildmat.2013.05.069>
- [13] A.Ojha, P.Aggarwal (2021) Fly Ash based Geopolymer Concrete: A comprehensive review; *Silicon*, 14(6), 2453–2472. <https://doi.org/10.1007/s12633-021-01044-0>
- [14] J.R.Yost, A.Radlińska, S.Ernst, M.Salera (2012) *Structural behavior of alkali activated fly ash concrete. part 1: Mixture design, material properties and sample fabrication*; *Materials and Structures*, 46(3), 435–447. <https://doi.org/10.1617/s11527-012-9919-x>
- [15] G.Saini, U.Vattipalli (2020) Assessing properties of alkali activated GGBS based self-compacting geopolymer concrete using nano-silica; *Case Studies in Construction Materials*, 12. <https://doi.org/10.1016/j.cscm.2020.e00352>
- [16] C.Luan, X.Shi, K.Zhang, N.Utashev, F.Yang, J.Dai, Q.Wang (2021) A mix design method of fly ash geopolymer concrete based on factors analysis; *Construction and Building Materials*, 272, 121612. <https://doi.org/10.1016/j.conbuildmat.2020.121612>
- [17] S.V.Patil, V.B.Karikatti, M.Chitawadagi (2018) Granulated blast-furnace slag (GGBS) based geopolymer concrete - review concrete – review; *International Journal of Advanced Science and Engineering*, 5(1), 879. <https://doi.org/10.29294/IJASE.5.1.2018.789-885>
- [18] K.Vijai, R.Kumutha, B.G. Vishnuram (2010) Effect of curing on strength of geopolymer concrete; *International journal of physical sciences*, 5(9), 1419-1423.
- [19] A.Noushini, A.Castel, J.Aldred, A.Rawal (2020) Chloride diffusion resistance and chloride binding capacity of fly ash-based geopolymer concrete; *Cement and Concrete Composites*, 105, 103290. <https://doi.org/10.1016/j.cemconcomp.2019.04.006>
- [20] S.Nagajothi S, S.Elavenil (2020) Effect of GGBS addition on reactivity and microstructure properties of ambient cured fly ash based geopolymer concrete; *Silicon*, 13(2), 507–516. <https://doi.org/10.1007/s12633-020-00470-w>
- [21] R.R.Bellum, R.Nerella, S.R.Madduru, C.S.Indukuri (2019) Mix Design and mechanical properties of fly ash and GGBFS-synthesized alkali-activated concrete (AAC); *Infrastructures*, 4(2), 20. <https://doi.org/10.3390/infrastructures4020020>
- [22] H.Ma, H.Zhu, C.Yi, J.Fan, H.Chen, X.Xu, T.Wang (2019) Preparation and reaction mechanism characterization of alkali-activated coal gangue–slag materials; *Materials* 12(14), 2250. <https://doi.org/10.3390/ma12142250>
- [23] IS 383 (2016) Indian Standard Coarse and Fine Aggregate for Concrete. Bureau of Indian Standards
- [24] M.S.Red, P.Dinakar, B.H.Rao (2018) Mix design development of fly ash and ground granulated blast furnace slag based geopolymer concrete; *Journal of Building Engineering*, 20, 712–722. <https://doi.org/10.1016/j.jobe.2018.09.010>
- [25] R.R.Bellum, K.Muniraj, S.R.Madduru (2020) Investigation on modulus of elasticity of fly ash-ground granulated blast furnace slag blended geopolymer concrete; *Materials Today: Proceedings*, 27, 718–723. <https://doi.org/10.1016/j.matpr.2019.11.299>
- [26] IS 456 (2000) Indian Standard Plain and Reinforced Concrete,” Bureau of Indian Standards,
- [27] ASTM C-293 (2002), Standard Test Method for Flexural Strength of concrete (using Simple Beam with Center-Point Loading) International Standard Organization
- [28] Y.Hu, Z.Tang, W.Li, Y.Li, V.W.Y.Tam (2019) Physical-mechanical properties of fly ash/GGBFS geopolymer composites with recycled aggregates; *Construction and Building Materials*, 226, 139–151. <https://doi.org/10.1016/j.conbuildmat.2019.07.211>
- [29] Diaz-Loya E I, Allouche E N, and Vaidya S (2011) Mechanical properties of fly-ash-based geopolymer concrete, *ACI Materials Journal*, 108(3). doi:10.14359/51682495
- [30] IS 5816 (1999) Indian Standard Splitting Tensile Strength of Concrete Method of Test,” Bureau of Indian Standards.

- [31] P.Nath, P.K.Sarker (2014) Effect of GGBFS on setting, workability and early strength properties of fly ash geopolymer concrete cured in ambient condition; *Construction and Building Materials*, 66, 163–171. <https://doi.org/10.1016/j.conbuildmat.2014.05.080>
- [32] Z.Tang, Y.Hu, V.W.Y.Tam, W.Li (2019) Uniaxial compressive behaviors of fly ash/slag-based geopolymeric concrete with recycled aggregates; *Cement and Concrete Composites*, 104, 103375. <https://doi.org/10.1016/j.cemconcomp.2019.103375>
- [33] J.Xie, J.Wang, R.Rao, C.Wang, C.Fang (2019) Effects of combined usage of GGBS and fly ash on workability and mechanical properties of alkali activated geopolymer concrete with recycled aggregate; *Composites Part B: Engineering* 164: 179–190. <https://doi.org/10.1016/j.compositesb.2018.11.067>
- [34] I.R.Mithanthaya, S.Marathe, B.S.Rao, V.Bhat (2017) Influence of superplasticizer on the properties of geopolymer concrete using industrial wastes; *Materials Today: Proceedings*, 4(9), 9803–9806. <https://doi.org/10.1016/j.matpr.2017.06.270>
- [35] S.Kuma, R.Kumar, S.P.Mehrotra (2010) Influence of granulated blast furnace slag on the reaction, structure and properties of fly ash based geopolymer; *Journal of Materials Science*, 45(3), 607–615. <https://doi.org/10.1007/s10853-009-3934-5>
- [36] ACI M318 (2005) Building Code Requirements for Structural Concrete and Commentary, American Concrete Institute.
- [37] P.Nath, P.K.Sarker (2016) Fracture properties of GGBFS-blended fly ash geopolymer concrete cured in ambient temperature; *Materials and Structures*, 50(1). <https://doi.org/10.1617/s11527-016-0893-6>
- [38] G.Fang, W.K.Ho, W.Tu, M.Zhang (2018) Workability and mechanical properties of alkali-activated fly ash-slag concrete cured at ambient temperature; *Construction and Building Materials*, 172, 476–487. <https://doi.org/10.1016/j.conbuildmat.2018.04.008>
- [39] Code, CEB-FIP Model(1995) Comité euro-international du béton. Bulletin d'information 213: 46.

IZVOD

KARAKTERISTIKE SVEŽEG I OČVRSLOG ALKALNO AKTIVIRANOG GEOPOLIMERNOG BETONA SA GGBFS

Razvoj infrastrukture jedne zemlje u velikoj meri se oslanja na upotrebu cementnog betona kao glavnog građevinskog materijala. Industrija cementa značajno doprinosi globalnom zagrevanju zbog značajne emisije ugljen-dioksida (CO₂). Smanjenje potrošnje cementa u betonu uz zadržavanje njegovih osnovnih karakteristika može dovesti do isplativijeg i ekološki prihvatljivijeg napretka građevinskog sektora.

Posmatrajući novu mešavinu betona koja uključuje leteći pepeo (FA) i mlevenu granuliranu šljaku iz visokih peći (GGBFS), ova studija ima za cilj razvoj betona bez cementa. Alkalno aktiviran rastvor (AAS) je korišćen kao tečno vezivo zajedno sa suvom mešavinom FA i GGBFS. Ova studija ispituje korišćenje i uticaj tečnih i čvrstih veziva u proizvodnji geopolimera betona (GPC) na bazi GGBFS aktiviranog alkalno, kao i optimalne količine potrebne za njihovu ugradnju.

Ekperimentisani su različiti odnosi AAS prema GSB da bi se odredila optimalna smeša. Da bi se pronašla optimalna mešavina GGBFS za GPC, različite količine GGBFS su korišćene kao delimična zamena za leteći pepeo. Nakon 28 dana, uzorci za testiranje, kao što su kocke, cilindri i grede, su liveni i stavljani na ispitivanje. GPC je takođe odlučio da koristi toplotno očvršćavanje da bi dobio dobre rezultate. Utvrđeno je da je odnos 0,5 između AAS i GSB i sastav od 75% GGBFS čini najjači materijal. Rezultati studije pokazuju da se upotrebom AAS i GGBFS u geopolimeru betonu dobija bolji proizvod, koji bi se mogao koristiti na mestima gde nema dovoljno vode.

Ključne reči: Geopolimer; Geopolimerno čvrsto vezivo; Alkalno aktivirani rastvor; Pepeo; GGBFS

Naučni rad

Rad primljen: 19.12.2023.

Rad prihvaćen: 08.01.2024.

Rad je dostupan na sajtu: www.idk.org.rs/casopis

Abdel Hafiz A. Ali^{1*}, Seddik S. Waheed², Salah M. Rabia²,
Nouby M. Ghazaly³

¹Assis. Lecturer at the Higher Institute of Engineering and Technology, Minia, Egypt, ²Emeritus Professor, Mechanical Engineering Department, Minia University, Egypt ³Technical College, Imam Ja'afar Al-Sadiq University, Baghdad, Iraq, ³Department of Mechanical Engineering, South Valley University, Egypt.

Scientific paper

ISSN 0351-9465, E-ISSN 2466-2585

<https://doi.org/10.62638/ZasMat1124>



Zastita Materijala 65 (2)
307 - 314 (2024)

Assessment of the effect of mixing polystyrene (PS) with sawdust (SD) on copyrolysis products

ABSTRACT

The co-pyrolysis process between biomass and solid waste especially plastics has attracted significant attention in research studies as a means to enhance both the quantity and quality of bio-oil derived from biomass decomposition. In this research paper, the PS/SD co-pyrolysis was carried out for six different concentrations ranging from 0% to 100%, with increments of 20% PS, inside a small laboratory reactor at 450 °C and heating rate (HR) of 20.5 °C min⁻¹. Results showed that an increase in the proportion of PS in the blend resulted in a higher bio-oil outcome. The highest bio-oil yield was recorded at the 80PSSD blend, indicating that co-pyrolysis had a positive effect on oil production in all mixtures. The most significant positive impact was observed at the 20PSSD blend, reaching [+11.54]. Conversely, gas production showed a negative effect, with gas quantities lower than expected for all mixtures, and the most significant negative impact was at 20PSSD, with a decrease of [-11.8]. As for char outcome, there was a minimal increase in its quantity, with the highest positive impact of charcoal observed at 80PSSD, reaching [+3.44]. Consequently, it can be observed that the quantity of char produced is not significantly affected by the co-blending process.

Keywords: PS plastic, biomass, sawdust, co-pyrolysis, bio-oil.

1. INTRODUCTION

The global population growth and expanding industrial operations have substantially increased energy consumption. The continued reliance on fossil fuels (FF) as the primary energy source has resulted in heightened pollution, significant greenhouse gas emissions, and considerable impacts on climate change, raising environmental and social concerns [1]. Despite the growing adoption of electric power as a cleaner alternative in various industrial applications, the dependence on FF remains inevitable [2].

Due to these previous challenges, many countries are shifting their policies towards the production of bio-fuels extracted from renewable energy sources to serve as a viable alternative to FF.

Biomass has been included on this list of energy sources, with reliance on biomass accounting for 70% of primary energy sources [3]. Biomasses, including materials like wood, crop residues, agricultural waste, energy crops, and organic industrial and household waste.

Biomasses can serve as a renewable energy source through processes like combustion, gasification, or fermentation. While bio-fuels from biomass are already in use as alternative energy sources, it's crucial to improve their low combustion efficiency to ensure their sustainable utilization in the future [4].

Nomenclature list

Nomenclature list			
20PSSD	20%PS+80%SD	HR	Heat rate
40PSSD	40%PS+60%SD	PS	Polystyrene
60PSSD	60%PS+40%SD	NSE	Negative synergistic effect
BOC	Bio-oil content	SD	Saw dust
FF	Fossil fuel	SWM	Solid waste materials

Corresponding author: A. Hafiz A.A. Ali

E-mail: ali5.engstar@gmail.com

Paper received: 30. 09. 2023.

Paper corrected: 25.12.2023.

Paper accepted: 11. 01. 2024.

Paper is available on the website: www.idk.org.rs/journal

Commercially implemented liquid bio-fuels suffer from significant disadvantages, such as a substantial proportion of oxygenated compounds may be up to 60%, limited thermal stability, increased viscosity, and acidity issues, resulting biofuel has low heating value [5]. Lately, numerous research studies have been conducted to enhance the efficiency of liquid biofuel, and one of the most significant strategies is the effectiveness of thermochemical methods as pyrolysis, anaerobic digestion, and gasification [6]. However, the most efficient technique is pyrolysis, it improves the properties of liquid, gas, and solid fractions of pyrolysis simultaneously, the main product is BOC, which can be refined into biodiesel and blended with gasoline [7].

Although the oil obtained from plastic pyrolysis has some good characteristics similar to conventional fuels in internal combustion engines, such as high heating value and hydrocarbon content, which partially solves the issues mentioned earlier regarding bio-oils, these oils contain a high percentage of polycyclic aromatic hydrocarbons (PAHs), which pose a serious health risk to humans (cancer). This restricts the widespread use of this technology or requires costly and complex pre-treatments [8].

The utilization of co-pyrolysis (biomass with SWM) especially waste plastic shows great potential as it can effectively handle waste materials and transform them into valuable fuels or chemicals. This process involves using plastics as a catalyst of sorts to enhance the production of aromatic hydrocarbons and reduce the presence of oxygenated compounds in the liquid portion. Consequently, employing waste biomass (such as wood chips, sawdust, and branches) along with discarded plastics offers a promising approach to address various challenges [9]. Until now, scientific studies efforts have been dedicated to discovering the most favorable conditions as (feedstock type, pyrolysis mechanisms, various parameters processes, and product yield) to use the co-pyrolysis process widely scale.

The authors [10], PS/SD co-pyrolysis was conducted in FBR. The study recorded the highest bio-oil yield of 83.86% for the 75% wt PS blend; however, the highest PSE in the bio-oil yield was observed (62.33% wt, against 31.39% wt for SD alone) for the 25% wt PS blend with a value of +17.44 between the expected and experimental values. On the other hand, the NSE in the production of bio-gas for all blends ratios. The study also showed that adding PS to the mixture increased HHV to 40.21 MJ/kg while reducing the O₂ content and increasing the aromatic compounds of the bio-oil fuel.

The authors in [11] examined the effect of increasing PS content on the co-pyrolysis with co-gasification of paper biomass using a lab-scale batch reactor at a temperature 1173 K. Their results showed a positive effect on the increase in the bio-gas yield with decreasing in the char fraction. Additionally, there was an improvement in the gas quality, with the hydrogen fraction almost doubling as the PC "polystyrene content" increased from 10% to 30%. These results can be attributed to the fact that the volatile materials from the paper pyrolysis increased the bio-gas PS pyrolysis, slowed the reaction rate, leading to a decrease in the charcoal yield during co-pyrolysis.

The study [12], the researchers studied the co-pyrolysis of PS and CS "corn stalk" biomass at 500°C in a fixed reactor and found that the maximum oil yield was obtained at a 1:3 CS to PS blend without catalyst, where synergistic effect was observed 5.75 during co-pyrolysis process.

Sanahuja et al. [13] evaluated the effect of PS/GS(grape seeds) co-pyrolysis by FBR, and they recorded that a positive synergistic effect PSE for bio-oil yield when PS in the range (5% to 40%) in the blend, also the study showed that a clear improvement in the bio-oil quality, which can be summarized as follows, maximum reduction in oxygen content to 6.3% wt of 40% wt PS compared to 14% wt GS biomass, increasing heating value to 39 MJ/kg of 20% and 40% wt PS compared to 36 MJ/kg of GS alone, increasing in PH value at 6 for 40% PS compared usually to 2-3 PH values of GS alone, which negatively affects the fuel efficiency and engine components.

In another study [14], a high calorific value was recorded 41.29 MJ/kg for the bio-oil produced from co-pyrolysis PS/ NES (non-edible seeds), using fixed reactor at a blend of 1:2 respectively, The study mentioned that this was due to an increase in the total heat flow of the co-pyrolysis process. Reduction in the oxygen content and viscosity, thereby improving the efficiency of the resulting oil compared to that produced from Karanja & Nijer NES. The authors concluded that co-pyrolysis of biomass and waste polystyrene has a successful economic direction for both plastic waste management and converting biomass to energy.

2. MATERIALS AND EXPERIMENTAL SET-UP

2.1. Feed-stocks

The co-pyrolysis process evaluated the effect of waste PS adding on SD biomass materials as six blends (0PSSD to 100PSSD) with increasment 20% of PS, SD was obtained from the wood feathers resulting from furniture manufacturing processes in carpentry workshops, Faculty of

Engineering, Minia University, Egypt The SD was a mixture of different proportions of beech wood and white musky sawdust was cut into small homogeneous samples about 1 to 2 mm average size, while PS has been collected from single-use dish waste from candy and fast food stores, then cleaned and cut into small pieces, approximately 1 to 2 cm² in size.

2.2. Experimental set-up

The previous two pure and four its blends feedstocks were tested in a small-scale pyrolysis reactor to convert plastic waste into liquid oil, gas, and char products Fig. (1). The reactor cylinder was made of cast iron with a thickness of 6 mm and wrapped with a loop of an electric heater, which was 2.5 meters in length and had a capacity

of 3 kW. The reactor had a height of 285 mm, a diameter of 101.5 mm, and a capacity of 2.2 liters (Table 1). It was connected to a 20 mm diameter tube that passed inside a condenser tube with a length of 550 mm and a diameter of 3.5 mm. The condenser tube was equipped with two entrances for cooling water, with the bottom serving as the entry and the top as the exit. The vapors of plastic waste produced in the heating chamber at high temperatures were condensed into liquid oil in the condenser tube. Water circulated through the condenser tube at a flow rate of 1.5 L/min., and the condensed liquid oil was collected in the oil collector tank located at the bottom of the system. The uncondensed products (gases) were exhausted outside the system.

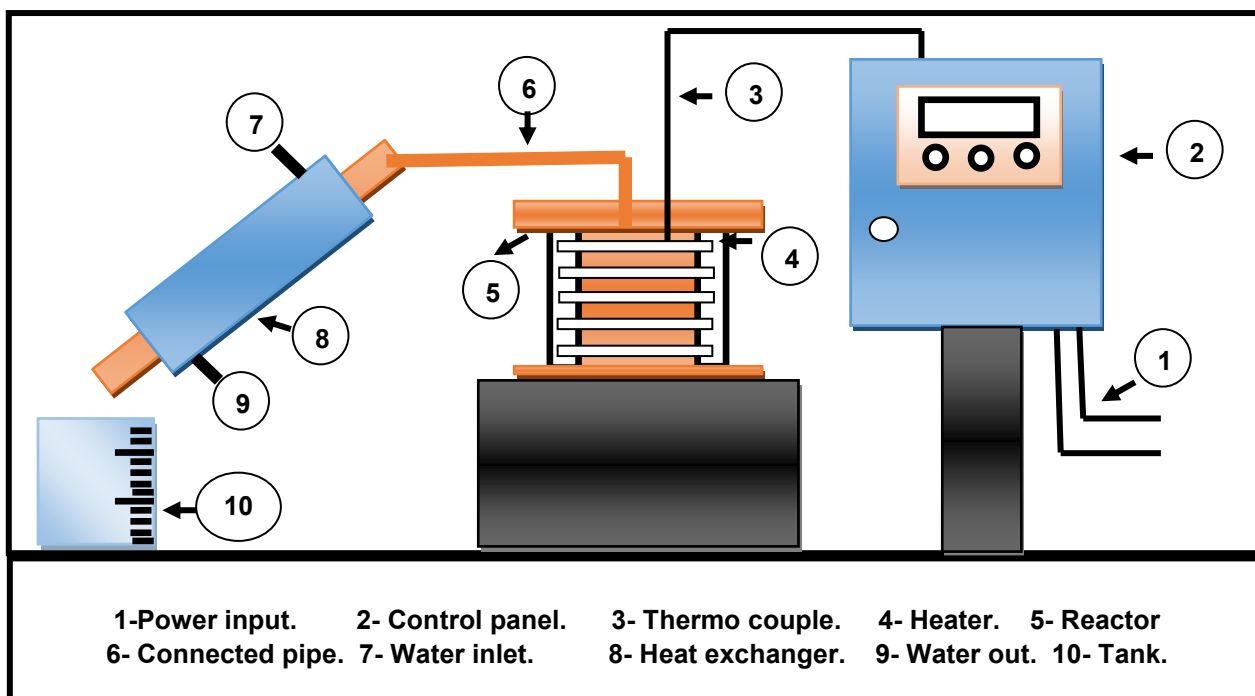


Figure 1. The schematic set up of the pyrolysis unit

Slika 1. Šematski prikaz jedinice za pirolizu

Table 1. Reactor components parameters

Tabela 1. Parametri komponenti reaktora

Component		Features
Reactor properties	Long	285 mm
	Out diam.	101.5 mm
	Thickness	6 mm
	Capacity	2.2 lit
Thermocouple		type K
Heater		2.5 m & 3 kW
condenser diameter		63.5 mm
condenser length		55cm

3. RESULTS

3.1. Pure PS, and SD pyrolysis

The current experiment was evaluated the SD pyrolysis at 450 °C, 20.5 °C /min HR. This is because it is the optimal conditions for obtaining the largest amount of bio-oil (83% wt) produced from PS pyrolysis, in order to have a clear effect on improving the characteristics of the fuel resulting from PS/SD co-pyrolysis.

The figure reviewed the outcomes of the thermal pyrolysis process of individual pure materials PS, and SD, by analyzing the figure, it is

concluded that PS recorded the highest oil content of up to 83% with a small product of coal and gas up to 3% and 14%, respectively, in contrast, SD recorded a product of bio-oil up to 36.7% wt, which

represents a small percentage if compared to PS, while a rise in char content was observed to record 33.3% wt SD, while the content of gas as 30% wt.

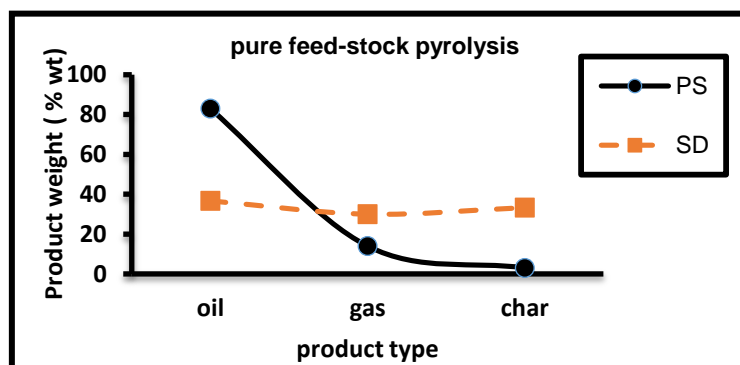


Figure 2. Pure feed stocks type's verses product yield percentage

Slika 2. Procenat prinosa proizvoda tipa čiste stočne hrane

The distribution of products in SD biomass and PS plastic pyrolysis exhibits significant differences, despite the similarity of operating conditions. This disparity can be attributed to the varying composition of biomass and plastics. Biomass pyrolysis product type is strongly influenced by the presence of cellulose, and hemicellulose, which promotes the production of bio-oil; this is due to the presence of weak bonds that are easily broken at a short range of temperatures (220 – 315 °C). While the high content of lignin (It is the second main component of biomass after cellulose and is usually in wood material from 20 to 35% depending on the type of wood. Lignin is characterized by strong bonds and a three-dimensional network that makes it a difficult and decomposition resistant material that is difficult to convert into valuable products (oil or gas) as biofuel [15]) in biomass indicates a rise in char yield [16]. On the other hand, PS plastics have a higher volatile content up

to 99.6 %, which favors liquid yield [17]. Consequently, the co-pyrolysis of plastics and biomass will be a promising technique to raise the efficiency of biomass pyrolysis outcomes.

3.2. Co-pyrolysis PS/SD outcome.

Figure 3 illustrated the co-pyrolysis products of PS/SD. Upon analyzing the figure, it becomes evident that the highest bio-oil content was obtained from a blend of 75% PS and 25% SD, reaching 76.25%. Gas and char contents were 11.25% and 12.5%, respectively. The bio-oil content increased with higher percentages of PS in the blend, while the char content decreased, reaching its peak value of 27.5% in the 20PSSD blend. The blend of 20PSSD yielded the highest non-condensed gas production at 15%. As the PS percentage increased in the mixture, there was a slight decrease in biogas content ranging from 12.5% to 11.25%.

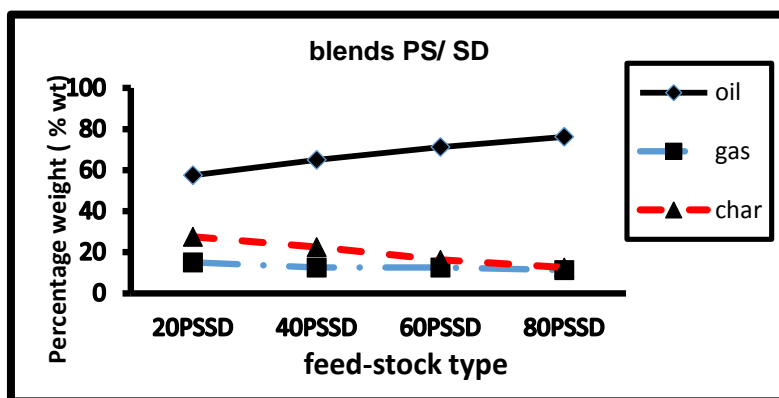


Figure 3. Blends PS/SD verses product yield percentage

Slika 3. Mešavine PS/SD u odnosu na procenat prinosa proizvoda

3.3. PS/SD Co-pyrolysis synergistic effect

Figure 4 illustrated the impact of the co-pyrolysis between PS and SD on the pyrolysis products. Figures. A, B, and C from Fig. 4 indicated that there is a PSE or NSE that confirms the presence of a new distribution in the content of the co-pyrolysis outcomes, which differs from the individual pyrolysis products of each material.

The SE is determined by comparing the actual experimental values of the co-pyrolysis product outputs with the expected theoretical values, Eq.1 is used to know the theoretical expected value, while the Eq.2 represents the extent of the impact of the joint decomposition process, if it is positive, it indicates an increase in the product yield than expected, and if it is negative, it indicates a decrease in the percentage of the product, and there are no differences indicating that the product resulting from the co pyrolysis is not affected.

$$X_{cal} = M_{SD}Y_{SD} + M_{PS}Y_{PS} \tag{1}$$

M_{SD}, M_{PS} = relative mass.

Y_{SD}/ Y_{PS} = oil yield.

$$\Delta Y = X_{exp} - X_{cal}. \text{ (Synergistic effect)} \tag{2}$$

Figure 4.A presented the effect of co-pyrolysis on bio-oil production. The data analysis concluded that all blends of PS/SD exhibited a PSE. Among the blends, 20PSSD blend achieved the highest PSE (+11.54) according to the table 2. The PSE decreases as the concentration of PS in the blend increases. This can be explained by the potential occurrence of internal interactions between PS and SD molecules, particularly when there is a larger proportion of SD biomass and a smaller percentage of PS present.

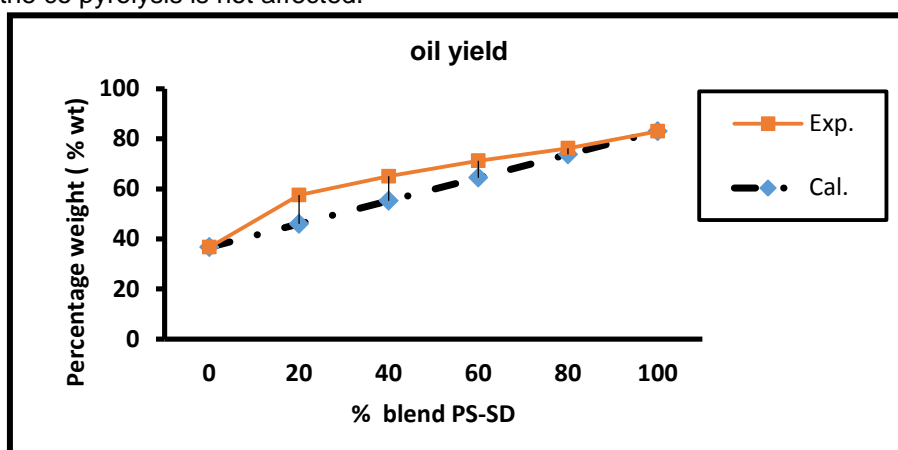


Figure 4A. Effect co-pyrolysis on bio-oil yield

Slika 4A. Efekat ko-pirolize na prinos bio-ulja

The SE of the char was evaluated in Fig. 4-B. The data showed that the PSE of all blends on the char yield resulting from the co-pyrolysis, but this effect is not noticeable, and the laboratory results are very close to the expected results.

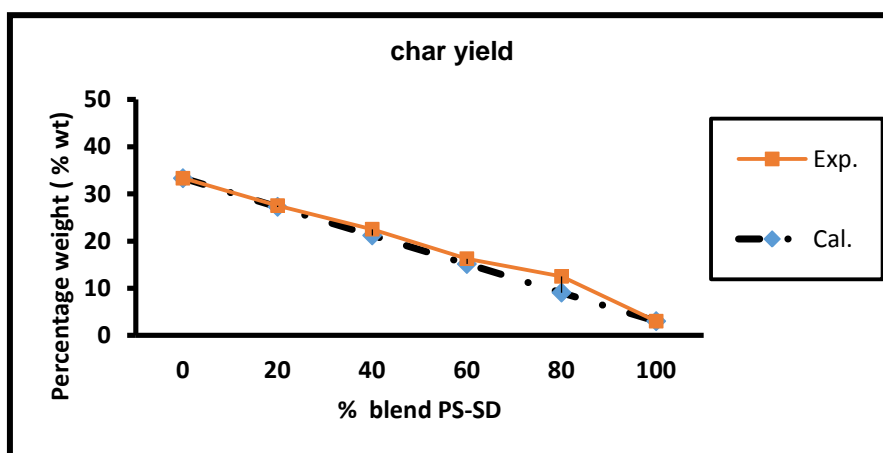


Figure 4B. Effect co-pyrolysis on bio-char yield

Slika 4B. Uticaj ko-pirolize na prinos bio-uglja

This indicates that the effect of PSSD co-pyrolysis on char production is limited to the amount of char produced from the pyrolysis of each individual. The greatest PSE (+3.44) was achieved with an 80PSSD blend.

Figure 4.C illustrates the effect of co-pyrolysis on the non-condensate gas content. It can be inferred from the presented data that the gas content exhibits a noticeable NSE on all blends. The 20PSSD blend demonstrates the highest NSE compared to the other blends. This can be

attributed to the high hydrogen content in the PS component. Consequently, when a certain quantity of PS is present in the SD biomass, it causes the condensation of some gas molecules, resulting in a decrease in the gas outcome and an increase in the bio-oil yield. As the concentration of PS in the mixture increases, the NSE decreases. This decrease could be attributed to the insufficient amount of biomass pyrolysis gases, leading to a reduction in gas condensation.

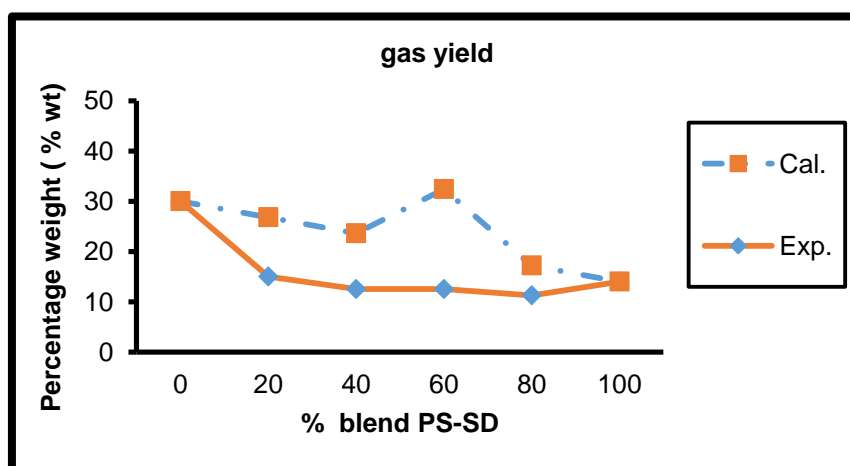


Figure 4C. Effect co-pyrolysis on bio-gas yield

Slika 4C. Efekat ko-pirolize na prinos biogasa

Table 2. Synergistic effect co-pyrolysis PS-SD outcome

Tabela 2. Sinergijski efekat ko-pirolize PS-SD ishod

Feed stock	Oil			char			gas		
	Cal.	Exp.	effect	Cal.	Exp.	effect	Cal.	Exp.	effect
SD	36.7	36.7	0	33.3	33.3	0	30	30	0
20PSSD	45.96	57.5	+11.54	27.24	27.5	+0.26	26.8	15	-11.8
40PSSD	55.22	65	+9.78	21.18	22.5	+1.32	23.6	12.5	-11.1
60PSSD	64.48	71.25	+6.77	15.12	16.25	+1.13	32.4	12.5	-19.9
80PSSD	73.74	76.25	+2.51	9.06	12.5	+3.44	17.2	11.25	-5.95
PS	83	83	0	3	3	0	14	14	0

3.4. Heating values of bio oil produced

The calorific value of fuel is the thermal energy that can be obtained from the combustion of a specific quantity of fuel. Therefore, this value serves as a clear indicator of the efficiency and quality of the fuel. Fuels with high calorific values achieve effective and economical performance, manifested in increased thermal system efficiency, reduced fuel consumption, and lower harmful emissions, in contrast to fuels with low calorific values.

Three samples of bio-oil resulting from the thermal pyrolysis of mixtures SD, 20PSSD, and PS were analyzed to determine their high heating value (HHV). The values obtained were 17.3, 22.5, and 39.5 MJ/kg, respectively. The samples were analyzed at the petroleum refining facility of Badr Company in Egypt. The decrease in HHV of SD bio-oil is attributed to an increase in moisture content and a decrease in the carbon and hydrogen ratio, in contrast to the HHV of PS bio-oil [18]. This explains the increase in HHV with an increasing proportion of PS in the co-pyrolysis blend.

4. CONCLUSION

The study emphasized the significance of co-pyrolysis of biomass and plastics in enhancing both the quantity and quality of the biofuel produced. The subsequent conclusion was derived based on the study's findings.

- 1 - co pyrolysis PS and SD biomass had a positive impact on the quantity and quality of the bio-oil produced by increasing the oil content and enhancing its thermal efficiency.
- 2 - 20PSSD blend recorded the largest PSE in obtaining bio-oil, exceeding expectations compared to other blends. Despite having PSE as well, the same blend had the largest NSE on the quantity of gas produced. On the other hand, there was an observed stability in the char content in terms of its SE.
- 3 - Co pyrolysis had PSE for both char and bio-oil, resulting in the blend 40PSSB having the largest PSE on the char content, while the blend 20PSSB had the largest PSE on the oil yield. Conversely, all blends exhibited NSE on bio-gas productivity, with the blend 20PSSB recording the largest NSE on gas production compared to the other blends.

Last but not least, researchers' efforts to further control the factors affecting the pyrolysis process are still ongoing, in order to achieve a larger quantity and better quality of bio-oil.

5. REFERENCES

- [1] E.Abokyi, P.Appiah, F.Abokyi, E.F.Oteng (2019) Industrial growth and emissions of CO₂ in Ghana: the role of financial development and fossil fuel consumption, *Energy Reports*, 5, 1339 – 1353. <https://doi.org/10.1016/j.egy.2019.09.002>.
- [2] A.Foley, Ab.Ghani Olabi (2017) Renewable energy technology developments, trends and policy implications that can underpin the drive for global climate change, *Renewable and Sustainable Energy Reviews*, 68(2), 1112-1114. <https://doi.org/10.1016/j.rser.2016.12.065>.
- [3] A.H.Zulkafli, H.Hassan, M.Ahmad, A.Mohd Din, S. Wasli (2023) Co-pyrolysis of biomass and waste plastics for production of chemicals and liquid fuel: A review on the role of plastics and catalyst types, *Arabian Journal of Chemistry*, 16, 104389. <https://doi.org/10.1016/j.arabjc.2022.104389>.
- [4] Jh.M.Aberilla, Al.Gallego-Schmid, Ad.Azapagic (2019) Environmental sustainability of small-scale biomass power technologies for agricultural communities in developing countries, *Renewable Energy*, 141, 493-506. <https://doi.org/10.1016/j.renene.2019.04.036>.
- [5] H.Hassan, J.K.Lim, B.Hameed (2016) Recent progress on biomass co-pyrolysis conversion into high-quality bio-oil. *Bioresour Technol.*, 221, 645-655. <https://doi.org/10.1016/j.biortech.2016.09.026>.
- [6] P.M.Gvero, S.Papuga, I.Mujanić, S.Vasković (2016) Pyrolysis as a key process in biomass combustion and thermochemical conversion, *Therm. Sci.*, 20(4), 1209–1222. <https://doi.org/10.2298/TSCI151129154G>.
- [7] M.Ch.Chiong, Ch.T.Chong, Jo-Han Ng, Su.Sh. Lam, M-Vu Tran, W. W. F. Chong, M. N. M. Jaafar, A. Valera-Medina (2018) Liquid biofuels production and emissions performance in gas turbines: A review, *Energy Conversion and Management*, 173, 640-658. <https://doi.org/10.1016/j.enconman.2018.07.082>.
- [8] E.E.Kwon, J.I.Oh, K.H.Kim (2015) Polycyclic aromatic hydrocarbons (PAHs) and volatile organic compounds (VOCs) mitigation in the pyrolysis process of waste tires using CO₂ as a reaction medium, *J. Environ. Manage.*, 160, 306–311. <https://doi.org/10.1016/j.jenvman.2015.06.033>.
- [9] J.Chatopadhyay, T.S.Pathak, R.Srivastava, A.C. Singh (2016) Catalytic co-pyrolysis of paper biomass and plastic mixtures (HDPE (high density polyethylene), PP (polypropylene) and PET (polyethylene terephthalate)) and product analysis, *Energy*, 103, 513– 521. <https://doi.org/10.1016/j.energy.2016.03.015>.
- [10] H.Stančin, M.Šafář, J.Růžičková, H.Mikulčić, H. Raclavská, X.Wang, N.Duić (2021) Co-pyrolysis and synergistic effect analysis of biomass sawdust and polystyrene mixtures for production of high-quality bio-oils, *Process Safety and Environmental Protection*, 145, 1-11. <https://doi.org/10.1016/j.psep.2020.07.023>.
- [11] N.Déparrois, P.Singh, K.G.Burra, A.K.Gupta (2019) Syngas production from co-pyrolysis and co-gasification of polystyrene and paper with CO₂, *Appl Energy*, 246, 1–10. <https://doi.org/10.1016/j.apenergy.2019.04.013>.
- [12] B.Muneer, M.Zeeshan, S.Qaisar, M.Razzaq, H. Iftikhar (2019) Influence of in-situ and ex-situ HZSM-5 catalyst on co-pyrolysis of corn stalk and polystyrene with a focus on liquid yield and quality, *J Clean Prod*, 237, 117762. <https://doi.org/10.1016/j.jclepro.2019.117762>.
- [13] O.Sanahuja-Parejo, A.Veses, M.V.Navarro, J.M. López, R.Murillo, M.S.Callén (2019) Drop-in biofuels from the co-pyrolysis of grape seeds and polystyrene, *Chem Eng J*, 377, 120246. <https://doi.org/10.1016/j.cej.2018.10.183>.
- [14] K.P.Shadangi, K.Mohanty (2015) Co-pyrolysis of Karanja and Niger seeds with waste polystyrene to produce liquid fuel, *Fuel*, 153, 492–8. <https://doi.org/10.1016/j.fuel.2015.03.017>.
- [15] D.Watkins, M.Nuruddin, M.Hosur, A.T.Narteh, S. Jeelani (2015) Extraction and characterization of lignin from different biomass resources, *Journal of Materials Research and Technology*, 4(1), 26-32. <https://doi.org/10.1016/j.jmrt.2014.10.009>.
- [16] Z.Xiao, S.Wang, M.Luo, J.Cai (2022) Combustion characteristics and synergistic effects during co-combustion of lignite and lignocellulosic components under oxy-fuel condition, *Fuel*, 310, Part B, 122399. <https://doi.org/10.1016/j.fuel.2021.122399>.

- [17] S.D.Anuar Sharuddin, F.Abnisa, W.M.A.W.Daud, M. Kheir eddine Aroua (2016) A review on pyrolysis of plastic wastes, Energy Conversion and Management, 115, 308–326. <http://dx.doi.org/10.1016/j.enconman.2016.02.037>.
- [18] Q.V.Nguyen, Y.S.Choi, S.K.Choi, Y.W.Jeong, Y.Su Kwon (2019) Improvement of bio-crude oil properties via co-pyrolysis of pine sawdust and waste polystyrene foam, Journal of Environmental Management, 237, 24-29. <https://doi.org/10.1016/j.jenvman.2019.02.039>.

IZVOD

PROCENA EFEKTA MEŠANJA POLISTIRENA (PS) SA PILJEVINOM (SD) NA PROIZVODE OD KOPIROLIZE

Proces kopirolize između biomase i čvrstog otpada, posebno plastike, privukao je značajnu pažnju u istraživačkim studijama kao sredstvo za poboljšanje i količine i kvaliteta bio-ulja dobijenog razgradnjom biomase. U ovom istraživačkom radu, PS/SD ko-piroliza je sprovedena za šest različitih koncentracija u rasponu od 0% do 100%, sa povećanjem od 20% PS, unutar malog laboratorijskog reaktora na 450 °C i brzini zagrevanja (HR) od 20,5 °C min⁻¹. Rezultati su pokazali da je povećanje udela PS u mešavini rezultiralo većim ishodom bio-ulja. Najveći prinos bio-ulja zabeležen je kod mešavine 80PSSD, što ukazuje da je kopiroliza imala pozitivan efekat na proizvodnju ulja u svim mešama. Najznačajniji pozitivan uticaj primećen je kod mešavine 20PSSD, dostižući [+11,54]. Suprotno tome, proizvodnja gasa je pokazala negativan efekat, sa količinama gasa manjim od očekivanih za sve meše, a najznačajniji negativan uticaj je bio na 20PSSD, uz smanjenje od [-11,8]. Što se tiče ishoda ugljenika, došlo je do minimalnog povećanja njegove količine, sa najvećim pozitivnim uticajem drvenog uglja zabeležen na 80PSSD, koji je dostigao [+3,44]. Shodno tome, može se primetiti da na količinu proizvedenog ugljenika ne utiče značajno proces zajedničkog mešanja.

Ključne reči: PS plastika, biomasa, piljevina, kopiroliza, bio-ulje

Naučni rad

Rad primljen: 30.09.2023.

Rad korigovan: 25.12.2023.

Rad prihvaćen: 11.01.2024.

Rad je dostupan na sajtu: www.idk.org.rs/casopis

Gayathri Thangavel*, Kavitha Balakrishnan,
Nirmala Murugesan

Department of Physics, Sri GVG Visalakshi College for Women,
Udumalpet, India

Scientific paper

ISSN 0351-9465, E-ISSN 2466-2585

<https://doi.org/10.62638/ZasMat1120>



Zastita Materijala 65 (2)
315 - 330 (2024)

NiO/MnO₂ nanocomposite in addition of layered Reduced Graphene Oxide (RGO) electrode for accountable supercapacitor application

ABSTRACT

(Reduced Graphene oxide/Nickel oxide/Magnesium dioxide) RGO/NiO/MnO₂ nanocomposite electrode was successfully prepared by simple co-precipitation method. The synthesised nanocomposite was characterised by XRD, FESEM, EDAX, FTIR, UV, CV, GCD, EIS. The RGO/NiO/MnO₂ nanocomposite was pretreated by ultrasonication, followed by thermal annealing at 350 °C. The crystalline face and size of nanocomposite were analysed by X-Ray Diffraction (XRD). The sandwich-like structure of RGO/NiO/MnO₂ was analysed by Scanning Electron Microscope (SEM). This structure promoted an efficient contact between electrolyte and active materials, and the distinct architecture could offer fast transfer channels of ion and electrons. The nanocomposite exhibited high conductivity owing to the presence of RGO. The electrochemical performance of prepared nanocomposite was done by Cyclic Voltammetry (CV), Galvanostatic charge discharge (GCD), Electrical Impedance Spectroscopy (EIS). The synthesised RGO/NiO/MnO₂ nanocomposite acquired high specific capacitance of 1167F/g at current density of 1 A/g. The low cost, low temperature RGO/NiO/MnO₂ nanocomposite electrode could be the promising electrode for Energy storage devices.

Keywords: Reduced Graphene Oxide (RGO), NiO/MnO₂ nanocomposite, pseudo-capacitor, cyclic voltammograms, Supercapacitor

1. INTRODUCTION

Supercapacitors have been in the limelight as a sort of energy storage technology among research groups and business for several decades. However, ongoing advancements in electrode development and manufacture are crucial for producing a low-cost supercapacitor with acceptable electrochemical properties [1]. Due to their high-power densities, large specific capacitance, rapid charge-discharge times, long cycle life, and hygienic electrochemical energy storage, supercapacitors (SCs) are the best solution for energy storage technology [2]. Consequently, it is widely stated that improving the electrochemical performance of supercapacitors may be achieved by material synthesis through sustainable synthesis and fabrication methodologies, specifically by changing the structure of the

electrode's active components [3]. Electrochemical double-layer capacitors (EDLCs) are made of carbon-based materials (graphene oxide, carbon nanotubes, etc.), but conducting polymers, metal oxides, metal sulphides and conducting polymers are employed in the construction of battery-and/or pseudo capacitive-type cells [4].

Metal oxides like NiO and MnO₂ are among the active materials utilized in pseudo capacitive and/or battery-type applications that are being thoroughly studied and analysed because of their higher chemical stability and eco-friendliness. The composition of these metal oxide-based nanomaterials may offer more active sites and a synergistic effect for improved electrochemical processes [5]. Several attempts have been reported in this context, especially with regard to the synthesis of metal oxide nanostructures. In order to reduce ionic/electronic resistance and shorten ion diffusion paths between the electrode and the electrolyte surface, metal oxides and their nanoscale morphologies are also utilized [6]. When creating pseudo-capacitors, a variety of transition metal oxide nanostructures, including MnO₂, CO₃O₄, V₂O₅, SnO₂, and NiO, are frequently

*Corresponding author: Gayathri Thangavel

E-mail: gayathrithangavel18@gmail.com

Paper received: 03. 12. 2023.

Paper corrected: 14.01. 2024,

Paper accepted: 16. 01. 2024.

Paper is available on the website: www.idk.org.rs/journal

utilized as electrode materials. Because of its appealing qualities, including its relative abundance, low cost, strong redox property, large electrochemical surface area, high specific capacitance value, and ease of production, nickel oxide (NiO) can be chosen as an appropriate electrode material among these [7].

NiO's high resistance in electrochemical capacitors is its primary disadvantage. Using highly conductive carbonaceous materials like RGO, graphene, and CNTs can help with this high resistivity issue. Here, by decreasing carbon nanostructure agglomeration and restacking, NiO nanostructures serve as a spacer between various carbon nanostructures and enhance the electrochemical surface area for redox reaction [8]. As a result, the two-dimensional (2D) structure with sp² hybridized carbon atoms, such as RGO, is an attractive choice due to its high conductivity, large specific surface area, and robust cycle stability, which can minimize the resistivity of NiO nanoflakes. Many researchers have created RGO-based nanocomposite materials that increase the electrochemical performance of supercapacitors [9]. The development of sophisticated materials with high capacitance and rate capacity is essential to achieve the aforesaid design. Complementary benefits are often produced by a composite that is constructed with the appropriate mix of two components [10]. Everyone knows that because of its high theoretical specific capacitance, huge specific surface area, and extraordinarily high electrical conductivity, reduced graphene oxide (RGO) is one of the most promising electrode materials for EDLCs. When appropriately included into the composite, RGO improves the electrode's structural stability in addition to the composite's electrical conductivity. Consequently, using reduced graphene oxide as a framework is a useful strategy for enhancing the composites' mechanical strengths [11].

Alsaieri et al., reported ZnO/NiO produced specific capacity of 350 F/g was found at 2 A/g current while the lowest specific capacity of 217 F/g was measured at 20 A/g [12]. Mohammad Shariq et al., synthesised nanocomposites of (Co₃O₄/NiO), the specific capacitance of which was 2769.2 F/g at 5 mV/s [13]. Geerthana Mummoorthi et al., researched that the ternary composite α-Fe₂O₃/NiO/rGO has shown a specific capacitance of 747 F/g@ a current density of 1 A /g in a 6 M KOH [14]. Qi An et al., prepared NiO-rGO, NiO nanoparticles uniformly distributed in rGO to achieve a high specific capacity at current density of 0.5 A /g[15]. O. C. Pore et al., synthesised NiO/rGO composite achieved the highest specific capacitance of 727.1 F/g at 1 mA cm⁻² current density and showed good cyclic stability of about 80.4% over 9000 cycles[16]. S. Seenivasan et al., notably, NiO@MnO₂@rGO modified structure exhibited excellent conductivity due to the presence of rGO, demonstrating a high charge storage capacity of 536 F/g at a current density of 1 A/g[17].

RGO (Reduced Graphene Oxide) is effectively integrated in NiO/MnO₂ nanocomposites to make better composites. The co-precipitation approach were used successfully to synthesize the RGO/NiO/MnO₂ composite.

2. EXPERIMENTAL METHOD

2.1. Preparation of RGO/NiO nanocomposite

For preparation of RGO/NiO nanocomposite, 0.01 g of commercially available RGO and 0.1 M of Nickel Nitrate hexahydrate (Ni(NO₃)₂·6 H₂O) was taken in 100 ml of deionized water and sonicated for 30 minutes. Then both the solutions were stirred for 2 hours. The pH was then gradually raised to 9 by adding 0.1M of sodium hydroxide (NaOH). After that, the particles were centrifuged with ethanol and deionized water. The particle was first dried for six hours at 100°C in an oven, and then it was calcined for 2 hours at 350°C.



Figure 1. Schematic representation of synthesis procedure of RGO/NiO/MnO₂ nanocomposite

Slika 1. Šematski prikaz postupka sinteze RGO/NiO/MnO₂ nanokompozita

2.2. Preparation of RGO/NiO/MnO₂ nanocomposite

To prepare the RGO/NiO/MnO₂ Nanocomposite, 0.01 g of RGO, 0.1M Nickel Nitrate hexahydrate Ni (NO₃)₂·6 H₂O and 0.1M of Manganese acetate tetrahydrate (CH₃COO)₂Mn 4H₂O were dissolved in 100 ml of deionised water. Then the solution were sonicated for 30 minutes and stirred for 2 hours. Following that, 0.1 M of Sodium hydroxide (NaOH) was added drop by drop until the pH reached 9. After that, the particle was centrifuged in deionized water and ethanol. The particle was dried in a 150°C oven for 6 hours before being calcinated in muffle furnace at 350°C for 2 hours.

2.3. Characterization

A Shimadzu X-ray diffractometer (D8 ADVANCE) with a vertical goniometer fitted with vanadium filter and copper radiation (CuK α λ =1.54 Å) with a step size of 1.01° was used for the structural analysis of the synthesised nanoparticles. FTIR spectrophotometer, (JASCO) FTIR spectrometer model FT/IR- 4600 series) ranging 500 cm⁻¹ to 4000 cm⁻¹ was used to determine chemical bonding and functional group present in the synthesised nanoparticles. The Morphological characterization of the synthesized NiO was studied using (Jeol 6390LV) for Scanning Electron Microscopy (SEM) analysis. A JASCO V-770UV double beam spectrophotometer was used for optical studies in the wavelength range 400-2500nm.

2.4. Electrochemical Measurements

The Electrochemical analyses such as cyclic voltammetry, electrochemical impedance, and galvanostatic charge–discharge (GCD) measurements were carried out using an electrochemical

workstation (Metrohm AutolabM204) with potential window of -0.1 to +0.5 at room temperature. The electrochemical analysis has been done with three electrode system, specifically, Nickel foam (substrate) was used as a working electrode, Ag/AgCl as reference electrode and Platinum electrode (Pt) electrode as counter electrode.

2.5. Fabrication of Electrode Material

Preparation of working electrode. RGO, RGO/NiO, RGO/NiO/MnO₂ coated Ni foam, Ag/AgCl, and platinum were used as working, reference, and counter electrode in a three-electrode cell system. All electrochemical studies were carried out in presence of 1 M KOH as electrolyte at room atmosphere. The working electrode was prepared by uniform mixing of NiO nanoparticles (75 wt%), acetylene black (15 wt%), and polyvinylidene difluoride (PVDF) (10 wt%) in 1-methyl-2- pyrrolidinone (solvent) under sonication to obtain slurry. An adequate amount of slurry was used to deposit on Ni foam with coating area of 1×1 cm². Before this process, Ni foam was washed with acid, detergent, ethanol, and deionized water to remove all surface impurities [18]

3. DISCUSSIONS AND FINDINGS

3.1. XRD Analysis

The prepared nanocomposite was investigated by XRD to evaluate the diffraction pattern and crystalline structure of synthesised nanocomposite. The XRD patterns of (a) RGO, (b) RGO/NiO, and (c) RGO/NiO/MnO₂ nanocomposite are shown in Figure 2. From the XRD diffraction pattern (curve a in Figure 2) the identifying peaks for prepared nanocomposites are at $2\theta=26.6^\circ$ and 44.0° corresponding to (002), (100), the pattern of RGO corresponded to carbon peaks [19-22].

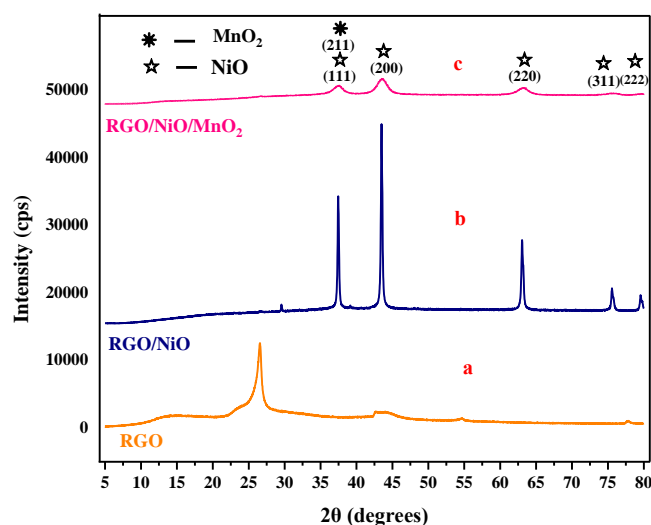


Figure 2. XRD diffractograms of (a) RGO, (b) RGO/NiO, (c) RGO/NiO/MnO₂ nanocomposite

Slika 2. XRD difraktogrami (a) RGO, (b) RGO/NiO, (c) RGO/NiO/MnO₂ nanokompozita

Observed peak position for the RGO/NiO nanocomposite (curve b in Figure 2) with 2θ values of 37.45°, 43.437°, 63.05°, 75.56° and 79.52° were indexed on the (111), (200), (220), (311) and (222) NiO crystal planes, respectively (JCPDS Sheet No. 78- 0429) [23]. The absence of additional peaks in the XRD spectrum indicates the purity of the synthesized nanocomposite. No peaks were found at about 26°, indicating that all graphite powder was oxidized and that the RGO was free of impurities or unreacted graphite [24]. All diffraction peaks were assigned to the centered cubic phase of NiO (FCC), with the lattice constant “a” calculated to be average 4.1634 Å [25].

From (curve c in Figure 2 RGO/NiO/MnO₂ nanocomposite's XRD peaks with 2θ values of 37.45°, 43.54°, 63.15°, 75.64° and 79.58° were indexed to (111) and (211), (200), (220), (311) and (222) respectively [26-28]. When compared to (curve b in Figure 2) the peak's intensity (reduction in height down the y axis) and width both decreased in (curve c in Figure 2.) [29-33]. This confirmed the development of the NiO, MnO₂, and RGO nanocomposite successfully. And as strain and dislocation density increase, crystalline size decreases [34, 35]. Structural parameters of synthesised RGO, RGO/NiO, RGO/NiO/MnO₂ nanocomposites are calculated using below formulas (1-4) [36] and its structural parameters listed in table 1.

From the observed ‘d’ spacing and (hkl) planes the lattice constant is evaluated using the relation

$$d = \frac{a}{\sqrt{h^2 + k^2 + l^2}} \quad (1)$$

Where

d — interplanar spacing, and a — lattice constant, (hkl planes). From the observed ‘d’ spacing various structural parameters such as lattice constant, crystalline size, dislocation density and strain have been estimated using the expressions,

The crystalline size of nanoparticles is determined using Debye Scherrer’ relation.

$$D = \frac{K\lambda}{\beta \cos \theta} \quad (2)$$

Where

β is the full width half- maximum value of the high intensity peak, θ is Bragg’s angle, K is the shape factor ($K= 0.94$) and λ is the wavelength (1.54 Å°) of the X-ray source used in the XRD. The crystal structure of the samples is FCC.

The dislocation density (δ) can be calculated using the equation

$$\delta = \frac{1}{D^2} \quad (3)$$

The micro strain (ϵ) can be calculated using the equation

$$\epsilon = \frac{\beta \cos \theta}{4} \quad (4)$$

Table.1. Structural parameters of synthesised RGO, RGO/NiO, RGO/NiO/MnO₂ nanocomposites

Tabela 1. Strukturni parametri sintetizovanih RGO, RGO/NiO, RGO/NiO/MnO₂ nanokompozita

Composite	2θ values (deg)	hkl	Crystalline size D (nm)	d value	Lattice constant a (Å)	Micro-strain (ϵ) 10^3	Dislocation density (δ) 10^{15}L/m^2
RGO	26.32	(002)	3.90	3.0775	-	-	-
RGO/NiO	37.46	(111)	27.4261	2.3991	4.155	2.4845	0.0364
	43.49	(200)	25.7554	2.0794	4.158	2.8801	0.0388
	62.05	(220)	17.1699	1.4733	4.171	5.4945	0.0582
	75.62	(311)	12.7043	1.2565	4.165	11.6322	0.0787
	79.61	(222)	12.1251	1.2033	4.168	14.8890	0.0824
			Average=19.0362			Average=4.1634	
RGO/NiO/MnO ₂	37.45	(111) and (211)	4.1450	2.3997	4.156	17.0634	0.2412
	43.54	(200)	4.1806	2.0768	4.154	19.2870	0.2425
	63.15	(220)	3.9405	1.4710	4.160	27.2288	0.2537
	75.64	(311)	3.8884	1.2561	4.166	30.6474	0.2571
	79.58	(222)	11.100	1.2036	4.173	10.9880	0.0901
			Average=5.4509			Average=4.1618	

3.2. FT-IR spectroscopy

Figure 3. displays FT-IR spectra of the RGO, RGO/NiO, and RGO/NiO/MnO₂ nanocomposite materials. The transmission maxima found in the electromagnetic spectrum between 400 and 4000 cm⁻¹ wave numbers. From (curve a in Fig.3) for RGO the C=O stretching vibrations are a result of the 1741.41 cm⁻¹ peak. Stretching of the C-O and O-H bonds is shown by the peak at 1369.21 cm⁻¹ in the carboxylic group, whereas stretching of the C-O-C bonds is indicated by the peak at 1221.68 cm⁻¹

in the epoxy group [37]. In RGO/NiO nanocomposite (curve b in Figure 3), the peaks at 444 cm⁻¹ and 673.99 cm⁻¹ are associated with Ni-O stretching vibrations, confirmed that NiO nanoparticles were present in RGO [38]. In (curve c in Figure 3) RGO/NiO/MnO₂ two distinct bands at 433 cm⁻¹ and 532 cm⁻¹ confirm the creation and formation of the MnO₂/NiO nanocomposite. It is also observed that the peak intensity is significantly lower in (curve c in Fig .3) than in (curve b in Figure 3) [39].

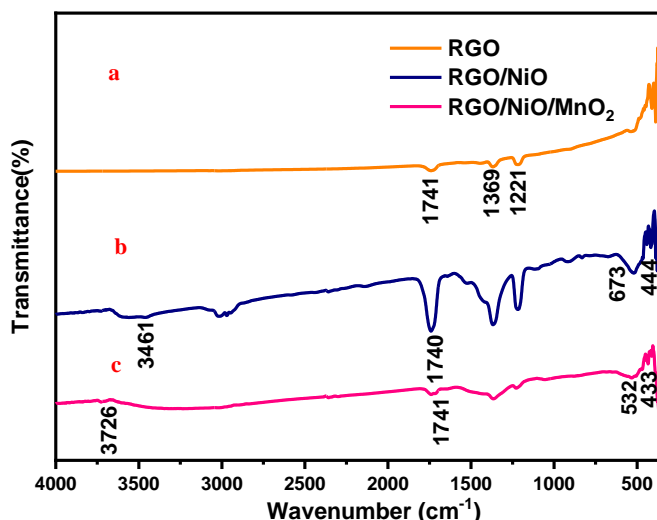


Figure 3. FT-IR spectra of (a) RGO, (b) RGO/NiO, (c) RGO/NiO/MnO₂ nanocomposite
 Slika 3. FT-IR spektri (a) RGO, (b) RGO/NiO, (c) RGO/NiO/MnO₂ nanokompozita

3.3. UV-Vis spectroscopy

The optical bandgap energy was estimated from the UV-Vis spectrum using the following (5)

$$\alpha = A(E_g - h\nu)^n / h\nu \tag{5}$$

For a straight transition, n equals 2, A is a constant, E_g is the bandgap, and α is the absorption coefficient. The bandgap was determined using a plot of (αhν)² vs photon energy (αhν). The UV-visible absorption spectra of RGO, RGO/NiO, and RGO/NiO/MnO₂ are shown in Fig. 4. The intercept of the tangent (tauc plot) to the figure best approximates the bandgap energy for this direct bandgap in Fig. 5. From (curve a in fig .4) displays the RGO absorbance spectrum, which has only one peak at a wavelength of 268 nm and peak has a π-π* transitional orbital correlation [40]. When the wavelength is longer, the absorbance is constant and resembles pure monolayer graphene. Around (curve a in Fig.5) depicts the tauc plot of the RGO and reveals that the bandgap is 3.25 eV.

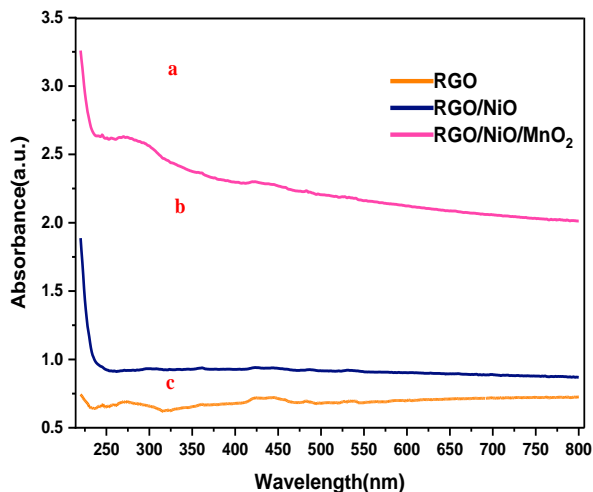


Figure 4. UV-vis absorption spectra of (a) RGO, (b) RGO/NiO, (c) RGO/NiO/MnO₂ nanocomposite
 Slika 4. UV-vis apsorpcioni spektri (a) RGO, (b) RGO/NiO, (c) RGO/NiO/MnO₂ nanokompozita

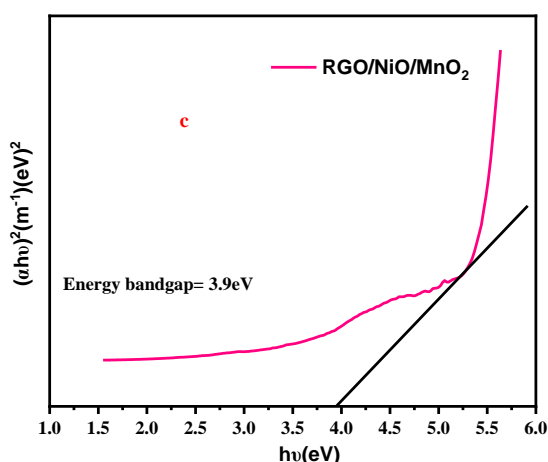
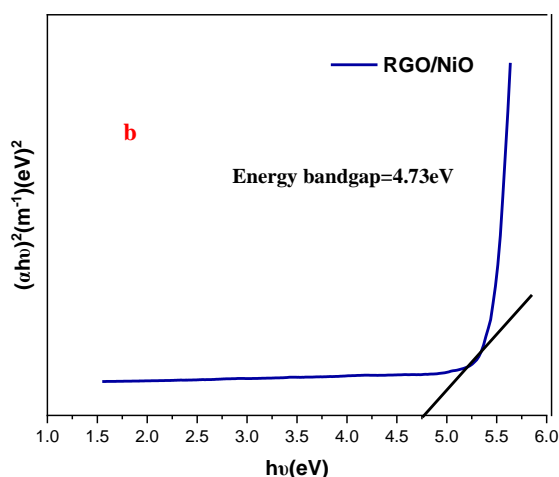
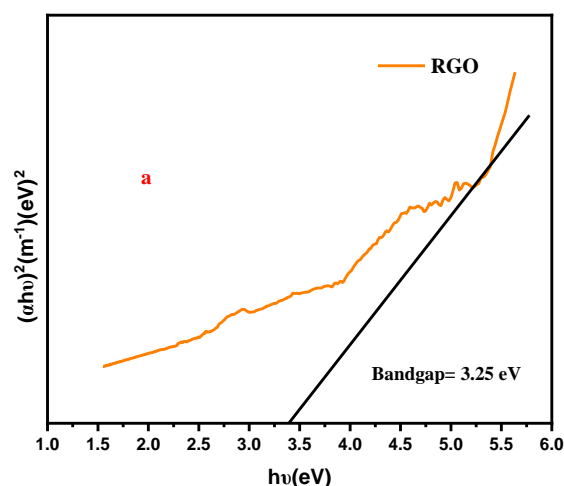


Figure 5. Method for calculating band gap energy (E_g) from the Tauc plot. (a) RGO, (b) RGO/NiO, (c) RGO/NiO/MnO₂ nanocomposite

Slika 5. Metoda za izračunavanje energije širine pojasa (E_g) iz Tauc grafikona. (a) RGO, (b) RGO/NiO, (c) RGO/NiO/MnO₂ nanokompozit

The (curve b in Figure 4) shows the absorbance spectra of RGO/NiO. There was an absorption peak at around 200 nm as a result of direct stimulation of the NiO. The enhanced absorption is due to the chemically decreased material. Based on taucplot (curve b in Figure 5) the estimated bandgap of RGO/NiO was determined to be 4.73 eV [41]. The largest absorption peak is seen in (curve c in Figure 4), a blueshift (below 300 nm) with the near-visible region's (300–400 nm) peak of RGO/NiO/MnO₂ composite [42]. From (curve c in Figure 5) the bandgap of RGO/NiO/MnO₂ was determined to be 3.9 eV.

3.4. Scanning electron microscopy

The morphological investigation of the synthesized nanocomposite were studied using SEM analysis. The SEM micrographs of the RGO(a–b), RGO/NiO(c– d), and RGO/NiO/MnO₂ nanocomposites (e–f) are shown in Fig. 6. The RGO's morphology shows a collection of thin, transparent sheets separated with a layer in between each sheet. The (image a,b in Fig. 6) shows the randomly distributed waves of silk-like RGO are seen. The RGO sheets' contact resulted in a sequence of minuscule waves. RGO takes on a structure akin to a membrane fold when Van der Waal contact is present, and RGO also seems to be more transparent and squasier. [43].

In the (image c,d in Figure 6) the NiO is a non-uniform, spherical ball-like substance, and its whole structure is composed of a smooth surface measuring around 40nm. It is evident that RGO is essentially transparent and that layers of RGO work together to form a 3D network with plenty of holes in it. SEM images of the two materials compared to one another show that the surface of the RGO/NiO nanocomposite is significantly rougher than that of RGO, which can be attributable to the homogeneous distribution of NiO nanoparticles on RGO [44]. In (image e,f in Figure 6) The cross-section SEM pictures of the manufactured RGO/NiO/MnO₂, show the sandwich-like structure. NiO and RGO are incorporated in the RGO/NiO/MnO₂ nanocomposite, and the particle size is determined to be around 17 nm [45].

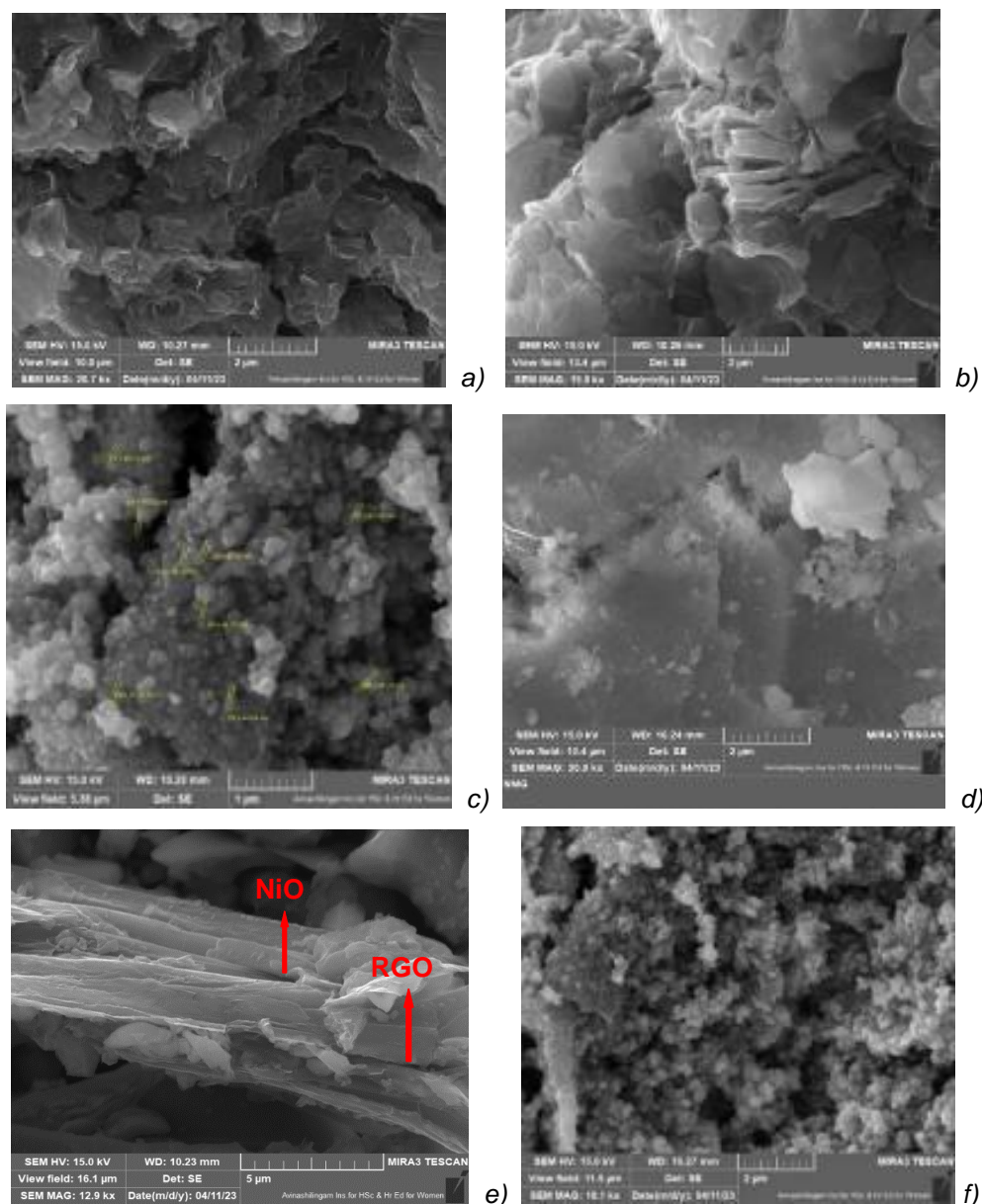


Figure 6. SEM micrographs of (a-b) RGO, (c-d) RGO/NiO, (e-f) RGO/NiO/MnO₂ nanocomposites

Slika 6. SEM mikrofotografije (a-b) RGO, (c-d) RGO/NiO, (e-f) RGO/NiO/MnO₂ nanokompozita

3.5. Energy-dispersive X-ray spectroscopy

Figure 7 represents the elemental distribution (EDAX) and mapping plots for (a) RGO, (b) RGO/NiO, and (c) RGO/NiO/MnO₂ electrodes. The Graph a in Figure 7 shows the elemental mapping and EDS spectra of RGO and reveals the presence of the elements O and C, confirming the phase purity of the material. Research on the constituent constituents of RGO confirms their existence and excludes the possibility of any impurities [46, 47].

Graph b in Figure 7 shows the EDAX and Elemental mapping of a RGO/NiO sample, which revealed the presence of C (from the RGO), O (from the NiO), and Ni (from the NiO and RGO). The sample's elemental mappings show that C, O, and Ni are all scattered in the same location, confirming the presence of the NiO/RGO nanocomposite [48]. The graph c in Figure 7 displays the EDAX and Elemental mapping of a RGO/NiO/MnO₂ sample, demonstrating the presence of Mn-7.94%, Ni-49%, C-20.81%, O-19.63%, and other elements due to environmental variables during the synthesis process [49].

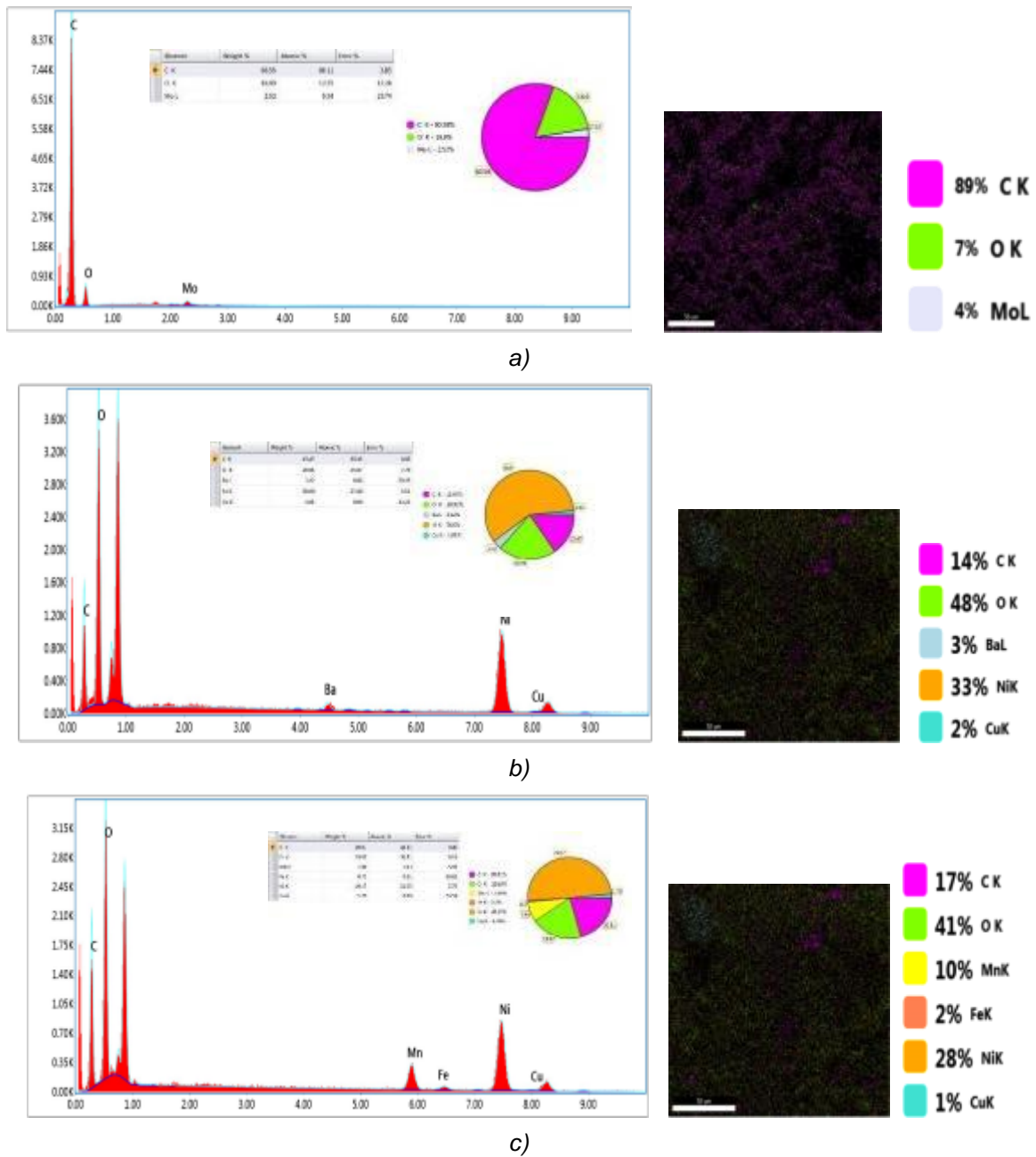


Figure 7. EDS and Elemental mapping of (a)RGO, (b)RGO/NiO, (c) RGO/NiO/MnO₂

Slika 7. EDS i elementarno mapiranje (a)RGO, (b)RGO/NiO, (c) RGO/NiO/MnO₂

4. ELECTROCHEMICAL ANALYSIS

4.1. Cyclic Voltammetry (CV)

Figure 8 depicts cyclic Voltammograms of (a) RGO, (b) RGO/NiO, and (c) RGO/NiO/MnO₂ nanoparticles. In (curve a in Figure .8) Electrochemical experiments were performed on the RGO. RGO electrode CV curves acquired at various scan rates (5, 10, 20, 30, 40, 50, 70, 80, 100, 120, 160, and 320 mV/s) in 1 M KOH electrolyte. The electrode displayed two significant

peaks on the anodic and cathodic sides, indicating typical pseudo capacitive behaviour in relation to RGO's faradaic redox reaction.

As a result of electron transport restriction, RGO on the electrode surface generated semi-irreversible behaviour. Surprisingly, the redox peaks of the RGO sample are enhanced due to lattice structures, as shown by the creation of easily reducible oxygen species, resulting in better electrocatalytic performance. Both the cathodic and anodic peak currents increased considerably [50].

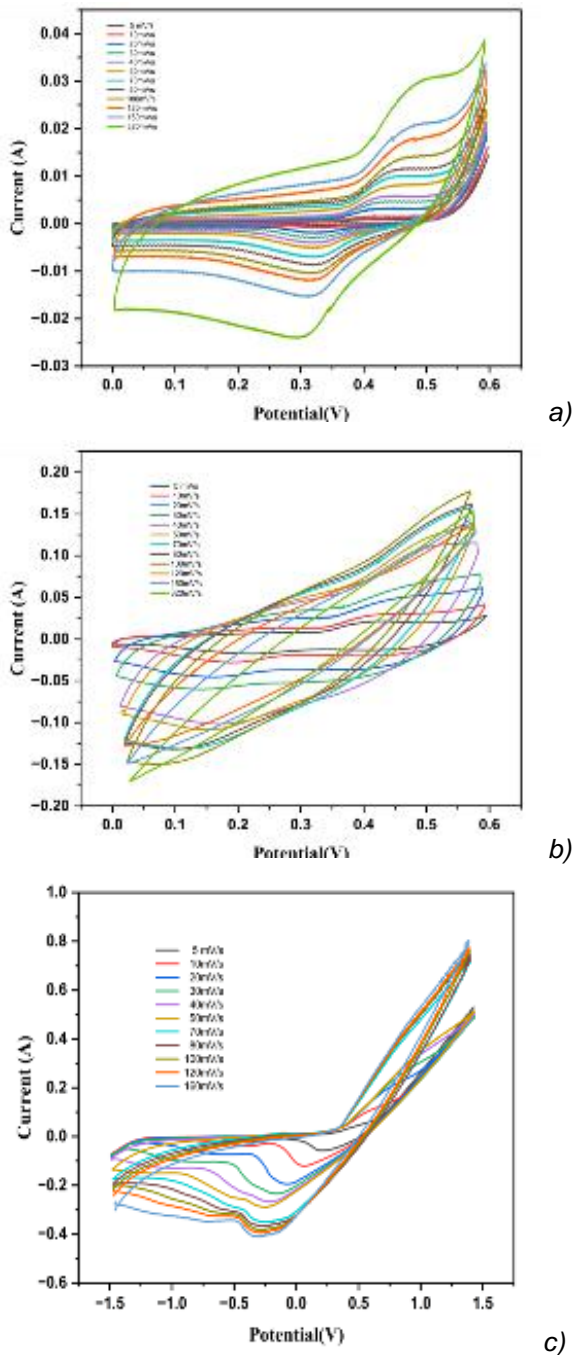


Figure 8. Cyclic Voltammograms of (a) RGO, (b) RGO/NiO, (c) RGO/NiO/MnO₂ nanoparticles.

Slika 8. Ciklični voltamogrami (a) RGO, (b) RGO/NiO, (c) RGO/NiO/MnO₂ nanočestica

In (curve b in Figure 8) two reduction peaks and one oxidation peak appear at low scan rates of (5-40mV/s), while at high scan rates of (50-320)mV/s), all curves are inclined, indicating a tremendous potential shift due to one or more types of polarizations that makes the equilibrium potential difficult to distinguish [51].

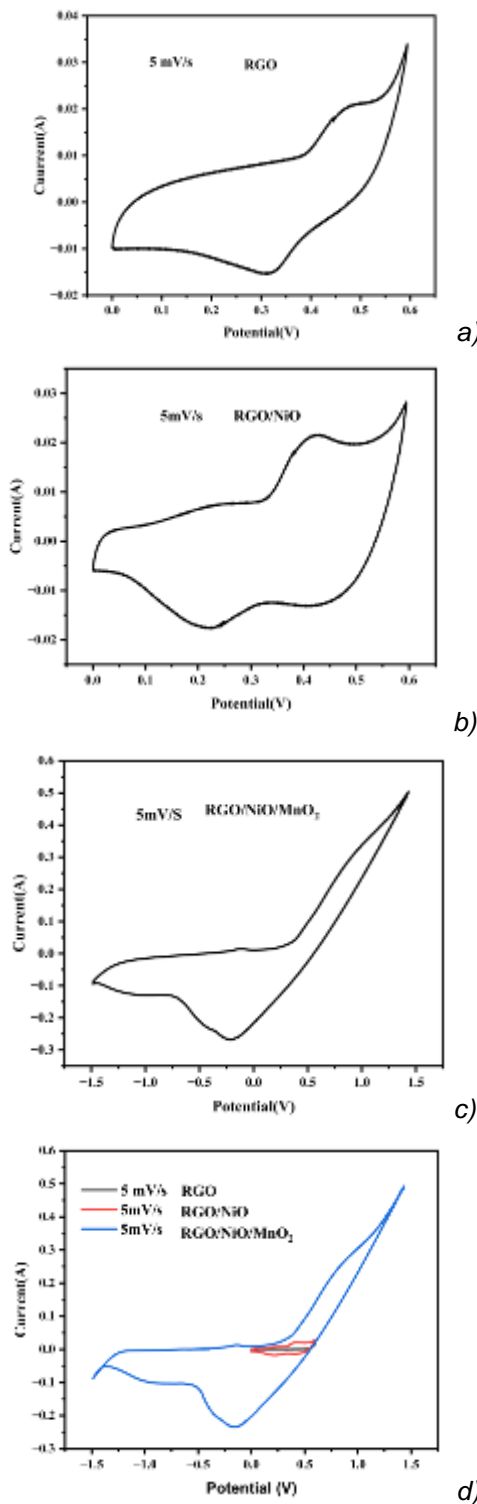


Figure 9. Shows the cyclic voltammograms at 5mV/s scan rate (a) RGO, (b) RGO/NiO, (c) RGO/NiO/MnO₂, (d) combination of RGO, RGO/NiO, RGO/NiO/MnO₂ at 5mV/s scan rate

Slika 9. Prikaz ciklične voltamogramne pri brzini skeniranja od 5mV/s (a) RGO, (b) RGO/NiO, (c) RGO/NiO/MnO₂, (d) kombinacija RGO, RGO/NiO, RGO/NiO/MnO₂ pri 5mV/s brzina skeniranja

The RGO/NiO/MnO₂ electrode's CV curve (curve c in Figure 8) clearly displays redox peaks, proving that it is a battery electrode. The peaks showed the Ni and Mn ion redox transition brought on by non-capacitive faradaic behavior. The electrolyte diffusion in the material is responsible for the redox peaks, suggesting that the RGO/NiO/MnO₂ electrode was operating like a battery. The electrode redox behavior, which was based on the Nernstian process, is described by the peak-shaped CV curves. Distinct redox peaks were seen at high scan speeds, suggesting that the working electrode had strong reversibility and a high rate of capability.

Figure 9 displays the cyclic voltammograms at 5mV/s scan rate (a) RGO, (b) RGO/NiO, (c) RGO/NiO/MnO₂, and the (curve d in Fig.9) shows the combination of RGO, RGO/NiO, and RGO/NiO/MnO₂ RGO, RGO/NiO electrodes in the 0 to 0.6 V range and RGO/NiO/MnO₂ electrodes in the -1.5to +1.5V range at a scan rate of 5 mV/s, respectively. Each curve had redox peaks. These findings showed that the capacitive process was regulated by faradaic reactions. Furthermore, the integral areas of the materials were in the order RGO < RGO/NiO < RGO/NiO/MnO₂, suggesting that the composite electrode outperformed the other electrodes in terms of capacitance performance.

4.2. Galvanostatic Charge/Discharge (GCD)

Figure 10 depicts the galvanostatic charge-discharge curves of (a) RGO, (b) RGO/NiO, and (c) RGO/NiO/MnO₂. For different current densities (1, 1.5, 2, 2.5, 3, and 3.5) at potentials ranging from -0.1 to 0.5 V in 1 M KOH electrolyte [53]. In Figure 10, the discharge time decreased as the current density increased. These semi symmetric discharge curves corroborate the pseudo capacitive nature of the a) RGO, b) RGO/NiO, and c) RGO/NiO/MnO₂ electrodes [54].

It is hypothesized that there is a redox reaction at the electrode-electrolyte interface. The specific capacitance of the a) RGO, b) RGO/NiO, and c) RGO/NiO/MnO₂ electrodes was calculated using equation (6) [55,56]. In table .2 calculated specific capacitance corresponding current densities of RGO, RGO/NiO, and RGO/NiO/MnO₂ are shown. RGO/NiO/MnO₂ show high Specific capacitance of 1167 F/g at current density 1A/g. Calculated using below Eq .6 were C_s = specific capacitance (F /g), I = (A /g) is the applied current density, Δt (s) is the discharging time, ΔV (V) is the maximum potential window to discharge the cell.

$$C_s = \frac{(1 + \Delta t)}{(\Delta V \times m)} \quad (6)$$

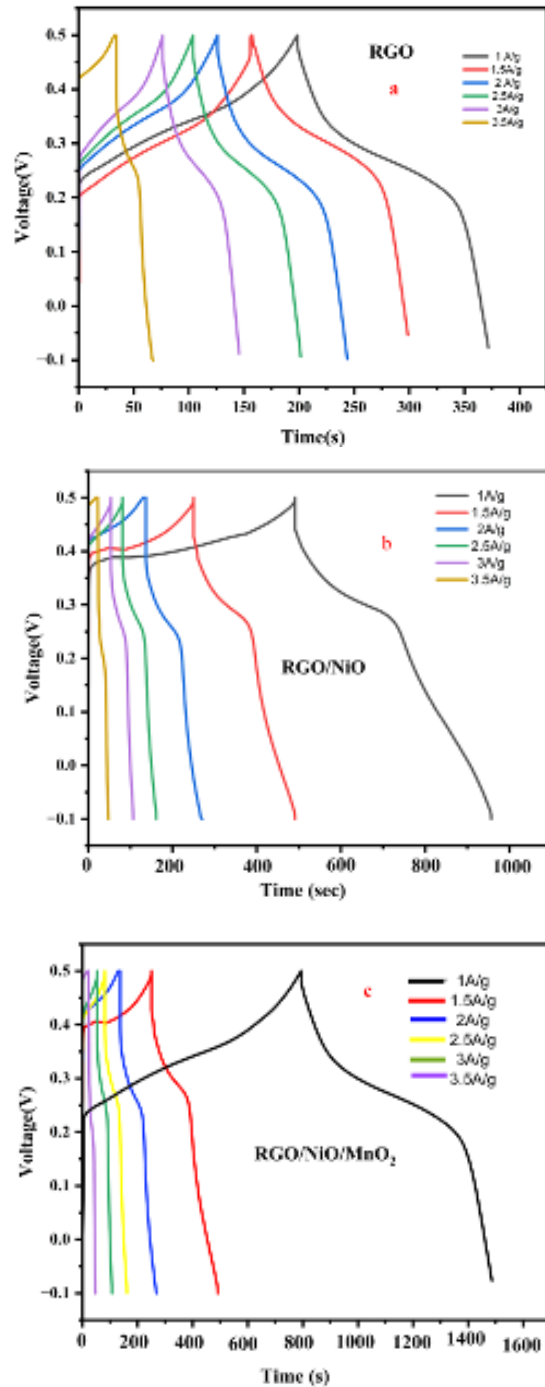


Figure 10. Galvanostatic charge/discharge of (a) RGO, (b) RGO/NiO, (c) RGO/NiO/MnO₂

Slika 10. Galvanostatsko punjenje/praznjenje (a) RGO, (b) RGO/NiO, (c) RGO/NiO/MnO₂

Figure 11 depicts the curve of specific capacitance versus discharge current densities for all electrodes. At low current density, the specific capacitance value is maximum, and it decreases at high current density. The electrode discharges faster at high current densities, resulting in a low specific capacitance value, whereas the electrode

discharges slowly at low current densities, resulting in a high Cs. Cs decreases at high current density and scan rate due to poor electrolyte ion transport. Because only the outer active surface is employed for charge storage, and because time is limited during the high-rate charge-discharge process and ionic mobility in the electrolyte is always regulated by diffusion.

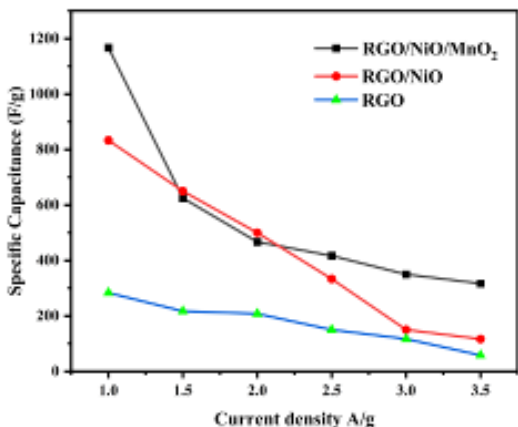


Figure 11. Comparison specific capacitance versus discharge current for Galvanostatic charge/discharge of RGO, RGO/NiO, RGO/NiO/MnO₂

Slika 11. Poređenje specifične kapacitivnosti u odnosu na struju pražnjenja zagalvanostatičko punjenje/pražnjenje RGO, RGO/NiO, RGO/NiO/MnO₂

Table 2. Calculation of specific capacitance at different current densities

Tabela 2. Proračun specifične kapacitivnosti pri različitim gustinama struje

Current density (A/g)	Specific capacitance (F/g)		
	RGO	RGO/NiO	RGO/NiO/MnO ₂
1	283	833	1167
1.5	217	625	625
2	208	500	467
2.5	150	333	417
3	117	150	350
3.5	58	117	317

4.3 .Electrochemical Impedance Spectroscopy (EIS)

EIS measurements were used to understand the interfacial chargetransfer process. Furthermore, electrochemical impedance spectroscopy measurements in the frequency range of 0.01 Hz to 100kHz were acquired from the EIS plots and the related equivalent electrical circuit of Nyquist plot of EIS of

RGO, RGO/NiO, RGO/NiO/MnO₂ nanocomposite are shown in (curve a,b,c in Figure 12). In (curve a in Figure .12) There is no semi-circular area in the Nyquist plot and Electron transfer between electrodes is boosted by RGO therefore RGO's conductivity is clearly high [57]. This is due to the restoration of RGO's graphitic nature (i.e., sp₂ bonds). It is noted that the diameter grew in (curve c in Figure 12) compared to (curve b in Figure 12) [58]. The (curve b,c in Figure 12) depicts the EIS curves in the high frequency zone, demonstrating that both semicircles are almost coincident, indicating that the electrolyte resistance and charge transfer resistance of the RGO/NiO/MnO₂ nanocomposite are similar [59].

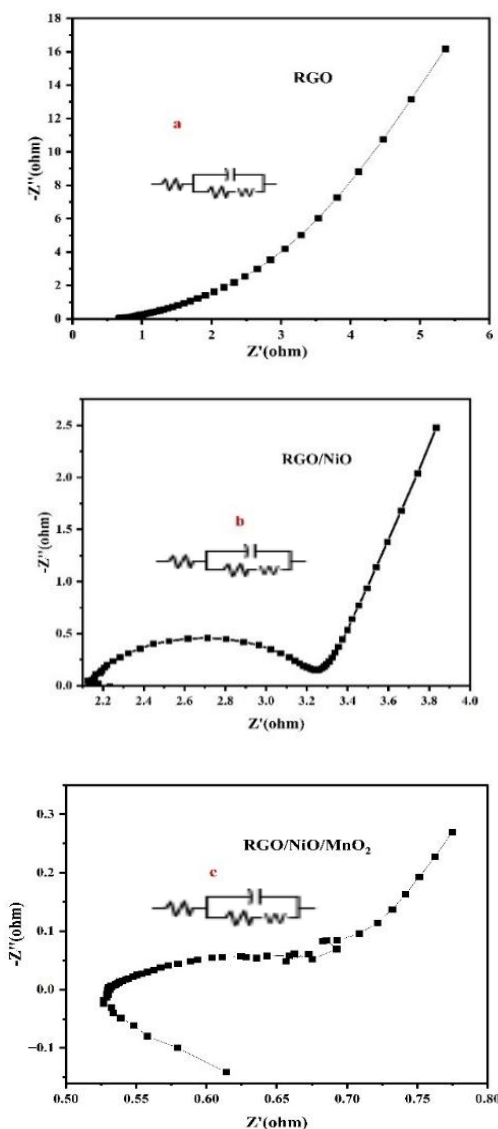


Figure 12. EIS Nyquist plot of (a) RGO, (b) RGO/NiO, (c) RGO/NiO/MnO₂

Slika 12. EIS Najkvist dijagram (a) RGO, (b) RGO/NiO, (c) RGO/NiO/MnO₂

Table 3. Comparison of the maximum capacitance values of the reported electrodes and the present electrode (RGO/NiO/MnO₂ nanocomposite)

Tabela.3. Poređenje maksimalnih vrednosti kapacitivnosti prijavljenih elektroda i sadašnje elektrode (RGO/NiO/MnO₂ nanokompozit)

Electrode material	Capacitance (F /g)	Ref.
1. Binary MnO ₂ -NiO oxides	160 (50 mV /s)	60
2. Porous nickel manganite composites	180 (0.25 A /g)	61
3. Nanosized Ni-Mn oxides	195 (10 mV /s)	62
4. Mn/Ni mixed oxides	210 (0.12 A /g)	63
5. Nickel-manganese oxide	284 (5 mV /s)	64
6. Ni(OH) ₂ -MnO ₂ core-shell nanostructures	355 (0.5 A /g)	65
7. Mesoporous Mn-Ni oxides	411 (2 mV /s)	66
8. Nanostructured NiO-MnO ₂ composite	453 (10 mV /s)	67
9. Graphene-MnO ₂ nano wall hybrids	122 (10 mV /s)	68
10. Graphene-MnO ₂ -carbon nanotubes	193 (0.2 A /g)	69
11. Graphene-honeycomb-like MnO ₂	210 (0.5 A /g)	70
12. Hydrothermally reduced graphene-MnO ₂	212 (2 mV /s)	71
13. Graphene porous NiO nanocomposite	430 (0.2 A /g)	72
14. RGO/NiO/MnO ₂ nanocomposite	1167 (1 A/g)	Present work

5. CONCLUSION

A RGO/NiO/MnO₂ nanocomposite was successfully synthesized by co-precipitation technique. The crystallographic, surface morphology, optical studies and capacitive behaviour of the nanocomposite were studied. Incorporation of RGO shows nanosheet like structure which is used not only to enhance the stability of NiO and MnO₂ but also to improve the electrochemical reactions of the nanocomposite electrode material. This behaviour resulted from the uniform distribution of NiO/MnO₂ on RGO nanosheets. This uniform morphology and the higher conductivity of the composite facilitate electrolyte diffusion and electron transfer in the nano-composite materials. The RGO/NiO/MnO₂ nanocomposite showed a highest specific capacitance of 1167 F/g at a current density of 1 A/g representing excellent electrochemical performance. Therefore, the results proved that the composite electrode material can be used as an active electrode material for supercapacitor application.

Acknowledgement

The authors are grateful to the Secretary, Director, Principal and Head of the Department of Physics, Sri G.V.G Visalakshi College for Women, Udumalpet for their excellent encouragement and support and Prof.C.N.R Rao Research Centre, Avinashilingam university, Coimbatore, Tamil Nadu, India. This research did not receive any specific grant from funding agencies in the public, commercial, or not-for-profit sectors.

Compliance with ethical standards

Conflict of interest the authors declare that they have no conflict of interest.

6. REFERENCE

- [1] N.A.Salleh, S.Kheawhom, N.A.A.Hamid (2023) Electrode polymer binders for supercapacitor applications: A review, J. of materials research and technology.,23, 3470-3491. <https://doi.org/10.1016/j.jmrt.2023.02.013>
- [2] S.Kalaiarasi, S.Shyamala, M.Kavitha (2022) Electrochemical performance of r-graphene oxide based MnO₂ nanocomposite for supercapacitor, nanosystems: Phys. Chem. Math., 13 (3), 320-330. DOI <http://dx.doi.org/10.17586/2220-8054-2022-13-3-320-330>
- [3] S.J.Park, Y.R.Son, Y.J.Heo (2018) Prospective Synthesis Approaches to Emerging Materials for Supercapacitor, Emerging Materials for Energy Conversion and Storage.,6,185-208. <https://doi.org/10.1016/B978-0-12-813794-9.00006>
- [4] C.An, Y.Zhang, H.Guo, Y.Wang (2019) Metal oxide-based supercapacitors: progress and perspectives, Nanoscale Advances., 12, 4644-4659. <https://doi.org/10.1039/C9NA00543A>
- [5] R.Kumar, R.Thangappan (2022) Electrode material based on reduced graphene oxide (rGO)/transition metal oxide composites for supercapacitor applications: a review, Emergent Materials .,5, 1881-1897. <https://doi.org/10.1007/s42247-021-00339-7>
- [6] S.Tamang, S.Rai, R.Bhujel (2023) A concise review on GO, rGO and metal oxide/rGO composites: Fabrication and their supercapacitor and catalytic applications, Journal of Alloys and Compounds., 947, 169588. <https://doi.org/10.1016/j.jallcom.2023.169588>.

- [7] S.Rusi , R.Majid (2015) Green synthesis of in situ electrodeposited rGO/MnO₂ nanocomposite for high energy density supercapacitors, *Sci Rep* **5**, 16195. <https://doi.org/10.1038/srep16195>
- [8] R.Rajeswari, A.Kavitha, B.Ananda, P.H. Gurumallesh (2021) A Review on Graphene Based Metal/Metal Oxide Composites and Enhanced Properties along with Biomedical Applications, *Nano Res Appl* **7**,3-6. doi: 10.1007/s40820-018-0206-4
- [9] S.M.Majhi, A.Mirzaei, H.W.Kim, S.S.Kim (2021) Reduced Graphene Oxide (rGO)-Loaded Metal-Oxide Nanofiber Gas Sensors: An Overview, *Sensors (Basel)*, **21**(4), 1352. <https://doi.org/10.3390/s21041352>
- [10] S.Yadav, N.Rani, K.Saini (2022) A review on transition metal oxides based nanocomposites, their synthesis techniques, different morphologies and potential applications, *IOP Conf. Ser.: Mater. Sci. Eng.*, **1225** 012004.doi:10.1088/1757- 899X/1225/1/012004
- [11] D.Selvakumar, P.Nagaraju, R.Jayavel (2018) Graphene-Metal Oxide based Nanocomposites for Supercapacitor Applications. *Advanced Materials: TechConnect Briefs.*, p.70–73.Graphene-Metal Oxide Based Nanocomposites for Supercapacitor Applications
- [12] N. S.Alsaiari, M.Ahmad, I.Shaheen, I. Ali , U.Amara (2023) Three-dimensional flower-like nanocomposites based on ZnO/NiO as effective electrode materials for supercapacitors, *Journal of Electroanalytical Chemistry*, **930**, 11715. <https://doi.org/10.1016/j.jelechem.2023.117158>
- [13] M.Shariq, A. BaQais, T.M.Althagafi, O.Madkhali, A. A.Alholaisi, S.Hussain , Y.Javed (2023) Synthesis of Co₃O₄/NiO nanospherical composites as electrode material for high-performance supercapacitors, *Eur. Phys. J. Plus.*, **138**, 389 . <https://doi.org/10.1140/epjp/s13360-023-04001-5>
- [14] G.Mummoorthi, S.Shajahan, M.A.Haija, U. Mahalingam, R.Rajendran (2022) Synthesis and Characterization of Ternary α -Fe₂O₃/NiO/rGO Composite for High- Performance Supercapacitors, *ACS Omega*, **7**, 31, 27390–27399. <https://doi.org/10.1021/acsomega.2c02418>
- [15] Q.An, X.Zhao, S.Bai (2021) Novel Lithium-Ion Capacitor Based on a NiO-rGO Composite, *Materials* **14**(13),3586. <https://doi.org/10.3390/ma14133586>
- [16] O.C.Pore, A.V.Fulari, V.G.Parale, H.H.Park, R. V. Shejwal, V.J.Fulari, G.M.Lohar (2022) Facile hydrothermal synthesis of NiO/rGO nanocomposite electrodes for supercapacitor and nonenzymatic glucose biosensing application. *J.of Porous Materials*, **29**(6), 1991-2001. <https://doi.org/10.1007/s10934-022-01313-2>
- [17] S.Seenivasan, S.Dhinesh, F.Maiz, M.Shkir (2023) Electrochemical investigation of NiO@MnO₂@rGO ternary nanocomposite-based electrode material for high-performance supercapacitor applications, *Ionics*, **29**, 3641–3652. <https://doi.org/10.1007/s11581-023-05110-y>
- [18] N.Duraisamy, K.Kandiah., R.Rajendran (2018) Electrochemical and photocatalytic investigation of nickel oxide for energy storage and wastewater treatment, *Res Chem Intermed* **44**, 5653–5667 . <https://doi.org/10.1007/s11164-018-3446-5>
- [19] S.A.Soomro, I.H.Gul, H.Naseer, S.Marwat (2019) Improved Performance of CuFe₂O₄/rGO Nanohybrid as an Anode Material for Lithium-ion Batteries Prepared Via Facile One-step Method, *Current Nanoscience*, **4**, 15, 420-429(10). <https://doi.org/10.2174/157341371466618111512201610>.
- [20] P. A .Mikhaylov, M. I. Vinogradov , I. S .Levin, G. A. Shandryuk, A.V.Lubchenko, V.G.Kulichikhin (2019) Synthesis and characterization of polyethylene terephthalate reduced graphene oxide composites, *IOP Conf. Series: Materials Science and Engineering*, **693**, 012036. 10.1088/1757-899X/693/1/012036.
- [21] Y.Zhang , Y.Shen , X.Xie , W.Du, L. K,Y,Wang , X. Sun , Z.Li , B.Wang (2020)One-step synthesis of the reduced graphene oxide@NiO composites for supercapacitor electrodes by electrode-assisted plasma electrolysis, *Materials & Design*, **196**,109111. <https://doi.org/10.1016/j.matdes.2020.109111>
- [22] T.G. Vladkova, I.A.Ivanova , A. D. Staneva , M. G. Albu, A.S. A. Shalaby , T. I. Topousova, A. S. Kostadinova (2017) Preparation and Biological Activity of New Collagen Composites Part II: Collagen/Reduced Graphene Oxide Composites, *Journal of Archives in Military Medicine*, **5**, 1 e13223. doi: 10.1007/s12010-016-2092-x.
- [23] J.Xu , L.Wu, Y.Liu et al. (2020) NiO-rGO composite for supercapacitor electrode, *Surfaces and Interfaces*, **18**, 100420 . <https://doi.org/10.1016/j.surfin.2019.100420>
- [24] T.R.Madhura, G.G.Kumar, R.Ramaraj (2020) Reduced graphene oxide supported 2D-NiO nanosheets modified electrode for urea detection, *J Solid State Electrochem*, **24**, 3073–3081. <https://doi.org/10.1007/s10008-020-04763-3>
- [25] H.Zhu, X.Zeng (2019) A nickel oxide nanoflakes/reduced graphene oxide composite and its high-performance lithium-storage properties, *J Solid State Electrochem*, **23**, 2173–2180 . <https://doi.org/10.1007/s10008-019-04281-x>
- [26] B.S.Singu, K.R.Yoon (2017) Synthesis and characterization of MnO₂- decorated graphene for supercapacitors. *Electrochimica Acta*, **231**, 749-758. <https://doi.org/10.1016/j.electacta.2017.01.182>
- [27] A.Khana , H. Wangb , Y. Liub (2018) Highly Efficient α -Mn₂O₃@ α -MnO₂-500 nanocomposite for Peroxymonosulfate Activation: Comprehensive Investigation of Manganese Oxides, *J. Mater. Chem.*, **A.6**, 1590-1600. <https://doi.org/10.1039/C7TA07942G>
- [28] P.J.S.Jennifer, S.Muthupandi, M.J.R.Ruban (2022) Interlacing Rod and Sphere Morphology of MnO₂ in RGO/NiO/MnO₂ Ternary Nanocomposites for Supercapacitive Applications,*J. Electrochem. Soc.*, **169** ,12350. DOI 10.1149/1945-7111/aca8d0 *J Solid State Electrochem.*, **24** 30, 5222–5232.

- [29] K. M. Racik, K.Guruprasad, M. Mahendiran (2019) Enhanced electrochemical performance of MnO₂/NiO nanocomposite for supercapacitor electrode with excellent cycling stability, *Int.J.Energy Research*, 46(12), 17163-17179. <https://doi.org/10.1007/s10854-019-00821-3>
- [30] S.G.Hwang, J.E.Hong, G.O.Ki, H.M.Jeong (2012) Graphene Anchored with NiO-MnO₂ Nanocomposites for Use as an Electrode Material in Supercapacitors, *ECS Solid State Letters*, 2(1): M8-M11. DOI:10.1149/2.010301ssl
- [31] E.Liu, W.Li, J.Li (2009) Preparation and characterization of nanostructured NiO/MnO₂ composite electrode for electrochemical super capacitors, *Materials Research Bulletin*, 44,5, 6:1122-1126. <https://doi.org/10.1016/j.materresbull.2008.10.003>
- [32] Y.F.Yuan, J.X.Lin, D.Zhang (2017) Freestanding hierarchical NiO/MnO₂ core/shell nanocomposite arrays for high-performance electrochemical energy storage, *Electrochimica Acta*, 227, 303-309. <https://doi.org/10.1016/j.electacta.2017.01.002>
- [33] J.Chen, Y.Huang, C.Li (2016) Synthesis of NiO@MnO₂ core/shell nanocomposites for supercapacitor application, *Applied Surface Science* 360, 534- 53. DOI:10.1016/j.apsusc.2015.10.187
- [34] T.F.Yi, J.Mei, B.Guan (2020) Construction of spherical NiO@MnO₂ with core- shell structure obtained by depositing MnO₂ nanoparticles on NiO nanosheets for high-performance supercapacitor, *Ceramics International*, 46(1), 421-429 . <https://doi.org/10.1016/j.ceramint.2019.08.278>
- [35] S.Ramesh, K.Karuppasamy, S.Msolli (2017) A nanocrystalline structured NiO/MnO₂@nitrogen-doped graphene oxide hybrid nanocomposite for high performance supercapacitors, *New Journal of Chemistry*, 24, 373-382. <https://doi.org/10.1039/C7NJ03730A>
- [36] S.Sivakumar, N. A.Mala (2021) Influence of Variant Temperatures in Optical, Magnetic Properties of NiO Nanoparticles and its Supercapacitor Applications via Precipitation Method, *Asian Journal of Chemistry*, 33(8), 1783-1790. <http://dx.doi.org/10.14233/ajchem.2021.23242>
- [37] I.Sengupta, S.Chakraborty, M.Talukdar (2018) Thermal reduction of graphene oxide: How temperature influences purity. *Journal of Materials Research*, 33:4113– 4122. <https://doi.org/10.1557/jmr.2018.338>.
- [38] A.Al Nafiey, A.Kumar, M.Kumar (2017) Nickel oxide nanoparticles grafted on reduced graphene oxide (rGO/NiO) as efficient photocatalyst for reduction of nitroaromatics under visible light irradiation, *Journal of Photochemistry and Photobiology A: Chemistry*, 336, 198-207. <https://doi.org/10.1016/j.jphotochem.2016.12.023>
- [39] K. Mohamed Racik, K.Guruprasad, M. Mahendiran (2019) Enhanced electrochemical performance of MnO₂/NiO nanocomposite for supercapacitor electrode with excellent cycling stability, *Journal of Materials Science: Materials in Electronics*, 30, 5222–5232. <https://doi.org/10.1007/s10854-019 - 00821 - 3>
- [40] F.Zheng,W.L. Xu, D.Jin (2015) Charge transfer from poly(3-hexylthiophene) to graphene oxide and reduced graphene oxide, *RSC Advances*, 5(109), 89515- 89520. doi: 10.1039/C5RA18540H.
- [41] P.Vijaya Kumar, A.Jafar Ahamed, M. Karthikeyan (2019) Synthesis and characterization of NiO nanoparticles by chemical as well as green routes and their comparisons with respect to cytotoxic effect and toxicity studies in microbial and MCF-7 cancer cell models, *SN Appl. Sci.*, 1, 1083 . <https://doi.org/10.1007/s42452-019-1113-0> <https://doi.org/10.1007/s42452-019-1113-0>
- [42] Y.Deng, W.Tang, W.Li, Y.Chen (2018) MnO₂-nanowire@NiO-nanosheet core- shell hybrid nanostructure derived interfacial Effect for promoting catalytic oxidation activity, *Catalysis Today*, 308, 58-63. <https://doi.org/10.1016/j.cattod.2017.07.007>
- [43] W.Gul, R.A.Shah (2023) Synthesis of graphene oxide (GO) and reduced graphene oxide (rGO) and their application as nano-fillers to improve the physical and mechanical properties of medium density fiberboard, *Front.Mater.*, Sec.Polymeric and Composite Materials., 10, 784-793. <https://doi.org/10.3389/fmats.2023.1206918>
- [44] V.Manikandan, R.Elancheran, P.Revathi et al. (2021) Synthesis, Characterization, Photocatalytic and Electrochemical Studies of Reduced Graphene Oxide Doped Nickel Oxide Nanocomposites, *Asian Journal of Chemistry*,33(2), 411- 422. DOI: 10.14233/ajchem.2021.22979
- [45] H.Fei, N. Saha, N.Kazantseva et al. (2017) A Highly Flexible Supercapacitor Based on MnO₂/RGO Nanosheets and Bacterial Cellulose-Filled Gel Electrolyte. *Materials*, 10, 1251. doi:10.3390/ma10111251
- [46] S.S.Mehta, D.Y.Nadargi, M. S.Tamboli et al. (2021) RGO/WO₃ hierarchical architectures for improved H₂S sensing and highly efficient solar-driving photodegradation of RhB dye, *Scientific Reports*, 11, 5023. <https://doi.org/10.1038/s41598-021-84416-1>.
- [47] N.Tiwari, S.Kulkarni (2022) Impact of Current Collector Base on Supercapacitive Performance of Hydrothermally Reduced Graphene Oxide Electrode, *ES Energy Environ.*, 15, 67-75. <https://dx.doi.org/10.30919/esee8c614>
- [48] L.Ma, X.Y.Pei, D.C. Mo, et al. (2019) Facile fabrication of NiO flakes and reduced graphene oxide (NiO/RGO) composite as anode material for lithium-ion batteries, *Journal of Materials Science: Materials in Electronics*, 30, 5874–5880 <https://doi.org/10.1007/s10854-019-00885-1>
- [49] B.Belay Etana (2019) Functionalization of textile cotton fabric with reduced graphene oxide/MnO₂/polyaniline based electrode for supercapacitor To cite this article before publication, *Mater. Res.*, 6, 125708. <https://doi.org/10.1088/2053-1591/ab669>
- [50] G. Vinodhkumara, R. Ramyab, M. Vimalanc (2018) Reduced graphene oxide based on simultaneous detection of neurotransmitters, *Progress in*

- Chemical and Biochemical Research., 1 (1), 40-49. DOI: 10.29088/SAMI/PCBR.2018.1.4049
- [51] X. Pu, D. Zhao, C. Fu, Z. Chen, S. Cao, C. Wang et al. (2021) Understanding and Calibration of Charge Storage Mechanism in Cyclic Voltammetry Curves, *Chem. Int. Ed.*, 10.1002/anie.202104167. <https://doi.org/10.1002/anie.202104167>
- [52] E. S. Agudosi, E. C. Abdullah, A. Numan et al. (2020) Fabrication of 3D binder-free graphene NiO electrode for highly stable supercapattery, *Sci Rep* 10., 11214. <https://doi.org/10.1038/s41598-020-68067-2>
- [53] L. G. Beka, X. Bu, X. Li et al. (2019) A 2D metal-organic framework/reduced graphene oxide heterostructure for supercapacitor application, *RSC Adv.*, 9, 36123-36135. DOI: 10.1039/C9RA07061C
- [54] S. Ge, Y. Zonglin, X. Lijing, B. Zhihong (2020) In-situ conversion of Ni₂P/rGO from heterogeneous self-assembled NiO/rGO precursor with boosted pseudocapacitive performance, *Chinese Chemical Letters.*, 31(6), 1392-1397. doi: 10.1016/j.ccllet.2020.03.046
- [55] S. Abbas, S. Manzoor, M. Abdullah (2022) One-pot synthesis of reduced graphene oxide-based PANI/MnO₂ ternary nanostructure for high-efficiency supercapacitor applications, *Journal of Materials Science: Materials in Electronics.*, 33, 25355-25370 (2022). <https://doi.org/10.1007/s10854-022-09242-1>
- [56] N. H. N. Azman, Y. Sulaiman, M. D. S. Mamat (2019) Novel poly(3,4-ethylenedioxythiophene)/reduced graphene oxide incorporated with manganese oxide/iron oxide for supercapacitor device, *Journal of Materials Science: Materials in Electronics.*, 30, 1458-1467. <https://doi.org/10.1007/s10854-018-0415-0>, 2018
- [57] Y. Ming, W. C. H. Zhang (2022) Reduced Graphene Oxide Derived from Low-Grade Coal for High-Performance Flexible Supercapacitors with Ultrahigh Cyclability, *Nanomaterials.* 12(17), 2989. <https://doi.org/10.3390/nano12172989>
- [58] L. Lu, S. Xu, J. An, S. Yan (2016) Electrochemical performance of CNTs/RGO/MnO₂ composite material for supercapacitor, *Nanomaterials and Nanotechnology.* 6, 1-7. <https://doi.org/10.1177/1847980416663687>
- [59] J. Huang, F. Li, B. Liu, P. Zhang (2020) Ni₂P/rGO/NF Nanosheets As a Bifunctional High-Performance Electrocatalyst for Water Splitting, *Materials.*, 13(3), 744. <https://doi.org/10.3390/ma13030744>
- [60] Y. S. Chen, C. C. Hu (2003) Capacitive Characteristics of Binary Manganese-Nickel Oxides Prepared by Anodic Deposition, *Electrochem Solid-State Lett.*, 6, A210-A213. <https://doi.org/10.1149/1.1601373>
- [61] H. Pang, J. Deng, S. Wang, S. Li, J. Du, J. Chen, J. Zhang (2012) Facile synthesis of porous nickel manganite materials and their morphology effect on electrochemical properties, *RSC Adv.*, 2, 5930-5934. <https://doi.org/10.1039/C2RA20245J>
- [62] J. Zhou, X. Shen, M. Jing (2006) Nanosized Ni-Mn Oxides Prepared by the Citrate Gel Process and Performances for Electrochemical Capacitors, *J. Mater. Sci. Technol.*, 22, 803-806. DOI 10.1149/1.1541675
- [63] H. Kim, B. N. Popov (2003) Synthesis and Characterization of MnO₂-Based Mixed Oxides as Supercapacitors, *J. Electrochem. Soc.*, 150, D56-D62. <https://doi.org/10.1021/cm0630800>
- [64] C. H. Wu, J. S. Ma, C. H. Lu (2012) Synthesis and characterization of nickel-manganese oxide via the hydrothermal route for electrochemical capacitors, *Curr. Appl. Phys.*, 12, 1190-1194. <https://doi.org/10.1016/j.cap.2012.02.056>
- [65] H. Jiang, C. Li, T. Sun, J. Ma (2012) Chem High-performance supercapacitor material based on Ni(OH)₂ nanowire-MnO₂ nanoflakes core-shell nanostructures, *Commun.*, 48, 2606-2608. <https://doi.org/10.1039/C2CC18079K>
- [66] D. L. Fang, B. C. Wu, Y. Yan, A. Q. Mao, C. H. Zheng (2012) Enhanced supercapacitor performance by incorporating nickel in manganese oxide, *J. Solid State Electrochem.*, 16, 135-142.
- [67] E. H. Liu, W. Li, J. Li, X. Y. Meng, R. Ding, S. T. Tan (2009) Progress in Research on Manganese Dioxide Electrode Materials for Electrochemical Capacitors, *Mater. Res. Bull.*, 44, 1122-1126.
- [68] C. Zhu, S. Guo, Y. Fang, L. Han, E. Wang, S. Dong (2011) One-step electrochemical approach to the synthesis of Graphene/MnO₂ nanowall hybrids, *Nano Res.*, 4, 648-657. [https://doi.org/10.1016/S1872-2040\(11\)60534-3](https://doi.org/10.1016/S1872-2040(11)60534-3)
- [69] Z. Lei, F. Shi, L. Lu (2012) Incorporation of MnO₂-Coated Carbon Nanotubes between Graphene Sheets as Supercapacitor Electrode, *ACS Appl. Mater. Interfaces.*, 4, 1058-1064. <https://doi.org/10.1021/am2016848>
- [70] J. Zhu, J. He (2012) Facile Synthesis of Graphene-Wrapped Honeycomb MnO₂ Nanospheres and Their Application in Supercapacitors. *Mater. Interfaces, ACS Appl.*, 4, 1770-1776. <https://doi.org/10.1021/am3000165>
- [71] Y. Jiang, D. Chen, J. Song, Z. Jiao, Q. Ma, H. Zhang, L. Cheng, B. Zhao, Y. Chu (2013) Synthesis of Shape-Controlled NiO/Graphene Nanocomposites with Enhanced Supercapacitive Properties, *Electrochim. Acta.*, 91, 173-178.
- [72] G. Yu, L. Hu, M. Vosgueritchian, H. Wang, X. Xie, J. R. McDonough, X. Cui, Y. Cui, Z. Bao (2011) Solution-Processed Graphene/MnO₂ Nanostructured Textiles for High-Performance Electrochemical Capacitors, *Nano Lett.*, 11, 2905 - 2911. <https://doi.org/10.1021/nl2013828>

IZVOD

NiO/MnO₂ NANOKOMPOZIT KAO DODATAK SLOJEVITIM ELEKTRODAMA SA REDUKOVANIM GRAFEN OKSIDOM (RGO) ZA ODGOVORNU PRIMENU SUPERKONDENZATORA

Smanjeni grafen oksid/nikl oksid/magnezijum dioksid, RGO/NiO/MnO₂, nanokompozitna elektroda je uspešno pripremljena jednostavnom metodom ko-precipitacije. Sintetizovani nanokompozit je okarakterisan XRD, FESEM, EDAX, FTIR, UV, CV, GCD, EIS. Nanokompozit RGO/NiO/MnO₂ je prethodno obrađen ultrazvukom, nakon čega je usledilo termičko žarenje na 350 °C. Kristalna površina i veličina nanokompozita su analizirani rendgenskom difrakcijom (XRD). Strukturalna analiza sendvič RGO/NiO/MnO₂ je analizirana skenirajućim elektronskim mikroskopom (SEM). Ova struktura je promovisala efikasan kontakt između elektrolita i aktivnih materijala, a posebna arhitektura bi mogla da ponudi brze kanale za prenos jona i elektrona. Nanokompozit je pokazao visoku provodljivost zahvaljujući prisustvu RGO. Elektrohemijske performanse pripremljenog nanokompozita urađene su cikličkom voltametrijom (CV), galvanostatskim pražnjenjem naelektrisanja (GCD), spektroskopijom električne impedanse (EIS). Sintetizovani nanokompozit RGO/NiO/MnO₂ dobija visoku specifičnu kapacitivnost od 1167 F/g pri gustini struje od 1 A/g. Niskotemperaturna RGO/NiO/MnO₂ nanokompozitna elektroda bi mogla biti elektroda koja obećava za uređaje za skladištenje energije.

Ključne reči: Redukovani grafen oksid (RGO), nanokompozit NiO/MnO₂, pseudokondenzator, ciklički voltamogrami, superkondenzator.

Naučni rad

Rad primljen: 03.12.2023.

Rad korigovan: 14.01.2024.

Rad prihvaćen: 16.01.2024

Rad je dostupan na sajtu: www.idk.org.rs/casopis

Abd El-Aziz S. Fouda^{1*}, Ibrahim S. El-Hallag²,
Ahmed A. El-Barbary², Fatma M. El Salamony¹

¹Department of Chemistry, Faculty of Science, Mansoura University,
Mansoura-35516, Egypt, ²Department of Chemistry, Faculty of Science,
Tanta University, Tanta, Egypt

Scientific paper

ISSN 0351-9465, E-ISSN 2466-2585

<https://doi.org/10.62638/ZasMat1150>



Zastita Materijala 65 (2)
331 - 342 (2024)

Electrochemical and theoretical evaluations of 3-(4-chlorophenyl)-7-methyl-5H-[1, 2, 4] triazolo [3,4-b][1,3,4]thiadiazin-6(7H)-one as corrosion inhibitor for copper in nitric acid environment

ABSTRACT

3-(4-chlorophenyl)-7-methyl-5H-[1,2,4]triazolo[3,4-b][1,3,4]thiadiazin-6(7H)-one (CTT) was synthesized and evaluated as corrosion inhibitor for copper in one molar HNO_3 . The adsorption properties for the synthesized CTT were determined by experimental and theoretical methods in acid environment. The chemical method such as mass loss method (ML), DC potentiodynamic polarization (PDP) and AC impedance (EIS) techniques were utilized to determine the inhibitive behavior of CTT. Outcome data obtained from these methods displayed that with increasing the concentration of CTT its inhibition efficiencies (%IE) increases and reached 91.5% at $24 \times 10^{-6} \text{ M}$, 25°C using EIS technique. The presence of CTT reduces the capacity of the double layer (C_{dl}) and improves the charge transfer resistance (R_{ct}) in a solution of one molar nitric acid. CTT is a mixed-type inhibitor from the data obtained from the polarization curves. The attained data indicated that CTT was physically adsorbed onto the Cu surface in accordance for the Langmuir adsorption. The surface protection examination was carried out using scanning electron microscopy (SEM), Energy Dispersive X-ray (EDX) and atomic force microscope (AFM). Also, The quantum chemical parameters of CTT were computed and discussed. The results of several methods are in agreement with each other.

Keywords: Corrosion inhibition, Copper, Nitric acid, 3-(4-chlorophenyl)-7-methyl-5H-[1,2,4]triazolo[3,4-b][1,3,4]thiadiazin-6(7H)-one (CTT), Langmuir isotherm.

1. INTRODUCTION

The fifth-most common metal on the planet, copper, is very beneficial both in its pure form and as an alloy [1]. Owing to their excellent properties such as good thermal and electrical conductivity, mechanical workability, low cost and high corrosion resistance, copper and its alloys were extensively used in various industries such as conductors, heat exchangers, and the electronic industry [2,3]. Copper has a relatively noble potential, despite this, it corrodes far more quickly in chloride and seawater conditions [4,5]. It is widely known that the amount of chloride ions in the environment affects how easily copper dissolves anodically. The formed CuCl , which is not sufficiently protective, and dissolves when it reacts with excess chloride [6–8]. In spite of its high corrosion resistance feature in atmospheric conditions, by forming an

oxide protective layer on its surface, copper and its alloys may easily undergo metal dissolution in the presence of an aggressive media like chloride having environment [6]. The primary technique for protecting metals and alloys is the use of inhibitors. Right now, green inhibitors show promise since they provide effective inhibition while having a minimal negative impact on the environment. Several investigators have reported [5–8] that organic compounds can act as possible corrosion inhibitors for numerous metals and alloys in various corrosive media. The inhibitors can be introduced to the medium or coated on the metal surface to slow down the corrosion process to avoid corrosion in the metal used in such corrosive media; both methods work well [9–13]. Heterocyclic compounds having N, O, S, P, or π -bonds make up many effective corrosion inhibitors by generating a physical barrier to reduce the transport of corrosive species to the metal surface [14–16].

Organic compounds that include conjugated double bonds and hetero atoms especially those, that can form polymeric complexes with copper by coordinating with CuO , Cu^+ , or Cu^{2+} through their

*Corresponding author: Abd El-Aziz S. Fouda

E-mail: asfouda@mans.edu.eg

Paper received: 03. 01. 2024.

Paper accepted: 16. 02. 2024.

Paper is available on the website: www.idk.org.rs/journal

lone pair electrons [17]. These adhere to the copper surface to produce a protective coating that prevents corrosion by serving as a wall against harmful ions like chloride [18]. 1,2,3-triazole (BTA) compound has been reported as a well-known effective corrosion inhibitors of copper in many environments [19]. The inhibition effect of 3-amino-1,2,4-triazole (ATA) on copper corrosion in 2M HNO₃ solution was studied by Zarrouk et al [20]. The inhibition efficiency reached 82.2% at 10-2M. Yaroslav et al [21] studied the protection of steels with a 3-substituted 1,2,4-triazole (3ST) in 2 M H₂SO₄ solution. The inhibition protection reached 97.8% at 4.2x10⁻⁷M. Additionally, the ability of some 1,2,4-triazole derivatives to suppress copper corrosion in a neutral aqueous environment has been investigated. These derivatives include 3-vanilidene amino 1,2,4-triazole phosphonate, 3-anisalidene amino 1,2,4-triazole phosphonate [22], and 3-amino-5-mercapto-1,2,4-triazole [23, 24]. 1,2,4-triazole derivatives, including 1,2,4-triazole, 3-amino-1,2,4-triazole, and 2-4-diamino-1,2,4-triazole in 1 M H₂SO₄ [25]; 3,5-bis(2-thienyl)-4-amino-1,2,4-triazole in 1 M HCl and 0.5 M H₂SO₄ [26,27]; 3,5-diamino-1,2,4-triazole in 2 M HNO₃ [28]; 5-amino-1,2,4 triazole, 5-amino-3-mercapto 1,2,4 triazole, 5-amino-3-methyl thio-1,2,4-triazole, 1-amino-3-methyl thio-1,2,4-triazole [29–33]; 4-amino-4H-1,2,4-triazole-3-thiol, 4-amino-5-methyl-4H-1,2,4-triazole-3-thiol [34, 35] in 0.5 M HCl have been studied in relation to copper corrosion. Chooto et al [36] reported the effect of thioureas and N, O, S-Ligating Ring Compounds as corrosion inhibitors for Cu in Cl⁻ ions. Wang et al. [37] investigate the inhibition mechanism of combined thiourea and hexamethylenetetramine as a corrosion inhibitor on the surface of copper in 0.5 M HCl solution.

With the improvement of hardware and software, recently, quantum chemical methods like functional density theory (DFT) has been used as fast and powerful tool to predict and understand corrosion inhibition performances of inhibitors [38]. Although there is an extensive literature on the corrosion properties of benzotriazole on steel and copper [39, 40], a protective coating is created by utilizing a tiny inhibitor dose to delay the corrosion reaction [41-43].

The organ-sulphur and heterocyclic compounds have the basic requirements to be considered as eco-friendly compounds. These compounds are adsorbed on the metal surface by blocking the active sites during the inhibition process. This leads to the need of development of new environmentally-friendly inhibitors for copper metal. A newly synthesized 3-(4-chlorophenyl)-7-methyl-5H-[1,2,4]triazolo[3,4-b][1,3,4]thiadiazin-6(7H)-one

one, was investigated for its ability to suppress the corrosion of copper in one molar HNO₃. The evaluation of the corrosion behavior of copper in aggressive media in the absence and presence of newly synthesized CTT using (PDP), (EIS), and ML methods were discussed".

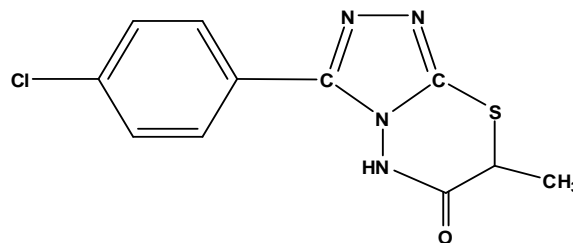
2. EXPERIMENTAL

2.1. Solutions and materials

The chemical composition of the Cu used in this paper is as follows: "(wt. %) 0.0023 Zn, 0.0023 Pb, 0.0023 P, 0.0019 Co, 0.0018 Al, 0.0015 Si, 0.004 Ni and the remainder is copper. Copper samples of measured (2 x 2 x 0.2) cm in triplicate, were mechanically polished. Samples were abraded with emery paper of grades levels from 250 and until 1200, then cleaned by distilled water, brushed using acetone and at end dried by filter papers. The strong solutions (5 M HNO₃) were prepared by diluting AR grade (70 %) HNO₃ with bi-distilled water and checking its concentration with standardized solution of NaOH, after that prepare one molar HNO₃ by diluting with bi-distilled water. 100 mL stock solutions (10⁻³ M) were prepared by dissolving an accurately weighed quantity of CTT in an appropriate volume of dimethyl formamide (DMF) and absolute ethanol, then diluting with bi-distilled water to the needed concentrations (4x10⁻⁶ - 24 x10⁻⁶ M).

2.2. Synthesis of 3-(4-chlorophenyl)-7-methyl-5H-[1,2,4]triazolo[3,4-b][1,3,4]thiadiazin-6(7H)-one [44].

The chemical structure and molecular formula of the 3-(4-chlorophenyl)-7-methyl-5H-[1,2,4]triazolo[3,4-b][1,3,4]thiadiazin-6(7H)-one (CTT) compound was shown in Figure 1. The studies were done at different concentrations (4x10⁻⁶, 8x10⁻⁶, 12x10⁻⁶, 16x10⁻⁶, 20x10⁻⁶ and 24x10⁻⁶ M) on the presence and absence of the investigated CTT. In thermostatic conditions, all experiments were conducted.



3-(4-chlorophenyl)-7-methyl-5H-[1,2,4]triazolo[3,4-b][1,3,4]thiadiazin-6(7H)-one

Figure 1 Optimized structure of CTT, (C₁₁H₉ClN₄OS), M. Wt. = 280.02 g/mol

Slika 1 Optimizovana struktura CTT, (C₁₁H₉ClN₄OS), M. Vt. = 280.02 g/mol

2.3. ML method

Specimens with emery paper were abraded, and bi-distilled water was used to clean it, then using filter papers for drying and weighed. In the existence and absence of various amounts of CTT, the samples were immersed into 100 mL of the acid medium. The CTT doses were between 1×10^{-6} – 24×10^{-6} M. The time of immersion is 30 to 180 minutes. After a certain time, the samples were weighed again. The corrosion rate (k_{corr}) of the metal specimens was determined using the following relationship” [45].

$$CR = \frac{\Delta W}{AT} \quad (1)$$

Where, ΔW (mg) as the reduction in mass, A (cm^2) as the area of the surface of Cu and t (min) as the time. The protection efficacy (% IE) in addition to specimen surface coverage (Θ) by CTT can be obtained as follows”:

$$\% IE = \theta \times 100 = \left(\frac{\Delta W_2 - \Delta W_1}{\Delta W_2} \right) \times 100 \quad (2)$$

with ΔW_1 as ML in the presence of the CTT and ΔW_2 as ML in the absence of the CTT.

2.4. Electrochemical techniques

For the electrochemical experiments, a standard electrochemical cell made-up from Pyrex glass was used. Cu (1 cm^2 exposed area) as working electrode, a saturated calomel electrode (SCE) and a platinum sheet as reference, and counter electrodes, respectively were used for electrochemical studies. Potentiodynamic current-potential graphs were documented by instantaneously shifting the electrode potential from -700 mV to $+700 \text{ mV}$ at a scanning rate of 0.2 mVs^{-1} (version 3.20). Corrosion current density (i_{corr}) and corrosion potential (E_{corr}) were assessed from the relationship of the correlation anodic and cathodic sections of Tafel plots in the absence and existence of various inhibitor doses. Before initiating the readings, the electrode potential was stabilized for 30 minutes. Gamry reference PCI300/4 Potentiostat/Galvanostat/Zra analyzer, DC105 corrosion, EIS300, Echem Analyst 5.5 software's were used for result plotting, graphing, data fitting, and calculating. The results of every experiment were checked at least three times. The degree of surface coverage (θ), and % IE were calculated using Eq. 3:

$$\% IE = \theta \times 100 = \left(\frac{i_{\text{corr}}(\text{free}) - i_{\text{corr}}(\text{inh})}{i_{\text{corr}}(\text{free})} \right) \times 100 \quad (3)$$

Where, “ $i_{\text{corr}}(\text{inh})$ and $i_{\text{corr}}(\text{free})$ to indicate the currents densities in absence and existence of CTT, individually”.

For impedance calculation, open circuit potential (OCP) has been applied and current signals range from 100 kHz to 10 Hz. The θ and % IE were calculated as follows:

$$\% IE_{EIS} = \left(\frac{R_{\text{ct}}^*(\text{inh}) - R_{\text{ct}}(\text{free})}{R_{\text{ct}}(\text{inh})} \right) \times 100 \quad (4)$$

with $R_{\text{ct}}(\text{free})$ as the resistance in blank solution and $R_{\text{ct}}(\text{inh})$ as the resistance of charge transfer in inhibited solution.

2.5. Surface morphology by SEM and EDX techniques

The specimens were placed in one molar HNO_3 solution for 24 hours, both with and without higher doses of CTT (24×10^{-6} M), after preparing their surfaces as before, then examined by Scanning electron microscope (SEM, JSM-T20, Japan) for the test. Furthermore, the copper samples were examined using energy dispersive X-ray (EDX) spectroscopy system provided (Zeiss Evo 10 instrument model)”. The beam accelerating voltage was 25 kV.

2.6. Computational chemical approaches

To study the relationship among the molecular structure and the reactivity of CTT, The density functional theory (DFT) in Materials Studio version 7.0 was utilized for theoretical computations.

3. RESULT AND DISCUSSION

3.1. ML tests

The ML of Cu in the acid environment at “ 25°C without and in presence of altered doses of CTT after several immersion periods from 30 to 180 min is given in Figure 2.

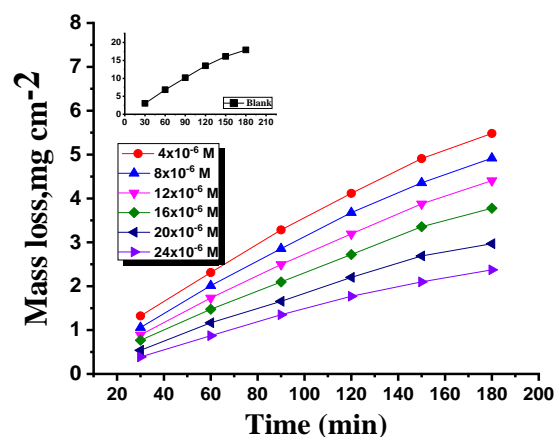


Figure 2. ML-Time diagrams at 25°C for the dissolution process of the Cu in one molar nitric acid in the absence and at various doses of CTT

Slika 2. ML-vremenski dijagrami na 25°C za proces rastvaranja Cu u jednoj molarnoj azotnoj kiselini u odsustvu i pri različitim dozama CTT-a

The ML was decreased as the CTT concentration increases. This due to the layer formed on the Cu surface from the adsorbed molecules of CTT which protects Cu surface from the corrosive environment and blocks the metal corrosive sites [46]. According to the data, the %IE value climbed to 85.9% as the CTT concentration was raised from the range of 4×10^{-6} to 24×10^{-6} M. The Cu outer surface area was sufficiently protected from corrosion when the k_{corr} declined and the CTT concentration grew. When the CTT level was raised from 4×10^{-6} to 24×10^{-6} M, the k_{corr} reduced from 0.0498 to 0.0237 $\text{mg cm}^{-2} \text{min}^{-1}$. It was observed that the % IE dropped after 24×10^{-6} M. This decrease is probably caused by the CTT

molecules saturating every active area on the Cu surface [47].

3.1.1. Impact of temperature

Corrosion rate (k_{corr}) of Cu, θ and % IE at various temperatures in the acid environment in the absence and at various doses of CTT were presented in Table 1. The (k_{corr}) decreased while θ and % IE improved with increased doses of CTT. % IE decreased by raising the temperature due to desorption process [48] illustrating that the CTT is physically adsorbed on the Cu surface. The impact of temperature on the desorption process on the metal surface was covered in earlier research [49].

Table 1. CR, θ and percent IE at various temperatures for corrosion of the Cu in the used acid medium in the absence and at various doses of CTT compound

Tabela 1. CR, θ i procenat IE na različitim temperaturama za koroziju Cu u korišćenom kiselom medijumu u odsustvu i pri različitim dozama CTT jedinjenja

Temp, °C	(30°C)			(35°C)			(40°C)			(45°C)		
Conc., M	k_{corr}	θ	IE %									
0.0	0.1683	---	---	0.2198	---	---	0.2848	---	---	0.3285	---	---
4×10^{-6}	0.0498	0.704	70.4	0.0736	0.665	66.5	0.1213	0.574	57.4	0.1679	0.489	48.9
8×10^{-6}	0.0449	0.733	73.3	0.0675	0.693	69.3	0.1170	0.589	58.9	0.1544	0.53	53.0
12×10^{-6}	0.0402	0.761	76.1	0.0589	0.732	73.2	0.1054	0.63	63.0	0.1386	0.578	57.8
16×10^{-6}	0.0340	0.798	79.8	0.0543	0.753	75.3	0.0883	0.69	69.0	0.1225	0.69	62.7
20×10^{-6}	0.0279	0.834	83.4	0.0459	0.791	79.1	0.0783	0.725	72.5	0.1061	0.725	67.7
24×10^{-6}	0.0237	0.859	85.9	0.0385	0.825	82.5	0.0720	0.747	74.7	0.0910	0.747	72.3

The following Arrhenius equation was used to estimate activation energy (E_a):

$$\log k_{corr} = \left(\frac{-E_a^*}{2.303RT} \right) + \log A \quad (5)$$

where A as (pre-exponential Arrhenius multiplier), R (8.314 Joule/ K. mol.) as universal gas constant. Figure 3 indicates Arrhenius plots without and with various dose of CTT for Cu corrosion in the used acid medium. Results of E_a^* were determined from the lines slope. Enthalpy (ΔH^*) and entropy (ΔS^*) of the activation process can be specified by application the transition state equation as follows:

$$\log k_{corr} = \log \left(\frac{R}{Nh} \right) + \frac{\Delta S^*}{2.303R} + \frac{\Delta H^*}{2.303RT} \quad (6)$$

With h (6.625×10^{-27}) as Planck's constant and N (6.025×10^{23} g/mol.) as Avogadro's number. Figure 4 displays $\log(k_{corr}/T)$ against $(1/T)$ diagrams without and with various doses of CTT for Cu corrosion in the used acid medium. Slopes and intercepts of the straight lines give values ΔH^* and ΔS^* , respectively. The determined activation parameters were depicted in Table 2. Values of E_a^* in Table 2 for solutions with CTT were high than that in its absence. The rise in the E_a^* shows that CTT molecules are physically adsorbed on the Cu surface. The exothermic activation process was

demonstrated by the negative sign of ΔH^* values. This proves that the Cu dissolution in the acid medium is a unimolecular reaction. The negative signals of ΔS^* showed that the disorder develops along the direction from the reactant to the activated complex [50].

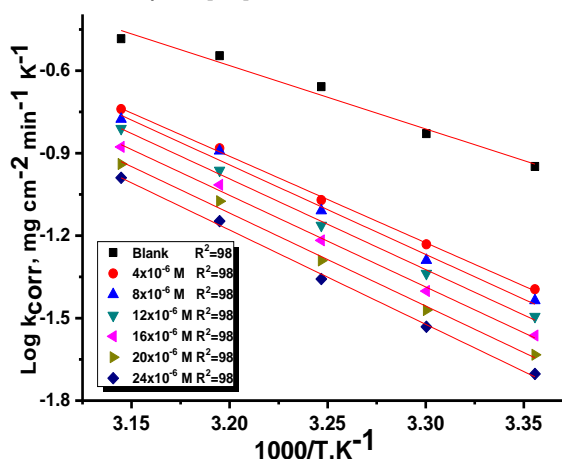


Figure 3. $\log k_{corr}$ against $1/T$ diagrams without and at various doses of CTT for Cu corrosion in the used acid medium

Slika 3. $\log k_{corr}$ naspram $1/T$ dijagrama bez i pri različitim dozama CTT za koroziju Cu u korišćenom kiselom medijumu.

Table 2. Thermodynamic activation parameters without and at various doses of CTT for Cu corrosion in the used acid medium

Tabela 2. Parametri termodinamičke aktivacije bez i pri različitim dozama CTT za koroziju Cu u korišćenom kiselom mediju

Conc. M	Activation parameters		
	E _a [*] , kJ mol ⁻¹	-ΔH [*] , kJ mol ⁻¹	-ΔS [*] , J mol ⁻¹ K ⁻¹
Blank	45.2	41.6	122.1
4x10 ⁻⁶	61.5	58.9	77.0
8x10 ⁻⁶	63.6	61.0	70.8
12x10 ⁻⁶	64.4	62.0	69.1
16x10 ⁻⁶	65.1	62.5	68.3
20x10 ⁻⁶	66.0	63.4	66.4
24x10 ⁻⁶	66.9	64.3	64.6

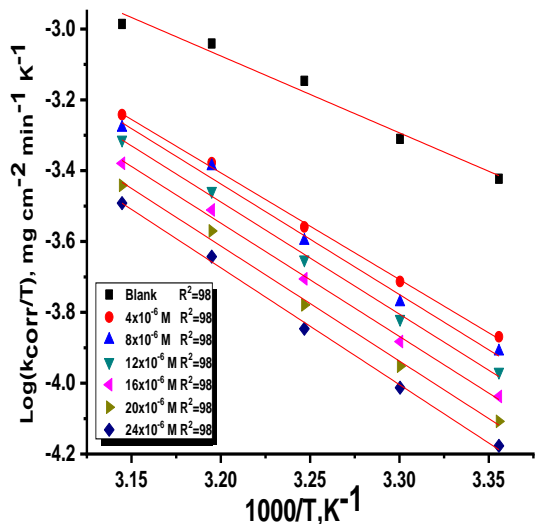


Figure 4. log (k_{corr}/T) against 1/T diagrams without and at various doses of CTT for Cu corrosion in the used acid medium

Slika 4. log (k_{corr}/T) naspram 1/T dijagrama bez i pri različitim dozama CTT-a za koroziju Cu u korišćenom kiselom mediju

3.1.2. Adsorption studies

The Langmuir model's isotherm for adsorption perfectly match the data (Figure 5). The following Eq. 7 can be used to show the Langmuir adsorption isotherm.

$$\frac{C_{inh}}{\theta} = \frac{1}{K_{ads}} + C_{inh} \tag{7}$$

with C as the dose of CTT inhibitor and K_{ads} as the adsorption constant. Eq. 8 can be applied to give the free energy of adsorption (ΔG^o_{ads}):

$$K_{ads} = \frac{1}{55.5} \exp\left(\frac{-\Delta G_{ads}^o}{RT}\right) \tag{8}$$

where the water dose at the Cu/solution interface is 55.5 (mol./L). By using the Vant Hoff equation, the enthalpy of adsorption (H^o_{ads}) was determined as follows:

$$\log K_{ads} = \frac{-\Delta H_{ads}^o}{2.303RT} + constant \tag{9}$$

Figure 6 indicates draw among 1/T and log K_{ads}. From the line slope, ΔH^o_{ads} value can be determined. ΔS^o_{ads} can be gotten by applying the next balance:

$$\Delta S_{ads}^o = \frac{\Delta H_{ads}^o - \Delta G_{ads}^o}{T} \tag{10}$$

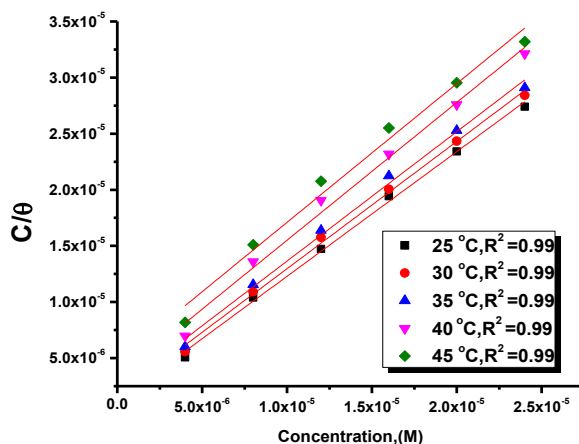


Figure 5. Langmuir adsorption plots of CTT on Cu surface at different temperatures
Slika 5. Langmuir-ovi adsorpcioni grafikoni CTT na površini Cu pri različitim temperaturama

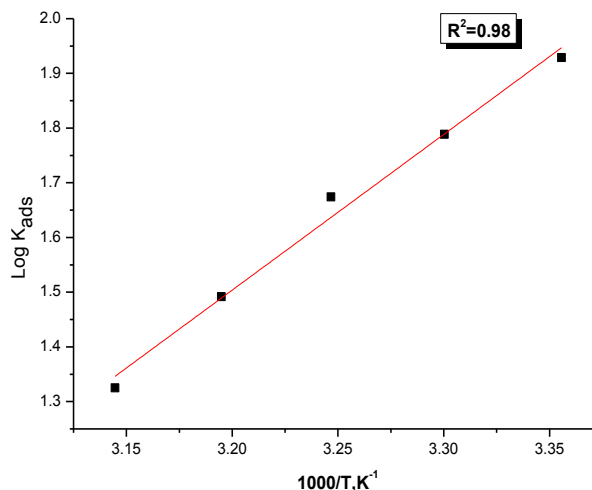


Figure 6. log K_{ads} against 1/T for adsorption of CTT on Cu surface

Slika 6. log K_{ads} prema 1/T za adsorpciju CTT na površini Cu

The negative value of ΔG^o_{ads} indicates the spontaneity and the stability of the CTT adsorption layer occurred on the Cu surface (Table 3). The

obtained values of ΔG°_{ads} , are around 20 kJ mol^{-1} indicates the physisorption of the CTT molecules on the Cu surface. Indicating that the adsorption procedure is exothermic this obtained from the negative values of ΔH°_{ads} .

Table 3. Adsorption parameters for CTT at different temperatures

Tabela 3. Parametri adsorpcije za CTT na različitim temperaturama

Temp. °C	$K_{ads} \text{ M}^{-1}$	$-\Delta G^{\circ}_{ads} \text{ kJ mol}^{-1}$	$-\Delta H^{\circ}_{ads} \text{ kJ mol}^{-1}$	$-\Delta S^{\circ}_{ads} \text{ J mol}^{-1} \text{ K}^{-1}$
25	85	20.9	54.0	70.1
30	61	20.4		67.4
35	47	20.1		65.2
40	31	19.3		61.7
45	21	18.7		58.5

Table 4. PP parameters for liquefaction of the Cu in the used acid environment without and at altered doses of CTT

Tabela 4. PP parametri za tečenje Cu u korišćenju kiseloj sredini bez i pri izmenjenim dozama CTT

Conc. M	$i_{corr}, \mu\text{A cm}^{-2}$	$-E_{corr}, \text{mV vs SCE}$	$\beta_a \text{ mV dec}^{-1}$	$-\beta_c \text{ mV dec}^{-1}$	C.R, 10^2 mpy	Θ	% IE
Blank	396	19	115	185	381	--	--
4×10^{-6}	244	23	111	177	272	0.384	38.4
8×10^{-6}	157	14	113	191	153	0.604	60.4
12×10^{-6}	142	19	109	187	149	0.641	64.1
16×10^{-6}	137	25	99	197	147	0.654	65.4
20×10^{-6}	103	26	88	201	58	0.740	74.0
24×10^{-6}	39	24	93	174	25	0.902	90.2

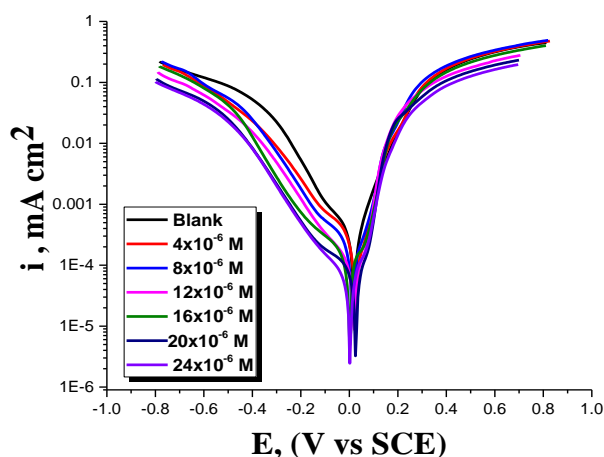


Figure 7. PDP curves for corrosion of the Cu in the used acid medium without and at various doses of CTT

Slika 7. PDP krive za koroziju Cu u korišćenju kiseloj sredini bez i pri različitim dozama CTT

3.2. Electrochemical Techniques

3.2.1. PDP tests

PDP curves in the absence and at different doses of CTT for Cu in the acid medium were presented in the Figure 7. It is apparent that the examined CTT retards the anodic dissolution of Cu and cathodic discharge of oxygen. PDP results such as (E_{corr}), (i_{corr}), slopes of Tafel lines (β_a and β_c), θ , and % IE were determined and tabulated in Table 4. Lowering the values of i_{corr} is because the CTT has been adsorbed on the surface of the Cu. There is no clear change in E_{corr} , β_a and β_c in the protect solutions associated with the uninhibited one, and there is no definite change in data of E_{corr} , these indicate that the CTT behaves as mixed kind inhibitor [51]. In addition, cathodic slope (β_c) moved to more negative direction and the anodic slope (β_a) moved to more positive direction in presence of the CTT inhibitor. The parallel Tafel lines indicate that the mechanism of the corrosion reaction is preserved and the basic adsorption mode prevents the corrosion reaction [52].

3.2.2. EIS tests

For the Cu electrode, Nyquist plots were produced in the presence and at different doses of CTT at their respective corrosive potential after 30 minutes of immersion in the acid medium. Figure 8 shows the resulting Nyquist and Bode plots. It is clear that the inductive loops in the blank solution are bigger when the CTT is present than when it is not, and that the size increases in direct proportion to the concentration of CTT [53]. Interestingly, the frequency dispersion effect causes the capacitive loops to diverge from perfect semicircles. The applied electrical circuit model equivalent for fitting EIS results was displayed in Figure 9, it explains the resistance of charge transfer (R_{ct}) values, constant phase element (CPE), resistance of solution (R_s) and quadratic resistance (W_d). The data in Table 5 include resistance (R_{ct}) to charge transfer, capacitance (C_{dl}) of double layer, (Θ) and (%IE) attained from EIS test. As the CTT dose is

increased, it is shown that R_s and R_{ct} values rise but C_{dl} values decrease; it may be demonstrated by exchange between the molecules of the water and

the CTT molecule which adsorb on the metal's surface and/or increasing the double layer thickness [54].

Table 5. EIS parameters for Cu corrosion in the used acid medium without and at various doses of CTT

Tabela 5. EIS parametri za Cu koroziju u korišćenom kiselom medijumu bez i pri različitim dozama CTT

Conc., M	R_{ct} , $\Omega \text{ cm}^2$	$C_{dl}, \times 10^{-3} \mu\text{F cm}^{-2}$	θ	%IE
Blank	23	142	---	---
4×10^{-6}	76	123	0.697	69.7
8×10^{-6}	102	101	0.775	77.5
12×10^{-6}	208	76	0.889	88.9
16×10^{-6}	220	68	0.895	89.5
20×10^{-6}	245	51	0.906	90.6
24×10^{-6}	270	37	0.915	91.5

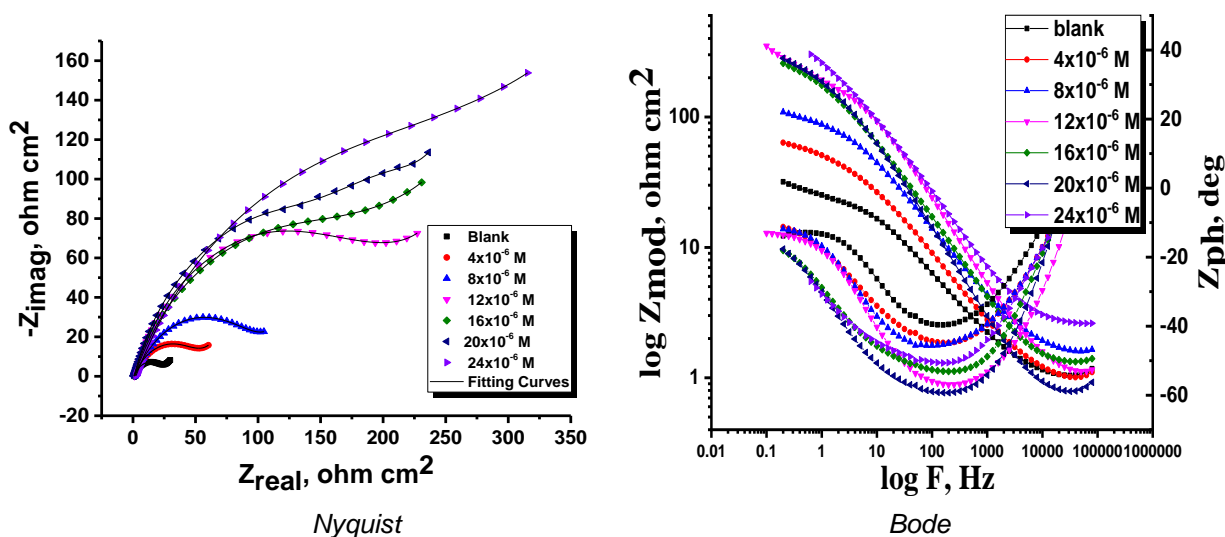


Figure 8. Nyquist and Bode graphs for Cu corrosion in the used acid medium without and at various doses of CTT

Slika 8. Nyquist i Bode-ov grafikon za koroziju Cu u korišćenom kiselom medijumu bez i pri različitim dozama CTT-a

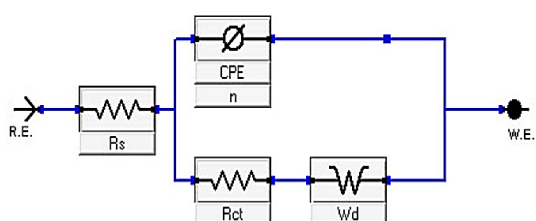


Figure 9. The circuit used to analyze the EIS values

Slika 9. Kolo koje se koristi za analizu EIS vrednosti

3.3. Surface examinations

3.3.1. SEM analysis

SEM analysis was performed on the Cu surface to determine whether the surface

morphology was changed when a specific concentration of CTT molecules was used. SEM micrographs obtained for Cu samples without and with 24×10^{-6} M CTT presented in Figure 10. When the tested inhibitor was present, it significantly reduced Cu surface corrosion as seen in Figure 10b and the Cu surface was smooth. In the absence of any inhibitor, corrosion significantly weakened the Cu's surface in HNO_3 (Figure 10a), resulting in visible pits and cavities [55]. We can deduce from the SEM results that when the inhibitor was utilized, a protective coating formed on the Cu superficial [56]. According to EDX analysis, the Cu surface is heavily damaged without the inhibited solution, where the images of inhibited Cu surface indicated less corrosion in the presence of examined inhibitors. Also, the percentage of iron in the Cu surface immersed in

inhibited solution is decreasing, while the percentage of the carbon and heteroatoms (S, O and N) is increasing. From the SEM-EDX tests, we can conclude that the examined CTT adsorbed on

the Cu metal surface shows an excellent image for preventing severe corrosion of the metal surface [57].

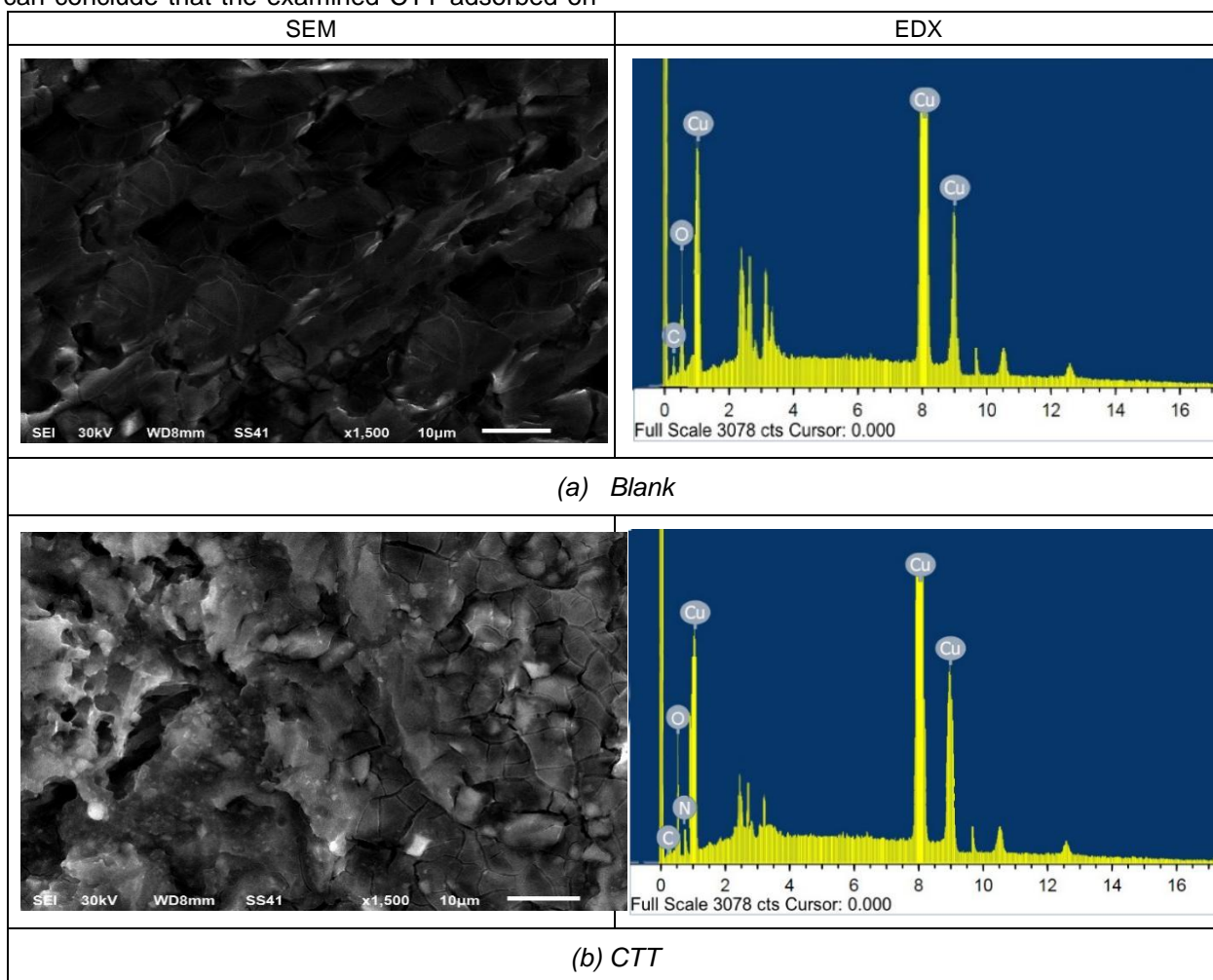


Figure 10. SEM and EDX profiles for: (a) After of 24-hour immersion in HNO_3 (1.0 M), (b) with 24×10^{-6} M CTT presented

Slika 10. SEM i EDX profili za: (a) Posle 24-časovnog potapanja u HNO_3 (1,0 M), (b) sa prikazanim CTT 24×10^{-6} M

3.4. Quantum Chemical Parameters

The highest (E_{HOMO}) occupied value of a molecule represents its ability to donate two unshared electrons. On the other hand, a larger E_{HOMO} indicates a greater likelihood that the molecule will provide protons to an electroscopic reagent [58]. A higher propensity for the molecule to absorb electrons from the metal atoms is shown by a lower energy of the empty molecular orbital (E_{LUMO}). The energy band gap ΔE_g ($\Delta E = E_{\text{HOMO}} - E_{\text{LUMO}}$) that the lower energy gap values are reflected to be great reactivity of the CTT molecule and have excellent corrosion behavior onto the Cu surface [59]. Different parameters were resulted via the calculations. The quantum parameters connotation with corrosion hindrance were

calculated containing ionization potential ($I_p = -E_{\text{HOMO}}$), molecular dipole moment (μ), electron affinity ($E_A = -E_{\text{LUMO}}$), global hardness (η), electronegativity (χ) that are used to calculate the electrons transfer from the inhibitor molecule to the metallic atom ΔN , electrophilicity index (ω), softness (σ), and back-donation (ΔE back-donation)", were calculated as Koopmans's theorem" [60] from the next balance:

$$\mu = -\chi = -\frac{I_p + E_A}{2} \quad (11)$$

$$\chi = \frac{I_p + E_A}{2} \quad (12)$$

$$\eta = \frac{I_p - E_A}{2} \quad (13)$$

$$\sigma = \frac{1}{\eta} \quad (14)$$

$$\omega = \frac{\mu^2}{2\eta} \quad (15)$$

$$\Delta E_{back\ donation} = -\frac{\eta}{4} \quad (16)$$

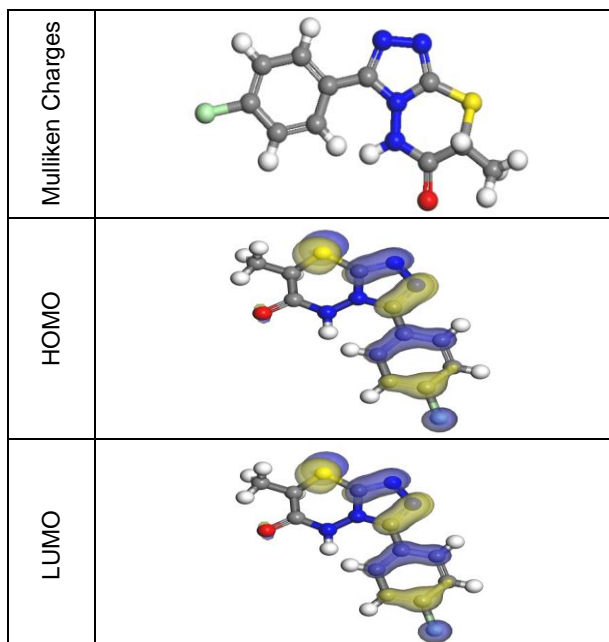


Figure 10 The electron density maps of HOMO and LUMO for the CTT Vilazodone are provided by the frontier molecular

Slika 10 Mape elektronske gustine HOMO i LUMO za CTT Vilazodon su obezbeđene od strane graničnog molekula

A molecule's polarity is determined by its molecular dipole moment (μ) [61]. A higher degree of polarization in the molecule is associated with a larger dipole moment. A recent research [62] claims that higher dipole moment levels and lower ΔE values both enhance % IE.

Table 6. Quantum statistics for the considered CTT inhibitor

Tabela 6. Kvantna statistika za razmatrani CTT inhibitor

Compound	CTT
E_{HOMO} , eV	-5.386
E_{LUMO} , eV	-3.313
ΔE , eV	2.07
I_p , eV	5.386
E_A , eV	3.313
η , eV	1.04
σ , eV	0.96
μ , eV	4.349
Dipole moment (Debye)	4.254

3.4. Inhibition mechanism analysis

There are two adsorption kinds, they are: chemisorption and physisorption. Usually, physisorption procedure requirements the attendance of charged molecules and charged Cu surface, while, chemisorption process contains sharing electrons or transferring them from the molecules of the CTT to the d-orbital of iron forming coordinate bond. CTT has electronegative donor atom O, N and π electrons of the aromatic rings. Effective CTT adsorption on the surface of the Cu is caused by these electronegative donor atoms or π electrons of the aromatic rings, or both of them. [63]. The positively charge of Cu surface in aqueous acid environment [64]. An electrostatic attraction causes the protonated CTT (cationic) to adsorb on the negatively charged metal surface created by the adsorbed Cl^- ions on the Cu sample. The specimen Cu sample could adsorb the protonated molecules. The adsorption process results in the formation of a corrosion-inhibiting layer on the surface of the Cu. Remove water from the Cu surface, then protect it from corrosion.

4. CONCLUSIONS

- 3-(4-chlorophenyl)-7-methyl-5H-[1,2,4] triazolo [3,4-b] [1,3,4]thiadiazin-6(7H)-one (CTT) shows high inhibition efficiency for corrosion of the Cu in one molar HNO_3 solutions.
- Langmuir adsorption isotherm was followed when CTT was adsorbed onto Cu surface. The process of the adsorption is physical adsorption.
- % IE increases as CTT dose increases and as the temperature decreases.
- According to PDP method, CTT inhibitor has cathodic and anodic inhibitory effects.
- C_{dl} decreases and R_{ct} increases as CTT concentration increased.
- Chemical and electrochemical tests showed that investigated CTT behaved as good corrosion inhibitor for Cu

5. REFERENCES

- X.J.Raj, N.Rajendran (2011) Corrosion inhibition effect of substituted thiadiazoles on brass. Int J Electrochem Sci.6(2), 348–66.
- S.Neupane, P.Losada-Pérez, U.Tiringer, P.Taheri, D.Desta, C.Xie (2021) Study of mercaptobenzimidazoles as inhibitors for copper corrosion: down to the molecular scale. J Electrochem Soc. 168(5), 51504. doi.org/10.1149/1945-7111/abf9c3
- C.U.Dueke-Eze, N.A.Madueke, N.B.Iroha, N.J. Maduelosi, L.A.Nnanna, V.C.Anadebe (2022) Adsorption and inhibition study of N-(5-methoxy-2-hydroxybenzylidene) isonicotinohydrazide Schiff base on copper corrosion in 3.5% NaCl. Egypt J Pet. 31(2), 31–7. doi.org/10.1016/j.ejpe.2022.05.001

- [4] A.S. Fouda, M.A. Ismail, M.A. Khaled, A. El-Hossiany (2022) Experimental and computational chemical studies on the corrosion inhibition of new pyrimidinone derivatives for copper in nitric acid. *Sci Rep.* 12(1), 16089. <https://doi.org/10.1038/s41598-022-20306-4>
- [5] E.M. Sherif, S.M. Park (2005) Inhibition of copper corrosion in 3.0% NaCl solution by N-phenyl-1, 4-phenylenediamine. *J Electrochem Soc.* 152(10), B428. doi.org/10.1149/1.2018254
- [6] S.H. Zaferani, M. Sharifi, D. Zaarei, M.R. Shishesaz (2013) Application of eco-friendly products as corrosion inhibitors for metals in acid pickling processes—A review. *J Environ Chem Eng.* 1(4), 652–657. doi.org/10.1016/j.jece.2013.09.019
- [7] M. Finšgara, I. Milošev, B. Pihlar (2007) Inhibition of Copper Corrosion Studied by Electrochemical and EQCN Techniques. *Acta Chim Slov.* 54(3), 591–597.
- [8] A. El Warraky, H.A. El Shayeb, E.M. Sherif (2004) Pitting corrosion of copper in chloride solutions. *Anti-Corrosion Methods Mater.* 51(1), 52–61. DOI: 10.1108/00035590410512735
- [9] S.H. Etaiw, G.S. Hassan, A.A. El-Hossiany, A.S. Fouda (2023) Nano-metal–organic frameworks as corrosion inhibitors for strengthening anti-corrosion behavior of carbon steel in a sulfuric acid environment: from synthesis to applications. *RSC Adv.* 13(22), 15222–35. doi.org/10.1039/D3RA01644G
- [10] M.B. Petrović Mihajlović, Ž.Z. Tasić, M.B. Radovanović, A.T. Simonović, M. Antonijević (2022) Electrochemical Analysis of the Influence of Purines on Copper, Steel and Some Other Metals Corrosion. *Metals (Basel)*. 12(7), 1150.
- [11] O.A.A. El-Shamy (2013) Effectiveness of some nonionic surfactants as corrosion inhibitors for carbon steel in hydrochloric acid solution. *Adv Mater Res.*, 787, 211–5. doi.org/10.4028/www.scientific.net/AMR.787.211
- [12] O.A.A. El-Shamy, M.A. Deyab (2023) Improvement of the corrosion resistance of epoxy coatings with the use of a novel zinc oxide-alginate nanoparticles compound. *Mater Lett.* 331, 133402. <https://doi.org/10.1016/j.matlet.2022.133402>
- [13] O.A.A. El-Shamy, M.A. Deyab (2023) Novel anti-corrosive coatings based on nanocomposites of epoxy, chitosan, and silver. *Mater Lett.* 330, 133298. <https://doi.org/10.1016/j.matlet.2022.133298>
- [14] A.M. Abdel-karim, R.A. Azzam, O. El-Said Shehata, M.A. Adly, O.A.A. El-Shamy, G.A. El Mahdy (2023) Synthesis of New Guanidine Benzothiazole Derivative and Its Application as Eco-Friendly Corrosion Inhibitor. *Egypt J Chem.* 66(7), 187–95. doi.org/10.21608/EJCHEM.2022.167419.7063
- [15] M.A. Deyab, O.A.A. El-Shamy, H.K. Thabet, A.M. Ashmawy (2023) Electrochemical and theoretical investigations of favipiravir drug performance as ecologically benign corrosion inhibitor for aluminum alloy in acid solution. *Sci Rep.* 13(1), 8680. doi.org/10.1038/s41598-023-35226-0
- [16] A. Lachiri, M. El Faydy, F. Benhiba, H. Zarrok, M. El Azzouzi, M. Zertoubi (2018) Inhibitor effect of new azomethine derivative containing an 8-hydroxyquinoline moiety on corrosion behavior of mild carbon steel in acidic media. *Int J Corros Scale Inhib.* 7(4), 609–32. doi.org/10.17675/2305-6894-2018-7-4-9
- [17] J. Saranya, F. Benhiba, N. Anusuya, R. Subbiah, A. Zarrouk, S. Chitra (2020) Experimental and computational approaches on the pyran derivatives for acid corrosion. *Colloids Surfaces A Physicochem Eng Asp.* 603, 125231. <https://doi.org/10.1016/j.colsurfa.2020.125231>
- [18] N.A. Madueke, N.B. Iroha (2018) Protecting aluminum alloy of type AA8011 from acid corrosion using extract from Allamanda cathartica leaves. *Int J Innov Res Sci Eng Technol.* 7(10), 10251–8. doi.org/10.15680/IJRSET.2018.0710014
- [19] A.T. Simonović, Z.Z. Tasić, M.B. Radovanović, M.B. Petrović Mihajlović, M.M. Antonijević (2020) Influence of 5-chlorobenzotriazole on inhibition of copper corrosion in acid rain solution. *ACS omega.* 5(22), 12832–41. <https://doi.org/10.1021/acsomega.0c00553>
- [20] A. Zarrouk, B. Hammouti, H. Zarrok, M. Bouachrine, K.F. Khaled, S.S. Al-Deyab, (2012) Corrosion Inhibition of Copper in Nitric Acid Solutions Using a New Triazole Derivative. *Int. J. Electrochem. Sci.*, 7, 89 – 105. [https://doi.org/10.1016/S1452-3981\(23\)13323-2](https://doi.org/10.1016/S1452-3981(23)13323-2)
- [21] Y.G. Avdeev, A. Tatyana, A. Nenasheva, An. Yu. Luchkin, An. I. Marshakov, Y. I. Kuznetsov (2023) Thin 1,2,4-Triazole Films for the Inhibition of Carbon Steel Corrosion in Sulfuric Acid Solution, *Coatings*, 15(19), 6989. doi.org/10.3390/ma15196989.
- [22] S Ramesh, S Rajeswari, S Maruthamuthu (2004) Corrosion inhibition of copper by new triazole phosphonate derivatives. *Appl Surf Sci*, 229, 214–225, <https://doi.org/10.1016/j.apsusc.2004.01.063>
- [23] J. Yu, L. Jiang, F. Gan (2010) Inhibition of copper corrosion in deionized water by 3-amino-5-mercapto-1,2,4-triazole. *J Chin Soc Corros Prot.* 30, 21–24. doi.org/10.1016/j.apsusc.2004.01.063
- [24] J. Yu, F. Gan, L. Jiang (2008) Inhibition effect of 3-amino-5-mercapto-1,2,4-triazole on copper corrosion. *Corrosion* 64, 900–904. doi.org/10.5006/1.3294405
- [25] A. Soumoue, B. El Ibrahimy, S. El Issami, L. Bazzi (2014) Some triazolic compounds as corrosion inhibitors for copper in sulphuric acid. *Int J Sci Res*, 3, 349–354.
- [26] Y.M. Tang, Y. Chen, Y. W. Zang, X.S. Yin, J.T. Wang (2010) 3,5-Bis(2-thienyl)-4-amino-1,2,4-triazole as a corrosion inhibitor for copper in acidic media. *Anti-Corros Methods Mater*, 57, 227–233
- [27] C. Y. hen, Y. Tang, W. Yang, Y. Liu, J. Wang (2009) Inhibition of 3,5-bis(2-thienyl)-4-amino-,2,4-triazole on copper in HCl media. *Corros Sci Prot Technol* 21, 406–409.
- [28] A. Zarrouk, B. Hammouti, S.S. Al-Deyab, R. Salghi, H. Zarrok, C. Jama, F. Bentiss (2012) Corrosion inhibition performance of 3,5-diamino-1,2,4-triazole for protection of copper in nitric acid solution. *Int J Electrochem Sci* 7, 5997–6011. [https://doi.org/10.1016/S1452-3981\(23\)19457-0](https://doi.org/10.1016/S1452-3981(23)19457-0)

- [29] A.Lalitha, S.Ramesh, S.Rajeswari (2005) Surface protection of carbon steel by hexanesulphonic acid-zinc ion system. *Electrochim Acta*, 51,47–55. 29. <https://doi.org/10.1155/2014/628604>
- [30] H.H.Hassan, E.Abdelghani, M.A.Amin (2007) Inhibition of mild steel corrosion in hydrochloric acid solution by triazole derivatives -Part I. *Electrochim Acta* 52, 6359–6364. <https://doi.org/10.1016/j.electacta.2007.08.021>
- [31] M.K.Awad, M.R.Mustafa, M.M.A.Elnga (2010) Computational simulation of the molecular structure of some triazoles as inhibitors for the corrosion of metal surface. *J Mol Struct (Theochem)*, 959, 66–74. <https://doi.org/10.1016/j.theochem.2010.08.008>
- [32] S.E.S.M.herif, R.M.Erasmus, J.D.Comins (2007) Effects of 3-amino-1,2,4-triazole on the inhibition of copper corrosion in acidic chloride solutions. *J Colloid Interface Sci*, 311,144–151. doi.org/10.1016/J.JCIS.2007.02.064
- [33] E.S.M.Sherif, R.M.Erasmus, J.D.Comins (2007) Corrosion of copper in aerated acidic pickling solutions and its inhibition by 3-amino-1,2,4-triazole-5-thiol. *J Colloid Interface Sci*,306, 96–104. doi.org/10.1016/j.jcis.2007.01.003
- [34] P.Sudheer, M.A.Quraishi (2013) Electrochemical and theoretical investigation of triazole derivatives on corrosion inhibition behavior of copper in hydrochloric acid medium. *Corros, Sci*, 70,161–169. <https://doi.org/10.1016/j.corsci.2013.01.025>
- [35] E.G.Demissie, S.B.Kassa, G.W.Woyessa (2014) Quantum chemical study on corrosion inhibition efficiency of 4-amino-5-mercapto-1,2,4-triazole derivatives for copper in HCl solution. *Int J Sci, Eng Res*, 5, 304–312. doi.org/10.14299/ijser.2014.06.001
- [36] Y.Wang, J.Hu, Y.Wang, Li.Yu (2016) A New Method for Preventing Corrosion Failure: Thiourea and Hexamethylenetetramine as Inhibitor for Copper, *Bull. Korean Chem. Soc.*, 37, 1797–1811. <https://doi.org/10.1002/bkcs.10978>
- [37] P. Chooto, W. Aemaek Tappachai, S. Duangthong, S. Manaboot (2020) Corrosion Inhibition of Copper by Thioureas, and N, O, S-Ligating Ring Compounds, *Port. Electrochim. Acta*, 38(5), 343-350. doi.org/10.4152/pea.202005343
- [38] R.Vaira Vignesh, R.Padmanaban, M.Govindaraju (2020) Synthesis and characterization of magnesium alloy surface composite (AZ91D—SiO₂) by friction stir processing for bioimplants. *Silicon*. 12(5),1085–102. <https://doi.org/10.1007/s12633-019-00194-6>
- [39] J. Liu, P.Hao, L.Jiang, L.Qian (2022) Novel Eco-friendly Slurries for Chemical Mechanical Polishing of GCr15 Bearing Steel. *Tribol Lett.* 70(3), 67-82. <https://doi.org/10.1007/s11249-022-01608-0>
- [40] H.Hussien, S.Shahen, A.M.Abdel-karim, I.M.Ghayad, O.A.A.El-Shamy, N.Mostfa (2023) Experimental and theoretical evaluations: Green synthesis of new organic compound bis ethanethioly oxalamide as corrosion inhibitor for copper in 3.5% NaCl. *Egypt J Chem.* 66(3),189–96. doi.org/10.21608/ejchem.2023.182301.7364
- [41] A.Fateh, M.Aliofkhazraei, A.R.Rezvanian (2020) Review of corrosive environments for copper and its corrosion inhibitors. *Arab J Chem.* 13(1),481–544. <https://doi.org/10.1016/j.jcis.2007.02.064>
- [42] A.M. Abdel-Karim, A.M.El-Shamy, Y. Reda (2022) Corrosion and stress corrosion resistance of Al Zn alloy 7075 by nano-polymeric coatings. *J Bio-and Tribo-Corrosion.* 8(2), 57. <https://doi.org/10.1007/s40735-022-00656-2>
- [43] B. Souad, S.Chafia, A.Hamza, M.Wahiba, B.Issam (2021) Synthesis, experimental and DFT studies of some benzotriazole derivatives as brass C68700 corrosion inhibitors in NaCl 3%. *Chemistry Select.* 6(6),1378–84. doi.org/10.1002/slct.202004383
- [44] A.A. El-Barbary, A.Z.Abou-El-Ezz, A.A.Abdel-Kader, M.El-Daly, C.Nielsen (2004) Synthesis of some new 4-amino-1, 2, 4-triazole derivatives as potential anti-HIV and anti-HBV. *Phosphorus, Sulfur, and Silicon.* 179(8),1497–508. <https://doi.org/10.1080/10426500490463989>
- [45] E.E.Oguzie, C.Unaegbu, C.N.Ogukwe, B.N.Okolue, A.I.Onuchukwu (2004) Inhibition of mild steel corrosion in sulphuric acid using indigo dye and synergistic halide additives. *Mater Chem Phys.* 84(2–3),363–8. <https://doi.org/10.1016/j.matchemphys.2003.11.027>
- [46] P.Desai (2010) Efficiency of xlenol orange as corrosion inhibitor for aluminum in trichloroacetic acid. *Indian Journal of Chemical Technology*, 17, 50- 55, <https://ssrn.com/abstract=4234402>, <http://dx.doi.org/10.2139/ssrn.4234402>
- [47] A.M.Ayuba, A.Uzairu, G.A.Shallangwa (2018) Theoretical study of aspartic and glutamic acids as corrosion inhibitors on aluminum metal surface', *Moroccan, Journal of Chemistry*, 6(1), 6-12. [doi:10.48317/IMIST.PRSM/MORJCHEM-V6I1.9111](https://doi.org/10.48317/IMIST.PRSM/MORJCHEM-V6I1.9111)
- [48] S.A.Umoren, I.B.Obot, A.Madhankumar, Z.M.Gasem (2015) Performance evaluation of pectin as ecofriendly corrosion inhibitor for X60 pipeline steel in acid medium: Experimental and theoretical approaches' *Carbohydrate polymers*, 124, 280-291. doi.org/10.1016/j.carbpol.2015.02.036
- [49] Q.B.Zhang, Y.X.Hua (2009) Corrosion inhibition of mild steel by alkyimidazolium ionic liquids in hydrochloric acid', *Electrochim. Acta*, 54(6), 1881-1887. <https://doi.org/10.1016/j.electacta.2008.10.025>
- [50] N.Iroha, N.Maduelosi (2020) 'Pipeline steel protection in oil well acidizing fluids using expired pharmaceutical agent', *Chemistry International*, 6(4), 267-276. <https://ssrn.com/abstract=3693741>
- [51] P.Desai, S.M.Kapopara (2014) Inhibitory action of xlenol orange on aluminum corrosion in hydrochloric acid solution. *Indian Journal of Chemical Technology*, 21, 139-145. <https://ssrn.com/abstract=4234403> or <http://dx.doi.org/10.2139/ssrn.4234403>
- [52] P.S.Desai, R.T.Vahi (2011) Inhibitive efficiency of sulphathiazole for Alcorrosion in trichloroacetic acid. *Anti-Corrosion Methods Mater.* 58(2),70–75. <https://doi.org/10.1108/00035591111110714>
- [53] L.Larabi, Y.Harek, M.Traisnel, A.Mansri (2004) Synergistic influence of poly (4-vinylpyridine) and potassium iodide on inhibition of corrosion of mild steel in 1M HCl. *J Appl Electrochem.* 34, 833–9. <https://doi.org/10.1023/B:JACH.0000035609.09564.e6>

- [54] B.I.Ita, O.E.Offiong (2001) The study of the inhibitory properties of benzoin, benzil, benzoin-(4-phenylthiosemicarbazone) and benzil-(4-phenylthiosemicarbazone) on the corrosion of mild steel in hydrochloric acid. Mater Chem Phys. 70(3), 330–5. [https://doi.org/10.1016/S0254-0584\(00\)00476-4](https://doi.org/10.1016/S0254-0584(00)00476-4)
- [55] K.F.Khaled (2009) 'Monte Carlo simulations of corrosion inhibition of mild steel in 0.5 M sulphuric acid by some green corrosion inhibitors', J. Solid State Electrochem.,13,1743-1756. <https://doi.org/10.1007/s10008-009-0845-y>
- [56] S.S.Salem, E.N. Hammad, A.A.Mohamed, W.El-DougDoug (2022) A comprehensive review of nanomaterials: Types, synthesis, characterization, and applications. Biointerface Res Appl Chem. 13(1), 41. doi.org/ 10.33263/BRIAC131.041
- [57] I.B.Onyeachu, S.Abdel-Azeim, D.S.Chauhan, M.A.Quraishi (2020) 'Electrochemical and computational insights on the application of expired metformin drug as a novel inhibitor for the sweet corrosion of C1018 steel', ACS omega, 6(1), 65-76. doi.org/ 10.33263/BRIAC131.041
- [58] M.A.Abu-Dalo, A.A.Othman, N.A.F.Al-Rawashdeh (2012) 'Exudate gum from acacia trees as green corrosion inhibitor for mild steel in acidic media', Int. J.Electrochem. Sci., 7(10), 9303-9324. [https://doi.org/10.1016/S1452-3981\(23\)16199-2](https://doi.org/10.1016/S1452-3981(23)16199-2)
- [59] A.M.A.li, A.M.Ouf, El- A.Hossiany, A.S.Fouda (2022) Eco-friendly approach to corrosion inhibition of copper in hno3 solution by the expired tylosin drug. Biointerface Res Appl Chem. 12(4),5116–30. <https://doi.org/10.33263/BRIAC124.51165130>
- [60] A.Zarrouk, B.Hammouti, A.Dafali, M.Bouachrine, H.Zarrok, S.Boukhris, S.S.Al-Deyab (2014) A theoretical study on the inhibition efficiencies of some quinoxalines as corrosion inhibitors of copper in nitric acid', J. Saudi Chem. Soc., 18(5),450-455. doi.org/10.1016/J.JSCS.2011.09.011
- [61] I.B.Obot, N.O.Obi-Egbedi (2010) 'Theoretical study of benzimidazole and its derivatives and their potential activity as corrosion inhibitors', Corros.Sci., 52(2), 657-660. <https://doi.org/10.1016/j.corsci.2009.10.017>
- [62] O.A.Elgyar, A.M.Ouf, A.El-Hossiany, A.S.Fouda (2021) The inhibition action of viscum album extract on the corrosion of carbon steel in hydrochloric acid solution. Biointerface Res Appl Chem. 11(6),14344–58. <https://doi.org/10.33263/BRIAC116.1434414358>
- [63] A.S.Fouda, E.S.El-Gharkawy, H.Ramadan, A.El-Hossiany (2021) Corrosion resistance of mild steel in hydrochloric acid solutions by clinopodium acinos as a green inhibitor. Biointerface Res Appl Chem. 11(2), 9786. doi.org/10.33263/briac112.97869803
- [64] A.S.Fouda, S.A.Abd El-Maksoud, A.A.M.Belal, A.El-Hossiany, A.Ibrahium (2018) Effectiveness of some organic compounds as corrosion inhibitors for stainless steel 201 in 1M HCl: experimental and theoretical studies. Int J Electrochem Sci. 13(10), 9826–46. <https://doi.org/10.20964/2018.10.36>

IZVOD

ELEKTROHEMIJSKE I TEORIJSKE PROCENE 3-(4-HLOROFENIL)-7-METIL-5H-[1, 2, 4] TRIAZOLO [3,4-B][1,3,4]TIADIAZIN-6(7H)-ONA KAO INHIBITOR KOROZIJE ZA BAKAR U OKRUŽENJU AZOTNE KISELINE

3-(4-hlorofenil)-7-metil-5H-[1,2,4]triazolo[3,4-b][1,3,4]tiadiazin-6(7H)-on (CTT) je sintetizovan i ocenjen kao inhibitor korozije za bakar u 1M HNO₃. Eksperimentalnim i teorijskim metodama u kiseloj sredini određena su adsorpciona svojstva sintetizovanog CTT. Za određivanje inhibitivnog ponašanja CTT korišćene su hemijske metode kao što su metoda gubitka mase (ML), DC potenciodinamička polarizacija (PDP) i AC impedansa (EIS). Podaci dobijeni ovim metodama pokazuju da sa povećanjem koncentracije CTT-a njegova efikasnost inhibicije (%IE) raste i dostiže 91,5% pri 24k10⁻⁶ M, 25°C primenom EIS tehnike. Prisustvo CTT smanjuje kapacitet dvostrukog sloja (Cdl) i poboljšava otpor prenosa naelektrisanja (Rct) u rastvoru jedne molarne azotne kiseline. CTT je inhibitor mešovito tipa iz podataka dobijenih iz krivulja polarizacije. Dobijeni podaci ukazuju da je CTT fizički adsorbovan na površinu Cu u skladu sa Langmuir adsorpcijom. Ispitivanje površinske zaštite obavljeno je pomoću skenirajuće elektronske mikroskopije (SEM), energetski disperzivnog rendgenskog zraka (EDKS) i mikroskopa atomske sile (AFM). Takođe, izračunati su i diskutovani kvantno hemijski parametri CTT-a. Rezultati nekoliko metoda se međusobno slažu.

Ključne reči: Inhibicija korozije, bakar, azotna kiselina, 3-(4-hlorofenil)-7-metil-5H-[1,2,4] triazolo [3,4-b][1,3,4]tiadiazin-6(7H)-on (CTT), Langmuir izoterma

Naučni rad

Rad primljen: 03.01.2024.

Rad prihvaćen: 16.01.2024.

Rad je dostupan na sajtu: www.idk.org.rs/casopis

Mukesh Kumar*

Department of Physics, Multan Modi College Modinagar,
Ghaziabad, UP 201204, India.

Scientific paper

ISSN 0351-9465, E-ISSN 2466-2585

<https://doi.org/10.62638/ZasMat1143>



Zastita Materijala 65 (2)

343 - 349 (2024)

Studies of structural and optical properties of sputtered SiC thin films

ABSTRACT

The present study explored the deposition of amorphous silicon carbide (a-SiC) thin films on Si (100) and glass substrates using RF-magnetron sputtering. The sputtering power is changed from 100 to 250 W to study its influence on the characteristics of a-SiC thin films. Raman spectroscopy reveals the formation of a-SiC as well as carbon clusters. The film deposited at 100 W clearly shows the presence of both transverse optical (TO) and longitudinal optical (LO) phonon modes. The average roughness of the a-SiC films found to follow an increasing trend with increase in the sputtering power. The optical band gap of the a-SiC films measured by UV-Visible spectrophotometer was found to increase up to 2.45 eV with decrease in sputtering power. All a-SiC thin films were highly transparent. The Photoluminescence (PL) spectroscopy results were in agreement with the data observed by UV-Visible spectroscopy.

Keywords: SiC thin films, Magnetron sputtering, Raman spectroscopy, PL spectroscopy

1. INTRODUCTION

Silicon carbide (SiC) is a promising semiconductor material because of its excellent physical and chemical properties. Due to its fine tunable properties, SiC have attracted a great scientific and technological interest and have been used in many kinds of optoelectronic devices, such as solar cell windows layer, color sensors, and thin film light emitting and detecting devices [1-4]. In addition, amorphous SiC (a-SiC) thin films are chemically inert and are an excellent alternate passivation layer for silicon solar cells as well as MEMS application. SiC is hard material and at the moh scale it is just below from the diamond. Some other materials like TiAlBN have studied for their structural and hardness properties [5]. Thin films of a-SiC are usually synthesized by glow discharge method and consequently are hydrogenated a-SiC (a-SiC:H) [6]. To establish electrodes for electrical contacts, the passivity layer bears the high temperature firing process. However, during high temperature firing process, hydrogen in the a-SiC films evaporated.

After the evaporation, many hydrogen molecules voids are generated. Therefore, the firing process brings degradation in the temperature stability of the films [7,8]. In this study, voids free a-SiC thin films have been deposited by RF magnetron sputtering on Si (100) substrate for solar cells and MEMS applications.

Several techniques are used for the synthesis of SiC thin films. Some of the common methods are chemical vapor deposition (CVD) [9,10], pulsed laser deposition (PLD) [11,12], molecular beam epitaxy [13,14] and reactive magnetron sputtering [15-17]. Among these techniques reactive magnetron sputtering is most attractive due to low substrate temperature deposition technique, good adhesion and less concentration of lattice defects [18].

In the present study we attempt to investigate the role of sputtering power on structural and optical properties of a-SiC thin films deposited at 400°C. It has been observed that the sputtering power has a great effect on the properties of SiC thin films.

2. EXPERIMENTAL DETAILS

RF-magnetron sputtering technique has been used to grow a-SiC thin films on glass (Corning 1737) and Si (100) substrates. A commercially available silicon carbide target (SCI-Engineered Materials, USA) with 99.99 % purity was used for deposition of films. The diameter and thickness of

*Corresponding Author: Mukesh Kumar

Email: mkjiit@gmail.com

Paper received: 25. 09. 2023.

Paper corrected: 22.01.2024.

Paper accepted: 31. 01. 2024.

Paper is available on the website: www.idk.org.rs/journal

the target were 50 mm and 5 mm, respectively. The substrate was cleaned in an ultrasonic bath using acetone and methanol. The Si substrate was passivated in 5 % HF solution to prevent the oxide formation on the Si surface. For the deposition of a-SiC films the sputtering pressure and substrate temperature were fixed at 10 mTorr and 400°C, respectively. However the sputtering power was varied in the range from 100 W to 250 W. A turbo-based pumping system was used to achieve a base pressure of $\sim 10^{-6}$ Torr. High-purity argon (99.99%) was used as sputtering gas. The distance between target and substrate was 6 cm and the deposition time for all the films was kept constant for 1 hour. Before each deposition the target was pre-sputtered for 5 min in order to ascertain the same state of the target. The sputtering parameters are shown in the table 1.

After deposition, the a-SiC thin films were characterized by X-ray diffractometer (Bruker D8 Advance), Raman spectrometer (Renishaw) and Atomic Force Microscopy (NT-MDT, model: NTEGRA) to study the structural properties. The optical properties of the a-SiC thin films have been studied by UV-Vis-NIR spectrophotometer (Cary 5000 Varian) and Photoluminescence spectrometer (Perkin Elmer LS 55). The thicknesses of the samples were examined by Surface Profilometer (Ambios Technology XP-200).

3. RESULTS AND DISCUSSION

Figure 1 shows the XRD pattern of a-SiC thin films deposited on Si (100) substrate at the substrate temperature of 400°C with varying sputtering power.

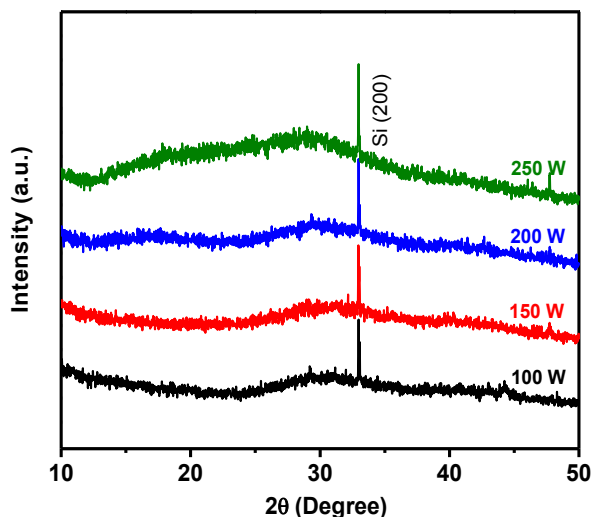


Figure 1. XRD pattern of a-SiC thin films deposited at various sputtering power

Slika 1. XRD uzorak a-SiC tankih filmova deponovanih pri različitoj snazi raspršivanja

Obviously no SiC diffraction peaks observed from the XRD patterns of the all samples, which show that the all samples are amorphous, because at the low substrate temperature there may not be sufficient energy to grow crystalline phase. The XRD peaks at angle ($2\theta \sim 33^\circ$) are corresponds to substrate peaks.

Figure 2 shows Raman spectra in the 100-1600 cm^{-1} region for the a-SiC thin films deposited on Si (100) substrate with varying sputtering power from 100 to 250 W. The Raman scattering measurements were performed at room temperature in the back-scattering configuration. Two broad bands are clearly observed in the regions of 600-1000 cm^{-1} and 1300-1600 cm^{-1} in the obtained Raman spectra. As the former band corresponds to the Raman band of a-SiC due to Si-C bond and the latter corresponding to that of amorphous carbon is due to C-C bonds [19].

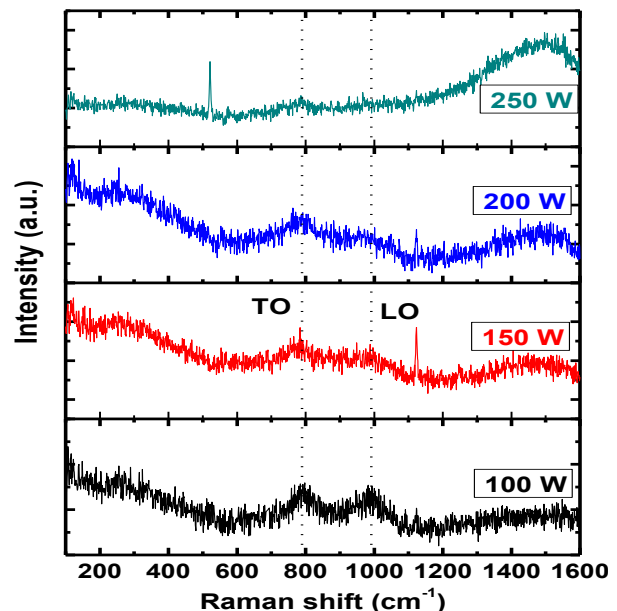


Figure 2. Raman spectra of a-SiC thin films deposited at various sputtering pressures (a) 5 mTorr, (b) 10 mTorr, (c) 15 mTorr, (d) 20 mTorr and (e) 25 mTorr

Slika 2. Ramanski spektri a-SiC tankih filmova deponovanih pri različitim pritiscima raspršivanja (a) 5 mTorr, (b) 10 mTorr, (c) 15 mTorr, (d) 20 mTorr i (e) 25 mTorr

The film deposited at sputtering power of 100 W clearly shows two phonon modes, namely a transverse optical (TO) phonon mode (795 cm^{-1}) and a longitudinal optical (LO) phonon mode (970 cm^{-1}) at the Γ - point of the Brillouin zone centre. Presence of the C-clusters was arising due to the superimposition of E_{2g} stretching mode and A_{1g}

mode of small crystallites of graphite [20]. In this paper, the sputtering power has been optimized to synthesize a-SiC thin films with TO and LO modes and the intensities of both modes decreases with increasing of sputtering power. Raman peak in the $630\text{-}1000\text{ cm}^{-1}$ band was observed due to phonon damping. The reason for this phonon damping may be attributed to the short range ordering of SiC crystallites and the effect of surroundings having Si as well as C-clusters at higher sputtering power.

The AFM images of a-SiC thin-films deposited at varying sputtering power from 100 to 250 W on

Si (100) substrates are shown in Figure 3. From the images we can observe that the thin-films grow in a way of columns or grains and the surface is very compact. The grains are uniformly distributed, and they are all in the shape of ellipse, which is consistent with Refs. [21]. It was observed that with increasing the sputtering power, the value of surface roughness increase. The average surface roughness of the films were observed from 8 nm to 11 nm with varying the sputtering power from 100 to 250 W, respectively as shown in Table 1.

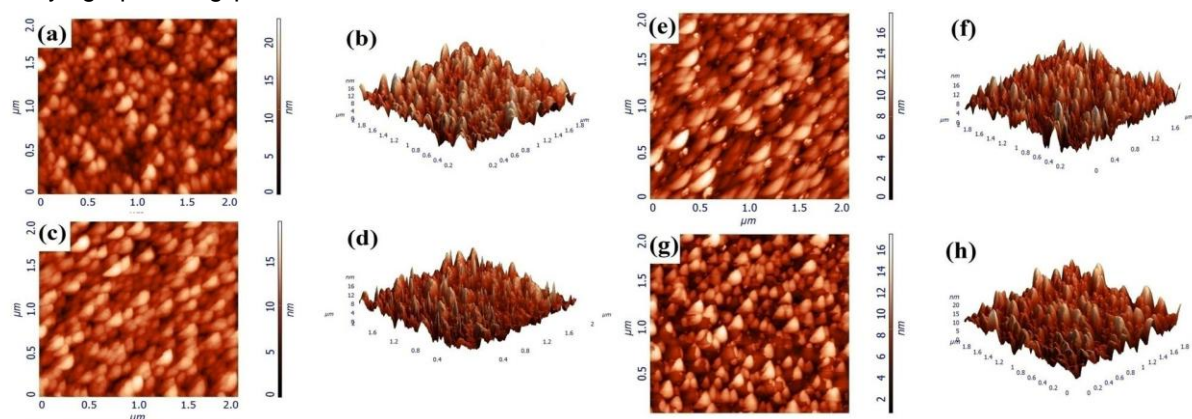


Figure 3. 2D and 3D AFM images of a-SiC thin films deposited at various sputtering power (a)&(b) 100 W, (c)&(d) 150 W, (e)&(f) 200 W and (g)&(h) 250 W

Slika 3. 2D i 3D AFM slike a-SiC tankih filmova deponovanih pri različitim snagama raspršivanja (a)&(b) 100 V, (c)&(d) 150 V, (e)&(f) 200 V i (g) i (h) 250 V

These smaller values of surface roughness indicate that the films were very smooth and have good adherence to the substrate. The surface roughness increases due to the increase in grain size with increasing the power from 100 to 250 W. In order to understand the effect of sputtering power it is necessary to understand the basic working principle of the rf magnetron sputtering. In sputtering process, Argon gas ionized and the argon ions hit the target due to positive charge on the ion and negative charge on the target. In this process the target atoms ejected and deposited on the substrate. If the substrate temperature is low then the sputtered atoms have not much time to move on the substrate surface. We have deposited

a-SiC at the temperature of $400\text{ }^{\circ}\text{C}$ which provide sufficient energy to the sputtered atoms to move on the surface which leads to grow in the column-shaped structure. When sputtering power increased to 150 W both the kinetic energy and deposition rate increased significantly. So the size and the shape has been significantly changed which leads to increase in the thickness of the films [22]. Further increase in the sputtering power up to 250 W, the sputtered atoms have the more kinetic energy which leads to the more increase in surface roughness. We have chosen the sputtering pressure 10 mTorr for all the depositions because we have optimized it in previous study [23].

Table 1. Properties of SiC thin films with variation of sputtering power

Tabela 1. Osobine tankih filmova SiC sa varijacijama snage raspršivanja

S. No.	Sputtering power (W)	Band gap (eV)	Refractive index	Thickness (nm)	Average Transmittance (%)	Average roughness (AFM) (nm)
1.	250	2.21	1.54	1088	84	11
2.	200	2.33	1.65	992	87	10
3.	150	2.40	1.69	967	89	9
4.	100	2.45	1.98	962	89	8

The spectral variations of transmission for the a-SiC films deposited onto glass substrate at various deposition pressure were measured over the wavelength range 200–1100 nm and are shown in Figure 4.

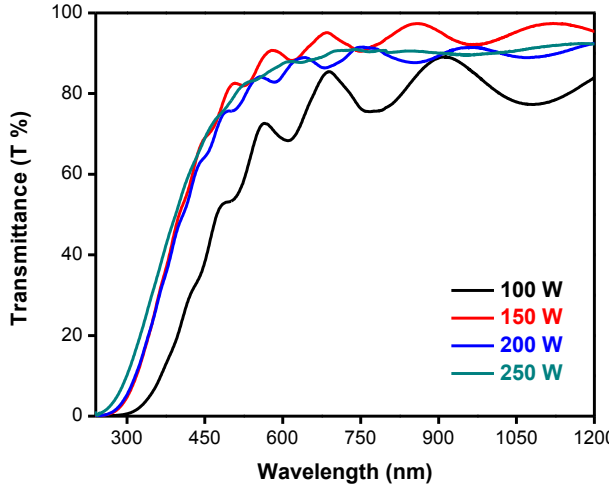


Figure 4. Optical transmittance spectra of a-SiC thin films deposited at various sputtering pressure

Slika 4. Spektri optičke propusnosti a-SiC tankih filmova deponovanih pri različitim pritiscima raspršivanja

The films show very good transmittance in the visible range. It can be clearly seen that transmittance decreases with decreasing of sputtering pressure. As described above, with increase in sputtering pressure, the surface of the films becomes rough and hence results in more scattered light and less transmittance. The film deposited at low sputtering power shows a high transmittance because of minimal scattering light loss caused by the rough surface [24]. The scattering light loss increases with increasing of sputtering power which leads to decrease in transmittance.

Refractive index (n) was estimated from the transmission spectrum by using envelope method and following expression was used to calculate the refractive index.

$$n = [N + (N^2 - n_0^2 n_1^2)^{1/2}]^{1/2}$$

where

$$N = \left[\frac{n_0^2 + n_1^2}{2} \right] + 2 n_0 n_1 (T_{max} - T_{min}) / T_{max} T_{min}$$

n_0 is the refractive index of air, n_1 is the refractive index of substrate, T_{max} and T_{min} are maximum and minimum transmittance values at the same wavelength. The calculated refractive

indices for the film deposited at 400 °C are shown in Table 1. The refractive indices were found to be decrease with decreasing of sputtering pressure up to a limit and increase further decreasing of sputtering pressure.

The absorption spectra of a-SiC thin film have been recorded as a function of the photon energy (hv) in the wavelength range of 200 to 1100 nm. In order to calculate the indirect optical band gap (E_g) of a-SiC thin film deposited at different sputtering pressure we have used the Tauc relation [25].

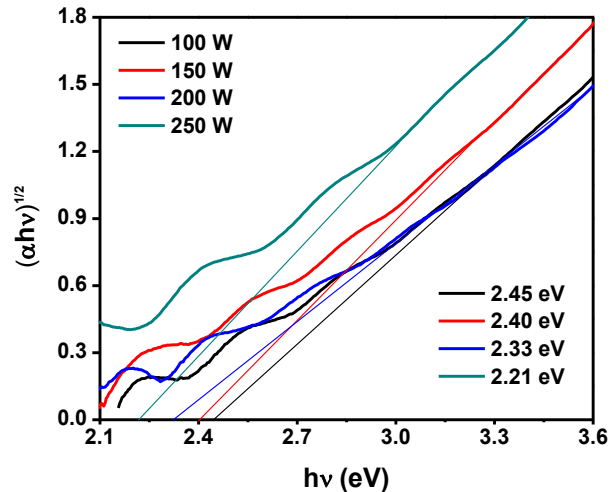


Figure 5. $(ahv)^{1/2}$ versus (hv) plot of a-SiC thin films deposited on glass substrate at various sputtering pressure

Slika 5. Grafikon $(ahn)^{1/2}$ u odnosu na (hn) tankih filmova a-SiC nanesenih na staklenu podlogu pri različitim pritiscima raspršivanja

The absorption spectra of a-SiC thin film have been recorded as a function of the photon energy (hv) in the wavelength range of 200 to 1100 nm. In order to calculate the indirect optical band gap (E_g) of a-SiC thin film deposited at different sputtering pressure we have used the Tauc relation [25].

The band gaps of the a-SiC thin films deposited at sputtering power 100, 150, 200 and 250 W was calculated 2.45 eV, 2.40 eV, 2.33 eV and 2.21 eV, respectively as shown in Figure 5 and Table 1. The band gap increase with decrease in the sputtering power up to 250 W could be due to increase in grain size as explained above in the AFM results (shown in Figure 3).

Figure 6 depicts the room temperature Photoluminescence (PL) spectra of the a-SiC thin films deposited on Si (100) at different sputtering pressure. The excitation wavelength for all a-SiC thin films was 450 nm. PL spectrum of a-SiC thin films deposited at 250 W shows a broad and intense peak at ~ 532 nm near the band gap

emission. This emission was attributed to the band edge emission from the a-SiC [26]. The band gap of SiC has been calculated using thin emission and found to be consistent with the values obtained from optical absorption. As the sputtering power decrease to 200 W, two PL peaks were observed. The one is located at 526 nm, and the other is located at 604 nm. Further decreasing of sputtering power to 150 W both PL peaks red shift to 528 nm and 609 nm respectively and the intensity of 609 nm peaks is low. It can be seen clearly that the PL peaks have been found to red shift by increasing the sputtering power from 100 W to 250 W. These PL spectra are similar to those observed SiC thin films and SiO₂/Si/SiO₂ structure [27]. The PL results are in accordance with the UV-visible spectroscopy results.

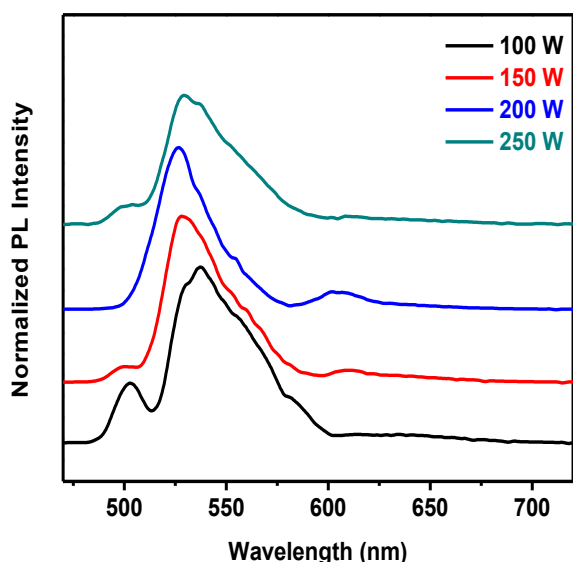


Figure 6. Photoluminescence spectra of a-SiC films deposited at various sputtering pressure

Slika 6. Spektri fotoluminiscencije a-SiC filmova deponovanih pri različitim pritiscima raspršivanja

Figure 6 depicts the room temperature Photoluminescence (PL) spectra of the a-SiC thin films deposited on Si (100) at different sputtering pressure. The excitation wavelength for all a-SiC thin films was 450 nm. PL spectrum of a-SiC thin films deposited at 250 W shows a broad and intense peak at ~ 532 nm near the band gap emission. This emission was attributed to the band edge emission from the a-SiC [26]. The band gap of SiC has been calculated using thin emission and found to be consistent with the values obtained from optical absorption. As the sputtering power decrease to 200 W, two PL peaks were observed. The one is located at 526 nm, and the other is located at 604 nm. Further decreasing of sputtering power to 150 W both PL peaks red shift to 528 nm

and 609 nm respectively and the intensity of 609 nm peaks is low. It can be seen clearly that the PL peaks have been found to red shift by increasing the sputtering power from 100 W to 250 W. These PL spectra are similar to those observed SiC thin films and SiO₂/Si/SiO₂ structure [27]. The PL results are in accordance with the UV-visible spectroscopy results.

4. CONCLUSION

In summary, a-SiC thin films were successfully grown on two substrates namely Si (100) and glass. The effect of sputtering power on structural and optical properties of a-SiC thin films were studied. No SiC peaks found in XRD pattern which show the amorphous nature of all samples deposited at different sputtering power ranging from 100 to 250 W. The amorphous nature of SiC has been confirmed by Raman spectrometer and both TO and LO modes were clearly present in the Raman spectra with very less carbon concentration in a-SiC films deposited at 100 W. The optical band gap of the a-SiC films was found to increase up to 2.45 eV with decrease in sputtering power from 250 to 100 W. The transmittance of the a-SiC films was found to decrease with increasing the sputtering power. Further it was observed that the band gap decreases with increase in sputtering power as confirmed by UV-visible and PL spectra. Thus, the sputtering parameters were found to have a great influence on the structural and optical properties of a-SiC thin films.

7. REFERENCES

- [1] J.C.Zopler, M.Skowronski (2005). Advances in Silicon Carbide Electronics, Mater. Res. Soc. Bull. 30. 273-278. doi: 10.1557/mrs2005.73.
- [2] H.Morkoc, S.Strite, G.B.Gao, M.E.Lin, B.Sverdlov, M.Burns (1994) Large-band-gap SiC, III-V nitride, and II-VI ZnSe-based semiconductor device technologies, Journal of Applied Physics 76(3), 1363-1398. doi:10.1063/1.358463.
- [3] B.Delley, E.F.Steigmeier (1993) Quantum confinement in Si nanocrystals, Phys. Rev. B, 47, 1397. doi: https://doi.org/10.1103/PhysRevB.47.1397.
- [4] L.Tsykeskov, J.V.Vandyshev, P.M.Fauchet (1994) Blue emission in porous silicon: Oxygen-related photoluminescence, Phys. Rev. B, 49, 7821 (R). doi: https://doi.org/10.1103/PhysRevB.49.7821.
- [5] M.A.Baker, M.A.Monclus, C.Rebholz, P.N.Gibson, A.Leyland, A.Matthews (2010) A study of the nanostructure and hardness of electron beam evaporated TiAlBN coatings, Thin Solid Films 518, 4273-4280. doi: https://doi.org/10.1016/j.tsf.2009.12.109.

- [6] D.A.Anderson, W.E.Spear (1977) Electrical and optical properties of amorphous silicon carbide, silicon nitride and germanium carbide prepared by the glow discharge technique, *The Philosophical Magazine: A Journal of Theoretical Exp. and App. Phys* 35(1), 1-16. doi: <https://doi.org/10.1080/14786437708235967>.
- [7] M.Künle, T.Kaltenbach, P.Löper, A.Hartel, S.Janz, O.Eibl, K.G.Nickel (2010) Si-rich a-SiC:H thin films: Structural and optical transformations during thermal annealing, *Thin Solid Films*, 519(1), 151-157. doi: <https://doi.org/10.1016/j.tsf.2010.07.085>.
- [8] W.S.Choi, B.Hong (2008) The effect of annealing on the properties of diamond-like carbon protective antireflection coatings, *Renewable Energy*, 33(2), 226-231. doi: <https://doi.org/10.1016/j.renene.2007.05.022>.
- [9] I.Golecki, F.Reidinger, J.Marti (1992) Single-crystalline, epitaxial cubic SiC films grown on (100) Si at 750° C by chemical vapor deposition, *Appl. Phys. Lett.* 60 (14), 1703-1705. doi: <https://doi.org/10.1063/1.107191>.
- [10] T.Nishiguchi, M.Nakamura, K.Nishio, T.Isshiki, S.Nishino (2004). Heteroepitaxial growth of (111) 3C-SiC on well-lattice-matched (110) Si substrates by chemical vapor deposition, *Appl Phys. Lett.* 84 (16), 3082. doi: 10.1063/1.1719270.
- [11] M.Kumar, R.Chandra, M.S.Goyat, R.Mishra, R.K.Tiwari, A.K.Saxena (2015) Structural and magnetic properties of pulsed laser deposited Fe-SiC thin films, *Thin solid films*, 579, 64-67. doi: <https://doi.org/10.1016/j.tsf.2015.02.012>.
- [12] T.Kusumori, H.Muto (2003) Influence of argon gas pressure on the crystallinity of α -SiC epitaxial films fabricated by Nd: YAG pulsed-laser deposition, *Optical Materials* 23(1), 55-60. doi: 10.1016/S0925-3467(03)00059-4.
- [13] A.J.Steckl, J.Devrajan, C.Tran, R.A.Stall (1996) SiC rapid thermal carbonization of the (111) Si semiconductor-on-insulator structure and subsequent metalorganic chemical vapor deposition of GaN, *Appl. Phys. Lett.* 69 (15), 2264-2266. doi: <https://doi.org/10.1063/1.117528>.
- [14] H.Nakazawa, M.Suemitsu (2001) Low-temperature formation of an interfacial buffer layer using monomethylsilane for 3C-SiC/Si (100) heteroepitaxy, *Appl. Phys. Lett.* 79, 755-757. doi: <https://doi.org/10.1063/1.1390476>.
- [15] Z.D.Sha, X.M.Wu, L.J.Zhuge (2005) Structure and photoluminescence properties of SiC films synthesized by the RF-magnetron sputtering technique, *Vacuum*, 79(3-4), 250-254. doi: <https://doi.org/10.1016/j.vacuum.2005.04.003>.
- [16] M.Liu, Y.Yang, Q.Mao, Y.Weil, Y.Li, N.Ma, H.Liu, X. Liu, Z.Huang (2021) Influence of radio frequency magnetron sputtering parameters on the structure and performance of SiC films, *Ceramics International*, 47(17), 24098-24105. doi: <https://doi.org/10.1016/j.ceramint.2021.05.120>.
- [17] M.Kumar, Y.K.Gautam, R.Chandra, M.S.Goyat, B.S.Tewari, R.K.Tewari (2020) Influence of SiC thin films thickness on the electrical properties of Pd/SiC thin films for hydrogen gas sensor, *Vacuum*, 182, 109750. doi: <https://doi.org/10.1016/j.vacuum.2020.109750>.
- [18] A.Costa, S.Camargo (2003) Amorphous SiC coatings for WC cutting tools, *Surface and coatings technology*, 163-164, 176-180. doi:[https://doi.org/10.1016/S0257-8972\(02\)00486-3](https://doi.org/10.1016/S0257-8972(02)00486-3).
- [19] Z.Xia, S.Huang (2010) Structural and photoluminescence properties of silicon nanocrystals embedded in SiC matrix prepared by magnetron sputtering, *Solid State Communications*, 150(19-20), 914-918. doi: <https://doi.org/10.1016/j.ssc.2010.02.032>.
- [20] F.Neri, S.Trusso, C.Vasi, F.Barreca, P.Valisa (1998) Raman microscopy study of pulsed laser ablation deposited silicon carbide films, *Thin Solid Films*, 332(1-2), 290-294. doi:[https://doi.org/10.1016/S0040-6090\(98\)00994-8](https://doi.org/10.1016/S0040-6090(98)00994-8).
- [21] R.A.Simao, A.K.Costa, C.A.Achete, S.S.Camargo (2000) Magnetron sputtering SiC films investigated by AFM, *Thin Solid Films*, 377-378, 490-494. doi: [https://doi.org/10.1016/S0040-6090\(00\)01371-7](https://doi.org/10.1016/S0040-6090(00)01371-7).
- [22] H.Tang, S.Tan, Z.Huang, S.Dong, D.Jiang (2005) Surface morphology of α -SiC coatings deposited by RF magnetron sputtering, *Surface & Coatings Technology*, 197(2-3) 161-167. doi: <https://doi.org/10.1016/j.surfcoat.2004.11.036>.
- [23] M.Kumar, R.Chandra, R.Mishra, R.K.Tiwari, A.K.Saxena (2012) Effect of Sputtering Gas on Structural and Optical Properties of Sputtered SiC Thin Films, *AIP Conf. Proc.* 1451, 260. doi: 10.1063/1.4732434.
- [24] J.K.Seo, Ki-han Ko, W.S.Choi, M.Park, J.H.Lee, J. S.Yi (2011) The effect of deposition RF power on the SiC passivation layer synthesized by an RF magnetron sputtering method, *Journal of Crystal Growth* 326(1),183-185. doi: <https://doi.org/10.1016/j.jcrysgro.2011.01.093>.
- [25] J.Tauc, (Ed.) (1974) *Amorphous, Liquid Semiconductor*, Plenum Press, New York, p.159. doi:<https://www.science.org/doi/10.1126/science.188.4184.141.b>.
- [26] N.M.A.Rashid, R.Ritikos, M.Othman, N.H.Khanis, S. M.A.Gani, M.R.Muhamad, S.A.Rahman (2013) Amorphous silicon carbon films prepared by hybrid plasma enhanced chemical vapor/sputtering deposition system: Effects of r.f. power, *Thin Solid Films*, 529, 459-463. doi: <https://doi.org/10.1016/j.tsf.2012.09.032>.
- [27] D.Chen, Z.M.Liao, L.Wang, H.Z.Wang, F.Zhao, W.Y.Cheung, S.P. Wong (2003). Photoluminescence from β -SiC nanocrystals embedded in SiO₂ films prepared by ion implantation, *Optical Materials* 23(1-2), 65-69. doi: [https://doi.org/10.1016/S0925-3467\(03\)00061-2](https://doi.org/10.1016/S0925-3467(03)00061-2).

IZVOD

STUDIJE STRUKTURNIH I OPTIČKIH OSOBINA RASPRŠENIH SiC TANKIH FILMOVA

Ova studija je istraživala taloženje tankih filmova amorfnog silicijum karbida (a-SiC) na Si (100) i staklene podloge korišćenjem RF-magnetronskog raspršivanja. Snaga raspršivanja je promenjena sa 100 na 250V da bi se proučavao njen uticaj na karakteristike a-SiC tankih filmova. Ramanova spektroskopija otkriva formiranje a-SiC kao i klastera ugljenika. Film deponovan na 100 V jasno pokazuje prisustvo i poprečnih optičkih (TO) i uzdužnih optičkih (LO) fononskih modova. Utvrđeno je da prosečna hrapavost a-SiC filmova prati rastući trend sa povećanjem snage raspršivanja. Utvrđeno je da se optički razmak a-SiC filmova meren UV-vidljivim spektrofotometrom povećava do 2,45 eV sa smanjenjem snage raspršivanja. Svi a-SiC tanki filmovi bili su veoma providni. Rezultati fotoluminiscencije (PL) spektroskopije bili su u saglasnosti sa podacima uočenim UV-vidljivom spektroskopijom.

Ključne reči: SiC tanki filmovi, Magnetronsko raspršivanje, Ramanova spektroskopija, PL spektroskopija

Naučni rad

Rad primljen: 25.09.2023.

Rad korigovan: 22.01.2024.

Rad prihvaćen: 31.01.2024.

Rad je dostupan na sajtu: www.idk.org.rs/casopis

Arunprasad Jaychandran^{1*}, Murugan Ramaiyan²,
Christian Johnson Singaram³, Anukarthika Balakrishnan³

¹Research Scholar, Department of Civil and Structural Engineering, Annamalai University, Tamilnadu, India, ²Department of Civil and Structural Engineering, Annamalai University, Tamilnadu-608002, India, ³Department of Civil Engineering, Erode Sengunthar Engineering College, Perundurai, Tamilnadu, India.

Scientific paper

ISSN 0351-9465, E-ISSN 2466-2585

<https://doi.org/10.62638/ZasMat1129>



Zastita Materijala 65 (2)
350 - 359 (2024)

Non-destructive evaluation of subsurface corrosion on hot steel angle sections embedded in concrete and its repair by cement slurry and nitozinc coating

ABSTRACT

This research article presents a comprehensive investigation into the materials and corrosion resistance of angle components critical to infrastructure construction. The study focuses on two key angle materials: steel angles and Fiber-Reinforced Plastic (FRP) angles, selected based on project-specific requirements. The concrete mix design, incorporating crucial components like chemicals (Calcium Chloride, Sodium Hydroxide, Calcium Hydroxide), aggregates (M Sand and 20 mm Aggregate), and cement (Portland Pozzolana Cement - 43 grade), ensures that the structural integrity and performance meet desired standards. The research also involves advanced corrosion assessment techniques, including the Half-Cell Potential Test and the Applied Voltage Test (Holiday Test), which offer insights into material conductance, corrosion resistance, and protective coating integrity. Moreover, a Chemical Resistance Test examines the impact of various solutions on these materials, highlighting their suitability for diverse industrial applications. The results underscore the importance of tailored material selection, proactive corrosion management, and the critical role of protective coatings in ensuring infrastructure longevity and safety. This study contributes to the advancement of corrosion assessment methods, supporting the durability of critical infrastructure materials.

Keywords: corrosion, coating, chemical resistance, durability, FRP, angle section

1. INTRODUCTION

Corrosion monitoring activities play a vital role in assessing the integrity of steel components within concrete foundations [1]. Corrosion can lead to the deterioration of the concrete surrounding the reinforcement, necessitating timely inspections and repairs [2]. Several methods are employed for assessing and addressing this corrosion-related damage [3]. One such method is the Half-Cell Potential Method, which measures electro-potential and helps in evaluating the condition of the steel reinforcement within the concrete [4,5]. It provides insights into the likelihood of corrosion occurring [6]. The Ultrasonic Pulse Velocity Test measures the velocity of ultrasonic waves through the concrete [7-9].

This test is invaluable for determining the concrete's quality and detecting any voids or defects within it [10-12]. The Rebound Hammer Test assesses the concrete's surface hardness and, by extension, its structural integrity [13,14]. This test is particularly useful in cases where manual repair is considered, provided there is no calcium chloride present in the concrete [15,16]. Cathodic Protection is a crucial technique used to halt the rusting process of steel reinforcement within the concrete [17]. This method is instrumental in preventing further corrosion damage, and preserving the structural integrity of the concrete [18].

Additional methods, such as Parallel Seismic Time Testing, Impulse Response, Impact-Echo, Ultrasonic Tomography, Ground Penetrating Radar, and Impedance Tomography, employ various physical quantities, including acoustic wave pass-through time, vibration frequency, magnetic flux, and electric potential, to assess different aspects of concrete and reinforced concrete structures [19-21]. These methods are employed for evaluating the condition of concrete and its

*Corresponding author: Jaychandran Arunprasad

Email ID: arunprasadcivil@esec.ac.in

Paper received: 26. 11. 2023.

Paper corrected: 26.02.2024.

Paper accepted: 09. 03. 2024.

Paper is available on the website: www.idk.org.rs/journal

reinforcing steel in various structural elements, including foundation slabs, columns, beams, walls, and more [22]. The experimentally proven coatings were applied in subsurface concrete models and the efficiency of the coatings, and admixtures in concrete were studied for durability [23]. Methodology for maintenance of subsurface corrosion of most susceptible to high rates of metal corrosion has been reviewed by *Petter*. Investigation on the application of protective coatings upon the reinforcements and addition of admixtures in the concrete have been carried out by S.Christian Johnson and G.Thirugnanam [24, 25]. Protective methods like applying zinc-rich coatings such as epoxy coatings in the stub angle concrete interface to combat the crevice corrosion, have been suggested for field applications in aggressive environments [26]. Several non-destructive techniques like half-cell potential tests, applied voltage tests, and chemical resistance tests including experimental investigations in the laboratory have been elaborately carried out [27].

This paper aims to find the effectiveness of coating and prevent the corrosion of steel angles induced in concrete which can reduce the durability of concrete structures. It leads to the formation of cracks in concrete. Corrosion of the structure can be reduced by using additives and anticorrosive coatings such as zinc coatings on the angles. In this work, an attempt is made to apply epoxy coating on angles and to study the corrosion of angles up to the cracking of concrete in a short time, the corrosion rate is increased by impressing direct current, and the corrosion process is monitored continuously. The durability of concrete is calculated by performing chemical resistance and applied voltage tests. It is aimed to study the effectiveness of coating applied on angles and its durability.

2. MATERIALS AND MIX DESIGN

In this research, two types of angle materials were considered for the construction: steel angles and FRP (Fiber-Reinforced Plastic) angles, with dimensions of 300x50x50mm and 150x50x50mm [28-30]. The choice of these materials depends on various factors, including their intended use and the specific requirements of the project. To create the concrete mix, several essential components were utilized, including chemicals and aggregates [31]. The chemicals included 3M of Calcium Chloride, 3M of Sodium Hydroxide, and a saturated solution of Calcium Hydroxide. These chemicals play a crucial role in influencing the concrete's properties, such as setting time and durability [32]. In terms of aggregates, fine aggregate (M Sand) and coarse aggregate (20 mm Aggregate) were

incorporated into the mix [33]. The selection of aggregates is vital in determining the concrete's strength and workability [34]. Lastly, the binding agent, cement, was chosen in the form of PPC (Portland Pozzolana Cement) - 43 grade. The specific grade of cement plays a significant role in determining the concrete's overall quality and performance [35]. The mix proportion employed for the study was based on a 1:1.5:3 ratio, which corresponds to M20-grade concrete [36]. This ratio was applied to ensure the concrete's desired properties [37]. The design mix ratio was then calculated by dividing the required weight of all materials by the weight of cement, resulting in the following proportions: Cement: Fine Aggregate: Coarse Aggregate: Water = 1: 1.85: 2.9: 0.5. This precisely defined mix ratio is critical for achieving the desired structural strength and performance characteristics of the concrete [38].

3. EXPERIMENTAL INVESTIGATIONS

3.1. Half-Cell Potential Test

This test method covers the estimation of the electrical half-cell potential of uncoated reinforcing steel in field and laboratory concrete, to determine the corrosion activity of the reinforcing steel [39]. This test method is limited by electrical circuitry. A concrete surface that has dried to the extent that it is a dielectric and surfaces that are coated with a dielectric material will not provide an acceptable electrical circuit [40]. The values stated in inch-pound units are to be regarded as the standard. For the Half-cell potential test, we cast 8 specimens for testing and the test is undertaken after 28 days of providing 2V while curing of specimens. As per ASTM C876 [32] limits below -350mV corrosion does not occur. From the -350mV to -200mV. Probability of occurrence of corrosion when potential head exceeds -200mV. The test setup is shown in Figure 1 and the ASTM standard value is presented in Table 1.

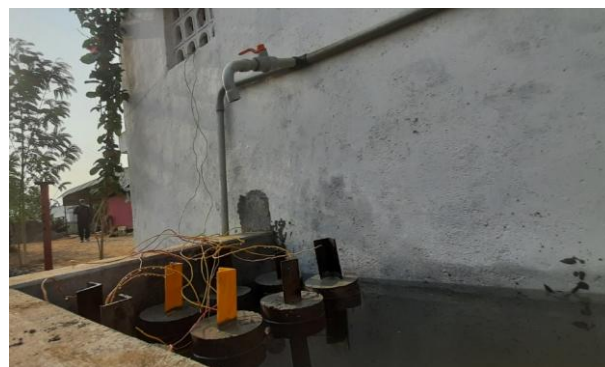


Figure 1. (a) Accelerated corrosion test setup
Slika 1. (a) Ubrzano podešavanje testa korozije



Figure 1. (b) HCP test on corroded specimen

Slika 1. (b) HCP test na korodiranom uzorku

Table 1. Potential Test Valve (ASTM Standard)

Tabela 1. Ventilzaispitivanje potencijala (ASTM standard)

Corrosion	Potential (C-CSE)
> 95%	More Negative than -350mV
50%	-200 to -350mV
< 5%	More Positive than -200mV

3.2. Applied Voltage Test

Non-conductive plastic material is used in a metallic vessel. The specimens are suspended

vertically in the vessel with at least 25 mm clearance from the bottom. Test specimens are separated by not less than 40 mm [41]. Test specimens shall be separated from any wall of the vessel by not less than 40 mm. The depth of the electrolyte is the test length of the specimen to be immersed, but the immersed area shall not be less than 23, 200 mm². AC power was used for powering the overlays. A VARIAC was used to regulate the applied voltage. A transformer was used to elevate the applied voltage to a maximum of 420 volts. The overlays were connected to the AC power in parallel. An amp-meter was used to record the electrical current going through each overlay. The total current going through both overlays was limited to the maximum capacity of the power source.

Epoxy coatings were applied on the angle for the voltage test. Dimensions of 300mm x 50mm x 6mm angles are used in this test. The effect of electrical and electrochemical stresses on the bond of coating to steel and the integrity of the coating shall be assessed [42]. The test setup is shown in Figure 2. The tests were conducted as per IS 13620:1993. In this test, the coated angles were tested and readings were noted.



Figure 2. Applied Voltage Test – Setup

Slika 2. Test primenjenog napona – podešavanje

3.3. Chemical Resistance Test

The chemical resistance test, conducted in accordance with IS 13620:1993, is a vital evaluation of coating durability for reinforcing bars. In this test, the coated reinforcing bars are subjected to immersion in various solutions to assess their resistance to chemical corrosion [43]. Figure 3 depicts the test setup of the chemical resistance test. The solutions used include distilled water, a 3M aqueous solution of CaCl₂, a 3M aqueous solution of NaOH, and a solution saturated with Ca(OH)₂. This comprehensive evaluation ensures that the coating can withstand exposure to a range of potentially corrosive

substances. It is important to note that this test is a physical inspection procedure, focusing on the coating's ability to withstand chemical exposure.

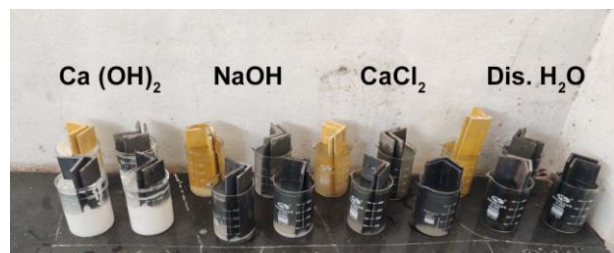


Figure 3. Chemical Resistance test setup

Slika 3. Podešavanje testa hemijske otpornosti

Following the designated experimental period, the test examines the formation of any holidays, imperfections, or defects in the coating. After the completion of 45 days, the test setup is meticulously investigated to determine the coating's performance under these challenging conditions, providing valuable insights into its durability and suitability for various applications.

4. RESULT AND ANALYSIS

4.1. Half Cell Potential Test Results

In an investigation aimed at assessing the electrical conductance of various angle materials, a test was initiated after 28 days of the curing process. This test was extended for an additional 8 days post-curing, encompassing a 6-hour test period. The objective was to chart the current, measured in amperes, against time in seconds, creating a graph that depicted the variations in electrical properties over time. This graph was then subjected to smoothing to provide a clear representation of the data. Subsequently, the area under the smoothed curve was integrated to

calculate the total charge passed during the 6-hour test period, expressed in ampere-seconds or coulombs. This measure of total charge passed served as a crucial indicator of the electrical conductance of the concrete during the testing phase.

The presented Table 2, and Figure 4 provide detailed data on the half-cell potential test readings for three types of angle specimens: Uncoated Angle, Nitozinc Coated Angle, and FRP (Fiber-Reinforced Plastic) Angle.

Uncoated Angle: The readings for the Uncoated Angle exhibited consistently negative potentials throughout the 6-hour test period, with values ranging from -159 to -218mV. These negative potential values suggest that the Uncoated Angle is susceptible to electrical conduction, and the increasing negative potential values signify the material's gradual degradation over time. This electrical conductance points to the angle's vulnerability to corrosion, making it an unfavorable choice for applications that require corrosion resistance.

Table2 Half-cell potential test readings

Tabela 2 Očitavanje test potencijalapolučelije

Specimens	Half-cell potential test readings (mV)			
	24	48	72	96
Uncoated Angle	-159	-165	-178	-194
	-168	-176	-189	-211
	-165	-179	-192	-218
Nitozinc Coated Angle	-142	-150	-162	-170
	-148	-152	-160	-180
	-134	-140	-164	-184
FRP Angle	0	0	0	0
	0	0	0	0
	0	0	0	0

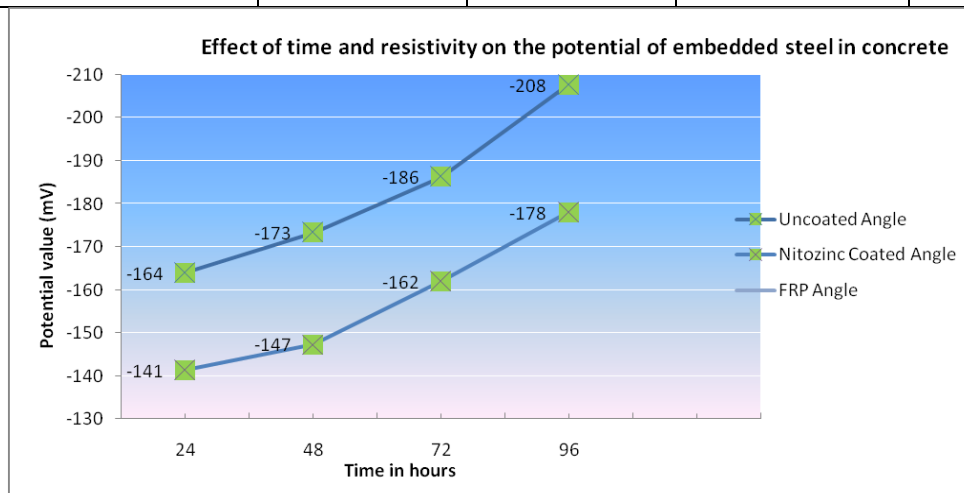


Figure 4. Effect of time and resistivity on the potential of embedded steel in concrete

Slika 4. Uticaj vremena i otpora na potencijal ugrađenog čelika u beton

Nitozinc Coated Angle: In contrast, the Nitozinc Coated Angle displayed positive potentials throughout the test, with values ranging from -142 to -184 mV. These consistent positive potentials signify the angle's ability to resist electrical conduction, indicating its corrosion resistance. The Nitozinc Coating effectively maintained its electrical integrity over the testing duration, highlighting its suitability for applications where corrosion resistance is of utmost importance.

FRP Angle: The FRP Angle consistently registered at zero amperes during the entire test period, signifying its complete lack of electrical conduction. This property underscores the angle's electrical non-conductivity, making it an ideal choice for applications where electrical insulation is a critical requirement.

The half-cell potential test results provide valuable insights into the electrical conductance and corrosion resistance of the tested angle materials. While the Uncoated Angle displayed negative potentials and susceptibility to corrosion, the Nitozinc Coated Angle demonstrated positive potentials and resistance to electrical conduction. The FRP Angle's consistent zero amperes confirmed its electrical non-conductivity. Nitozinc Coating is resistive against corrosion compared to Uncoated steel angles. FRP angle does not conduct any current.

4.2. Applied Voltage Test Results

The Applied Voltage test, often referred to as a holiday test, is a critical method used in the field of material inspection and quality control. It involves assessing the integrity of coatings or linings on various substrates, specifically looking for the presence of holidays. Holidays, in this context, refer to imperfections or discontinuities in the coating or lining film, such as pinholes, voids, cracks, inclusions, or contaminants. These defects, though often invisible to the naked eye, can compromise the protective properties of the coating and pose significant risks, especially in applications designed for critical services, such as immersion, chemical storage, or transportation.

The Applied Voltage test is an essential tool to ensure the reliability and safety of coated or lined materials, as a failure to detect these holidays could potentially lead to catastrophic events. The test is conducted after a specified experimental period during which the coated or lined materials are exposed to various conditions and stresses. At the end of this period, the formation of holidays is assessed through readings obtained from the test.

The test results, as summarized in Table 3, provide valuable insights into the condition of the coated or lined specimens, with specific

observations for Nito Zinc Coated Angle, Uncoated Angle, and FRP (Fiber-Reinforced Plastic) Angle.

1. Nito Zinc Coated Angle: Observation: Low holidays.

The Nito Zinc Coated Angle, after undergoing the Applied Voltage test, demonstrated a low presence of holidays. This observation suggests that the Nito Zinc coating effectively protected the underlying substrate from the formation of imperfections or defects. The low holiday count signifies that the coating is of high quality, and the material is suitable for applications that require a high level of protection against corrosive or environmental factors.

2. Uncoated Angle: Observation: Severe Holidays.

In contrast, the Uncoated Angle exhibited severe holidays following the Applied Voltage test. This observation highlights the vulnerability of uncoated materials to imperfections or defects. The presence of severe holidays indicates that the material is at high risk of corrosion or other forms of degradation. It underscores the critical importance of applying protective coatings or linings to substrates, especially in environments where materials are subjected to harsh conditions.

3. FRP Angle: Observation: Very Low Holidays.

The FRP Angle displayed very low holidays, indicating that the fiber-reinforced plastic coating effectively protected the substrate from imperfections. FRP is known for its corrosion-resistant properties and durability, and these results validate its effectiveness in maintaining a high level of protection. This observation underscores the suitability of FRP in applications where corrosion resistance and material integrity are paramount.

The observations from this test demonstrate the significance of protective coatings and linings in preserving material integrity and preventing catastrophic failures. The ability to detect imperfections that are often invisible to the naked eye underscores the importance of 100% inspection of coated or lined surfaces. Whether applied to newly coated materials or those that have aged, the test equipment's portability makes it a versatile and practical choice for quality control and maintenance in various industrial settings.

4.3. Chemical Resistance Test

It is a physical inspection test. After the test experiment period, the information on holidays was calculated. After 45 days of completion, the test setup is investigated. In this comparative analysis of various chemical treatments, it can be observed the effects of different solutions on four different types of angle materials, namely NitoZinc Coated,

Cement Slurry Coated, Uncoated, and FRP Angles. The experiment involved immersing these angles in four different solutions: Distilled Water, 3M CaCl₂, 3M NaOH, and Ca(OH)₂. The study was conducted over a specified period, and the results are summarized in the table below, indicating the number of angles that exhibited specific characteristics after exposure to each solution. In the case of NitoZinc Coated Angle, the weight changes after exposure to these solutions were as follows: 20% for Distilled Water, 19% for 3M CaCl₂, 19% for 3M NaOH, and 19% for Ca(OH)₂. For Cement Slurry Coated Angle, the weight changes were 17% for Distilled Water, 18% for 3M CaCl₂, 15% for 3M NaOH, and 15% for Ca(OH)₂. Uncoated Angle displayed weight changes of 10% for Distilled Water, 11% for 3M CaCl₂, 12% for 3M NaOH, and 12% for Ca(OH)₂. Lastly, the FRP Angle exhibited consistent weight changes of 20% for all the tested solutions. The graphical representation of test results is shown in Figure 5.

Distilled Water:

NitoZinc Coated Angle showed no significant weight change (20%). This indicates its excellent resistance to pure water, suggesting that the coating effectively protects the underlying material from corrosion in a water-rich environment. Cement Slurry Coated Angle exhibited a relatively small weight change (17%), implying good resistance to pure water, although slightly less effective than NitoZinc Coated Angle. The uncoated Angle experienced a moderate weight change (10%). While it's less susceptible to water than coated angles, this change suggests potential vulnerability to water-induced corrosion over time. FRP Angle demonstrated no significant weight change (20%), indicating its exceptional water resistance. This material is ideal for applications requiring high water resistance.

3M CaCl₂ Solution:

NitoZinc Coated Angle displayed a minor weight change (19%), signifying good resistance to chloride-rich solutions. Cement Slurry Coated Angle exhibited a slightly higher weight change (18%), indicating slightly reduced resistance to calcium chloride compared to NitoZinc Coated

Angle. Uncoated Angles showed a moderate weight change (11%), suggesting moderate susceptibility to chloride-induced corrosion. FRP Angle experienced no significant weight change (20%), showcasing its excellent resistance to calcium chloride.

3M NaOH Solution:

NitoZinc Coated Angle demonstrated a slight weight change (19%), suggesting good resistance to alkaline conditions. Cement Slurry Coated Angle had a relatively higher weight change (15%), indicating it might be slightly more vulnerable to sodium hydroxide. The uncoated Angle showed a moderate weight change (12%), implying some vulnerability to strong alkali. FRP Angle displayed no significant weight change (20%), highlighting its strong resistance to alkaline solutions.

Ca(OH)₂ Solution:

NitoZinc Coated Angle showed minimal weight change (19%), emphasizing its resistance to highly alkaline environments. Cement Slurry Coated Angle exhibited a slightly higher weight change (15%), indicating it can withstand alkaline conditions. Uncoated Angle displayed a moderate weight change (12%), suggesting it might be moderately susceptible to strong alkalinity. FRP Angle showed no significant weight change (20%), underscoring its resistance to highly alkaline solutions.

These scientific observations reveal the chemical resistance and durability of the tested angle materials in different environmental conditions. NitoZinc Coated Angle and FRP Angle consistently exhibited strong resistance across various chemicals does not produce any holidays making them suitable for applications demanding robust corrosion resistance. On the other hand, Uncoated Angle and Cement Slurry Coated Angle showed large number of holidays showing varying degrees of susceptibility to different chemicals and loss of weight, underlining the importance of protective coatings and material selection for specific industrial contexts.

Table 3. Test results of chemical resistance of samples

Tabela 3. Rezultati ispitivanja hemijske otpornosti uzoraka

Chemicals	Weight changes (%)			
	NitoZinc Coated Angle	Cement Slurry Coated Angle	Uncoated Angle	FRP Angle
Distilled Water	20	17	10	20
3M CaCl ₂	19	18	11	20
3M NaOH	19	15	12	20
Ca(OH) ₂	19	15	12	20

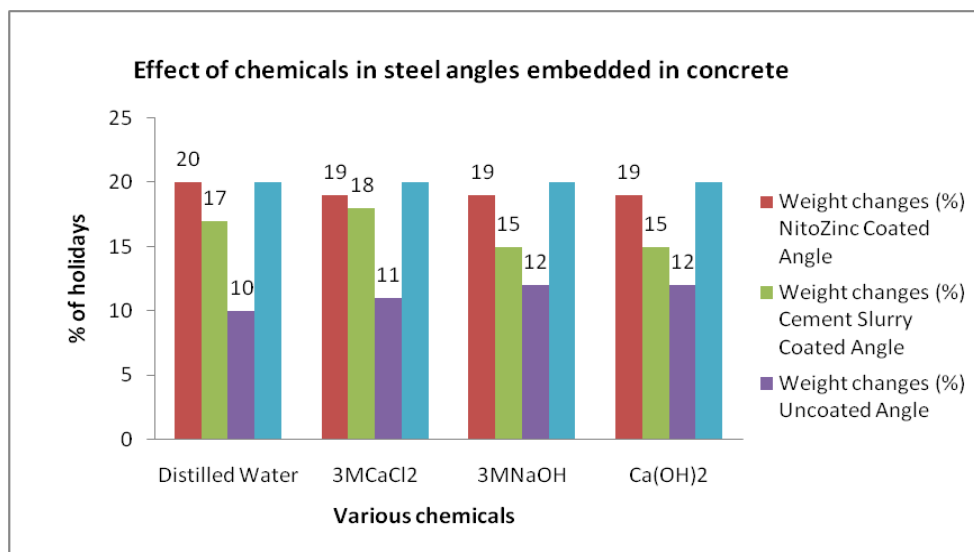


Figure 5. Effect of chemicals in steel angles embedded in concrete

Slika 5. Uticaj hemikalija na čelične uglove ugrađene u beton

5. CONCLUSION

The conducted investigations involving the Applied Voltage test and the Chemical Resistance test provide significant insights into the electrical conductance and chemical resistance properties of various angle materials. These findings hold substantial implications for material selection in applications where corrosion resistance and electrical integrity are critical.

1. The Uncoated Angle exhibited negative potentials (-159 to -218 mV), indicating susceptibility to corrosion and electrical conduction, making it unsuitable for corrosion-sensitive applications. In contrast, the Nitozinc Coated Angle maintained positive potentials (142 to -184 mV), highlighting its corrosion resistance and electrical integrity, suitable for applications demanding protection. The FRP Angle consistently registered zero amperes, confirming its electrical non-conductivity, making it an ideal choice for applications requiring insulation.
2. The Uncoated Angle demonstrated a consistent negative potential, indicating its susceptibility to electrical conduction and corrosion. It is, therefore, an unfavorable choice for applications requiring corrosion resistance. The Nito Zinc Coated Angle consistently displayed a positive potential, signifying its ability to resist electrical conduction and maintain its corrosion resistance. This makes it a suitable choice for environments where protection against corrosion is paramount. The FRP Angle exhibited a consistent zero potential, highlighting its electrical non-conductivity and

making it ideal for applications where electrical insulation is essential.

3. The experiments conducted with different chemical solutions showcased varying effects on the tested angle materials. Distilled Water had no significant impact on any of the angle types. 3M CaCl₂ produced minor changes in the NitoZinc Coated, Uncoated, and Cement Slurry Coated angles, while affecting 11 angles of the FRP category. 3M NaOH and Ca(OH)₂ had similar effects, leaving the NitoZinc Coated, Uncoated, and Cement Slurry Coated angles mostly unchanged, but causing alterations in all FRP angles.
4. These results are crucial in the context of material selection for applications demanding high corrosion resistance and electrical integrity. The Nito Zinc Coated Angle consistently demonstrated resistance to both electrical conduction and chemical-induced alterations, rendering it a preferred choice for critical services where protection against corrosion is paramount. The Uncoated Angle, with its susceptibility to corrosion, serves as a cautionary example of the importance of protective coatings in such applications. Lastly, the FRP Angle's electrical non-conductivity and varying chemical resistance make it a versatile material suitable for specific applications.
5. These tests provide essential data for informed decision-making in industries requiring materials capable of withstanding harsh conditions. The choice of materials should consider not only their inherent properties but also the environmental factors they will be exposed to, ensuring the longevity and safety of the

applications. The results reaffirm the significance of protective coatings and linings in preserving material integrity and preventing catastrophic failures, while also emphasizing the role of electrical conductance and resistance in specific industrial contexts.

Acknowledgments

The authors wish to acknowledge the Department of Civil Engineering, Annamalai University, and Erode Sengunthar Engineering College, Tamil Nadu for the facility and support extended for the research work.

6. REFERENCES

- [1] R.Alfred, J.Mathew (2013) Electrical Indication of Concrete's Ability to Resist chloride Ion Penetration. *International Journal of Advanced Scientific and Technical Research.*,3(6), 51-59.
- [2] A.Ahmad, A.Kumar(2013)Chloride ion migration/diffusion through concrete and test methods. *International Journal of Advanced Scientific and Technical Research.*, 6(3), 151-180.
- [3] B.P.Baltazar-García, B.Zamora, et al. (2024) Behavior of Potential of Half-Cell AISI 1018 and GS in Concrete Buried in Sand in the Presence of MgSO₄. *European Journal of Engineering and Technology Research.*, 9(1), 32-36. DOI:<https://doi.org/10.24018/ejeng.2024.9.1.3123>.
- [4] N.Kumar, S.Prakash, S.Ghani, M.Gupta, S. Saharan (2024) Data-driven machine learning approaches for predicting permeability and corrosion risk in hybrid concrete incorporating blast furnace slag and fly ash. *Asian Journal of Civil Engineering.*, 1-13. <https://doi.org/10.1007/s42107-023-00977-8>
- [5] M.A.M.Ariffin, M.A.R.Bhutta, M.W.Hussin, M.Mohd Tahir, Nor Aziah, Sulfuric acid resistance of blended ash geopolymer concrete. <https://doi.org/10.1016/j.conbuildmat.2013.01.018>
- [6] R.Mohanraj, K.Vidhya (2024) Evaluation of compressive strength of Euphorbia tortilis cactus infused M25 concrete by using ABAQUS under static load. *Materials Letters.*, 356, 135600. <https://doi.org/10.1016/j.matlet.2023.135600>
- [7] T.Bakharev, J.G.Sanjayan, Y.B.Cheng (2003) Resistance of alkali-activated slag concrete to acid attack, *Cement and Concrete Research*, 33, 1607 – 1611.[https://doi.org/10.1016/S0008-8846\(03\)00125-X](https://doi.org/10.1016/S0008-8846(03)00125-X)
- [8] M.T.Bassuoni, M.L.Nehdi (2007) Resistance of self-consolidating concrete to sulfuric acid attack with consecutive pH reduction.*Cement and Concrete Research.*, 37, 1070–1084.<https://doi.org/10.1016/j.cemconres.2007.04.014>
- [9] R.Mohanraj, S.Senthilkumar, P.Padmapoorani (2022) Mechanical properties of RC beams With AFRP sheets under a sustained load. *Materials and Technology.*, 56(4), 365–372. <https://doi.org/10.17222/mit.2022.481>
- [10] C. Bilim, C.D.Atis, H. Tanyildizi, O. Karahan (2009) Predicting the compressive strength of ground granulated blast furnace slag concrete using artificial neural network.*Advances in Engineering Software.*, 40, 334–340.<https://doi.org/10.1016/j.advengsoft.2008.05.005>
- [11] M.Velumani, R.Mohanraj, R.Krishnasamy, K. Yuvaraj (2023)Durability Evaluation of Cactus-Infused M25 Grade Concrete as a Bio-Admixture. *Periodica Polytechnica Civil Engineering.*, 67(4), 1066-1079 . <https://doi.org/10.3311/PPci.22050>
- [12] Ch.Kennedy, Ph. Kpae, W. Oruene(2018) Comparative Half Cell Potential and Concrete Resistivity Corrosion Probability Assessment of Embedded Coated Steel Reinforcement in Concrete Accelerated Environment. *International Journal of Scientific & Engineering Research.*, 9(5).141-159. DOI:10.14299/ijser.2018.05.06
- [13] R. Krishnasamy, C. J.Singaram, S. Palanichamy, R. Mohanraj (2024) Testing and Evaluation of Buckling and Tensile Performance of Glass Fiber–Reinforced Polymer Angle Section with Different Joints/Connections. *Journal of Testing and Evaluation.*, 52(1), 1-16. <http://doi.org/10.1520/JTE20230010>
- [14] L.V.Dias, S.M.Soares J.A.Salvador Filho, F.G.S. Ferreira (2021)Evaluation of chloride migration in ultra-high performance concrete (UHPC) with glass powder.11(2), 61-75. <https://doi.org/10.21041/ra.v11i2.512>
- [15] D.Mills, P.Lambert, Sh.Yang (2021) Electrochemical Noise Measurement to Assess Corrosion of Steel Reinforcement in Concrete. 14(18), 5392. <https://doi.org/10.3390/ma14185392>
- [16] R.Mohanraj, S.Senthilkumar, Pr. Goel, R. Bharti (2023) A state-of-the-art review of Euphorbia Tortilis cactus as a bio-additive for sustainable construction materials. *Materials Today: Proceedings.* <https://doi.org/10.1016/j.matpr.2023.03.762>
- [17] S.Gunaselvi, P.Satheeshkumar, M.Jeganathan (2020) Surface Modification of Steel by Nickel Coating in Electrochemical Process. *Journal of New Materials for Electrochemical Systems.*, 23(2), 112-122. DOI:<https://doi.org/10.14447/jnmes.v23i2.a08>
- [18] K. Chansuriyasak, Ch. Wanichlamlart, P. Sancharoen, W. Kongprawechnon S. Tangtermsirikul (2010) Comparison between half-cell potential of reinforced concrete exposed to carbon dioxide and chloride environment. *Songklanakarin J. Sci. Technol.*, 32 (5), 461-468.
- [19] L.Maria Nicula,O.Corbu, M.Iliescu, A.V.Sandu, An. Hegyi (2021) Study on the Durability of Road Concrete with Blast Furnace Slag Affected by the Corrosion Initiated by Chloride. *Hindawi Advances in Civil Engineering.*, p.1-16.<https://doi.org/10.1155/2021/8851005>
- [20] R.Mohanraj, S.Senthilkumar, S. Shanmugasundaram, P.Padmapoorani (2022) Torsional performance of reinforced concrete beam with carbon fiber and aramid fiber laminates. *Revista de la Construcción.*, 21(2), 329-337. <https://doi.org/10.7764/RDLC.21.2.329>

- [21] L. Sadowski (2016) Methodology for Assessing the Probability of Corrosion in Concrete Structures on the Basis of Half-Cell Potential and Concrete Resistivity Measurements. *The Scientific World Journal*. <http://dx.doi.org/10.1155/2013/714501>
- [22] S.C.Johnson, G.S.Thirugnanam (2010) Experimental study on corrosion of transmission line tower foundation and its rehabilitation. *International Journal of Civil & Structural Engineering*., 1(1), 27-34.
- [23] P. Claisse, J. L. Marriaga (2012) The effect of other ions on chloride migration in concrete. 3rd International Conference on the Durability of Concrete Structures., p.17-19.
- [24] R. Siddique, J. Klaus (2009) Influence of metakaolin on the properties of mortar and concrete. *Applied Clay Science*., 43(3-4), 392-400. <https://doi.org/10.1016/j.clay.2008.11.007>
- [25] P.Padmappoorani, S.Senthilkumar, R.Mohanraj (2023) Machine Learning Techniques for Structural Health Monitoring of Concrete Structures: A Systematic Review. *Iranian Journal of Science and Technology, Transactions of Civil Engineering*, 47(4). <https://doi.org/10.1007/s40996-023-01054-5>
- [26] R. Rodrigues, St. Gaboreau, J. Gance, I. Ignastiadis St. Betelu(2020) Numerical Insights into Its Physical Aspect and Its Ability to Locate Highly Corroding Areas in Macrocell Corrosion of Steel in Concrete. *Corros. Mater. Degrad.*, 1, 373-407. <https://doi.org/10.3390/cmd1030018>
- [27] R.Paul Borg, E.Gatt, St.Sammut(2017) Chloride Ion Detection in Concrete through Galvanic Voltage and Resistivity. *Jordan Journal of Civil Engineering*., 11(4), 638-645.
- [28] V.L.Satish (2020) Half Cell Potential Studies for Durability Studies of Concrete Structures in Coastal Environment., *NDE2020*. e12608.
- [29] R.Mohanraj, S.Senthilkumar, P.Loganathan, R. Krishnasamy (2023) Confinement effectiveness of 2900psi concrete using the extract of *Euphorbia tortilis cactus* as a natural additive. *Matéria (Rio de Janeiro)*., 28(1). <https://doi.org/10.1590/1517-7076-RMAT-2022-0233>
- [30] S.Irico, L.De Meyst, D.Qvaeschning, M.Cruz Alonso, Kristina Villar, and Nele De Belie (2020) Severe Sulfuric Acid Attack on Self-Compacting Concrete with Granulometrically Optimized Blast-Furnace Slag-Comparison of Different Test Methods. *Materials*., 13, 1431. <https://doi.org/10.3390/ma13061431>
- [31] W.Yourey, Y.Fu, N.Li, V.Battaglia, W.Tong (2021) Design Considerations for Fast Charging Lithium Ion Cells for NMC/MCMB Electrode Pairs. *Batteries*., 7(1), 4 <https://doi.org/10.3390/batteries7010004>
- [32] ASTM C 876-91(2008) Standard test method for half-cell potentials of uncoated reinforcing steel in concrete.
- [33] K.Ravikumar, S.Palanichamy, C.J.Singaram, M. Rajendran (2023) Crushing performance of pultruded GFRP angle section with various connections and joints on lattice towers. *Matéria (Rio de Janeiro)*., 28, e20230003. <https://doi.org/10.1590/1517-7076-RMAT-2023-0003>
- [34] P.Loganathan, R.Mohanraj, S.Senthilkumar, K. Yuvaraj (2022) Mechanical performance of ETC RC beam with U-framed AFRP laminates under a static load condition. *Revista de la Construcción*., 21(3), 678- 691. <https://doi.org/10.7764/RDLC.21.3.678>
- [35] G.Palanisamy, V.Kumarasamy (2023) Rehabilitation of damaged RC exterior beam-column joint using various configurations of CFRP laminates subjected to cyclic excitations. *Matéria (Rio de Janeiro)*., 28(2), e20230110. doi: <http://dx.doi.org/10.1590/1517-7076-rmat-2023-0110>.
- [36] A.A.Rajesh, S.Senthilkumar, S.Samson (2023) Optimal proportional combinations of rubber crumbs and steel slag for enhanced concrete split tensile strength. *Matéria (Rio de Janeiro)*., 28(4), e20230206. doi: <http://dx.doi.org/10.1590/1517-7076-rmat-2023-0206>.
- [37] P.Prasanthni, B.Priya, G.Dineshkumar, G.N. gobinath (2023) Mechanical properties of coal ash concrete in the presence of graphene oxide. *International Journal of Coal Preparation and Utilization*. In press. doi: <http://dx.doi.org/10.1080/19392699.2023.2284991>
- [38] A.R.Krishnaraja, S.Kandasamy (2018) Flexural performance of hybrid engineered cementitious composite layered reinforced concrete beams. *Periodica Polytechnica Civil Engineering*., 62(4), 921-929. doi: <http://dx.doi.org/10.3311/PPci.11748>.
- [39] S.C.Johnson, G.S.Thirugnanam (2015) Structural integrity assessment of transmission line tower foundations: a comprehensive approach. *CIGRE India Journal*, 4(2), 42-49.
- [40] R.Krishnasamy, S.C.Johnson (2020) Experimental investigations on glass fibre reinforced polymer composite pultruded sections and transmission line towers modules. *Water and Energy International*., 62(10), 33-37. doi.org/10.1007/976-3-030-31680-8
- [41] K.Gurunaathan, S.C.Johnson, G.S.Thirugnanam (2017) Anticipated and actual performance of composite girder with pre-stressed concrete beam and RCC top flange. *Structural Engineering and Mechanics International Journal*., 61(1), 117-124.
- [42] A.R.Krishnaraja, S.Anandakumar, M.Jegan, et al. (2019) Study on impact of fiber hybridization in material properties of engineered cementitious composites. *Matéria (Rio de Janeiro)*., 24(2), e12347. doi: <http://dx.doi.org/10.1590/s1517-707620190002.0662>.
- [43] A.A.Rajesh, S.Senthilkumar, K.Sargunan (2023) Interpolation and extrapolation of flexural strength of rubber crumbs and coal ash with graphene oxide concrete. *Matéria (Rio de Janeiro)*. 28(4), e20230179. doi: <http://dx.doi.org/10.1590/1517-7076-rmat-2023-0179>.

IZVOD

NEDESTRUKTIVNA PROCENA PODZEMNE KOROZIJE NA UGAONIM PROFILIMA OD VRUĆEG ČELIKA UGRAĐENIH U BETON I NJIHOVA SANACIJA CEMENTNOM SUSPENZIJOM I NITOCINK PREMAZOM

Ovaj istraživački članak predstavlja sveobuhvatno istraživanje materijala i otpornosti na koroziju ugaonih komponenti kritičnih za izgradnju infrastrukture. Studija se fokusira na dva ključna ugaona materijala: čelične uglove i uglove od plastike ojačane vlaknima (FRP), odabrane na osnovu zahteva specifičnih za projekat. Dizajn betonske mešavine, koji uključuje ključne komponente kao što su hemikalije (kalcijum hlorid, natrijum hidroksid, kalcijum hidroksid), agregati (M pesak i 20 mm agregat) i cement (Portland Pozzolana cement - 43 stepen), osigurava da se strukturalni integritet i performanse ispune željeni standardi. Istraživanje, takođe, uključuje napredne tehnike procene korozije, uključujući test potencijala polučelije i test primenjenog napona (Holiday Test), koji nude uvid u provodljivost materijala, otpornost na koroziju i integritet zaštitnog premaza. Štaviše, test hemijske otpornosti ispituje uticaj različitih rešenja na ove materijale, naglašavajući njihovu pogodnost za različite industrijske primene. Rezultati naglašavaju važnost odabira materijala po meri, proaktivnog upravljanja korozijom i kritične uloge zaštitnih premaza u obezbeđivanju dugovečnosti i bezbednosti infrastrukture. Ova studija doprinosi unapređenju metoda procene korozije, podržavajući trajnost kritičnih infrastrukturnih materijala.

Ključne reči: korozija, premaz, hemijska otpornost, trajnost, FRP, ugaoni presek

Naučni rad

Rad primljen: 26.11.2023.

Rad korigovan: 26.02.2024.

Rad prihvaćen: 09.03.2024.

Rad je dostupan na sajtu: www.idk.org.rs/casopis

Rajasundaravadivel Jeya Prakash¹, Balu Soundara²,
Singaram Christian Johnson³

¹Nandha Engineering College, Erode, Tamilnadu, India,

²The College of Engineering Guindy, Anna University, Chennai, India,

³Erode Sengunthar Engineering College, Erode, Tamilnadu, India

Scientific paper

ISSN 0351-9465, E-ISSN 2466-2585

<https://doi.org/10.62638/ZasMat1044>



Zastita Materijala 65 (2)
360- 370 (2024)

Serviceability performance of fibre reinforced no fine concrete pavement

ABSTRACT

The massive development of the construction industry demands sustainability, and the studies on No Fines Concrete (NFC) will support sustainable development in the field of transportation and highway industry. It is the key requirement of all developing countries like India in order to satisfy three main criteria namely sustainability, serviceability and feasibility in addition to its performance. Application of NFC pavement is itself a sustainable method to manage and discharge the retaining stormwater during heavy floods. Fibre Reinforced No Fine Concrete (FRNFC) was considered, with findings suggesting that the inclusion of fibres has minimal impact on strength characteristics and only marginally reduces the permeability of NFC. However, NFC pavements require regular maintenance to prevent clogging of pores with dust, sediments, and debris, which impairs water flow. A 2 m x 2 m span real-time FRNFC pavement was cast and subsequently subjected to assessment of its serviceability performance. The study examines the performance of FRNFC under clogging and suggests rehabilitation methods to reinstate infiltration capacity. Pressure wash combined with vacuum sweep shows the highest Drainage Efficiency Restoration (DER), maintaining drain ability from 99% to 90% after 12 cycles. Routine pressure wash monthly and vacuum sweep yearly are recommended for proper pavement serviceability and effective stormwater runoff mitigation.

Keywords: No fine concrete, fibre reinforcement, serviceability, clogging, drainage efficiency

1. INTRODUCTION

The increase in the infrastructural development and urbanization of several countries around the world resulted in decreasing the Earth's overall permeability. It also encounters serious environmental effects such as global warming, reduction in groundwater recharge, water pollution, and water stagnation during heavy rainfalls. Poor drainage with the impermeable surface will result in difficulties in using road transport facilities and accessing the basement of surrounding buildings in heavy rainfall prone areas. Installation of NFC pavement replacing the conventional impervious one is an efficient and sustainable solution to avoid flooding frequently. A numerous study has been conducted to evaluate the material properties of

NFC. This study extensively made the effort of adding fibre to NFC thereby increasing its durability without compromising its structural or hydraulic behaviour. FRNFC pavement system differed from conventional rigid concrete pavement systems by their complexity of inherent and flexible porosity along with multi-layer arrangements. The application of NFC is restricted for light loading conditions such as parking lots and sidewalks of residential areas [1]. The prototype developed was proposed to serve as a highway shoulder, where the runoff due to high precipitation can be drained. This can highly reduce the requirement of stormwater control structures constructed specially for highway runoff. When an FRNFC pavement is designed to be a highway shoulder, it should survive the wheel loadings from invading truck. Nevertheless, the incorporation of polypropylene fibres is aimed at enhancing durability aspects such as abrasion and resistance to freeze-thaw cycles, which are ongoing considerations for practical application. Pervious or NFC pavements are categorized under rigid pavement design. Still, there are some fundamental differences between them such as strength, stiffness, subbase and subgrade [2].

*Corresponding author: Rajasundaravadivel Jeya Prakash

E-mail: drjpcivil@gmail.com

Paper received: 26. 02. 2024.

Paper corrected: 13. 03. 2024.

Paper accepted: 17. 03. 2024.

Paper is available on the website: www.idk.org.rs/journal

2. TYPE OF PAVEMENTS

The pavements are the structural elements used in highway applications with the primary function of transmitting load to the subbase and underlying soil. Pavements are categorized into three major types including flexible or asphalt pavement, rigid or cement concrete pavement and

composite pavements. The composite pavements are constructed with a combination of flexible (top layer) and rigid (bottom layer) pavements. Hot mix asphalt and Portland cement concrete are generally used in the construction of composite pavements. Rigid pavements are further classified based on the joints and reinforcement as shown in Figure 1.

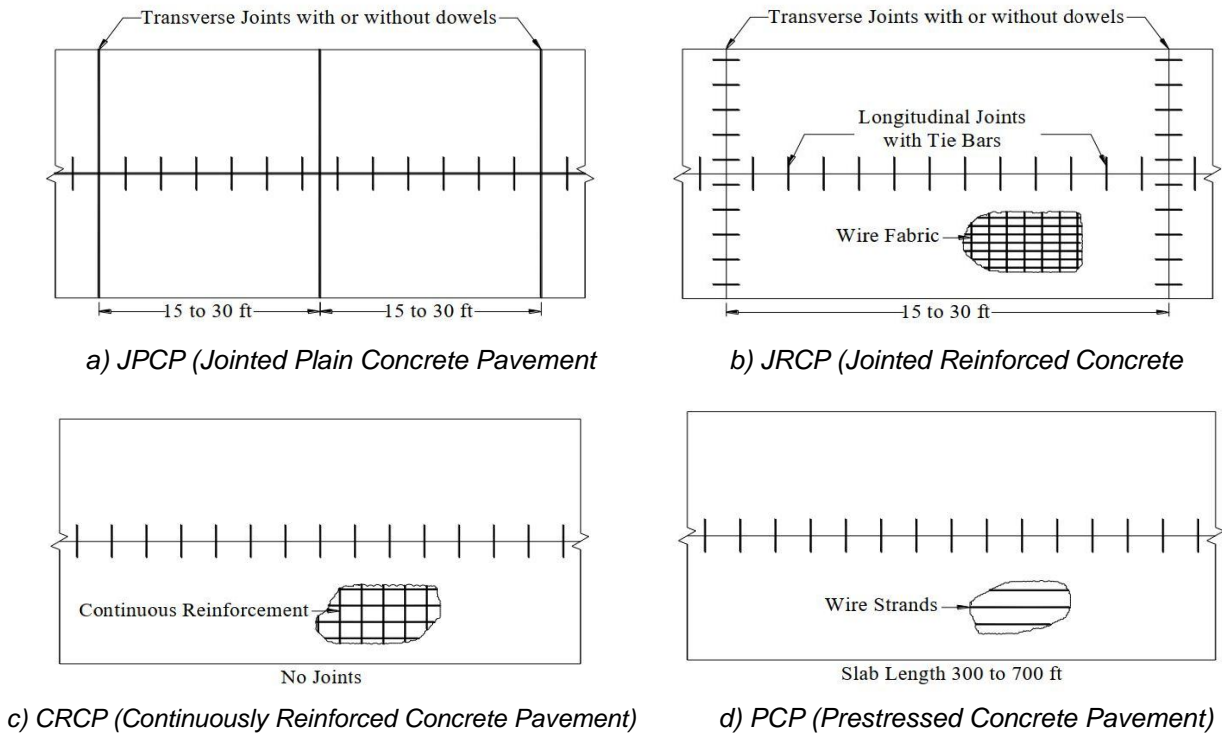


Figure 1 Types of Rigid Pavement
Slika 1 Tipovi krutih kolovoza

A traditional rigid pavement consists of three layers, concrete, subbase and subgrade or soil strata as shown in Figure 2. The traffic volume and the expected pavement loading are the key factors for designing the depth of the concrete and

subbase layer. The subbase layer was latterly introduced for resisting the high traffic volume and pavement loading, it is also used to reduce the water thrusting of the concrete layer by the subgrade.

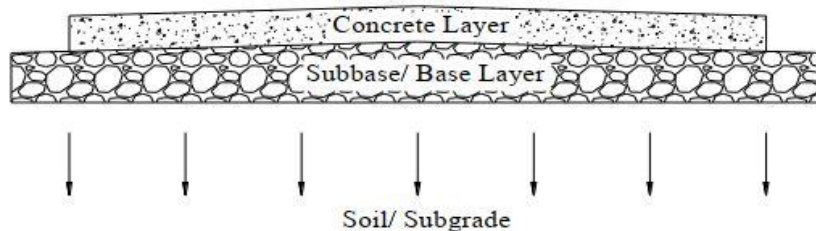


Figure 2 Cross section of Rigid Pavement
Slika 2 Poprečni presek krutog kolovoza

NFC pavements are generally considered under Low Impact Development (LID) techniques, which practices the natural infiltration and control the runoff volume [3]. For NFC pavement, the design depth of the subbase is larger than that of traditional rigid pavement. And usually, the subbase is not compacted as much tight as practising for normal rigid pavement. This is to increase the

volume of storage packets (voids) and thereby increasing the retention period to support natural infiltration of stormwater [4]. An additional property of noise absorption by these types of pavements can serve as a sustainable solution for the reduction of noise pollution during heavy traffic conditions [5].

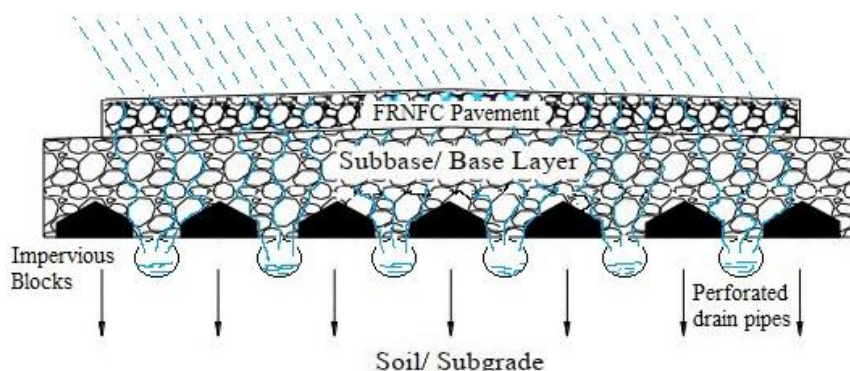


Figure 3. Cross section of Proposed FRNFC Pavement

Slika 3. Poprečni presek predloženog FRNFC kolovoza

Figure 3 shows the cross-section of the proposed FRNFC pavement, with increased subbase thickness and perforated drainpipes separated by impervious blocks just below the subbase. These blocks are used to break the infiltration link to the subgrade (underlying soil) which affects the bearing capacity of soil and cause failure to the pavement.

2.1. Subgrade

The subgrade is also known as formation level, i.e., the natural layer present underneath the pavement to be constructed. The characteristics of a given soil are taken before the review of the soil

profile for determining the settlement. The investigation of the subgrade is much important before preparation for permeable pavement since the infiltrated water has an adverse effect on both the pavement and subbase. The values of modulus of elasticity and Poisson's ratio of a particular soil varies with respect to the degree of saturation and drainage condition [6]. Preferably for FRNFC pavements also subgrade with a higher drainage ratio is chosen to increase the efficiency of stormwater runoff management. Table 1. gives the values of the modulus of elasticity and Poisson's ratio based on the soil's drainage condition.

Table 1. Moduli of elasticity and Poisson's ratio of soils (Coduto, 1994)

Tabela 1. Moduli elastičnosti i Poissonov odnos tla (Coduto, 1994)

Soil Type		Modulus of elasticity (GPa)	Soil Type	Poisson's ratio
Clay (Undrained condition)	Soft	0.0015-0.01	Saturated soil (Undrained condition)	0.50
	Medium	0.005-0.05		
	Stiff	0.015-0.075		
Clay (Drained condition)	Soft	0.0003-0.0015	Partially saturated clay	0.30-0.40
	Medium	0.0005-0.0035		
	Stiff	0.0012-0.02		
Sand (Drained condition)	Loose	0.01-0.025	Loose sand (Drained condition)	0.30-0.40
	Medium dense	0.02-0.06	Dense sand (Drained condition)	0.10-0.30
	Dense	0.05-0.1		
Sandstone	-	7.0-20.0	Sandstone	0.25-0.30
Granite	-	25.0-50.0	Granite	0.23-0.27

In drained condition, the rate of drainage is greater than the infiltration rate and for the undrained condition, the rate of drainage is less than the infiltration rate. The drainage rate is the function of permeability coefficient or hydraulic conductivity. For example, sand and gravel hold

drained condition easily as the coefficient of permeability is high, and clay soils hold in undrained condition often due to less coefficient of permeability. Generally, subgrade with a higher drainage ratio is preferred for rigid pavements to reduce the effect of water thrusting which affects the soil stability with respect to time.

2.2. . Subbase

Subbase is one of the layers of pavement laid over the subgrade, specially designed for bearing the load from the pavement and distribute it to the soil strata. The subbase quality is highly important to increase the serviceability of the pavement. Generally, natural aggregates of size not less than 20 mm are used for the subbase. The thickness of the subbase is obtained from Table 2. Since the proposed pavement design is adopted for highway shoulder application, the thickness of 10" (0.25 m) is taken for this study. However, Subbase does not bring any structural strength to the pavement but distributes the load uniformly to the subgrade. Generally bounded subbases are recommended for rigid pavements in design guides, for permeable rigid pavements unbounded subbase are preferred. The thickness of subbase and concrete pavement does not change with the subgrade strength as in the case of flexible pavement. Still, the material selection, proper design and effective construction is very much important for the long-term serviceability of the pavement.

Table 2. Thickness of Subbase

Tabela 2. Debljina podloge

S. No.	Road Application	Standard Thickness (in)
1	Garden Pathway	3 – 4
2	Driveway and public foot path	4 – 6
3	Heavy used Roadways	6 – 9
4	Highway	> 10

3. FRNFC PAVEMENT

The construction of given pervious or FRNFC pavement systems involves 3 layers (bottom quarter, middle half and top quarter) with an assumption of the faultless bond between the layers [7-10]. The porosity of these three sections varies with the time period, and an average porosity is finally considered as the system porosity. The porosity of the top quarter changes with respect to time due to the clogging effects and reduces the system porosity. And the bottom quarter porosity varies with the selection of subgrade (coarser subgrade permits higher discharge rate) [11]. Whereas the porosity of the middle half remains the same and is influenced by poor placement practicing, which can be enhanced during pavement casting.

The distribution of wheel load is uniform to the area under the slab. The load on the slab is

transmitted through beam action, and hence with sufficient beam strength, the pavement can withstand any areas within adequate support and localize subgrade failures [12]. Figure 4 illustrate the wheel load distribution of concrete pavements.

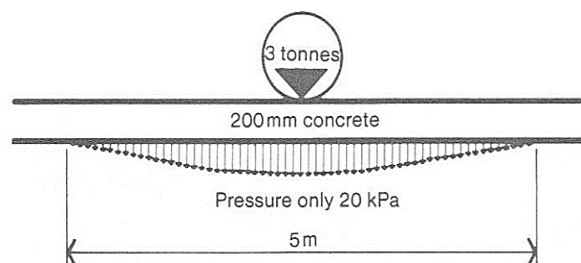


Figure 4 Wheel load distribution of concrete pavements

Slika 4 Raspodela opterećenja na točkove betonskih kolovoza

3.1. Highway Shoulders

An adjacent portion connected with highway specially meant for parking the trucks or any emergency drives, and to provide support for the subbase and pavement along lateral direction [13]. Thus, shoulders are subjected to similar loading as that of the main pavement. FRNFC pavement with thickness ranging from 200 to 300 mm is considered to be effective for replacing highway shoulders based on the usage intensity [14-15].

3.2. Site Preparation and Placement

Before the placement of pavement, the subgrade should be maintained in moist condition with no standing water. The excess water present in the subgrade can eradicate the binder from the bottom portion of the pavement. High porosity without compromising strength and durability is the main target of the NFC pavement, care must be taken to avoid the premature drying of the concrete mixture [16]. The concrete placement with high evaporation rates must be avoided to reduce the chance of loss in water content. The factors like high voids content and less w/c ratio support the rapid drying of mixtures followed by a reduction in strength and durability.

Site preparation and placement includes preparation of subbase and pavement placement. Figure 5 shows the preparation of subbase including the a) excavation for subbase preparation, b) arrangements for perforated pipes and impervious block, c) filling of aggregates as subbase and d) cross-section of perforated pipe connected to side drain to collect runoff water. Whereas Figure 6 illustrates the transportation and placement of FRNFC pavement in the site.

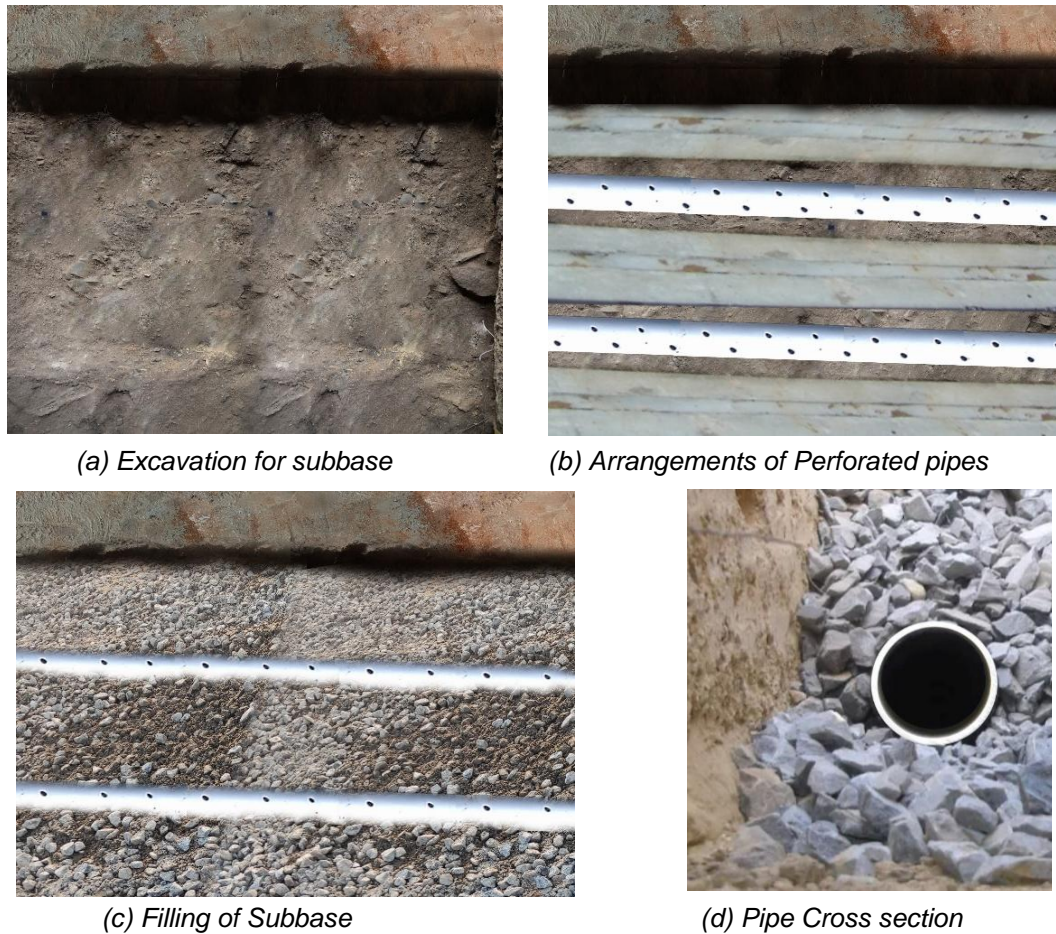


Figure 5. Preparation of Subbase

Slika 5. Priprema podloge

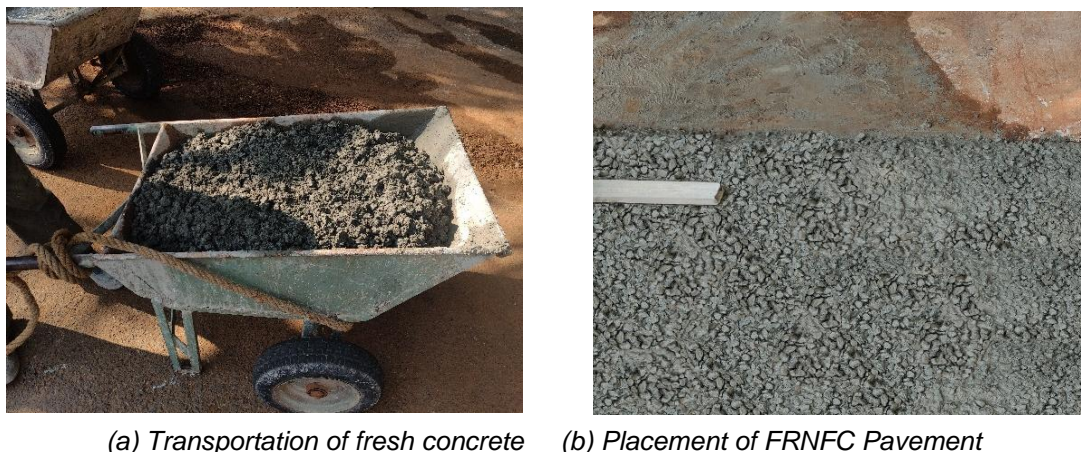


Figure 6 Pavement Placement

Slika 6 Postavljanje kolovoza

3.3. Pavement Configuration

The dimension of the slab is taken as 6.5' x 6.5' (2 m x 2 m) and the thickness of the FRNFC pavement, subbase and subgrade layers were considered to resemble a typical roadway

pavement thickness. There is a difference observed between traditional concrete and FRNFC in the values of stiffness, compressive strength and flexural behaviour. Generally, for pavements, the stiffness of subbase and subgrade are also taken into consideration as given in Table 3.

Table 3. Material Properties obtained from laboratory testing

Tabela 3. Svojstva materijala dobijena laboratorijskim ispitivanjem

Material/Layer	Youngs Modulus E (Mpa)	Poisson's ratio, ν_u (no units)	Density, ρ kg/m ³
Polypropylene Fibre	4.0 - 4.5	0.4	910
FRNFC Slab	18875	0.2	1875
Subbase	5000	0.2	1542
Subgrade	200	0.4	1430

3.4. Thickness Design

An FRNFC slab model of thickness 8" (0.2 m) was cast in the laboratory parking area. The pavement was placed over an unbound subbase of thickness 10" (0.25 m) prepared by aggregates of size 20 mm. A partially saturated with the undrained condition is taken as a subgrade with a thickness of 39" (1 m) as shown in Figure 7. The design depth of the subbase used for an FRNFC pavement is usually larger than that of a traditional impervious rigid pavement [17]. And also, the subbase is not compacted as much tight as practising for normal rigid pavement. This is to increase the volume of storage packets (voids) and thereby increasing the retention period to support natural infiltration of stormwater [18-19].

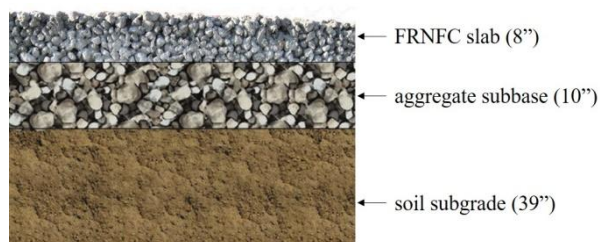


Figure 7 Pavement Thickness Design

Slika 7 Projektovanje debljine kolovoza

3.5. Drainage Design

The infiltration of water subsequently affects the stability and bearing capacity of the subbase and subgrade, which in turn affects the serviceability of the pavements. Figure 8 shows a typical cross-section of drainage design of the proposed FRNFC pavement specially used to break the infiltration link to the subgrade (underlying soil), with perforated drainpipes separated by impervious blocks just below the subbase. The collected stormwater from the

perforated drainpipes is directed to common outfall drain from where they can be sent to treatment units.

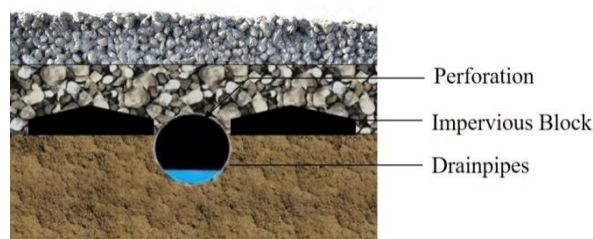


Figure 8 Drainage Design

Slika 8 Dizajn drenaže

4. SERVICEABILITY BEHAVIOUR

No fines concrete is most commonly known as sustainable concrete that helps in stormwater mitigation, pollutants load reduction, temperature mitigation, noise absorption, air quality improvement, etc., [20]. Besides these benefits, their serviceability is likely to be affected by several factors like clogging and less surface abrasion resistance. However, the fibre reinforcement was incorporated to improve its abrasion resistance [21]. The performance of FRNFC under the clogging effect was examined and the change in infiltration capacity of the specimens was discussed. To reinstate the infiltration capacity, certain rehabilitation methods were suggested, and their efficiencies were discussed [22]. This study provides security for the investment made on no fines concrete; the pavement must serve for a minimum service life by providing resistance against all these factors.

4.1. Clogging

NFC pavements have a high chance of clogging after every rainy event. Clogging is one of the significant issues associated with the serviceability of NFC pavements as it reduces its infiltration capacity. It is also considered to be one of the main restrictions against the practical application of pervious pavements [23]. Clogging takes places due to the deposition of dust, sediments, debris, and other inorganic particles over the pores on the pavement surface during stormwater runoff.

The slab specimens cast for determining the infiltration capacity, are subjected to clogging by allowing dirt muddy water containing different types of clogging materials such as sand, clay, and silt as shown in Figure 9. Twelve cycles of clogging and cleaning were carried out and its drain ability was tested after every clogging (reduced infiltration) and cleaning cycle (recovery infiltration).



a) Test Setup



b) Specimen after clogging

Figure 9. Clogging test on FRNFC Pavement

Slika 9. Test začepljenja na FRNFC kolovozu

4.2. Rehabilitation Methods

NFC pavements need proper maintenance or rehabilitation since dust, sediments, debris, and other inorganic particles get deposited into the pores of the pavement surface and clog the water flow. Periodic removing of surface sediment particles prevents their deeper penetration inside the concrete matrix and thereby affecting the drain ability of the pavements. The FRNFC specimens subjected to clogging test are then rehabilitated to restore the infiltration rate by standard cleaning methods such as pressure wash (wet cleaning), vacuum sweep (dry cleaning), and combined method [24].

Pressure Wash

Pressure wash technique can be adopted to remove the surface clogging by applying a concentrated water using power nozzle sprayer over the surface of the FRNFC pavements after scrubbing to get out the debris as shown in Figure 10. This pressurized water from the nozzle will wash off all the surface dirt by weakening the bond between the concrete and clogged particles. Small particles will penetrate deep into the concrete matrix and reaches the subbase layer, gets deposited on the aggregate reservoir. This method is highly recommended for high load of sediments or debris.



Figure 10. Pressure Wash

Slika 10. Pranje pod pritiskom

Vacuum Sweep

The surface of the FRNFC pavements can be subjected to a dry vacuum sweep method annually to dislodge the hidden clogged particles and debris. It consists of three units, a blower, suction tube, and a hopper. This method of cleaning is considered to be more effective than pressure wash which requires plenty of water to wash off the debris from the surface, whereas vacuum sweep implements a simple tool of vacuum cleaner to remove the debris off from the pavement surface and dump it into a hopper as shown in the Figure 11.



Figure 11. Vacuum sweep

Slika 11. Vakuumsko čišćenje

The silt carried by the runoff water plugs into the concrete matrix, on saturated conditions the silt starts bulged and gets sticky to the matrix. Hence, this method is usually carried when the pavement is in dry condition, as the silt loosen its grip with the matrix by shrinking and get sucked by the suction tube.

Combined Method

This combined method of cleaning FRNFC pavement includes a vacuum sweep followed by a pressure wash, which produces the best results in improving the efficiency of infiltration after a

clogging cycle. The clogged debris get dislodged from the interconnected voids, by using pressure wash and vacuum sweep once after drying the pavement simultaneously.

4.3. Drainage Efficiency Restoration

In recent days, the construction of pervious pavement attracts the attention of the engineers mainly to prevent splashing and to control erosion.

Thus, the porous pavement with a storage reservoir to collect the surface runoff should be maintained appropriately for higher drainage efficiency. The effects of clogging and different methods of cleaning for 12 cycles on the infiltration rate of the FRNFC pavement by double-ring infiltrometer test setup is given below in Table 4 and graphically shown in Figure 12.

Table 4. Drainage Efficiency Restoration

Tabela 4. Obnova efikasnosti drenaže

Cycle	Pressure Wash			Vacuum Sweep			Combined Method		
	Infiltration rate, I (cm/sec)		DER	Infiltration rate, I (cm/sec)		DER	Infiltration rate, I (cm/sec)		DER
	Clog	Clean	%	Clog	Clean	%	Clog	Clean	%
0	-	0.291	-	-	0.291	-	-	0.291	-
1	0.223	0.261	89.77	0.223	0.276	94.99	0.223	0.287	98.63
2	0.222	0.257	88.35	0.222	0.274	94.16	0.222	0.281	96.56
3	0.222	0.252	86.72	0.222	0.271	93.28	0.222	0.278	95.53
4	0.220	0.249	85.64	0.220	0.269	92.44	0.220	0.273	93.81
5	0.218	0.248	85.37	0.218	0.266	91.27	0.218	0.269	92.44
6	0.215	0.247	84.85	0.215	0.264	90.59	0.215	0.268	92.10
7	0.212	0.241	82.93	0.212	0.259	88.85	0.212	0.266	91.41
8	0.210	0.241	82.80	0.210	0.258	88.67	0.210	0.265	91.07
9	0.208	0.237	81.58	0.208	0.257	88.28	0.208	0.264	90.72
10	0.205	0.236	81.11	0.205	0.255	87.63	0.205	0.263	90.38
11	0.205	0.235	80.76	0.205	0.251	86.25	0.205	0.262	90.03
12	0.201	0.233	80.07	0.201	0.247	84.88	0.201	0.261	89.69

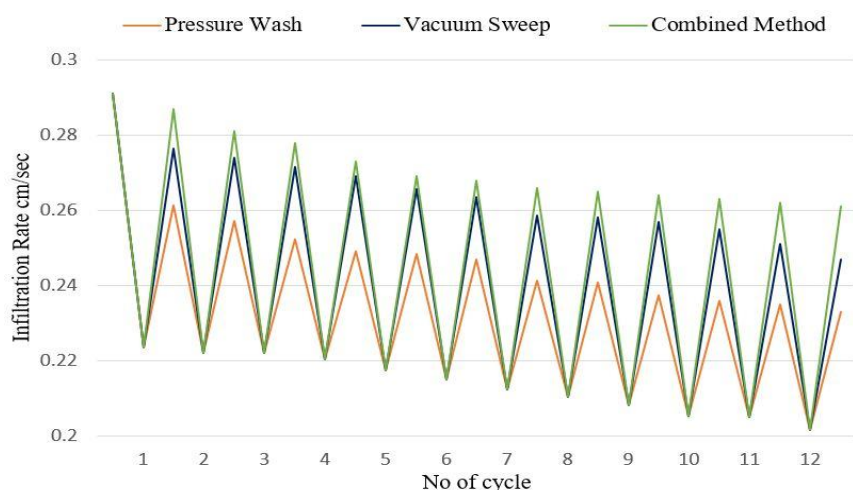


Figure 12. Drainage Efficiency Restoration

Slika 12. Obnova efikasnosti drenaže

The selection of the rehabilitation method highly depends on the clogging percentage and sediment characteristics. Both pressure wash and vacuum sweep combinedly produce the maximum

Drainage Efficiency Restoration (DER) from 99% (first cycle) to 90% after 12 cycles of clogging and cleaning. Whereas pressure wash retains drain ability from 90% (first cycle) to 80% after 12 cycles

and vacuum sweep retains drain ability from 95% (first cycle) to 85% after 12 cycles.

From the test results, the clogging cycle reduces the rate of infiltration of FRNFC pavement by about 73.6% and it is suggested to routine pressure wash at a frequency of monthly once and vacuum sweep at a frequency of yearly once to ensure proper serviceability of the pavement, to achieve max DER % and effective stormwater runoff mitigation.

4.4. Cost Benefit Analysis

No fines concrete pavements are constructed to support the soil and water conservation practices. The replacement of conventional impervious asphalt pavements by pervious FRNFC pavements would increase the infiltration capacity and supports groundwater recharges and thereby reducing the stormwater runoff. Hence, a cost-benefit analysis is highly essential to answer the question, 'Whether FRNFC is a cost-effective alternative or not?'.

Table 5. Construction and Maintenance cost comparison for 1 m²

Tabela 5. Poređenje troškova izgradnje i održavanja za 1 m²

Particulars	Frequency in 20 years	FRNFC Pavements (₹)	Frequency in 20 years	Asphalt Pavements (₹)
Installation	1	6000	1	4000
Drainage Design	1	450	0	0
Vacuum Sweep	20	15 x 20	0	0
Pressure Wash	240	5 x 240	0	0
Restore Permeability	5	65 x 5	0	0
Crack Sealing	0	0	20	10 x 20
Seal Coat	0	0	5	750 x 5
Stripping	0	0	1	115 x 1
Patching	0	0	5	5 x 5
Surface Replace	0	0	1	1175 x 1
Construction Cost	-	6450	-	4000
Maintenance Cost	-	1825	-	5265
Total Cost per 1 m ²	-	8275	-	9260

Detailed cost comparison between conventional impervious asphalt pavements and pervious FRNFC pavements including the construction and maintenance cost for a unit square meter is evaluated and discussed in Table 5. The serviceability of FRNFC pavement is assumed to be 20 years [25].

The installation of pervious pavements by replacing the existing impervious one will not be initially considered as economical, since it also includes the demolition cost. However, counting the benefits and environmental sustainability obtained over time from installation will make it cost-effective. From the above analysis, it is clear that the initial cost required for the construction is high for pervious FRNFC pavements comparing to the impervious Asphalt pavements. This is because FRNFC requires a large amount of excavation and additional design for proper drainage to improve its durability. The base layers in FRNFC pavements are designed to not only offers structural stability but also to assist the infiltration process. While considering the maintenance requirement of

Asphalt pavements over the service life it cost higher (almost three times) than the FRNFC pavements. Asphalt pavement includes the cost for crack sealing, seal coat, stripping and patching works whereas FRNFC only requires periodical pressure washing and vacuum sweeping to maintain its drain ability.

Generally, Asphalt pavements are with high surface tension and thereby highly pretentious by temperature, weathering, and minimum geographical stress (ground uplift, earthquakes and swallet). Thus, any difference in stress easily propagates cracks in asphalt pavement and requires regular maintenance to ensure safe drives. This makes asphalt over its service period an expensive choice comparing FRNFC pavements, which have an additional provision for stormwater management.

5. CONCLUSION

The total depth of FRNFC pavement is divided into three layers (top quarter 2", middle half 4" and bottom quarter 2"). The porosity of these three

layers varies, and an average is finally considered as the system porosity. Thus, to increase the overall system porosity of given pervious pavements, each of the three layers must follow different strategies.

- The top quarter porosity changes to time due to the clogging effects and can be recovered, and the efficiency can be restored by practising a few rehabilitation techniques like pressure wash, vacuum sweep, and combined method.
- The bottom quarter porosity varies with the selection of subgrade and is boosted by placing the pervious pavement over a coarser unbounded subgrade which permits a higher discharge rate.
- The middle half porosity remains the same and is influenced by poor placement practising, which can be enhanced during casting.

The infiltration of water to the subgrade subsequently affects its stability and bearing capacity. The proposed FRNFC pavement implements a specific drainage design to break the infiltration link to the subgrade, with perforated drainpipes and impervious blocks just below the subbase. The collected stormwater is directed to a common outfall drain from where it can be sent to treatment units.

From the detailed study of the clogging effect on FRNFC, it is suggested to follow a routine pressure wash at least once a month followed by an annual vacuum sweep to ensure proper drainability of the pavement. And from a cost-benefit analysis, construction of FRNFC pavement over conventional impervious asphalt for a parking lot of ½ acre would save about ₹ 20,13,310 over a service life of 20 years. This makes FRNFC pavement a cost-effective replacement for impervious asphalt pavement.

6. REFERENCES

- [1] Al.Ralinska, A.Welker, K.Greising, B.Campbell, D. Littlewood (2012) Long-term field performance of pervious concrete pavement, *Advances in Civil Engineering*, p.1-9.
- [2] American Concrete Institute - ACI (2010) Report on pervious concrete, ACI Committee 522, Report number: ACI 522R-10.
- [3] E.J.Elizondo-Martínez, VC.Andrés, D.Jato-Espino, J.Rodríguez (2019) Review of porous concrete as multifunctional and sustainable pavement, *Journal of Building Engineering*, 27, 100967. <https://doi.org/10.1016/j.job.2019.100967>
- [4] E.Fassman, S.Blackbourn (2010) Urban runoff mitigation by a permeable pavement system over impermeable soils, *Journal of Hydrologic Engineering*, 15(6), 475-485.
- [5] AS.Gandage, V.Vinayaka-Ram, M.Panwar, M.Shah, R.Singhvi (2016) Study on Reduction of Pavement Noise Using Porous Concrete, *Indian Concrete Journal*, 90(3), 12–21.
- [6] P.Coduto Donald (1994) *Foundation Design: Principles and Practices : Solutions Manual*, Prentice Hall.
- [7] ASTM C 1202, Standard Test Method for Electrical Indication of Concrete's Ability to Resist Chloride Ion Penetration, American Society for Testing and Materials, West Conshohocken, PA, USA.
- [8] ASTM C 1747, Standard Test Method for Determining Potential Resistance to Degradation of Pervious Concrete by Impact and Abrasion, American Society for Testing and Materials, West Conshohocken, PA, USA.
- [9] ASTM C 944, Standard Test Method for Abrasion Resistance of Concrete or Mortar Surfaces by the Rotating-Cutter Method, American Society for Testing and Materials, West Conshohocken, PA, USA.
- [10] ASTM D 3385-94, Standard Test Method for Infiltration Rate of Soils in Field Using Double-Ring Infiltrometer, American Society for Testing and Materials, West Conshohocken, PA, USA.
- [11] A.K.Chandrappa, KP.Biligiri (2016) Pervious concrete as a sustainable pavement material – Research findings and future prospects: A state-of-the-art review, *Construction and Building Materials*, 111, 262-274.
- [12] NJ.Garber, LA.Hoel (2002) *Traffic and Highway Engineering*, Third edition, Brooks Cole Publishing Company.
- [13] YH.Huang (2004) *Pavement Analysis and Design*, 2nd ed., Pearson Prentice Hall, Upper Saddle River, NJ, USA.
- [14] R.Jeya Prakash, B.Soundara, S.Christian Johnson (2020) Sustainability of No-Fine Concrete with Fibre reinforcement, *The Journal of Environmental Protection and Ecology*, 21(6), 2131-2143.
- [15] R.Jeya Prakash, B.Soundara, K.S.Elango, S.Christian Johnson (2023) Performance Evaluation of Fibre Reinforced Pervious Concrete Pavement, *Romanian Journal of Materials*, 53(3), 237-247.
- [16] R.Karthik Navada, BM. Mithun, M.Shriram (2018) Pervious Concrete for Transportation Application, *International Research Journal of Engineering and Technology*, 5(5), 3461-3463.
- [17] U. Magesvari, VL.Narasimha (2013) Studies on characterization of pervious concrete for pavement Applications, *Procedia – Social and Behavioral Sciences*, 104, 198-207. <https://doi.org/10.1016/j.sbspro.2013.11.112>
- [18] T.Su-Lin, C.Kevin, C.Dylan, M.Johnathon (2015) Cost and Benefit Analysis of Permeable Pavements in Water Sustainability, *ESM*, Final report, 25/5/2015.
- [19] CY.Sung, YI.Kim (2012) Void ratio and durability properties of porous polymer concrete using recycled aggregate with binder contents for permeability pavement, *Journal of Applied Polymer Science*, 126, 338-348. <https://doi.org/10.1002/app.36974>

- [20] L. Akand, M. Yang, X. Wang (2018) Effectiveness of chemical treatment on polypropylene fibres as reinforcement in pervious concrete, *Construction and Building Material*, 163, 32–39. <https://doi.org/10.1016/j.conbuildmat.2017.12.068>
- [21] JT. Kevern, T. Biddle (2015) Effects of Macrosynthetic Fibres on Pervious concrete Properties, *Journal of Materials in Civil Engineering*, 27(9), [https://doi.org/10.1061/\(ASCE\)MT.1943-5533.0001213](https://doi.org/10.1061/(ASCE)MT.1943-5533.0001213).
- [22] C. Lian, Y. Zhuge, S. Beecham (2011) The relationship between porosity and strength for porous concrete, *Construction and Building Materials*, 25(11), 4294-4298.
- [23] X. Shu, B. Huang, H. Wu, Q. Dong, G. Edwin Burdette (2011) Performance comparison of laboratory and field produced pervious concrete mixtures, *Construction and building materials*, 25(8), 3187-3192.
- [24] M. Yaolu, C. Xianhua, G. Yanfen, Z. Xinlan (2020) Effect of Clogging on the Permeability of Porous Asphalt Pavement, *Advances in Materials Science and Engineering*, Article ID 4851291, <https://doi.org/10.1155/2020/4851291>.
- [25] R. Sri Ravindrarajah, S.J. Kassis (2014) Effect of supplementary cementitious materials on the properties of pervious concrete with fixed porosity', *Proceedings of the 23rd Australasian conference on the Mechanics of Structures and Materials*, p. for publication 53-58.

IZVOD

MOGUĆNOST UPOTREBE PERFORMANSE OBLOGA OJAČANOG VLAKNIMA BEZ FINOG BETONA

Masivan razvoj građevinske industrije zahteva održivost, a studije o betonu bez finog kamenca (NFC) će podržati održivi razvoj u oblasti transporta i industrije autoputeva. To je ključni zahtev svih zemalja u razvoju kao što je Indija kako bi se zadovoljila tri glavna kriterijuma, a to su održivost, upotrebljivost i izvodljivost, pored svog učinka. Primena NFC kolovoza je sama po sebi održiva metoda za upravljanje i ispuštanje atmosferske vode koja se zadržava tokom velikih poplava. Razmatran je beton ojačan vlaknima bez finog betona (FRNFC), sa nalazima koji sugerišu da uključivanje vlakana ima minimalan uticaj na karakteristike čvrstoće i samo neznatno smanjuje propustljivost NFC-a. Međutim, NFC kolovozi zahtevaju redovno održavanje kako bi se sprečilo začepljenje pora prašinom, sedimentima i ostacima, što otežava protok vode. FRNFC kolovoz u realnom vremenu raspona 2 m x 2 m je izliven i naknadno podvrgnut proceni performansi njegove upotrebljivosti. Studija ispituje učinak FRNFC-a pod začepljenjem i predlaže metode rehabilitacije za ponovno uspostavljanje kapaciteta infiltracije. Pranje pod pritiskom u kombinaciji sa vakuumskim čišćenjem pokazuje najveću restauraciju efikasnosti drenaže (DER), održavajući sposobnost drenaže od 99% do 90% nakon 12 ciklusa. Rutinsko pranje pod pritiskom mesečno i čišćenje usisivačem godišnje se preporučuju za ispravnu upotrebljivost kolovoza i efikasno ublažavanje oticanja atmosferskih voda.

Ključne reči: Bez finog betona, vlaknasta armatura, upotrebljivost, začepljenje, efikasnost drenaže

Naučni rad

Rad primljen: 26. 02. 2024.

Rad korigovan: 13. 03. 2024.

Rad prihvaćen: 17. 03. 2024.

Rad je dostupan na sajtu: www.idk.org.rs/casopis

RECENZENTI – REVIEWERS

Prof.dr Milan Antonijević, Univerzitet u Beogradu, Tehnički fakultet u Boru, Bor, Srbija
 Prof. dr Miomir Pavlović, Univerzitet u Beogradu, Tehnološko-metalurški fakultet, Beograd, Srbija
 Prof. dr Časlav Lačnjevac, Univerzitet u Beogradu, Poljoprivredni fakultet, Beograd, Srbija
 Prof. dr Radomir Folić, Emeritus, Univerzitet u Novom Sadu, Fakultet tehničkih nauka, Novi Sad, Srbija
 Prof. dr Vesna Mišković-Stanković, Univerzitet u Beogradu, Tehnološko metalurški fakultet, Beograd, Srbija
 Prof. dr Miodrag Maksimović, Univerzitet u Beogradu, Tehnološko metalurški fakultet, Beograd, Srbija
 Prof. dr Vladimir Panić, Univerzitet u Beogradu, Tehnološko metalurški fakultet, Beograd, Srbija
 Prof. dr Dragica Jevtić, Univerzitet u Beogradu, Građevinski fakultet, Beograd, Srbija
 Dr Miodrag Stojanović, Vojnotehnički institut, Beograd, Srbija
 Prof. dr Petar Živković, Univerzitet u Podgorici, Metalurško-tehnološki fakultet, Podgorica, Crna Gora
 Prof. dr Branislav Nikolić, Univerzitet u Prištini, Fakultet tehničkih nauka, Kosovska Mitrovica, Srbija
 Prof. dr Dragan Veselinović, Univerzitet u Beogradu, Fakultet za fizičku hemiju, Beograd, Srbija
 Prof. dr Veselin Batalović, Univerzitet u Beogradu, Rudarsko-geološki fakultet, Beograd, Srbija
 Dr Nebojša Nikolić, Naučni savetnik, Univerzitet u Beogradu, IHTM, Beograd, Srbija
 Prof.dr Jelena Pješčić, Univerzitet u Podgorici, Metalurško-tehnološki fakultet, Podgorica, Crna Gora
 Prof.dr Refik Zejnilović, Univerzitet u Podgorici, Metalurško-tehnološki fakultet, Podgorica, Crna Gora
 Dr Mile Dimitrijević, Univerzitet u Beogradu, Tehnološko metalurški fakultet, Beograd, Srbija
 Prof. dr Karlo Raić, Univerzitet u Beogradu, Tehnološko metalurški fakultet, Beograd, Srbija
 Dr Mirjana Stojanović, Naučni savetnik, ITNMS, Beograd, Srbija
 Dr Zvonko Gulišija, Naučni savetnik, ITNMS, Beograd, Srbija
 Dr Zoran Karastojković, Naučni saradnik, Visoka tehnička škola, Novi Beograd, Srbija
 Prof. dr Nedeljko Krstajić, Univerzitet u Beogradu, Tehnološko metalurški fakultet, Beograd, Srbija
 Dr Ljiljana Gajić-Krstajić, Naučni savetnik, Institut tehničkih nauka SANU, Beograd, Srbija
 Dr Jasmina Stefanović, Naučni savetnik, Univerzitet u Beogradu, IHTM, Beograd, Srbija
 Prof. dr Miladin Gligorić, Univerzitet Istočno Sarajevo, Tehnološki fakultet, Zvornik, Republika Srpska
 Prof. dr Nikola Ristić, Emeritus, Univerzitet u Beogradu, Poljoprivredni fakultet, Beograd, Srbija
 Prof. dr Milan Jakšić, Institute of Chemical Engineering Sciences, FORTH, Patras, Greece
 Prof. dr Dragica Čamovska, Univerzitet "Kirilo i Metodije", TMF, Skopje, Makedonija
 Prof. dr Fehim Korać, Univerzitet u Sarajevu, Tehnološki fakultet, Sarajevo, BiH
 Prof. dr Evica Ivanović, Univerzitet u Beogradu, Poljoprivredni fakultet, Beograd, Srbija
 Prof.dr Aleksandar Đorđević, Univerzitet u Beogradu, Poljoprivredni fakultet, Beograd, Srbija
 Prof.dr Jelena Đorđević, Univerzitet u Beogradu, Poljoprivredni fakultet, Beograd, Srbija
 Prof.dr Zoran Rajić, Univerzitet u Beogradu, Poljoprivredni fakultet, Beograd, Srbija
 Prof.dr Sreten Jelić, Univerzitet u Beogradu, Poljoprivredni fakultet, Beograd, Srbija
 Prof.dr Dejan Bezbradica, Univerzitet u Beogradu, Tehnološko-metalurški fakultet, Beograd, Srbija
 Dr Zoran Avramović, Naučni saradnik, RTB, Bor, Srbija
 Dr Vlada Jović, Naučni savetnik, Univerzitet u Beogradu, IMSI, Beograd, Srbija
 Dr Nevenka Elezović, Naučni savetnik, Univerzitet u Beogradu, IMSI, Beograd, Srbija
 Dr Uroš Lačnjevac, Viši naučni saradnik, Univerzitet u Beogradu, IMSI, Beograd, Srbija
 Dr Borka Jović, Naučni savetnik, Univerzitet u Beogradu, IMSI, Beograd, Srbija
 Prof. dr Milorad Tomić, Univerzitet Istočno Sarajevo, Tehnološki fakultet, Zvornik, Republika Srpska
 Prof. dr Ace Dimitrov, Univerzitet "Kirilo i Metodije", TMF, Skoplje, R.Makedonija
 Prof. dr Filip Kokalj, Univerzitet u Mariboru, Tehnički fakultet, Maribor, Slovenija
 Prof. dr Sonja Martinez, Univerzitet u Zagrebu, Fakultet za strojarstvo, Zagreb, Hrvatska
 Prof.dr Vesna Alar, Univerzitet u Zagrebu, Tehnološki fakultet Zagreb, Hrvatska
 Prof. dr Ivan Stojanović, Univerzitet u Zagrebu, Fakultet za strojarstvo, Zagreb Hrvatska
 Dr Ivan Krastev, Naučni savetnik, Institut tehničkih nauka, Bulgarian Academy of Sciences, Sofija, Bugarska
 Prof. dr Nebojša Ralević, Univerzitet u Beogradu, Poljoprivredni fakultet, Beograd, Srbija
 Prof. dr Blažo Lalević, Univerzitet u Beogradu, Poljoprivredni fakultet, Beograd, Srbija
 Prof. dr Milovan Jotanović, Univerzitet Istočno Sarajevo, Tehnološki fakultet, Zvornik, Republika Srpska
 Dr Anžej Koval, Naučni savetnik, Institut Krakov, Krakov, Poljska
 Prof. dr Kozeta Vaso, Univerzitet u Tirani, Tehnički fakultet, Tirana, Albanija
 Prof. dr Vaso Novaković, Univerzitet Istočno Sarajevo, Tehnološki fakultet, Zvornik, Republika Srpska
 Prof. dr Slobodan Sokolović, Univerzitet u Novom Sadu, Tehnološki fakultet, Novi Sad, Srbija
 Prof. dr Radmila Šećerov-Sokolović, Univerzitet u Novom Sadu, PMF, Novi Sad, Srbija

Dr Miroslav Sokić, naučni savetnik, ITNMS, Beograd, Srbija
 Dr Marija Mihajlović, viši naučni saradnik, ITNMS, Beograd, Srbija
 Dr Zoran Janjušević, viši naučni saradnik, ITNMS, Beograd, Srbija
 Prof. dr Đendi Vaštag, Univerzitet u Novom Sadu, PMF, Novi Sad, Srbija
 Dr Branka Kaluđerović, naučni savetnik INN Vinča, Beograd, Srbija
 Dr Jelena Milojčić, naučni saradnik, ITNMS, Beograd, Srbija
 Dr Marija Petrović, naučni saradnik, ITNMS, Beograd, Srbija
 Dr Srećko Manasijević, viši naučni saradnik, Institut Lola, Beograd, Srbija
 Prof.dr Borislav Milinović, Univerzitet u Banja Luci, Tehnološki fakultet, Banja Luka, R.Srpska
 Prof. dr Borko Matijević, Univerzitet u Novom Sadu, PMF, Novi Sad, Srbija
 Prof. dr Ljiljana Rašković, Univerzitet u Nišu, Tehnološki fakultet, Leskovac, Srbija
 Prof. dr Milan Jaić, Univerzitet u Beogradu, Šumarski fakultet, Beograd, Srbija
 Prof. dr Milanka Điporović, Univerzitet u Beogradu, Šumarski fakultet, Beograd, Srbija
 Prof. dr Branislav Grgur, Univerzitet u Beogradu, TMF, Beograd, Srbija
 Prof. dr Milica Radovanović, Univerzitet u Beogradu, Tehnološko metalurški fakultet, Beograd, Srbija
 Prof.dr Milan Sak Bosner, Univerzitet u Zagrebu, Tehnološki fakultet, Osjek, Hrvatska
 Prof.dr Ivana Grmuša, Univerzitet u Beogradu, Šumarski fakultet, Beograd, Srbija
 Prof.Dr.habil. Marian Jaskula, Full Professor - Jagiellonian University, Cracow, Poland
 D-r enj. Bogomil Velikov Kolev, Institute of technical scientific Sofia, Bulgaria
 Prof. dr Radu Claudiu Fierascu, ICECHIM, Bucharest, Romania
 Prof. dr Dumitru Tsiulyanu, Technical University, Chisinau, Moldava
 Prof. dr Jadranka Malina, Univerzitet u Zagrebu, Metalurški fakultet, Sisak, Hrvatska
 Prof. dr Štefan Nižnik, Technical University of Košice, Faculty of Metallurgy, Košice, Slovakia
 Prof. dr Kiril Lisichkov, Univerzitet "Kirilo i Metodije", TMF, Skopje, R. Makedonia
 Prof. dr Vineta Srebrekoska, Goce Delčev University, Faculty of Technology, Štip, R. Makedonia
 Prof. dr Emilija Fidancevska, Univerzitet "Kirilo i Metodije", TMF, Skopje, R. Makedonia
 Prof. dr Vesna Dimova, Univerzitet "Kirilo i Metodije", TMF, Skopje, R. Makedonia
 Prof. dr Romulus Dima, Politehnica University of Bucharest, Romania
 Dr Biljana Bobić, naučni savetnik, IHTM, Beograd, Srbija
 Dr Bore Jegdić, Univerzitet u Beogradu, IHTM, Beograd, Srbija
 Prof.dr Irena , Bulgarian Academy of Sciences, Sofia, Bulgaria
 Prof. dr Abd El-Aziz S. Fouda, El-Mansoura University, Faculty of Science, El-Mansoura, Egypt
 Prof. dr Ayman. Y. El-Khateeb, Mansoura University, Faculty of Agriculture, Mansoura, Egypt
 Prof.dr Hesham H. El-Zhery, Umm Al-Qura University, Health Science College at Al Leith, KSA, Egypt
 Prof.dr Mohamed Fakih, Health Science College at Al Leith, KSA, Egypt
 Prof.dr Samar A. Abd El-Maksoud, Port Said University, Faculty of Science, Port Said, Egypt
 Prof. dr Samar A. Abd El-Salam, Port Said University, Faculty of Science, Port Said, Egypt
 Prof.dr H.M.Mostafa, Port Said University, Faculty of Science, Port Said, Egypt
 Prof.dr Nabila M.Elbahrawi, Mansoura University, Faculty of Agriculture, Mansoura, Egypt
 Prof.dr Ayman Y. El-Khateeb, Mansoura University, Faculty of Science, Mansoura, Egypt
 Dr.sc.Antonija Višekruna, University of Split, Faculty of Electrical Engineering, Mechanical Engineering and Naval Architecture, Split, Croatia,
 Prof.dr Jagoda Radošević, University of Split, Faculty of Electrical Engineering, Mechanical Engineering and Naval Architecture, Split, Croatia
 Dr Petar Ljumović, University of Split, Faculty of Electrical Engineering, Mechanical Engineering and Naval Architecture, Split, Croatia
 Dr Srdjan Matijašević, viši naučni saradnik, ITNMS, Beograd, Srbija
 Dr Branislav Marković, naučni saradnik, ITNMS, Beograd, Srbija
 Dr Nebojša Labus, naučni saradnik, Institute of Technical Sciences of the SASA, Belgrade, Serbia
 Prof.dr Szilvia Ormándi, Dept. of Mineralogy, Eötvös Loránd University, Budapest, Hungary
 Prof. dr István Dódon, Dept. of Mineralogy, Eötvös Loránd University, Budapest, Hungary
 Prof. dr Munhjargal Dashnyam, Defenve university of Mongolia, Department of Mathematics and Computer Technology, Ulan Bator, Mongolia
 Dr Oyuntsetseg Janchiv, Institute of Chemistry and Chemical technology, of Mongolian Academy of Sciences, Ulan Bator, Mongolia
 Dr Ulambayar Renchinhand, Institute of Chemistry and Chemical technology, of Mongolian Academy of Sciences, Ulan Bator, Mongolia

Dr Ganbaatar Jamsranjav, Institute of Chemistry and Chemical technology, of Mongolian Academy of Sciences, Ulan Bator, Mongolia

Prof. dr Ljubica Vasiljević, Univerzitet Istočno Sarjevo, Tehnološki fakultet, Zvornik, Republika Srpska

Prof.dr Branislav Škundrić, Akademija nauka i umjetnosti R. Srpske, Banja Luka, Republika Srpska

Prof.dr Dragan Tošković, Univerzitet Istočno Sarjevo, Tehnološki fakultet, Zvornik, Republika Srpska

Prof. dr Dušan Stanojević, Univerzitet Istočno Sarjevo, Tehnološki fakultet, Zvornik, Republika Srpska

Prof.dr Vesna Grekulović, Univerzitet u Beogradu, Tehnički fakultet u Boru, Bor, Srbija

Prof.dr Mirjana Rajčić-Vujasinović, Univerzitet u Beogradu, Tehnički fakultet u Boru, Bor, Srbija

Prof.dr Zoran Stević, Univerzitet u Beogradu, Tehnički fakultet u Boru, Bor, Srbija

Prof.dr F.M. Mulimbayan, Department of Mining, Metallurgical and Materials Engineering, University of the Philippines, Diliman, Quezon City, Philippines

Prof.dr E.M. Olegario-Sanchez, Department of Mining, Metallurgical and Materials Engineering, University of the Philippines, Diliman, Quezon City, Philippines

Prof.dr A.A. Parreño, Department of Mining, Metallurgical and Materials Engineering, University of the Philippines, Diliman, Quezon City, Philippines

Prof.dr R.M. Cervera, Department of Mining, Metallurgical and Materials Engineering, University of the Philippines, Diliman, Quezon City, Philippines

Prof.dr D.M. Aguila, Department of Mining, Metallurgical and Materials Engineering, University of the Philippines, Diliman, Quezon City, Philippines,

Prof.dr M.V. Ligaray, Department of Mining, Metallurgical and Materials Engineering, University of the Philippines, Diliman, Quezon City, Philippines

Prof.dr R.V. Mariano, University of the Philippines, Diliman, Quezon City, Philippines

Prof.dr H.D. Mendoza, University of the Philippines, Diliman, Quezon City, Philippines

Dr Valentina A. Nikashina, Vernadsky Institute of Geochemistry and Analytical Chemistry RAS, Moscow, Russia

Dr Inna B. Serova, Vernadsky Institute of Geochemistry and Analytical Chemistry RAS, Moscow, Russia

Dr Tatjana G. Kusmina, Vernadsky Institute of Geochemistry and Analytical Chemistry RAS, Moscow, Russia

Dr Irma A. Roschina, Vernadsky Institute of Geochemistry and Analytical Chemistry RAS, Moscow, Russia

Dr Irina N. Gromyak, Vernadsky Institute of Geochemistry and Analytical Chemistry RAS, Moscow, Russia

Dr Nadezhda Lihareva, Institute of Mineralogy and Crystallography, BAS,Sofia, Bulgaria

Dr Ognjan Petrov, Institute of Mineralogy and Crystallography, BAS,Sofia, Bulgaria

Prof.dr Vincenzo Leone, Department of Environmental, Biological and Pharmaceutical Science and Technologies, Second University of Naples, Caserta, Italy

Prof.dr Pasquale Iovino, Department of Environmental, Biological and Pharmaceutical Science and Technologies, Second University of Naples, Caserta, Italy

Prof.dr Elio Coppola, Department of Environmental, Biological and Pharmaceutical Science and Technologies, Second University of Naples, Caserta, Italy

Prof.dr Stefano Salvestrini, Department of Environmental, Biological and Pharmaceutical Science and Technologies, Second University of Naples, Caserta, Italy

Prof.dr Sante Capasso, Environmental Technologies University Spin-off, Second University of Naples, Caserta, Italy

Prof.dr Tore Krogstad, Norwegian University of Life Sciences, Faculty of Environmental Science and Technology, Norway

Prof.dr Nevenka Rajić, Univerzitet u Beogradu, TMF, Beograd, Srbija

Dr Milan Kragović, naučni saradnik, ITNMS, Beograd, Srbija

Dr Aleksandra Daković, naučni savetnik, ITNMS, Beograd, Srbija

Prof.dr Blagica Cekova, MIT University, Faculty of ecological resources menagment, Skopje, R.Macedonia

Prof.dr Filip Jovanovsk, University of Skopje, Faculty of Technology and Metallurgy, Skopje, R. Macedonia

Dr Jelena Pavlović, University of Belgrade, Innovation Centre of the Faculty of TMF, Belgrade, Serbia

Dr Jelena D. Rusmirović, University of Belgrade, Innovation Centre of the Faculty of TMF, Belgrade, Serbia

Prof.dr Milica Rančić, Univerzitet u Beogradu, Šumarski fakultet, Beograd, Srbija

Prof.dr Aleksandar D. Marinković, Univerzitet u Beogradu, TMF, Beograd, Srbija

Dr Branimir Jugović, Univerzitet u Beogradu, Tehnički institut SANU, Beograd, Srbija

Prof.dr Zorica Jugović, Univerzitet u Beogradu, TMF, Beograd, Srbija

Dr Karmina Miteva, University of Skopje, Faculty of Technology and Metallurgy, Skopje,R. Macedonia

Prof.dr Slavčo Aleksovski, University of Skopje, Faculty of Technology and Metallurgy, Skopje, R. Macedonia

Prof.dr Gordana Bogoeva-Gaceva, University of Skopje, Faculty of Technology and Metallurgy, Skopje,R.Macedonia

Prof.dr Ivan Juranić, University of Belgrade, Faculty of Chemistry and Center for Chemistry IChTM, Belgrade, Serbia

Prof.dr Slađana Č. Alagić, Univerzitet u Beogradu, Tehnički fakultet u Boru, Bor, Srbija

Prof.dr Dragana V. Medić, Univerzitet u Beogradu, Tehnički fakultet u Boru, Bor, Srbija

Prof.dr Mile D. Dimitrijević, Univerzitet u Beogradu, Tehnički fakultet u Boru, Bor, Srbija

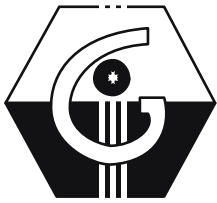
Prof.dr Snežana B. Tošić, Univerzitet u Nišu, Fakultet za nauku i matematiku, Niš, Srbija
 Dr Ljiljana Avramović, naučni savetnik, Institut za metalurgiju i rudarstvo, Bor, Srbija
 Dr Zoran Stevanović, naučni savetnik, Institut za metalurgiju i rudarstvo, Bor, Srbija
 Dr Mile Bugarin, naučni savetnik, Institut za metalurgiju i rudarstvo, Bor, Srbija
 Dr Radojka Jonović, naučni savetnik, Institut za metalurgiju i rudarstvo, Bor, Srbija
 Dr Radmila Marković, naučni savetnik, Institut za metalurgiju i rudarstvo, Bor, Srbija
 Dr Vojka Gardić, naučni savetnik, Institut za metalurgiju i rudarstvo, Bor, Srbija
 Dr Marko Jonovic, Univerzitet u Beogradu, IHTM, Beograd, Srbija
 Prof.dr Blažo Lalević, Univerzitet u Beogradu, Poljoprivredni fakultet, Beograd, Srbija
 Prof.dr Vera Raičević, Univerzitet u Beogradu, Poljoprivredni fakultet, Beograd, Srbija
 Prof.dr Aleksandar Đorđević, Univerzitet u Beogradu, Poljoprivredni fakultet, Beograd, Srbija
 Docent dr Aleksandar Kostić, Univerzitet u Beogradu, Poljoprivredni fakultet, Beograd, Srbija
 Prof.dr Dragan Kiković, Univerzitet u Prištini, Prirodno-matematički fakultet, Kosovska Mitrovica, Srbija
 Prof.dr Dragana Kukić, Univerzitet u Novom Sadu, Tehnološki fakultet, Novi Sad, Srbija
 Prof.dr Marina Šćiban, Univerzitet u Novom Sadu, Tehnološki fakultet, Novi Sad, Srbija
 Prof.dr Jelena Pejjin, Univerzitet u Novom Sadu, Tehnološki fakultet, Novi Sad, Srbija
 Dr Zorica Lopičić, naučni saradnik, ITNMS, Beograd, Srbija
 Dr Tatjana Šošćarić, naučni saradnik, ITNMS, Beograd, Srbija
 Dr Jelena Dragišić Maksimović, naučni savetnik, Univerzitet u Beogradu, IMSI, Beograd, Srbija
 Prof.dr Miloš Mojović, Univerzitet u Beogradu, Fakultet za fizičku hemiju, Beograd, Srbija
 Dr Vuk Maksimović, naučni savetnik, Univerzitet u Beogradu, IMSI, Beograd, Srbija
 Prof.dr Djurdja Kerkez, Univerzitet u Novom Sadu, PMF, Novi Sad, Srbija
 Prof.dr Milena Bečelić-Tomin, Univerzitet u Novom Sadu, PMF, Novi Sad, Srbija
 Prof.dr Božo Dalmacija, Univerzitet u Novom Sadu, PMF, Novi Sad, Srbija
 Prof.dr Dragana Tomašević Pilipović, Univerzitet u Novom Sadu, PMF, Novi Sad, Srbija
 Prof.dr Miljana Prica, Univerzitet u Novom Sadu, fakultet tehničkih nauka, Novi Sad, Srbija
 Prof.dr Marko Milojković, Univerzitet u Beogradu, Fakultet za biologiju, Beograd, Srbija
 Dr Bogdan Nikolić, naučni savetnik, Institut za zaštitu bilja i životnu sredinu, Beograd, Srbija
 Prof.dr Miloš Marinković, Univerzitet u Nišu, PMF, Niš, Srbija
 Dr Panić Ivan, naučni saradnik, Institut Jaroslav Černi, Beograd, Srbija
 Dr Martina Ormai, Univerzitet u Novom Sadu, Poljoprivredni fakultet, Novi Sad, Srbija
 Prof.dr Vera Pavlović, Univerzitet u Beogradu, Mašinski fakultet, Beograd, Srbija
 Dr Ranko Grujić, Univerzitet Istočno Sarajevo, TF Zvornik, Republika Srpska
 Prof.dr Vlada Veljković, Univerzitet u Nišu, Tehnološki fakultet, Leskovac, Srbija
 Prof.dr Goran Ilić, Univerzitet u Nišu, Tehnološki fakultet, Leskovac, Srbija
 Prof.dr Suzana Cakić, Univerzitet u Nišu, Tehnološki fakultet, Leskovac, Srbija
 Prof.dr Slavka Stanković, Univerzitet u Beogradu, TMF, Beograd, Srbija
 Dr Tamara Jakovljević, naučni savetnik, Hrvatski institut za istraživanje prirode, Jastrebarsko, Hrvatska
 Prof.dr Ivana Radojčić Redovniković, Univerzitet u Zagrebu, Fakultet za prehrambenu tehnologiju, Zagreb, Hrvatska
 Prof.dr Vjekoslav Sajfert, Univerzitet u Novom Sadu, Tehnički fakultet u Zrenjaninu, Zrenjanin, Srbija
 Prof.dr Dragan Rakovic, Univerzitet u Beogradu, Elektrotehnički fakultet, Beograd, Srbija
 Prof.dr Goran Jankes, Univerzitet u Beogradu, Mašinski fakultet, Beograd, Srbija
 Akademik Vlatko Doleček, Akademija nauka i umjetnosti Bosne i Hercegovine, Sarajevo, BiH
 Prof.dr Slaviša Putić, Univerzitet u Beogradu, TMF, Beograd, Srbija
 Prof.dr Aleksandar Marinković, Univerzitet u Beogradu, TMF, Beograd, Srbija
 Docent dr Milica Rančić, Univerzitet u Beogradu, Šumarski fakultet, Beograd, Srbija
 Docent dr Tanja Pralija, Univerzitet u Beogradu, Šumarski fakultet, Beograd, Srbija
 Prof.dr Željko Kamberović, Univerzitet u Beogradu, TMF, Beograd, Srbija
 Prof.dr Enes Dzunuzovic, Univerzitet u Beogradu, TMF, Beograd, Srbija
 Prof.dr Gordana Kokeza, Univerzitet u Beogradu, TMF, Beograd, Srbija
 Prof.dr Pero Dugić, Univerzitet u Banja Luci, Tehnološki fakultet, Banja Luka, R.Srpska
 Docent dr Ivan Ristić, Univerzitet u Novom Sadu, Tehnološki fakultet, Novi Sad, Srbija
 Prof.dr Miroslav Spasojević, Univerzitet u Kragujevcu, Agronomski fakultet, Čačak, Srbija
 Prof.dr Lenka Grbić, Univerzitet u Kragujevcu, Agronomski fakultet, Čačak, Srbija
 Dr Dragoslav Bekrić, naučni saradnik, Univerzitet u Beogradu, Mašinski fakultet, Beograd, Srbija
 Prof.dr Jovan Šetrajčić, Univerzitet u Novom Sadu, Prirodno-matematički fakultet, Novi Sad, Srbija
 Prof. dr Gordana Topličić Čurčić, Univerzitet u Nišu, Građevinsko-arhitektonski fakultet, Niš, Srbija,
 Dr Nebojša Marinković, Synchrotron Catalysis Consortium and Columbia University, New York, NY, USA

Prof.dr Kotaro Sasaki, Brookhaven National Laboratory, Upton, NY, USA
 Prof.dr Dragana Grujić, Univerzitet u Banjoj Luci, Tehnološki fakultet, Banja Luka, BiH
 Prof.dr Mirjana Kostić, Univerzitet u Beogradu, Tehnološko-metalurški fakultet, Beograd, Srbija
 Doc.dr Branko Neral, Univerza v Mariboru, Fakulteta za strojništvo, Maribor, Slovenija
 Prof. dr Tatjana Kaluđerović-Radoičić, Univerzitet u Beogradu, Tehnološko-metalurški fakultet, Beograd, Srbija
 Prof. dr Branko Bugarski, Univerzitet u Beogradu, Tehnološko-metalurški fakultet, Beograd, Srbija
 Prof. dr Aleksandar Sedmak, Univerzitet u Beogradu, Mašinski fakultet, Beograd, Srbija
 Dr Vencislav Grabulov, naučni savetnik, Institut za ispitivanje materijala Srbije, Beograd, Srbija
 Prof.dr Milovan Vukovic, Univerzitet u Beogradu, Tehnicki fakultet u Boru, Bor, Srbija
 Prof.dr Ljiljana Takic, Univerzitet u Niš, Tehnoloski fakultet u Leskovcu, Niš, Srbija
 Docent dr Ivan Ristić, University of Novi Sad, Faculty of Technology Novi Sad, Novi Sad, Srbija
 Prof.dr Sanja Podunavac-Kuzmanović, University of Novi Sad, Faculty of Technology Novi Sad, Novi Sad, Srbija
 Prof.dr Lidija Jevrić, University of Novi Sad, Faculty of Technology Novi Sad, Novi Sad, Srbija
 Prof.dr Slavko Djuric, Univerzitet u Novom Sadu, Fakultet inženjerskih nauka, Novi Sad, Srbija
 Prof. dr Aleksandar Jovović, Univerzitet u Beogradu, Mašinski fakultet, Univerzitet u Beogradu, Beograd, Srbija
 Prof.dr Despo Fatta-Kassinis, Nireas-IWRC, University of Cyprus, Nicosia, Cyprus
 Prof.dr C.S.Poon, Polytechnic University, Department of Civil and Structural Engineering, The Hong Kong, Hong Kong
 Prof.dr Jagos Radovic, University of Calgary, Department of Geoscience, Calgary, Canada
 Prof.dr, Milica Velimirovic, University of Vienna, Department of Environmental Geosciences, Vienna, Austria
 Prof.dr Mukesh Kumar Sinha, Defence Materials & Stores Research, Kanpur, Uttar Pradesh, India
 Prof.dr Marta Trninic, Univerzitet u Beogradu, Mašinski fakultet, Univerzitet u Beogradu, Beograd, Srbija
 Prof.dr Ivani Banković-Ilić, Univerzitet u Nišu, Tehnološki fakultet u Leskovcu, Leskovac, Srbija
 Prof.dr Dragan Đorđević, Univerzitet u Nišu, Tehnološki fakultet u Leskovcu, Leskovac, Srbija
 Prof.dr Slađana Alagić, Univerzitet u Beogradu, Tehnički fakultet u Boru, Bor, Srbija
 Prof.dr Aleksandra Porjazoska Kujundziski, University of Skopje, Faculty of Engineering, Skopje, R. Macedonia
 Dr Sanja Petronic, University of Belgrade, Innovation Center, Faculty of Mechanical Engineering, Belgrade, Serbia
 Dr Jana Štrbački, naučni saradnik, Univerzitet u Beogradu, Rudarsko-geološki fakultet, Beograd, Srbija
 Prof.dr Sanja Mrazovac, Univerzitet Union „Nikola Tesla“, Beograd, Srbija
 Dr Milena Marinovic-Cincovic, naucni savetnik, Univerzitet u Beogradu, INN Vinca, Beograd, Srbija
 Prof. dr Goran Nikolic, Univerzitet u Nisu, Tehnološki fakultet u Leskovcu, Leskovac, Srbija
 Prof.dr Dragan Zunic, Karnegi Melon Univerzitet, Doha, Katar
 Prof.dr Milovan Vukovic, Univerzitet u Beogradu, Tehnicki fakultet u Boru, Bor, Srbija
 Dr Marija Babić, Univerzitet u Beogradu, Inovacioni centar TMF, Beograd, Srbija
 Prof.dr Dusan Cvetkovic, Univerzitet u Nisu, Gradjevinski fakultet, Nis, Srbija
 Prof. dr Grozdanka Bogdanović, Univerzitet u Beogradu, Tehnički fakultet u Boru, Bor, Srbija
 Prof. dr Aleksandra Zarubica, Univerzitet u Nišu, Prirodno-matematički fakultet, Nis, Srbija
 Prof.dr Dragan Povrenovic, Univerzitet u Beogradu, TMF, Beograd, Srbija
 Prof.dr Ivana Boskovic, Univerzitet Crne Gore, Metalursko-tehnoloski fakultet, Podgorica, Podgorica, Crna Gora
 Dr Vojislav Stanić, Univerzitet u Beogradu, Institut za nuklearne nauke Vinča, Beograd, Srbija
 Dr Marin Tadić, Univerzitet u Beogradu, Institut za nuklearne nauke Vinča, Beograd, Srbija
 Dr Jasmina Glamoclija, IBI "Siniša Stanković", Beograd, Srbija
 Prof.dr Shadi Darvish, Florida International University, Department of Materials Engineering, USA
 Prof.dr Iman Khakpour, Florida International University, Department of Materials Engineering, USA
 Docent dr Aleksandar Kostić, Univerzitet u Beogradu, Poljoprivredni fakultet, Beograd, Srbija
 Prof. dr Snežana Tošić, Univerzitet u Nišu, Prirodno-matematički fakultet, Nis, Srbija
 Dr Ana Kostov, Institut za rudarstvo i metalurgiju Bor, Bor, Srbija
 Dr Aleksandra Mitovski, Univerzitet u Beogradu, Tehnicki fakultet u Boru, Bor, Srbija
 Dr El-Sayed M. Sherif, Advanced Manufacturing Institute (AMI), King Saud University, Saudi Arabia
 Dr Michael E. G. Lyons, School of Chemistry, University of Dublin Trinity College, Ireland
 Prof. Dr Radmila Jančić-Heinemann, Univerzitet u Beogradu, TMF, Beograd, Srbija
 Dr Dejan Momčilović, Institut IMS, Beograd, Srbija
 Dr Sanja Stevanović, IHTM, Univerzitet u Beogradu, Beograd, Srbija
 Prof.dr Suzana Samaržija-Jovanović, Univerzitet u Pristini, Prirodno-matematički fakultet, Kosovska Mitrovica
 Prof. Zora Pilić, University of Mostar, Faculty of Science and Education, Mostar, Bosnia and Herzegovina
 Prof. A. Y. El-Etre, Benha University, Faculty of Science, Department of Chemistry, Benha, Egypt
 Prof. Femiana Gapsari, Brawijaya University, Faculty of Engineering, Mechanical Engineering Department, Malang, Indonesia
 Dr Amin Rabiei, Islamic Azad University, Najafabad, Iran

Prof.dr Farid I. El-Dossoki, Port-Said University, Chemistry Department, Faculty of Science, Port-Said, Egypt
 Prof.dr Alaa El-Hussein, Mansoura University, Chemistry Department, Faculty of Science, Mansoura, Egypt
 Prof.dr Hamd Abu El-Nadr, Mansoura University, Chemistry Department, Faculty of Science, Mansoura, Egypt
 Dr Nataša V. Valentić, University of Belgrade, Faculty of Technology and Metallurgy, Belgrade, Serbia
 Dr Jelena M. Lađarević, University of Belgrade, Faculty of Technology and Metallurgy, Belgrade, Serbia
 Doc.Bojan Đ. Božić, University of Belgrade, Faculty of Biology, Belgrade, Serbia
 Prof.dr Dušan Ž. Mijin, University of Belgrade, Faculty of Technology and Metallurgy, Belgrade, Serbia
 Prof.dr Gordana S. Uščumlić, University of Belgrade, Faculty of Technology and Metallurgy, Belgrade, Serbia
 Dr Darko Manjenčić, Univerzitet u Novom Sadu, Tehnološki fakultet, Novi Sad, Srbija
 Dr Marina Kolundžić, University of Belgrade, Faculty of Pharmacy, Department of Pharmacognosy, Belgrade, Serbia
 Dr Jelena Radović, University of Belgrade, Faculty of Pharmacy, Department of Pharmacognosy, Belgrade, Serbia
 Dr Ana Tačić, University of Niš, Faculty of Technology, Leskovac, Serbia
 Dr Vesna Nikolić, University of Niš, Faculty of Technology, Leskovac, Serbia
 Prof.dr Tatjana Kundaković, University of Belgrade, Faculty of Pharmacy, Belgrade, Serbia
 Prof.dr Milena Bečelić-Tomin, Univerzitet u Novom Sadu, Prirodno-matematički fakultet, Novi Sad, Srbija
 Prof.dr Nataša Slijepčević, Univerzitet u Novom Sadu, Prirodno-matematički fakultet, Novi Sad, Srbija
 Prof.dr Ratko Ivković, Univerzitet u Prištini, Fakultet tehničkih nauka, Kosovska Mitrovica, Srbija
 Prof.dr Lazar Kopanja, Alfa BK Univerzitet, Fakultet informacionih tehnologija, Beograd, Srbija
 Prof.dr Mirjana Kostić, University of Belgrade, Faculty of Technology and Metallurgy, Belgrade, Serbia
 Prof.dr Marija Vukčević, University of Belgrade, Faculty of Technology and Metallurgy, Belgrade, Serbia
 Dr Sahar Zolfaghari, Islamic Azad University, Najafabad, Iran
 Dr Ali Ashrafi, Isfahan University of Technology, Department of Materials Engineering, Isfahan, Iran
 Dr Ahmad Saatchi, Department of Materials Science and Engineering, University of Wisconsin-Madison, USA
 Dr Leposava Filipović-Petrović, Visoka medicinska i poslovno-tehnološka škola strukovnih studija, Šabac, Srbija
 Dr Mirjana Antonijević-Nikolić, Visoka medicinska i poslovno-tehnološka škola strukovnih studija, Šabac, Srbija
 Dr Ljubica Mijić, Visoka medicinska i poslovno-tehnološka škola strukovnih studija, Šabac, Srbija
 Dr Slađana B. Tanasković, University of Belgrade, Faculty of Pharmacy, Belgrade, Serbia
 Prof.dr Branka Dražić, University of Belgrade, Faculty of Pharmacy, Belgrade, Serbia
 Dr Aleksandra S. Patarić, ITNMS, Beograd, Srbija
 Dr Mihailo Mrdak, Istraživački i razvojni Centar, IMTEL komunikacije a.d., Beograd, Srbija
 Dr Suzana R. Polić, Central institute for conservation, Belgrade, Serbia
 Dr Danijela N. Jovanović, Central institute for conservation, Belgrade, Serbia
 Docent dr Dalibor Petkovic, University of Nis, Faculty of Mechanical Engineering, Nis, Serbia
 Prof.dr Larisa Jovanovic, University of Educon, Sremska Kamenica, Serbia
 Prof.dr Vesna Stankov-Jovanovic, PMF, Univerzitet u Niu, Nis, Srbija
 Prof.dr Aleksandar Jokić, Faculty of Technology, University of Novi Sad, Novi Sad, Serbia
 Prof.dr Leonardo S.G.Teixeira, Instituto de Química-Universidade Federal da Bahia, Salvador, Bahia
 Prof.dr M.P. Dorado, Department of Physical Chemistry and Applied Thermodynamics, EPS, Edificio Leonardo da Vinci, Universidad de Córdoba, Campus de Excelencia Internacional Agroalimentario, Córdoba, Spain
 Prof.dr K.Noipin, School of Environment, Resources and Development, Asian Institute of Technology, Klong Luang, Thailand
 Prof. dr sc. med. dr Srđan Lazić, Institut za epidemiologiju VMA, Beograd, Srbija
 Prof.dr Marie-Josée Dumont, Bioresource Engineering Department, McGill University, Ste-Anne-de-Bellevue, Canada
 Prof.dr B. Ghobadian, Biosystems Engineering Department, Tarbiat Modares University, Tehran, Iran
 Dr Nina Obradović, Institut tehničkih nauka, Srpska akademija nauka i umetnosti, Beograd, Srbija
 Dr Katarina Čolić, Inovacioni centar, Univerzitet u Beogradu, Mašinski fakultet, Beograd, Srbija
 Dr Đorđe Veljović, Univerzitet u Beogradu, Tehnološko metalurški fakultet, Beograd, Srbija
 Dr Milan Milivojevic, Inovacioni centar, Univerzitet u Beogradu, Tehnološko metalurški fakultet, Beograd, Srbija
 Prof. dr Mlađan Popović, Univerzitet u Beogradu, Šumarski fakultet, Beograd, Srbija,
 Prof.dr Stevo Jacimovski, Univerzitet u Beogradu, Fakultet policijske akademije, Beograd, Srbija
 Dr Maja Kokunešoski, Univerzitet u Beogradu, Institut za nuklearne nauke „Vinča“, Beograd, Srbija
 Prof.dr Ivica Dimkic, Univerzitet u Beogradu, Bioloski fakultet, Beograd, Srbija
 Prof.dr Vedrana Komlen, Agromediterranski fakultet Mostar, Mostar, R BiH
 Prof.dr Snežana Urošević, Univerzitet u Beogradu, Tehnički fakultet u Boru, Bor, Srbija
 Prof. dr Violeta Mitić, Univerzitet u Nišu, Prirodno-matematički fakultet, Niš, Srbija
 Prof. dr Oskar Bera, Univerzitet u Novom Sadu, Tehnološki fakultet, Novi Sad, Srbija
 Prof. dr Milena Miljković, Univerzitet u Nišu, Prirodno-matematički fakultet, Hemija, Niš, Srbija,
 Prof. dr. sc. Zora Pilić, University of Mostar, Faculty of Science and Education, Mostar, BiH,

Doc. dr. sc. Sunčana Smokvina Hanza, Sveučilište u Rijeci, Tehnički fakultet, Rijeka, R.Hrvatska
 Prof. dr. sc. Veselinka Grudić, Univerzitet Crne Gore, Metalurško-tehnološki fakultet, Podgorica, Crna Gora
 Prof. dr.B.Muralidaran, Birla Institute of Technology Pilani, Sauthi Arabia
 Prof.dr Jelena Lađarević, Univerzitet u Beogradu, Tehnološko metalurški fakultet, Beograd, Srbija
 Prof.dr Ivana Savić Gajić, Univerzitet u Nišu, Tehnološki fakultet Leskovac, Leskovac, Srbija
 Prof. dr A.Subramania, Pondicherry University, India
 Prof.dr Jasmina Nikolić, Univerzitet u Beogradu, Tehnološko metalurški fakultet, Beograd, Srbija
 Prof.dr John Amalraj, Periyar EVR Govt Arts College, Trichy, India
 Prof.dr Peter Pascal Regis, St Joseph' College, Trichy, India
 Prof. dr Maja Radetić, Tehnološko metalurški fakultet, Univerzitet, Beograd, Srbija,
 Dr Biljana Popović, Visoka tekstilna strukovna škola za dizajn, tehnologiju i menadžment, Beograd, Srbija,
 Dr Stanko Ostojić, Univerzitet u Beogradu, Tehnološko metalurški fakultet, Beograd, Srbija,
 Dr Zoran Janjušević, ITNMS, Beograd, Srbija,
 Prof. dr sc.med.dr Srđan Lazić, Institut za epidemiologiju VMA, Beograd, Srbija
 Prof.dr Sanjin Gutić, Univerzitet u Sarajevu, Prirodno-matematički fakultet, Sarajevo, R.BiH
 Prof.dr Snezana Tosic, PMF, departman za hemiju, Univerzitet u Nisu, Nis, Srbija
 Dr. Ivana Perović, Institut za nuklearne nauke Vinča, Univerzitet u Beogradu, Beograd, Srbija
 Dr. Jelena Lović, IHTM - Centar za elektrohemiju, Univerzitet u Beogradu, Beograd, Srbija
 Dr A. S. Aisha, Federal University, Lokoja, Nigeria
 Prof.dr Victor Jamila Salihu Ahuiza, Tafawa Balewa University, Bauchi, Nigeria
 Dr. Malik Abdulwahab, Ahmadu Bello University, Nigeria
 Dr Milena Rašeta, naučni saradnik, PMF, Univerzitet u Novom Sadu, Novi Sad, Srbija,
 Dr Aleksandra Božić, naučni saradnik, IC, TMF Beograd, Univerzitet u Beogradu, Beograd, Srbija
 Prof.dr Goradana Drazic, Univerzitet Singidunum, Beograd, Srbija
 Prof.dr Sergej Medvedev, Univerzitet u Ljubljani, Ljubljana, Slovenija
 Prof.dr Aleksandar Dasic, Univerzitet u Istocnom Sarajevu, Tehnoloski fakultet, Zvornik, R.BiH
 Prof.dr Boris Agarski, Fakultet tehnickih nauka, Univerzitet u Novom Sadu, Novi Sad, Srbija
 Dr Memon Hafeezullah, College of Textile Science and Engineering, Zhejiang Sci-Tech University, Hangzhou, China
 Prof. dr Predrag Zivkovic, TMF, University of Belgrade, Belgrade, Serbia
 Prof. dr Svetlana Janjic, Faculty of Technology, University of Banjaluka, Banjaluka, BiH,
 prof.dr *Branka Dražić*, Faculty of Pharmacy, University of Belgrade, Belgrade, Serbia,
 prof.dr Mirjana Antonijević-Nikolić, Academy of applied studies Šabac, Sabac, Serbia
 Dr Vojislav Stanić, Vinca Institute of Nuclear Sciences, Belgrade, Serbia
 Prof. dr Vukosava Živković-Radovanović, Faculty of Chemistry, University of Belgrade, Belgrade, Serbia
 Prof. dr Djordje Djatkov, Faculty of Technical Sciences, University of Novi Sad, Novi Sad, Serbia
 Dr Zorica R. Lopičić, Institute for Technology of Nuclear and Other Mineral Raw Materials, Belgrade, Serbia
 Prof. dr Maja Trumić, Univerzitet u Beogradu, Tehnički fakultet Bor, Bor, Srbija
 Dr. Bojana Danilovic, Univerzitet u Nišu, Tehnološki fakultet Leskovac, Leskovac, Srbija
 Dr Sanja Martinovic, TMF, Univerzitet u Beogradu, Beograd, Srbija
 Prof. dr Natalia Lesnych, Fakulttt fur Ingenieurwissenschaften, Hochschule Wismar, Germany,
 Prof. dr Leonid Dvorkin, Рівне, Україна,
 Prof. dr Elena Yatsenko, Platov South Russian State Polytechnic University (NPI), Новочеркасск, Россия
 Prof. dr Vitaliy Petrovskyy, Київ, Україна
 Dr. Abdulhameed Al-Hashem, Kuwait Institute for Scientific Research (KISR), Kuwait
 Prof. dr Rajendran Maria Joany, Sathyabama Deemed University, Chennai,Tamilnadu, India
 Prof.dr S. Senthil Kumaran, Vellore Institute of Technology (VIT), Tamilnadu, India
 Prof.dr Jamal Khatib, Beirut Arab University, Beirut, Jordan
 Prof. dr Mohammed Sonebi, Queen's University of Belfast, United Kingdom
 Prof.dr Lev Chernyak, National Technical University of Ukraine, Kyiv, Ukraine
 Prof.dr Nataša Đurišić-Mladenović, Univerzitet u Novom Sadu, Tehnoloski fakultet, Novi Sad, Srbija
 Prof.dr Mirjana Kostić, Univerzitet u Beogradu, Tehnološko metalurški fakultet, Beograd, Srbija
 Prof. dr S Santhana Prabha, PSNA College of Engineering and Technology, Dindigul, Tamilnadu, India
 Prof.dr Piyush Kumar, Madan Mohan Malaviya University of Technology, Gorakhpur, India
 Prof.dr Sivaganesh Selvaraj, The Hong Kong Polytechnic University, Hong Kong
 Prof.dr R. Vijayalakshmi, Nandha Engineering College, Erode, Tamilnadu, India
 Dr. Srdjan Perisic, IHTM, Belgrade, Serbia
 Dr Dragutin Nedeljkovic, IHTM, Belgrade, Serbia
 Dr Aleksandar Grujic, IHTM, Belgrade, Serbi

Dr Srdjan Perisic, IHTM, Belgrade, Serbia
 Prof. dr Vera Obradovic, TMF, University of Belgrade, Belgrade, Serbia
 Prof. dr R Joseph Rathish, PSNA College of Engineering and Technology, Dindigul, Tamilnadu, India
 Prof. dr K Kavipriya, PSNA College of Engineering and Technology, Dindigul, Tamilnadu, India
 Prof. dr Gurmeet Singh, Pondicherry University, Puducherry, India
 Prof.dr T Shanthi, ARASU COLLEGE OF ARTS & SCIENCE FOR WOMEN, Karur, Tamilnadu, India
 Prof.dr Safija Herenda, PMF, Univerzitet u Sarajevu, Sarajevo, R.BiH
 Prof.dr Sanjin Gutic, PMF, Univerzitet u Sarajevu, Sarajevo, R.BiH
 Dr Dimitrije Petrović, National Institute of the Republic of Serbia, University of Belgrade, Serbia
 Prof.dr Marjan Ranđelović, Prirodno-matematički fakultet Niš, Univerzitet u Nišu, Niš, Srbija
 Prof.dr Tijana Djuricic, TF, Univerzitet u Banja Luci, R.BiH
 Dr Sasa Papuga, Masinski fakultet, Univerzitet u Banja Luci, R.BiH
 Prof.dr Heba Adnan Ahmed, Sulaimani Polytechnic University, Sulaymaniyah, KRI,Iraq
 Dr Sarvat Gull, National Institute of Technology, Hazaratbal, Srinagar, India
 Prof.dr A Krishnaveni, PG Department of Chemistry, Yadava College, Maduai, India
 Prof.dr Roman Tselms, State University of Aerospace Instrumentation, Russia
 Prof.dr Mikhail Egorov, State University of Aerospace Instrumentation, Russia
 Prof.dr Ekaterina Tsobkallo, State University of Industrial Technologies and Desig, Saint Petersburg, Russia
 Prof.dr R.Y. Hiranmai, School of Environment and Sustainable Development, Central University of Gujarat, Gandhinagar, India
 Prof.dr Jelena Vukmirović, University of Novi Sad, Faculty of Technology, Novi Sad, Serbia
 dr Jelena Petrović, Institut ITNMS, Beograd, Srbija
 dr Jelena Nikolić, Institut ITNMS, Beograd, Srbija
 Prof.dr Pramod K Singh, Sharda University, India
 Prof.dr Bhaskar Bhattacharya, Banarus Hindu University, India
 Prof.dr Snezana Grujic, TMF, University of Belgrade, Belgrade, Serbia
 Dr Sasa Miletic, Institut IMS, Belgrade, Serbia
 Prof. dr Marija Petrović Mihajlović, TMF, University of Belgrade, Belgrade, Serbia
 Prof. dr Marjan Ranđelović PMF, Univerzitet u Nisu, Nis, Srbija
 Prof.dr Sanja Panić, University of Novi Sad, Faculty of Technology, Novi Sad, Novi Sad, Serbia
 Prof.dr Jelena Pavličević, University of Novi Sad, Faculty of Technology, Novi Sad, Novi Sad, Serbia
 Dr Mirjana Petronijević, University of Novi Sad, Faculty of Technology, Novi Sad, Novi Sad, Serbia
 Docent Olga Govedarica, University of Novi Sad, Faculty of Technology, Novi Sad, Novi Sad, Serbia
 Prof. dr Ali I. Al-Mosawi, University of Baghdad, Baghdad, Iraq
 Prof.dr Kadhim F. Al-Sultani, University of Babylon, Babylon, Iraq
 Dr. Vesna Teofilovic, University of Novi Sad, Faculty of Technology, Novi Sad, Novi Sad, Serbia
 Prof.dr Shaymaa Abbas, Department of Materials Engineering, Faculty of Engineering, University of Kufa, Iraq
 Prof.dr Sreekanth B Jonnalagadda, School of Chemistry & Physics, College of Agriculture, Engineering & Science, University of KwaZulu-Natal, Durban, South Africa
 Dr. Kryzhanovskiy Vitaliy, University of Stuttgart, Germany
 Prof.dr Sergii Tolmachov, Kharkiv National Automobile and Highway University, KharkOv, Ukraine
 Prof.dr Iakov Iskhakov, Department of Civil Engineering, Ariel University, Israel
 Mehdi Shahedi Asl, Department of Mechanical Engineering, University of Mohaghegh Ardabili, Ardabil, Iran
 Dr. Natalia Rey-Raap, CSIC-Instituto de Ciencia y Tecnología del Carbono, (INCAR) This link is disabled., Oviedo, Spain
 Dr. Yong-Kang Lv, Key Laboratory of Coal Science and Technology of Ministry of Education and Shanxi Province, Taiyuan University of Technology, Taiyuan 030024, Shanxi, China
 Prof.dr Tanja Palija, University of Belgrade, Faculty of Forestry, Belgrade, Serbia
 Dr. Rui-Peng Ren, Key Laboratory of Coal Science and Technology of Ministry of Education and Shanxi Province, Taiyuan University of Technology, Shanxi, China
 Dr. Belén Lobato, Instituto de Ciencia y Tecnología del Carbono, INCAR-CSIC, Oviedo, Spain
 Dr. Arzu Karayel, Hitit University, Faculty of Arts and Sciences, Corum, Turkey
 Prof. Dr. Noor Haida, School of Chemical Sciences, Universiti Sains Malaysia, Penang, Malaysia
 Prof.dr K. Kavitha, Department of chemistry, National college, Trichy, India
 Prof.dr Gurmeet Singh, Pondicherry University, Puducherry, India
 Prof.dr Enis Dzunuzovic, TMF, University of Belgrade, Belgrade, Serbia
 Prof.dr S,Santhana Praba, PSNA College of engineering and technology, Dindigul, India
 Prof.dr R. Joseph Rathish, PSNA College of engineering and technology, Dindigul, India



G A L F O S d.o.o.

Batajnički put 23, 11080 Zemun - Beograd, Srbija
tel: 011/2193-893, tel/fax: 011/3070-383
e-mail: galfos@galfos.co.rs



Proizvodni program Galfosa

Preparati za pripremu površine metala pre zaštite
Preparati za nanošenje hemijskih i galvanskih prevlaka
Preparati za naknadnu obradu metalnih prevlaka
Preparati za fosfatiranje
Preparati za održavanje saobraćajnih sredstava
Preparati razvijeni po zahtevu kupaca

Prisutni smo na tržištima Srbije, Crne Gore,
Bosne i Hercegovine i Makedonije

Galfos je sertifikovan prema standardima:

Menadžment kvaliteta **ISO 9001:2008** i
Menadžment zaštite životne sredine **ISO 14001:2005**

Drugi su potvrdili kvalitet našeg rada,
vreme je da nas i Vi posetite ili pozovite

Generalni sponzor
Međunarodne konferencije YUCORR



INSTITUT ZA PREVENTIVU

ZAŠTITU NA RADU, PROTIVPOŽARNU ZAŠTITU I RAZVOJ D.O.O.
21000 Novi Sad, Kraljevića Marka 11, Tel/Fax: 021/420-571, 420-572, 420-573

prevex@eunet.yu

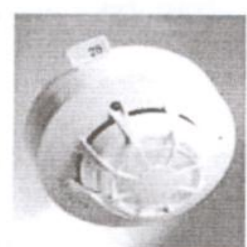
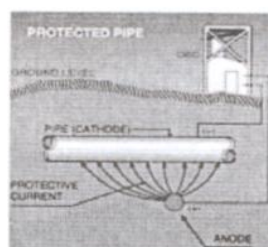
Institut za preventivu, zaštitu na radu, protivpožarnu zaštitu i razvoj – Novi Sad, osnovan je 1990. godine, pod nazivom "Centar za preventivu", sa ciljem da kao ovlašćena organizacija, u skladu sa zakonskim propisima, standardima i konvencijama, pruži stručnu pomoć u oblasti zaštite na radu, zaštite od požara i eksplozije, zaštite životne sredine i drugim delatnostima privrede.

Institut za preventivu, predstavlja savremeno preduzeće, koje je tako organizovano i tehnički opremljeno da može odgovoriti na brojne zahteve potencijalnih korisnika usluga. Naše preduzeće se bavi poslovima iz domena bezbednosti i zdravlja na radu, zaštite životne sredine, protivpožarne i protiveksplozivne zaštite. U dosadašnjem poslovanju, stekli smo preko 3000 poslovnih partnera.

Za obavljanje delatnosti Institut poseduje odgovarajuće licence, akreditacije i rešenja, dobijene od resornih ministarstava i Akreditacionog tela Srbije i Crne Gore.



BEZBEDNOST I ZDRAVLJE NA RADU
ZAŠTITA ŽIVOTNE SREDINE
ZAŠTITA OD POŽARA I EKSPLOZIJA
IZRADA PROJEKTNE DOKUMENTACIJE
I TEHNIČKI PRIJEM OBJEKATA
STRUČNE TRIBINE





Институт за водопривреду "Јарослав Черни" АД

Београд, Пиносава, ул. Јарослава Черног 80, Тел. 390 64 50, Факс 390 64 81

Водећа научноистраживачка организација у Србији у области вода.

Поред научноистраживачких активности, делатност Института обухвата планирање и пројектовање водних, енергетских и инфраструктурних објеката и система, надзор над извођењем хидротехничких објеката, консултантске услуге везане за управљање водним ресурсима и изграђеним објектима и системима, израду стратешких докумената и експертиза, као и помоћ приликом припреме законске регулативе, стандарда и методологија.

Институт за водопривреду "Јарослав Черни" је основан 1947. године, а име је добио по свом првом директору. Посебно треба истаћи да реноме Института превазилази локалне оквири, јер је његов значај признат не само у региону, већ и у Европи и свету. Захваљујући успешним активностима на просторима бивше Југославије и у преко 20 иностраних земаља, име Института "Јарослав Черни" је постало препознатљиво широм света.

Институт располаже са научним и стручним кадром, опремом и искуством да уз примену најновијих знања и технологија може успешно да решава и најсложеније задатке у домену вода и заштите животне средине. Институт има преко 240 запослених, од којих преко половине чине сарадници са високом стручном спремом, а значајан број има научна или истраживачка звања. Развој Института је подразумевао перманентно увођење савремених метода истраживања и пројектовања, уз коришћење нових технологија и софистициране мерне опреме.

Институт "Јарослав Черни" има и значајну образовну улогу у области водопривреде. Научни радници Института учествују у настави на факултетима универзитета у Београду, Новом Саду, Нишу и Бања Луци. Поред тога, у Институту је 10 година одржаван међународни курс из водопривредног инжењерства за стручњаке из земаља у развоју. Ову међународну активност су подржале владе Холандије и Југославије, као и УНЕСКО.

Високи реноме Института потврђују бројне и врло значајне референце: изграђени хидротехнички објекти у Србији, на простору бивше Југославије и свету, као и студије, планови, пројекти и водопривредне основе. У претходном периоду, Институт је учествовао у пројектовању и реализацији најзначајнијих водопривредних система и објеката у нашој земљи. У том оквиру, треба истаћи истраживања и студије за потребе пројектовања великих система - Хидроенергетског и пловидбеног система "Ђердап I" и "Ђердап II", Хидросистема Дунав-Тиса-Дунав, као и бројних хидроенергетских објеката. Поред тога, треба поменути студије и пројекте лука и пристаништа на обали Јадранског мора, на Дунаву и Сави.

Поред приказаних студија и пројеката на подручју бивше Југославије, треба истаћи да Институт има значајно међународно искуство у пројектима који су реализовани у земљама Африке, Средњег и Далеког Истока, Средње и Јужне Америке и Европе. Највеће учешће Института је било у Либији, Ираку, Ирану, Алжиру и Перуу.

У периоду од 2001 до 2010. године, Институт је учествовао у свим значајним активностима у области вода у Србији. Ове активности се могу сврстати у следеће основне категорије:

- **Припрема стратешких докумената из области вода:** Водопривредна основа Републике Србије, Студија одрживог развоја водопривреде Србије, Инструменти за развој сектора вода у Републици Србији, припрема новелација Водопривредне основе и друго;
- **Студијска припрема законодавних докумената:** Закон о водама Републике Србије, као и пратећа подзаконска акта;
- **Активно учешће у међународним активностима у области вода:** активности у оквиру Међународне комисије за заштиту реке Дунав (ICPDR), активности у оквиру Међународне комисије за слив реке Саве, студијске припреме предлога основа за преговоре и израду нацрта билатералних споразума са Мађарском, Румунијом, Бугарском, Хрватском, БиХ и Црном Гором и друго;
- **Израда комплексних студија и пројеката у свим областима сектора вода:** Студија Београдског изворишта подземних вода, Осматрања, мерења и анализе утицаја успора Дунава на приобаље изазваног радом ХЕ "Ђердап 1" и ХЕ "Ђердап 2", Студија о могућностима водоснабдевања Шумадије и Поморавља, Студија унапређења поузданости прогнозе и упозорења о наиласку великих вода, Истраживања за потребе развоја и унапређења заштитно-дренажних система, Главни пројекат бране и акумулације "Првонек", Хидроинформациони систем "Дрина", Генерални пројекти уређења ерозионих и бујичних подручја, Проучавање екстремних хидролошких ситуација - поплава и суша у Србији, Студија мера и радова за успостављање међународног пловног пута на реци Сави, Студија одбране од леда на Дунаву и друго.

PITURA

za nijańsu drugačija

Nudimo vam:

- › širok asortiman proizvoda
- › u željenim količinama
- › fleksibilnost i otvorenost za specifične zahteve
- › stručne savete
- › visok kvalitet
- › sigurnost da će vaši zahtevi biti ispoštovani



boje verne vašoj mašti

drvo

- poliuretanski dvokomponentni lak za parket
- poliuretanski emajli
- poliuretanski lakovi
- osnovna boja za drvo
- emajl lak
- lazurni premaz likol
- lak za čamce
- nitro bajc
- nitro lak
- nitro emajl

metal

- osnovna boja za metal
- termostabilna boja za metal
- antikorozione boje
- autoreparatur
- wash-primer

beton i fasade

- fasadon
- betonal
- signalin - boja za horizontalnu signalizaciju

poliuretanski i epoksidni premazi za zaštitu metala od korozije
epoksi samolivi podovi

PITURA fabrika boja i lakova

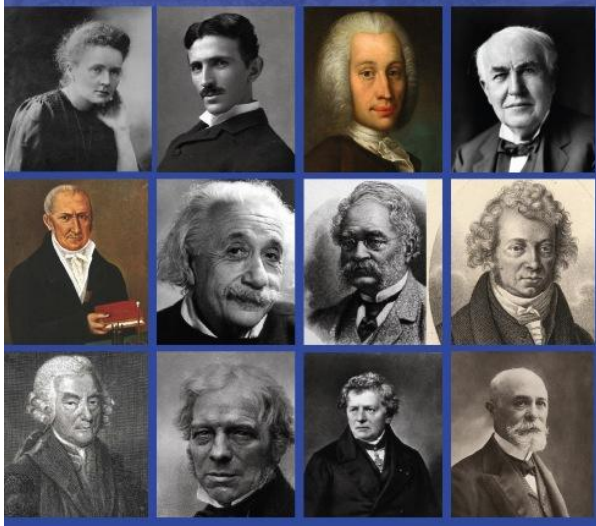
Batajnicki drum 10V, 11080 Zemun

tel./fax: (+381 11) 3755434, 3077840

e-mail: info@pitura.co.rs

Радмило М. ИВАНКОВИЋ
Бранислав А. БОШКОВИЋ

МЕРНЕ ЈЕДИНИЦЕ И СЛАВНИ ФИЗИЧАРИ



Inženjersko društvo za koroziju izdalo je monografiju **“Merne jedinice i slavni fizičari”**.

Monografija se sastoji iz dva dela:

- U prvom delu se iznose merne jedinice iz Međunarodnog sistema jedinica i objašnjava kako je razvoj nauke doprineo uvođenju merila i mernih jedinica radi poređenja rezultata eksperimenata i merenja;
- U drugom delu su predstavljeni svi fizičari čija imena nose pojedine merne jedinice, od Ampera do Siverta, uključujući i Nikolu Teslu. U biografijama svakog naučnika dati su osnovni biografski podaci i prikazi njihovih naučnih doprinosa. Pri tome je poseban naglasak stavljen na prikaze i rezultate njihovih istraživanja na osnovu kojih su odgovarajuće merne jedinice dobile njihova imena.

Rukopis veoma korisno može poslužiti kao naučno-popularna literatura, ali i kao dopunska literatura iz oblasti fizike počevši od učenika završnih razreda osnovne škole.

Cena ove publikacije je 500,00 dinara i može se poručiti preko izdavača na tel. 011/32 30 028.

Inženjersko društvo za koroziju izdalo je monografiju **“Vekovi klasične fizike”**.

Nakon dugog stagniranja, nauka je otpočela svoj trijumfalni put pojavom Leonarda da Vinčija. Svoj nagli razvoj postiže u XVII veku, veku velikih otkrića koja su trasirala dalji razvoj civilizacije. U tom periodu ističu se radovi Isaka Njutna. Klasična fizika svoj zenit je dostigla u XIX veku radovima dvojice naučnika – Faradeja i Maksvela. Njihov rad je vrhunac klasične fizike i predstavlja preokret u shvatanju fizičke realnosti.

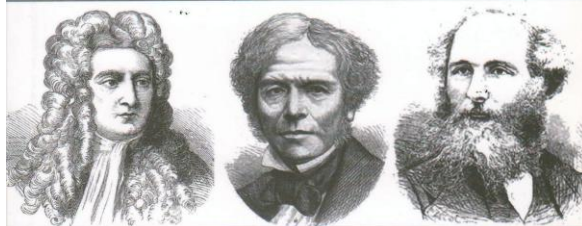
Razlog za izdavanje ove knjige je želja da se još jednom podsetimo života i rada velikana nauke – Njutna, Faradeja i Maksvela, čiji pregalački i stvaralački rad može biti inspirativan mladom naraštaju zainteresovanom za osnove egzaktno nauke. Izložen je razvoj ideja u fizici u širem kontekstu prilika, prikazujući život i rad fizičara u spletu raznih društvenih okolnosti koje su i omogućile taj razvoj.

Ako ova knjiga podstakne na razmišljanje o nauci i naučnicima koji su svojim radom unapredili naša znanja o fizičkoj stvarnosti, ona je postigla cilj.

Cena ove publikacije je 500,00 dinara i može se poručiti preko izdavača na tel. 011/32 30 028.

Радмило М. ИВАНКОВИЋ

ВЕКОВИ КЛАСИЧНЕ ФИЗИКЕ





Upotreba neobnovljivih izvora energije: uglja, nafte i derivata nafte i prirodnog gasa, od industrijske revolucije, a koja traje i danas, je dovela do enormne emisije gasova koji formiraju efekat staklene bašte. Na ovaj način površina zemlje i atmosfera postaju sve toplije i iz godine u godinu temperature su sve više, što dovodi do niza štetnih posledica.

Cilj ove monografije je da ukaže na potencijale, kao i na osnovne principe konverzije i akumulacije energije dobijene iz alternativnih izvora sa osvrtom na raspoložive potencijale Republike Srbije.

Cena ove publikacije je 750,00 dinara i može s poručiti preko izdavača na telefon 011/323 00 28 ili

e-mail: idd@idd.org.rs

Kraj XIX i početak XX veka u Srbiji je obeležen prvim značajnijim koracima u naučnom i prosvetnom životu. U prirodno-matematičkim naukama osećaju se prvi začeci i nagoveštaji daljeg napretka i uključivanja u naučne tokove tadašnje Evrope i sveta. Na drugoj strani, naučni život u domovini poprima sve življe trendove. Naši naučnici, školovani u inostranstvu, stečena znanja ugrađuju u domaću nauku. Unapređuju je, ali svojim talentom bitno utiču i na tokove svetske nauke.

Četiri pomenuta naučnika, četiri predstavnika srpske nauke, bila su snažan zamajac kako u našim naučnim krugovima, tako i u nauci svetskih razmera. To su razlozi iz kojih želimo da čitaoce bliže upoznamo sa njihovim životom i radom.

Cena ove publikacije je 400,00 dinara i može s poručiti preko izdavača na telefon 011/323 00 28 ili

e-mail: idd@idd.org.rs

